Exploring Star Formation in Dwarf Galaxies at z$\sim$1

Riona Ramraj

08 November 2013

A minor dissertation submitted in partial fulfilment of the requirements for the degree M.Sc.
in the Department of Astronomy, as part of the National Astrophysics and Space Science Programme

UNIVERSITY OF CAPE TOWN

Supervisors: Dr. D.G Gilbank and Dr S.L Blyth

Abstract

This dissertation presents the first Hα measurements of star formation rates (SFRs) for dwarf galaxies at z$\sim$1 (when the Universe was approximately half its current age) using the *Hubble Space Telescope (HST)*. We target a sample derived from the Redshift One LDSS3 Emission Line Survey (ROLES), which used $[\mathrm{OII}]_{\lambda3727}$ as a tracer of star formation to target very low stellar masses ($\mathrm{M}_{*}\sim10^{8.5}\mathrm{M}_{\odot}$) at this epoch.

In this dissertation, we study these low mass ROLES galaxies using near-infrared slitless spectroscopy from *HST*. We target and measure the luminosity of the Hα emission line. Even though Hα is a more direct SFR indicator, Hα derived SFRs still need to be corrected for dust which is normally done using Balmer decrement measurements that are not available for our spectra. We find that using SED-fitted dust estimates, in the V-band, underestimates the extinction in high mass galaxies, in agreement with a recent result obtained by Price et al. (2013). We instead derive an empirical mass-dependent dust correction to take into account the extra extinction needed in high mass galaxies.

We compare our dust corrected Hα SFRs to the [OII] SFRs from ROLES. The [OII] SFRs were calculated using a mass-dependent empirical correction derived for galaxies in the Local Universe (Gilbank et al. 2010a). We find that the empirically corrected [OII] SFRs agree quite well with our dust corrected Hα SFRs, having a slope of 1.6±0.7. This confirms that the mass-dependent empirical correction to [OII] works at $z\sim1$.

We study the Hα SSFR-mass relation for galaxies. We confirm previous results that at similar redshifts, low mass galaxies form their stars later and on longer timescales than high mass galaxies. However, our study probes down to lower limiting SFRs and lower stellar masses than any other previous studies, placing tighter constraints on galaxy evolution at this epoch.

Plagiarism Declaration

I, Riona Ramraj, know the meaning of plagiarism and declare that all of the work in the document, save for that which is properly acknowledged, is my own.

Contents

List of Figures

List of Tables

This work is based on observations taken by the 3D-HST Treasury Program (GO 12177 and 12328) with the NASA/ESA HST, which is operated by the Association of Universities for Research in Astronomy, Inc., under NASA contract NAS5-26555.

Chapter 1

Introduction

1.1 Observational History

Before the invention of telescopes, the Moon, a few thousand stars, "wandering stars" (planets), a diffuse band stretching across the sky (Milky Way) and some faint, diffuse nebulae were all that could be seen in the night sky with the naked eye. In 1610, Galileo pointed his telescope to the sky and discovered, among other things, that the Milky Way is made up of a large number of faint stars. This led to the speculation, by astronomer Thomas Wright, that the Milky Way is a flattened rotating disk of stars, and that other such nebulae visible in the night sky may be separate "Milky Ways". Philosopher Immanuel Kant introduced the term "island universes" for these distant nebulae in 1755.

Towards the end of the 18th century, Charles Messier compiled a catalog of about a hundred brightest nebulae (re-published by Messier & Niles 1981). He was searching for comets at the time and recorded these nebulae so that they would not be confused with his intended targets. Another catalogue was made by William Herschel for about five thousand nebulae (Herschel 1786) in the northern hemisphere. His aim was to determine the size of the Universe. He used a telescope with a 1.2m mirror to count stars in many different directions and assumed that the star density was uniform so that he could estimate the distances needed to count a certain number of stars in each direction. Hence, in any given direction, he could estimate the relative size of the universe of stars. From his data, he created a map of the Milky Way that included all the stars he counted and their distances from Earth, with the Sun located near the centre (Herschel 1785). Later his catalogue was expanded by his son, Sir John Herschel, to include nebulae from the southern hemisphere. Herschel's catalog was followed by Dreyer's New General Catalogue (Dreyer 1888), which was based on the Herschels' work, and contained about 8000 objects.

Around the end of the 19th century, Lord Rosse built a 1.8m telescope which was the largest telescope at the time. Using this telescope, he observed that some nebulae had spiral features and he was also able to identify point sources in some of them. He believed these spiral nebulae were systems of stars similar to the Milky Way but others still thought that they were gas clouds within the Milky Way.

In 1922, Jacobus Kapteyn postulated a model for the Milky Way which he believed to be the entire Universe, that was made up of a flat system of stars whereby the density of stars decreases with increasing distance from the centre. He estimated the the size of the Milky Way to be 10 kpc* wide and 3 kpc thick. He used the parallax method to calibrate the distance to the nearest stars. In his model, he placed the Sun close to the centre of the Galaxy.

1.1.1 The Great Debate

On 26 April 1920, two astronomers, Heber Curtis and Harlow Shapley, met to argue about the nature of these nebulae and the size of the Milky Way

---

*1 kpc = 3.08×10^{19}m

in what has become known as the Great Debate. Shapley believed that the nebulae were part of the Milky Way while Curtis believed that they were extragalactic.

Shapley's argument was based on his observations of globular clusters, compact spherical clusters of stars bound by gravity, in the Milky Way. In these globular clusters he observed Cepheid variable stars, whose brightness fluctuates with a regular period related to their luminosities. He then used the relation between the pulsation period and intrinsic luminosities of Cepheids (Leavitt & Pickering 1912) to determine the distances to the globular clusters. Shapley found that the distribution of globular clusters was asymmetrical with respect to the Earth's position, and based on this he estimated the diameter of the Milky Way to be 100 kpc (10 times larger than Kapteyn's estimate). This large estimate was one of the reasons which led him to believe that the Milky Way was the entire Universe. It was later found that he had actually observed RR Lyrae variable stars, which are fainter than Cepheids, to estimate distances, which led to an inflated size for the Milky Way.

Curtis's arguments were based on the novae he had observed in the Andromeda nebula. These novae were much fainter than those observed in the Milky Way. A nova is a star whose brightness increases rapidly and then goes back to being quiescent. He found that the novae were ten times fainter than novae in the Milky Way which implied they should be 100 times more distant. Curtis also argued that high radial velocities of spiral nebulae, measured by Vesto Slipher, meant that these nebulae could not stay gravitationally bound within the Kapteyn model of the Milky Way. Furthermore, he stated that if the transverse velocities and radial velocities of the spiral nebulae were similar, their proper motions could be measured if they were within the Milky Way, but no such measurements had been made. Lastly, he pointed out that dark bands could be seen in photographs of spiral nebulae which he believed were dust absorption lanes also found in the Milky Way.

The outcome of the Great Debate was inconclusive but the matter was settled a few years later by Edwin Hubble. He observed Cepheid variable stars in Andromeda and used the period-luminosity relation to calculate its distance. His estimate of the distance (285 kpc) proved that the Andromeda nebula was at a much greater distance than any other objects in the Milky Way. It was then conclusively established that there are other galaxies that exist beyond the Milky Way.

1.2 Structure and Galaxy Formation and Evolution

Understanding how and when galaxies formed and assembled their stellar mass is one of the biggest questions in modern astrophysics. Viewing the Universe on large scales, one sees a "cosmic web" consisting of sheets and filaments of galaxies separated by large voids with massive galaxy clusters appearing as nodes (Davis et al. 1982, de Lapparent et al. 1986). These structures formed from tiny density perturbations in the early Universe (Starobinsky 1982, Hawking 1982) which can be seen as temperature fluctuations in the Cosmic Microwave Background (CMB).

The CMB is thermal radiation from the surface of last scattering when the Universe was 400 000 years old. The surface of last scattering is the point at which the Universe became transparent to radiation. The CMB was discovered accidentally by Penzias & Wilson (1965). The radiation appeared as steady, low noise (2.7K) in their radio antenna which they were using to detect radio signals in the Milky Way. After ruling out sources of interference, including pidgeon droppings on their equipment, they concluded that the noise was coming from somewhere outside our galaxy. At the same time, Dicke et al. (1965) and his team at Princeton University had predicted the existence of the CMB and were searching for it. After contacting Dicke, Penzias realized that they had observed the cosmic background radiation.

Currently, the most accepted model of structure formation in the Universe is the cold dark matter model with a dark energy term (Λ-CDM) (Blumenthal et al. 1984, Davis et al. 1985, Frenk et al. 1985). This theory is based on non-relativistic particles (cold dark matter) which only interact through gravity, and includes the accelerated expansion of the Universe (caused by dark energy). The expansion of the Universe has been known since the work of Hubble (1929) who showed that galaxies are receding from us with a recessional velocity, v, proportional to their distance, d, away from us.

$$v = H_0 d \tag{1.1}$$

where H_0 is the Hubble constant which is the value for the expansion rate of the Universe at present. A galaxy's recession velocity can be measured from the redshift, z , of its emitted light,

$$z = v/c \tag{1.2}$$

where c is the speed of light. The light emitted by an object moving away from the observer is shifted to longer wavelengths (redshifted) while the light emitted by an object moving towards the observer is shifted to shorter wavelengths (blueshifted). The light emitted by a distant galaxy will be stretched because space is expanding and so the light received by the observer is redshifted. The cosmological redshift measures how much space has expanded between the time the light was emitted and the time it was received. This is our primary method for determining distances to galaxies outside the local Universe.

In the context of the Λ-CDM framework, the initial tiny density perturbations in the Early Universe caused the dark matter to undergo gravitational collapse and form cold dark matter haloes (Starobinsky 1982, Hawking 1982). Haloes grew hierarchically such that smaller haloes merged to form larger, more massive haloes (e.g. White & Frenk 1991, Sheth et al. 2001). The baryonic matter (hydrogen and helium gas) present in the early

Universe was attracted to the dense regions formed by the haloes and channeled towards the centre of the haloes gravitational potential wells. The gas then cooled, condensing to form the first stars. Gas cooling is central to the formation of galaxies because it sets the rate at which the material for star formation becomes available (Blumenthal et al. 1984). Rees & Ostriker (1977) gave arguments about how gas cools and this was used as the framework upon which White & Frenk (1991) based their basic model of how gas cools inside dark matter haloes. Radiative processes (e.g. Compton cooling, bremsstrahlung, recombination, etc.) are essentially responsible for the cooling of gas such that it decouples from the dark matter and settles into a star-forming disk (e.g. Mo et al. 1998).

The structures that formed in the early Universe continued to grow as the Universe aged, resulting in the clumpy matter distribution observed today. The baryonic distribution follows the dark matter distribution since they interact gravitationally over large scales. The mass function of dark matter haloes (which is the number density of haloes as a function of mass, at a given time) was derived analytically by Press & Schechter (1974). Technological advancements since then have led to the development of numerical N-body simulations (e.g. Millennium simulation; Springel et al. 2006). These simulations improve upon the analytically derived mass function and have the advantage that they can track the accretion and merging history of individual haloes with spatial information.

The different shapes between the theoretical halo mass function predicted from Λ-CDM and the observed galaxy mass function can be seen in Fig. 1.1. This is because the dark matter mass function is governed by gravity only, whereas the galaxy mass function includes much more complicated physics. The slope of the halo mass function is steeper than the observed mass function for the low and high mass ends. In other words, the number of low mass galaxies ($<10^9\mathcal{M}_\odot$) and high mass galaxies ($>10^{11}\mathcal{M}_\odot$) are lower than the predicted number of haloes corresponding to the same masses. This is due to feedback mechanisms which cause the cold gas needed for star formation to be heated. In low mass galaxies, supernova (SN) explosions (death of very massive stars) are responsible for heating the gas and expelling the gas from the galaxy thereby halting star formation. The reason the gas gets expelled from the galaxy is because low mass galaxies have very shallow potential wells. In high-mass galaxies, SN do not have the same effect as they do in the low mass galaxies because high mass galaxies have deeper potential wells. Active galactic nuclei (AGN), which are the compact regions of galaxy cores, with higher than normal luminosity thought to originate from the accretion of mass by the black hole at the centre of the galaxy) are responsible for feedback in high mass galaxies to shut down star formation.

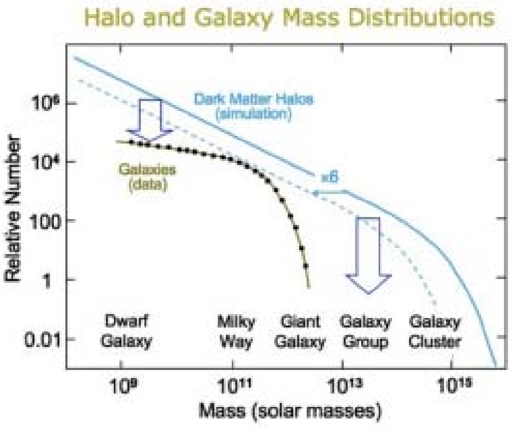

Figure 1.1: The theoretical halo mass function compared to the observed galaxy stellar mass function. The halo mass function does not follow the observed galaxy mass function for high and low mass galaxies (See text for discussion). Credit: Moster et al. (2010)

Once the galaxy and halo have assembled, they evolve simultaneously. There are many physical processes governing the evolution of galaxies such as galaxy harassment, gas stripping, strangulation and heating by AGN (Balogh et al. 2000, Weinmann et al. 2006, van den Bosch et al. 2008). We can model the evolution by making physical assumptions based on what we see in the observable Universe. Semi-analytic models (SAMs) describe the baryonic evolution of galaxies using simple analytic recipes for the complex physical processes (gas cooling and heating, star formation, feedback, etc.) that govern galaxy evolution (e.g. Baugh 2006, Silk & Mamon 2012). The complex processes are "painted" onto N-body codes. These simulations reproduce the observed distribution of matter remarkably well. Fig. 1.2 (taken from Springel et al. 2006) shows the observed distribution of large scale structure from two Local Universe surveys viz. Two-degree Field Galaxy Redshift Survey (2dFGRS; Colless et al. 2003) and the Sloan Digital Sky Survey (SDSS), together with surveys constructed from SAMs to simulate the evolution of galaxies within the evolution of the dark matter distribution in the Millennium simulation. On large scales, the distribution of matter between the observations and simulations is indistinguishable. However, on smaller scales there are many complex physical processes that occur in galaxies which are still not well understood.

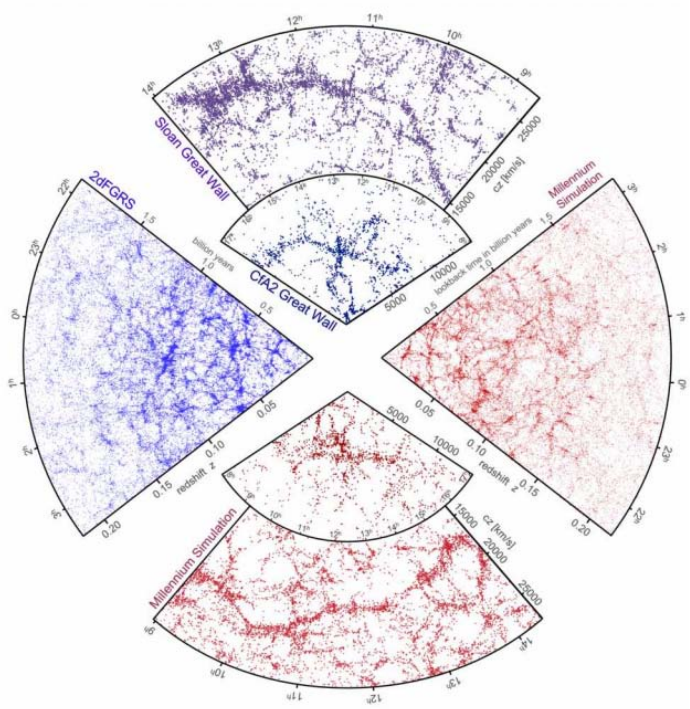

Figure 1.2: Large scale distribution of matter from observations and simulations. The observations come from the SDSS (purple) and 2dFGRS (blue) redshift surveys in the Local Universe. Artificial surveys (red) were constructed to simulate the evolution of galaxies described using semi-analytic models with the evolving dark matter from the Millennium simulation. There is a striking resemblance between the observations and simulations. Credit: Springel et al. (2006)

1.2.1 Patterns in Galaxy Properties

Galaxies exhibit many patterns in their observed properties which can help to reveal the physical processes which likely shape their formation and evolution. In recent years, it has become clear that the most fundamental parameters shaping a galaxy's evolution appear to be its stellar mass and the environment in which it resides (Brinchmann et al. 2004, Baldry et al. 2004, Baldry et al. 2006, Elbaz et al. 2007, Noeske et al. 2007b, Peng et al. 2010). The epoch at which a galaxy is observed (its redshift) is also fundamental in determining its observed properties at that time. Thus, to understand galaxy evolution, we would like to observe galaxies as a function of stellar mass and/or environment at different redshifts. Some of the observed properties which appear to show these strong correlations with mass/environment are: galaxy shape (morphology), colour, star-formation activity, metallicity[†].

1.2.1.1 Stellar Masses

Stars in a galaxy span a range of masses. The stellar mass cannot be directly observed but has to be derived from an observable quantity such as the luminosity of a galaxy. In order to measure the mass in stars via modeling, one must know how the mass of stars were initially distributed. The initial mass function (IMF) describes the distribution of mass for a population of stars when a galaxy first formed its stars. This function tells us the relative number of low to high mass stars. There are many more low mass stars than high mass stars and low mass stars are longer-lived than high mass stars. Hence, they dominate the stellar mass of the galaxy. The bulk of light from low mass stars is emitted at NIR wavelengths. Measuring light using the K-band gives the luminosity from the low mass stars.

There are many forms of the IMF and these have been extensively stud-

---

[†] Fraction of chemical elements in any astronomical object excluding hydrogen and helium

ied (e.g. Salpeter 1955, Scalo 1986, Kroupa 2001, Chabrier 2003). There have also been numerous studies that show variations and evolution of the IMF (e.g. Gunawardhana et al., 2011, Wilkins et al., 2008, Weidner et al., 2013, Bekki & Meurer, 2013). The derived stellar mass is sensitive to the choice of IMF. If, for example, an IMF is chosen where there is a larger fraction of low mass stars compared to another IMF, the mass-to-light ratio will be higher and hence, the computed stellar mass will be larger.

1.2.1.2 Star Formation Rates

The star-formation activity in a galaxy can be measured by the star formation rate (SFR). The SFR is a quantity that measures the rate at which a galaxy converts its cold gas into stars. There are many different SFR indicators (e.g. ultraviolet (UV) continuum, recombination lines, forbidden lines, far-infrared (FIR) continuum, radio continuum) that have been defined across the electromagnetic spectrum. SFR indicators essentially measure the flux from young, hot massive stars. These stars are short-lived which means that their presence in a galaxy implies that the galaxy is currently forming stars. Most of the flux emitted by these young stars is at UV wavelengths. The ionizing flux from nebular emission lines (e.g. Hα recombination line and [OII] forbidden line) in a galaxy's spectrum is one way of measuring the SFR of a galaxy (See §4.1 for a detailed description). These nebular emission lines give a measure of the unobscured star formation in a galaxy. At mid-to-far infrared wavelengths, the flux comes from dust heated by the hot, young stars and re-emitted at infrared wavelengths. Therefore measuring the SFR at infrared wavelengths gives a measure of the galaxy's obscured star formation. The radio wavelengths measure synchrotron radiation from supernova remnants and thermal radio emission. SFRs derived from radio wavelengths is found empirically to correlate with other (more direct) SFR indicators (Condon 1992).

There are systematic effects associated with estimating the SFR from different indicators. The main effect in the UV/optical is the amount of dust extinction in the galaxy and contamination from more evolved stellar populations. The dust extinction attenuates the UV continuum and emission line luminosities (Kennicutt 1998a, Kewley et al. 2004). An estimate of the dust can be obtained from the UV slope or the Balmer decrement (Hα/Hβ flux ratio) (Calzetti 2001). The most difficult property to correct for is dust geometry especially when the object of interest is resolved. Even after correcting for dust, other systematic uncertainties can limit the measurement of the SFR such as the metallicity, ionization parameter (for [OII]) (e.g. Kewley et al. 2004) and the assumed IMF. As described above, the IMF shows that the most massive stars are less numerous than the low mass stars. Since the luminous massive stars are rare, estimating the total mass of stars being formed requires an assumption about the relative number of low mass stars for a given mass in high mass stars. This is achieved through assuming a particular form for the IMF. If, for example, an IMF is chosen where there is a larger fraction of low mass stars compared to another IMF, the mass-to-light ratio will be higher and hence, the computed SFR will be larger.

1.2.1.3 Hα Studies

In order to study evolution, one would ideally like to measure the SFR using a single indicator which can be applied from low to high redshifts. In practice this is difficult since each indicator is subject to different biases and selection effects as mentioned above. However, Hα is considered the most direct indicator because it traces the current SF in a galaxy and is less affected by dust (e.g. Garn et al. 2010 , Gilbank et al. 2010a) than shorter wavelength emission lines (such as [OII]) and has a small dependence on metallicity (Charlot & Longhetti 2001).

At $0 < z \leq 0.4$ the Hα line is typically used for studying evolution because it can be observed optically (e.g. Ly et al. 2007, Dale et al. 2010). Hα moves out of the optical range at $z > 0.4$ into the NIR. For this reason, the [OII] emission line which is available in the optical out to $z\sim1.5$ has been used instead (e.g. Zhu et al. 2009, Gilbank et al. 2010b, Bayliss et al. 2011). Previously, NIR spectrographs on large telescopes enabled observations of only a few tens of galaxies at a time at z $\sim$1 because these were restricted to longslit spectroscopy (e.g. Glazebrook et al. 1999, Tresse et al. 2002). Recently, the development of multi-object spectrographs has enabled large ground-based Hα surveys to be conducted (e.g. High Redshift Emission line Survey (HiZELS; Geach et al. 2008, Villar et al. 2008, Twite et al. 2012, NewHα narrowband survey; Momcheva et al. 2013, Kashino et al. 2013) out to $z\sim$ 2.5. It is difficult to deal with atmospheric effects, such as seeing (atmospheric turbulence) which blurs the image and the sky brightness which adds background noise, from ground-based observations. Space-based telescopes provide a better alternative because they are above the atmosphere, meaning that atmospheric effects are not a problem. Hα spectroscopic surveys with the *Hubble Space Telescope* (*HST*) for example, provide much deeper observations than possible from the ground (e.g. McCarthy et al. 1999, Shim et al. 2009). The Wide-Field Camera (WFC 3) and grism on *HST* has been used to conduct slitless spectroscopic surveys. For example 3DHST (Brammer et al. 2012, van Dokkum et al. 2011) and WISP (Atek et al. 2010).

1.2.1.4 Star formation Rate Density and Specific Star formation rate

Making detailed measurements of the properties for a single galaxy is difficult therefore we study ensembles of galaxies to obtain their average properties. Also, we study populations of galaxies instead of one galaxy so that we can get a representative sample. Furthermore, studying large samples of galaxies at different epochs can provide us with a better understanding of the way galaxies evolve over cosmic time. The star formation rate density (SFRD) is a measure of the cosmic SFR of a sample of galaxies divided by volume of the Universe they reside in. By measuring the SFRD at different redshifts and within different volumes one can obtain the overall star formation history (SFH) of the Universe. The SFRD as a function of redshift in the Universe, has declined by an order of magnitude from $z{\sim}1$ to $z{\sim}0$ (e.g. Lilly et al. 1996, Madau et al. 1996, Hopkins & Beacom 2006, Elbaz et al. 2007). The contribution by galaxies to the SFRD depends on their stellar mass whereby the massive galaxies contribute more to the total SFRD at higher redshifts than similar mass galaxies at the present epoch. This idea was labelled "cosmic downsizing" by Cowie et al. (1996), to denote that star formation proceeds to progressively less-massive galaxies over cosmic time. Many studies have recently found evidence for this downsizing effect (e.g. Juneau et al. 2005, Noeske et al. 2007b, Zheng et al. 2007, Bundy et al. 2006).

The specific star formation rate (SSFR; SFR per unit stellar mass) is a quantity which represents the efficiency at which a galaxy forms stars. A strong correlation between SFR and stellar mass has been found for star-forming galaxies in the local Universe (e.g. Brinchmann et al. 2004, Schiminovich et al. 2007) such that lower mass galaxies have higher SSFRs than higher mass galaxies. This correlation has also been seen in studies at higher redshift (e.g. Bundy et al. 2006, Santini et al. 2009, Bauer et al 2011, Noeske et al. 2007a, Noeske et al. 2007b) where the normalization shifts to higher SSFRs with increasing redshift. Noeske et al. (2007b) called this the "main sequence" of star-forming galaxies. Here again can be seen the downsizing effect whereby the number of galaxies exceeding some SSFR threshold shifts from higher to lower masses with increasing redshift. This relation becomes unclear when lower mass galaxies are included due to the fact that there are not many surveys that probe down to extremely low stellar masses. Studies of the SSFR-mass relation and its evolution have been carried out by many others. Some used different SFR indicators (or a combination of indicators) (e.g. Juneau et al. 2005, Noeske et al. 2007b, Sobral et al. 2011) to determine the SFR. Others used photometric redshifts from which the SFR, redshift and dust extinction are estimated from the same dataset (e.g. Zheng et al. 2007, Feulner et al. 2005). Studies that used spectroscopic redshifts and the same indicator at all redshift have mostly probed the most massive galaxies at higher redshifts (e.g Maier et al. 2009, Fumagalli et al. 2012, Twite et al. 2012, Kashino et al. 2013). One survey that used spectroscopic redshifts and probed down to low stellar masses ($10^{8.5}$ $M_\odot$ yr^{-1}) is the Redshift One LDSS3 Emission line Survey (ROLES; Gilbank et al. 2010b) to study the SSFR-mass relation (Gilbank et al. 2011). Low mass galaxies are much more numerous than their higher mass counterparts and are the building blocks of high mass galaxies in the hierarchical formation scenario. Studying these systems are therefore important to get a better idea of how galaxies form and evolve.

1.2.2 Dissertation Outline

In this dissertation, we study low mass galaxies using NIR spectroscopy at $z\sim1$.

This dissertation is presented as follows: Chapter 2 introduces the data used and explains how the reduction is done to extract the spectra for our sample of galaxies. A line detection algorithm is developed to analyze the extracted spectra which is described in Chapter 3. The algorithm produces measurements of the line luminosity which we convert into SFR measurements and compare with other SFR indicators in chapter 4. The SSFR-mass relation is also studied in Chapter 4. Chapter 5 includes a summary of the results and a discussion of future work with upcoming telescopes and surveys. Throughout we adopt a ΛCDM cosmology with Ω_m=0.3, Λ=0.7 and H_0=70 km s^{-1} Mpc^{-1}. All magnitudes are quoted on the AB system. All SFRs are calculated using a Kroupa (2001) IMF.

Chapter 2

HST Grism Data

HST data is used for performing follow up spectroscopy on the galaxies from ROLES. In particular, we use near-infrared slitless spectroscopic data, and a general description of this type of spectroscopy is given in this chapter. The rest of the chapter describes the reduction of the data and its outputs (i.e. extracted spectra).

2.1 Sample Selection

2.1.1 ROLES

ROLES was designed to specifically target dwarf galaxies at z$\sim$1. This was the first time these galaxies have been studied with spectroscopy. They did this by targeting K-faint ($22.5 < K_{AB} < 24$) star-forming galaxies using the Low Dispersion Spectrograph 3 (LDSS-3) on the Magellan Telescope. The aim was to probe down to low stellar masses ($8.5 < \log(\frac{M_*}{M_\odot}) < 9.5$) at mid-to-high redshifts in order to better understand how dwarf galaxies form and evolve. The targeted fields were the Great Observatories Origins Deep

Survey-South (GOODS-S) field and the FIRES field. The survey looked at the redshift range $0.89 < z < 1.15$. The results are presented in Davies et al. (2009), Gilbank et al. (2010b), Gilbank et al. (2011) and Li et al. (2011). The [O II]$_{\lambda 3727}$ emission line was used to obtain spectroscopic redshifts and [OII] luminosities of the targeted star-forming galaxies. TThe emission line is a doublet at wavelengths 3736Å and 3729Å. Throughout we use [O II] as a shorthand for the doublet. SFRs were obtained down to a limit of ∼0.1 $M_{\odot}yr^{-1}$. The ROLES data were supplemented with an external subsample of emission line galaxies from ESO public spectroscopy (Vanzella et al. 2008) to extend the mass range of their work so that they could study the mass dependence of galaxy properties such as the SSFR-mass, SFRD, luminosity function, etc., at $z{\sim}1$. This sample overlaps the same region of sky as ROLES in the GOODS-S field. Only those galaxies within the ROLES redshift range were selected. The [OII] SFRs were measured in the same way as for ROLES by Gilbank et al. (2010b). To first order, the ESO public and ROLES are just different mass sub-samples of otherwise similar data. The full data sample (i.e. ROLES and ESO galaxies) and the sample containing ROLES galaxies only is hereafter referred to as WFC3-OII and WFC3-ROLES respectively. In this thesis, we study only the 311 WFC3-OII galaxies from ROLES in the GOODS-S field.

2.2 Slitless Spectroscopy

In traditional slit spectroscopy, slits are used to allow only light from the object of interest and a small amount of sky to enter the dispersing element (e.g. prism or grism). In slitless spectroscopy, the location of a spectrum is defined by the sky position of the object itself within the detector's field of view (FoV). The sky positions of the objects, their shapes and sizes, define the slits in analogy to slit spectroscopy. Each pixel on the detector can receive light of any wavelength within the instrument's sensitivity range, meaning that there is no unique correspondence between pixel coordinates and wavelength. Usually a direct image is taken with an imaging filter to

establish the wavelength zeropoint of the spectra. The light dispersed in a slitless spectrum for an object can be thought of as defining the object's own virtual slit (Freudling et al. 2008), that modulates the height of the 2D spectrum and the resulting spectral resolution through the width of the object in the dispersion direction (Kümmel et al. 2009).
Since the positions of these virtual slits are set by the object's position on the sky, overlapping of spectra, called contamination, occurs frequently. This can be seen in the top left corner of the 2D slitless spectrum shown in Fig. 2.2. It is for these reasons that slitless spectra are often considered difficult to extract and calibrate.

On the other hand, slitless spectroscopy is considered a powerful survey tool because spectra of all objects within the detector's FoV are recorded. Many slitless surveys have been conducted from the ground (eg. Wisotzki et al. 1996, Kurk et al. 2004, Worseck et al. 2008). The high sky background, however, is a disadvantage of ground-based slitless spectroscopy. Space-based observations, such as observations with the *Hubble Space Telescope* (*HST*) in slitless mode, are more effective because the background is many orders of magnitude lower than from Earth and there are no variable atmospheric absorption and emission components (Kümmel et al. 2009). Some surveys with *HST* slitless spectroscopy include the NICMOS/*HST* Grism Parallel Survey (McCarthy et al. 1999), GRAPES study of the Hubble Ultra-Deep Field using the Advanced Camera for Surveys (Pirzkal et al. 2004) and the PEARS survey of the GOODS fields (Straughn et al. 2008).

The GOODS-S region is an extragalactic field well studied by many surveys, one of which is 3D-HST*. 3D-HST is a NIR spectroscopic survey with the *HST* surveying ∼650 square arcminutes of other well studied extragalactic survey fields (such as AEGIS, COSMOS, GOODS-N, and UKIDSS/UDS) (Brammer et al. 2012). The survey provides low resolution (R∼130) slitless spectroscopy of ∼7000 galaxies at $1 < z < 3.5$ (van Dokkum et al. 2011; Brammer et al. 2012) with *HST* grisms in the optical and NIR.
The spectral feature of interest for this work is the Hα emission line because

---

*`http://3dhst.research.yale.edu/`

it is our SFR indicator of choice. We can get this by using data from the G141 grism. The WFC3/G141 spectra have a wavelength coverage from approximately 11000Å to 16000Å at a spatial resolution of $\sim 0''.13$, which, combined with their depth, makes them a unique resource for studying galaxy evolution (Brammer et al. 2012). The corresponding direct images were obtained with the broad F140W filter on the (Wide Field Camera (WFC3)) that spans the gap between the standard J and H passbands and lies roughly in the center of the G141 grism sensitivity range. WFC3 has two UV/visible detecting CCDs and a separate IR detector. The NIR channel has a 123 x 137 arcsec FoV (Brammer et al. 2012). The mean dispersion of the primary spectral order of the G141 grism is 47Å/pixel and the size of the resolution element is ∼100 Å ($R\sim120$ at 13000Å).

2.3 Data Sample

We used the NIR slitless spectra from 3D-HST to target the Hα emission line in the [OII]-selected WFC3-OII galaxies. Out of the 311 WFC3-OII galaxies in the GOODS-S field, 12 galaxies (green points in Fig. 2.1) fell in gaps in between pointings and 3 galaxies (cyan crosses in Fig. 2.1) were unable to be recovered by the spectroscopic reduction pipeline (this will be explained in §2.5). This reduced our sample to 296 galaxies that had a spectrum covering the Hα wavelength range. Of these, 14 galaxies (red and blue crosses in Fig. 2.1) had a spectrum not covering the wavelength range where the Hα emission line was expected. In total we were left with 282 WFC3-OII galaxies out of which 201 were WFC3-ROLES galaxies and 81 were ESO public spectroscopy galaxies (red and blue points in Fig. 2.1 respectively).

The mosaic map in Fig. 2.1 is made up of 38 individual pointings which were downloaded from the MAST archive[†] together with their associated pre-processed calibrated direct image-slitless spectrum pairs. Each slitless spectrum pointing had a total exposure time of $\sim$ 4712 seconds. These im-

---

[†] `http://archive.stsci.edu/hst`

age pairs were pre-processed using the `calwf3`[‡] pipeline. The pipeline does standard data pre-processing such as bias subtraction, dark subtraction, flat-fielding, and computation of the photometric zero-point in the header of the direct images. The reduction of the 2D slitless spectra by `calwf3` is slightly more restricted because of the individual wavelength coverage of each object which means that no single flat-field image can be correctly applied to 2D slitless spectra since each pixel contains light from different wavelengths[§]. The science products produced (`.flt` images) are used in the subsequent reduction.

[‡] `http://www.stsci.edu/hst/wfc3/documents/handbooks/currentDHB/wfc3_Ch33.html`

[§] The flat-field method for the slitless spectrum can be found in Chapter 7 of Rajan (2011).

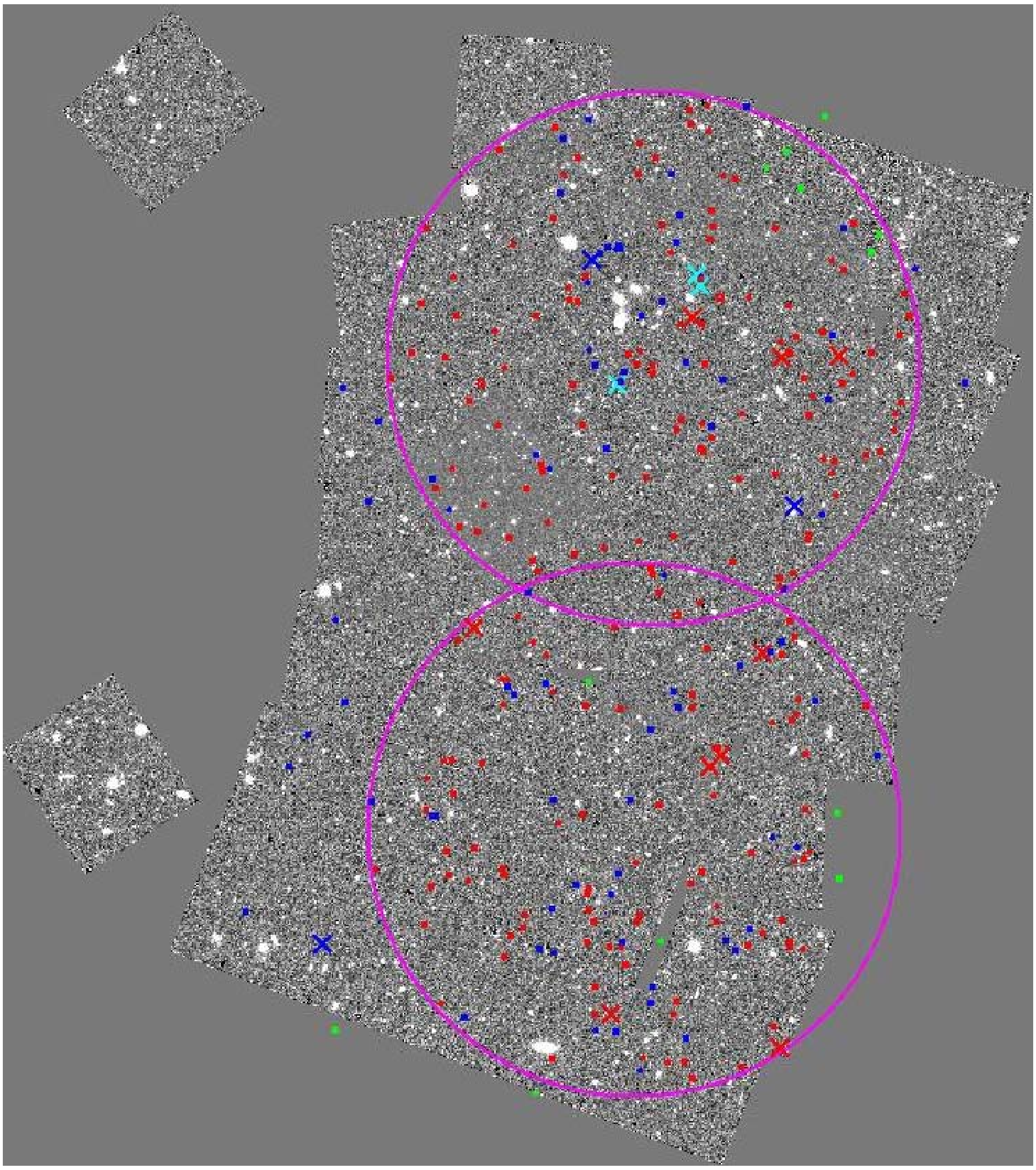

Figure 2.1: Direct image mosaic map (comprising 38 pointings) of the GOODS-S (RA: 3h 32m 30s, Dec: -27°48m 54s) region of the CDFS field. The size of each pointing can be seen from the two outlying fields on the left of the image. The image shows the WFC3-ROLES galaxies and ESO Public spectroscopy galaxies which have a spectrum covering the Hα wavelength range (red and blue points respectively) and the galaxies that do not have a spectrum (red and blue crosses respectively) covering the wavelength range where Hα is expected. Galaxies not reduced by the spectroscopic reduction pipeline are indicated by cyan crosses. Galaxies which fall in between gaps of pointings (green circles) are not counted as part of the WFC3-OII sample. The ROLES field is indicated by two magenta circles of roughly 8 arcminute diameter.

2.4 Data Reduction Method

2.4.1 Spectral Extraction using a "First Principles" Approach

Before running the automated reduction package, a first-principles approach was used to get an idea of what the extractions from the pipeline should look like.

Catalogues containing the objects' sky coordinates were made for the direct images of each pointing to determine which WFC3-OII galaxies they contained. These gave the object positions on the slitless spectrum which is a requirement in slitless spectroscopy as mentioned in Section 2.2. The object positions on the 2D slitless spectra were used as reference positions to determine the zeropoint wavelength of the spectrum. This was done as follows:

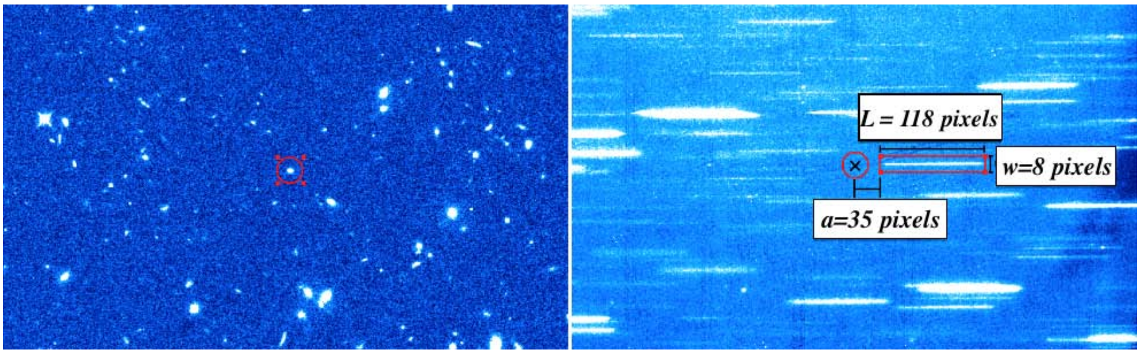

Figure 2.2: Example showing how the object position from the direct (*Left*) image was used as a reference position on the 2D slitless spectra (*Right*) to determine the wavelength scale of the spectrum. The values for a, L and w are the same for all spectra.

- A few bright objects were chosen from the direct image and a circle was placed around them. The same circle was also placed on the slitless spectrum at the same CCD pixel location. Figure 2.2 shows an example for one bright object.

- Boxes were placed on the corresponding shifted spectra of the chosen objects. The dispersion of the G141 grism is 46.5Å/pixel (Brammer et al. 2012) and the wavelength coverage of the grism is approximately 11000Å -16500Å as shown in Fig. 2.3. Assuming this 5500Å spectral range implies that the box length, L, is 118 pixels.

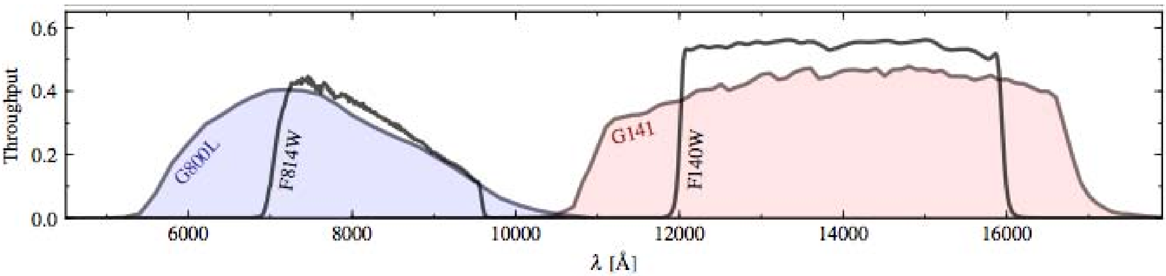

Figure 2.3: Throughput curves of the WFC3/G141 (primary) and ACS/G800L (parallel) grisms and the WFC3/F140W and ACS/F814W imaging filters used to define the wavelength reference for the grisms. For WFC3/G141, it can be seen that the reference wavelengths are not exactly 11000Å and 16000Å as assumed in the "first principles" approach. Credit: Brammer et al. 2012

- The galaxies' sky coordinates (RA and Dec) were converted to pixel coordinates using the WCS[¶](World Coordinate System) in the image header, from the MAST pipeline. Only galaxies for which the spectrum fell entirely on the detector were extracted.

After placing the spectral boxes, the spectral position of the the observed Hα emission pixel within the box was determined.

- The expected wavelength of Hα was calculated using,

$$\lambda_{obs} = (1 + z) \times \lambda_{rest} \tag{2.1}$$

where $\lambda_{rest} = 6562.8$ Å and z was the galaxy's spectroscopic WFC3-OII redshift from ROLES.

[¶] Documentation can be found at `http://stsdas.stsci.edu/astrolib/pywcs/api_wcs.html`

- The expected emission line wavelength was then converted to a pixel value

$$x_{em} = \frac{(\lambda_{obs} - 11000)}{46.5} \tag{2.2}$$

- The emission pixel position along the spectral box was then,

$$x_{obs} = x + a + x_{em} \tag{2.3}$$

where x is the spatial x-coordinate of the galaxy and a is the displacement in the spectral direction from the centre of the galaxy to the blue end of its spectrum.

- Sub-images of the image enclosing just the 2D spectra, as defined above, were then extracted. These 2D spectra were converted to 1D spectra by summing up the pixels in the spatial direction. 424 WFC3-OII spectra were extracted out of which 299 were unique spectra. An example of an extracted 2D and 1D spectrum is shown in Fig. 2.4. These spectra will later be compared to the extractions from the spectroscopic reduction pipeline to identify bad extractions. The spectra extracted from the first principles approach were not corrected for contamination, flat-fielding and background subtraction. These tasks will be performed when the data is run through the automated reduction pipeline.

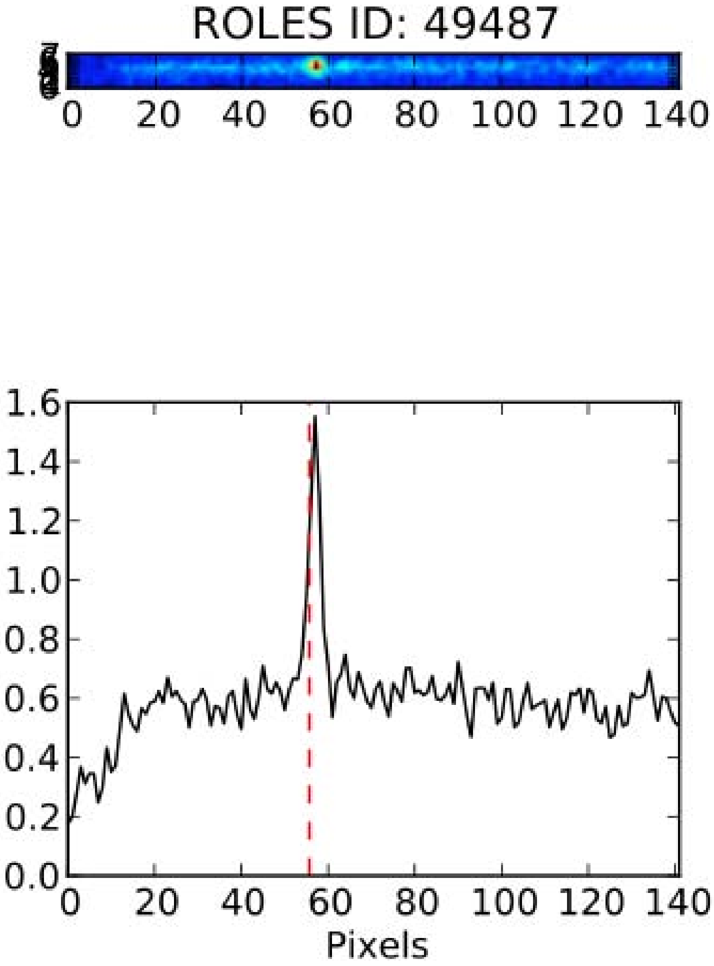

Figure 2.4: Example 2D and 1D spectra extracted using the "First Principles" approach described in §2.4.1. The red dashed line indicates the expected position of the emission line.

2.5 Spectral Extraction using `aXe`

This first principles approach described in the previous section has many other limitations such as no flux calibration, contamination by neighbouring sources, no background determination and no flat-fielding. These limitations were circumvented by running the data through the spectral extraction software package, `aXe` [‖]. `aXe` was designed to automatically extract and calibrate data from various slitless spectroscopy modes of HST instruments (Kümmel et al. 2009). It produces flux and wavelength calibrated 2D and 1D spectra for all objects in the field. The extraction process is outlined below[**].
Before any spectra were extracted, a few preparatory steps were performed. The WFC3/G141 configuration file, associated calibration files and a master sky background file were obtained from the Space Telescope Science Institute (STScI) website[††]. The configuration files contained information about the location and extent of the different spectral orders, spectral trace (location of the centre of gravity in the spatial direction) descriptions, dispersion solutions and names of the calibration files to be used. The calibration files were part of the regular pipeline calibration procedure performed by STScI.

2.5.1 Combined Images

Each pointing had multiple exposures (i.e. many `flt` direct images and 2D slitless spectra). These were combined using the software `Multidrizzle` (Koekemoer et al. 2006) to obtain a deep exposure direct image and corresponding slitless spectrum. Advantages of combining multiple exposures are the rejection of bad pixels (e.g. cosmic rays), removal of geometric distortions, increased spatial resolution and the deeper magnitude limit.

[‖] http://axe-info.stsci.edu/

[**] `aXe` User Manual: `http://axe.stsci.edu/axe/manual/Manual_2.3.pdf` contains information on all the file formats and reduction tasks

[††] `http://www.stsci.edu/hst/wfc3/analysis/grism_obs/calibrations/wfc3_g141.html`

A particular advantage for combining 2D slitless spectra is that running `Multidrizzle` performs cosmic ray detections and updates the `flt` images with the information of the detected cosmic rays. Figure 2.5 shows an example of a combined direct image with an individual direct image for comparison and Figure 2.6 shows the combined slitless spectrum and a individual slitless spectrum.

2.5.2 Object Detection

The object positions were obtained by running the object detection algorithm, `SExtractor`, (Bertin & Arnouts 1996) on each combined direct image with the following parameters:

```
DETECT_THRESH 2.0 # <sigmas>
ANALYSIS_THRESH 2.0 # <sigmas>
```

This produced, for each combined direct image, a master catalogue of all objects with a flux of more than twice the background noise (i.e. $>2\sigma$) in N connected pixels, where N was chosen to be 14 pixels. Other object parameters such as its width, source brightness, etc., were also included in the catalogue to be used in further reduction steps. The master catalogue was then projected back to the individual direct images so that individual catalogues for each slitless spectrum could be obtained. The `aXe` task `iolprep` was used to do this and it produced an Input Object List (IOL) for each direct image and an Input Image List. The Input Image List defined the combinations of IOLs, 2D slitless spectra and direct images used in the spectral extraction. All further `aXe` tasks used the Input Image Lists.

2.5.3 Background Determination

Each pixel not only contains all light from the object but also light from the background sky. There are two ways `aXe` does sky background subtraction, globally and locally. Global background subtraction was used whereby the

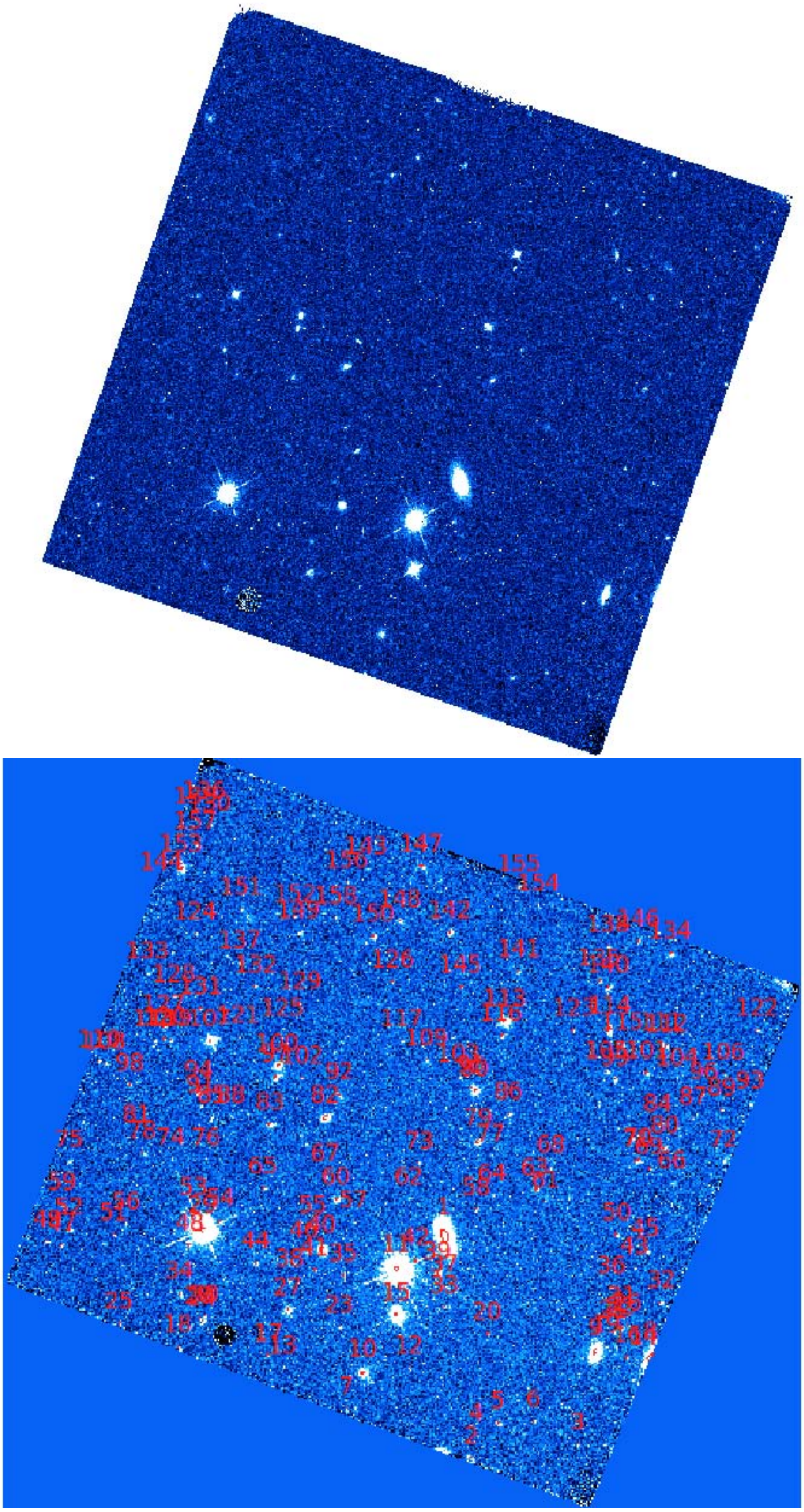

Figure 2.5: Multiple individual direct images (*Top*) were combined with `Multidrizzle` to form a combined direct image (*Bottom*) on which the object detection algorithm, SExtractor, was run to form a master object catalogue.The detected objects are indicated in red with their catalogue ID.

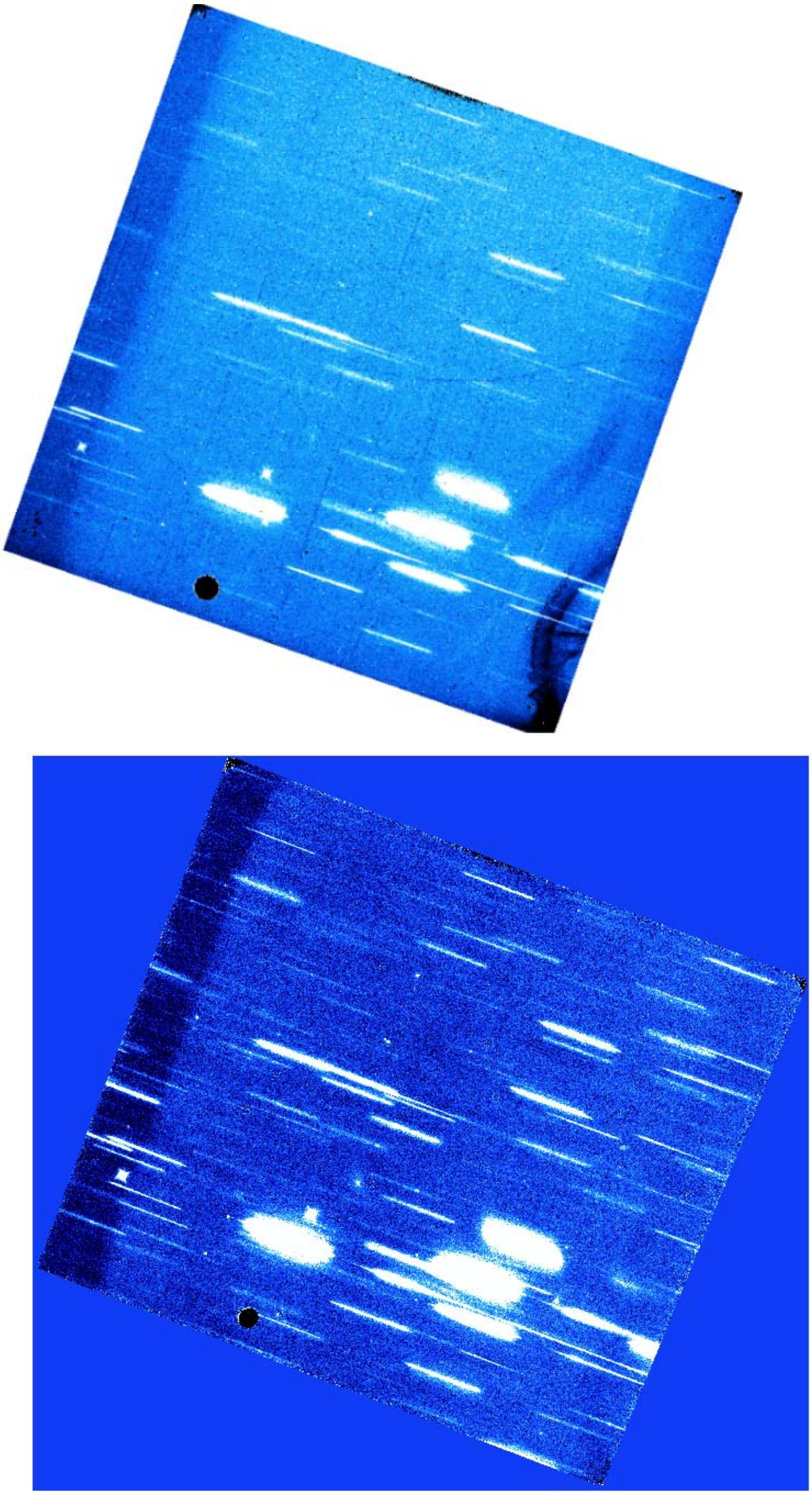

Figure 2.6: Multiple individual 2D slitless spectra (*Top*) were combined with `Multidrizzle` to form a combined slitless spectrum (*Bottom*). Notice the increased depth and decreased noise in the combined image.

2D master sky image (Fig. 2.7) was scaled to the background of the 2D slitless spectra automatically and then subtracted. The task `axeprep` was used to do this taking as inputs the master sky background file, the object catalogue and the configuration file.

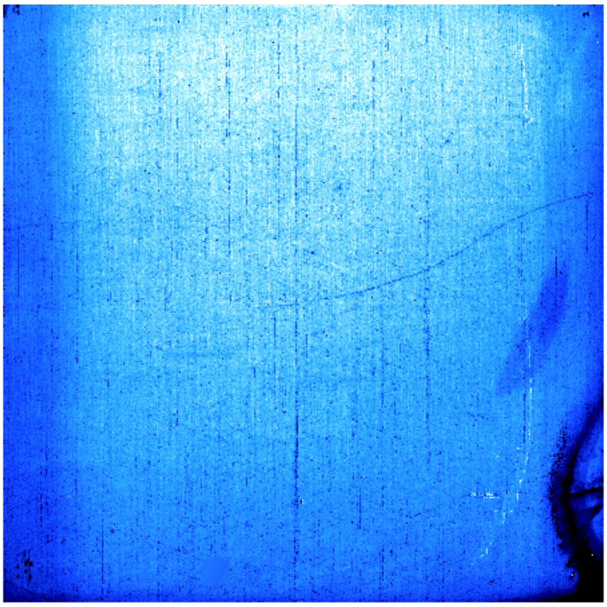

Figure 2.7: The master sky image for the G141 grism which was scaled to the background of the 2D slitless spectra and then subtracted.

2.5.4 Flat-fielding

In contrast to direct images, no single flat-field image can be correctly applied to 2D slitless spectra because each pixel contains signal arising from different wavelengths. Flat-fielding is therefore applied during the extraction of spectra once the wavelength corresponding to each pixel is known. Each pixel receives a flat-field correction dependent on the wavelength falling on that pixel, as specified by the position of the direct image and the dispersion solution. A 3D flat-field cube is used whereby the detector coordinates are the two spatial dimensions and the wavelength-dependent behavior of the flat field, characterized by a series of direct image flat fields taken at various central wavelengths, is the third dimension (Kümmel et al. 2009).

2.5.5 Contamination

There are two different methods `aXe` uses to deal with the problem of contamination. In geometrical contamination the areas covered by different spectral orders of all objects are recorded. For every pixel in each spectrum, the number of spectra falling on this pixel is calculated using these areas.

Quantitative contamination gives, for each spectral bin, an estimate on the contaminating flux from all other sources. It uses emission models to compute the contamination. The dispersed contribution of every object to the slitless spectrum is modeled and using the model information, the contaminating flux for each pixel is recorded and processed through the extraction process. This results in a contaminating flux spectrum for each extracted spectrum. The task `fcubeprep` produced a fluxcube file for every slitless spectrum by using the information provided in the slitless and direct images created using `Multidrizzle`.

2.5.6 Spectral Extraction

The contamination, flat-fielding and extraction of 1D and 2D spectra of all objects in the catalogue, were done with the task `axecore`. In this task, the object position and size from a given F140W direct image was projected to the associated slitless spectrum. The region containing the spectral information for each object and grism order was then determined and the pixel values stored in a *Pixel Extraction Table* (PET). A PET is a multi-extension fits-table that stores, in each extension, the complete spectral description of all pixels of one beam (one spectral order of one object). For a detailed description of how `aXe` extracts a single object spectrum from a slitless spectrum see sections 2.3 and 2.4 of Kümmel et al. (2009). The PET contained a wavelength assigned to each pixel and so the flat-field correction values derived from the 3D flat-field cubes were applied. Quantitative contamination was added to the PET from the created fluxcube files. For each object the 2D spectra from the four individual 2D slitless spectra were combined to form a single deep 2D slitless spectrum with `aXedrizzle`. This spectrum resembled a traditional spectrum, with the dispersion direction parallel to the x-axis and spatial direction parallel to the y-axis. The 1D spectrum was then extracted from the coadded 2D slitless spectrum. In conventional spectroscopy the extraction of the 1D spectra from the 2D data is done along the direction of the slit. In slitless spectroscopy, there is no predefined extraction direction. In `aXe` the default action is to set the extraction direction to be parallel to the object position angle as returned by SExtractor, given in the IOL. The flux calibration was done using sensitivity curves which were derived through observations of flux standard stars. In extended objects, however, the spectral resolution is degraded by the object size in the dispersion direction since the object acts as its own virtual slit. `aXe` takes into account the degraded spectral resolution of extended sources by smoothing the point source sensitivity function.

2.6 Summary

The RA and Dec of the WFC3-OII galaxies were matched to the closest RA and Dec in the master catalogue produced by SExtractor within a radius of 1 arc second.

In some special cases, there were galaxies that were too close together meaning that the match could not separate them to distinguish which galaxy is the real WFC3-OII galaxy. An example is shown in Fig. 2.8. There were 5 such cases, and we removed these spectra from our sample.

Below is a description of the extracted spectra, summarized in Table 2.1:

- There were 424 WFC3-OII spectra extracted by `aXe` in total. This included objects that had multiple spectra.

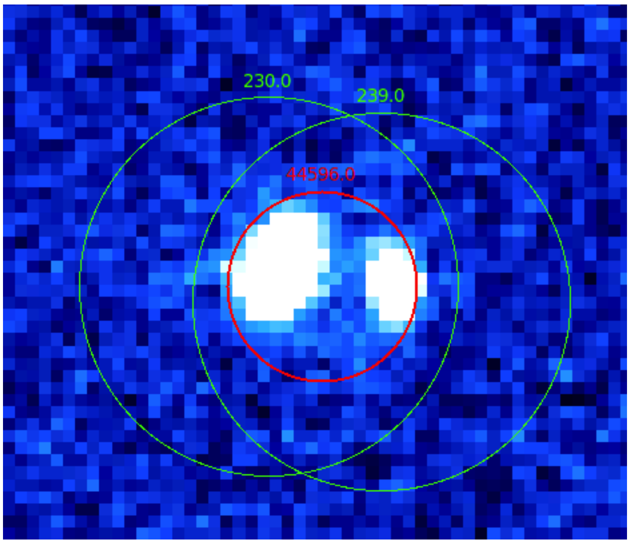

Figure 2.8: An example of showing the match for a WFC3-OII galaxy from the SExtractor catalogue for a pointing. The match picks both galaxies leading to two spectra that match the WFC3-OII galaxy. We cannot tell which is the match, so this system is rejected from our analysis.

- 42 extracted spectra did not belong to unique galaxies. These multiple spectra came from 20 individual galaxies. These multiple spectra will be used in §3.2 to test the wavelength, flux and S/N repeatability.

- Extractions from the "first principles" approach were compared to the `aXe` extractions visually to identify bad extractions (i.e. those which look significantly worse than from the first principles approach) in `aXe`. An example showing extractions that match is shown in Fig. 2.9 and an example where the extractions do not match is shown in Fig. 2.10. There were six spectra with bad extractions and attempts were made to extract these using higher SExtractor threshold parameters (§2.5.2) but to no avail. These spectra were excluded from all further analysis. Only two galaxies were lost because the other 4 had spectra in other pointings. Also, `aXe` did not find spectra for three galaxies that had spectra extracted using the first principles approach.

Due to the various issues noted above, the final catalogue contains 257 unique spectra which can be searched for Hα .

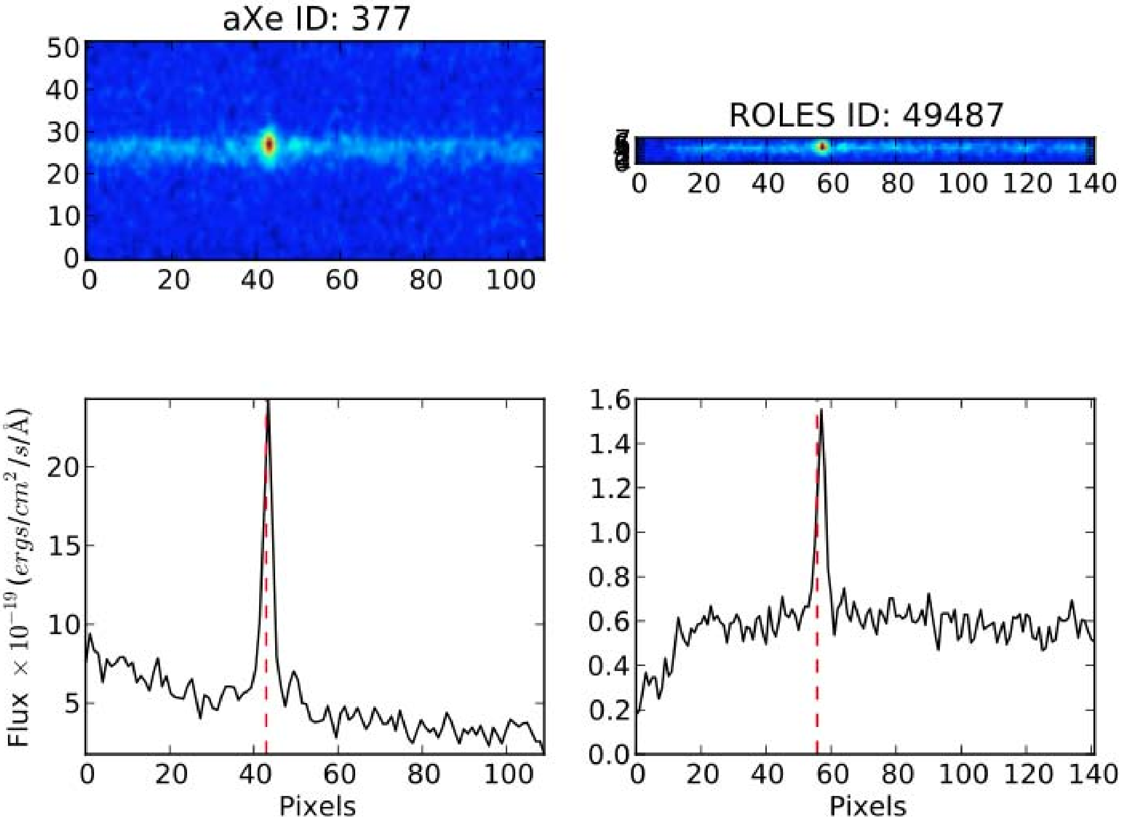

Figure 2.9: *Left Panel* shows a 2D and 1D spectrum extracted by `aXe` and the *Right Panel* shows the same spectrum extracted using the "First Principles" approach. Bearing in mind the limitations of the "First Principles" approach, these extractions agree. All spectra were compared in this way to identify bad extractions in `aXe`.

Total number of all spectra from `aXe` (with multiple spectra)	424 (42)
Unique galaxies with multiple spectra	20
Galaxies not found by `aXe`	3
Spectra lost to bad extractions in `aXe`	6
Unique galaxies with partial spectra not covering expected Hα wavelength	14
Unique galaxies with partial spectra covering Hα wavelength	30
Number of unique galaxies with spectra from first principles extraction	299
Number of unique galaxies from `aXe` with spectra	257

Table 2.1: Table summarizing the number of WFC3-OII spectra lost due to various factors and the number of spectra that remain.

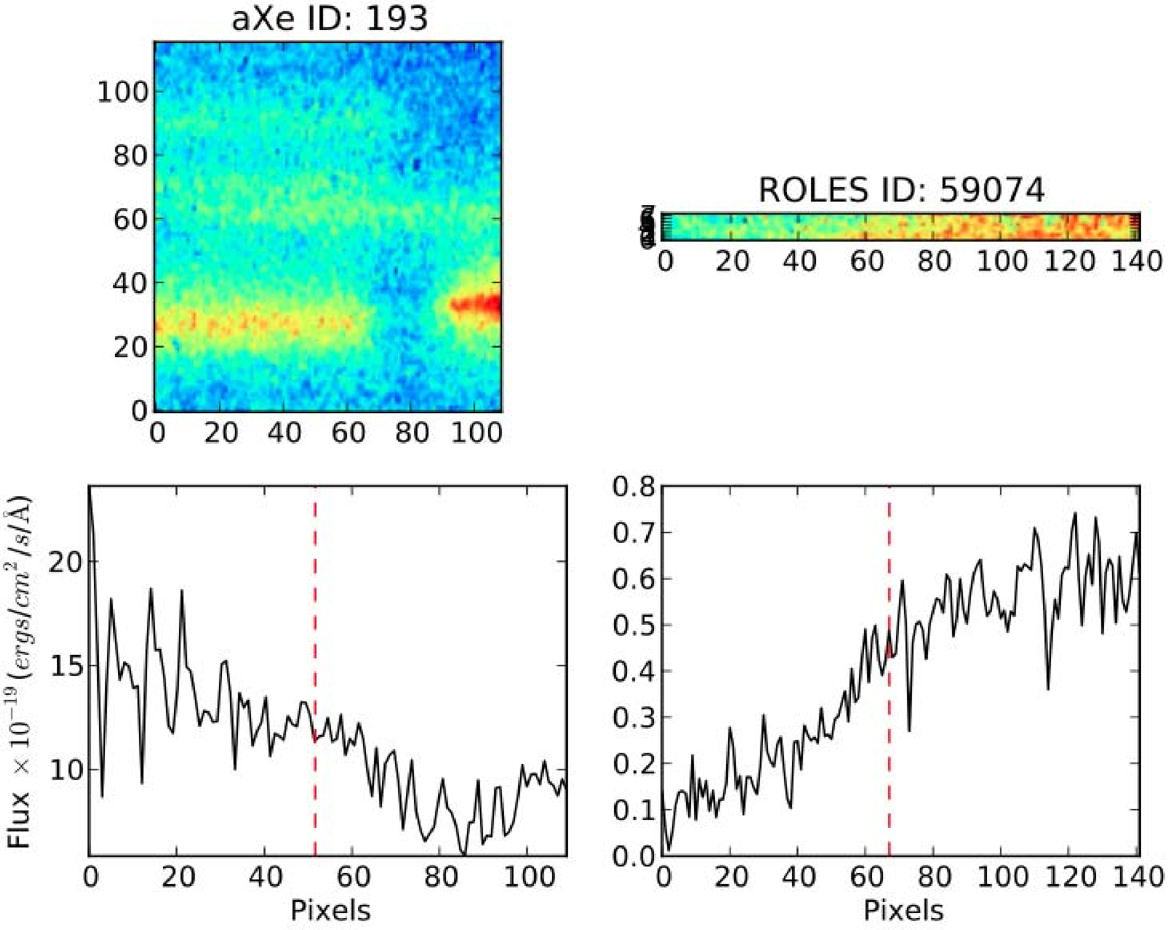

Figure 2.10: *Left Panel* shows a 2D and 1D spectrum extracted by `aXe` and the *Right Panel* shows the same spectrum extracted using the "First Principles" approach. In the top left panel, the middle spectrum is the one extracted by the pipeline but it is contaminated by the spectra above and below it. This is an example of a bad extraction by `aXe` because the two spectra do not agree. The `aXe` spectrum is contaminated by other objects.

Chapter 3

Spectral Analysis

In this chapter, we analyze the 1D spectra produced by `aXe` for the WFC3-OII galaxies. An automated pipeline was developed to detect and measure the Hα luminosities. We test the repeatability of our measurements (flux, wavelength, S/N) using galaxies that have multiple spectra.

3.1 Spectral Analaysis

An automated algorithm is needed to verify the presence of each emission line and measure its luminosity. The advantage of having an automated pipeline is that it is objective, meaning that the results can be reproduced by others using the same method. If this were to be done by humans, the results would be subjective, meaning that the measurements would differ from person to person.

For this dataset, we have the spectroscopic redshifts, for each galaxy, from the [OII] emission line in ROLES (Gilbank et al. 2010b) which means that we know where to search for the expected wavelength of Hα. The expected position of Hα is given by Eq. 2.1. However, we do not always expect to detect an emission line. This is because the galaxies we are targeting have low masses and therefore low SFRs ($\sim$0.1 $M_\odot$ yr^{-1}, Gilbank et al. 2010b). We can estimate the approximate limiting SFR of the Hα data by using the standard relation from Kennicutt (1998a) (converted to our assumed IMF) and setting this equal to the typical flux limit (3σ) of the HST spectra ($\sim 5\times10^{-18}$ erg/cm^2/s). This equates to a SFR limit of $\sim$0.9 $M_\odot$ yr^{-1}. This is slightly higher than the nominal ROLES limit for [OII] which means that we do not expect to detect the lowest SFR galaxies. (This conversion to Hα SFR has many simplifications which will be discussed in detail in Chapter 4.) In addition, these galaxies are so faint that we do not expect to detect continuum for most of them.

Our spectra are unusual in the sense that they are mostly noise (undetected continuum), but a fraction of these will have a significant emission line. Furthermore, they are unusual because they are very low resolution spectra (R=120 as mentioned in §2.2), meaning that the line is unresolved. In fact, the resolution element is so wide that the NIIλ6548 and NIIλ6583 lines will be blended with the Hα.

3.1.1 Line Verification

As described above, we need an algorithm which searches for a possible emission line signal around an expected wavelength. The reason a line may not be found at its expected position is either because of uncertainties in the wavelength calibration of the G141 grism or in the wavelength calibration used by ROLES to determine the redshifts of the galaxies. All spectra were visually inspected, and a few were found to have obvious emission lines (lines with a signal much higher than the noise). These were used to initially calibrate the sample by visually inspecting the typical offsets between the expected and observed position of the emission line (simply identified from the position of the peak). Based on the typical offset, a 4 pixels ($\sim$200Å) wide window, centred on the expected wavelength, was defined and the line peak within the window was found as shown in Figure

3.1.

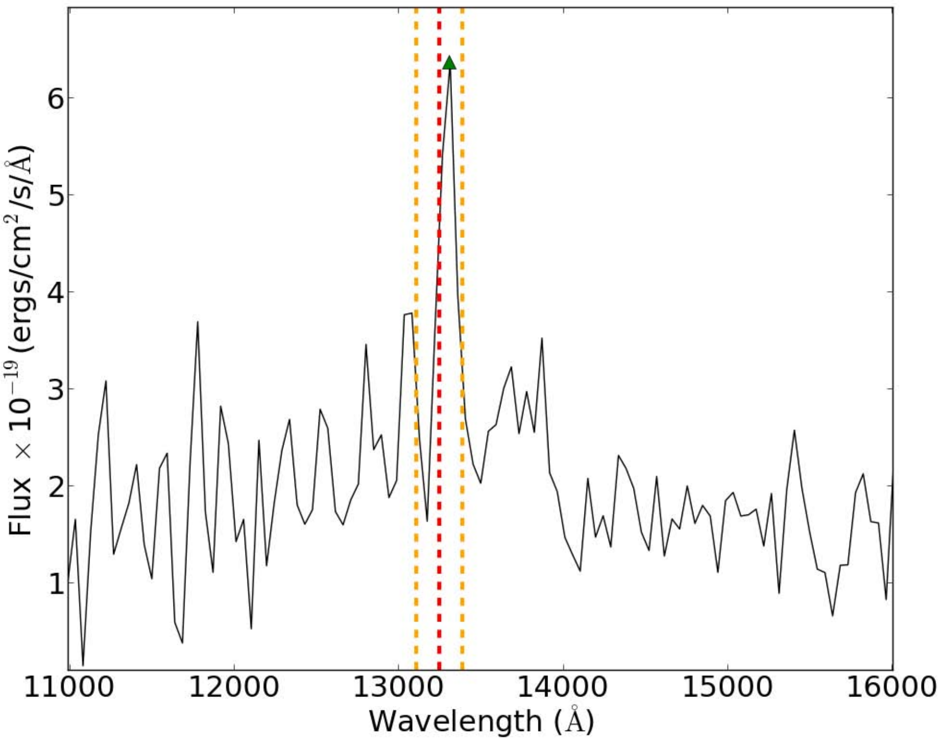

Figure 3.1: Example of a spectrum showing the expected position of the emission line (*dashed red line*) around which the 4 pixels (∼200Å) window (*dashed orange lines*) was centered to account for any uncertainty in the redshift. The emission line peak (*green triangle*) was found within this window.

3.1.2 Continuum Estimate

Now that the observed wavelength of the line is known, the algorithm needs to measure the flux of the line. The flux at the position of the line contains flux from both the line and the continuum and this has to be estimated and subtracted from the line before determining the true line flux. This is done by calculating the continuum in two 1D sidebands on either side of the line as shown in Fig. 3.2. All spectra with obvious emission lines were checked by eye to decide firstly, how far from the line to position the sideband so that the line flux is not included when calculating the continuum and secondly, how wide to make the sidebands to ensure that they contain enough continuum flux such that a linear fit to the continuum is valid. It can be seen in Fig. 3.2 that a width of 20 pixels, ranging from (x_{peak} -15) pixels to (x_{peak} - 35) pixels and (x_{peak}+15) pixels to (x_{peak} + 35) pixels, is a reasonable estimate for the sidebands. The mean in each side band was calculated and the continuum was estimated from a straight line fit to the mean values. The fitted continuum was then subtracted from the spectrum. One disadvantage of estimating the continuum in this way is that if the sideband contains a very bright pixel (Fig. 3.3), it will give an overestimate of the mean and therefore overestimate the slope of the continuum. However, this only affected a small fraction of our sample.

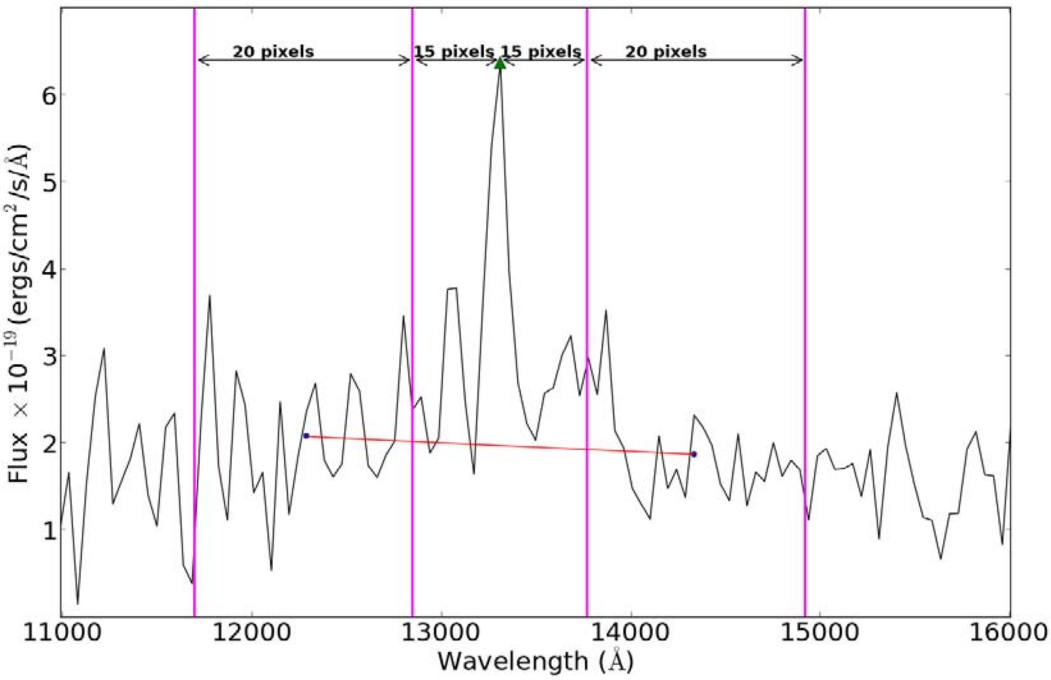

Figure 3.2: Example of a spectrum showing the two sidebands (*Magenta lines*) used to estimate the continuum. The median of all pixels (*blue circles*) was calculated in each sideband. The best fit line to the continuum is shown by the red line.

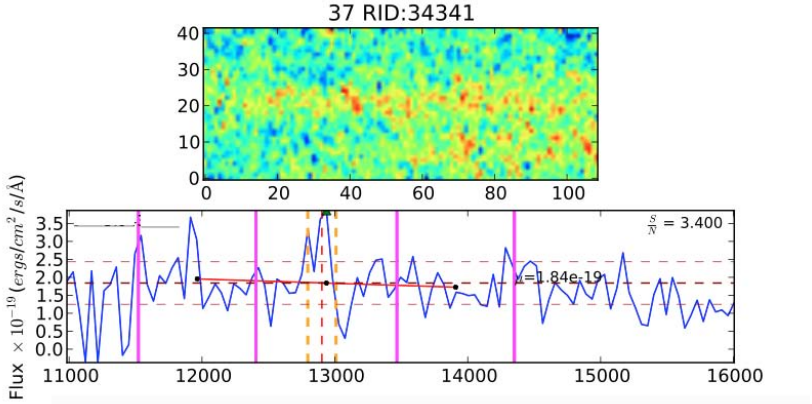

Figure 3.3: Example of a spectrum with a bright pixel in the left sideband which overestimates the mean continuum in the sideband. Top panel shows the 2D spectrum and the bottom panel shows the 1D spectrum. The magenta solid lines indicate the sidebands used to calculate the continuum with the black solid circles indicating the mean of all pixels in the sidebands. The red line is the best fit line to the continuum.

3.1.3 Signal-to-Noise

In order to determine the significance of the emission line, the noise level over the flux measurement aperture had to be determined. This is calculated by integrating over a region the same width as the integration region of the emission line (10 pixels or 480Å) on either side of the emission line and taking the mean integrated noise. The S/N ratio is then calculated as follows,

$$\frac{S}{N} = \frac{F(H\alpha)}{\sigma} \tag{3.1}$$

where F(Hα) is the integrated flux of the emission line after continuum subtraction and σ is the mean noise of the spectrum."

3.1.4 Line Luminosity Measurement

The final step in the algorithm is to measure the line luminosity. The line has some width so to calculate the total flux of the line, we have to integrate over a finite region. Choosing an integration region was a trade off between including too much noise by making the region too wide and not including all the emission line flux by making the region too narrow. To determine how wide a region to integrate over, spectra were visually inspected and a width of 480Å, centred on the peak of the emission line, was chosen as a reasonable estimate. The integrated flux was calculated using the composite Simpson's rule. This is simply dividing the integration region into a number of smaller subregions and applying Simpson's rule to each in turn. The built-in Python function `scipy.integrate.simps`* was used to do the integration.

Since the Hα line is blended with the adjacent [NII] lines, we assume a [NII]/(Hα+ [NII]) flux ratio of 0.25 (Sobral et al. 2012) to correct our Hα derived SFRs in all further analysis. This means that F(Hα)=0.75(F(Hα+[NII])). The Hα line luminosity was calculated as follows,

$$L(H\alpha) = 4\pi F(H\alpha)(D_L^2) \tag{3.2}$$

where F(Hα) is the integrated line flux and D$_L$ is the luminosity distance. The luminosity distance is defined by the relationship (Hogg 1999),

$$D_L \equiv \sqrt{\frac{L}{4\pi S}} \tag{3.3}$$

where L is the bolometric luminosity and S is the bolometric flux. The function `astCalc.dl(z)` from astLib was used to calculate D$_L$ using the galaxy's [OII] redshift from ROLES. We now have an automated algorithm that verifies the presence of emission lines, estimates the continuum, calculates the S/N and measures the luminosity of the line.

---

*Documentation can be found at`http://docs.scipy.org/doc/scipy/reference/generated/scipy.integrate.simps.html`

3.1.5 Detection Limit

As mentioned before, we do not always expect to detect an emission line. For this reason, a detection threshold has to be defined for our sample. Choosing a threshold is a trade off between purity and completeness. A very high threshold means that one has a completely pure sample which is incomplete (i.e., missing real detections). On the other hand, as one moves to lower thresholds, the sample becomes more complete but the probability of including spurious detections increases. By visually inspecting the emission lines of spectra such as those in Fig. 3.4, all lines that had a S/N $\geq$ 5 were obvious bright emission lines and not just noise. Based on this, an initial threshold of S/N ≥ 5 (5σ) was chosen meaning that all galaxies with line fluxes $< 5\sigma$ become limits while those with line fluxes $\geq 5\sigma$ are detections. An example of a limit is shown in Fig 3.5. A histogram of the S/N of the 282 unique WFC3-OII galaxies is shown in Figure 3.6. Table 3.1 summarizes the number of detections and limits for the sample.

	WFC3-ROLES	**ESO Public**
Number of unique galaxies with WFC3 spectra	177	80
Number of emission line detections	34	26
Number of emission line limits	143	54

Table 3.1: Table showing the number of Hα emission line detections and limits for a S/N $\geq$ 5 threshold for the WFC3-ROLES and ESO Public spectroscopy galaxies.

3.2 Repeatability tests of catalogue

In our sample there are galaxies that have multiple spectra. These spectra are used to test the repeatability of our flux measurements, the S/N and wavelength accuracy.

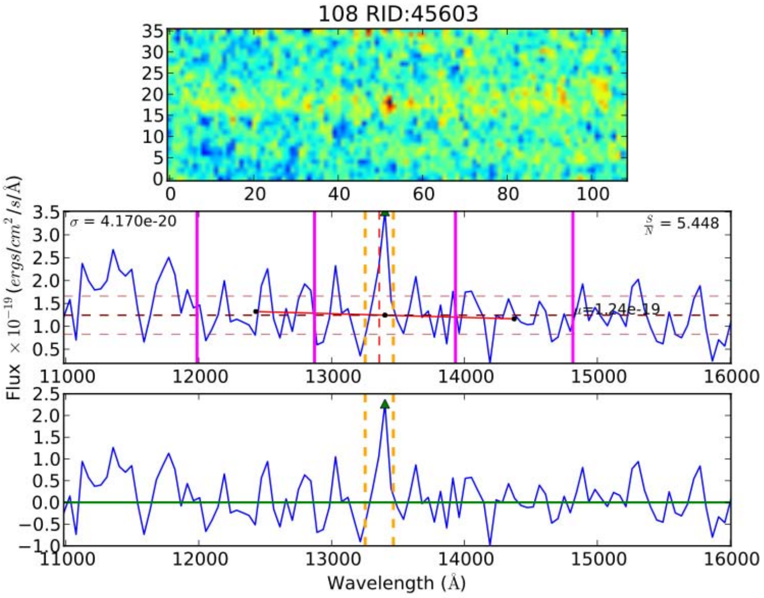

Figure 3.4: Example of one of the best WFC3-ROLES spectra. Spectra such as this, where the emission line is clearly visible, were looked at when deciding what S/N threshold to use, how wide to make the sidebands to estimate the continuum and how wide to make the integration region to determine the line flux. Top panel shows the 2D spectrum, the middle panel shows the 1D spectrum with the sidebands (magenta lines) and the solid black circles indicating the mean of all pixels in the sidebands as well as the continuum under the emission line. Maroon dashed line shows an estimate of the continuum. Brown dashed lines indicate 1σ continuum limits. The red line indicates a linear fit to the continuum. Red dashed vertical line indicates the emission line position. Yellow dashed lines indicate the window in which the line peak should be found. Green triangle indicates the peak in the defined window. The plots are annotated with the significance of the line. and the bottom panel shows the continuum subtracted spectrum.

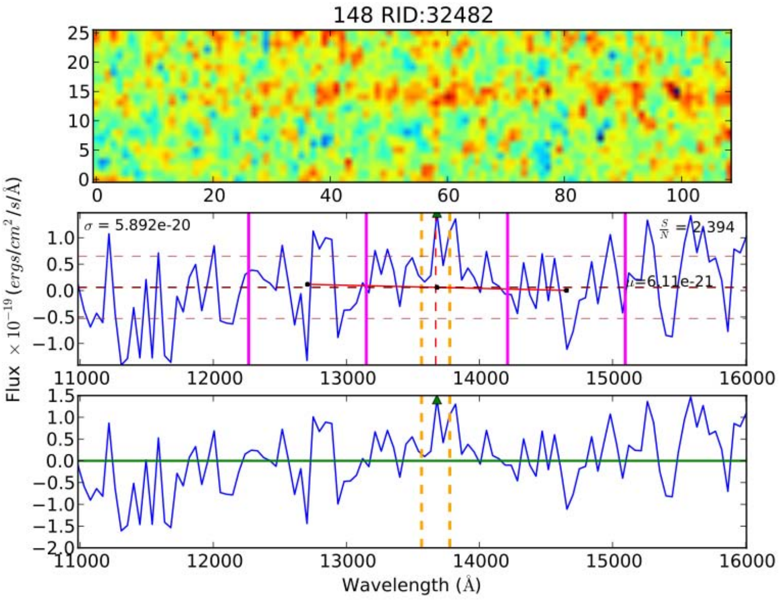

Figure 3.5: Example of a typical WFC3-ROLES spectrum. The spectrum is very noisy and it's difficult to say whether the line found is an actual emission line. Spectra like these are limits in the sample. Top panel shows the 2D spectrum, the middle panel shows the 1D spectrum with the sidebands (magenta lines) and the solid black circles indicating the mean of all pixels in the sidebands as well as the continuum under the emission line. Maroon dashed line shows an estimate of the continuum. Brown dashed lines indicate 1σ continuum limit. The red line indicates a linear fit to the continuum. Red dashed vertical line indicates the emission line position. Yellow dashed lines indicate the window in which the line peak should be found. Green triangle indicates the peak in the defined window. The plots are annotated with the significance of the line. and the bottom panel shows the continuum subtracted spectrum.

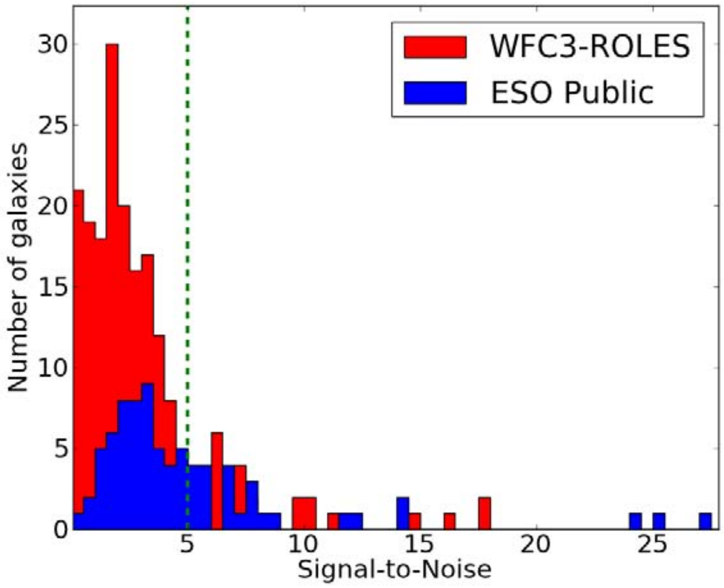

Figure 3.6: Histogram showing the significance of the emission lines for all 282 unique galaxies in the sample separated into WFC3-ROLES (*Red*) and ESO Public Spectroscopy galaxies (*Blue*). This shows the relative number of detections and limits expected for any chosen S/N threshold. A S/N greater than the threshold are detections and those less than the threshold are limits. A S/N$\geq$5 (*green dashed line*) was chosen by visually inspecting the emission lines to see if they did indeed look like a bright emission line and not just noise.

3.2.1 Flux repeatability test

Originally, the spectrum with the highest S/N was chosen for our catalogue (as is commonly done when combining catalogues). We show why this leads to a bias in the Hα measurements, and our alternate approach to negate this bias.

The repeatability of our flux measurements was tested by comparing the ratio of the observed errors to the expected errors for each. The error on the flux measurement is the noise level in the spectrum. This ratio was computed as follows,

$$\frac{F(H\alpha)_{used} - F(H\alpha)_{rep}}{\sqrt{\sigma_{used}^2 + \sigma_{rep}^2}} \tag{3.4}$$

where $F(H\alpha)_{used} - F(H\alpha)_{rep}$ is the observed error obtained from the difference between the line flux used in the catalogue (F(Hα)$_{used}$) and the flux from repeat observations (F(Hα)$_{rep}$). The expected error is the sum in quadrature of the errors on the flux measurement used in the catalogue (σ_{used}) and from repeat observations (σ_{rep}). If these errors have been calculated properly, a normal distribution, with a mean of zero, is expected. Always choosing the highest S/N measurements from duplicate measurements for a catalogue leads to an offset in the mean. We found an offset of μ ~1.5 in the mean. We use the noise level in the spectrum as the error on the flux measurement. Each galaxy has some associated true flux but all measurements of this flux are perturbed by the measurement error on the flux, some increasing and some decreasing the measured flux relative to the true flux. Assuming that the noise level, or measurement error, is similar for each measurement, the measurement with the highest S/N will preferentially be an overestimate of the true flux, since it is more likely to correspond to a case where the underlying true flux has been boosted by the noise, rather than suppressed. By choosing randomly between the multiple duplicate measurements, the bias is removed." We corrected this bias by replacing the highest S/N spectrum for a galaxy with multiple spectra with a randomly selected spectrum, using all spectra, to use in the catalogue.

The repeatability of our flux measurements is shown in the top left panel of Fig. 3.7. Most of the 1σ error bars do not overlap the 1-1 line and in some cases they do not overlap each other as seen in the top right panel of Fig. 3.7, meaning that the errors have been underestimated. The bottom panel of Fig. 3.7 shows the distribution of our errors. The distribution does not follow a normal distribution but is Gaussian with a width of 4.3 and a mean of 0.68. The offset in the mean from choosing a randomly selected measurement is much smaller (and closer to zero), than choosing the highest S/N measurement. The width indicates that our errors have been underestimated by a factor of 4.3 so we empirically correct our observed errors and replot Fig. 3.7 in Fig. 3.8. The 1σ error bars now mostly overlap the 1-1 line and each other as expected.

3.2.2 S/N Repeatability

In §3.1.5 we chose a detection threshold of 5σ (S/N$\geq$5) based on visually looking at spectra where there were obvious bright emission lines. In this section, we test whether this threshold is reasonable and if it really corresponds to a 5σ detection. As mentioned before, choosing a threshold is a trade off between purity and completeness. We can test our threshold by determining the reproducibility of the emission lines for galaxies that have multiple spectra. Our criteria for whether a detection is real or not is that the line should be found in the majority of the spectra (e.g. if a galaxy has four spectra, the line should be seen in three out of the four spectra) to be considered reproduced. The best way to test this is to pick a spectrum where the line has a very high S/N because it is more likely to be a real detection. An example of a galaxy that has four spectra, with a high S/N, is shown in Fig. 3.9. A line is seen in all the spectra meaning that the line is reproduced.

In the top panel of Fig. 3.10 we plot the S/N used in our catalogue against the S/N from repeat spectra. Moving from right to left (high to low σ) in the top panel of Fig. 3.10, we look at the points in the vertical

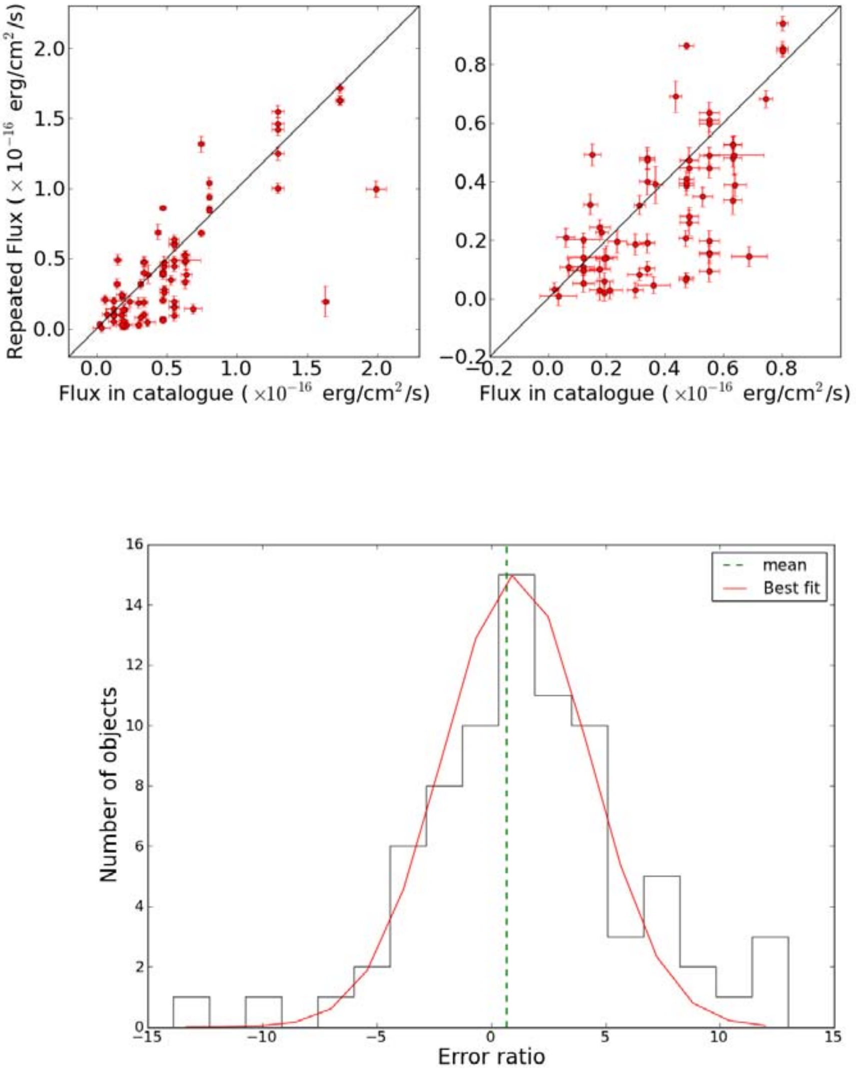

Figure 3.7: Repeatability of flux measurements from repeat observations to determine how reproducible the fluxes and their errors are. *Top Left Panel*: The repeat flux measurement is plotted against the flux used in the catalogue. *Top Right Panel*: Shows a zoomed in region of the top left panel. It can be seen that the errors have been underestimated because the 1σ error bars do not overlap the 1-1 line in the zoomed in region. *Bottom Panel*: The histogram shows the distribution of flux difference divided by the combined flux errors. The best fit curve (*Red*) is a Gaussian with width of 3.2 and a mean of 0.68.

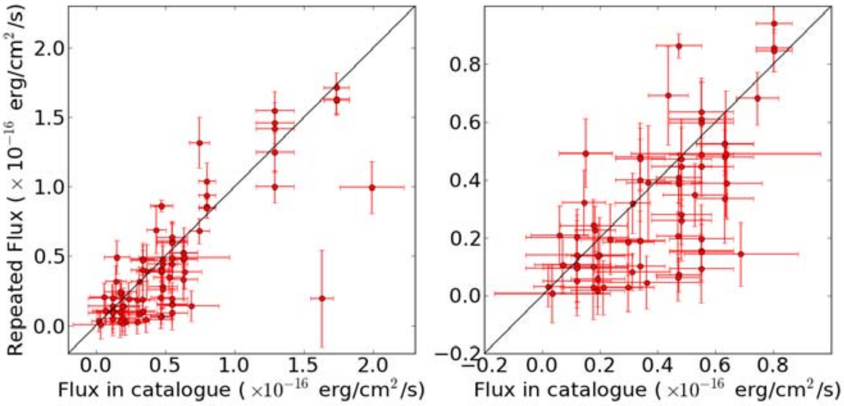

Figure 3.8: Repeatability of flux measurements from repeat observations after empirically correcting the observed errors. The right panel is a zoomed in plot of the left panel. The majority of the 1σ error bars now overlap the 1-1 line and each other as expected. This means that our expected errors are in better agreement with the observed errors.

direction because these correspond to the same galaxy and check to see if they lie above our chosen threshold. If they do, we count them as recovered. However, the chosen threshold has some uncertainty on it, so when deciding if a spectrum is recovered, we also count those points that lie fairly close, within 0.3σ, to the chosen threshold as recovered. We only go down to 3σ to see how many galaxies we can recover because we do not believe any detections below 3σ. The fraction of recovered galaxies is plotted in the bottom panel of Fig. 3.10. This plot shows that for our sample of galaxies that have repeat spectra, we recover 60-100% of galaxies between 3σ and 5σ. Based on Fig. 3.10, if we look at the S/N distribution in our catalogue (see Fig. 3.6) and apply a 4.5σ threshold, for example, we get 18 detections out of which 80% are real and 20% are spurious. Our initial threshold of 5σ thus gives us a pure sample but we are missing some real detections.

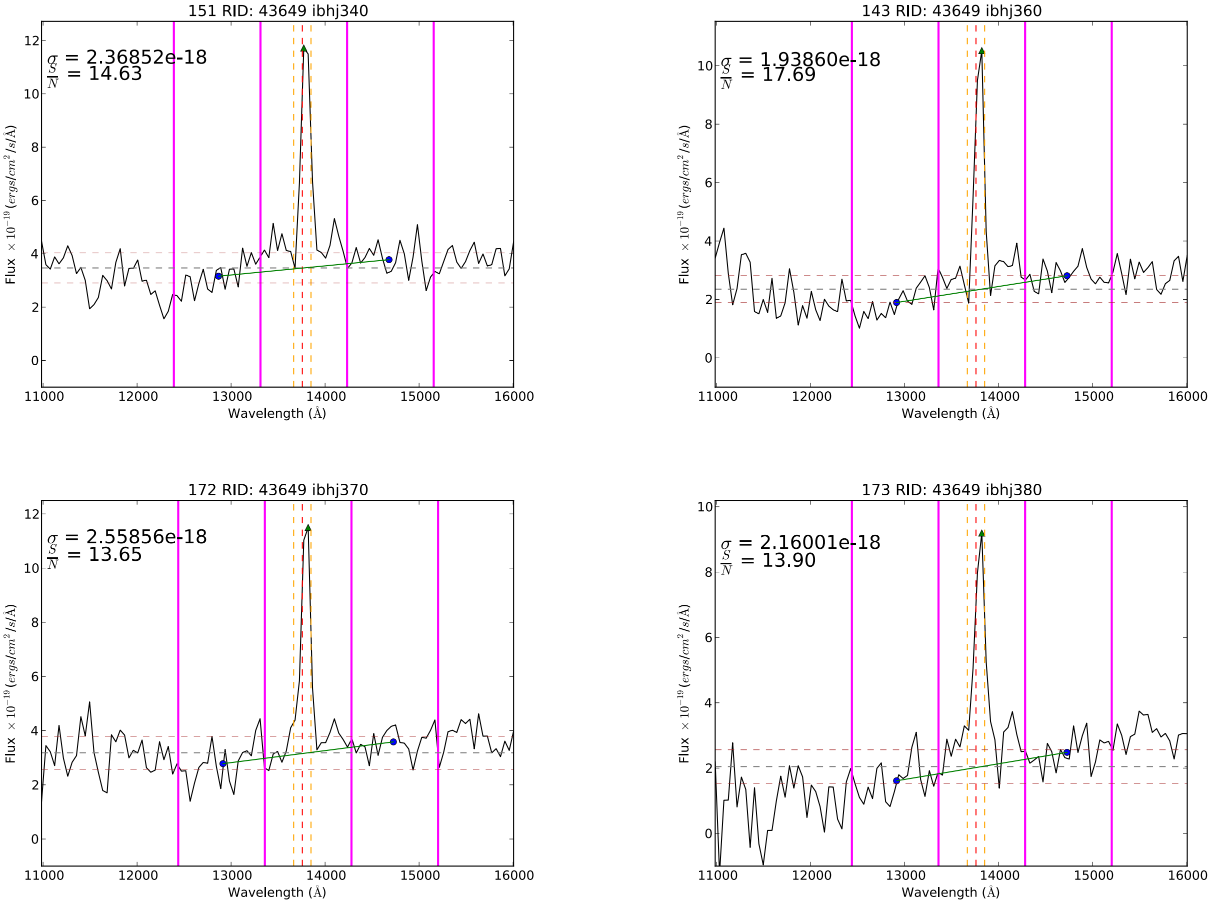

Figure 3.9: Example of a galaxy's spectrum with a high S/N emission line in four pointings. The emission line is seen in all pointings meaning that it is reproduced.

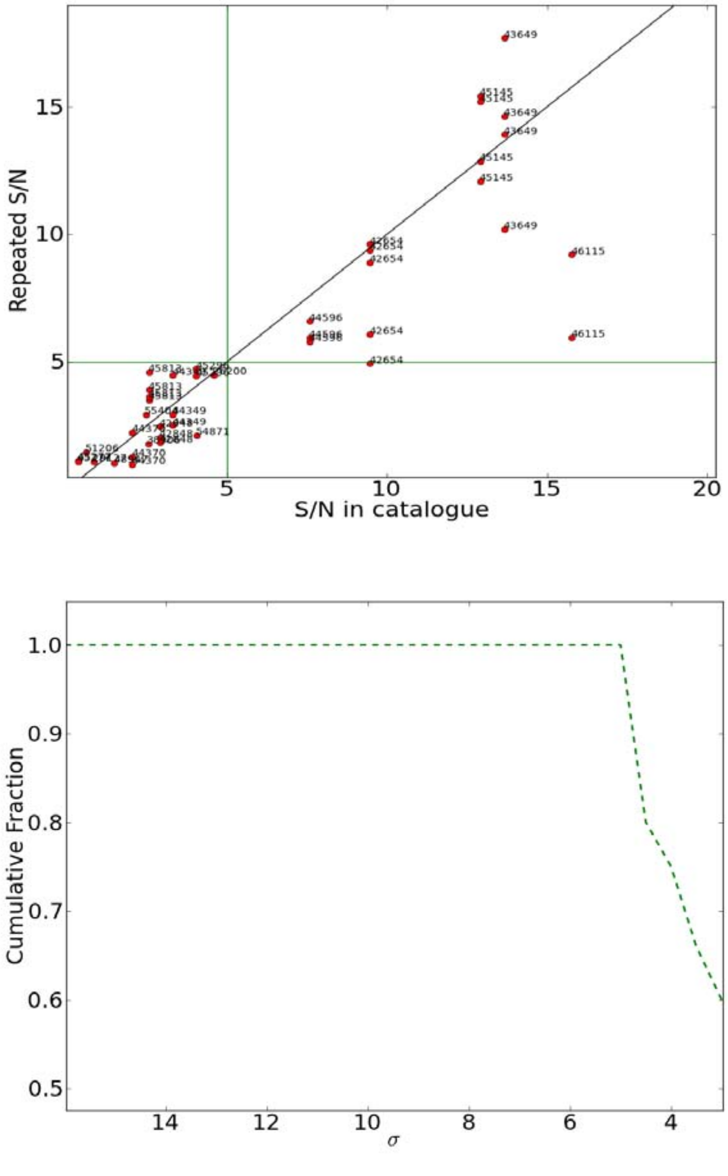

Figure 3.10: Top panel: S/N from repeat spectra against S/N used in catalogue. Green lines indicate the 5σ threshold. Bottom panel: Recovered fraction of galaxies from our sample of galaxies with multiple spectra.Note that the y-axis does not extend all the way to zero.

3.2.3 Wavelength Repeatability

The wavelength calibration of the G141 grism was tested by looking at a galaxy that had four repeat observations (Fig. 3.9). Computing the difference between the observed wavelengths, we found that our measurements were repeatable to within one pixel (46.5Å).

Chapter 4

Star Formation Rates and the SSFR-mass relation

At the end of Chapter 1, we noted that there is an observed correlation between the rate at which a galaxy forms stars (SFR) and stellar mass (M_*). In this chapter, the SFRs for our sample are estimated from the Hα and [OII] SFR indicators, using a variety of methods. These are compared against each other and against SED-fitted SFRs to determine which indicator gives the best estimate of the SFR. We then study the relation between the SSFR, which is a measure of the efficiency of star formation in a galaxy, and stellar mass for our sample of low-mass galaxies at $z\sim1$ using our Hα derived SFRs.

4.1 Introduction

As mentioned in §1.2.1.2, emission arising from hydrogen recombination lines and forbidden lines (Hα and [OII] in this work, respectively) can be used to estimate the SFR of a galaxy. The molecular gas clouds in galaxies are composed mainly of hydrogen and a smaller amount of helium and other heavier elements. In the centres of these clouds reside young, hot, high-mass

OB type stars. These stars emit large amounts of UV radiation shortward of the Lyman-limit (i.e. $\lambda < 912$Å) which have enough energy ($E_\gamma >= 13.6$eV) to ionize the surrounding hydrogen atoms, forming an HII region (also called a Strömgren sphere; e.g. Carroll & Ostlie 2006). The free electrons floating within the HII region can recombine with the protons to form hydrogen atoms. Recombination occurs when a proton captures a free electron and the electron cascades from its high energy level down to its ground state, releasing photons at each transition between energy levels (e.g. Foot 2005). The Balmer transition from the n=3 to n=2 energy level produces the Hα emission line at a rest wavelength of 6563Å. The process of recombination occurs because the lifetime of OB stars (~20 Myr) is much greater than the timescale for an electron to remain free (hundreds of years depending on the cloud's density). The hydrogen atom formed from recombination can again be reionized by the hot, young stars. Hence, the process of recombination and reionization of hydrogen continues until an equilibrium is reached. This enables the number of ionizing photons (assuming all photons are absorbed) needed to reach equilibrium to be determined, which relates directly to the UV luminosity from the OB stars. The Hα line luminosity is therefore directly coupled to the incident number of ionizing photons from young stars and is proportional to the SFR. The Hα SFR was calibrated by Kennicutt (1998b) (K98) for solar abundances and a 0.1-100 M$_\odot$ yr^{-1} Salpeter IMF (Salpeter 1955)

$$\frac{\mathrm{SFR}}{[\mathrm{M}_\odot\,\mathrm{yr}^{-1}]} = \frac{7.9 \times 10^{-42}\mathrm{L}(\mathrm{H}\alpha)}{[\mathrm{erg\,s}^{-1}]} \tag{4.1}$$

where L(Hα) is the line luminosity.

As with all indicators, there are uncertainties associated with estimating the SFR from Hα. Firstly, there is some dependence on the metallicity of the gas. However, Charlot & Longhetti (2001) showed that the efficiency factor in converting SFR to Hα line luminosity varies weakly with metallicity.

The biggest uncertainty in Hα-derived SFRs is the correction for dust extinction. A value of 1 mag of extinction at Hα is usually assumed for a typical galaxy based on extinction measurements in the Local Universe

(K98). The value for extinction at Hα for galaxies at higher redshifts is not well determined. Ideally, correcting for extinction on a galaxy-by-galaxy basis would give the best estimate of the Hα SFRs. The different ways that dust extinction can be estimated is explained further in §4.1.2.

Oxygen is also present in the HII star-forming regions and it too gets ionized by UV radiation from the OB stars. The conditions for [OII] to become collisionally excited are a critical temperature of $T > 10^4$ K and an electron density of $n_e \sim 10^{-4}$ cm^{-3} which are met in HII regions (Osterbrock 1989). Excited [OII] cannot de-excite to a lower energy level according to the selection rules of quantum mechanics for atomic transitions and is therefore called a forbidden transition (e.g. Carroll & Ostlie 2006). It must either lose its energy via spontaneous emission or collisions with other atoms in the surrounding region. The more [OII] there is (the higher the metallicity), the higher the probability of collisional de-excitation which makes [OII] very sensitive to metallicity. In the low density environment of HII regions, the timescale for collisions is longer than the lifetime of [OII] in its excited state, and it therefore decays via spontaneous emission. The collisionally excited [OII] line is also sensitive to the ionization parameter and its luminosity is more strongly affected by dust than Hα (Kewley et al. 2004). [OII] is therefore an indirect SFR indicator because its luminosity is less directly coupled to the ionizing flux from hot, young stars stars than Hα. Attempts to empirically correct the [OII] SFR for dust and metallicity have been made (e.g. Moustakas et al. 2006, Weiner et al. 2007).

The SFRs derived from different indicators are sensitive to stars of different ages, therefore masses, which means that the derived SFR is sensitive to the choice of IMF. Hα measures SFRs on short timescales ($\sim$20 M$_\odot$ yr^{-1}) whereas SFRs from UV-luminosity have much longer timescales (e.g. ≤ 1 Gyr for the FUV).

4.1.1 SED-Fitting

The amount of light emitted at different wavelengths gives the spectral energy distribution (SED) of a galaxy. The SED of a galaxy contains information about the SFH, IMF, total stellar mass, amount of dust, etc. SED-fitting is a technique used for extracting these quantities from the observed SED of a galaxy. Quantities such as the stellar mass, SFR and dust extinction can be obtained from SED-fitting[*]. A model SED is constructed from a stellar population synthesis (SPS) model. SPS models start with a simple stellar population (SSP) that describes the evolution in time of a single, coeval stellar population at a single metallicity and abundance pattern. The necessary ingredients for an SSP are the IMF, stellar evolution by isochrones and stellar spectral libraries (see Conroy 2013 for details). These SSPs are the building blocks for more complex stellar systems consisting of composite stellar populations (CSPs). CSPs contain stars with a range of ages given by their SFH, a range in metallicities and dust. These SSP models are fit to data in the form of broadband SEDs, moderate resolution optical/NIR spectra or spectral indices. However, deriving any quantity is model dependent and there are many uncertainties associated with SSP models. There are also a lot of degeneracies in fitting these models (e.g. age, metallicity, dust).

Fig. 4.1 (taken from Fig. 1 in Conroy 2013) is used to illustrate how the quantities mentioned above are obtained. The SED shape for a star-forming galaxy has most of its flux at the blue end of the spectrum because it is dominated by UV light from young stars (purple and blue spectra in Fig. 4.1). Moving from a star-forming galaxy to non star-forming galaxy, the SED-shape changes with the dominant flux at longer wavelengths (optical and NIR), making the galaxy redder (red and orange spectra in Fig. 4.1).[†] Placing broadband filters at bluer wavelengths will therefore give a measure SED-fit SFR of a galaxy. The UV slope changes as a galaxy moves from highly star-forming to less star-forming, and also as the galaxy becomes

---

[*] See Conroy (2013) for an excellent recent review on SED-fitting

[†] In the NIR, nearly all galaxies have a similar shaped SED.

dustier. One method of estimating dust attenuation is by measuring the UV slope (e.g. Meurer 1999). Most of the stellar mass in a galaxy comes from old stars. By measuring the 4000Å-break one can get an age of the stellar population. The 4000Å-break gets larger for older ages.

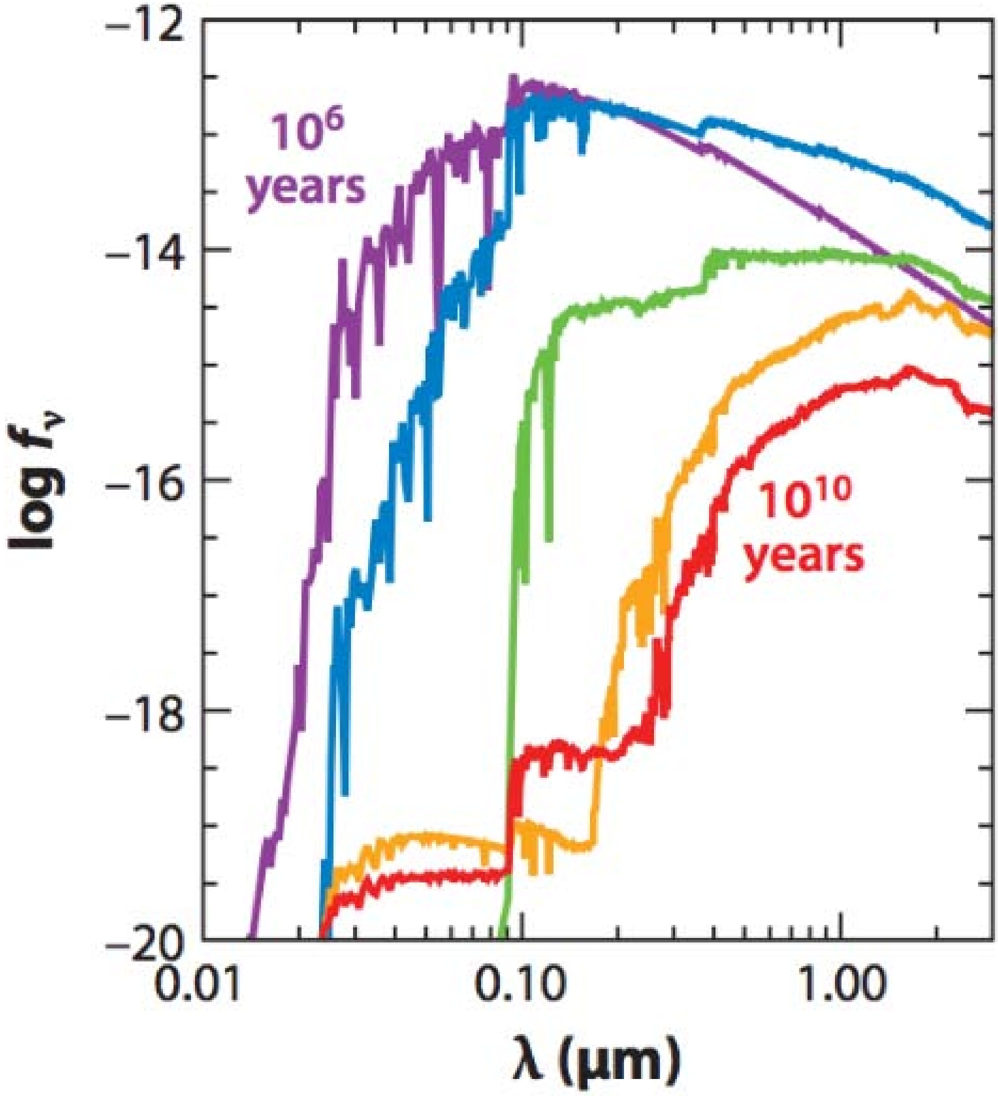

Figure 4.1: SEDs for young, star-forming (blue, purple and green) and old, passively evolving galaxies (orange and red). The shape changes moving from one to the other. Broadband filters placed at strategic wavelengths can be used to obtain the SFR, dust extinction and stellar mass of a galaxy. Credit: Conroy (2013)

4.1.1.1 Recent Hα studies at z~1

Only a handful of studies have investigated Hα SFRs at z~1. These have all been done in recent years because multi-object NIR spectrographs have only become available recently.

The High-Redshift Emission Line Survey (HiZELS) uses the Wide Field Camera on the United Kingdom Infrared Telescope (UKIRT) and a set of narrow-band filters to detect Hα emitters. A study by Sobral et al. (2009) used deep NIR narrow-band imaging (J, H and K bands) from HiZELS to obtain a sample of Hα emitters. Sobral et al. (2011) studied star-forming emission line galaxies from the Sobral et al. (2009) sample. Fumagalli et al. (2012) used 3DHST space-based spectroscopic data to study a mass-selected sample of galaxies between $0.8 < z < 1.2$. Momcheva et al. (2013) used ground-based spectroscopy to measure Hα luminosities and dust extinction at Hα at z~0.8. Twite et al. (2012) studied Hα SFRs at z~1 with ground-based NIR MOS using the Long-slit Intermediate Resolution Infrared Spectrograph on the William Herschel Telescope. Sobral et al. (2012), use a matched Hα + [OII] dual narrow-band survey at z~1.5. Kashino et al. (2013) studied Hα SFRs and dust extinction using ground-based FMOS spectroscopy at z~1.7.

4.1.1.2 Selection biases

Sample selection biases are important to consider in any study. Imagine we have to measure the SFR for a sample of galaxies using two SFR indicators, one more sensitive to dust (indicator A) than the other (indicator B). Let us assume that the SFR scales the same way with flux for both indicators, the only difference being that indicator A is more sensitive to dust than indicator B. Assume that both indicators go down to roughly similar flux (SFR) limits. For a galaxy with a given amount of dust, indicator A will measure a lower flux than indicator B. If this dust is sufficient to reduce the flux of the galaxy below the flux limit, then the galaxy drops out of the sample.[‡] However, if indicator A goes to a much deeper flux limit than indicator B, this effect is reduced or potentially completely removed. The galaxies that were being missed when the surveys were at similar depths will now be included in the sample. This is the case with ROLES. Even though ROLES uses an indicator that is more sensitive to dust (i.e., [OII]), the survey goes down to an extremely deep flux limit.

Using a SFR indicator that is insensitive to dust, such as radio, would be ideal. However at radio wavelengths, only the most highly star-forming galaxies will be detected. It is not possible to go down to as deep a flux limit at radio wavelengths at z$\sim$1 as in ROLES.

4.1.2 Derived Quantities

In this section we define the different SFRs, dust estimates and stellar mass estimates that are used in the rest of the chapter .

4.1.2.1 Nominal Hα SFR assuming 1 mag extinction (HαK98)

The nominal Hα SFR was estimated using the basic K98 calibration in Eq. 4.1 divided by 1.5 to convert to a Kroupa (2001) IMF (Brinchmann et al. 2004),

$$\frac{\mathrm{SFR}}{[\mathrm{M}_\odot\,\mathrm{yr}^{-1}]} = \frac{10^{0.4\mathrm{A}_{\mathrm{H}\alpha}}}{1.5}\frac{\mathrm{L(H}\alpha)}{1.27\times10^{41}[\mathrm{erg\,s}^{-1}]} \tag{4.2}$$

where $A_{H\alpha}$ is the magnitude of extinction at Hα (1 mag in this case) and L(Hα) is the measured Hα line luminosity (see §3.1.4).

[‡] Many studies have shown that dust extinction correlates with stellar mass and SFR. In particular, low mass galaxies, which also have low SFRs, are the least dusty. Since these galaxies have low SFRs, in a SFR selected sample, they will lie close to the survey's selection limit. Now, because they contain little dust, their observed fluxes (SFRs) are not greatly reduced by this. Hence the fraction of galaxies extinguished below the flux limit is in fact much lower than it would be if this correlation were not present.

4.1.2.2 Hα SFR with SED-fitted dust using Calzetti law (HαSC)

As mentioned above, a major source of uncertainty in Hα derived SFRs is dust extinction. The dust extinction estimates for each galaxy was obtained by the ROLES team using SED-fitting (explained in §4.1.2.7). These SED-fitted dust estimates in the V-band (A$_V$) were scaled as follows using a standard Calzetti et al. (2000) law to obtain the magnitude of extinction at Hα:

$$A_{H\alpha} = 0.44 \frac{k_{H\alpha}}{k_V} A_V \tag{4.3}$$

The values of $k_{H\alpha}$ and k_V come from the polynomial parameterization of Calzetti et al. (2000) (Eq. 4 in their paper):

$$k(\lambda) = 2.659(-2.156+1.509/\lambda-0.198/\lambda^2+0.011/\lambda^3)+4.05, \quad 1200\ \text{Å} \leq \lambda < 6300\ \text{Å}$$

$$k(\lambda) = 2.659(-1.857 + 1.040/\lambda) + 4.05, \qquad 6300\ \text{Å} \leq \lambda \leq 22000\ \text{Å} \tag{4.4}$$

where the wavelengths of 5500Å and 6563Å were substituted into the relevant polynomial to obtain the ratio of $\frac{k_{H\alpha}}{k_V} = 0.82$. A Milky Way-like screen law (e.g. Cardelli et al. 1989) was used in the Calzetti et al. (2000) method to estimate the reddening experienced by the nebular gas emission line. The reddening suffered by the stellar continuum is approximately 0.44 times the reddening experienced by emission lines. This has been empirically measured in terms of the color excess (E(B-V)) by Calzetti et al. (2000) as

$$E(B-V)_{stars} = 0.44 E(B-V)_{gas}. \tag{4.5}$$

The Hα SFR was then calculated using Eq. 4.2 correcting for dust extinction on a galaxy-by-galaxy basis with Eq. 4.4.

4.1.2.3 Hα SFR with SED-fitted dust using Calzetti law without 0.44 (HαSC$'$)

The Calzetti et al. (2000) empirical relation (Eq. 4.5) was derived for low-redshift starburst galaxies. However, it is not well determined whether the correction to the colour excess for the stellar continuum applies to high-redshift galaxies (Buat et al. 2002). Some studies suggest that the correction does not hold at high redshifts because it overpredicts Hα SFRs with respect to UV SFRs (e.g. Erb 2006, Hayashi 2009, Twite et al. 2012, Kashino et al. 2013). For this case, we calculated the Hα SFR using Eq. 4.2 without applying the 0.44 factor in Eq. 4.4 when correcting for dust extinction at Hα.

4.1.2.4 Hα SFR with mass-dependent dust extinction (HαM)

Several studies have looked at how the extinction varies with stellar mass (e.g. Brinchmann et al. 2004, Garn & Best 2010, Gilbank et al. 2010a). We calculate the extinction as a function of stellar mass using the relation from Gilbank et al. (2010a):

$$A_{H\alpha} = a + b \log(\mathrm{M}_*/\mathrm{M}_\odot) + \mathrm{c}\,[\log(\mathrm{M}_*/\mathrm{M}_\odot)]^2 \tag{4.6}$$

where a=51.201, b=-11.199, c=0.615 and is set to a constant value for $\log(\mathrm{M}_*/\mathrm{M}_\odot) \leq 9.0$. This relation was derived using Balmer decrement measured dust extinction for galaxies in the Local Universe. The Balmer decrement measures the ratio of the $H\alpha/H\beta$ line flux.

Garn & Best (2010) derived a similar relation where the dust extinction as a function of stellar mass is modeled as a fourth order polynomial:

$$A_{H\alpha} = 0.91 + 0.77\,X + 0.11\,X^2 - 0.09\,X^3 \tag{4.7}$$

where X=log(M$_*$/10^{10}M$_\odot$). This relation was also calibrated locally using Balmer decrement measured dust extinction (Eq. 4.7). We show the Garn & Best (2010) relation on some of our plots for comparison purposes.

Kashino et al. (2013) found a best fit relation to their dust extinction estimates as a function of stellar mass at 1.4<z<1.7 as follows (which we also use for comparison):

$$A_{H\alpha} = 0.72 + 1.38\log(\mathrm{M}_*/10^{10}\mathrm{M}_\odot). \tag{4.8}$$

4.1.2.5 Nominal [OII] SFR ([OII]K98)

The SFR measured from [OII] luminosity was calibrated by K98 by scaling between the [OII] and Hα luminosity as:

$$\frac{SFR}{[M_\odot yr^{-1}]} = \frac{10^{0.4A_{H\alpha}}}{1.5r_{lines}}\frac{L([OII])}{1.27\times10^{41}[ergs^{-1}]} \tag{4.9}$$

where $A_{H\alpha}$ is the magnitude of extinction at Hα (1 mag assumed), L([OII]) is the [OII] luminosity and r_{lines} is the ratio of [OII] to Hα flux. A ratio of 0.5 is usually assumed (e.g., Kennicutt 1998a). This ratio depends on metallicity and the ionisation parameter (e.g. Kewley et al. 2004). However, [OII] mass-dependent relation in the next section accounts for the metallicity variation at low redshift and if we assume that the dependence of metallicity and dust behave the same way as locally then the [OII]G10 correction will account for this line ratio at z$\sim$1.

4.1.2.6 Mass-dependent Empirical [OII] SFR ([OII]G10)

In Gilbank et al. (2010a), it was determined that the L([OII])-based SFR was dependent upon stellar mass. The constant L([OII]) conversion to SFR in Eq. 4.9 was found to overestimate the SFR at low stellar masses, and underestimate the SFR at higher masses. The stellar mass-dependent empirical correction of Gilbank et al. (2010a) is given by:

$$\mathrm{SFR_{emp,corr}} = \frac{\mathrm{SFR_0}}{\mathrm{a\tanh[(x-b)/c]+d}} \tag{4.10}$$

where x=log($M_*/M_\odot$), a=-1.424, b=9.827, c=0.572, d=1.700 and $\mathrm{SFR_0}/(\mathrm{M_\odot}$ $\mathrm{yr^{-1}}) = \mathrm{L([O\ II])}/(2.53\times\ 10^{40}$ ergs $\mathrm{s^{-1}})$.

This relation was empirically calibrated using Balmer-decrement corrected Hα SFRs and therefore encodes the extinction correction and metallicity dependence of [OII] implicitly by assuming these quantities are correlated with stellar mass. The calibration was done for galaxies in the Local Universe and using this relation at z$\sim$1 assumes that the dependance of metallicity and dust on stellar mass behave in the same way as locally.

4.1.2.7 SED-fit SFRs

The SED-fit SFRs from ROLES are complementary to (and independent of) the emission line SFR measurements. The SFRs estimated from SED fits by Gilbank et al. (2010b) were used as the independent indicator. They obtained these SFRs by fitting deep multiwavelength photometry at each galaxy's spectroscopic redshift to a grid of SPS models (using PEGASE.2; Navarro et al. 1997) as described in Glazebrook et al. (2004). This included U_{38}, B_{435}, B, V, V_{606}, R, i_{38}, I, z_{38}, J, H, K, [3.6 μm], [4.5 μm], [8.0 μm] photometry (see Wuyts et al. 2008 for details). Since the photometry was aperture-based, any luminosity-dependent fitted quantities such as SFR had to be scaled from the aperture measurements to total light measurements. This was done by multiplying the SFR obtained from the fitting by $10^{-0.4(K_{total}-K_{aperture})}$ where $K_{aperture}$ and K_{total} are the K-band aperture and total magnitude, respectively. This is largely equivalent to a UV luminosity SFR (Gilbank et al. 2010b).

4.1.2.8 Stellar masses

The stellar masses were also obtained from ROLES (Gilbank et al. 2010b). Since stellar mass is a luminosity-dependent SED-fitted quantity, it too was scaled from the aperture measurements to total light measurements. The masses obtained from the fitting were multiplied by $10^{-0.4(K_{total}-K_{aperture})}$ where $K_{aperture}$ and K_{total} are the K-band aperture and total magnitude, respectively.

4.1.2.9 Optimal dust correction to the Hα SFR

The biggest uncertainty on our Hα SFR measurements is due to dust extinction. A common way of measuring dust extinction is by using the Balmer decrement, which is the ratio of the Hα/Hβ emission line flux. The expected line ratio depends on the temperature and electron density in the HII regions. The expected value of the Balmer decrement, in the absence of dust extinction, can then be compared to the observed line ratio to determine the reddening in the HII region via an extinction law which describes the wavelength dependence of dust extinction (see §4.1.2.2).

Our spectra do not cover the wavelength range of the Hβ emission line which means that the extinction cannot be measured using the Balmer decrement. To test whether our SED-fitted dust extinction measurements are a good estimate of dust extinction, we compare to other works where the extinction has been measured using the Balmer decrement. Since dust is created in stars, one might expect dust extinction to depend on the number of stars (stellar mass), and the rate at which they are formed (SFR), in a galaxy. Previous studies have shown that dust extinction correlates with stellar mass (e.g. Garn & Best 2010, Gilbank et al. 2010a). Other studies have found a correlation between dust extinction and Hα luminosity (or SFR) (e.g. Hopkins et al. 2001, Pérez-González et al. 2003, Buat et al. 2005, Schmitt et al. 2006, Caputi et al. 2008). Furthermore, there have been studies that show that the dust extinction as a function of stellar mass and Hα luminosity evolves with redshift. We explore these relations in Fig. 4.2 and Fig. 4.3. In Fig. 4.2 and Fig. 4.3 we plot our SED-fitted dust estimates using Eq. 4.6 as a function of stellar mass and observed Hα luminosity to determine which property correlates better with dust.

The Momcheva et al. (2013) and Sobral et al. (2012) measurements are again plotted for comparison in Fig. 4.3. The two local relations from Hopkins et al. (2001) and Pérez-González et al. (2003) together with the relation derived by Garn et al. (2010) at $z\sim0.84$ are also shown. In Fig. 4.2, we plot, for comparison, the median dust extinction and mass values of Momcheva et al. (2013), Sobral et al. (2012) and Kashino et al. (2013). The local relations derived by Garn & Best (2010) and Gilbank et al. (2010a) at $z\sim$ 0.1 and are also shown.

4.1.3 Dust Correction Comparisons

Previous studies have found evidence that dusty massive galaxies contain less dust at the present epoch than at higher redshifts (e.g. Dunne et al. 2003, Bourne et al. 2012, Rowlands et al. 2014). However, whether or not this is intrinsic to all galaxies at all masses is unknown. Furthermore, this could be an artifact arising because the samples being compared span high-mass (high-obscuration) at high-z and relatively much lower masses (low-obscuration) at low-z. One must be careful when comparing a galaxy at a fixed stellar mass at low-z and high-z because it is not obvious how the dust has evolved. The evolution of dust obscuration in a galaxy remains an open issue. Fig. 4.2 shows our SED-fitted dust extinction estimates as a function of stellar mass. We compare these with other studies that measured dust extinction using standard Balmer-decrement. For low mass galaxies ($\log(\frac{M_*}{M_\odot}) < 10$) our dust estimates agree well with the median Balmer decrement dust measurements of Momcheva et al. (2013) within uncertainties. The Momcheva et al. (2013) sample at $z\sim0.8$ is the closest to our redshift range. Our dust estimates for low masses also fall on the

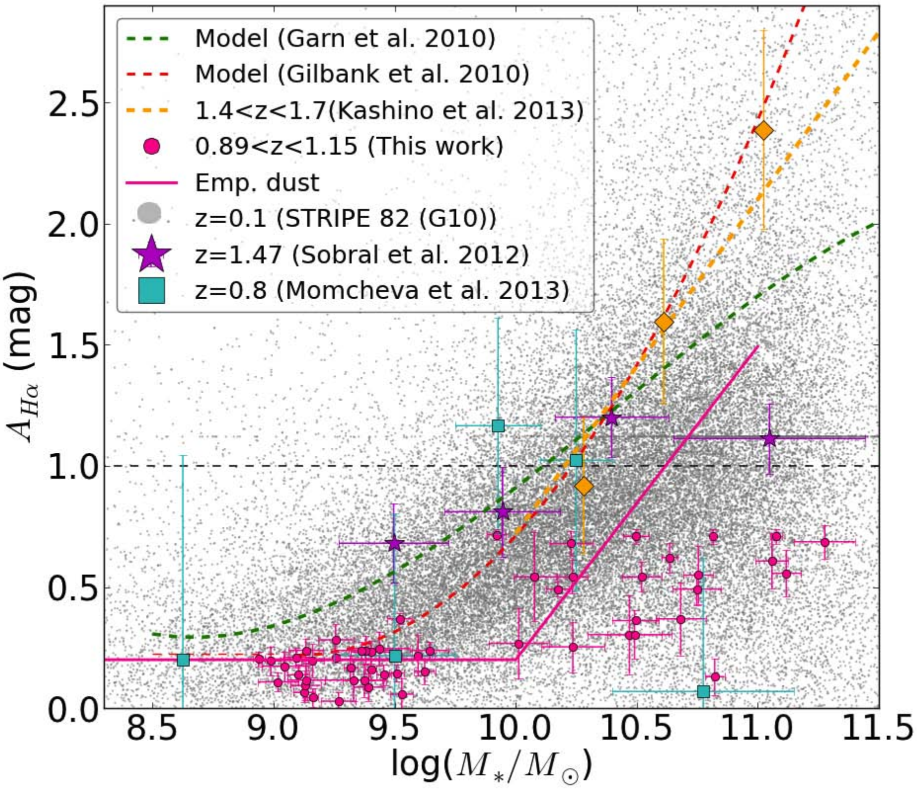

Figure 4.2: The relation between dust extinction ($A_{H\alpha}$) and stellar mass. All comparison samples estimate dust using Balmer decrement. Our SED-fitted dust estimates (pink points) for the low mass galaxies agree well with the Momcheva (2013) data. The low mass galaxies also follow the locally derived Gilbank et al. (2010a) extinction relation within uncertainties. At higher masses our dust estimates are underestimated so we derive a mass dependent dust correction (pink line) to account for this (See text for discussion).

Gilbank et al. (2010a) local relation (Eq. 4.6) that was calibrated using SDSS Stripe 82 measurements. At higher masses however, our measurements fall significantly below the local relation. Although the highest mass data point by Momcheva et al. (2013) also lies below the local relation, they attribute this to the possible contamination of their stacked sample by unidentified AGN at this mass range. At higher redshifts ($z\sim1.5$), Sobral et al. (2012) and Kashino et al. (2013) measure higher values for dust extinction for high mass galaxies. If dust extinction is expected to decrease monotonically towards the current epoch, then we do not expect our values at $z\sim1$ to suddenly drop below the local value and then increase again.

To correct for the dust that is underestimated at high masses, we derive an empirical dust correction as a function of stellar mass for all galaxies in our sample. The relation, shown in Fig. 4.2, is flat for low masses and increases linearly for high masses as,

$$\begin{aligned} A_{H\alpha} &= 0.2, && \log(M_*/M_\odot) < 10 \\ A_{H\alpha} &= 1.29\log(M_*/M_\odot) - 12.65, && \log(M_*/M_\odot) \geq 10. \end{aligned} \tag{4.11}$$

We chose the value of 0.2 for the intercept for the low mass part of the relation because it agrees with the Gilbank et al. (2010a) local relation and the Momcheva et al. (2013) points at low masses. For the higher mass part of the relation we chose two points at (10.0,0.3) and (11.1,1.7) from which the slope and intercept were determined. The first point was chosen based on the minimum mass value for the high mass galaxies. The second point was chosen by picking a value approximately between the Sobral et al. (2012) and Kashino et al. (2013) values for their highest mass bins, and above the Garn & Best (2010) local relation, because this is where the dust extinction should lie for our highest mass galaxies if dust is expected to decrease with decreasing redshift.

In Fig. 4.3, our SED-fitted dust extinction as a function of observed Hα luminosity (SFR) is compared with other studies that used the Balmer-decrement to estimate the dust extinction. The local measurements and the higher redshift measurements set the range within which one might expect to find extinction values at $z\sim1$. However, the Sobral et al. (2012) sample at $z\sim1.47$ follows the locally derived Garn & Best (2010) relation indicating no evolution in dust at higher luminosities. The measurements of our sample are much lower than those of Garn et al. (2010), Sobral et al. (2012) and fall below the local relations derived by Pérez-González et al. (2003), Hopkins et al. (2001) and Garn & Best (2010). Our measurements agree well with the median Momcheva et al. (2013) measurements across all luminosities.

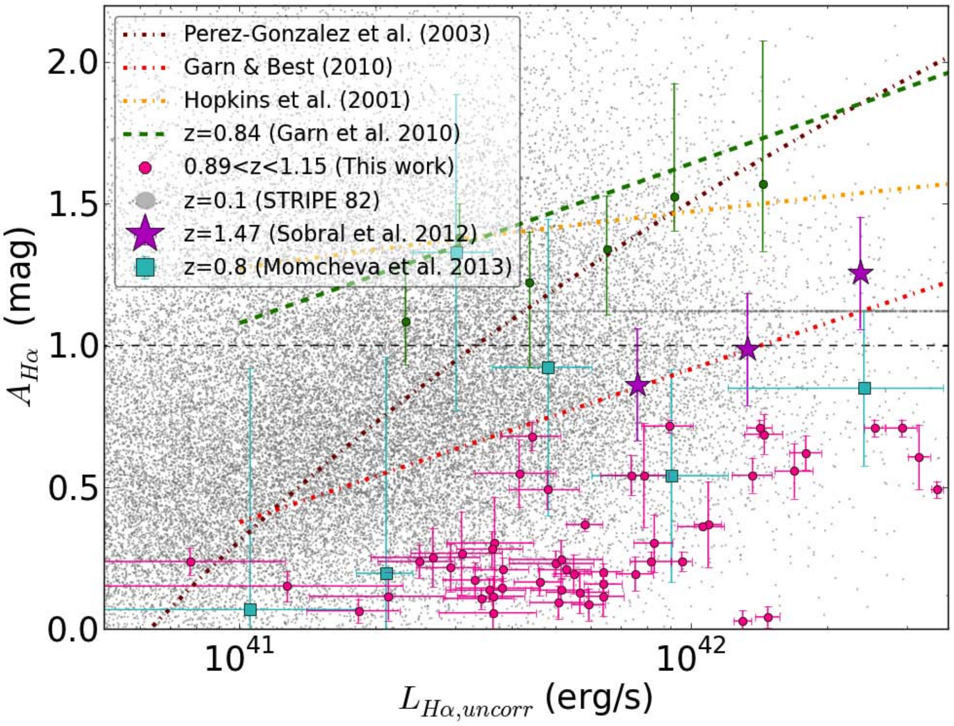

Figure 4.3: The relation between dust extinction ($A_{H\alpha}$) and observed Hα luminosity. All comparison samples estimate dust using Balmer decrement. Our SED extinction estimates do not follow the local relations or the Garn & Best (2010) relation at z=0.84.

However, as discussed for Fig. 4.2, the extinction values for the high mass galaxies are underestimated for both Momcheva et al. (2013) and our data. High luminosities (high SFRs) are due only to high mass galaxies (from the SFR-mass relation). On the other hand, high mass galaxies can also have lower luminosities (lower SFRs) which then means that they span a range in luminosities resulting in the lower extinction values seen in Fig. 4.3.

It can be seen that there is more scatter in our sample as a function of luminosity (SFR) compared to the scatter as a function of stellar mass. This indicates that stellar mass is a better predictor of dust extinction than luminosity as found by Gilbank et al. (2010a) and Garn & Best (2010).

As noted above, our SED-fitted dust extinction values agree well for low mass galaxies ($\log(\frac{M_*}{M_\odot}) < 10$) with extinction measurements from the literature that used Balmer decrement. SED-fitted dust extinction values for higher mass galaxies underestimate extinction compared to Balmer decrement measurements. For simplicity we adopt the mass-dependent empirical correction (Eq. 4.11, referred to as Mass-dependent Riona Ramraj (MRR)) to estimate dust extinction as our standard method.

4.1.3.1 Comparison of SFR indicators

Having obtained the optimal dust correction to the Hα SFR in the previous section, we compare it to the SFR derived from the [OII]K98 and [OII]G10. In Fig. 4.4, the HαMRR SFR is compared to the [OII]K98 and [OII]G10. Here, we want to check how well the [OII]G10 calibration works for galaxies at $z{\sim}1$.
We also want to test the agreement between the Hα and [OII] SFR measurements. We modeled the data using a linear regression model of the form:

$$SFR(H\alpha) = m \times SFR([OII])_{emp.corr} \tag{4.12}$$

where SFR(Hα) is obtained from HαMRR, SFR([OII])$_{emp.corr}$ is obtained from [OII]G10 and m, the slope, is the unknown parameter that has to be estimated.

Two methods are used to determine the slope. First, the ratio of the two SFRs (i.e. SFR(Hα)/SFR([OII])$_{emp.corr}$) is calculated and the median is taken to be the slope of the best fit line (solid green line in Fig. 4.5). The scatter (shaded green region bound by the dashed green lines in Fig. 4.5) is calculated by finding the standard deviation of the residuals i.e. difference between the observed SFR and the fitted SFR provided by the model,

$$\text{Residuals} = SFR(H\alpha) - (SFR([OII])_{emp.corr} \times \tilde{m}) \tag{4.13}$$

where $\tilde{m}$ is the median of the ratio values, $\frac{SFR(H\alpha)}{SFR([OII])_{emp.corr}}$ and, SFR(Hα) and SFR([OII])$_{emp.corr}$ have the same meaning as in Eq. 4.12. The advantage of this method is that it will allow us to study any residual trends as a function of stellar mass.

In the second method, a least squares fitting routine, `kmpfit`[§], is used to find the line of best fit (solid magenta line in Fig. 4.5). The method of least squares adjusts the parameters of a model function by minimizing the sum of squared residuals. The scatter about the best fit line is computed as in the previous method, using Eq. 4.13, but now using the best fit slope obtained from the fitting routine instead of the median (shaded cyan region bound by the dashed cyan lines in Fig. 4.5). The advantage of using this method over the median method is that it takes into account the errors on the data points. The errors in both variables, (i.e. SFR(Hα) and SFR([OII]$_{emp.corr}$)) are summed in quadrature and used as weights in the fit. The error on the best fit slope is too small so we bootstrap the data. The bootstrap method creates a number of resampled datasets, each of which have the same number of points as the original dataset, obtained from random sampling with replacement of the original dataset. The fit is then performed for each of the resampled datasets. We used 1000 bootstraps (shaded magenta region in Fig. 4.5) to obtain the minimum and maximum slopes of the resampled datasets (dashed magenta lines in Fig. 4.5).

We plot the ratio of HαMRR and [OII]G10 SFRs as a function of stellar mass in Fig. 4.6. Our HαMRR and [OII]G10 SFR measurements were then compared to the SED-fitted SFRs. In Fig. 4.7 the HαMRR and [OII]G10 SFRs were plotted against SED-fitted SFRs. The same fitting procedure described above was used.

Our fitting procedure was also used to compare the HαSC, HαSC$'$ and HαM to [OII]G10 SFR and SED-fitted SFRs. However, these were not used in the analysis because they did not give the best prediction for dust as HαMRR.

[§] Documentation can be found at `http://www.astro.rug.nl/software/kapteyn/kmpfittutorial.html`

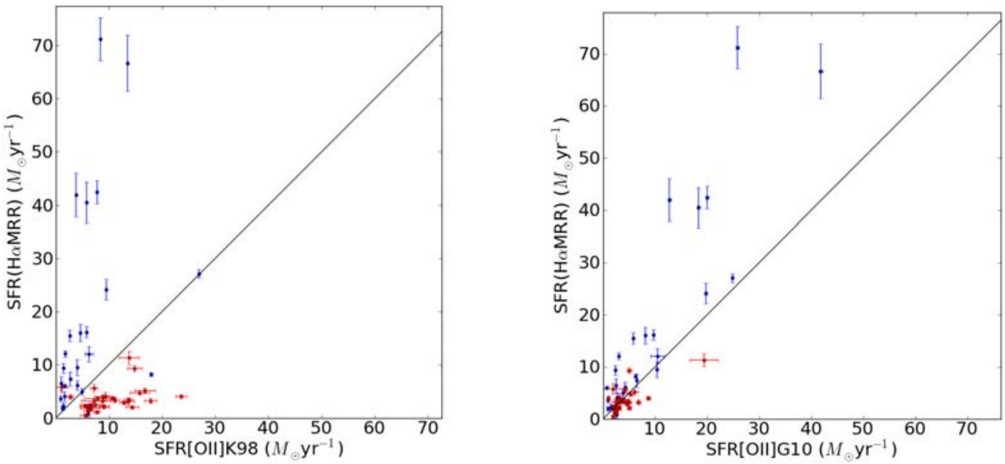

Figure 4.4: Left panel: The HαMRR SFR versus the nominal [OII]K98 SFR. The ESO sample (blue points) seems to have a steeper slope than the WFC3-ROLES (red points) sample. Right panel: The mass-dependent empirical correction ([OII]G10) was applied to the [OII]K98 SFRs and plotted against the HαMRR SFR. The black line is the 1-1 relation between the Hα SFR and [OII] SFR calibrated in the local Universe by Gilbank et al. (2010a).

4.1.4 Discussion

4.1.4.1 SFR Comparison

Seeing that our MRR dust extinction estimates give a good measure of the dust extinction, we now compare all further measurements using HαMRR as our nominal method. The scatter between the WFC3-ROLES and ESO Public data is large as seen in the left panel of Fig. 4.4 which shows the HαMRR SFRs with the [OII]K98 SFRs. The [OII]K98 calibration overestimates the SFR at the low-mass end and underestimates it at the high-mass end. We can also see that higher SFRs are predicted by Hα. In the right panel of Fig. 4.4, the two samples are brought into agreement using the [OII]G10 SFR, with the scatter between the two samples reduced. This shows that there is indeed a need to apply the mass-dependent empirical correction to [OII]. At the highest SFRs (highest masses), there are a few outliers that do not lie close to the 1-1 line. Most of our measurements, however, are at low SFRs (low masses). The best fit line has a slope of

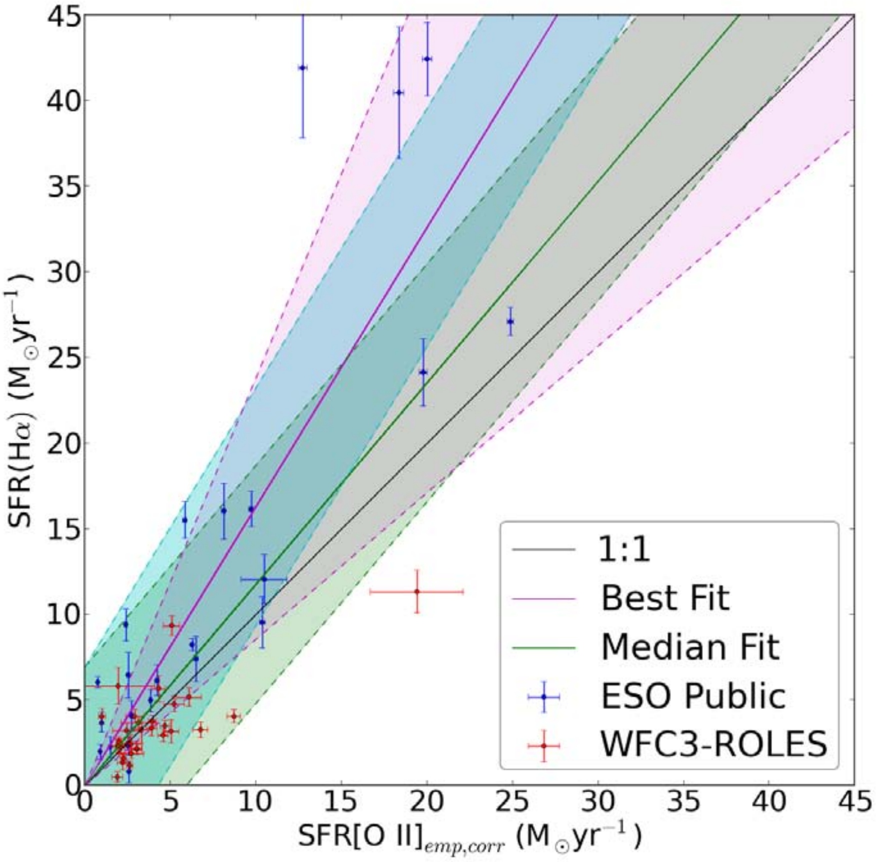

Figure 4.5: HαMRR SFR versus the mass-dependent empirically corrected [OII]G10 SFR of the WFC3-ROLES (red points) and ESO PUBLIC (blue) galaxies. The solid magenta line is the best fit line using the method of least squares and the shaded region is the confidence region from bootstrapping the data. The cyan shaded region shows the scatter about the best fit line from least squares fitting. The green line is the best fit line using the median of the ratios of the two indicators and the shaded green region shows the scatter. The black solid line is the 1:1 line.

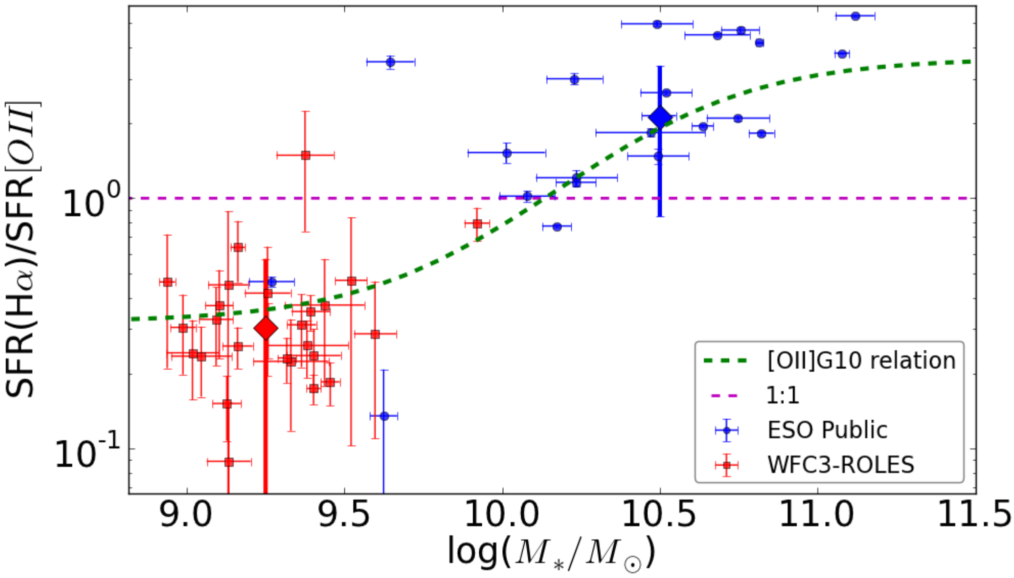

Figure 4.6: The Hα and [O II]K98 SFR ratio as a function of stellar mass. A clear residual trend is seen between the low and high masses where the median of the low mass galaxies (WFC3-ROLES; large red diamond) is lower than the high mass galaxies (ESO Public; large blue diamond). The green dashed line is the [OII]G10 relation. This confirms that [OII]G10 relation at z$\sim$1 is consistent with the [OII]G10 mass-dependent relation calibrated at z=0.1

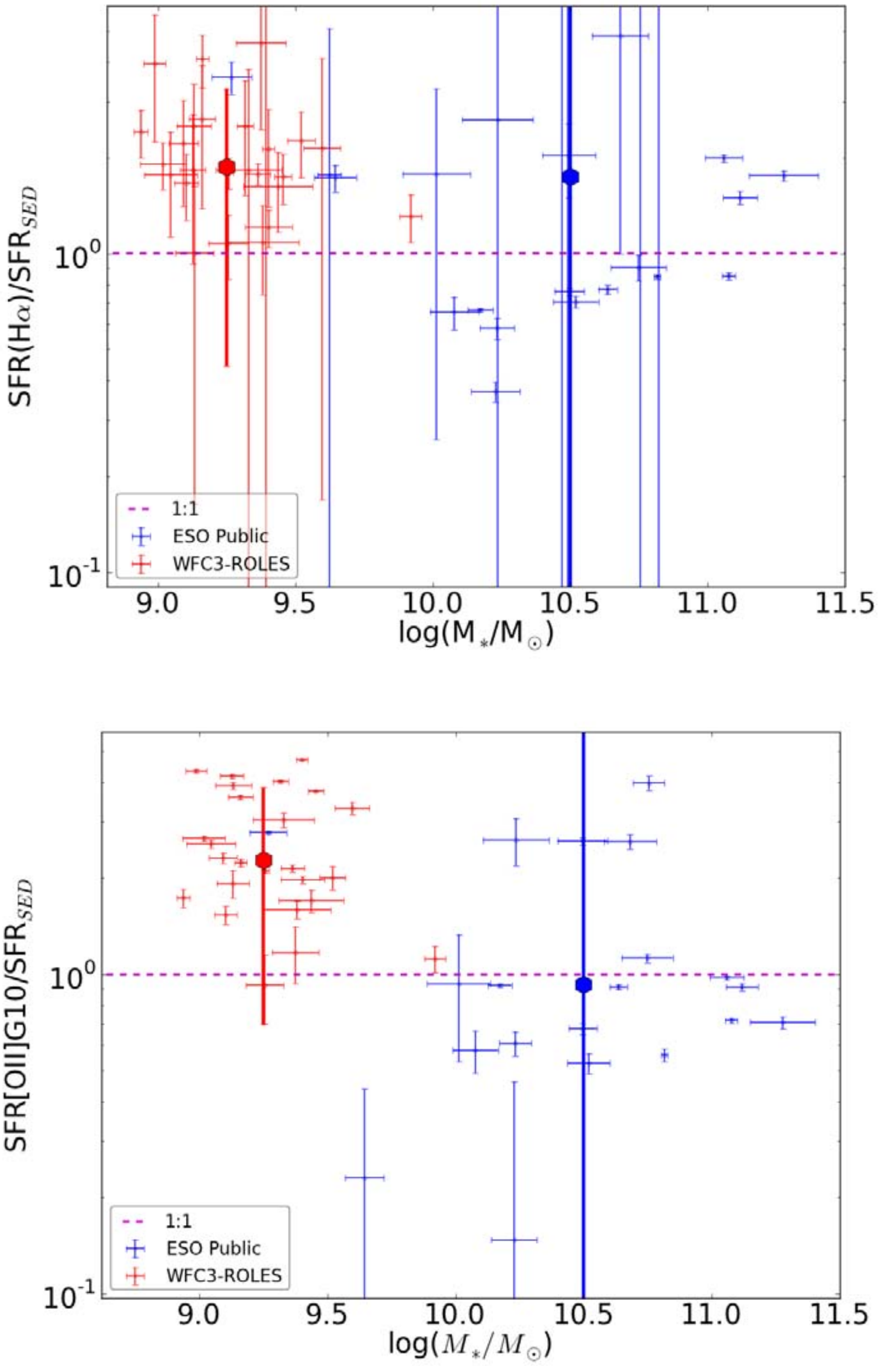

Figure 4.7: Same as Fig. 4.6 but taking the ratio of the HαMRR and [OII]G10 with the SED-fitted SFRs from Gilbank et al. (2010b).

1.1±0.5. The steep slope is probably driven by the few high mass outliers. This means that [OII]G10 SFR agrees well with HαMRR SFRs at $z\sim1$ and follows the 1-1 relation derived locally, within uncertainties.

In Fig. 4.6 we plot the ratio of the Hα and [OII]K98 SFRs as a function of stellar mass. A clear residual mass trend between the high and low mass galaxies is seen. Most of the WFC3-ROLES data (mostly low mass galaxies) lie below unity whereas most of the ESO Public data (mostly high mass galaxies) lie above unity. The median of the WFC3-ROLES data is 0.31±0.26 and the median for ESO Public data is 2.11±1.23. There is more scatter in the ESO Public data than the WFC3-ROLES data which means that the data are less well constrained at high masses. Most interesting is that the measurements follow the [OII]G10 relation (Eq. 4.10) within uncertainties. We see that at low masses and high masses the ratio is flat, and increases linearly in between. At low masses, the constant [OII] luminosity to SFR conversion underestimates the SFR relative to Hα by a factor of 3 and at high masses it overestimates the SFR relative to Hα by a factor of 2. This shows us that it is necessary to apply the mass-dependent [OII]G10 correction to [OII] SFRs rather than simply assuming a constant [OII] luminosity to SFR conversion. Furthermore, this confirms that the [OII]G10 relation at z∼1 is consistent with the [OII]G10 mass-dependent empirical relation calibrated at z∼0.1. We now compare the ratio of the HαMRR and SED-fitted SFRs as a function of stellar mass in the top panel of Fig. 4.7. There is no obvious residual trend with mass. The medians of the low mass and high mass samples are almost the same and lie close to unity. In the bottom panel of Fig. 4.7 we show the the ratio of the [OII]G10 and SED-fitted SFRs as a function of stellar mass. There is an obvious residual trend with mass where the median of the low mass galaxies is 2.5 times higher than the median of the high mass galaxies. Gilbank et al. (2010b) found that the SED-fitted SFRs are approximately 1.7 times higher than [OII]G10 for ROLES. We find that SED-fitted SFRs are 1.5 times higher than [OII]G10 which is consistent with the value in Gilbank et al. (2010b).

Other studies have used the [OII]G10 empirical correction. Mostek et al.

(2012) show how [OII]G10 correction compares to SFRs measured at z$\sim$1 using SFR fits from the UV/optical SEDs in the AEGIS survey. They found that the SED-fitted SFRs and the [OII]G10 empirically calibrated SFRs agree with 0.27 dex (1.86) scatter and have a mean offset of -0.06 dex (0.87).

Mok et al. (2013) used the [OII]G10 correction to obtain SFRs for a sample of galaxy groups from the Group Environment Evolution Collaboration 2 (GEEC2; Balogh 2011). They compared the SFRs derived from this method to SFRs calculated from using FUV SED-fits combined with 24μm. This measures the total star formation in the galaxy (obscured and unobscured). They noticed a systematic normalization offset between the difference of the two indicators. They found that the [OII] SFR estimated using [OII]G10 is underestimated by a factor of 3.1.

The reason that the SED-fitted values do not agree with each other from the two samples could be because of assumptions made in the fitting process (e.g. using different models). Also, the 24μm used by Mok et al. (2013) could be including some SF that we and Mostek et al. (2012) do not measure in our SED-fitted SFRs.

4.2 Systematic Uncertainties

The two main sources of uncertainty in our Hα SFRs are the [NII] correction to the blended (Hα+[NII]) flux and the correction for dust extinction. We used an average [NII]/Hα correction from Sobral et al. (2012) that was calibrated using local star-forming galaxies which is slightly less than the conventionally used 33%. Some studies have shown that the [NII]/Hα ratio increases with stellar mass (e.g. Erb et al. 2006). Furthermore the ratio, at any particular stellar mass, evolves with redshift (e.g. Erb et al. 2006). If the ratio has been overestimated for the low mass galaxies and underestimated for the high mass galaxies, it would result in the trend seen in our data. The typically used [NII]/Hα ratio is in the range 0.3-0.5 (Kennicutt & Kent 1983, Kennicutt 1992). Applying the extremes of this ratio to the data, bring the Hα SFR relative to [OII] SFR close to unity as possible but there still is a residual trend. Our results are therefore robust against any choice of [NII]/Hα correction in the range mentioned.

To investigate the effects that our choice of dust extinction model has on the measured SFRs, we consider what range of extreme fits to the data in Fig. 4.2 will best constrain our dust extinction values. First we want to check whether the residual mass trend seen in Fig. 4.6 is real or mainly due to systematic uncertainties. From Fig. 4.6 we see that to eliminate the mass-dependence (i.e., bring the Hα and [OII]SFRs into agreement), the Hα SFR must increase in the low mass galaxies and decrease in the high mass galaxies. This translates to increasing the extinction in the low mass galaxies and decreasing it in the high mass galaxies (SFR(Hα)$\propto 10^{0.4 A_{H\alpha}}$, Eq. 4.2). When we fitted the MRR relation (Eq. 4.11) for the high mass galaxies, we chose a point midway between the highest mass data points ($\log(M_*/M_\odot)$=11) of the Sobral et al. (2012) and Kashino et al. (2013) data. The reason being that this is where the dust extinction is expected to lie for our highest mass galaxies, if dust is expected to decrease with decreasing redshift. If we now fit a line through the median mass point ($\log(M_*/M_\odot)$=10.6) of the high mass galaxies in Fig. 4.2 and take this to be the minimum best fit, the dust extinction decreases by 0.5 mag. Hence, the Hα SFR relative to [OII] SFR decreases by a factor of 1.6 for the high mass galaxies. For the low mass galaxies, we fitted a constant extinction of 0.2 mag because it agreed with the Gilbank et al. (2010a) relation. If we now consider the maximum fit for the low mass galaxies to be consistent with the Garn & Best (2010) relation, the extinction increases by 0.3 mag. Hence, the Hα SFR relative to [OII] SFR increases by a factor of 1.3 for the low mass galaxies. Since these extreme fits do not flatten out the relation in Fig. 4.6, we can conclude that the mass dependence is not due to systematic uncertainties from the dust extinction.

Most of the uncertainty in dust extinction comes from the high mass galaxies. In Fig. 4.2, it can be seen that other studies measure higher values of dust extinction using Balmer decrement than our SED-fitted dust measurements for high mass galaxies. Furthermore, most of the data points from these studies follow the Garn & Best (2010) local relation. If we assume that the maximum best fit for high mass galaxies is the Garn & Best (2010) relation, then the extinction for the median mass point increases by 0.2 mag. This means that the Hα SFR increases by a factor of 1.2.

Another source of uncertainty comes from the number of active galactic nuclei (AGN) that may be present in our sample. The AGN contribution of the ROLES sample was tested in Gilbank et al. (2011) (Appendix C). They found that contamination by AGN is minimal (only 15 out of 311) and therefore neglecting them in the analysis will not affect our results significantly.

Model	Slope$_{med}$	σ_{res}	Slope$_{bestfit}$	σ_{res}
Hα[K98] vs [OII]G10	2.0	10.8	1.5±0.9	8.3
HαSC vs [OII]G10	1.1	4.9	1.0±0.06	4.552
HαSC$'$ vs [OII]G10	1.650	7.81	1.3±0.8	8.6
HαMRR vs [OII]G10	1.2	8.1	1.6±0.8	7.8
SFR(SED) vs HαSC	0.9	13.0	0.6±0.5	13.2
[OII]G10 vs SFR(SED)	0.91	12.0	0.6±0.4	3.1
HαMRR vs [OII]G10	1.0	4.2	0.7±0.4	3.1
HαMRR vs SFR(SED)	1.2	7.8	0.8±0.5	7.0

Table 4.1: Parameters and statistics from fit using the median of the ratio of the two indicators as the slope and from least squares fitting (`kmpfit`). The minimum and maximum slopes are from bootstrapping the data.

4.2.0.2 SSFR-mass Relation

The SSFR was computed by dividing the HαMRR SFR measurement by the galaxy's stellar mass (obtained from SED-fitting described in §4.1.2.8). We compare our measurements, as a function of stellar mass, with other studies at different redshifts in Fig. 4.8. The median SSFR in bins of stellar mass are shown as solid pink circles. The bin widths and median SSFRs are tabulated in Table 4.2.

Bin width ($\log(M_*/M_\odot)$)	N_{gal}	Median SSFR (yr^{-1})
8.5 - 9.5	28	-9.61 ± 0.06
9.5 - 10.5	19	-9.35 ± 0.09
10.5 - 11.5	8	-8.73 ± 0.13

Table 4.2: The sizes of the bins and the number of galaxies they contain. The median SSFR for each bin is also shown.

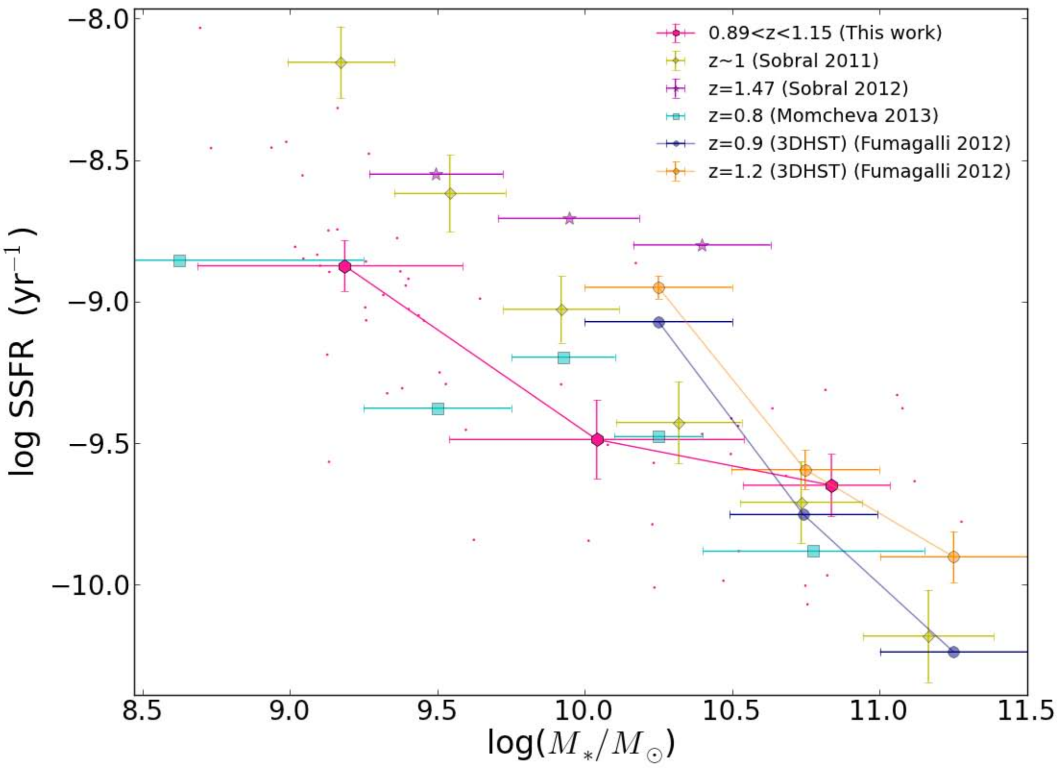

Figure 4.8: SSFR-mass relation where the SSFR has been measured with Hα. We compare our median SSFR measurements (pink circles; individual galaxies shown as pink dots) to the measurements from Momcheva et al. (2013) (cyan squares), Fumagalli et al. (2012) (navy and orange circles), Sobral et al. (2011) (yellow diamonds) and Sobral et al. (2012) (magenta stars). The trend is that low mass galaxies have higher SSFRs than high mass galaxies.

Fig. 4.8 shows that our SSFRs decline with increasing stellar mass which is consistent with the trend seen in the comparison samples at similar redshifts using Hα. The low mass galaxies have a higher SSFR than the more massive galaxies. The median SSFRs of our WFC3-OII sample at z∼1 decreases from log(SSFR) = -8.7 yr^{-1} in the lowest mass bin to log(SSFR)= -9.6 yr^{-1} in the highest mass bin. The samples closest to our redshift range are the Fumagalli et al. (2012) and Sobral et al. (2011) at z∼0.9 and z=1 respectively.

The median SSFR in our highest mass bin agrees within uncertainty with the mean SSFR in the middle mass bin of Fumagalli et al. (2012). Their sample uses HST data from the WFC3 grism which is the same as our data. Their measurements also include the blending of Hα and [NII]. Their measurements also include the blending of Hα and [NII]. We corrected for this by assuming the same [NII]/(Hα+ [NII]) ratio (i.e., 0.25) we used to correct our Hα fluxes. This now makes their results a fair comparison to our results. However, they state that they only probe the massive galaxies ($>10^{10}M_{\odot}$) at a detection limit corresponding to SFR = 2.8 M$_{\odot}$ yr^{-1} .

Our SSFRs in the intermediate and highest mass bins agree well, within the uncertainties, with the Sobral et al. (2011) sample. At low masses our SSFRs are much lower than Sobral et al. (2011). This is because of a selection bias in their sample due to the fixed SFR limit of >3 M$_{\odot}$ yr^{-1} . At the lowest masses probed, low SSFR galaxies fall below the selection limit, biasing the median SSFRs upwards. They found that this bias becomes significant at masses below $\sim 10^{10}M_{\odot}$. Hence, our sample gives a better SSFR measurement for the low mass (low SFR) galaxies.

We converted the binned stellar masses and SFRs from Momcheva et al. (2013) into binned SSFRs. Their data also agree with our measurements across stellar masses. The mass limit for their sample is $M_{*}>10^{9}M_{\odot}$ but they have a few galaxies with masses as low as $10^{8}M_{\odot}$. They used stacking techniques to obtain their measurements. The problem with stacking is mainly systematics. One can only obtain the average properties of the stacked sample and not individual measurements.

The data from Sobral et al. (2012) also show the downward trend in SSFRs with mass but their values are all higher than the other studies shown. They have a limiting SFR of $7\mathrm{M}_{\odot}$ yr^{-1} and a mass limit of $9.5M_{\odot}$ meaning that they only detect the brightest galaxies with high SFRs at their low mass limit and are incomplete.

In terms of evolution, the SSFR-mass relation has a lower normalization at $z{\sim}0.1$ than it did at $z{\sim}1$ as seen in Fig. 4.10. At higher masses the relation evolves almost in parallel as shown by Gilbank et al. (2011) using [OII]. Our Hα measurements are consistent with the ROLES [OII] measurements at the lower masses ($\log(\frac{M_*}{M_\odot}) < 9.5$) where we have most of our data. One can see that lowering the detection threshold for Hα in our sample (as discussed in §3.2.2) will bring the slope closer to the [OII]SSFR for low masses. At higher masses we see that some of the detection limits fall below the local value.

We have mentioned that for the high mass galaxies (low SSFR), the SED-fitted dust extinction is underestimated which is why we empirically correct our dust measurements as a function of stellar mass. Our SED-fitted dust measurements only measure the dust extinction experienced by the stellar continuum (Eq. 4.5). At the same time as this work, a study by Price et al. (2013) also found that estimating the dust extinction experienced by stellar continuum only, underestimates the dust extinction in high mass (low SSFR) galaxies. They find that an extra amount of extinction, experienced by the nebular gas emission line, is needed. For low mass (high SSFR) galaxies, the extinction experienced by the stellar continuum and the extinction suffered by the emission line is the same. This is illustrated in Fig. 4.9.

4.2.1 Comparison of SSFR-mass with a Tau Model

The SSFR-mass relation can be modeled using a simple toy (τ) model (e.g. Noeske et al. 2007a, Leitner 2012). We use the method employed by Gilbank

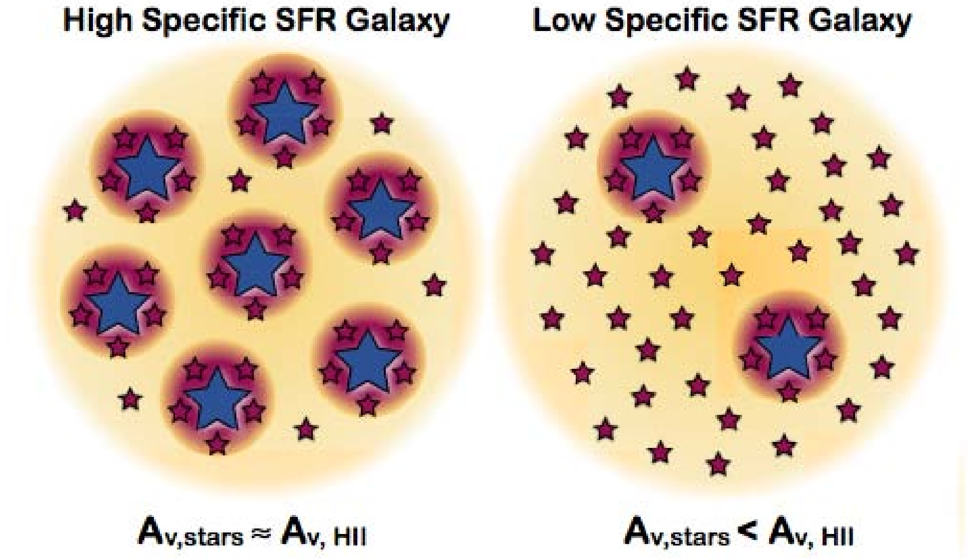

Figure 4.9: Illustration by Price et al. (2013) showing that for low mass (high SSFR) galaxies, the dust extinction from gas and stars is the same. However, in high mass (low SSFR) galaxies, the dust extinction from gas is lower than from the stars meaning that high mass galaxies require an extra extinction correction. The result is confirmed in this work.

et al. (2011) who followed the prescription of Noeske et al. (2007a). This toy model parameterizes the SFH of galaxies as a function of their baryonic mass.

The toy model was constructed by assuming a closed-box model and making the instantaneous recycling approximation. The baryonic mass is initially all gas and over time some of this gas forms stars making the baryonic mass a sum of the stellar mass and gas mass. If the SFR is related to the mass of the gas, M$_g$, by a star formation efficiency factor ϵ,

$$SFR = \epsilon M_g \tag{4.14}$$

and then assume a fraction, R of the stellar mass formed is returned to the interstellar medium instantly, this leads to an SFR that declines exponentially with a timescale of τ (or e-folding time),

$$SFR(M_b, z) = SFR(M_b, z_f)\exp(\frac{-T}{\tau}) \tag{4.15}$$

where τ=1/[ϵ(1-R)] , z_f is the formation redshift for when the stars first formed and M$_b$ is the baryonic mass of the galaxy (M$_b$ =M$_g$ at z=z_f initially),

$$T = t(z) - t(z_f) \tag{4.16}$$

where $t(z)$ is the cosmic time at which the galaxy is observed (i.e. at z) and $t(z_f)$ is the cosmic time at z_f. This then implies that,

$$SFR(M_b, z_f) = \epsilon M_b = \frac{M_b}{\tau(1-R)} \tag{4.17}$$

Then using the following for the relation for the stellar mass, M_*, which is the integrated SFR at time t,

$$M_* = \int_{t(z_f)}^{t(z)} SFR(t)\,\mathrm{d}t, \tag{4.18}$$

and combining this with Eq. 4.18 gives

$$SFR(M_b, z) = \frac{M_b}{\tau(1-R)}[1 - \exp(\frac{-T}{\tau})] \tag{4.19}$$

This 4.19 gives M_* and the SFR in terms of the star formation timescale τ, baryonic mass M_b and formation redshift (z_f) of the stars. The value of R used is 0.5 (Kroupa IMF; Bell et al. 2005)¶. This value can be estimated from stellar population theory. In Noeske et al. (2007a), they parameterized τ as a power law of the baryonic mass,

$$\tau = c_\alpha M_b^\alpha. \tag{4.20}$$

Initially Noeske et al. (2007a) assumed a constant formation redshift (z_f ~2) but found that this only reproduces the SSFR and its evolution for galaxies with masses $\geq 10^{10}$M$_\odot$ yr^{-1} . For the low mass galaxies, the model underestimates the SSFR and he obtains a flat slope (Fig.1 in Noeske et al. 2007a). They then parameterized z_f as a power law of the baryonic mass so that the average onset of SF is delayed in the less massive galaxies and the high SSFRs in the low-mass galaxies are reproduced.

$$1 + z_f = c_\beta M_b^\beta \tag{4.21}$$

This model interprets high SSFRs (low masses) as the early epoch of smooth SFH with lower formation timescales. The best fit parameters for Eq. 4.20 and Eq. 4.21 depends on systematics of the SFR and mass estimates and the IMF. Also the dependence of τ is mainly constrained by the high mass galaxies and the dependence of z_f by the lower masses.

Due to the high-mass limit in the DEEP2 data used by Noeske et al. (2007a), they could only measure the SSFRs for the highest mass galaxies (~10^{11}). Gilbank et al. (2011) fitted the SSFR for the low mass ROLES galaxies and the local SDSS data (shown in Fig. 4.10) and found best fit parameters of [logc_α=20.42, α=-0.99, logc_β -2.68, β=0.31]. Our SSFRs are all systematically higher than the ROLES [OII] SSFRs with the highest

---

¶Leitner (2012) developed a model where the gas fraction is allowed to vary offset seen at the lowest masses. Assuming that the Gilbank et al. (2011) model gives the minimum formation timescale, we can change the slope of z_f to obtain the maximum formation timescale. However, this is not simultaneously fit at multiple redshifts as done by Gilbank et al. (2011) and Noeske et al. (2007a). We do this for illustrative purposes to check that we get a slope that is reasonably consistent to constrain the formation timescale. If we decrease the slope by 0.1, our median SSFRs agree well with the model, so β lies between 0.29 and 0.31. Gilbank et al. (2011) found that with the best fit parameters of the model, a galaxy with $\log(M_{\odot}/M_{*})$=[9, 11], the typical z_f would be [1.7, 4.0] and τ=[34, 4] Gyr. With our slope of 0.29, the formation redshift for a galaxy with $\log M_{\odot}/M_{*}$=9 is 1.2 with a τ of 17 Gyr. This long SF timescale, with an e-folding time longer than the age of the Universe, means that low mass galaxies have essentially constant SFRs.

Our steeper slope translates into a more recent formation redshift (z_f=1.2) meaning that, in this toy model, the low mass galaxies have just been formed at the epoch of observation. If we take our results and the Gilbank et al. (2011) results to bracket the range of formation redshifts for low mass galaxies, this gives us $1.2 \leq z_f \leq 1.7$ for $\log(M_{\odot}/M_{*})$=9.

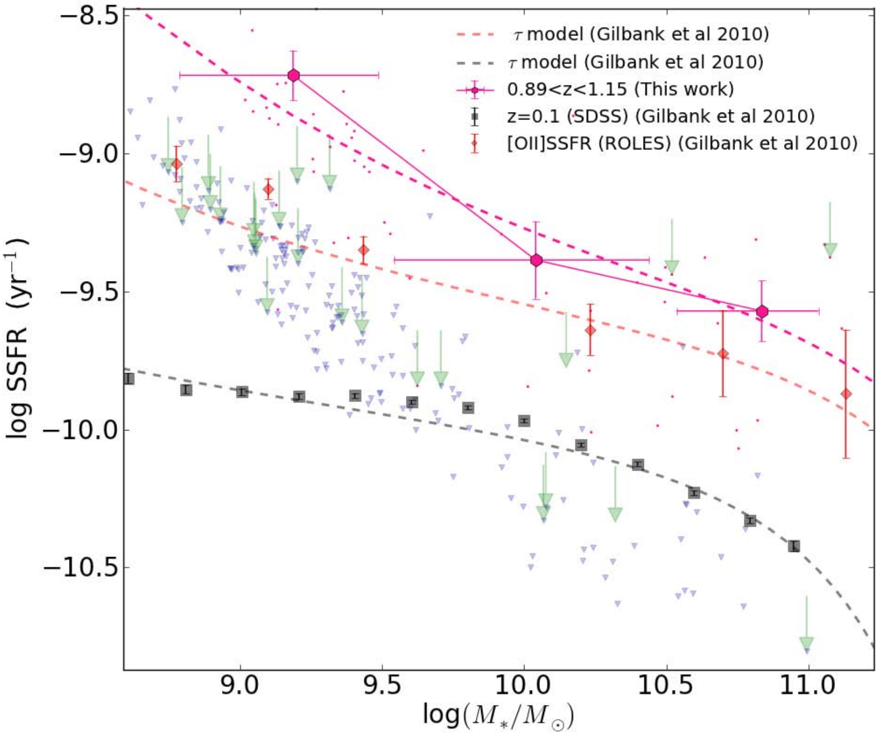

Figure 4.10: SSFR-mass relation where the SSFR has been measured with Hα for this work Pink circles and [OII] from Gilbank et al. (2010a). The local SSFR using Hα is also shown black squares. The 5σ limits (green arrows) and 4σ detection limits for the Hα line (blue triangles) are also shown. The dashed lines represent τ model fits to the data (see text for details). The SSFRs in low mass galaxies have a steeper relation at $z{\sim}1$ than locally. This means that they form their stars later than massive galaxies and on shorter timescales.

Chapter 5

Conclusion and Future Work

We have studied a sample of low-mass galaxies ($M_{*}<10^{9.5}M_{\odot}$) taken from the ROLES survey at $z{\sim}1$ with the aim of determining their SFRs using a more reliable SFR indicator, Hα . These systems were analyzed using NIR slitless spectroscopic data from HST. We measured the Hα emission line luminosities and converted these into SFRs.

We have shown that SED-fitted dust extinction in the V-band is a good diagnostic to estimate extinction in the absence of Balmer decrement measurements (which is the standard way of estimating dust) for low mass galaxies. However, SED-fitted dust measurements underestimate the dust extinction for high mass galaxies. This result was recently confirmed by Price et al. (2013) who showed that high mass galaxies require extra extinction. We derived an empirical mass-dependent correction to correct for the extra dust extinction needed in high mass galaxies. This correction was then used to correct our Hα SFRs for dust extinction. For the low mass galaxies, our dust extinction estimates follow the local relation derived by Gilbank et al. (2010a) meaning that dust does not evolve significantly between $z{\sim}1$ and the present day.

In ROLES, they studied galaxy properties by measuring [OII] emission line luminosities. In this study, we were able to compare their SFRs with our more direct Hα SFRs. Their [OII] SFRs were determined using a mass-dependent empirical correction by Gilbank et al. (2010b), which was calibrated for galaxies in the Local Universe. We have shown that the empirically corrected SFRs agree well with our dust corrected Hα SFRs. This confirms that the locally derived relation does indeed work at $z\sim1$ for the low mass galaxies.

We studied the Hα SSFR-mass relation of these low mass galaxies for the first time with spectroscopy. We have confirmed previous results that at $z\sim1$ the low mass galaxies form their stars later and on longer timescales than their high mass counterparts. However, we have pushed to lower limiting SFRs and lower stellar masses than any previous studies, placing tighter constraints on the evolution of galaxies at this epoch.

5.1 Future work

One of the factors that impact our results is the incompleteness (but we are still more complete than any Hα other study at $z\sim1$) of our sample. We were only able to obtain a handful of detections because 3DHST does not go deep enough to probe the SFRs expected for these low stellar masses ($M_* \sim 10^{8.5} M_\odot$) of our selected sample from ROLES. This is the main problem with the majority of galaxy surveys. They do not probe down to very low stellar masses (low SFRs) and therefore any observed trends in galaxy properties are biased towards the brightest, most massive galaxies. It is therefore necessary to have surveys that probe down to the low mass regime at high redshifts in order to get a complete understanding of galaxy formation. Future telescopes such as the *James Webb Space Telescope*[*] (*JWST*) and *Euclid*[†], will have NIR instruments that provide

---

[*] http://www.jwst.nasa.gov/

[†] http://www.euclid-ec.org/

better sensitivity to carry out deep large field infrared surveys. This will also increase the number of low mass galaxies observed meaning that we can get a better statistical representation of their properties. We cannot consider the MIPS-24 data in our analysis. The details for this are given in (Appendix B1.1 and Appendix B2.2) of Gilbank et al. (2011). Briefly, the main disadvantage of MIPS photometry is that the PSF is fairly large (6 arcseconds) and so faint sources (such as the low mass galaxies) become confused. By considering only isolated ROLES galaxies, they found that the majority of the WFC3-ROLES galaxies are not detected down to the SFR limit ($0.7\mathrm{M}_{\odot}\ \mathrm{yr}^{-1}$) of the 24um photometry in the GOOD-S field at z∼1.

Two new current and upcoming radio facilities will give us a new window into the physical conditions for star formation in these galaxies. In December 2013, we proposed for ALMA[‡] cycle 2 time, to observe CO (as a proxy for molecular hydrogen) in our sample. This traces directly the cold molecular gas which is the fuel for star formation. The Hα spectroscopic redshifts presented in this thesis greatly strengthen the case (by both confirming the [OII] redshift and providing a cleaner tracer of SFR) for obtaining ALMA time.

Using radio continuum observations, we will be able to measure the SFR without having to correct for dust, leading to more accurate measurements. There are existing deep radio observations of the GOOD-S field from the VLA[§] but these do not go deep enough to measure the SFR of our galaxies. For example, the upcoming deep survey MIGHTEE on the MeerKAT[¶] will observe this field as part of their observations starting in 2017. In the more distant future, the Square Kilometre Array (SKA) will provide the best sensitivity to study these galaxies at radio wavelengths. This work can be extended to even higher redshifts ($z>1$) in the future to study the evolution of this important galaxy population.

[‡] http://www.almascience.eso.org

[§] http://www.vla.nrao.edu/

[¶] South Africa's SKA precursor array

Furthermore, our field is scheduled to be observed by the MeerKAT LADUMA survey (Holwerda et al. 2012), starting 2017, which will be the deepest survey of neutral hydrogen (HI) to date. In combination, all these techniques will enable the study of the interplay of the gas and star formation processes in this previously unexplored regime.

Appendix A

All spectra used in catalogue

Presented here are plots of all the spectra used in our final catalogue. The magenta vertical lines indicate sidebands within which the continuum was estimated. The blue circles are the median values of the continuum flux in each sideband and the green line shows the straight line fit to the continuum. The red dashed line shows the expected position of the emission line. The green triangle represents the position of the peak within the defined search window represented by the dashed orange lines. Also shown in each panel are the values of the S/N of the line and uncertainty on the flux (ergs cm^{-2} s^{-1}) The first value in the title of each spectrum is the aXe ID, the second is the ROLES ID and the third is the pointing number.

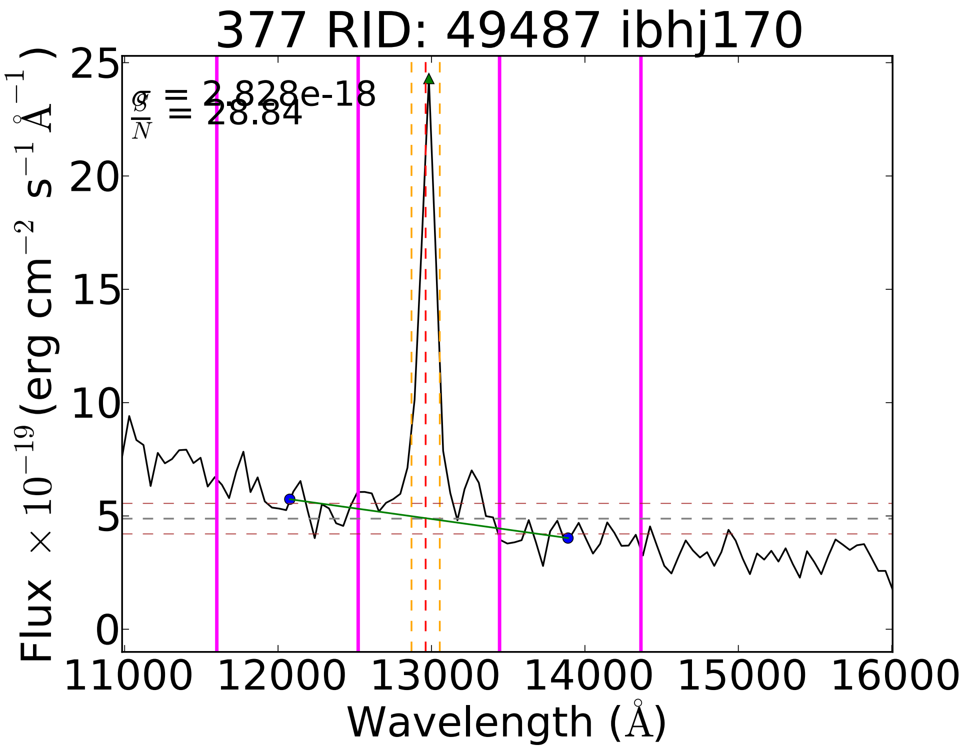
377 RID: 49487 ibhj170

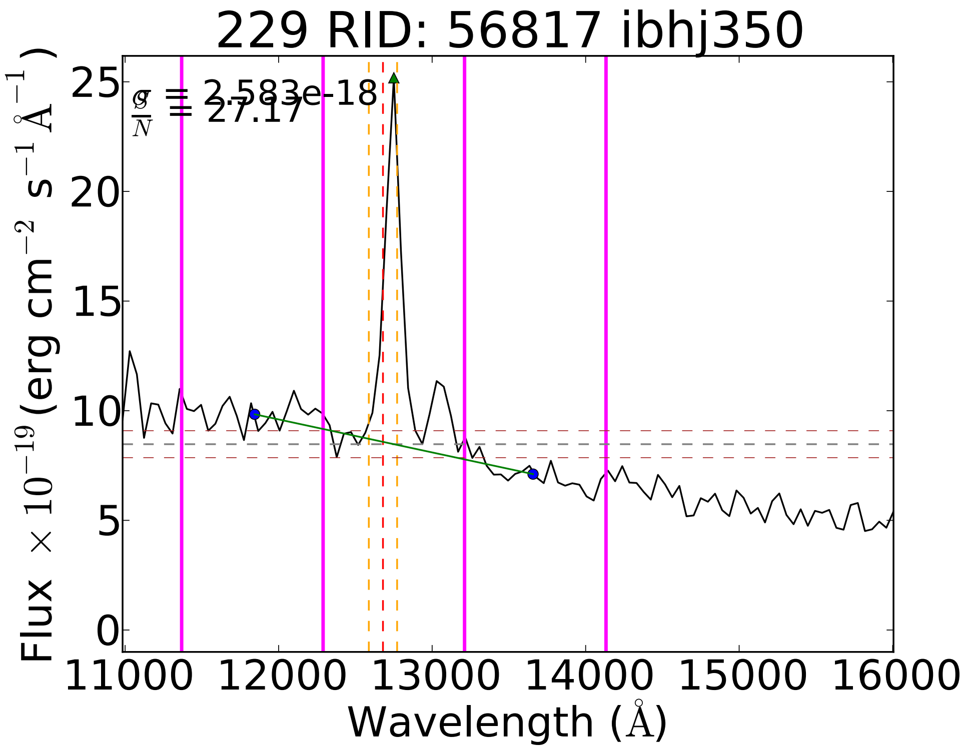
229 RID: 56817 ibhj350

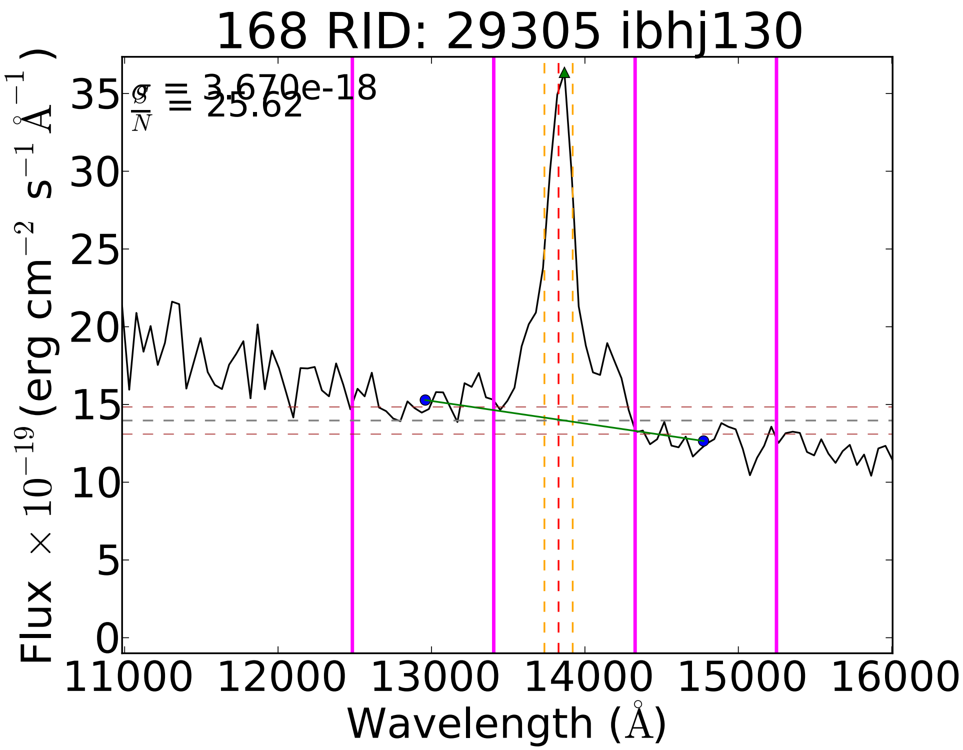
168 RID: 29305 ibhj130

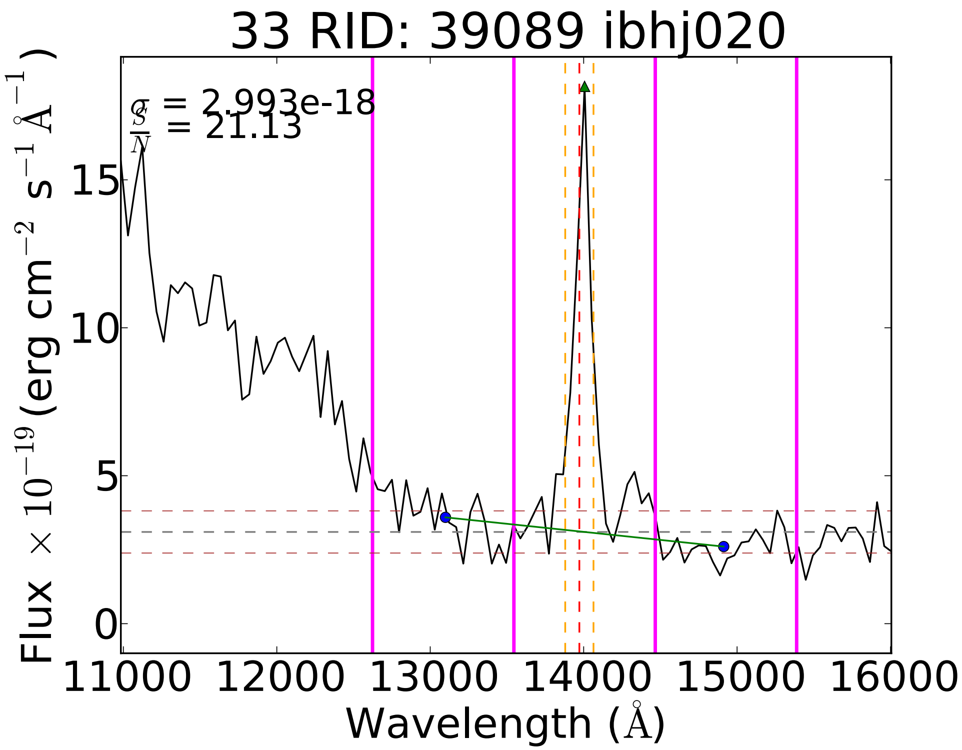
33 RID: 39089 ibhj020

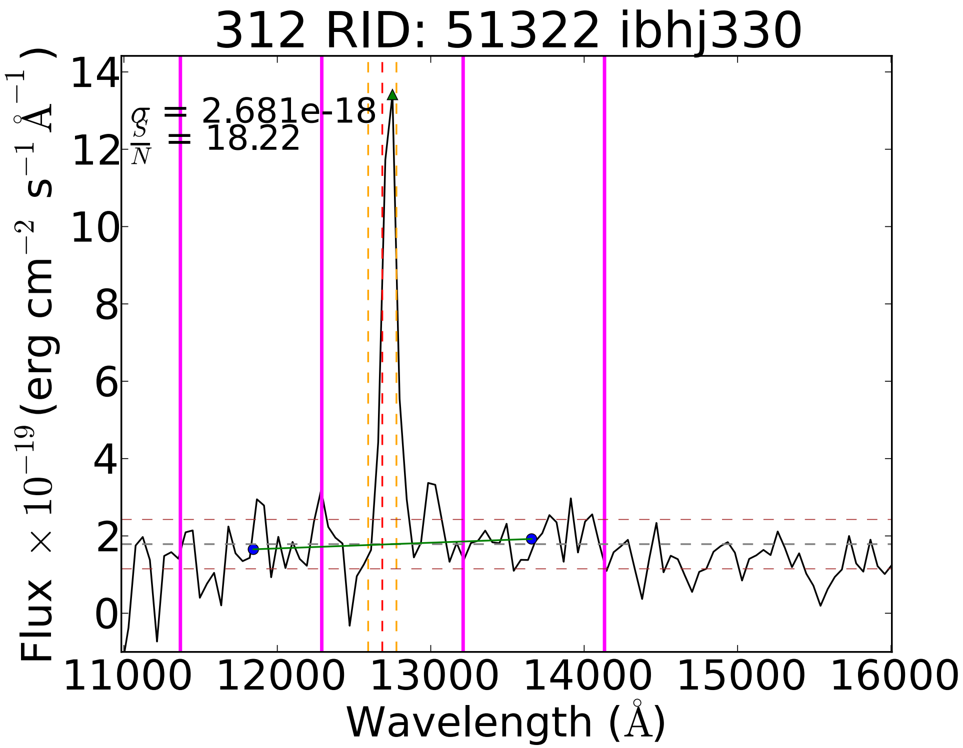
312 RID: 51322 ibhj330
σ = 2.681e-18
$\frac{S}{N}$ = 18.22
Flux $\times 10^{-19}$ (erg cm^{-2} s^{-1} Å^{-1})
Wavelength (Å)
0
2
4
6
8
10
12
14
11000
12000
13000
14000
15000
16000

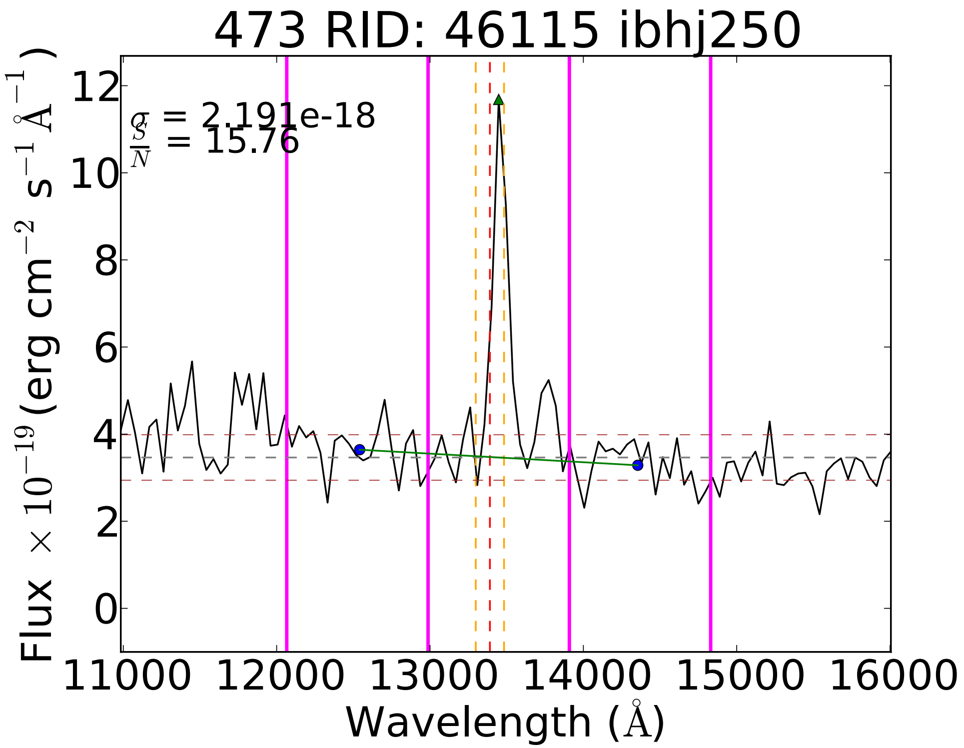
473 RID: 46115 ibhj250
σ = 2.191e-18
$\frac{S}{N}$ = 15.76
Flux $\times 10^{-19}$ (erg cm^{-2} s^{-1} Å^{-1})
Wavelength (Å)
0
2
4
6
8
10
12
11000
12000
13000
14000
15000
16000

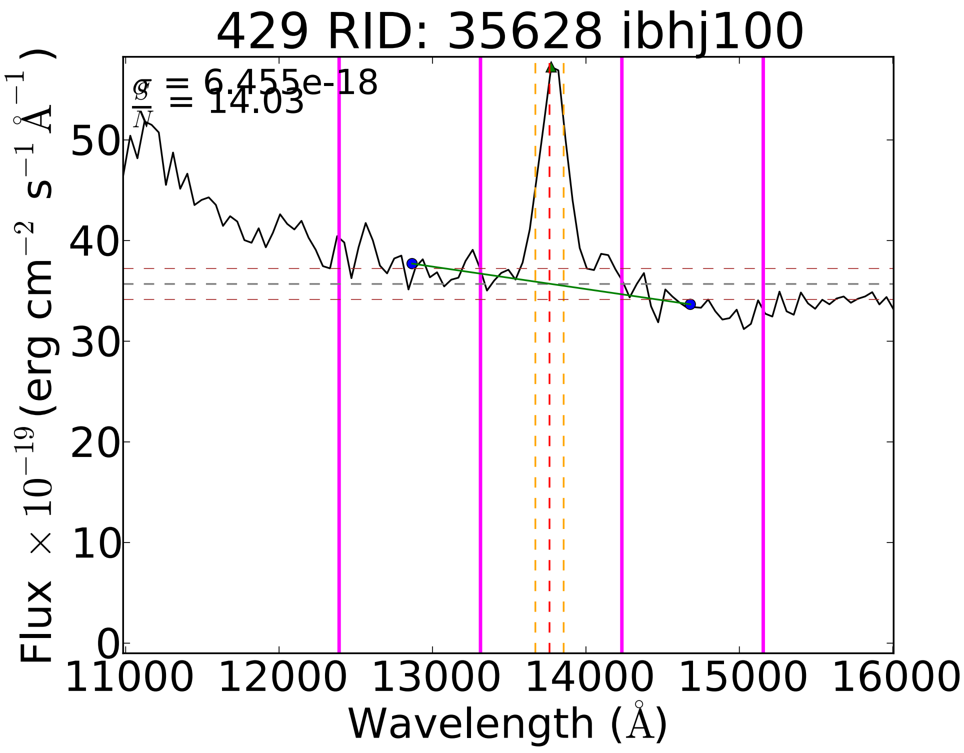
429 RID: 35628 ibhj100
σ = 6.455e-18
$\frac{S}{N}$ = 14.03
Flux $\times 10^{-19}$ (erg cm^{-2} s^{-1} Å^{-1})
Wavelength (Å)
0
10
20
30
40
50
11000
12000
13000
14000
15000
16000

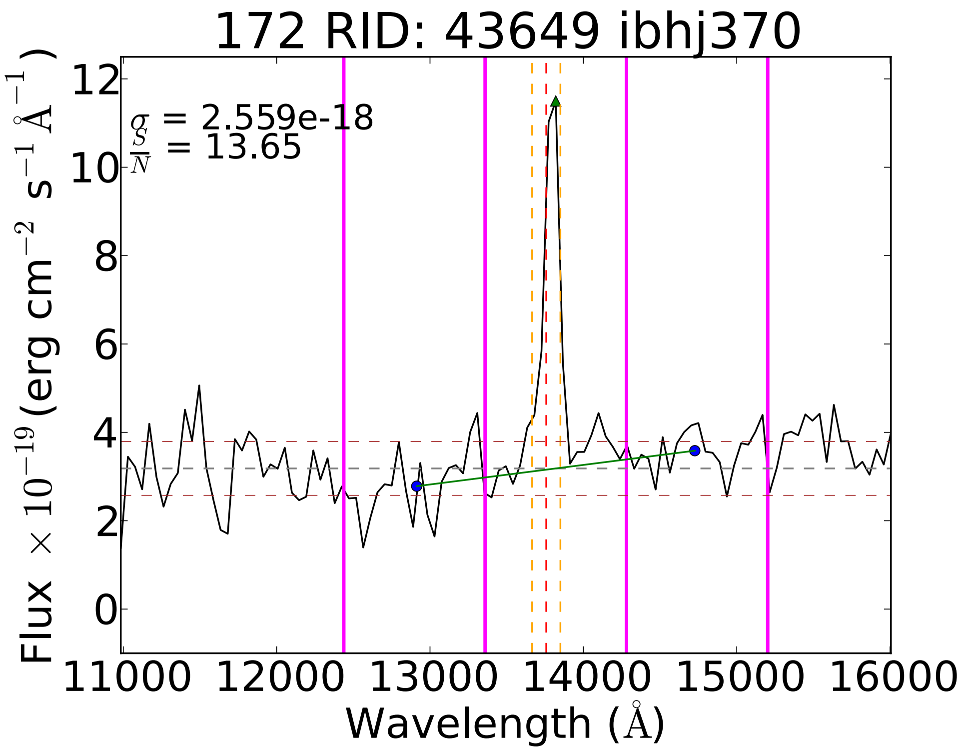
172 RID: 43649 ibhj370
σ = 2.559e-18
$\frac{S}{N}$ = 13.65
Flux $\times 10^{-19}$ (erg cm^{-2} s^{-1} Å^{-1})
Wavelength (Å)
0
2
4
6
8
10
12
11000
12000
13000
14000
15000
16000

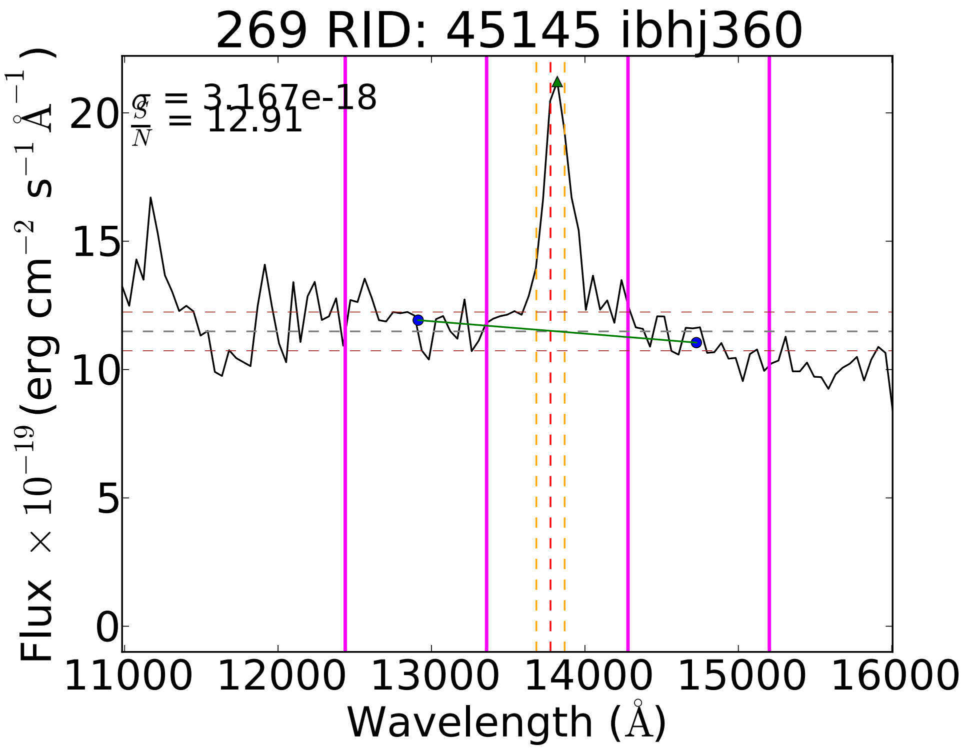
269 RID: 45145 ibhj360
σ = 3.167e-18
$\frac{S}{N}$ = 12.91
Flux $\times 10^{-19}$ (erg cm^{-2} s^{-1} Å^{-1})
Wavelength (Å)
0
5
10
15
20
11000
12000
13000
14000
15000
16000

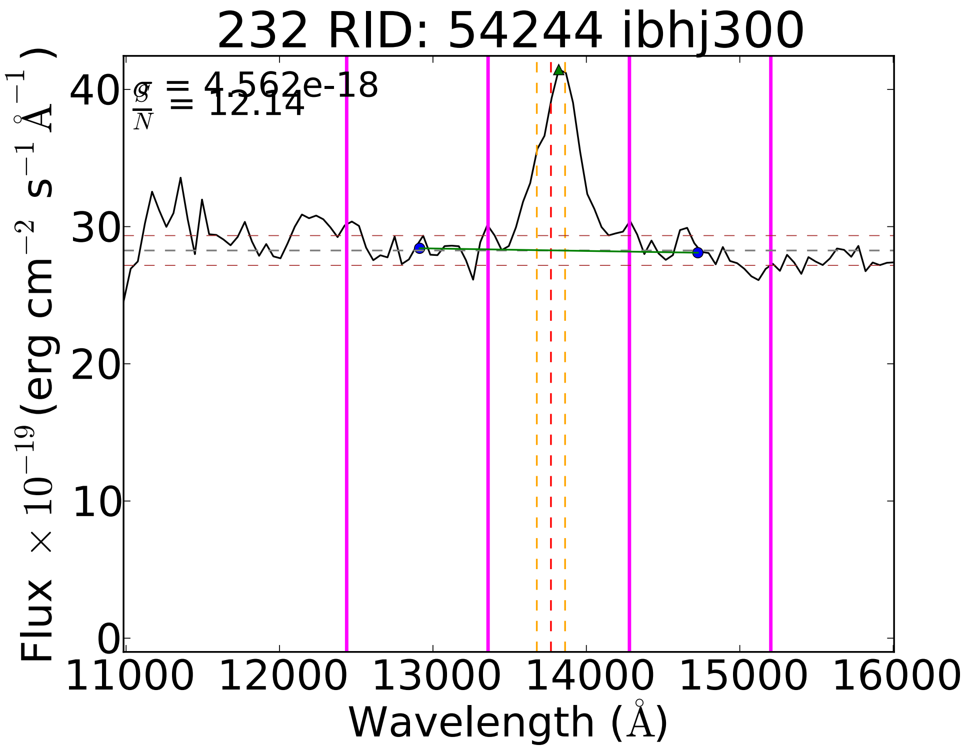
232 RID: 54244 ibhj300
σ = 4.562e-18
$\frac{S}{N}$ = 12.14
Flux $\times 10^{-19}$ (erg cm^{-2} s^{-1} Å^{-1})
Wavelength (Å)
0
10
20
30
40
11000
12000
13000
14000
15000
16000

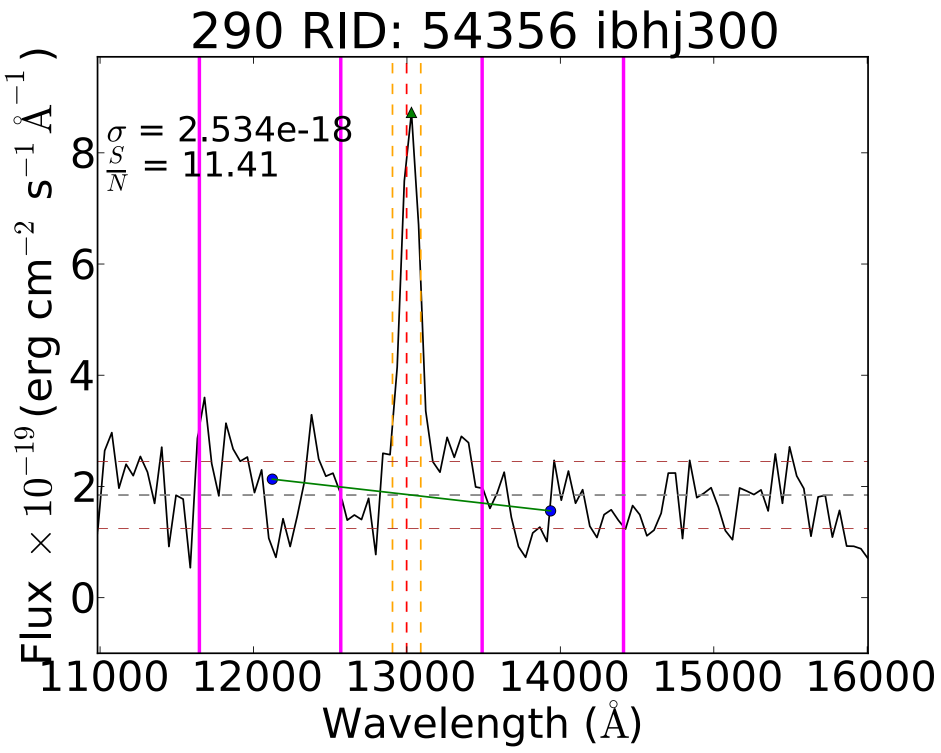
290 RID: 54356 ibhj300
σ = 2.534e-18
$\frac{S}{N}$ = 11.41
Flux $\times 10^{-19}$ (erg cm^{-2} s^{-1} Å^{-1})
Wavelength (Å)
0
2
4
6
8
11000
12000
13000
14000
15000
16000

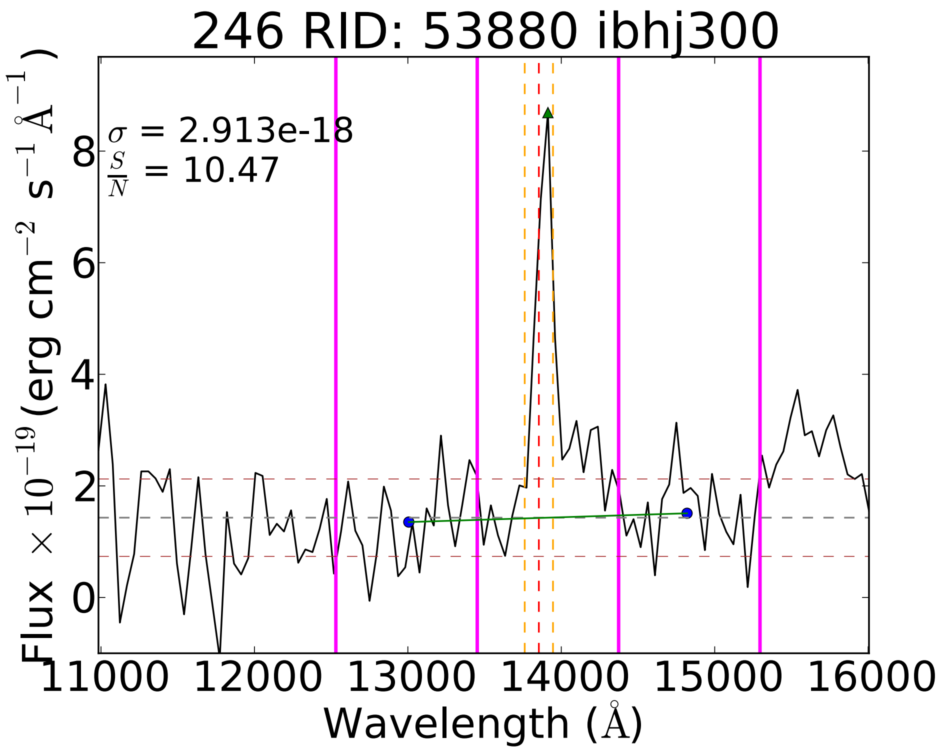
246 RID: 53880 ibhj300
σ = 2.913e-18
$\frac{S}{N}$ = 10.47
Flux $\times 10^{-19}$ (erg cm^{-2} s^{-1} Å^{-1})
Wavelength (Å)
0
2
4
6
8
11000
12000
13000
14000
15000
16000

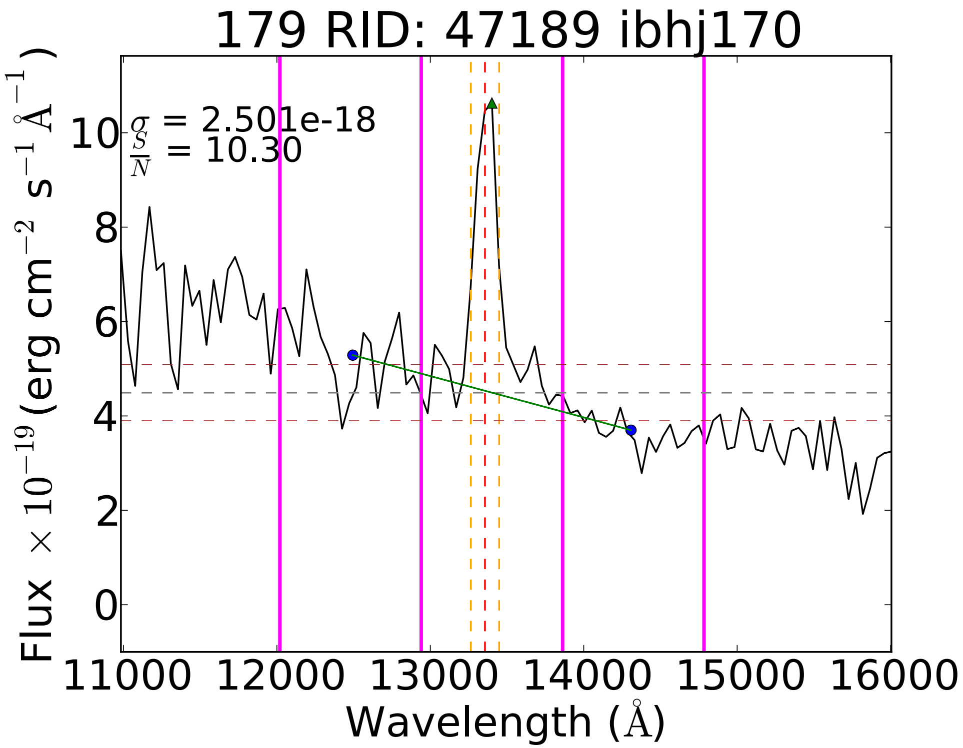
179 RID: 47189 ibhj170
σ = 2.501e-18
S/N = 10.30
Flux × 10^−19 (erg cm^−2 s^−1 Å^−1)
Wavelength (Å)
0
2
4
6
8
10
11000
12000
13000
14000
15000
16000

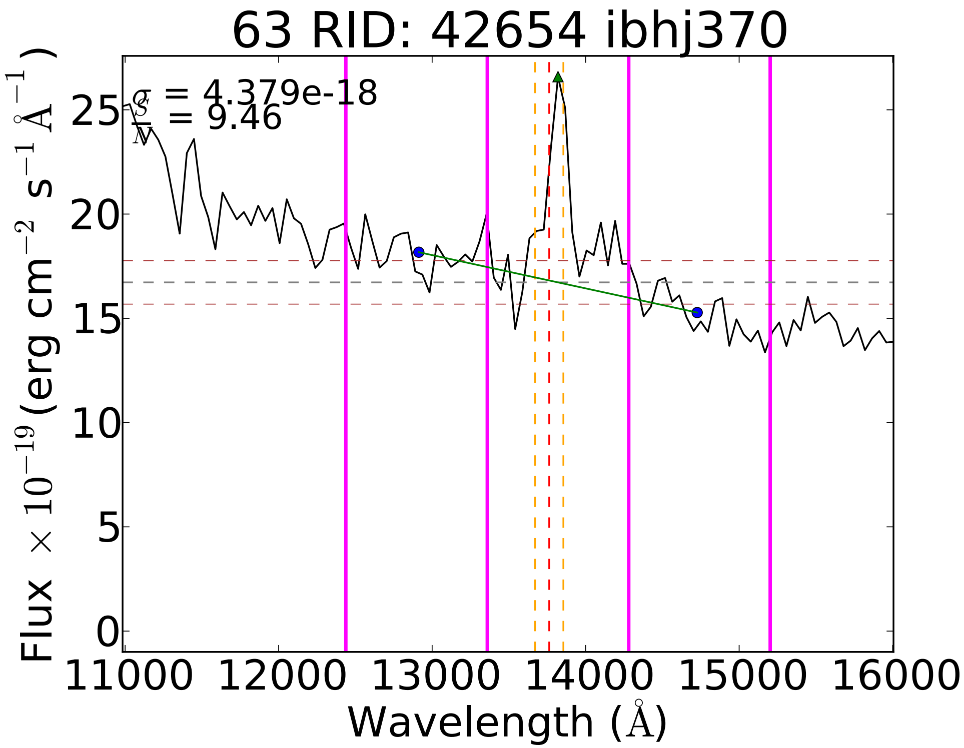
63 RID: 42654 ibhj370
σ = 4.379e-18
S/N = 9.46
Flux × 10^−19 (erg cm^−2 s^−1 Å^−1)
Wavelength (Å)
0
5
10
15
20
25
11000
12000
13000
14000
15000
16000

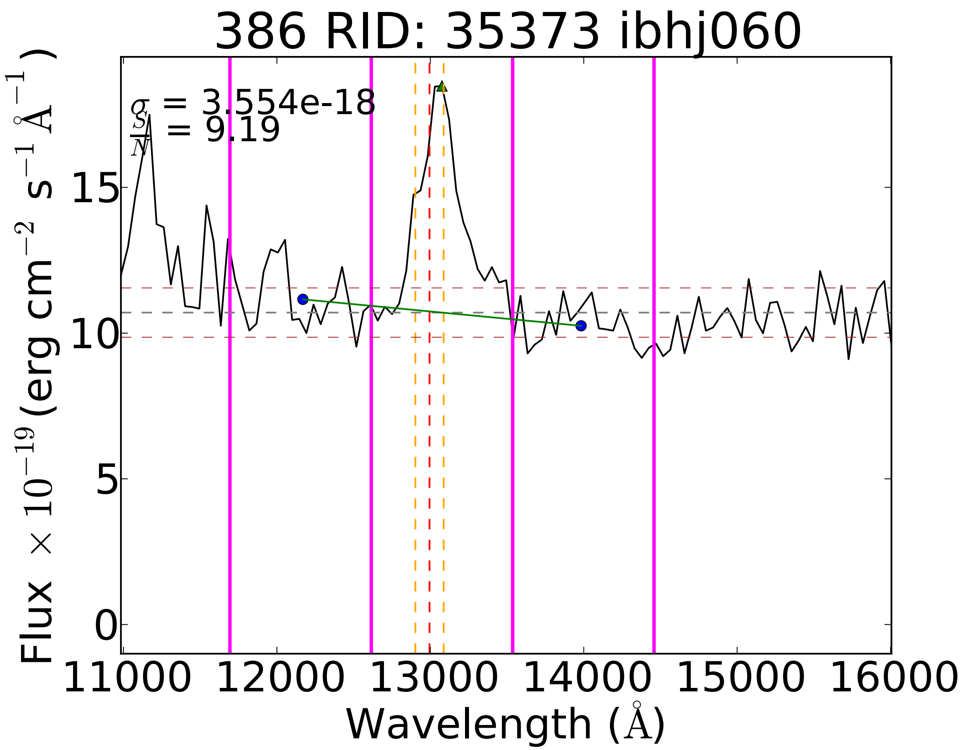
386 RID: 35373 ibhj060
σ = 3.554e-18
S/N = 9.19
Flux × 10^−19 (erg cm^−2 s^−1 Å^−1)
Wavelength (Å)
0
5
10
15
11000
12000
13000
14000
15000
16000

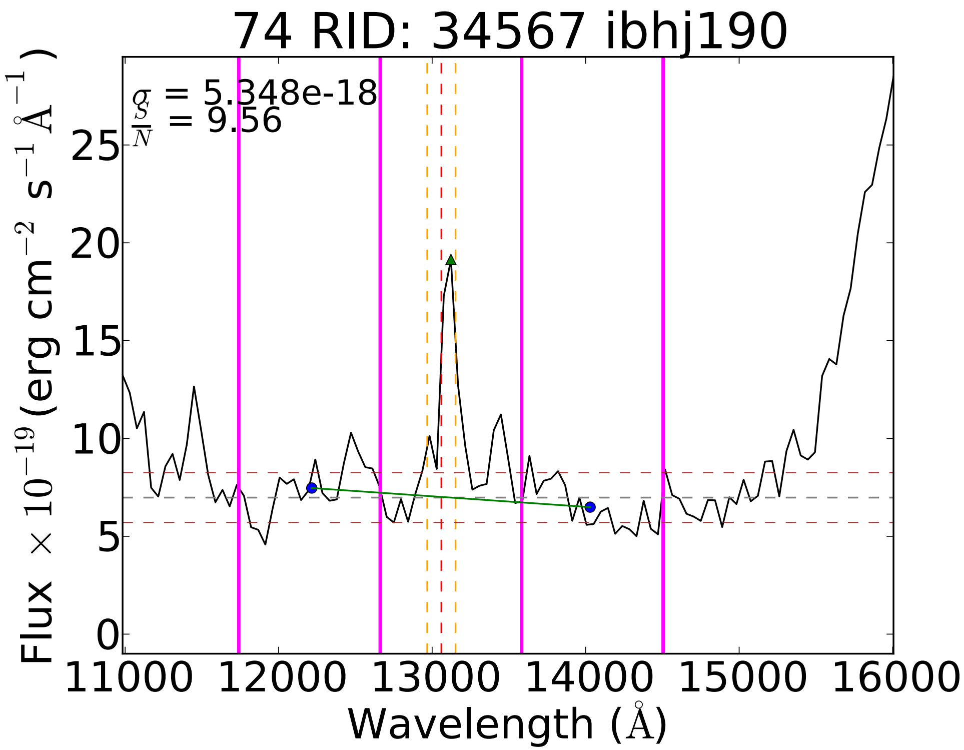
74 RID: 34567 ibhj190
σ = 5.348e-18
S/N = 9.56
Flux × 10^−19 (erg cm^−2 s^−1 Å^−1)
Wavelength (Å)
0
5
10
15
20
25
11000
12000
13000
14000
15000
16000

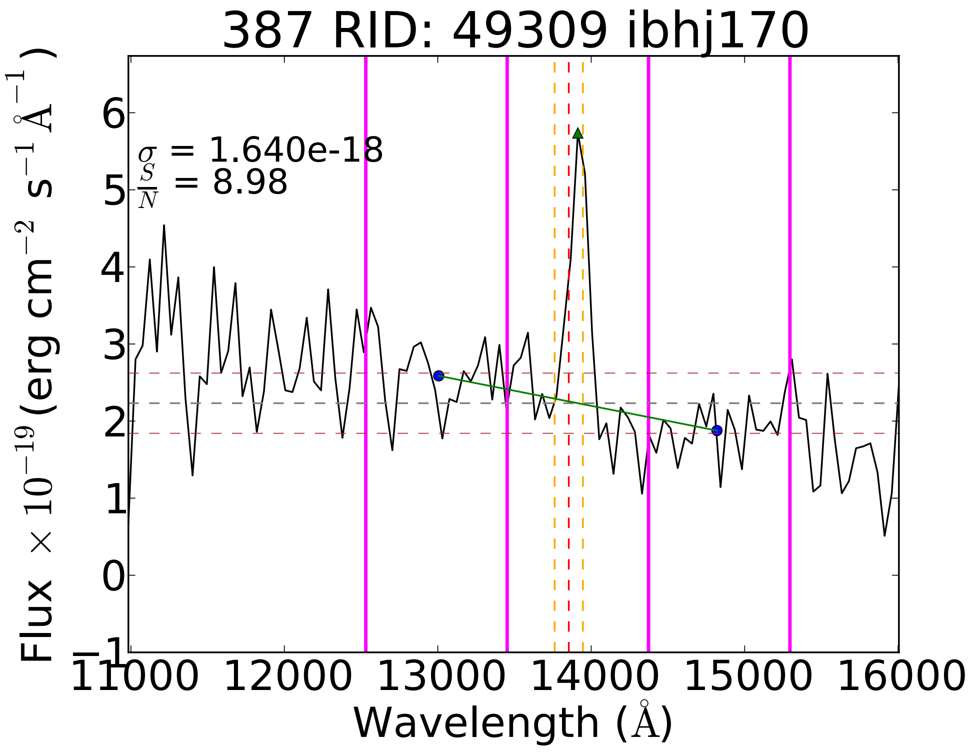
387 RID: 49309 ibhj170
σ = 1.640e-18
S/N = 8.98
Flux × 10^-19 (erg cm^-2 s^-1 Å^-1)
Wavelength (Å)
-1
0
1
2
3
4
5
6
11000
12000
13000
14000
15000
16000

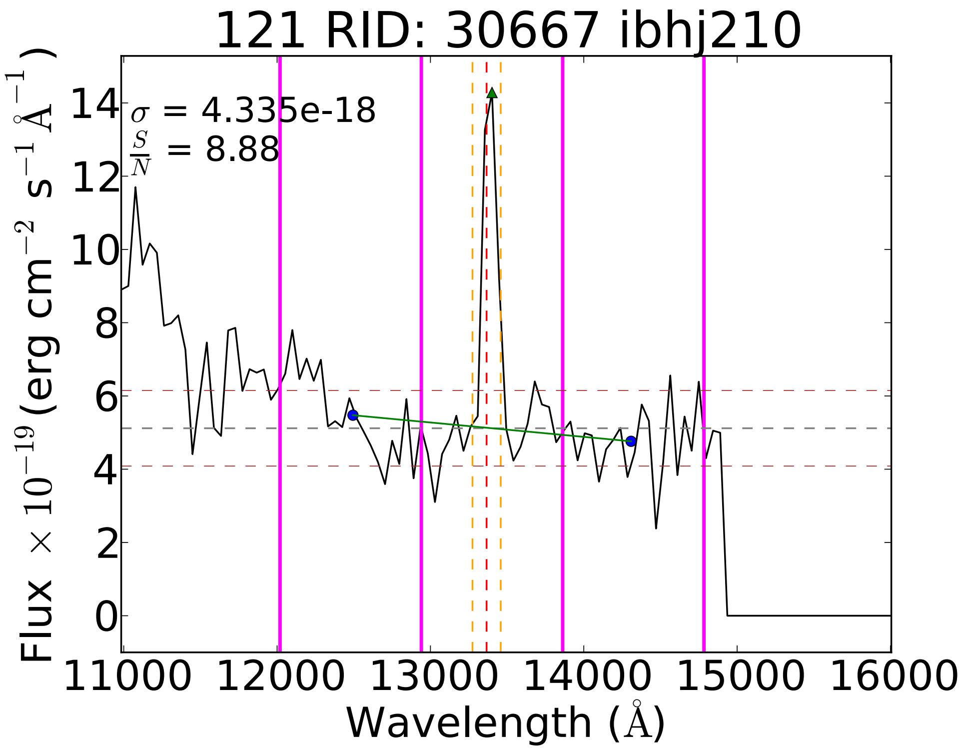
121 RID: 30667 ibhj210
σ = 4.335e-18
S/N = 8.88
Flux × 10^-19 (erg cm^-2 s^-1 Å^-1)
Wavelength (Å)
0
2
4
6
8
10
12
14
11000
12000
13000
14000
15000
16000

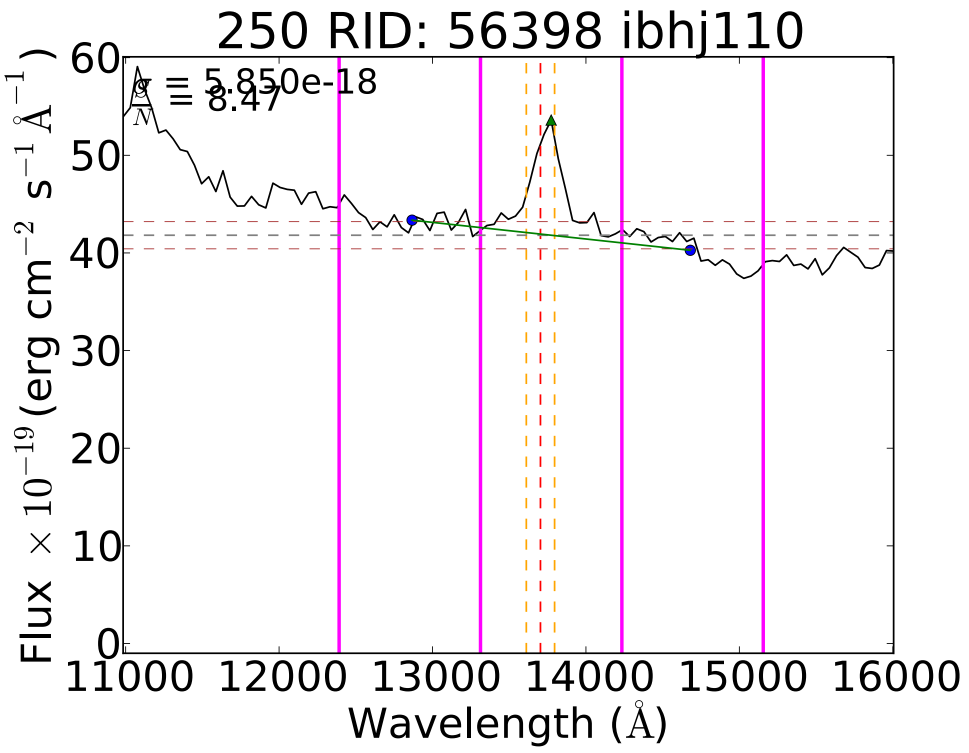
250 RID: 56398 ibhj110
σ = 5.850e-18
S/N = 8.47
Flux × 10^-19 (erg cm^-2 s^-1 Å^-1)
Wavelength (Å)
0
10
20
30
40
50
60
11000
12000
13000
14000
15000
16000

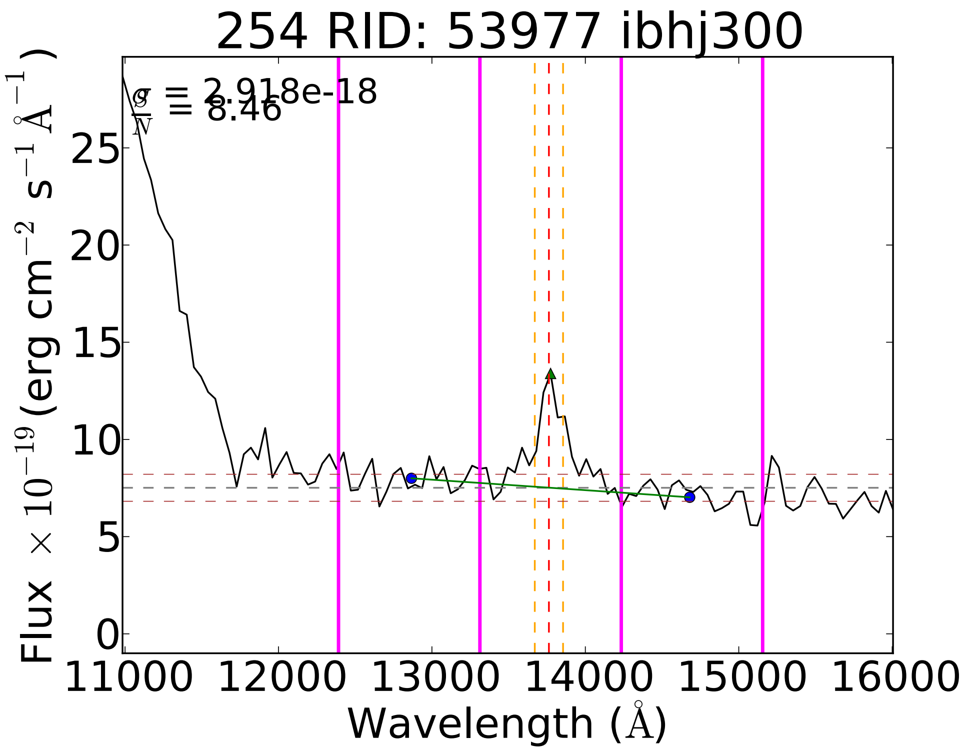
254 RID: 53977 ibhj300
σ = 2.918e-18
S/N = 8.46
Flux × 10^-19 (erg cm^-2 s^-1 Å^-1)
Wavelength (Å)
0
5
10
15
20
25
11000
12000
13000
14000
15000
16000

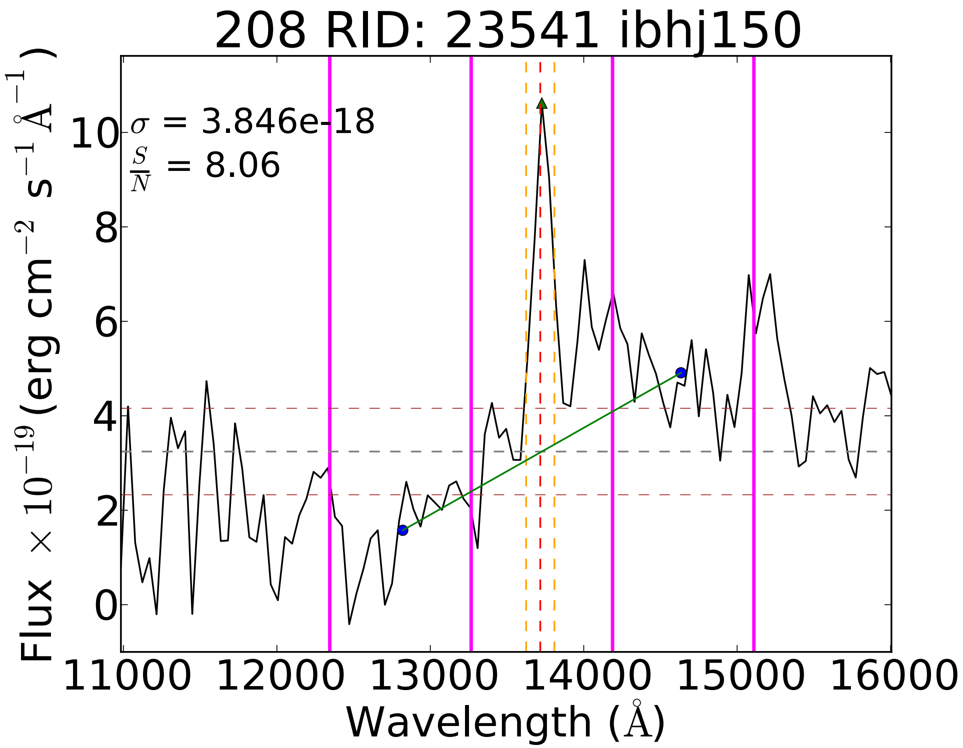
208 RID: 23541 ibhj150
σ = 3.846e-18
$\frac{S}{N}$ = 8.06
Flux $\times 10^{-19}$ (erg cm^{-2} s^{-1} Å^{-1})
Wavelength (Å)
0
2
4
6
8
10
11000
12000
13000
14000
15000
16000

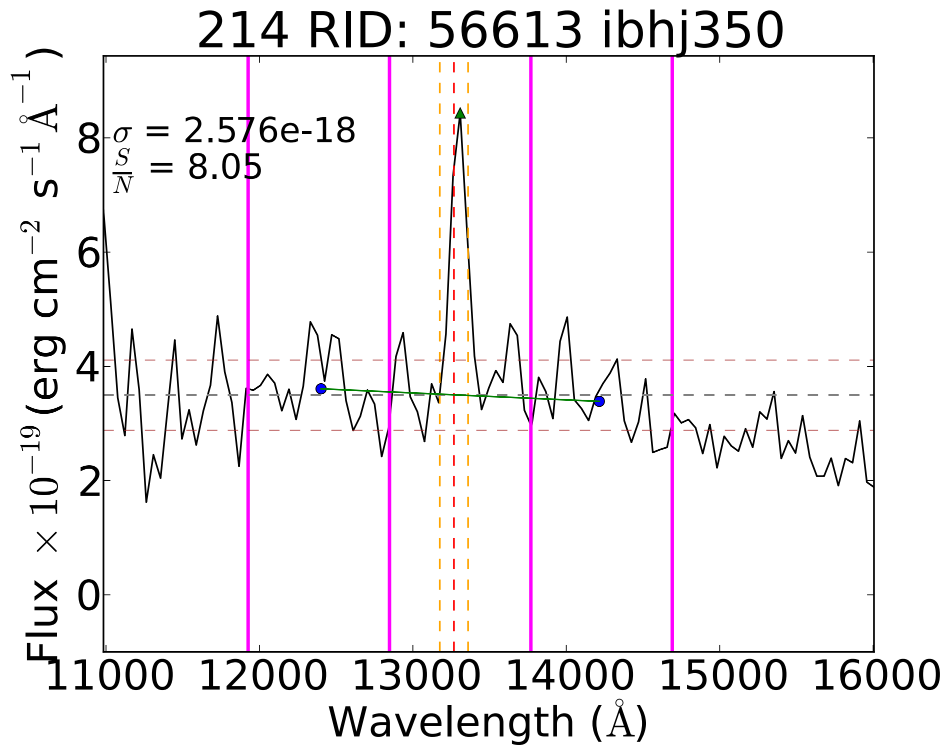
214 RID: 56613 ibhj350
σ = 2.576e-18
$\frac{S}{N}$ = 8.05
Flux $\times 10^{-19}$ (erg cm^{-2} s^{-1} Å^{-1})
Wavelength (Å)
0
2
4
6
8
11000
12000
13000
14000
15000
16000

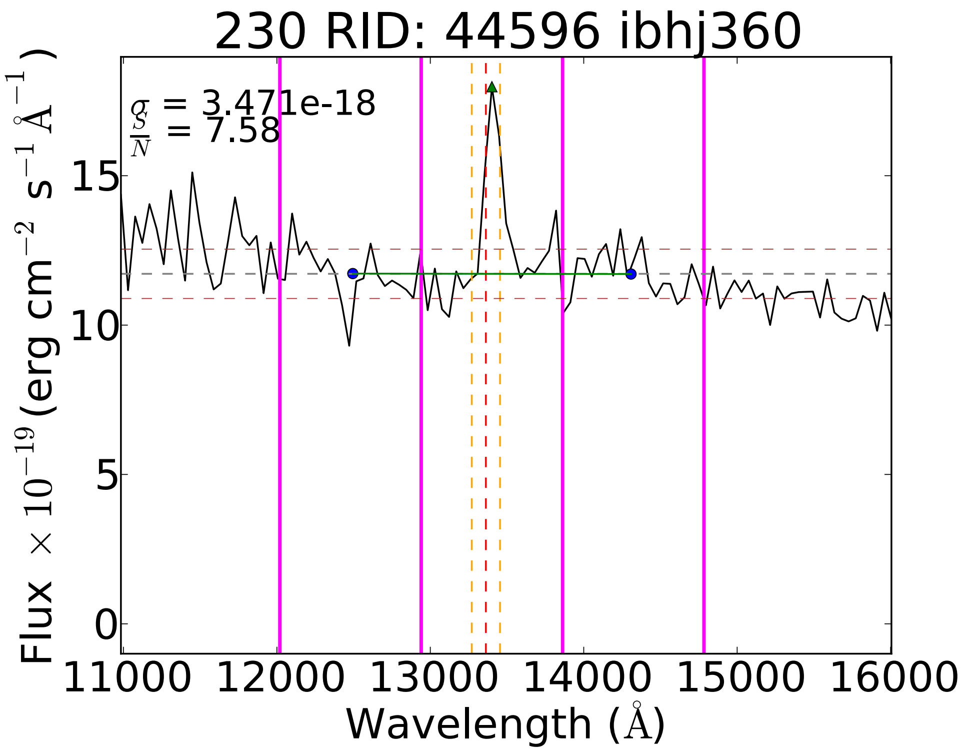
230 RID: 44596 ibhj360
σ = 3.471e-18
$\frac{S}{N}$ = 7.58
Flux $\times 10^{-19}$ (erg cm^{-2} s^{-1} Å^{-1})
Wavelength (Å)
0
5
10
15
11000
12000
13000
14000
15000
16000

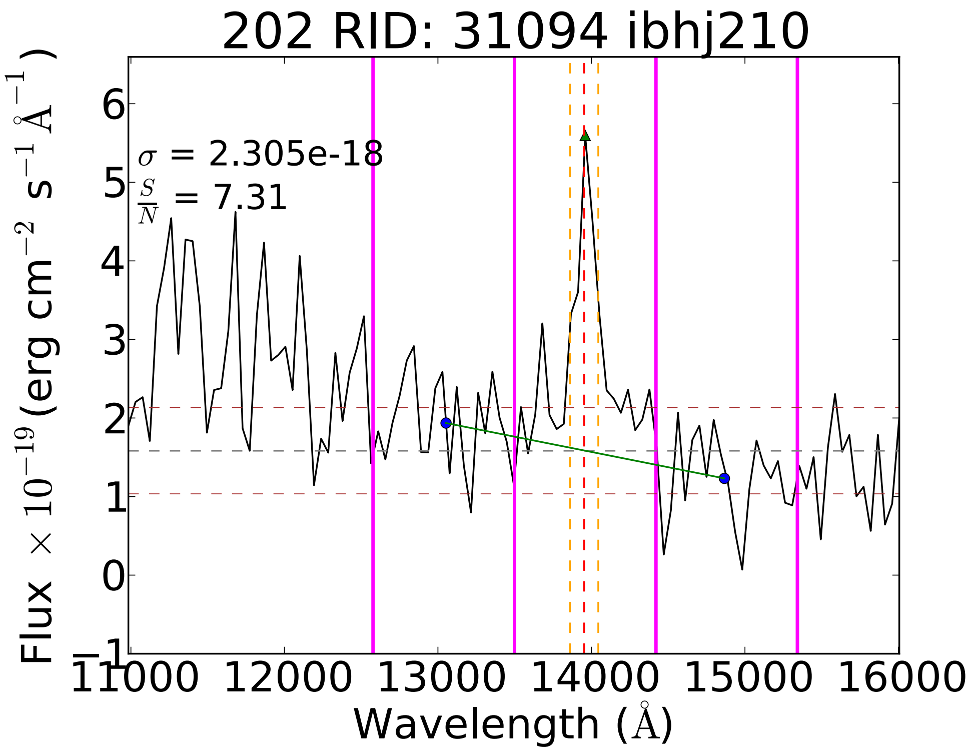
202 RID: 31094 ibhj210
σ = 2.305e-18
$\frac{S}{N}$ = 7.31
Flux $\times 10^{-19}$ (erg cm^{-2} s^{-1} Å^{-1})
Wavelength (Å)
−1
0
1
2
3
4
5
6
11000
12000
13000
14000
15000
16000

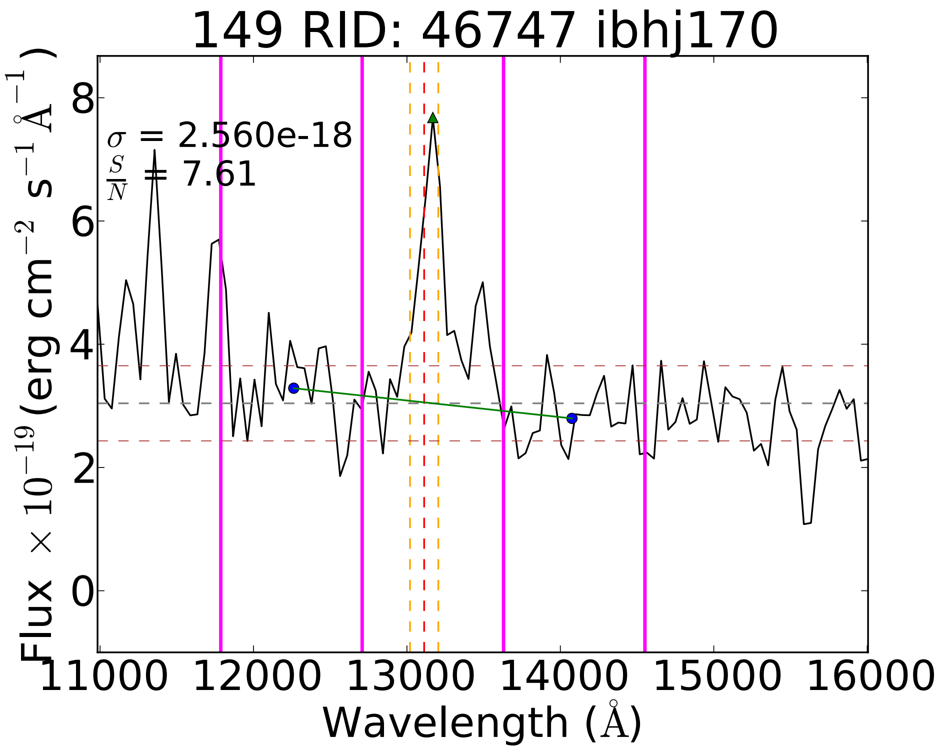
149 RID: 46747 ibhj170

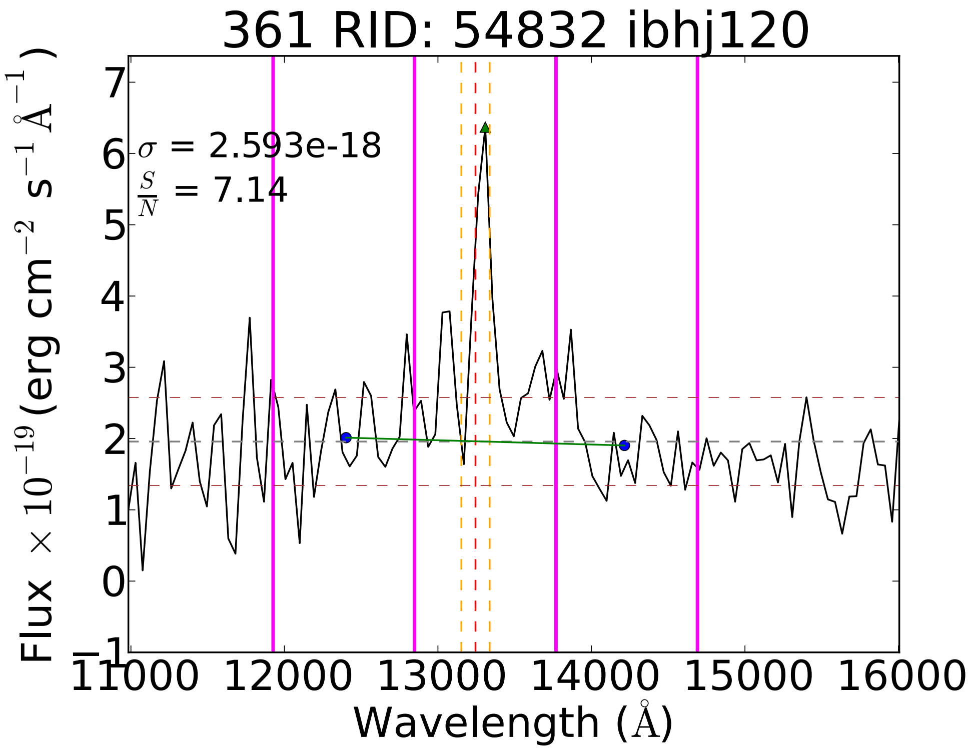
361 RID: 54832 ibhj120

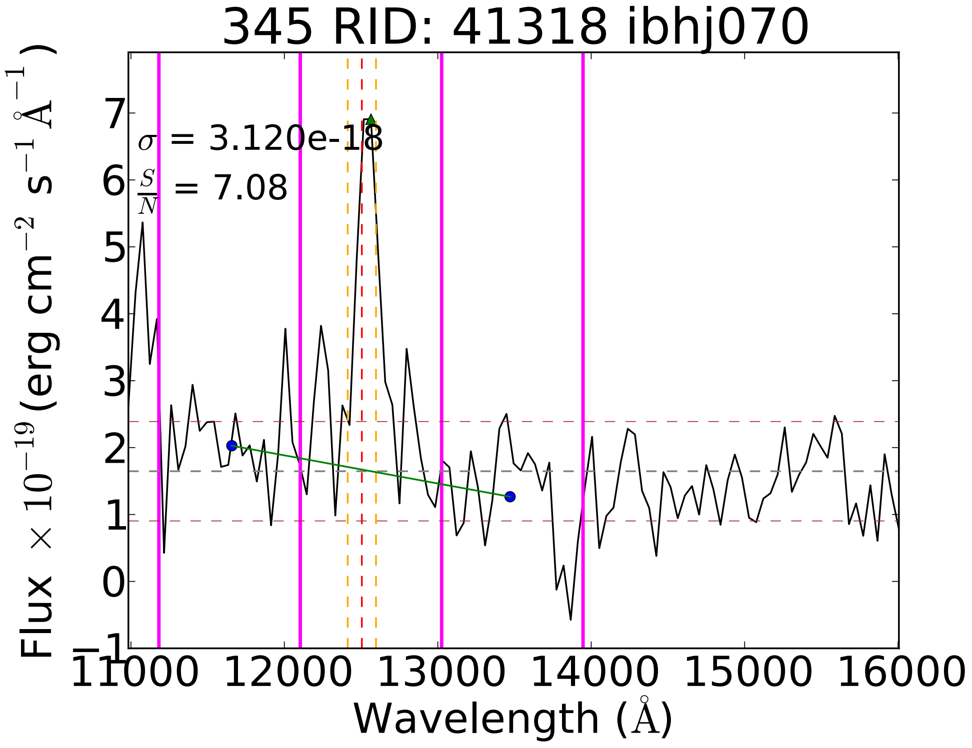
345 RID: 41318 ibhj070

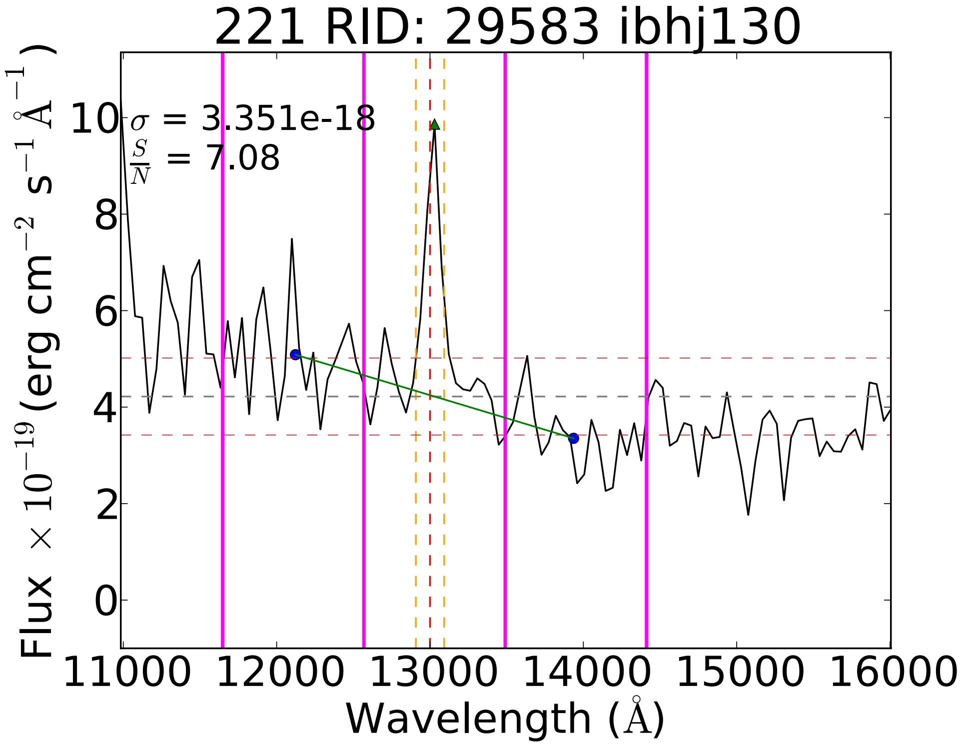
221 RID: 29583 ibhj130

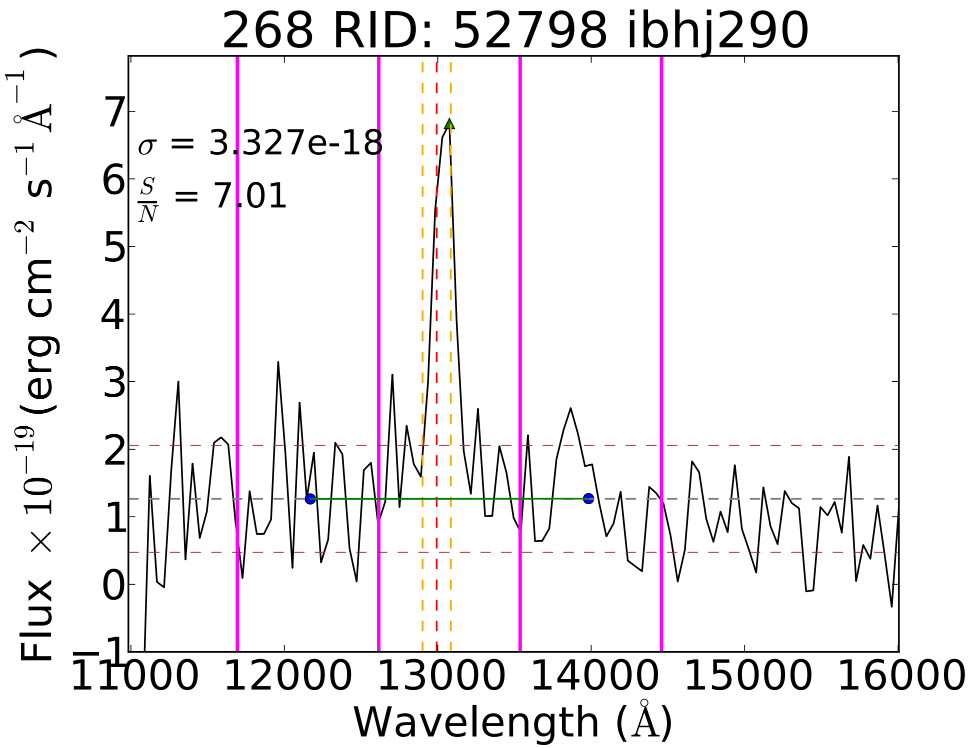
268 RID: 52798 ibhj290
σ = 3.327e-18
$\frac{S}{N}$ = 7.01
Flux $\times 10^{-19}$ (erg cm^{-2} s^{-1} Å^{-1})
Wavelength (Å)
−1
0
1
2
3
4
5
6
7
11000
12000
13000
14000
15000
16000

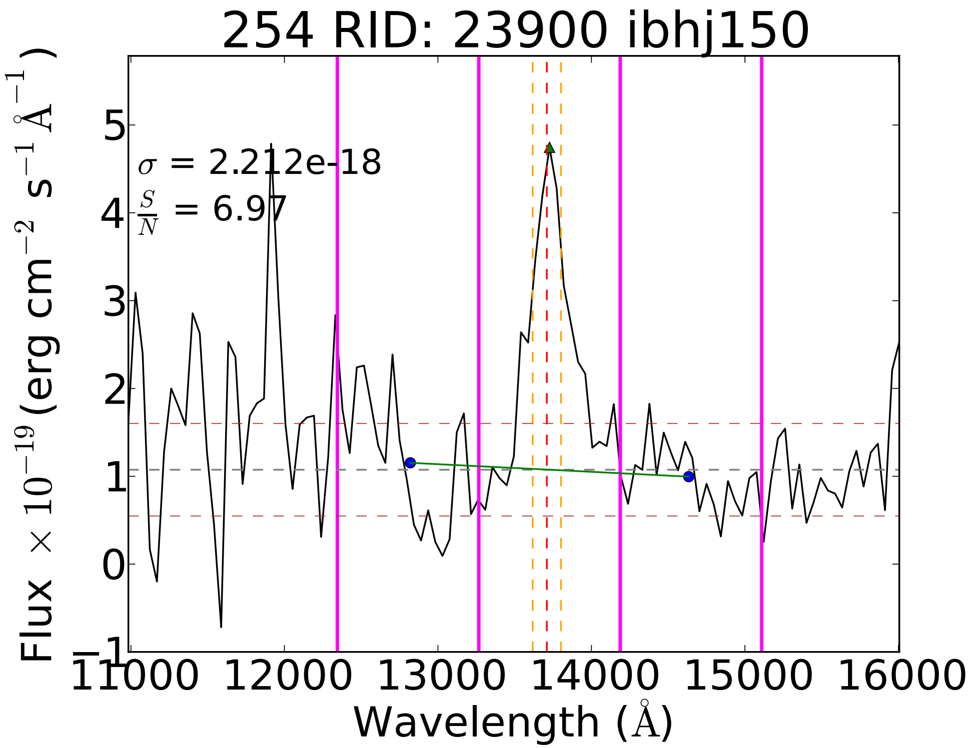
254 RID: 23900 ibhj150
σ = 2.212e-18
$\frac{S}{N}$ = 6.97
Flux $\times 10^{-19}$ (erg cm^{-2} s^{-1} Å^{-1})
Wavelength (Å)
−1
0
1
2
3
4
5
11000
12000
13000
14000
15000
16000

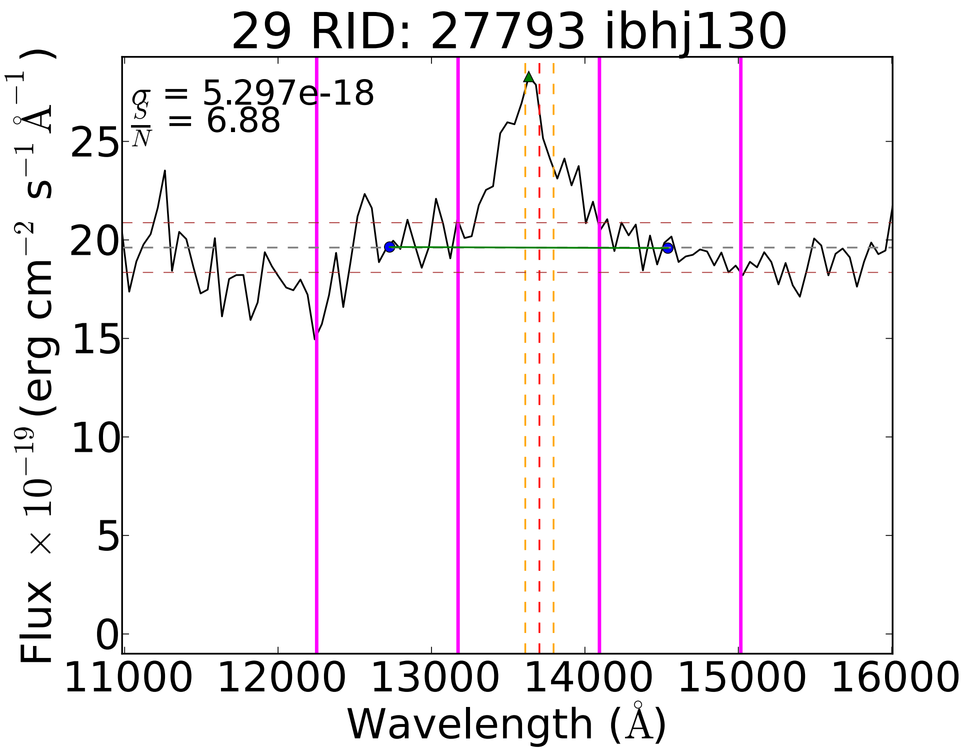
29 RID: 27793 ibhj130
σ = 5.297e-18
$\frac{S}{N}$ = 6.88
Flux $\times 10^{-19}$ (erg cm^{-2} s^{-1} Å^{-1})
Wavelength (Å)
0
5
10
15
20
25
11000
12000
13000
14000
15000
16000

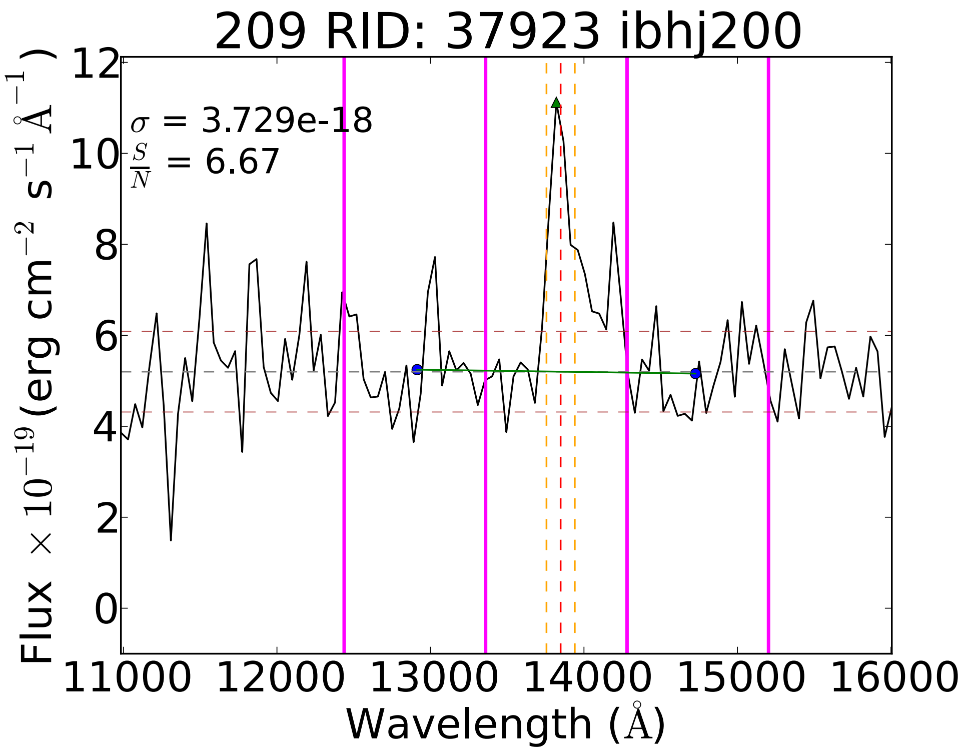
209 RID: 37923 ibhj200
σ = 3.729e-18
$\frac{S}{N}$ = 6.67
Flux $\times 10^{-19}$ (erg cm^{-2} s^{-1} Å^{-1})
Wavelength (Å)
0
2
4
6
8
10
12
11000
12000
13000
14000
15000
16000

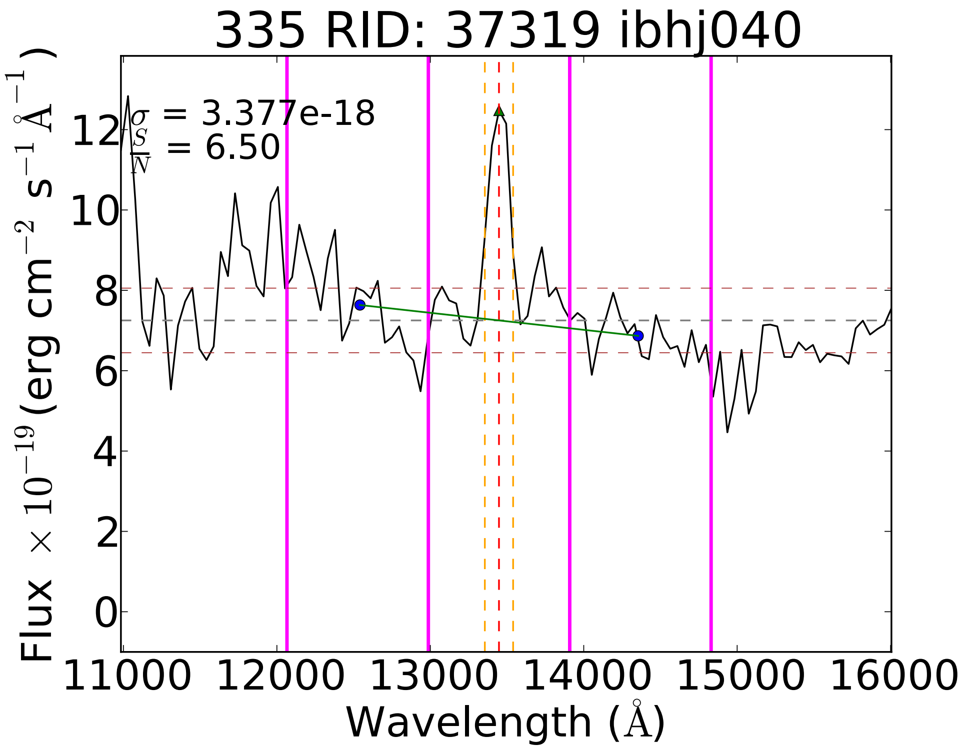
335 RID: 37319 ibhj040
σ = 3.377e-18
$\frac{S}{N}$ = 6.50
0
2
4
6
8
10
12
11000
12000
13000
14000
15000
16000
Wavelength (Å)
Flux $\times 10^{-19}$ (erg cm^{-2} s^{-1} Å^{-1})

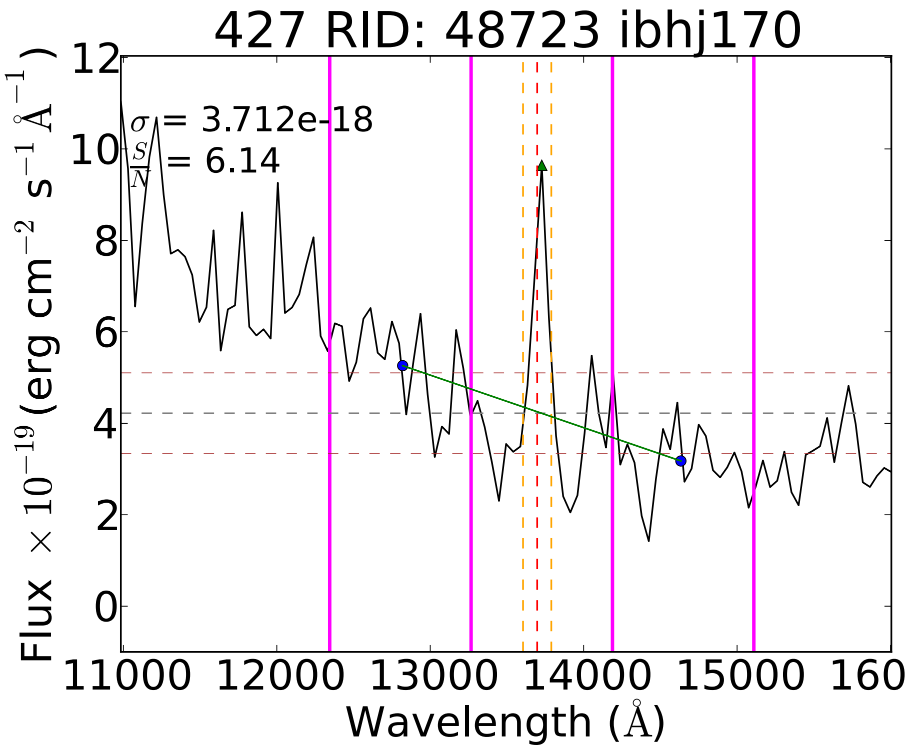
427 RID: 48723 ibhj170
σ = 3.712e-18
$\frac{S}{N}$ = 6.14
0
2
4
6
8
10
12
11000
12000
13000
14000
15000
16000
Wavelength (Å)
Flux $\times 10^{-19}$ (erg cm^{-2} s^{-1} Å^{-1})

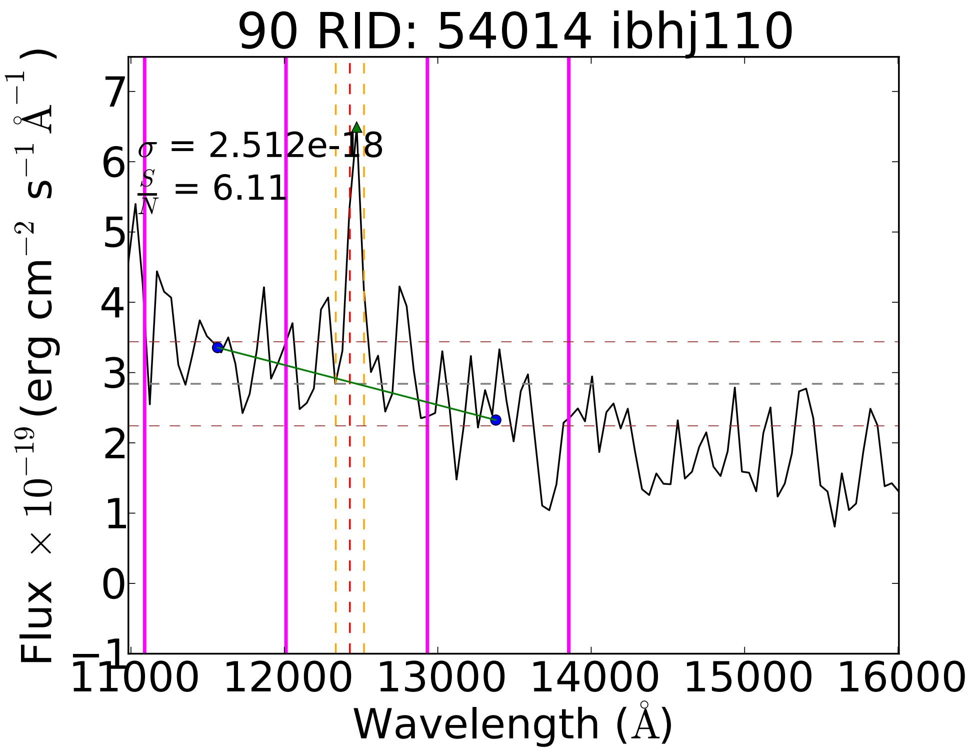
90 RID: 54014 ibhj110
σ = 2.512e-18
$\frac{S}{N}$ = 6.11
−1
0
1
2
3
4
5
6
7
11000
12000
13000
14000
15000
16000
Wavelength (Å)
Flux $\times 10^{-19}$ (erg cm^{-2} s^{-1} Å^{-1})

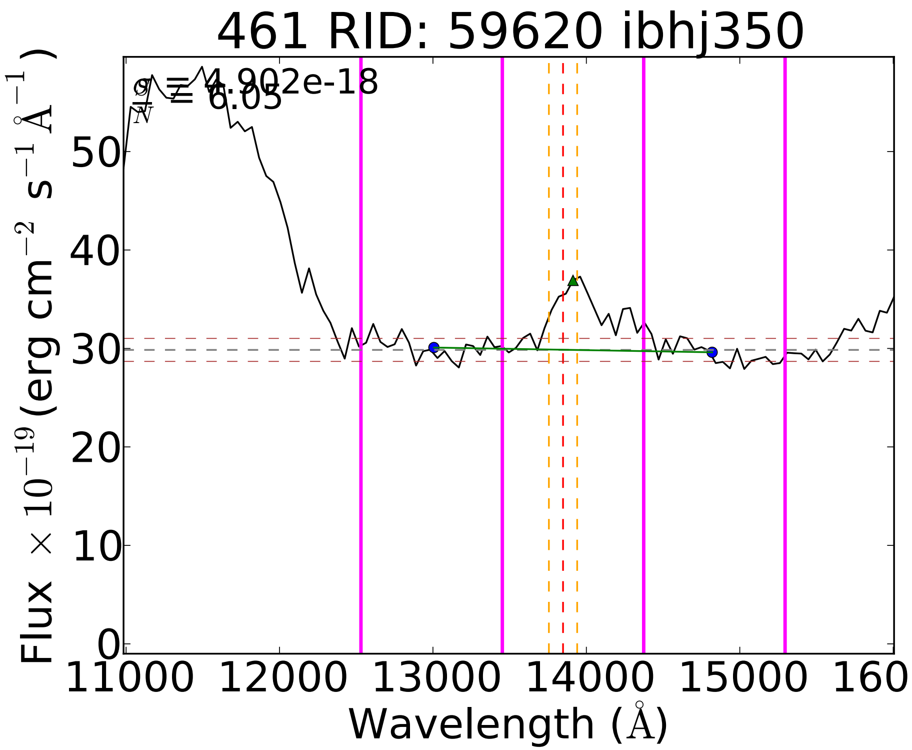
461 RID: 59620 ibhj350
σ = 4.902e-18
$\frac{S}{N}$ = 6.05
0
10
20
30
40
50
11000
12000
13000
14000
15000
16000
Wavelength (Å)
Flux $\times 10^{-19}$ (erg cm^{-2} s^{-1} Å^{-1})

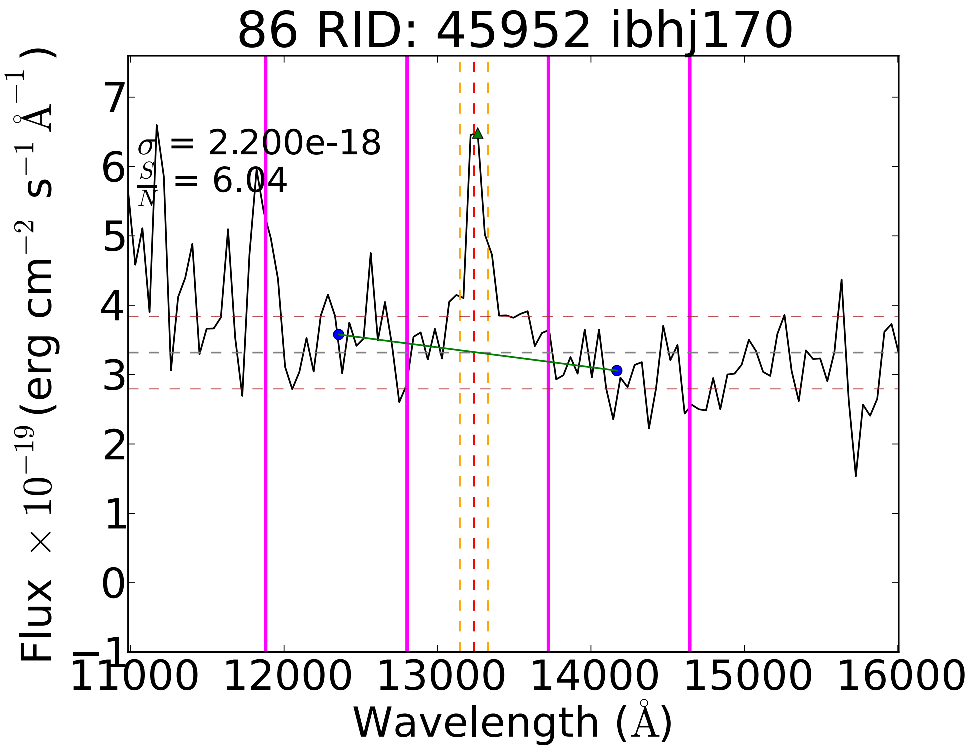

86 RID: 45952 ibhj170

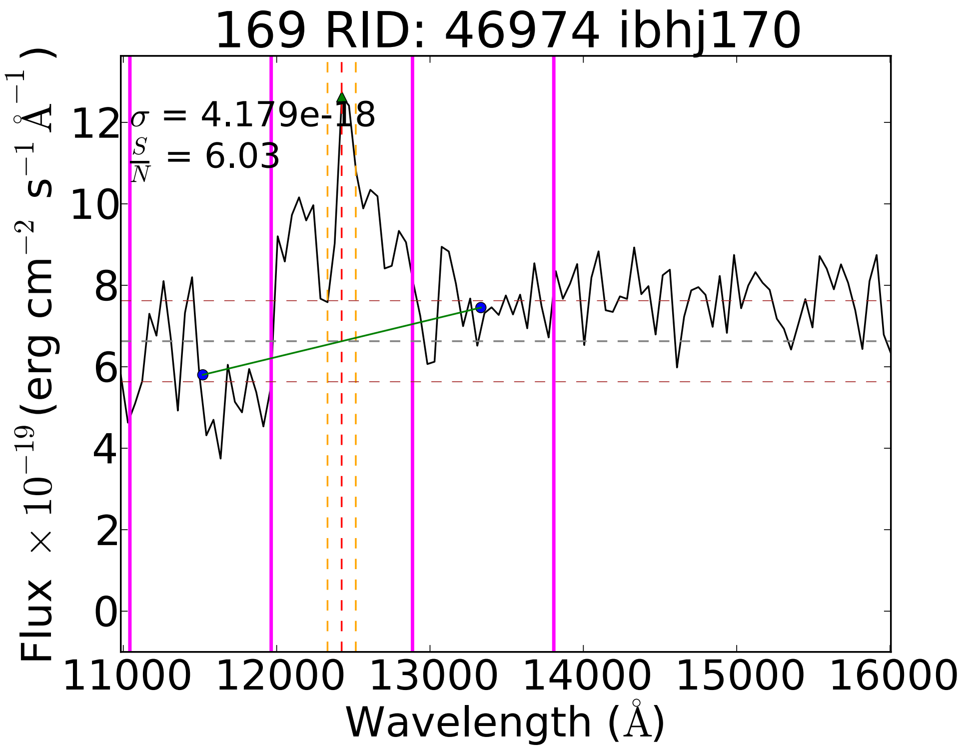

169 RID: 46974 ibhj170

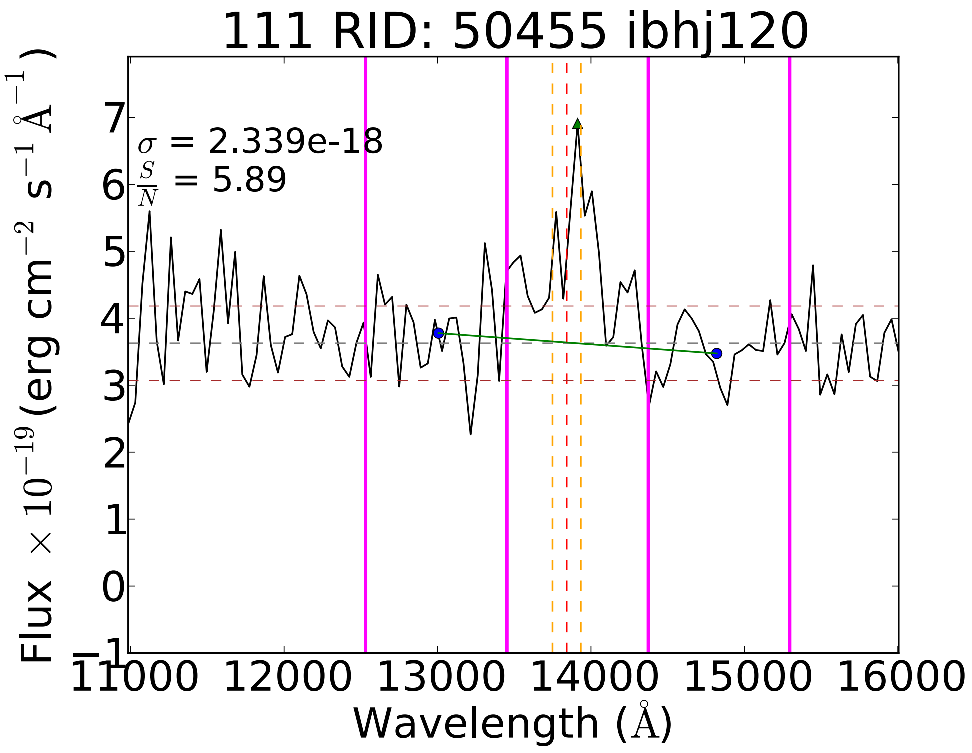

111 RID: 50455 ibhj120

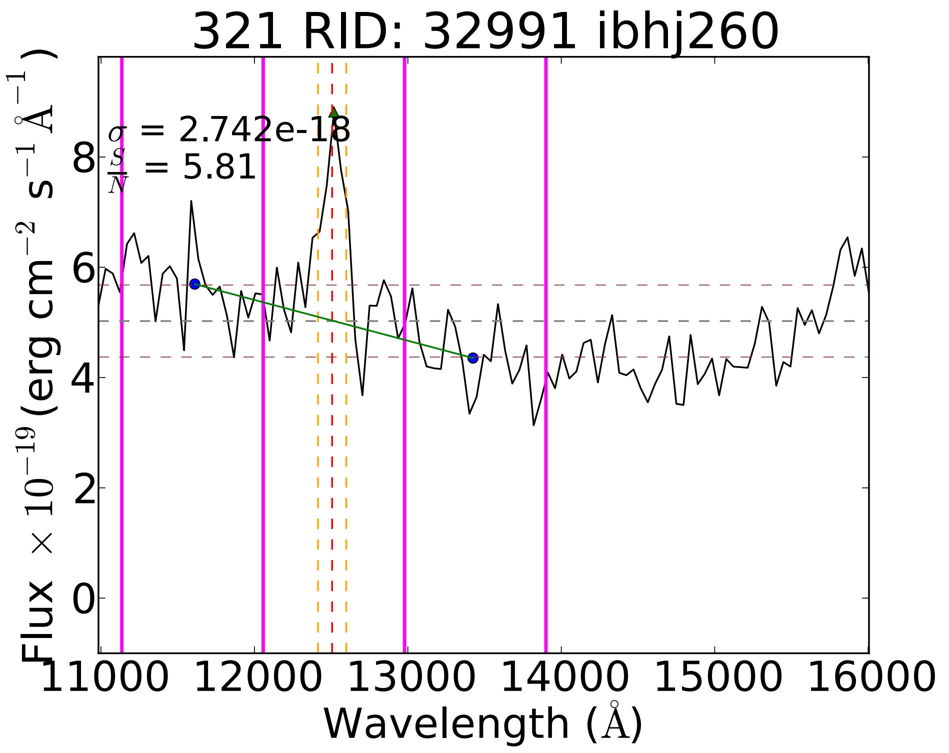

321 RID: 32991 ibhj260

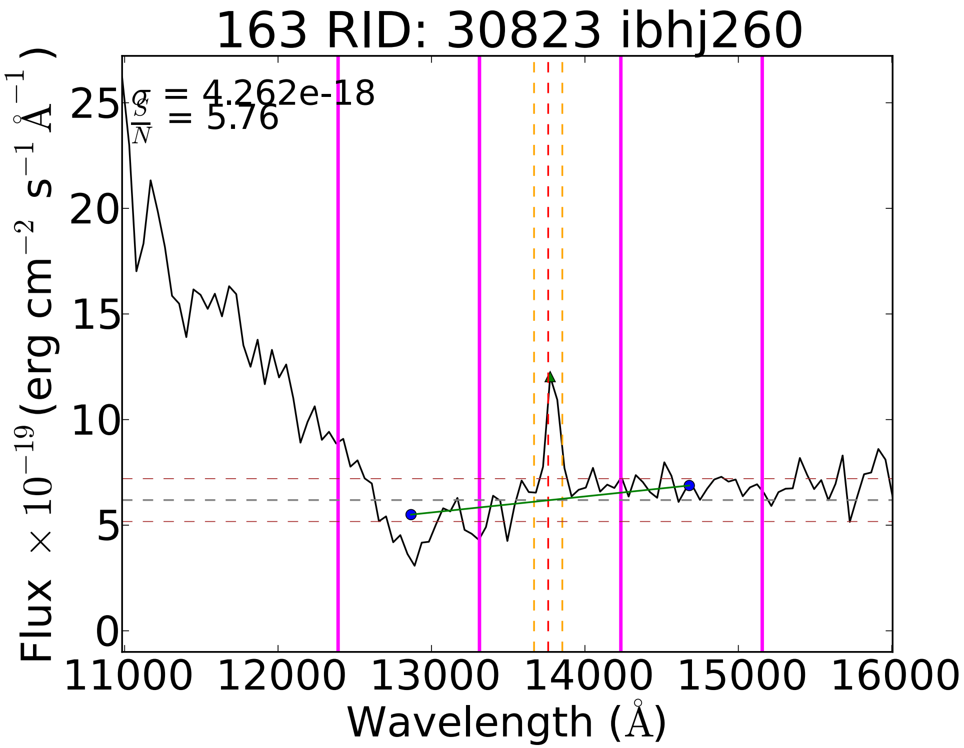
163 RID: 30823 ibhj260
σ = 4.262e-18
$\frac{S}{N}$ = 5.76
Flux $\times 10^{-19}$ (erg cm^{-2} s^{-1} Å^{-1})
0
5
10
15
20
25
11000
12000
13000
14000
15000
16000
Wavelength (Å)

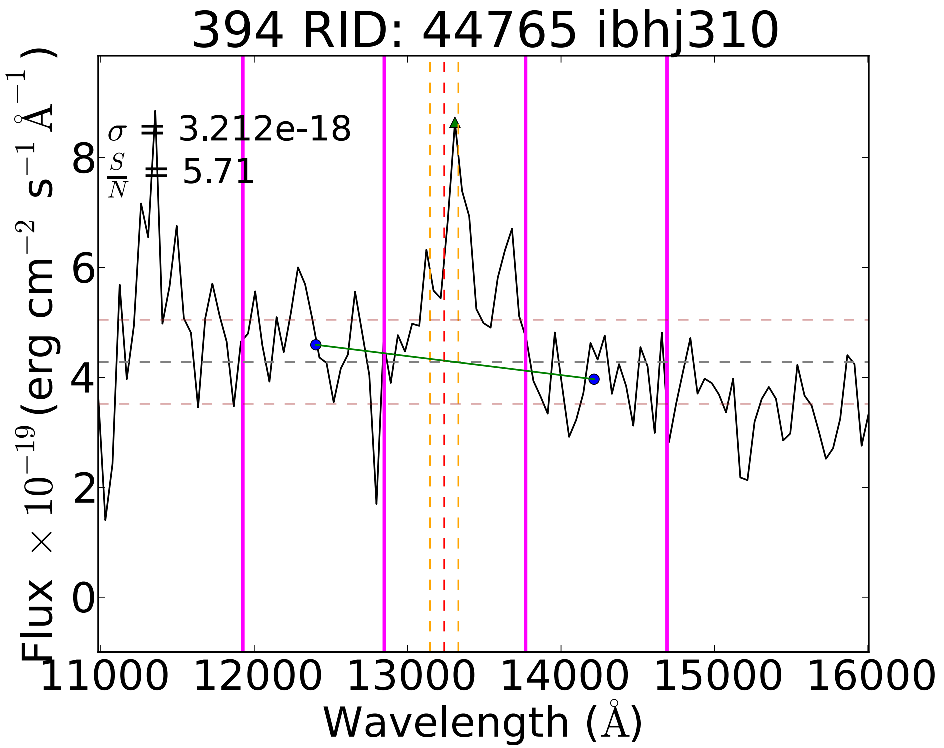
394 RID: 44765 ibhj310
σ = 3.212e-18
$\frac{S}{N}$ = 5.71
Flux $\times 10^{-19}$ (erg cm^{-2} s^{-1} Å^{-1})
0
2
4
6
8
11000
12000
13000
14000
15000
16000
Wavelength (Å)

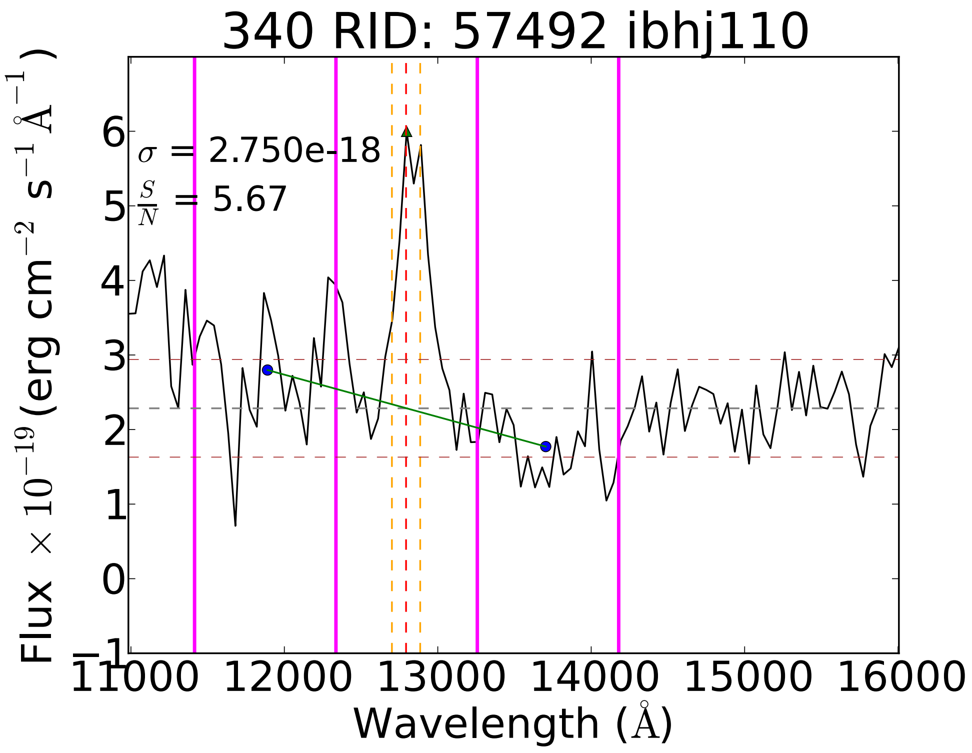
340 RID: 57492 ibhj110
σ = 2.750e-18
$\frac{S}{N}$ = 5.67
Flux $\times 10^{-19}$ (erg cm^{-2} s^{-1} Å^{-1})
−1
0
1
2
3
4
5
6
11000
12000
13000
14000
15000
16000
Wavelength (Å)

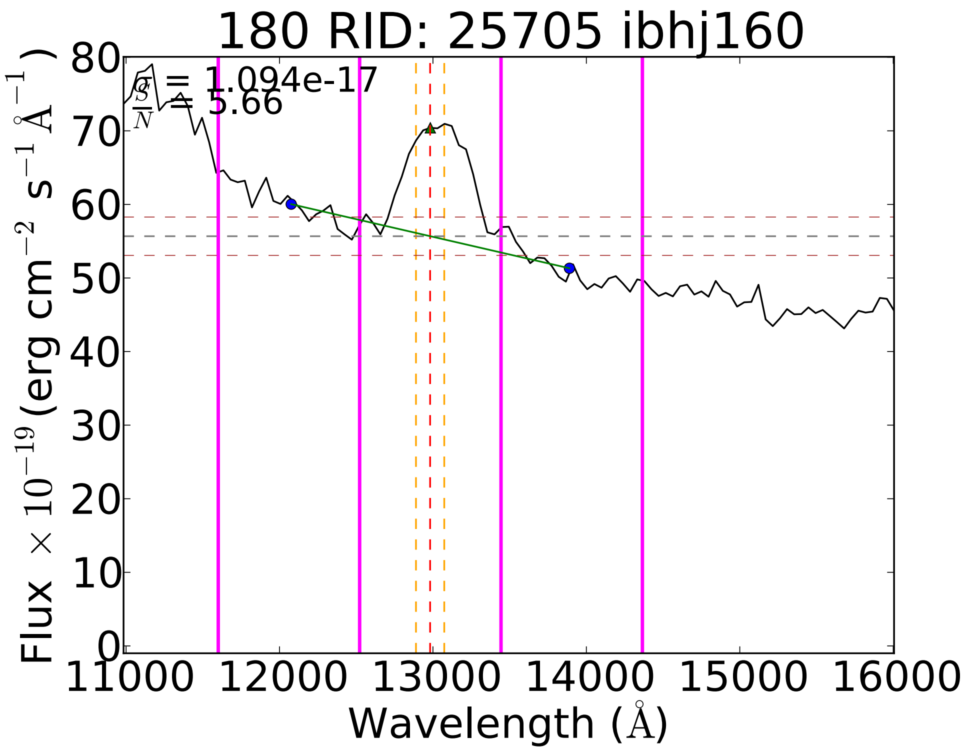
180 RID: 25705 ibhj160
σ = 1.094e-17
$\frac{S}{N}$ = 5.66
Flux $\times 10^{-19}$ (erg cm^{-2} s^{-1} Å^{-1})
0
10
20
30
40
50
60
70
80
11000
12000
13000
14000
15000
16000
Wavelength (Å)

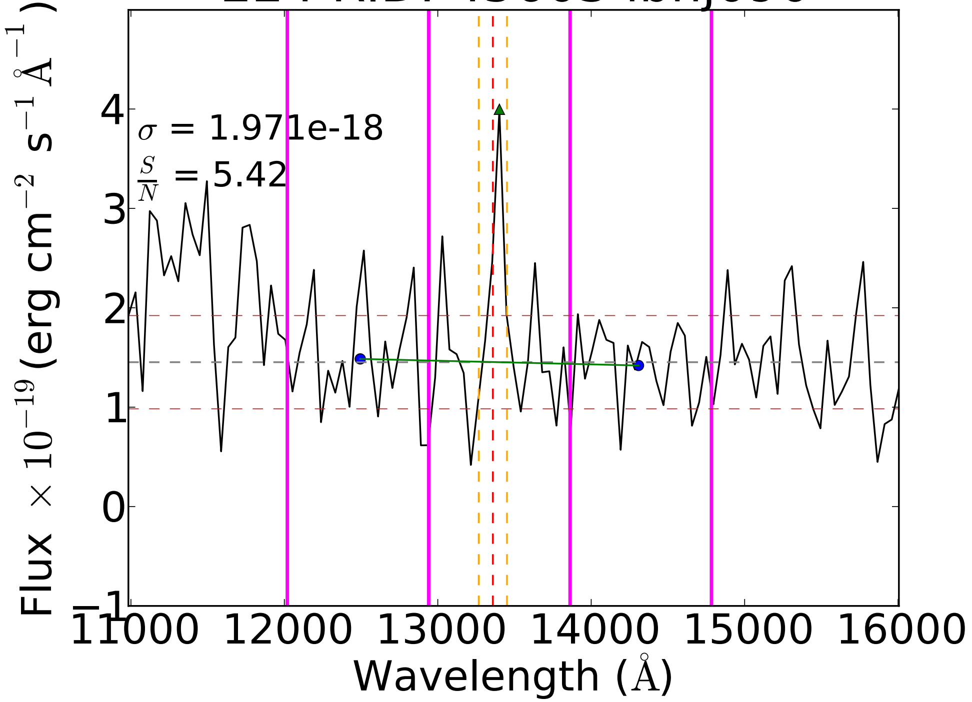
224 RID: 45603 ibhj090

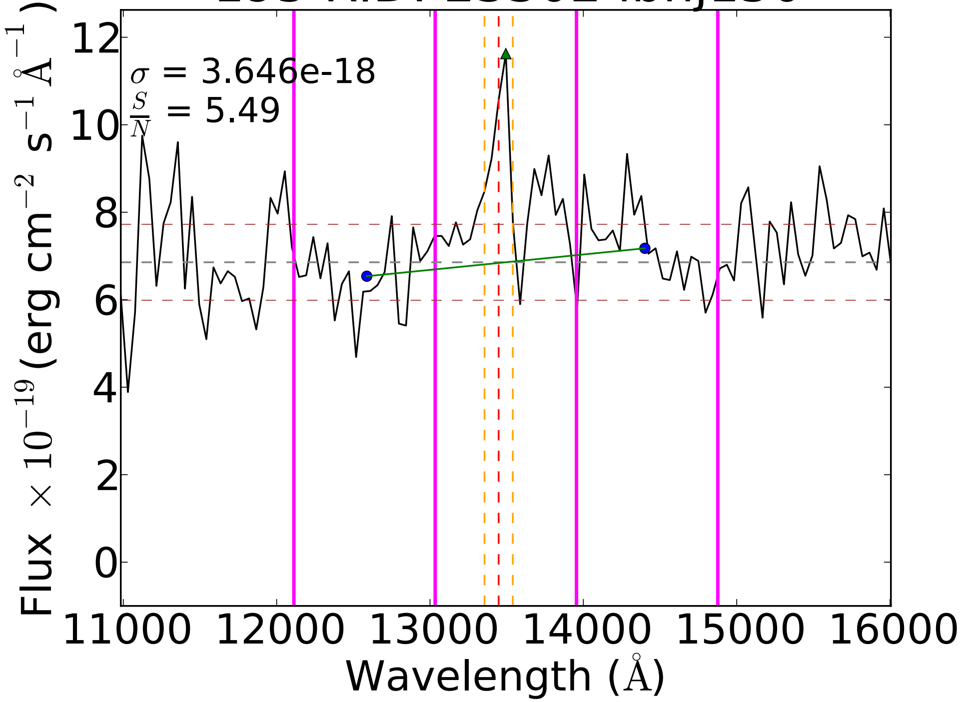
195 RID: 23302 ibhj150

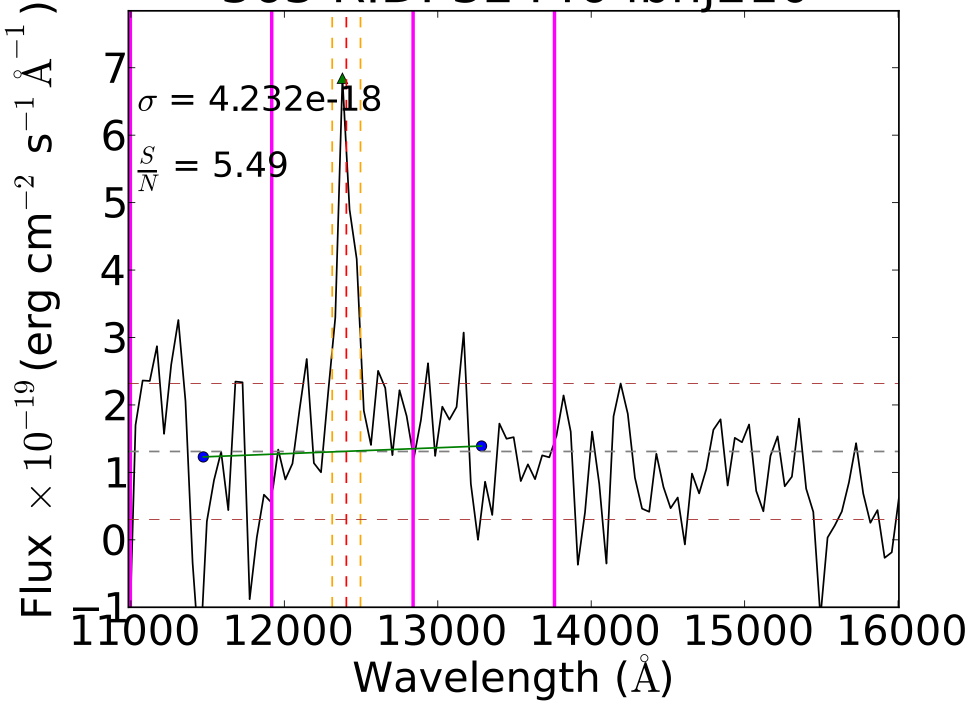
363 RID: 32446 ibhj210

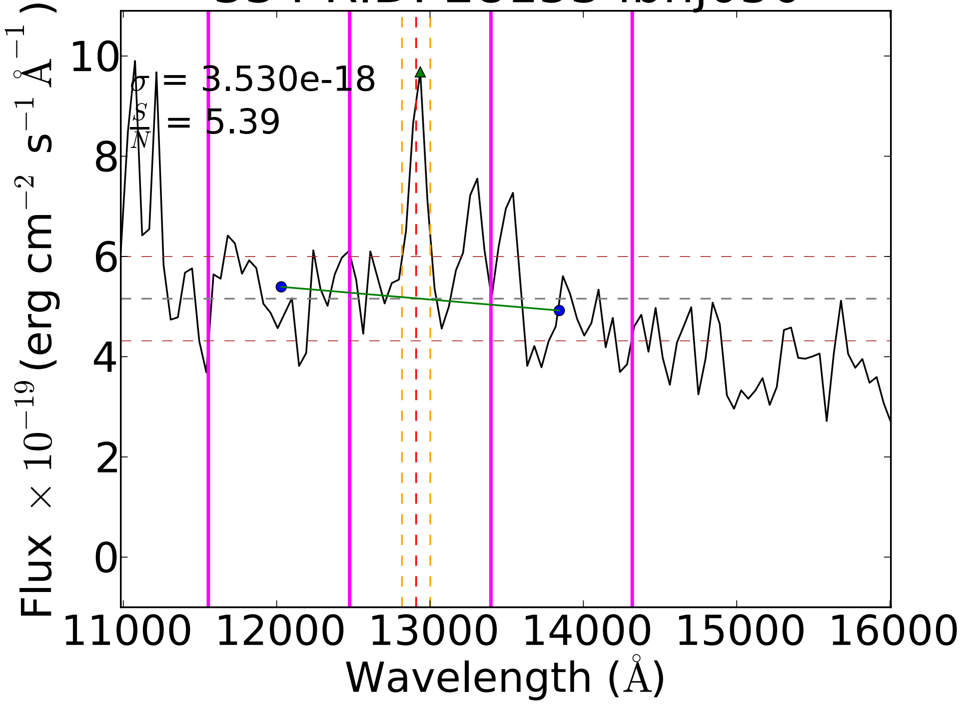
334 RID: 28153 ibhj050

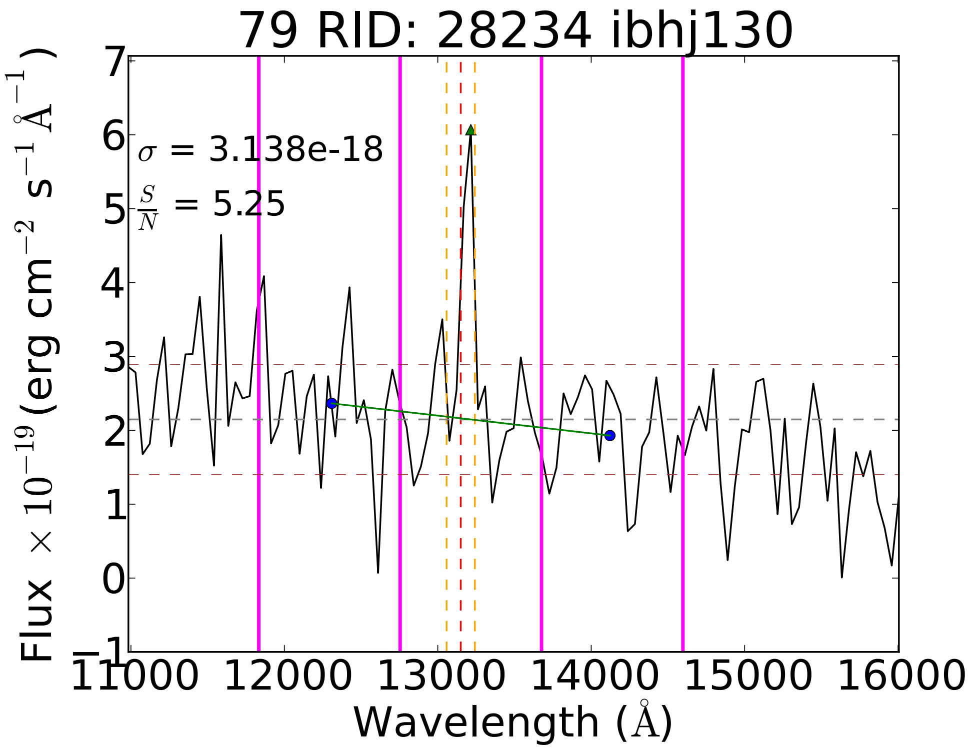
79 RID: 28234 ibhj130
σ = 3.138e-18
S/N = 5.25
Flux × 10^−19 (erg cm^−2 s^−1 Å^−1)
Wavelength (Å)
−1
0
1
2
3
4
5
6
7
11000
12000
13000
14000
15000
16000

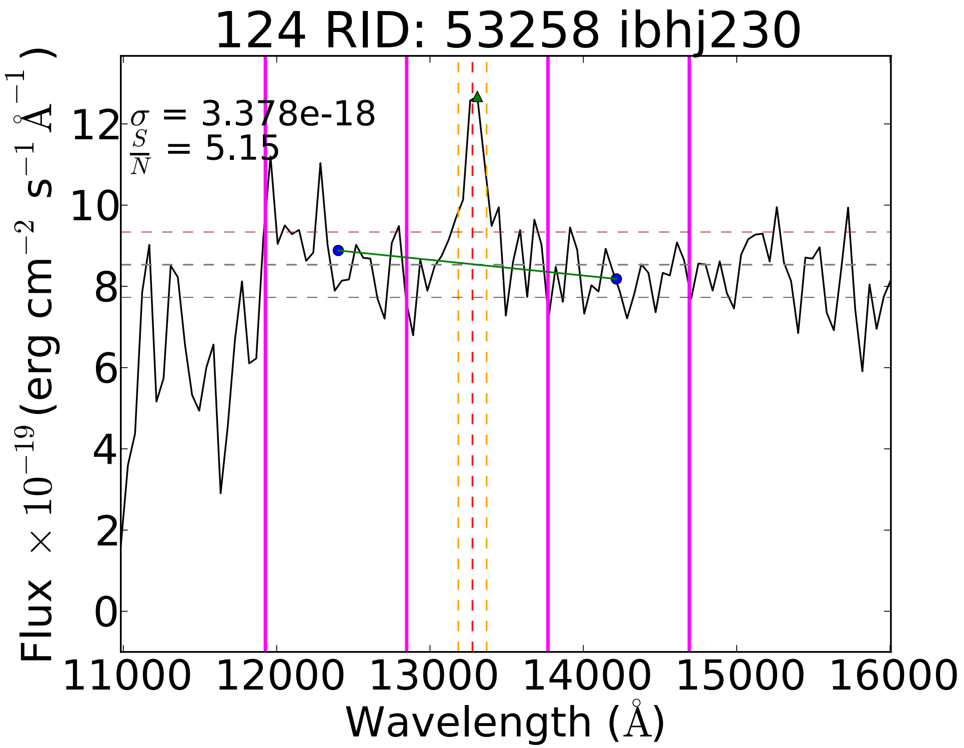
124 RID: 53258 ibhj230
σ = 3.378e-18
S/N = 5.15
Flux × 10^−19 (erg cm^−2 s^−1 Å^−1)
Wavelength (Å)
0
2
4
6
8
10
12
11000
12000
13000
14000
15000
16000

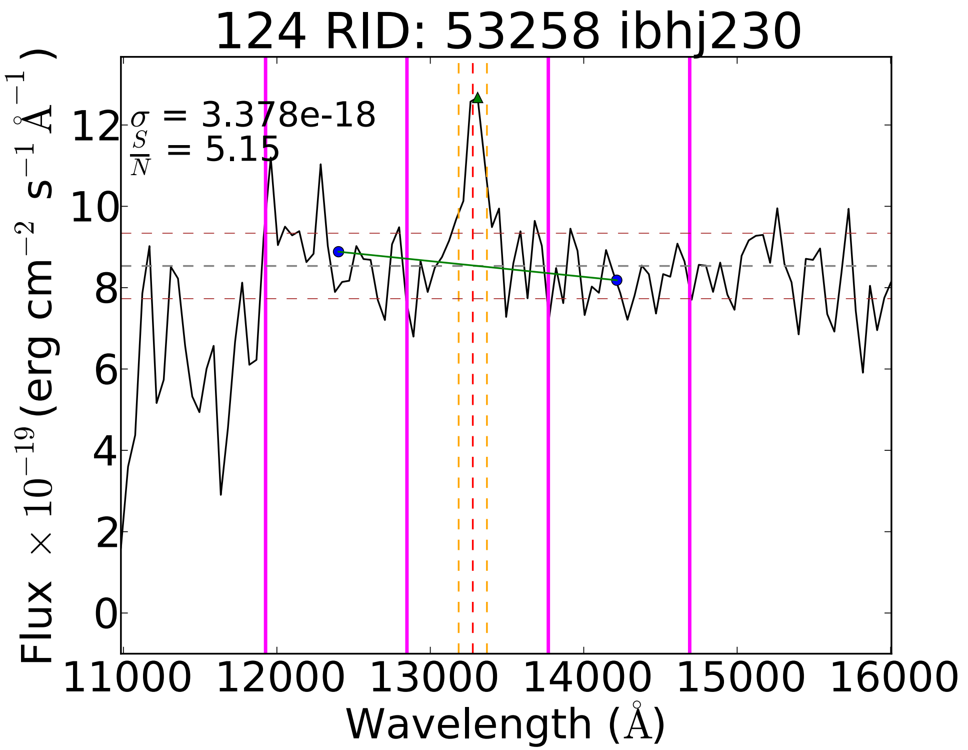
124 RID: 53258 ibhj230
σ = 3.378e-18
S/N = 5.15
Flux × 10^−19 (erg cm^−2 s^−1 Å^−1)
Wavelength (Å)
0
2
4
6
8
10
12
11000
12000
13000
14000
15000
16000

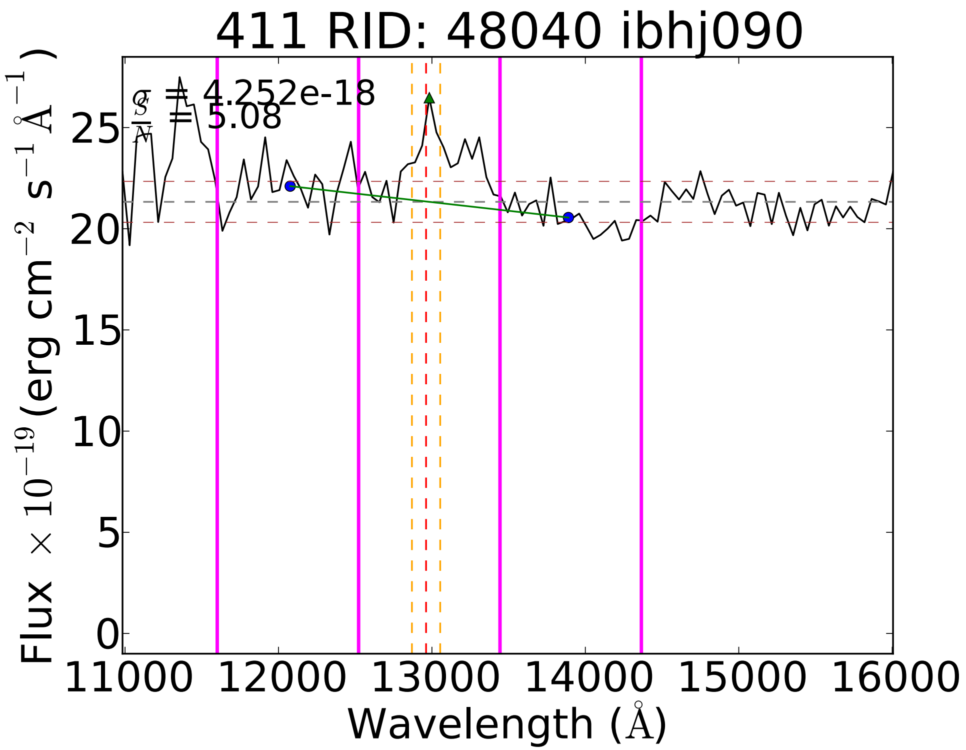
411 RID: 48040 ibhj090
σ = 4.252e-18
S/N = 5.08
Flux × 10^−19 (erg cm^−2 s^−1 Å^−1)
Wavelength (Å)
0
5
10
15
20
25
11000
12000
13000
14000
15000
16000

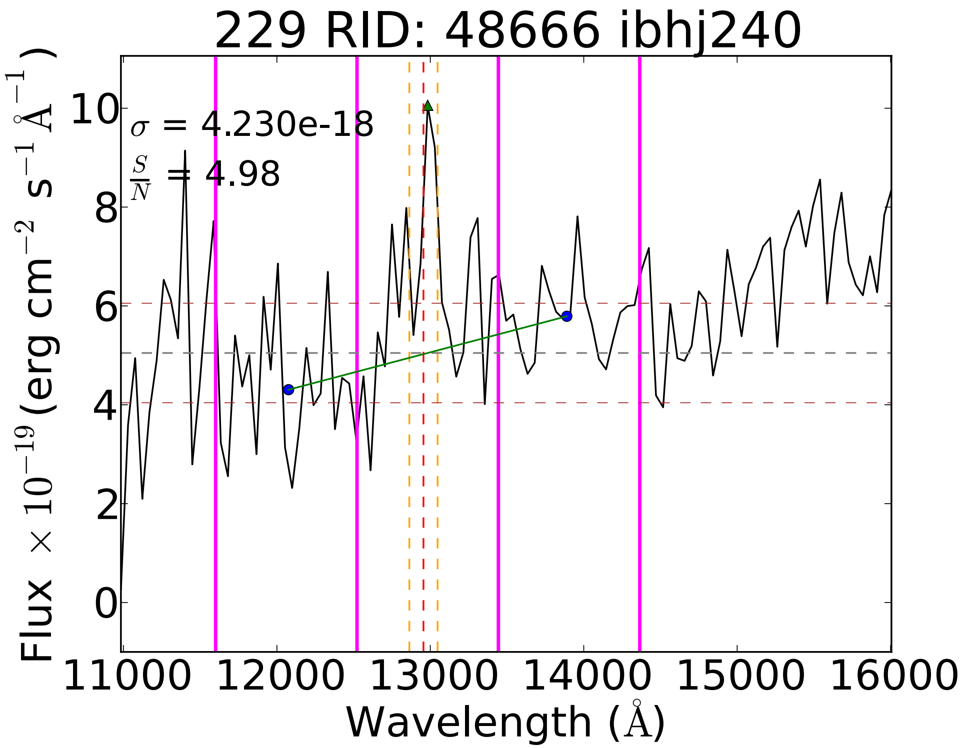
229 RID: 48666 ibhj240
σ = 4.230e-18
$\frac{S}{N}$ = 4.98
Flux $\times 10^{-19}$ (erg cm^{-2} s^{-1} Å^{-1})
Wavelength (Å)
0
2
4
6
8
10
11000
12000
13000
14000
15000
16000

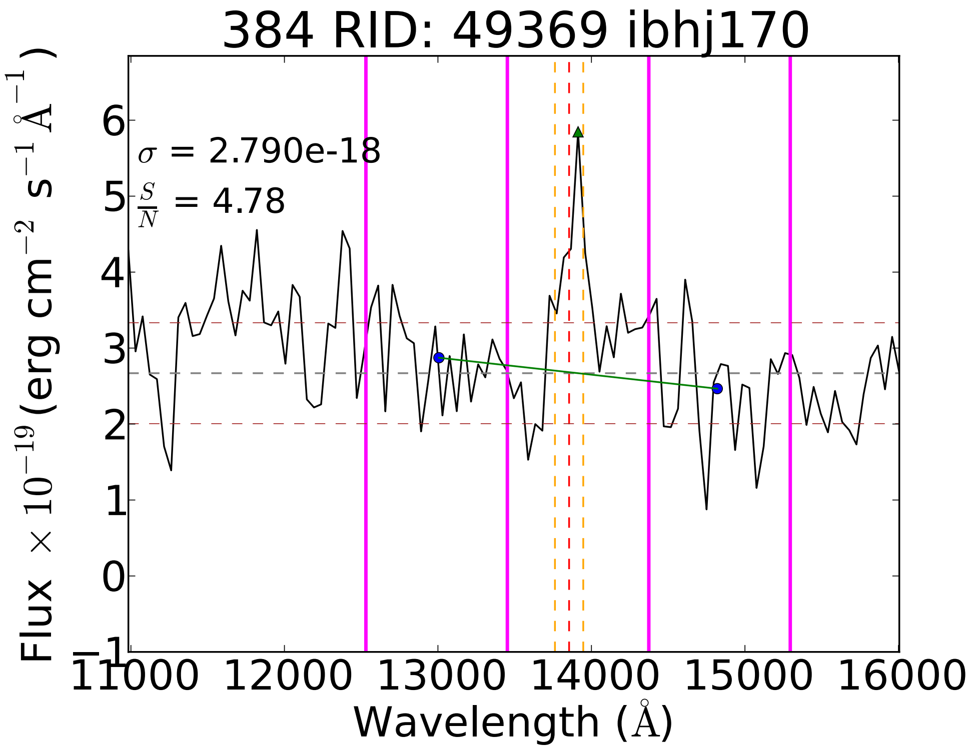
384 RID: 49369 ibhj170
σ = 2.790e-18
$\frac{S}{N}$ = 4.78
Flux $\times 10^{-19}$ (erg cm^{-2} s^{-1} Å^{-1})
Wavelength (Å)
−1
0
1
2
3
4
5
6
11000
12000
13000
14000
15000
16000

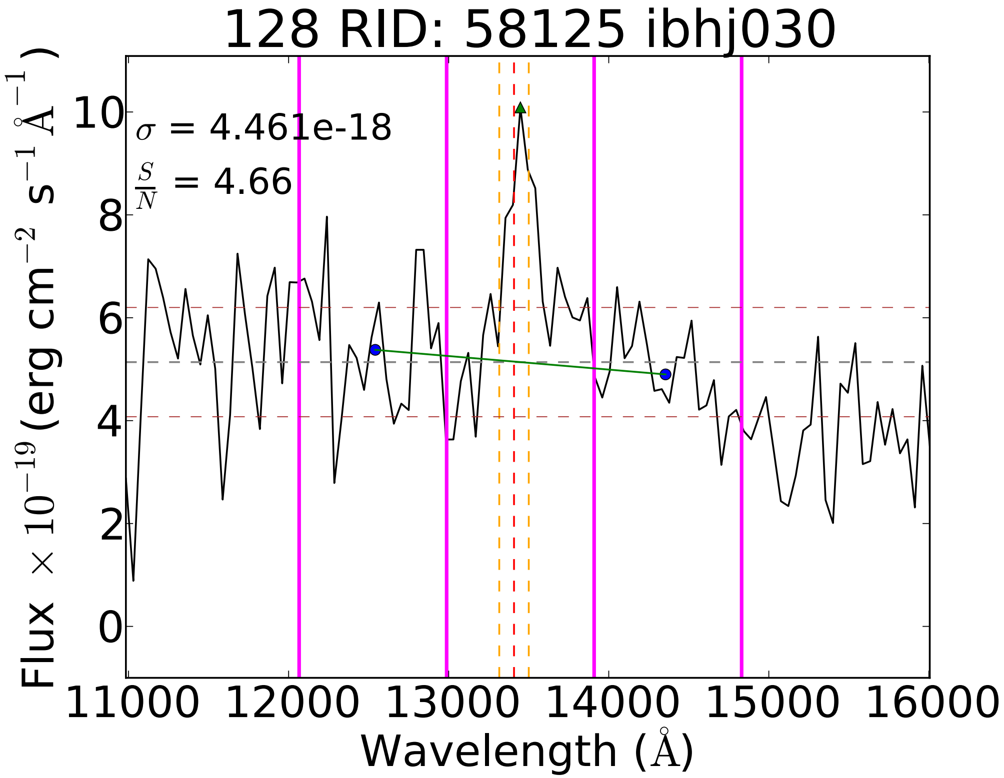
128 RID: 58125 ibhj030
σ = 4.461e-18
S/N = 4.66
Flux × 10^-19 (erg cm^-2 s^-1 Å^-1)
0
2
4
6
8
10
11000
12000
13000
14000
15000
16000
Wavelength (Å)

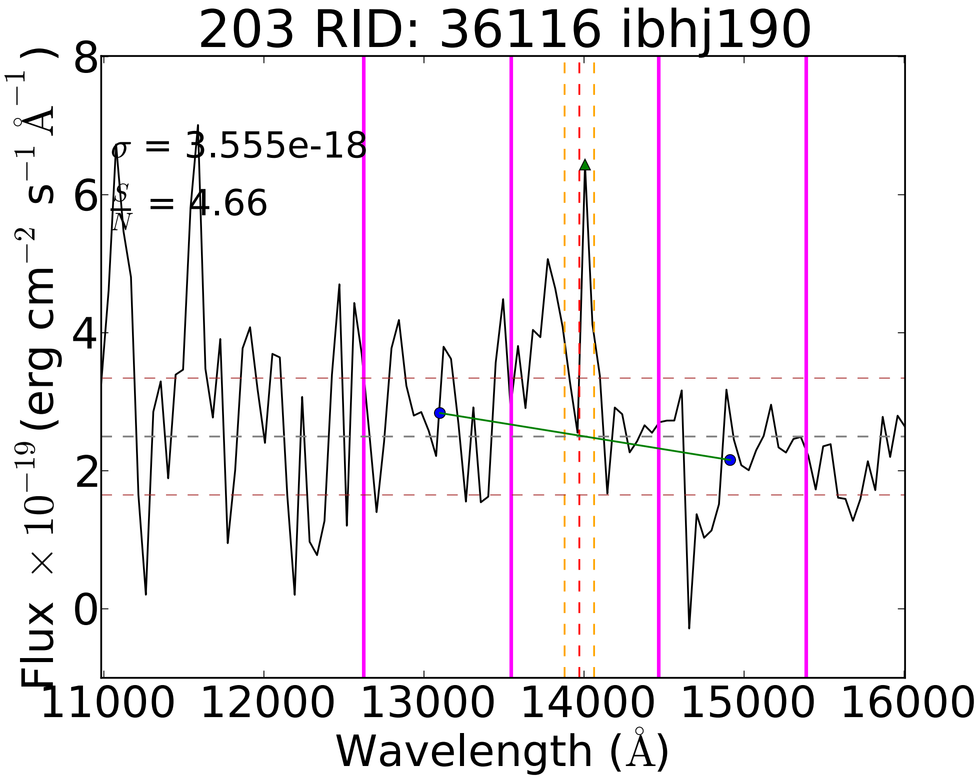
203 RID: 36116 ibhj190
σ = 3.555e-18
S/N = 4.66
Flux × 10^-19 (erg cm^-2 s^-1 Å^-1)
0
2
4
6
8
11000
12000
13000
14000
15000
16000
Wavelength (Å)

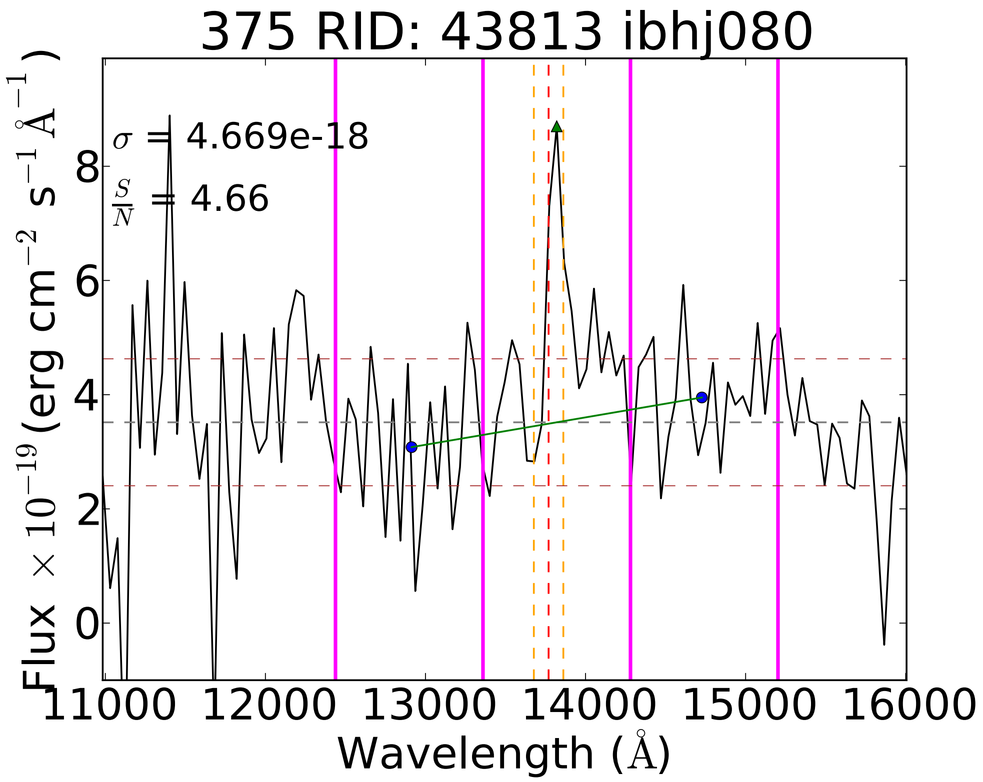
375 RID: 43813 ibhj080
σ = 4.669e-18
S/N = 4.66
Flux × 10^-19 (erg cm^-2 s^-1 Å^-1)
0
2
4
6
8
11000
12000
13000
14000
15000
16000
Wavelength (Å)

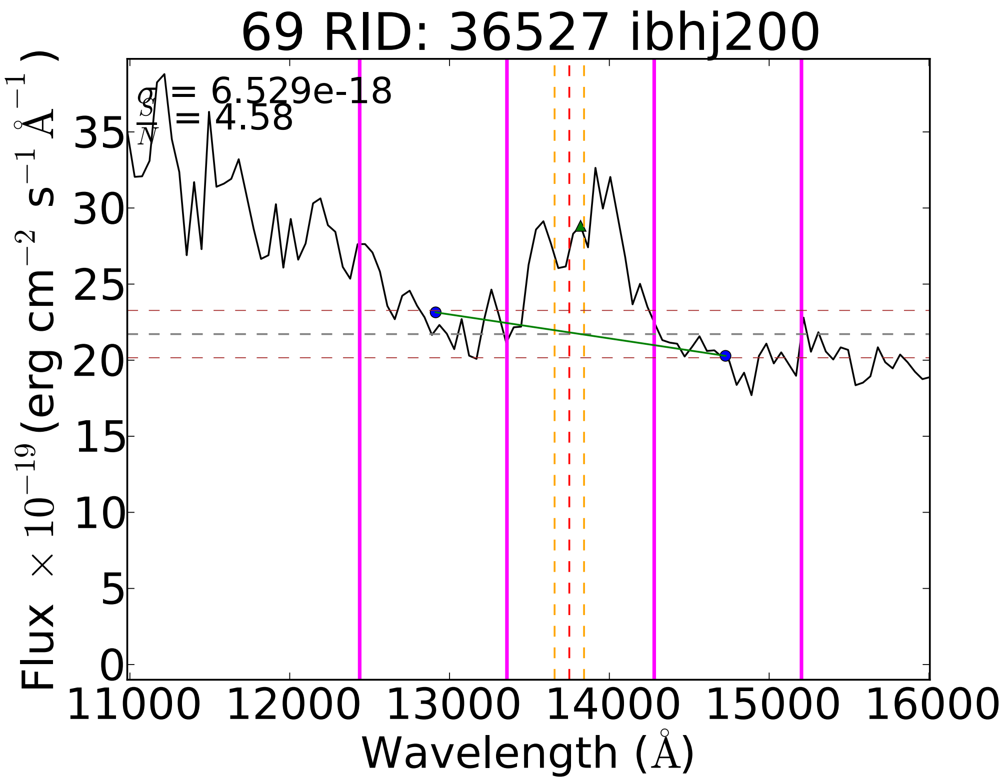
69 RID: 36527 ibhj200
σ = 6.529e-18
S/N = 4.58
Flux × 10^-19 (erg cm^-2 s^-1 Å^-1)
0
5
10
15
20
25
30
35
11000
12000
13000
14000
15000
16000
Wavelength (Å)

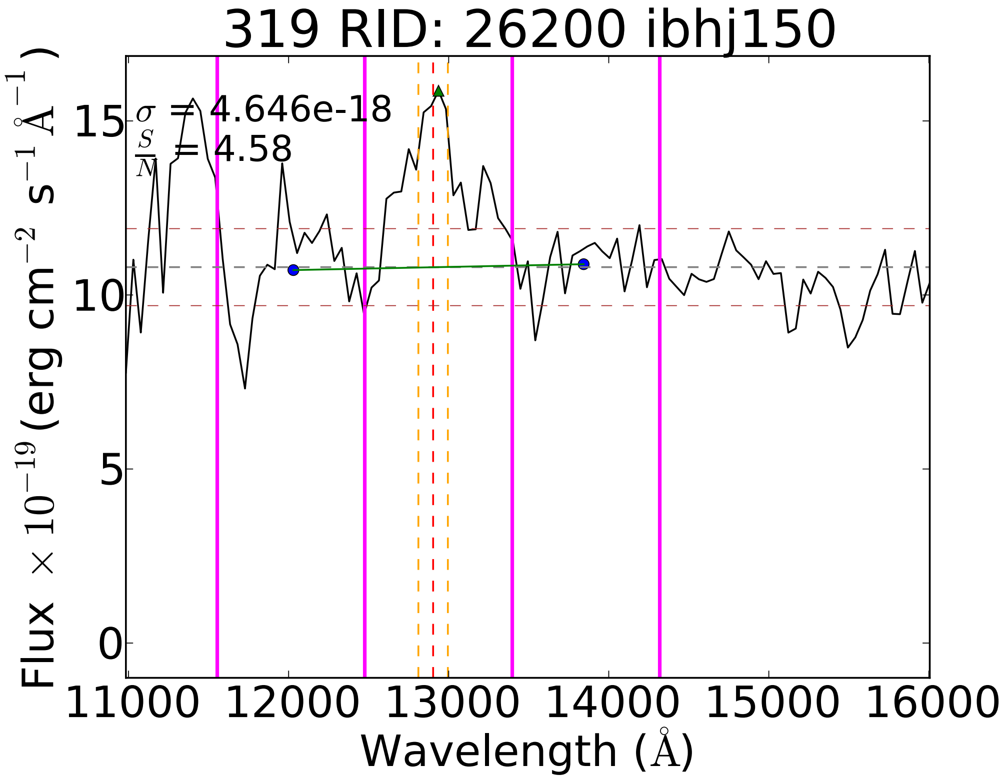
319 RID: 26200 ibhj150
σ = 4.646e-18
$\frac{S}{N}$ = 4.58
Flux × 10^{-19} (erg cm^{-2} s^{-1} Å^{-1})
Wavelength (Å)
0
5
10
15
11000
12000
13000
14000
15000
16000

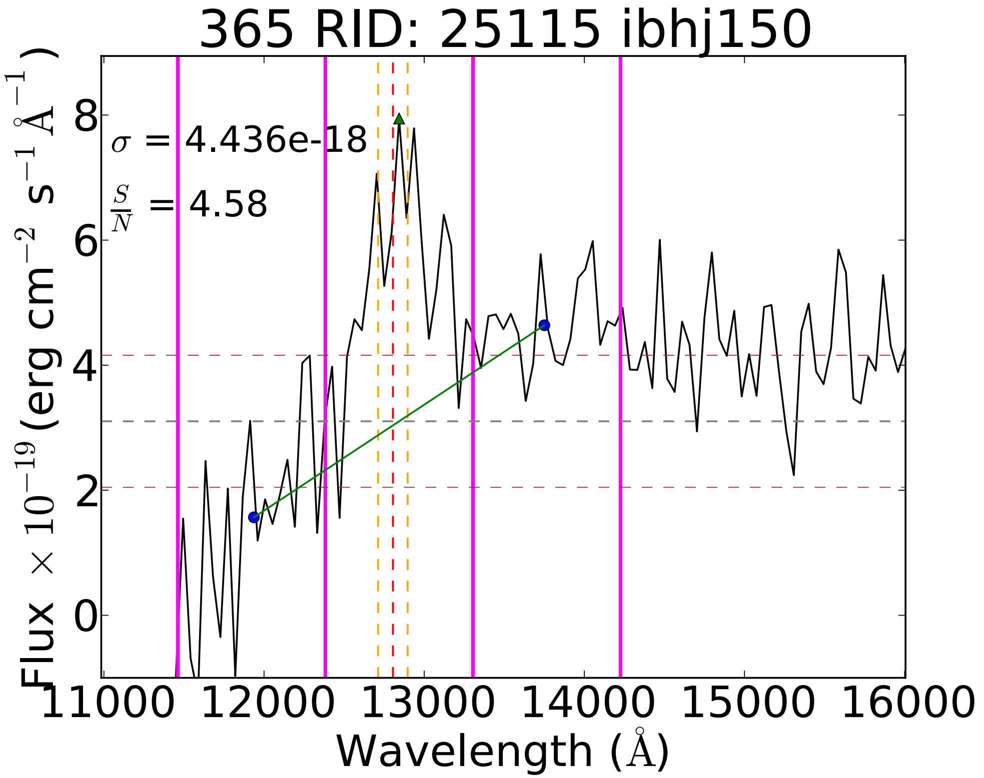
365 RID: 25115 ibhj150
σ = 4.436e-18
$\frac{S}{N}$ = 4.58
Flux × 10^{-19} (erg cm^{-2} s^{-1} Å^{-1})
Wavelength (Å)
0
2
4
6
8
11000
12000
13000
14000
15000
16000

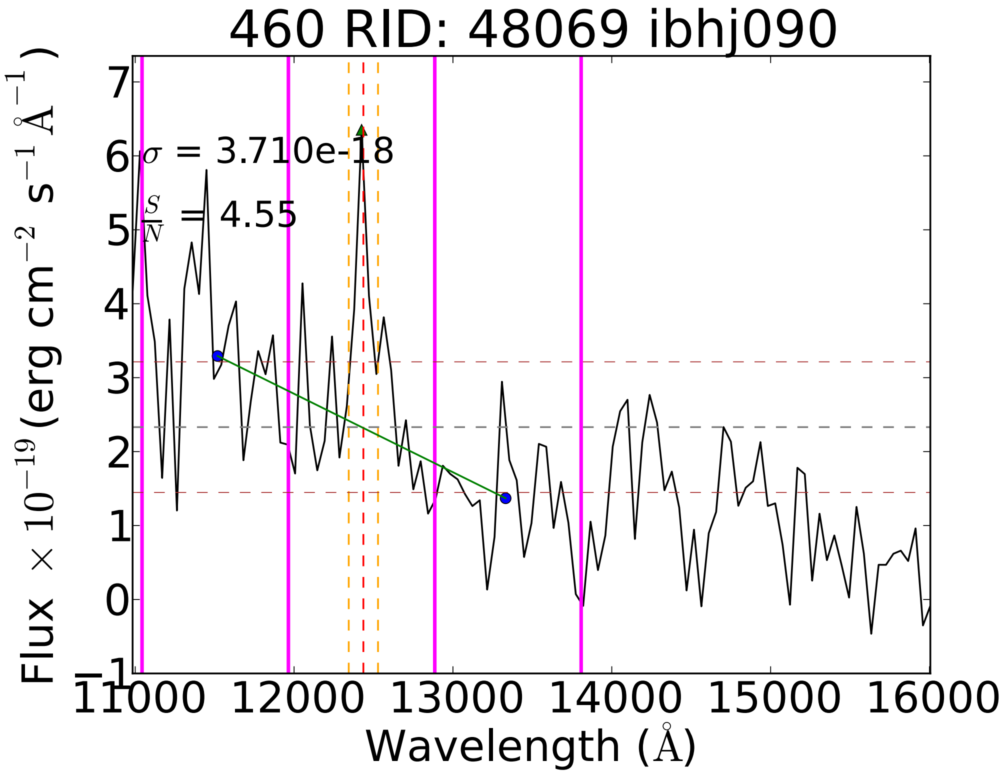
460 RID: 48069 ibhj090
σ = 3.710e-18
$\frac{S}{N}$ = 4.55
Flux × 10^{-19} (erg cm^{-2} s^{-1} Å^{-1})
Wavelength (Å)
−1
0
1
2
3
4
5
6
7
11000
12000
13000
14000
15000
16000

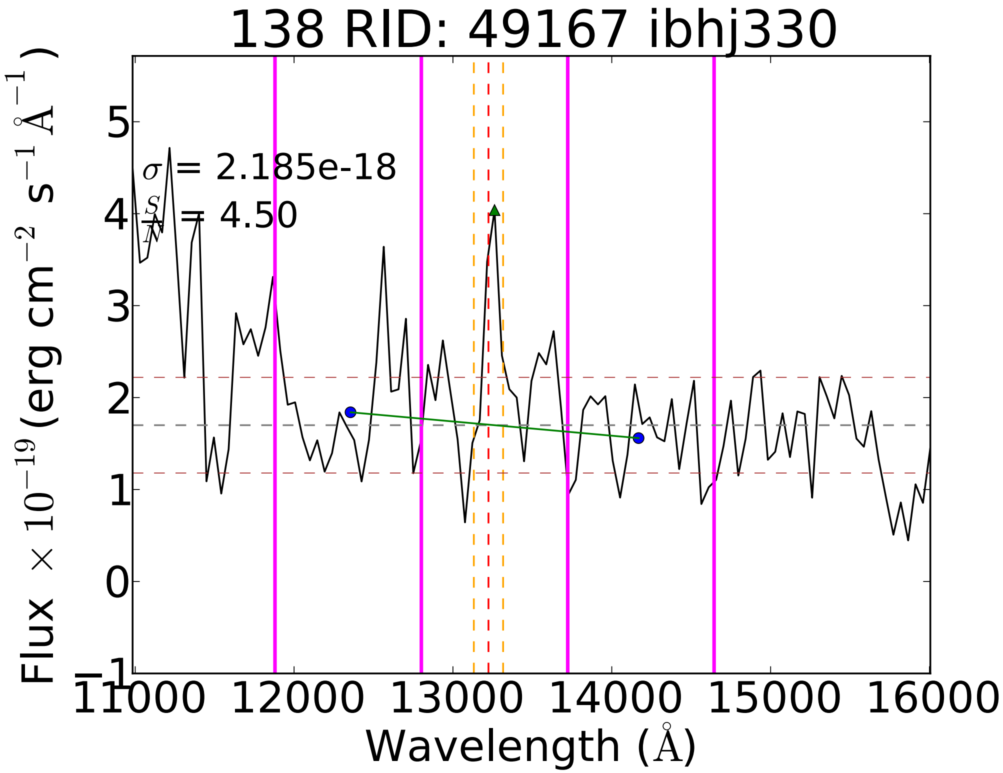
138 RID: 49167 ibhj330
σ = 2.185e-18
$\frac{S}{N}$ = 4.50
Flux × 10^{-19} (erg cm^{-2} s^{-1} Å^{-1})
Wavelength (Å)
−1
0
1
2
3
4
5
11000
12000
13000
14000
15000
16000

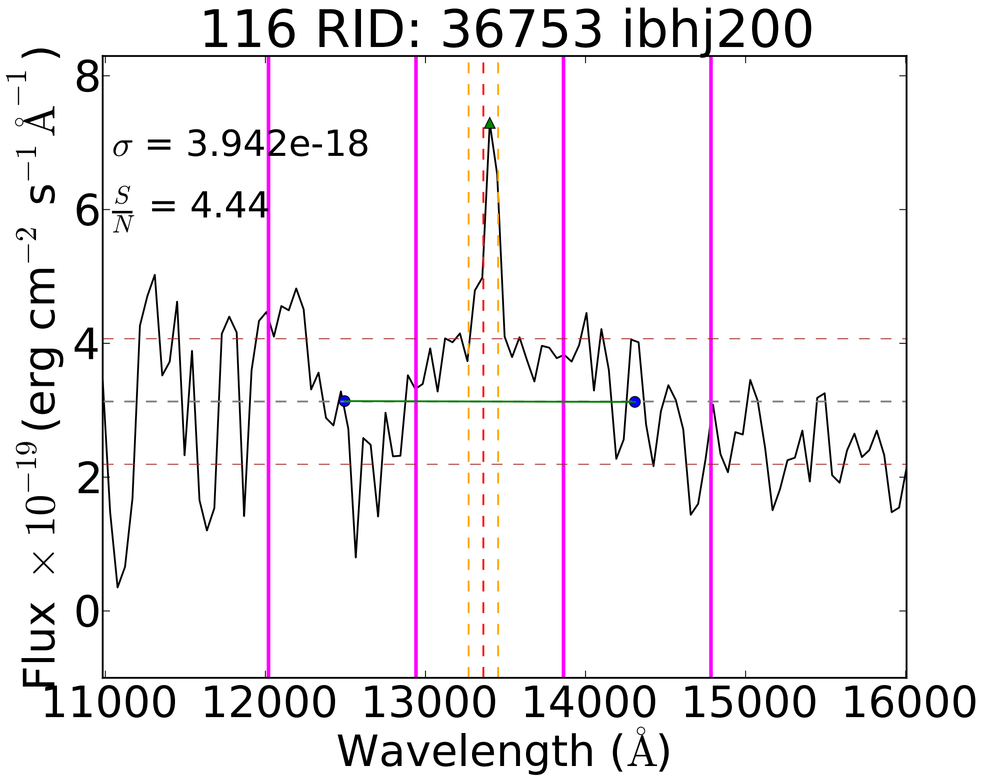
116 RID: 36753 ibhj200

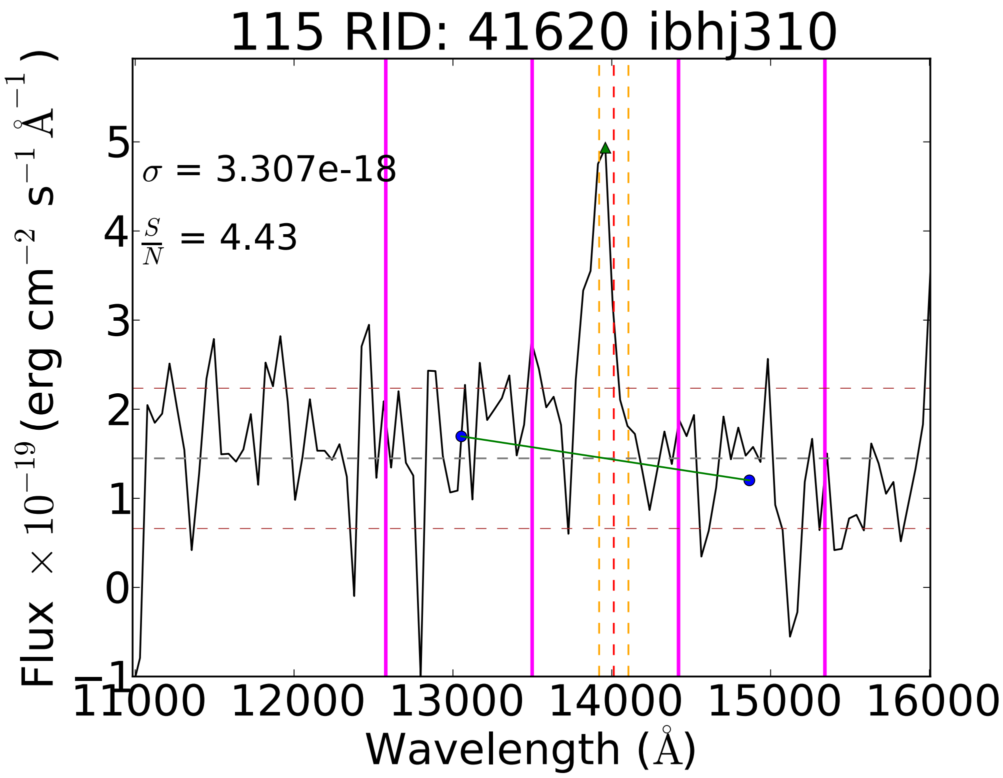
115 RID: 41620 ibhj310

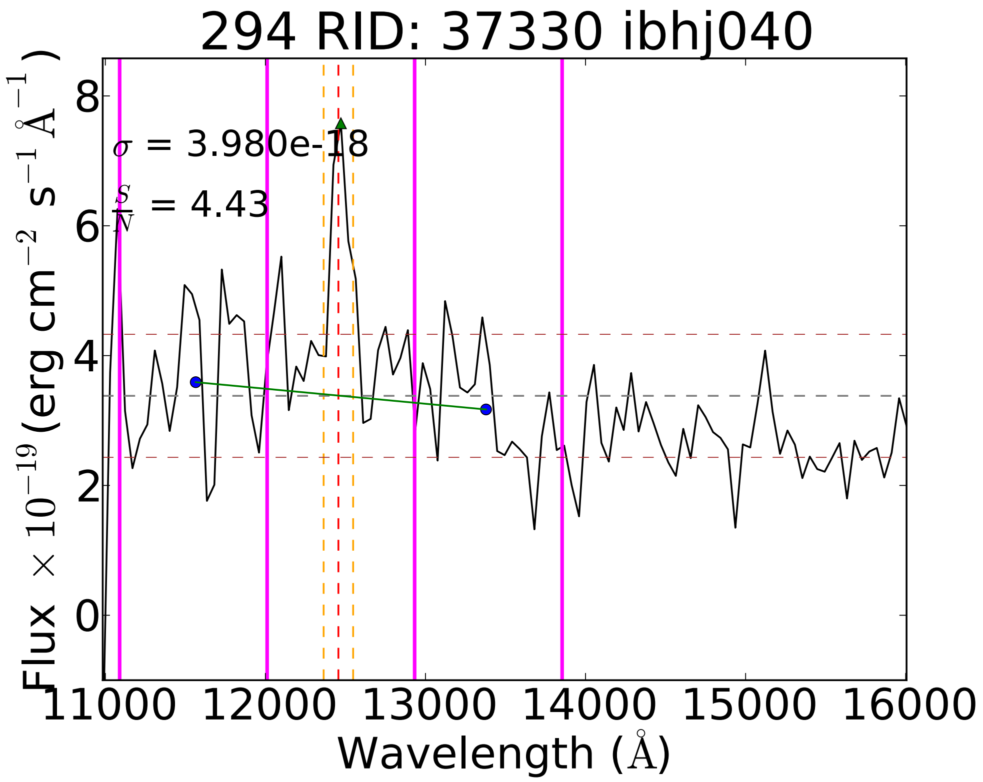
294 RID: 37330 ibhj040

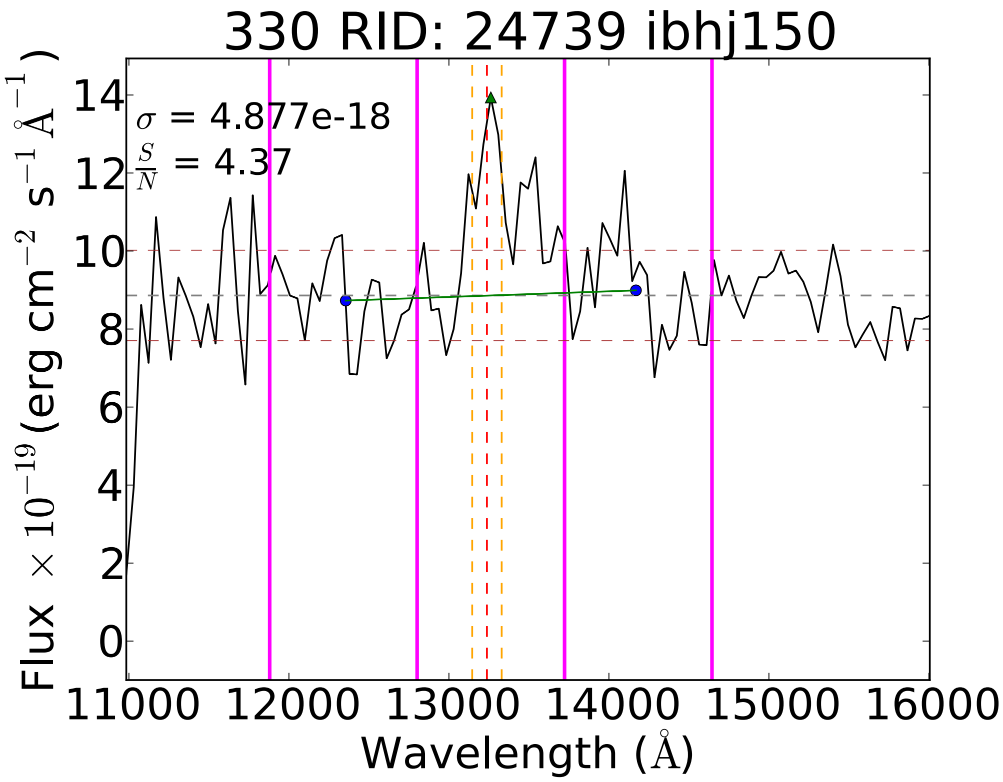
330 RID: 24739 ibhj150

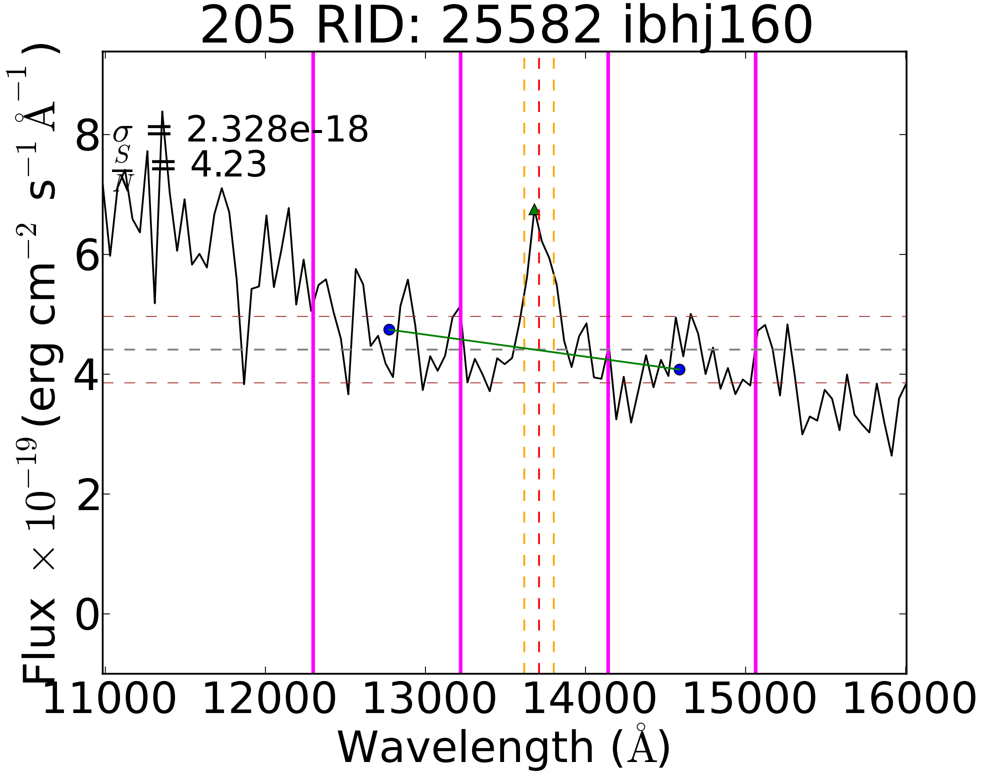
205 RID: 25582 ibhj160

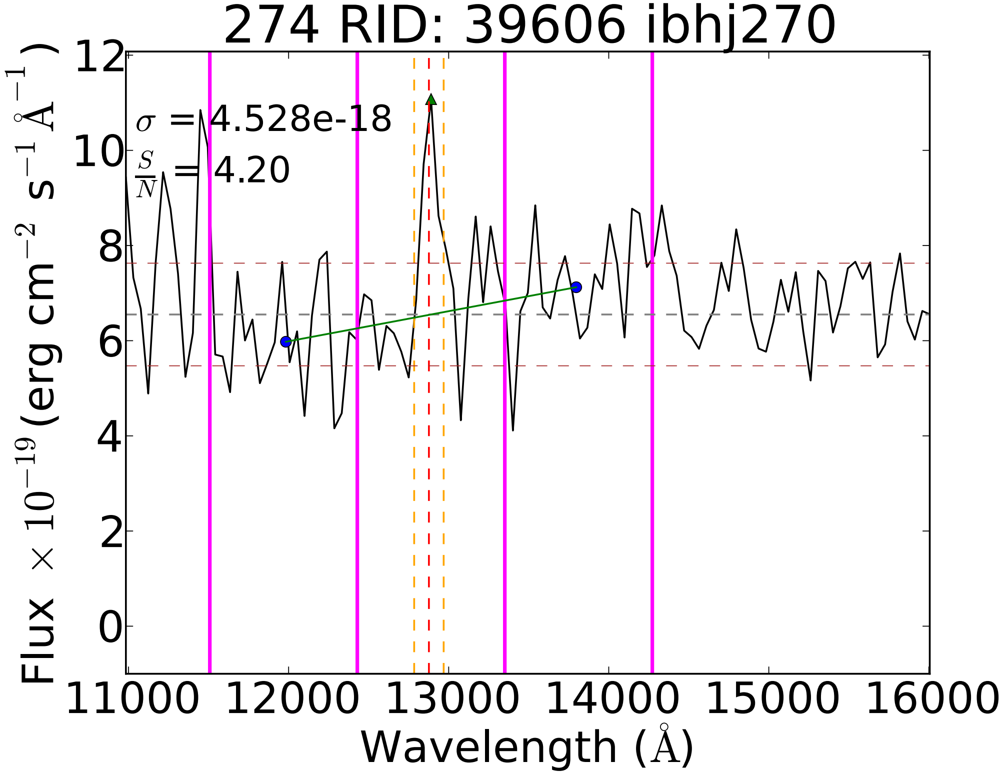
274 RID: 39606 ibhj270

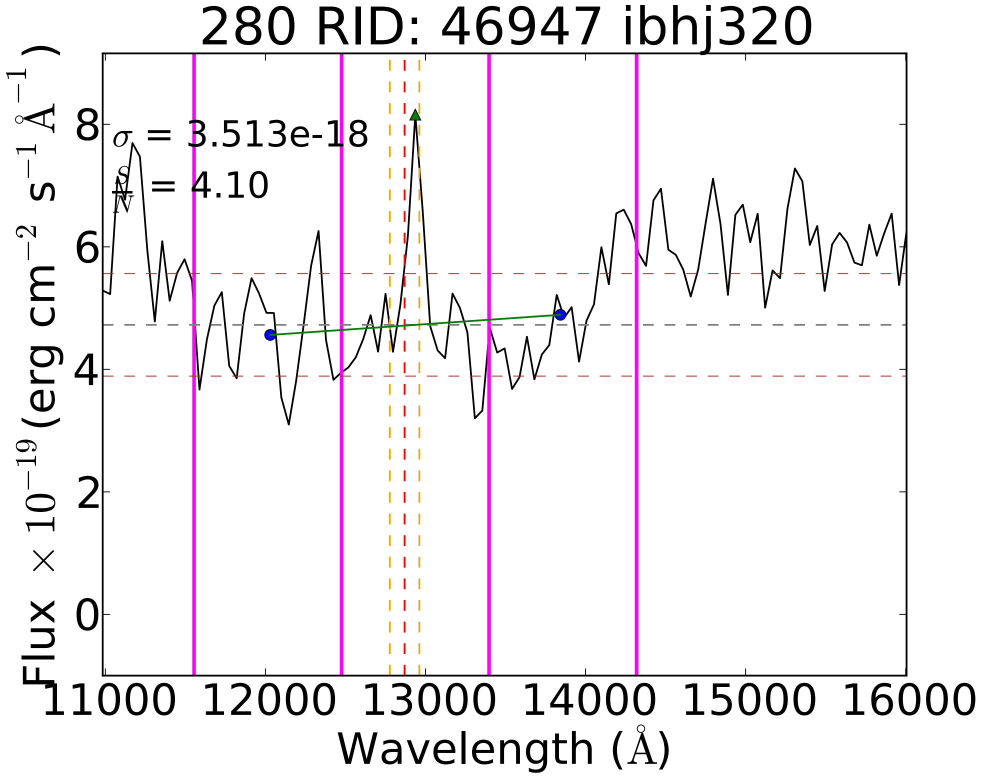
280 RID: 46947 ibhj320

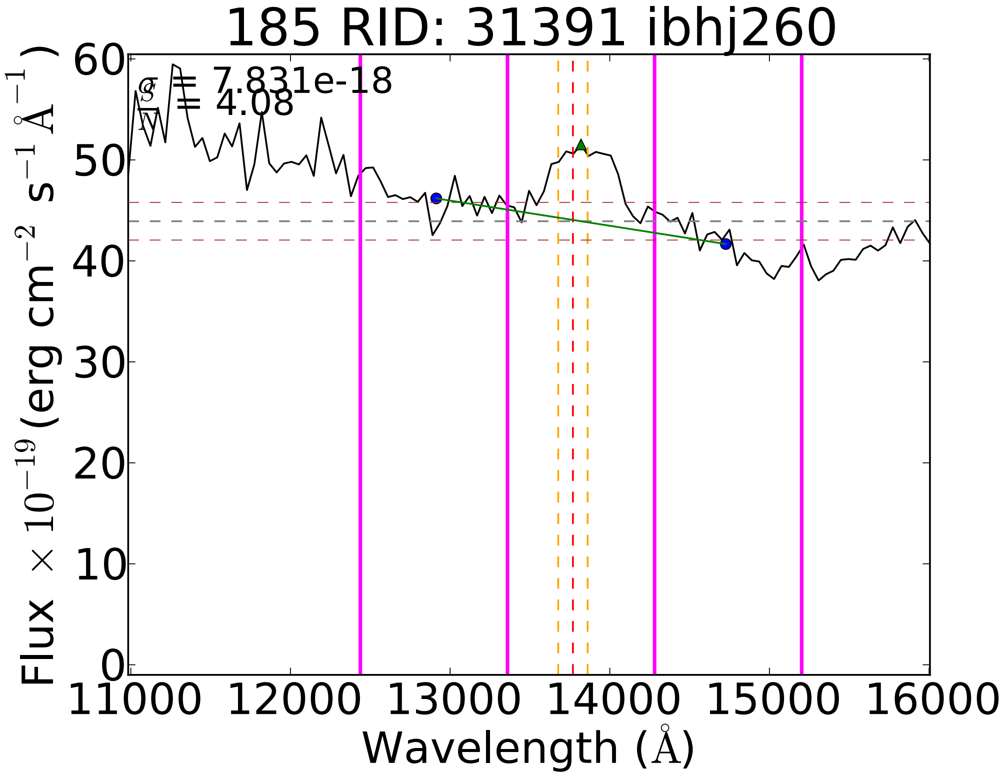
185 RID: 31391 ibhj260

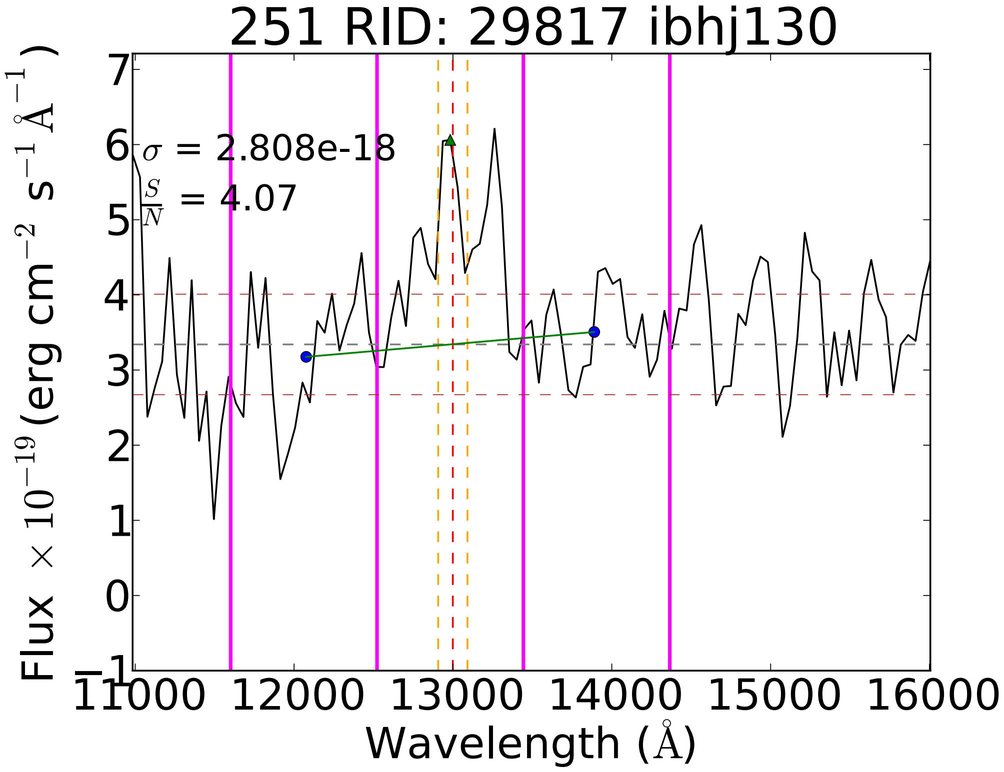
251 RID: 29817 ibhj130
σ = 2.808e-18
$\frac{S}{N}$ = 4.07
Flux $\times 10^{-19}$ (erg cm^{-2} s^{-1} Å^{-1})
Wavelength (Å)
−1
0
1
2
3
4
5
6
7
11000
12000
13000
14000
15000
16000

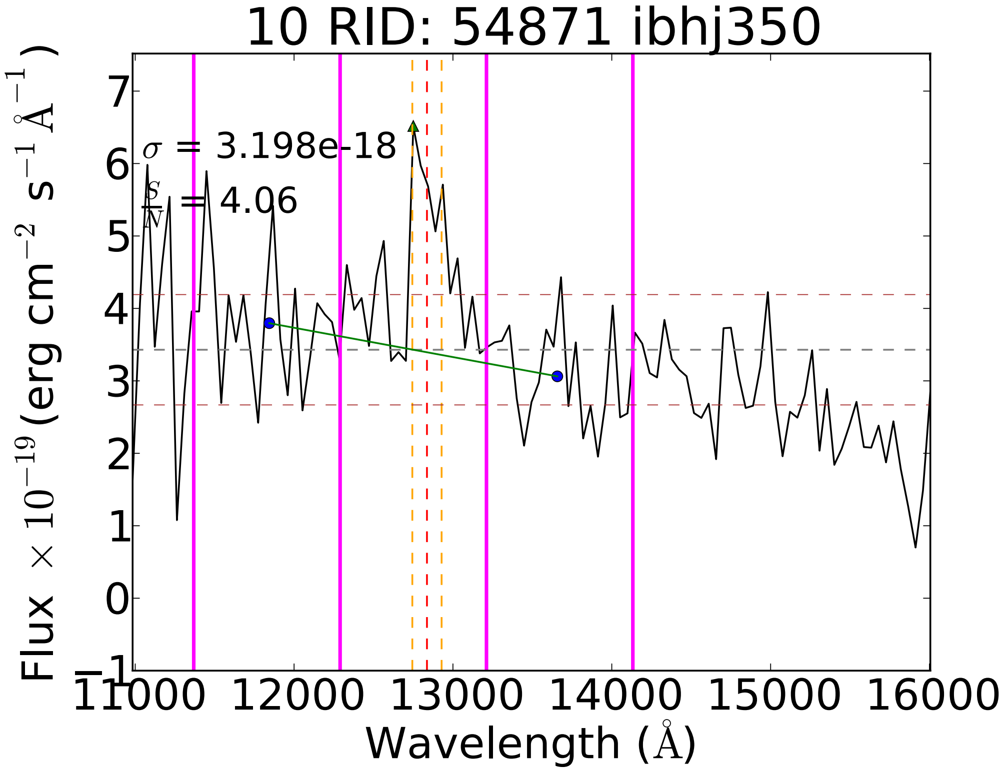
10 RID: 54871 ibhj350
σ = 3.198e-18
$\frac{S}{N}$ = 4.06
Flux $\times 10^{-19}$ (erg cm^{-2} s^{-1} Å^{-1})
Wavelength (Å)
−1
0
1
2
3
4
5
6
7
11000
12000
13000
14000
15000
16000

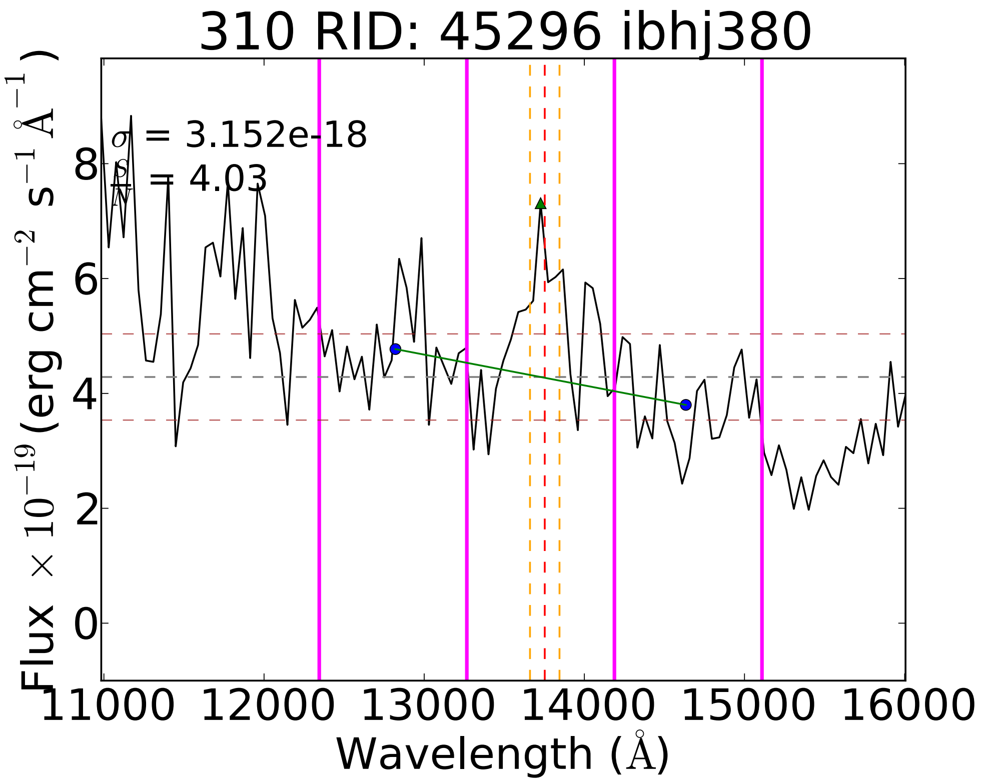
310 RID: 45296 ibhj380
σ = 3.152e-18
$\frac{S}{N}$ = 4.03
Flux $\times 10^{-19}$ (erg cm^{-2} s^{-1} Å^{-1})
Wavelength (Å)
0
2
4
6
8
11000
12000
13000
14000
15000
16000

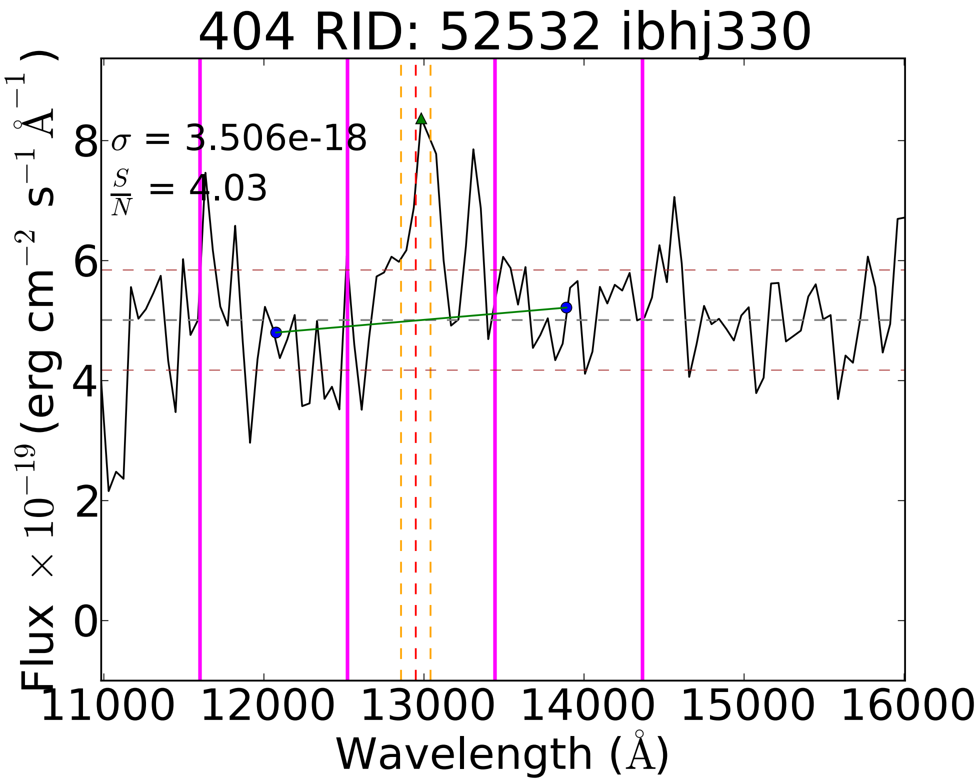
404 RID: 52532 ibhj330
σ = 3.506e-18
$\frac{S}{N}$ = 4.03
Flux $\times 10^{-19}$ (erg cm^{-2} s^{-1} Å^{-1})
Wavelength (Å)
0
2
4
6
8
11000
12000
13000
14000
15000
16000

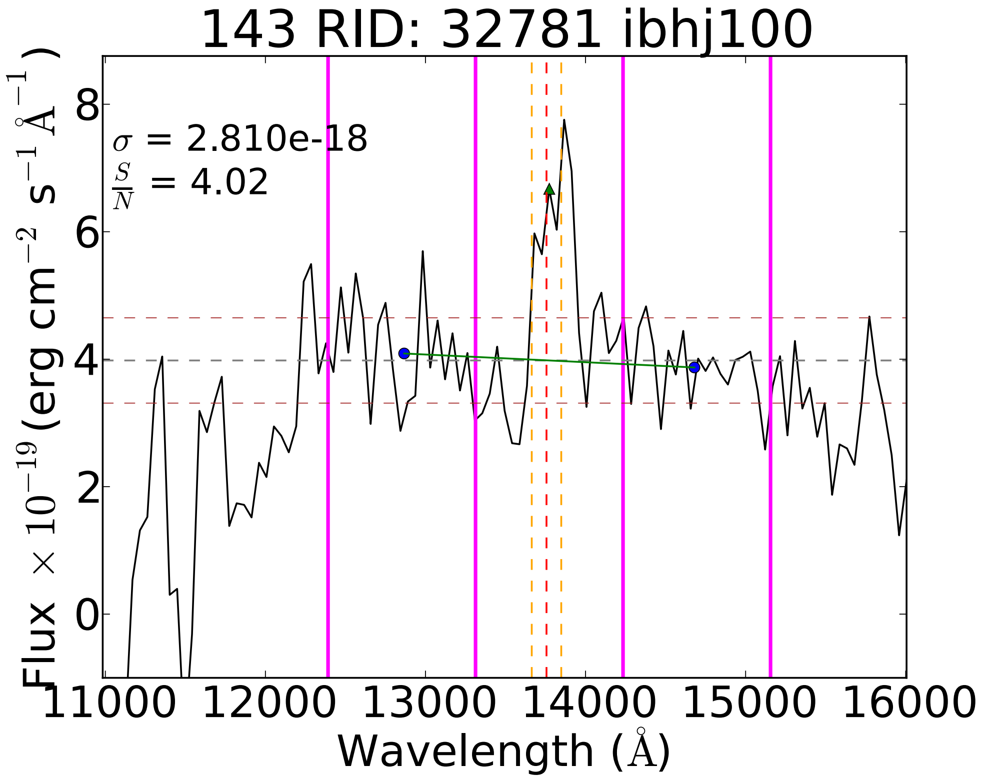
143 RID: 32781 ibhj100
σ = 2.810e-18
S/N = 4.02
Flux × 10^−19 (erg cm^−2 s^−1 Å^−1)
Wavelength (Å)
0
2
4
6
8
11000
12000
13000
14000
15000
16000

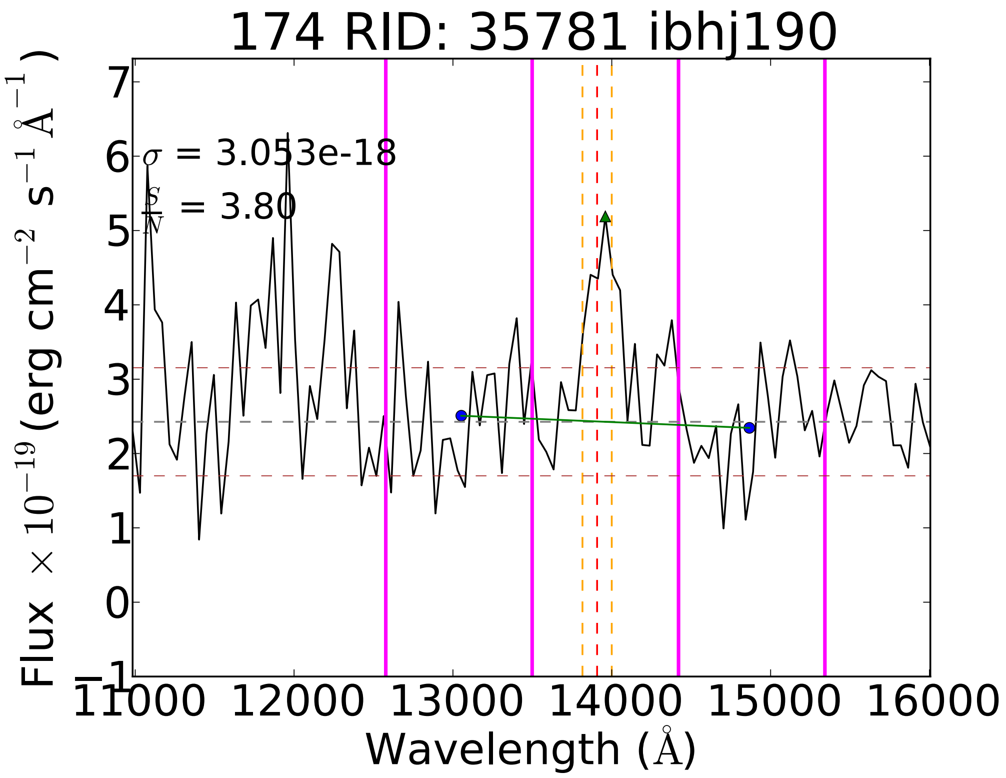
174 RID: 35781 ibhj190
σ = 3.053e-18
S/N = 3.80
Flux × 10^−19 (erg cm^−2 s^−1 Å^−1)
Wavelength (Å)
−1
0
1
2
3
4
5
6
7
11000
12000
13000
14000
15000
16000

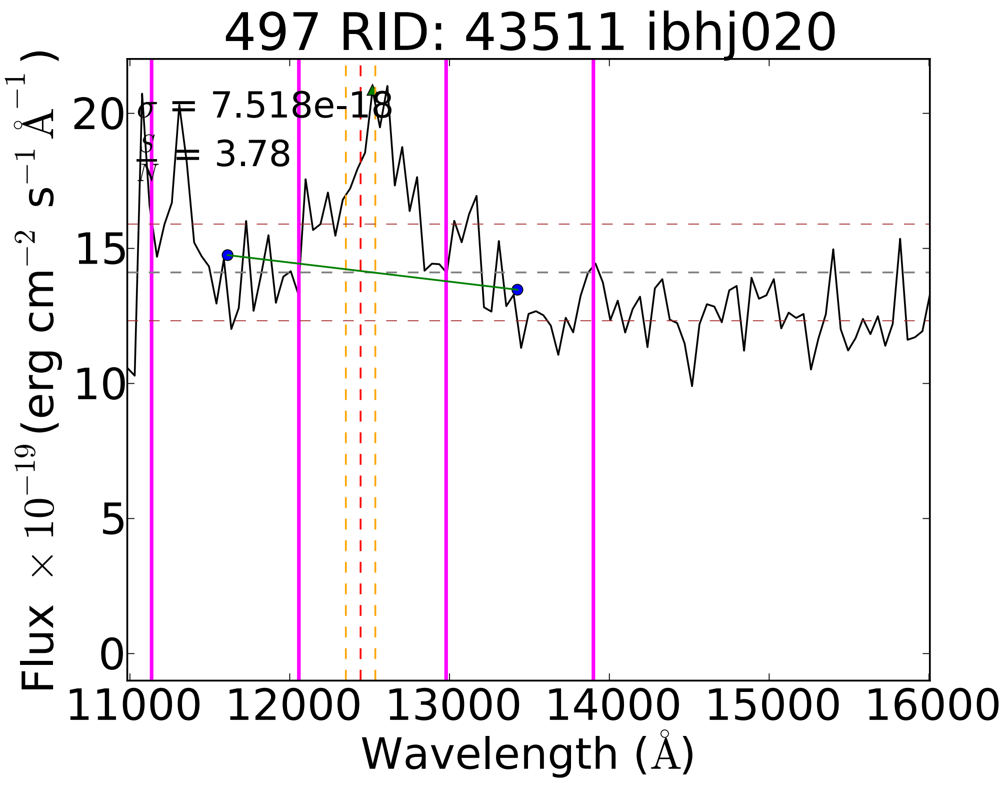
497 RID: 43511 ibhj020
σ = 7.518e-18
S/N = 3.78
Flux × 10^−19 (erg cm^−2 s^−1 Å^−1)
Wavelength (Å)
0
5
10
15
20
11000
12000
13000
14000
15000
16000

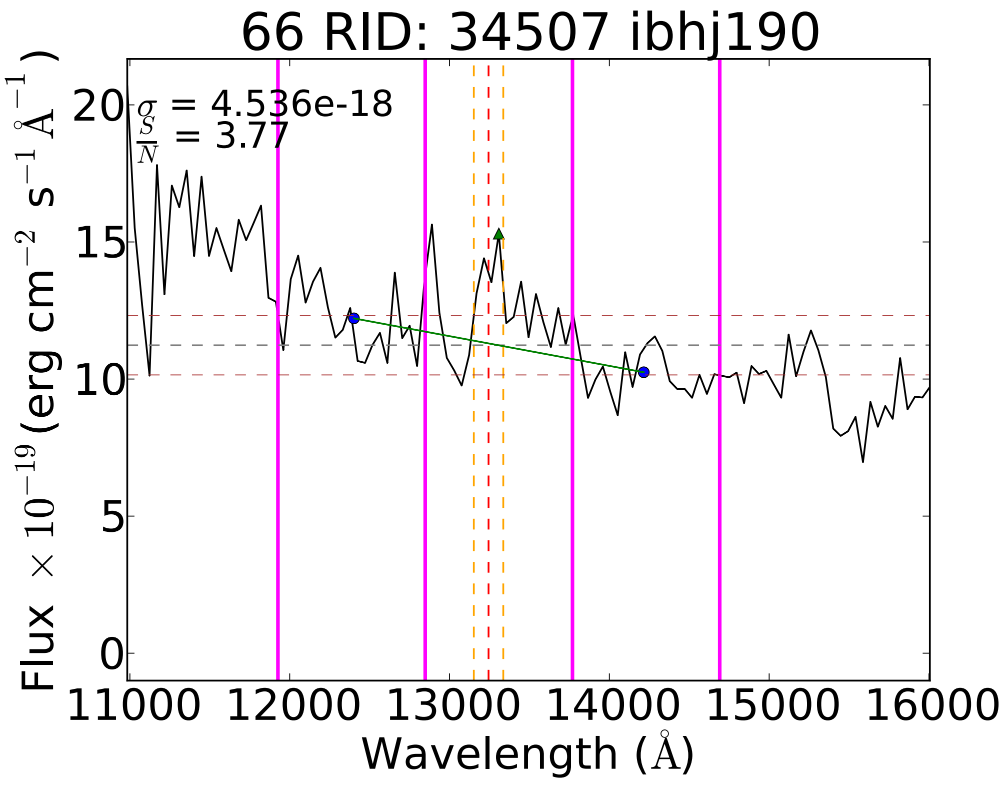
66 RID: 34507 ibhj190
σ = 4.536e-18
S/N = 3.77
Flux × 10^−19 (erg cm^−2 s^−1 Å^−1)
Wavelength (Å)
0
5
10
15
20
11000
12000
13000
14000
15000
16000

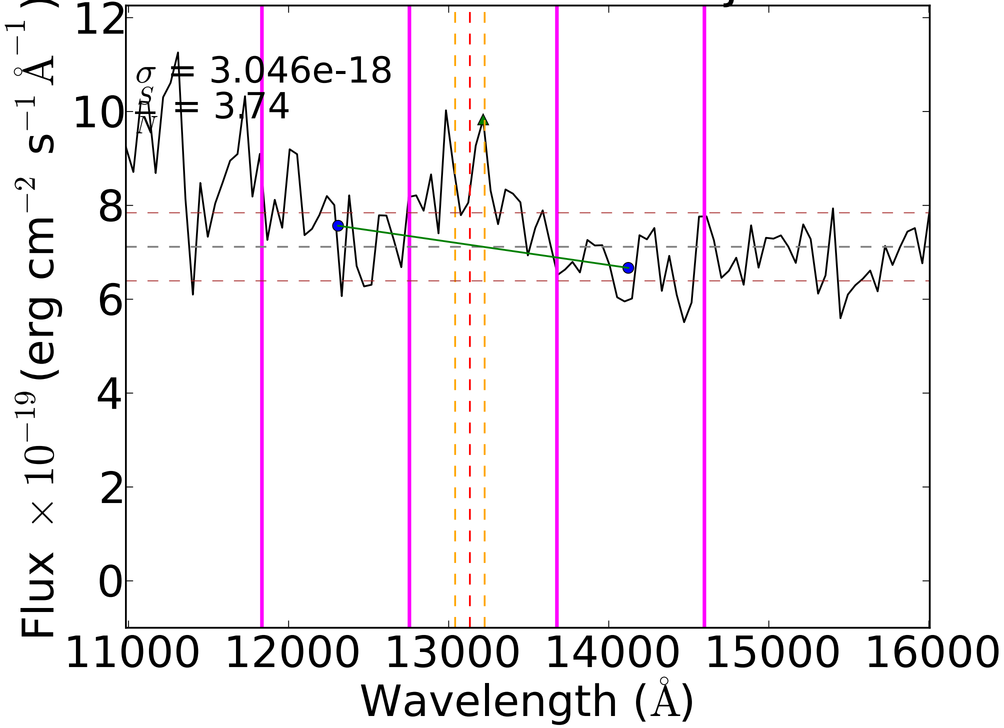

262 RID: 27844 ibhj050

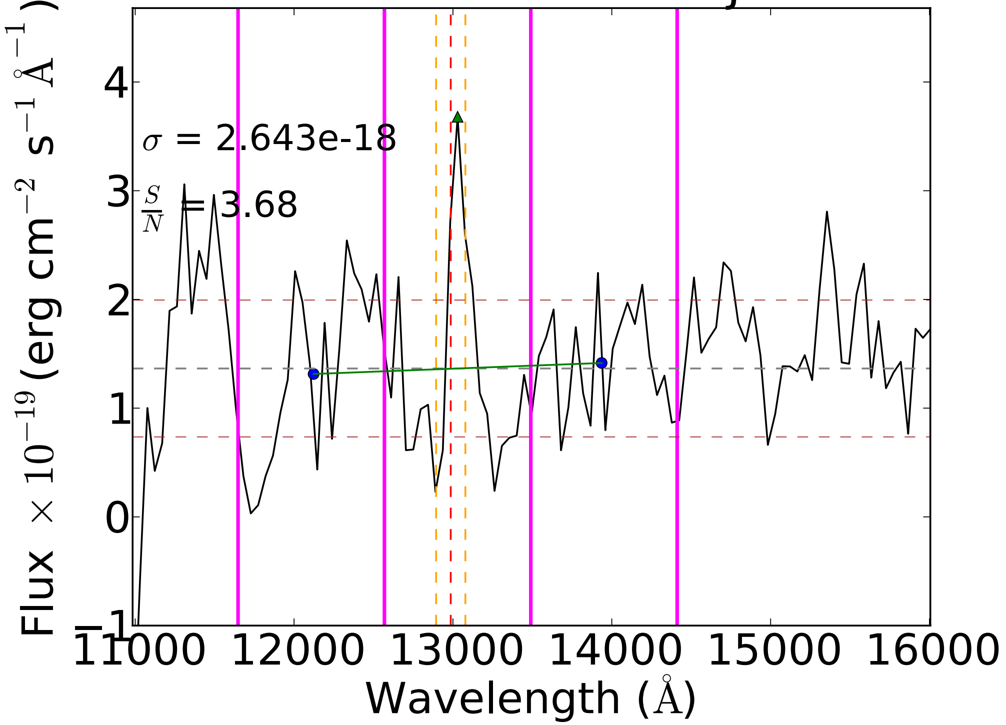

411 RID: 54692 ibhj290

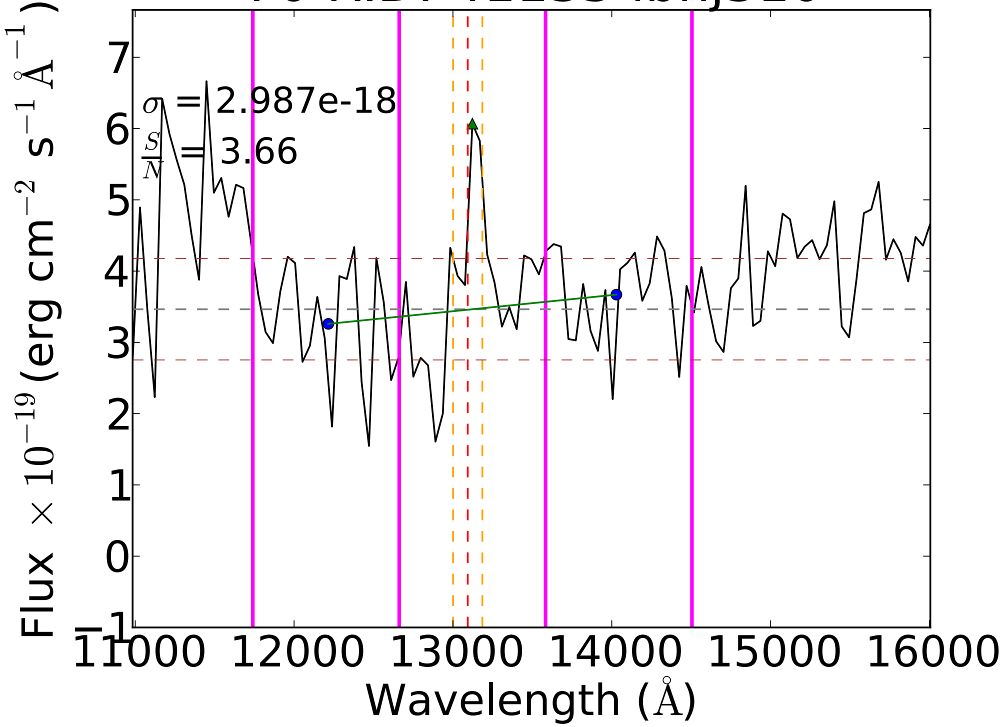

70 RID: 41135 ibhj310

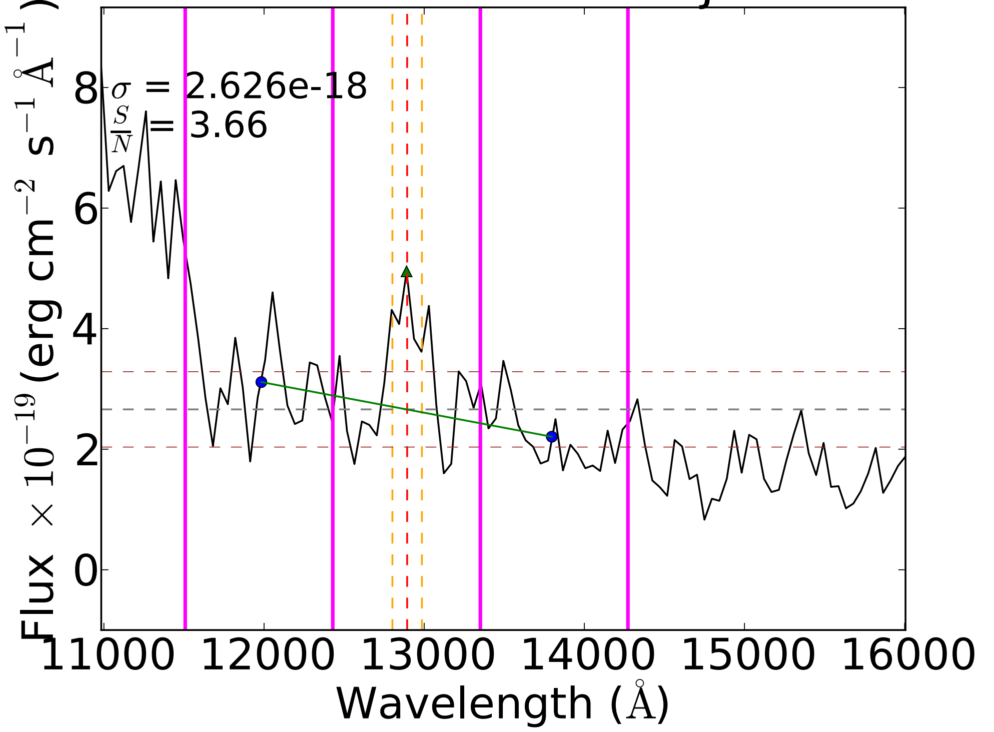

157 RID: 45021 ibhj090

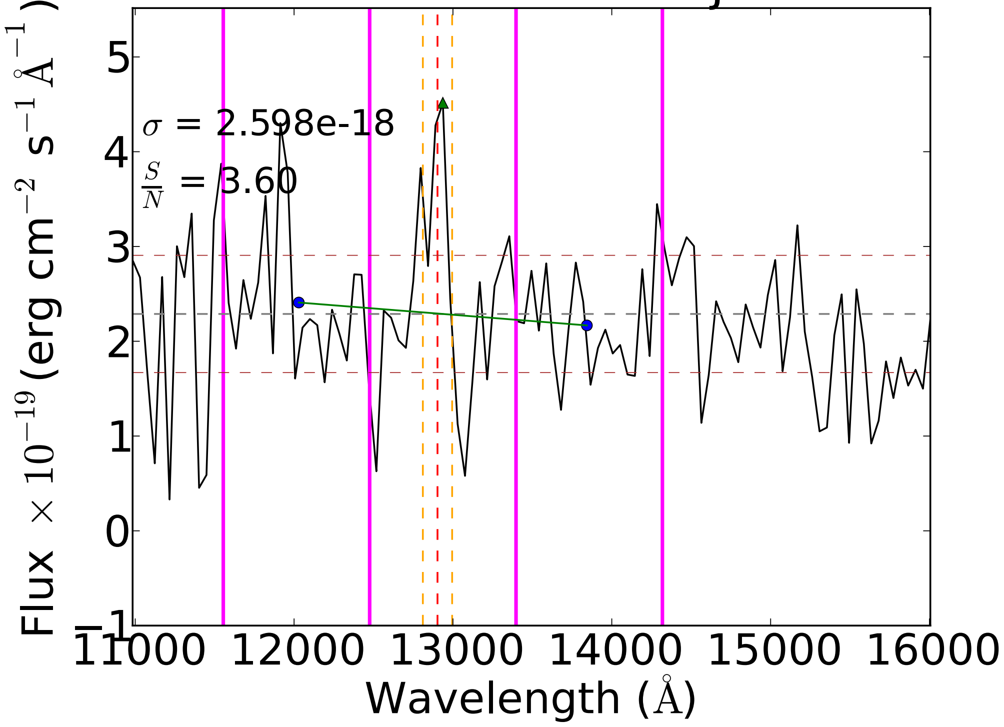
62 RID: 34341 ibhj040

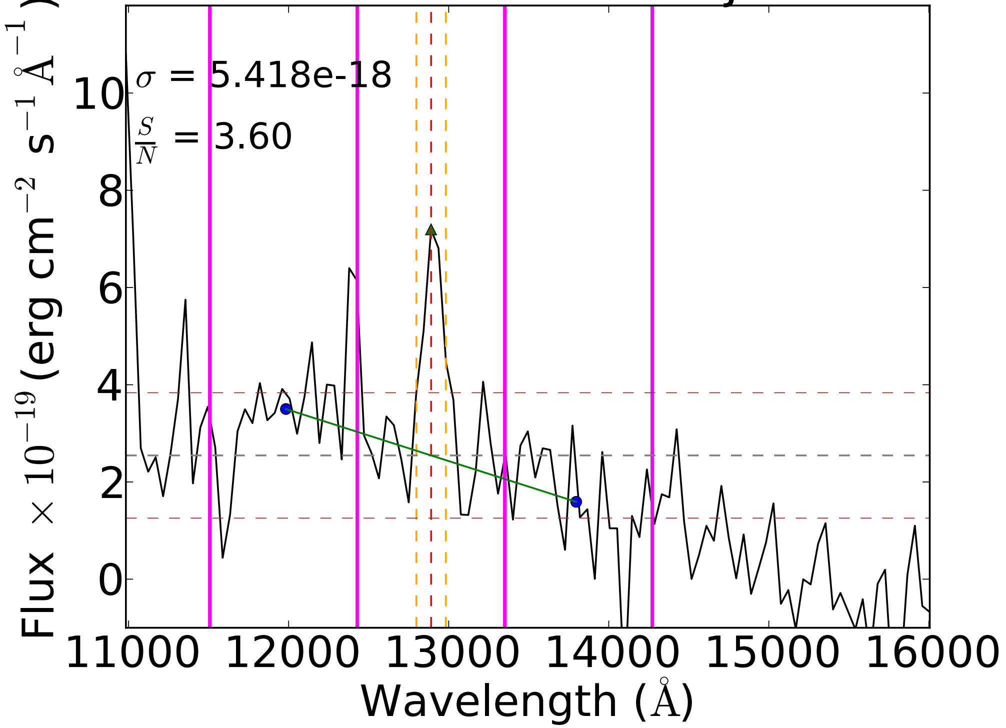
295 RID: 38359 ibhj190

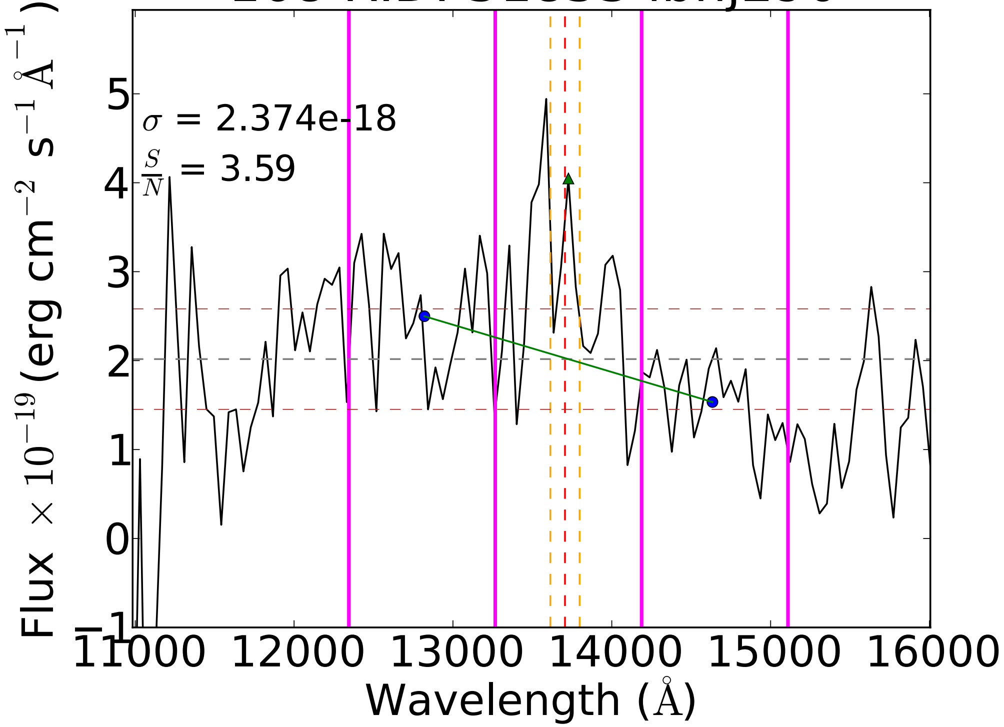
168 RID: 51853 ibhj290

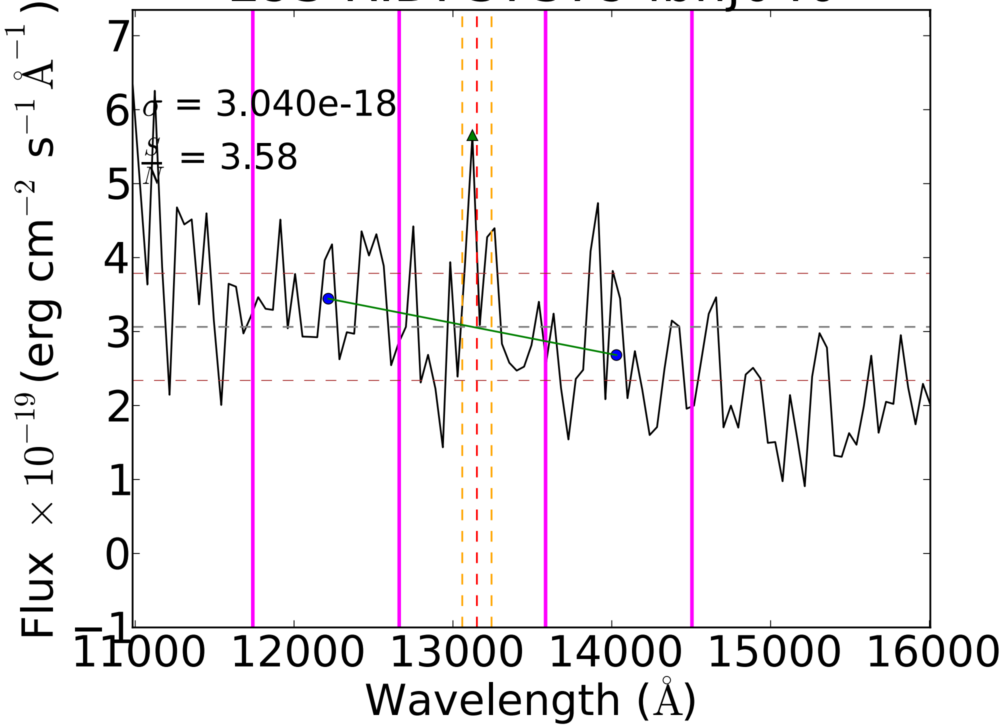
293 RID: 37379 ibhj040

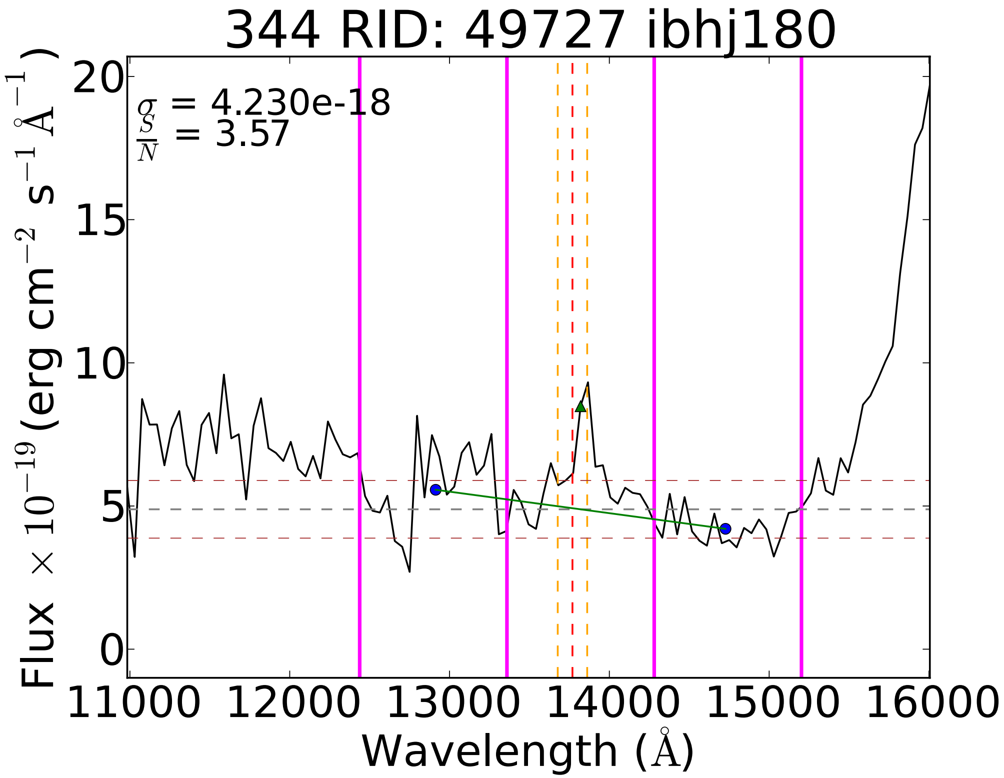
344 RID: 49727 ibhj180
σ = 4.230e-18
S/N = 3.57
Flux × 10^-19 (erg cm^-2 s^-1 Å^-1)
0
5
10
15
20
11000
12000
13000
14000
15000
16000
Wavelength (Å)

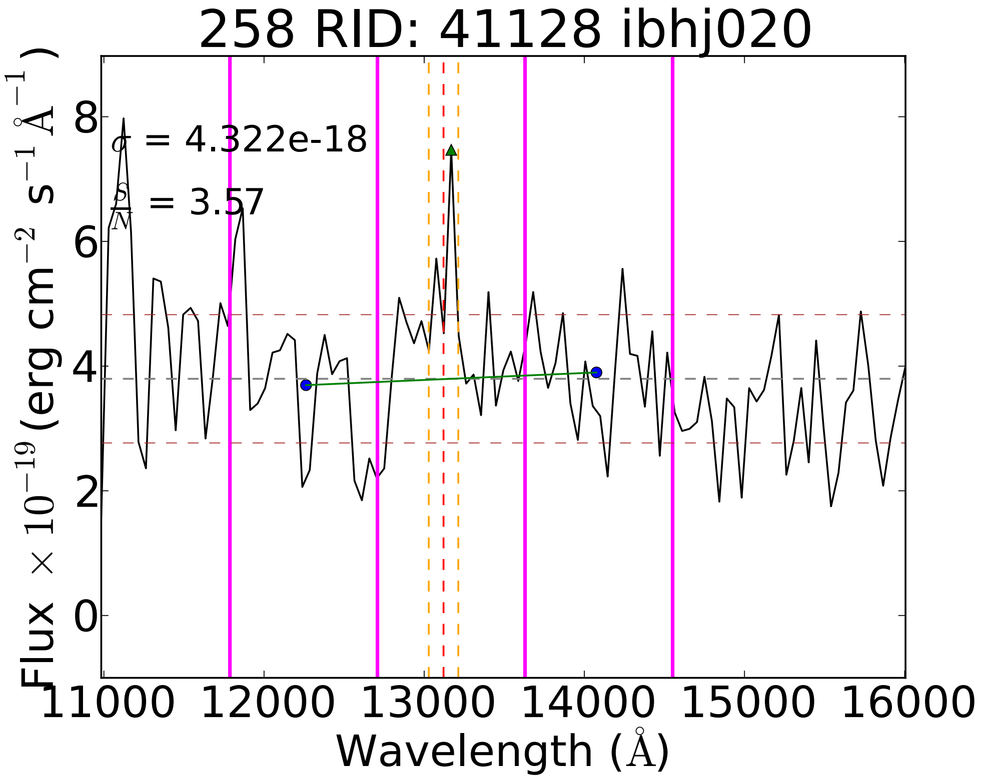
258 RID: 41128 ibhj020
σ = 4.322e-18
S/N = 3.57
Flux × 10^-19 (erg cm^-2 s^-1 Å^-1)
0
2
4
6
8
11000
12000
13000
14000
15000
16000
Wavelength (Å)

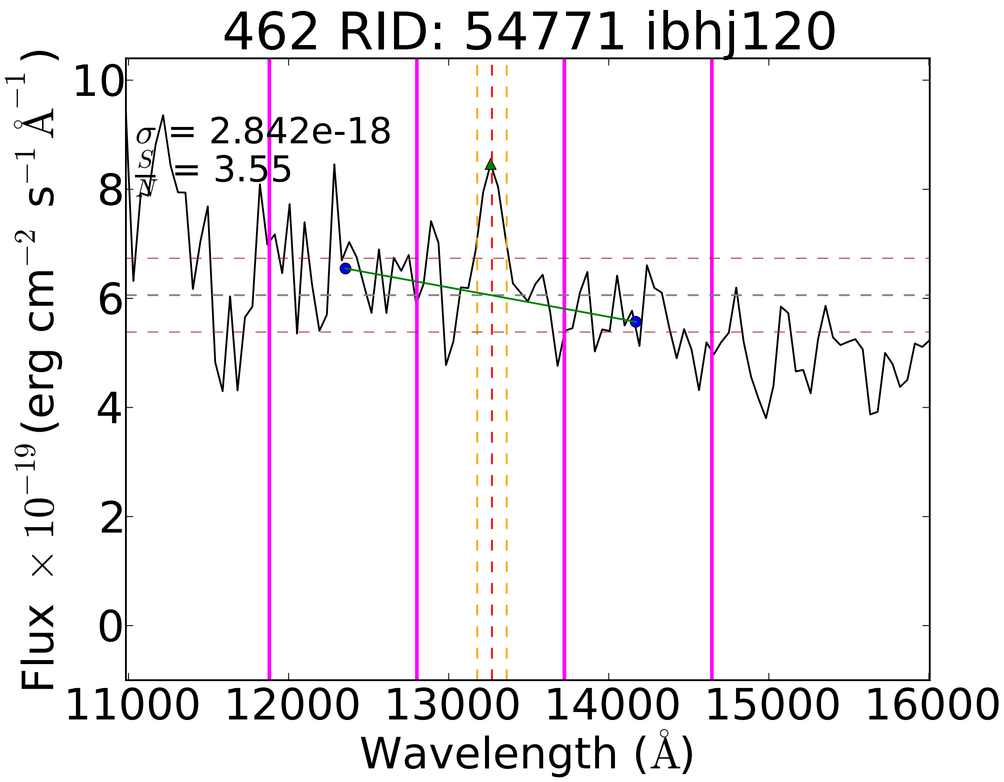
462 RID: 54771 ibhj120
σ = 2.842e-18
S/N = 3.55
Flux × 10^-19 (erg cm^-2 s^-1 Å^-1)
0
2
4
6
8
10
11000
12000
13000
14000
15000
16000
Wavelength (Å)

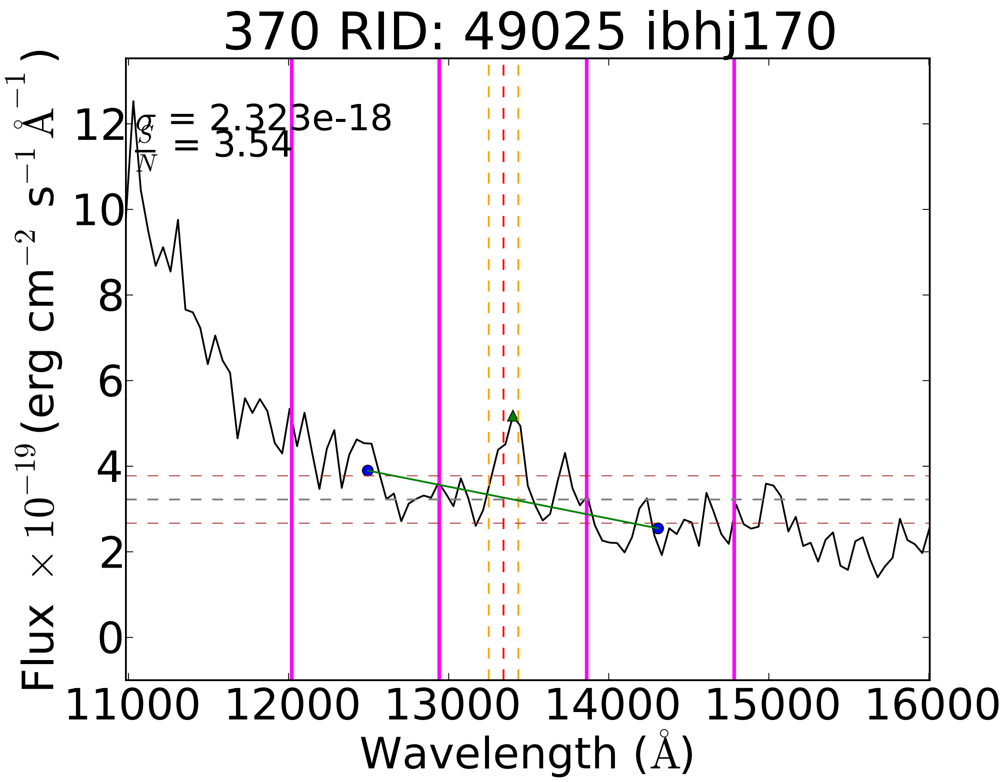
370 RID: 49025 ibhj170
σ = 2.323e-18
S/N = 3.54
Flux × 10^-19 (erg cm^-2 s^-1 Å^-1)
0
2
4
6
8
10
12
11000
12000
13000
14000
15000
16000
Wavelength (Å)

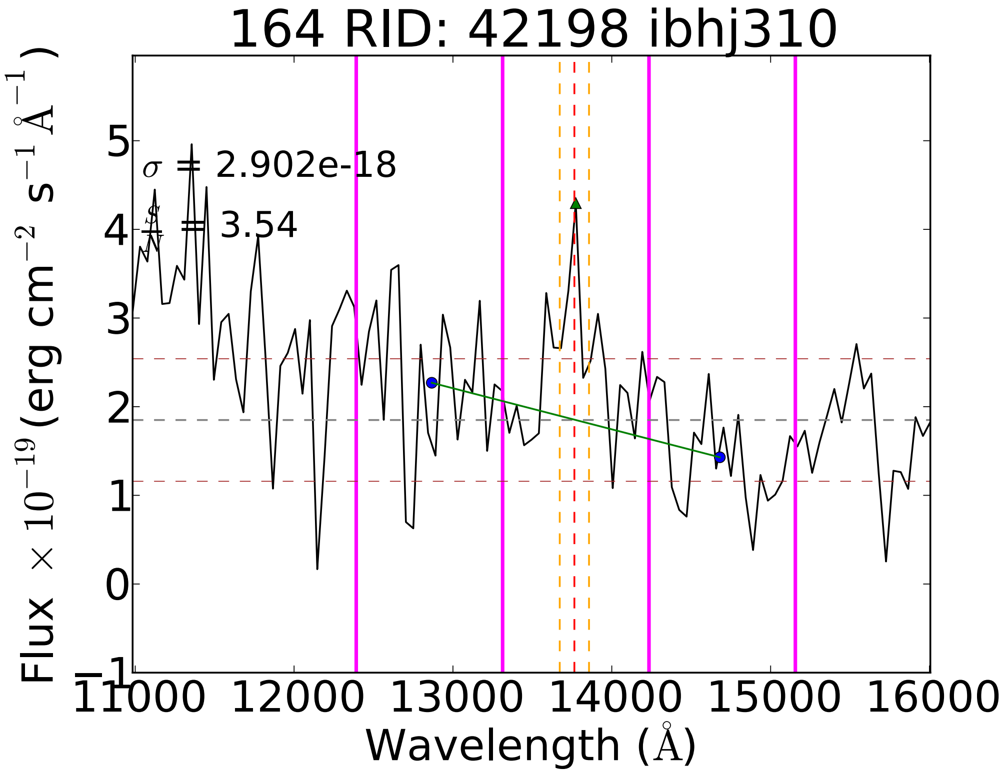
164 RID: 42198 ibhj310
σ = 2.902e-18
$\frac{S}{N}$ = 3.54
Flux $\times 10^{-19}$ (erg cm^{-2} s^{-1} Å^{-1})
Wavelength (Å)
−1
0
1
2
3
4
5
11000
12000
13000
14000
15000
16000

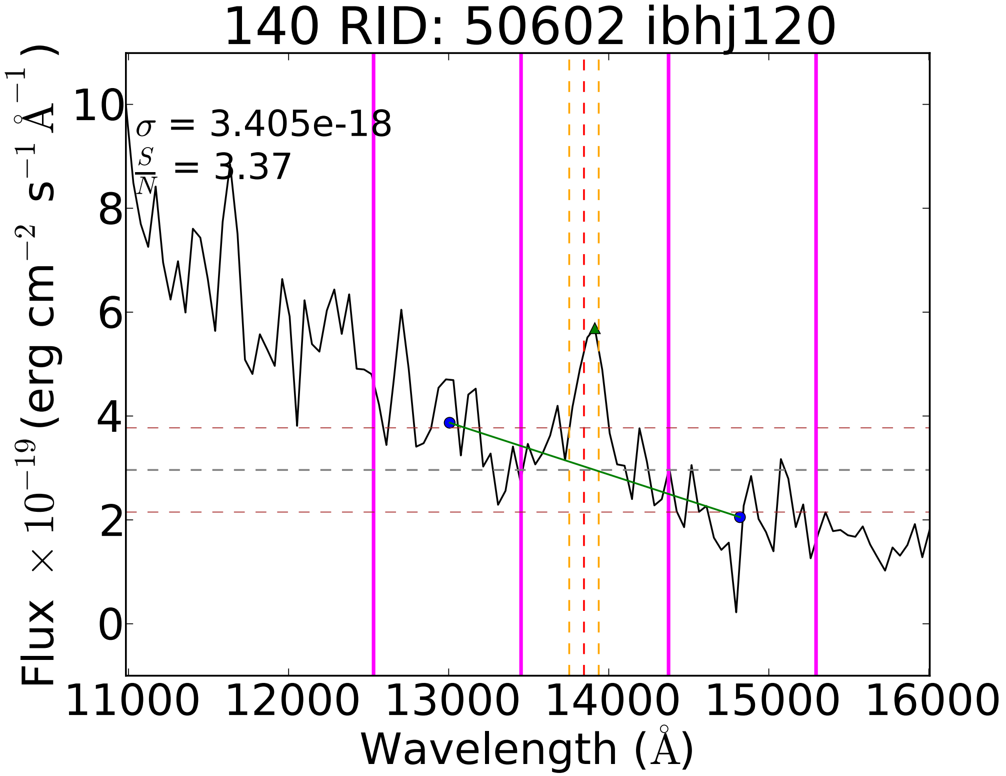
140 RID: 50602 ibhj120
σ = 3.405e-18
$\frac{S}{N}$ = 3.37
Flux $\times 10^{-19}$ (erg cm^{-2} s^{-1} Å^{-1})
Wavelength (Å)
0
2
4
6
8
10
11000
12000
13000
14000
15000
16000

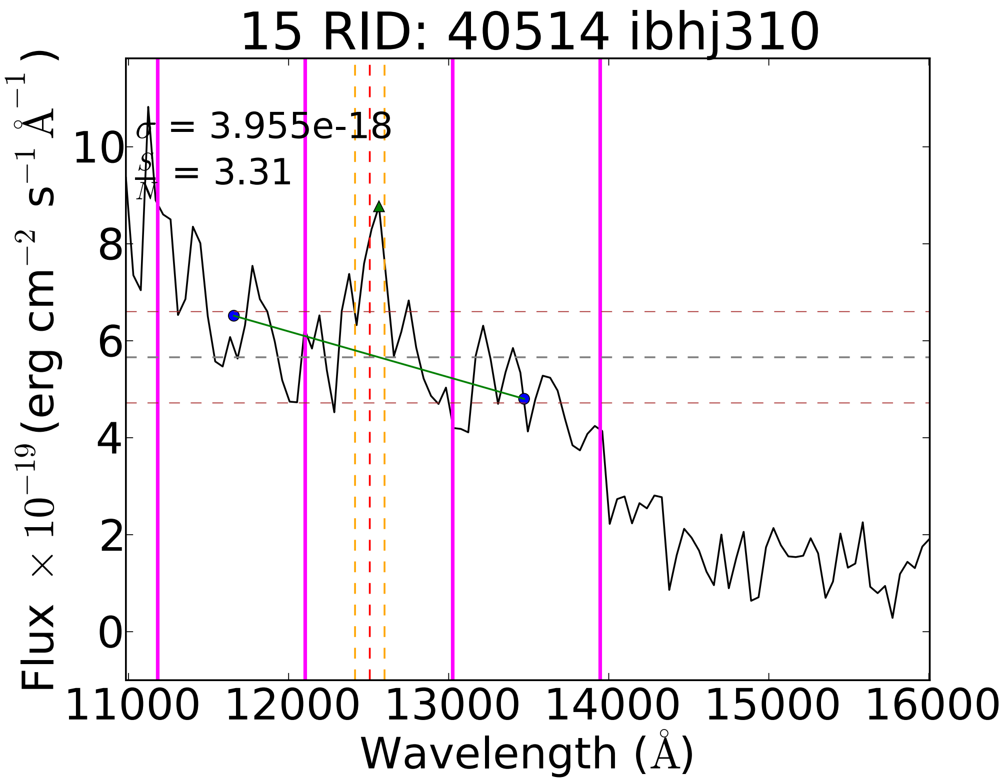
15 RID: 40514 ibhj310
σ = 3.955e-18
$\frac{S}{N}$ = 3.31
Flux $\times 10^{-19}$ (erg cm^{-2} s^{-1} Å^{-1})
Wavelength (Å)
0
2
4
6
8
10
11000
12000
13000
14000
15000
16000

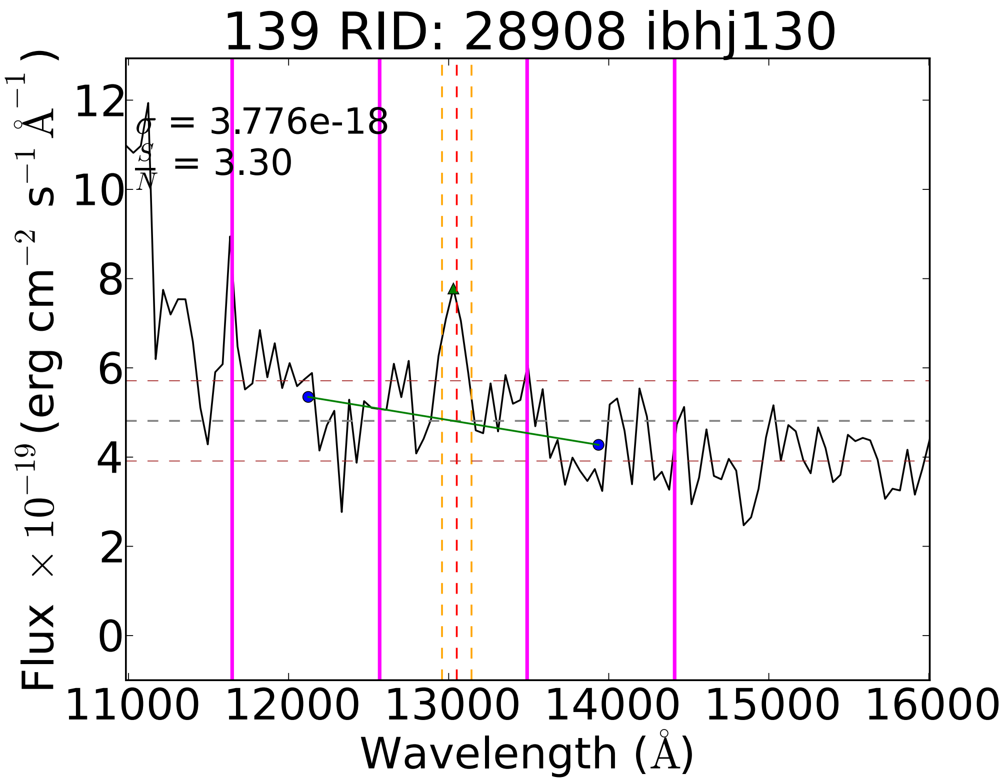
139 RID: 28908 ibhj130
σ = 3.776e-18
$\frac{S}{N}$ = 3.30
Flux $\times 10^{-19}$ (erg cm^{-2} s^{-1} Å^{-1})
Wavelength (Å)
0
2
4
6
8
10
12
11000
12000
13000
14000
15000
16000

331 RID: 49842 ibhj170

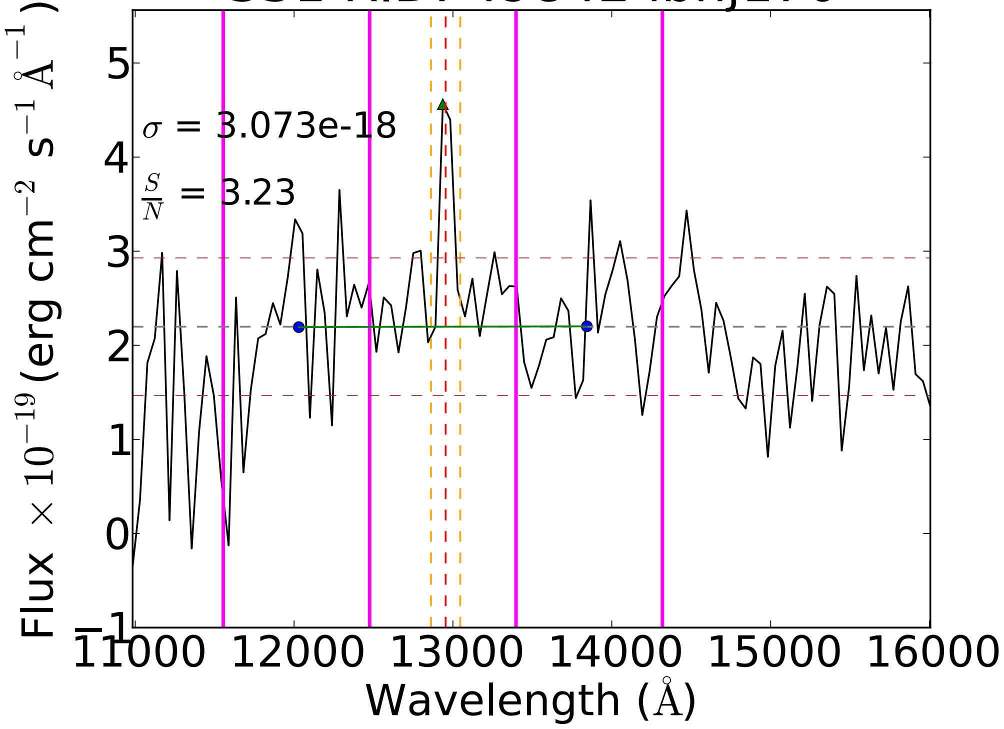

344 RID: 30681 ibhj130

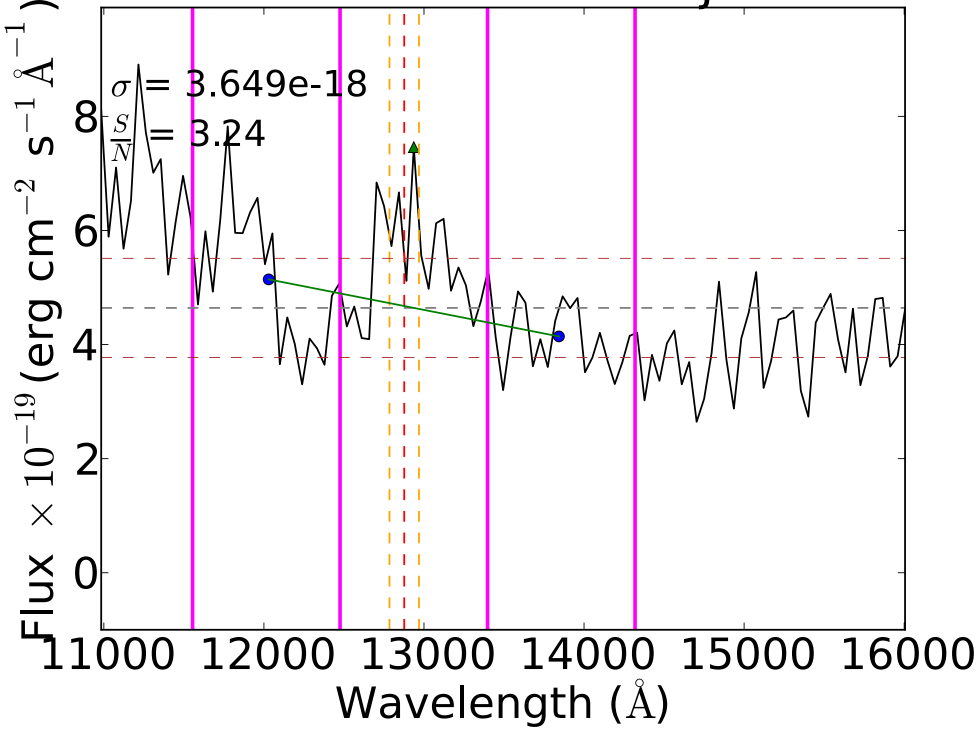

75 RID: 52072 ibhj300

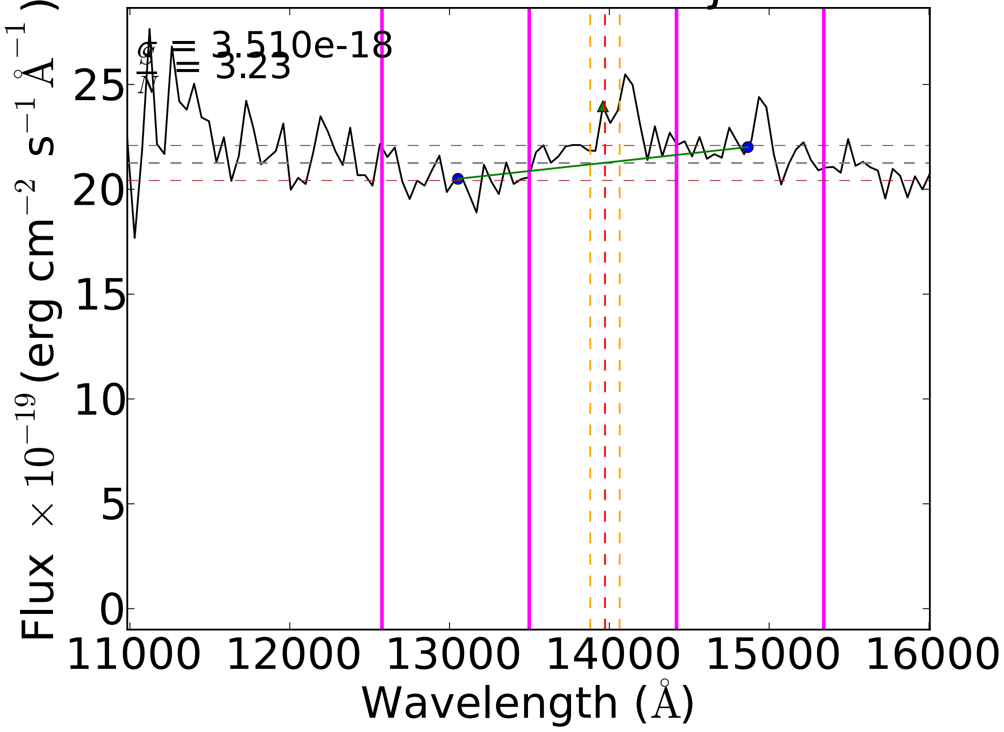

101 RID: 30407 ibhj210

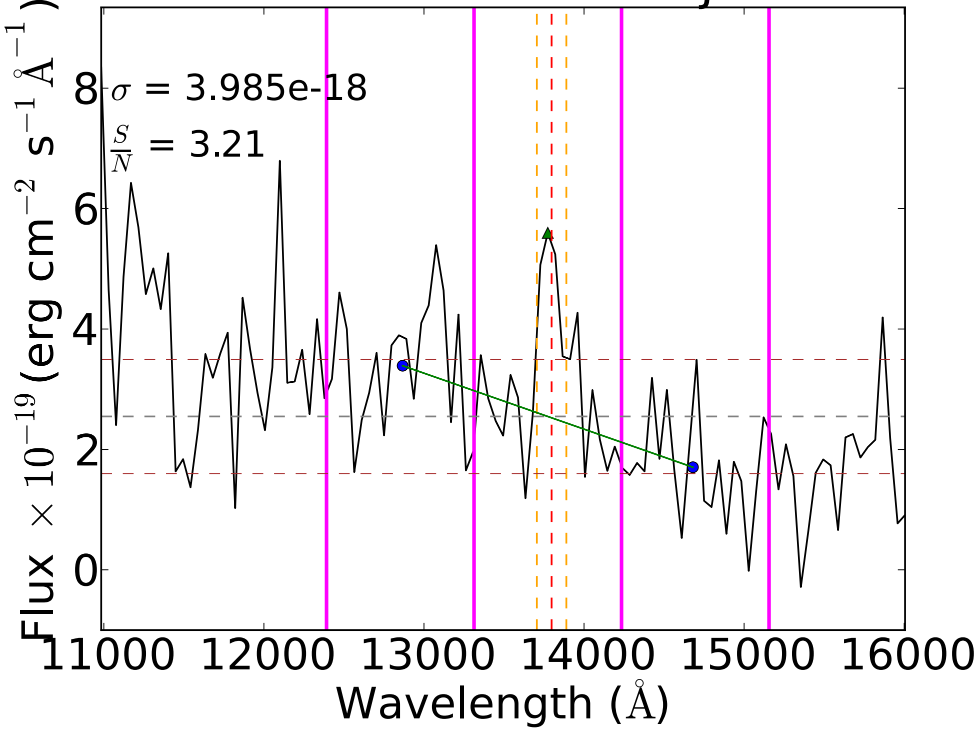

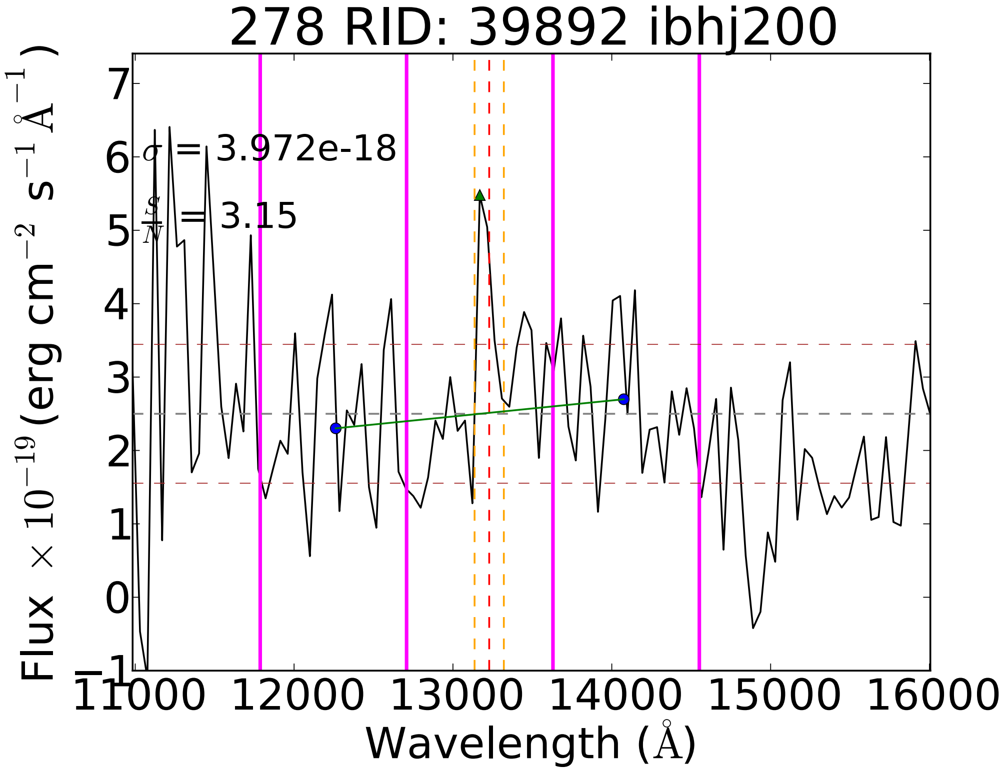
278 RID: 39892 ibhj200
σ = 3.972e-18
S/N = 3.15
Flux × 10^−19 (erg cm^−2 s^−1 Å^−1)
−1
0
1
2
3
4
5
6
7
11000
12000
13000
14000
15000
16000
Wavelength (Å)

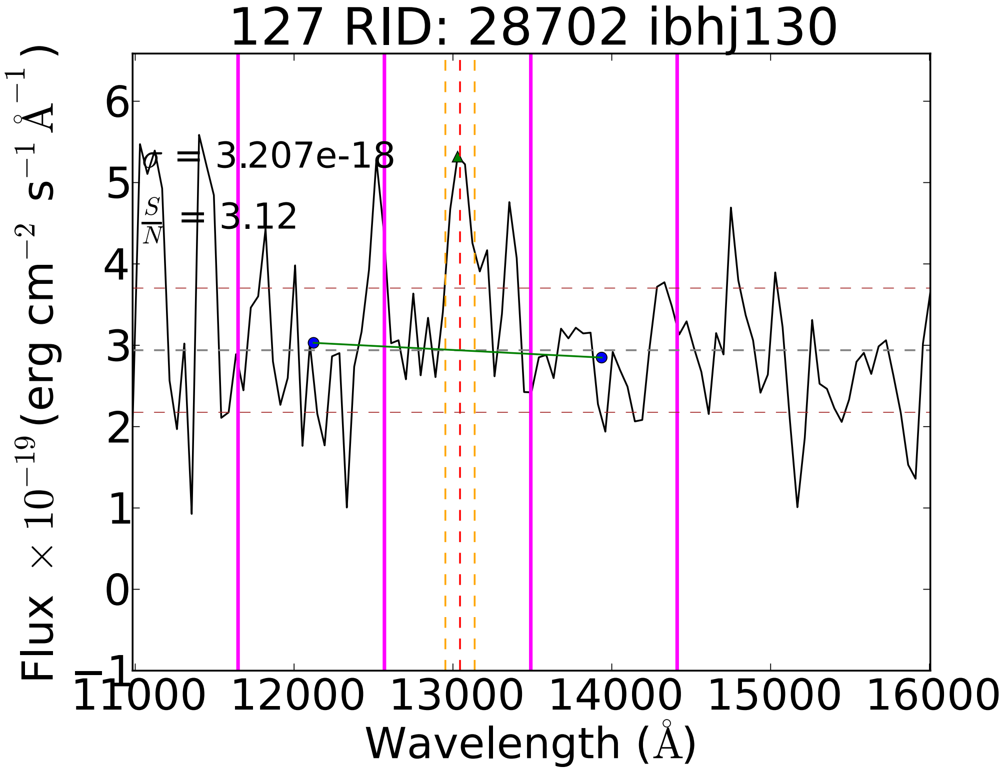
127 RID: 28702 ibhj130
σ = 3.207e-18
S/N = 3.12
Flux × 10^−19 (erg cm^−2 s^−1 Å^−1)
−1
0
1
2
3
4
5
6
11000
12000
13000
14000
15000
16000
Wavelength (Å)

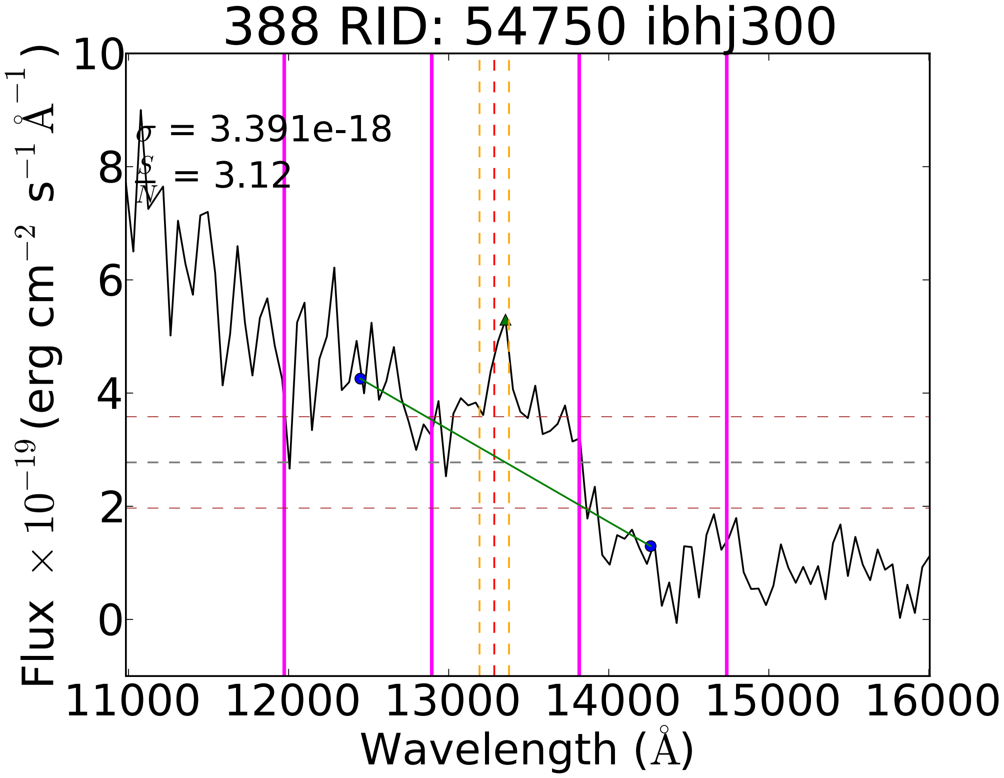
388 RID: 54750 ibhj300
σ = 3.391e-18
S/N = 3.12
Flux × 10^−19 (erg cm^−2 s^−1 Å^−1)
0
2
4
6
8
10
11000
12000
13000
14000
15000
16000
Wavelength (Å)

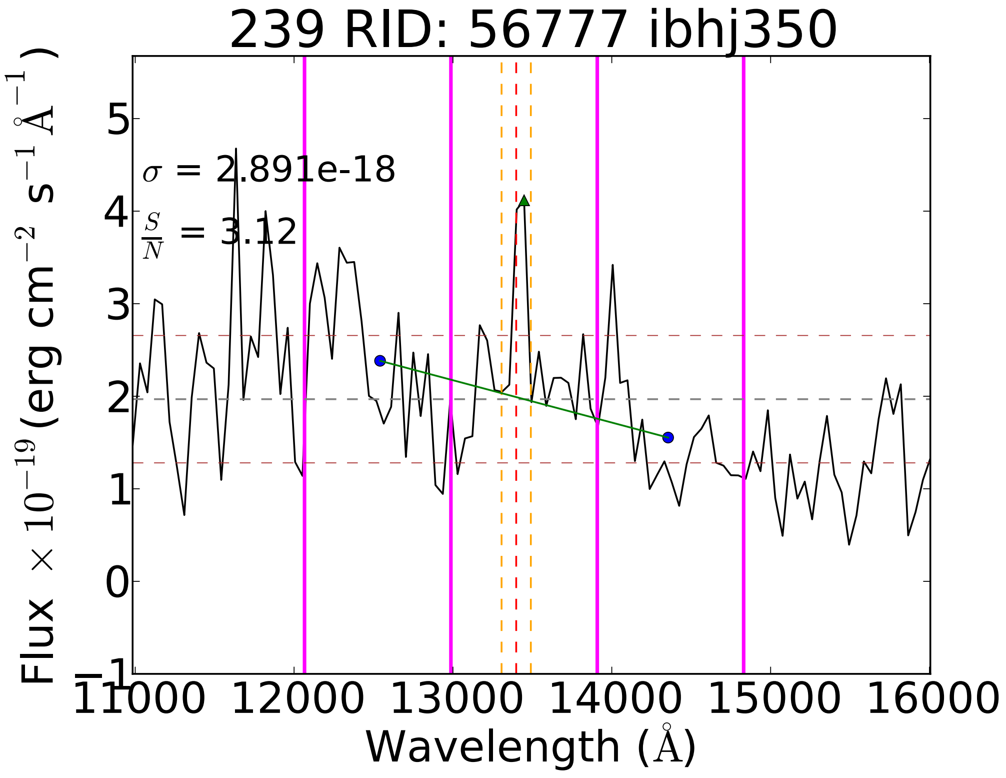
239 RID: 56777 ibhj350
σ = 2.891e-18
S/N = 3.12
Flux × 10^−19 (erg cm^−2 s^−1 Å^−1)
−1
0
1
2
3
4
5
11000
12000
13000
14000
15000
16000
Wavelength (Å)

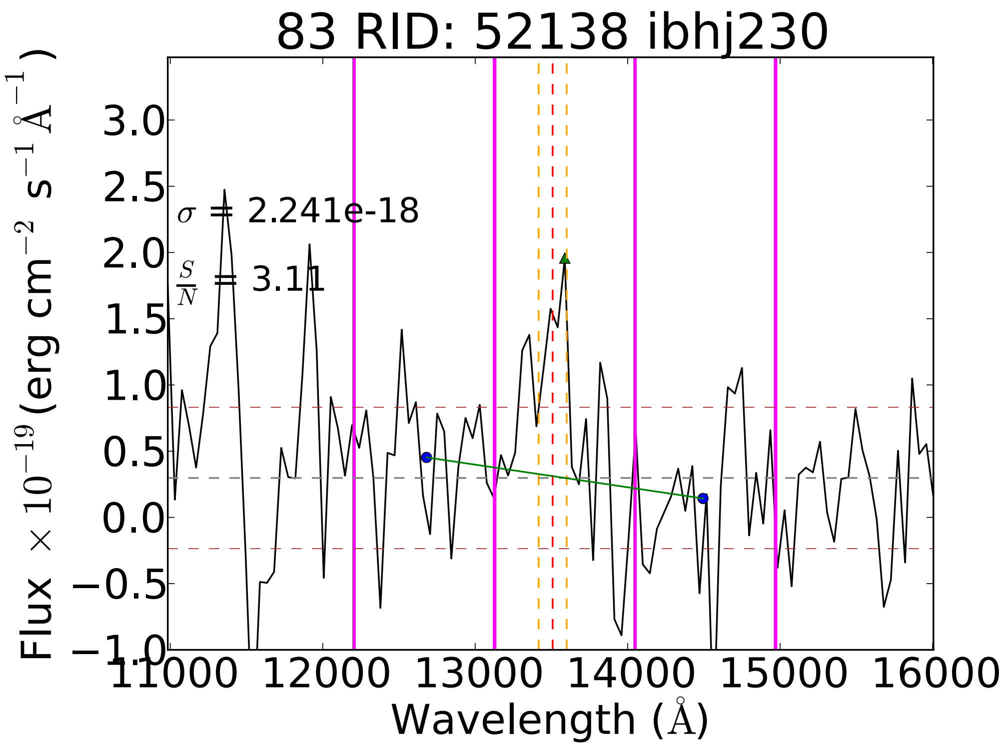
83 RID: 52138 ibhj230
σ = 2.241e-18
$\frac{S}{N}$ = 3.11
Flux $\times 10^{-19}$ (erg cm^{-2} s^{-1} Å^{-1})
Wavelength (Å)
−1.0
−0.5
0.0
0.5
1.0
1.5
2.0
2.5
3.0
11000
12000
13000
14000
15000
16000

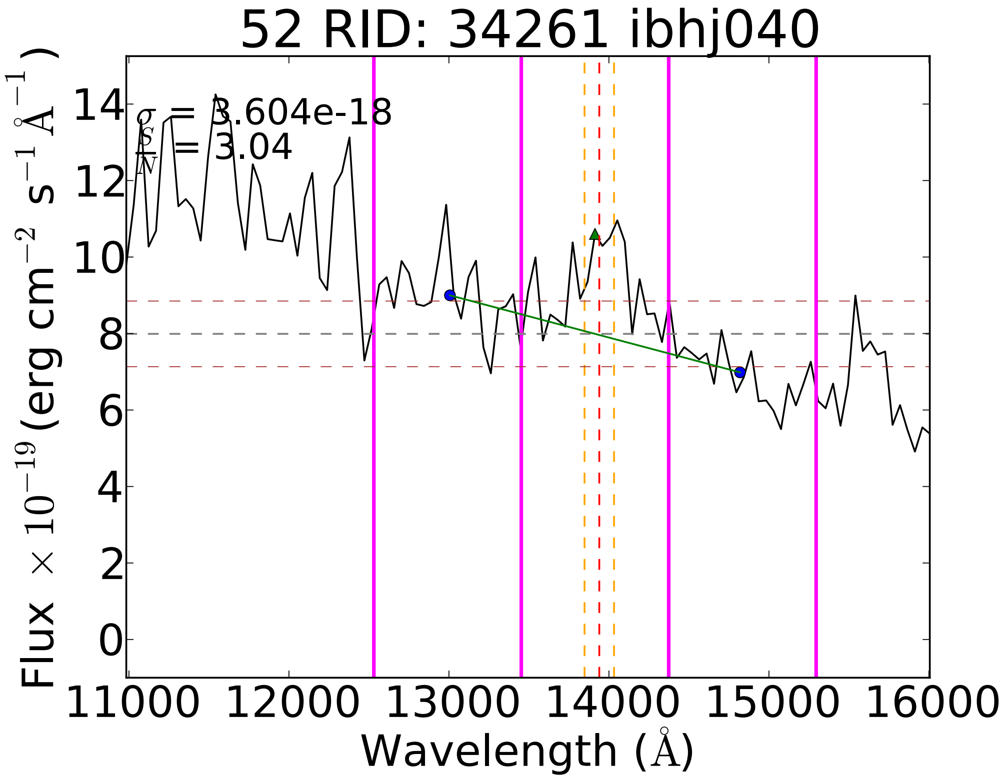
52 RID: 34261 ibhj040
σ = 3.604e-18
$\frac{S}{N}$ = 3.04
Flux $\times 10^{-19}$ (erg cm^{-2} s^{-1} Å^{-1})
Wavelength (Å)
0
2
4
6
8
10
12
14
11000
12000
13000
14000
15000
16000

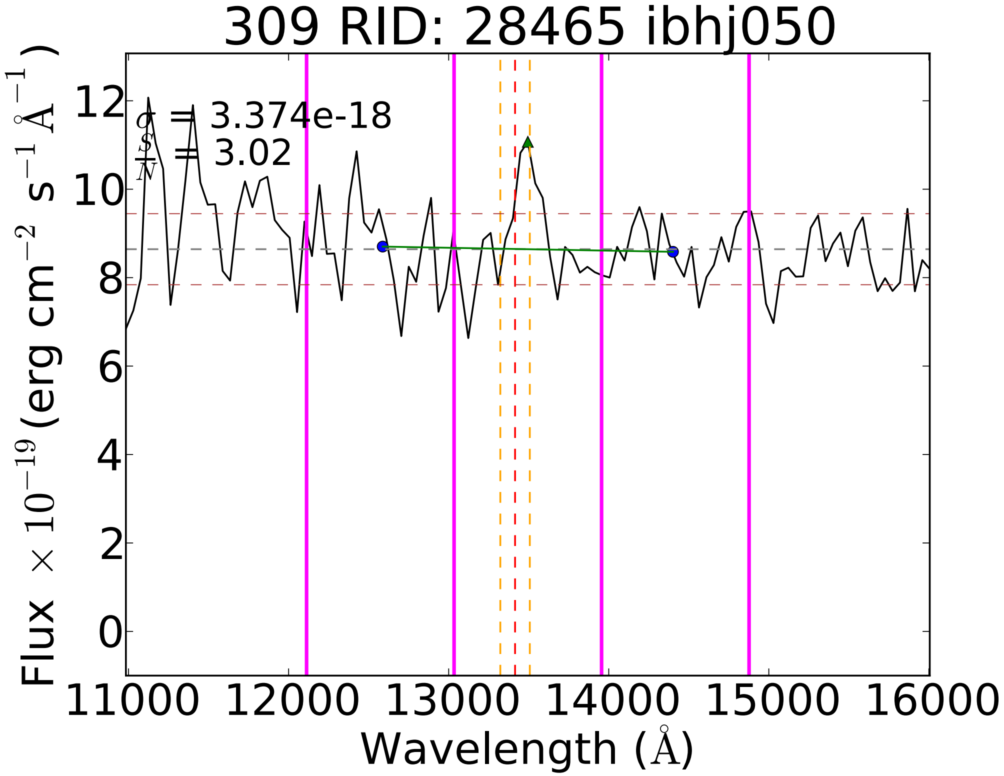
309 RID: 28465 ibhj050
σ = 3.374e-18
$\frac{S}{N}$ = 3.02
Flux $\times 10^{-19}$ (erg cm^{-2} s^{-1} Å^{-1})
Wavelength (Å)
0
2
4
6
8
10
12
11000
12000
13000
14000
15000
16000

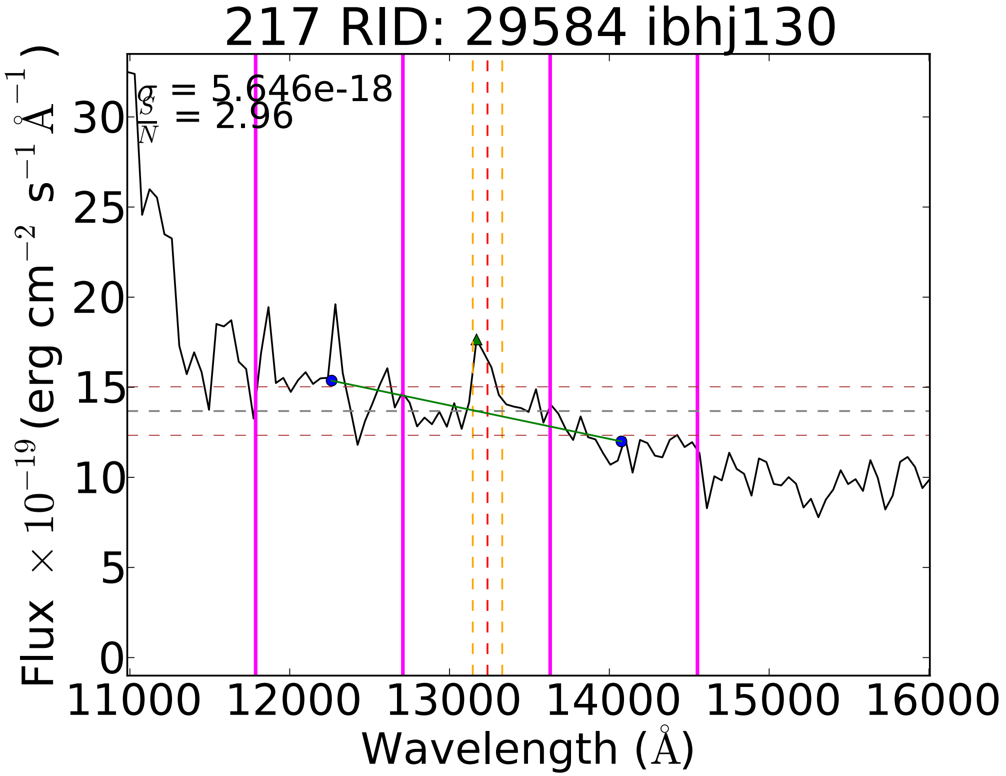
217 RID: 29584 ibhj130
σ = 5.646e-18
$\frac{S}{N}$ = 2.96
Flux $\times 10^{-19}$ (erg cm^{-2} s^{-1} Å^{-1})
Wavelength (Å)
0
5
10
15
20
25
30
11000
12000
13000
14000
15000
16000

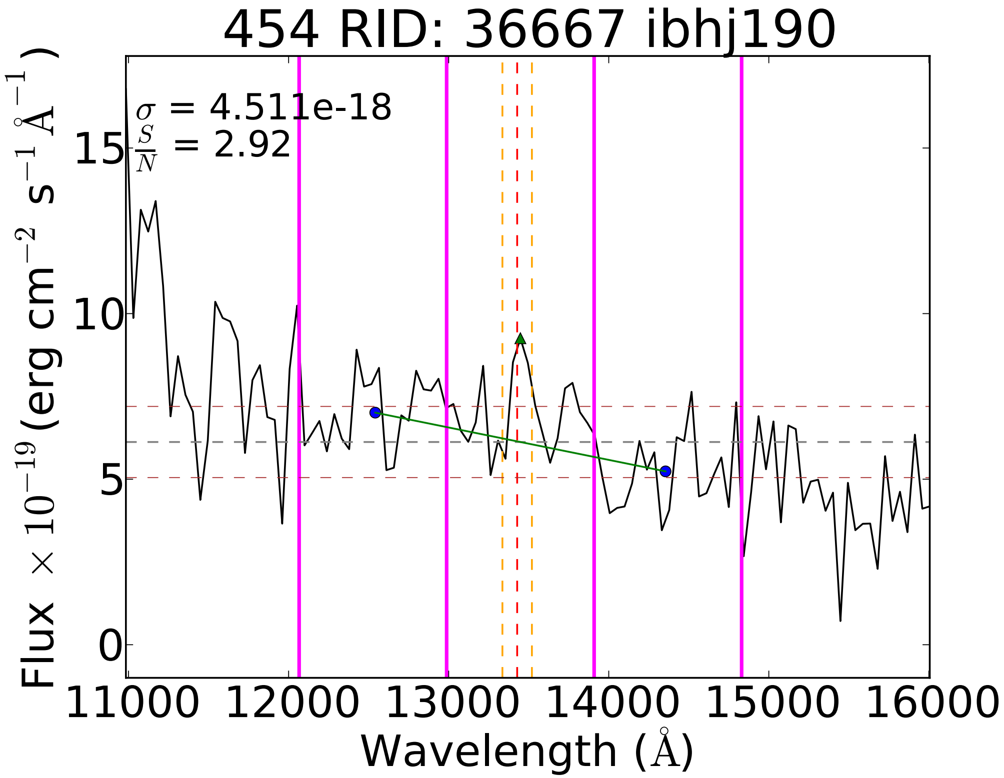
454 RID: 36667 ibhj190
σ = 4.511e-18
$\frac{S}{N}$ = 2.92
Flux $\times 10^{-19}$ (erg cm^{-2} s^{-1} Å^{-1})
0
5
10
15
11000
12000
13000
14000
15000
16000
Wavelength (Å)

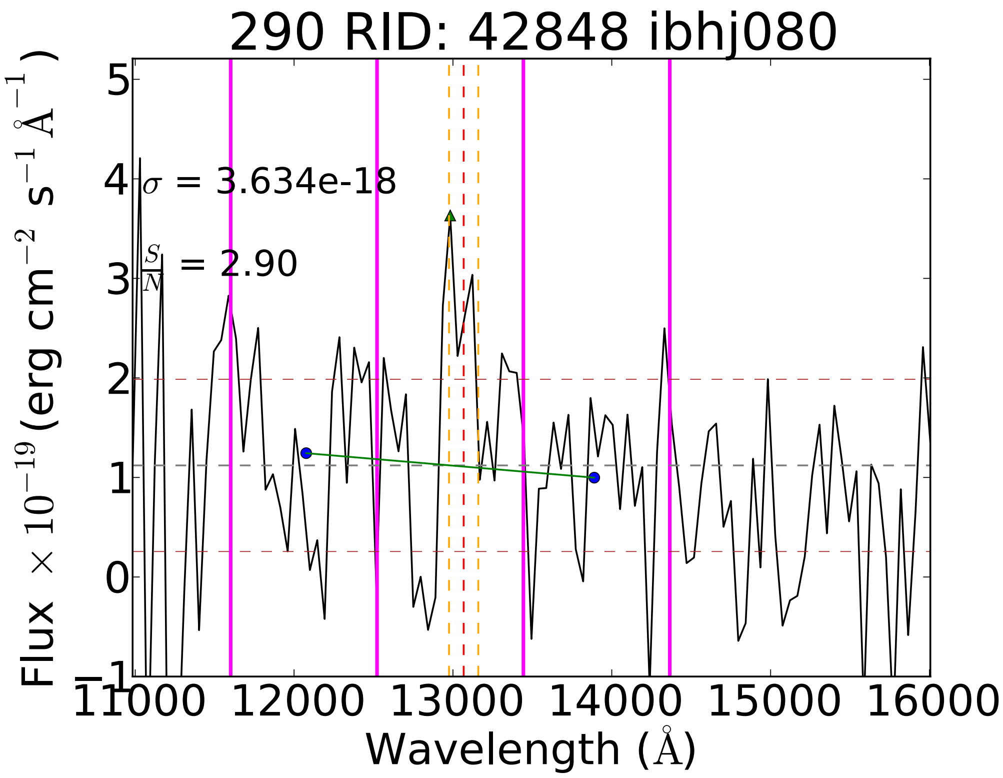
290 RID: 42848 ibhj080
σ = 3.634e-18
$\frac{S}{N}$ = 2.90
Flux $\times 10^{-19}$ (erg cm^{-2} s^{-1} Å^{-1})
−1
0
1
2
3
4
5
11000
12000
13000
14000
15000
16000
Wavelength (Å)

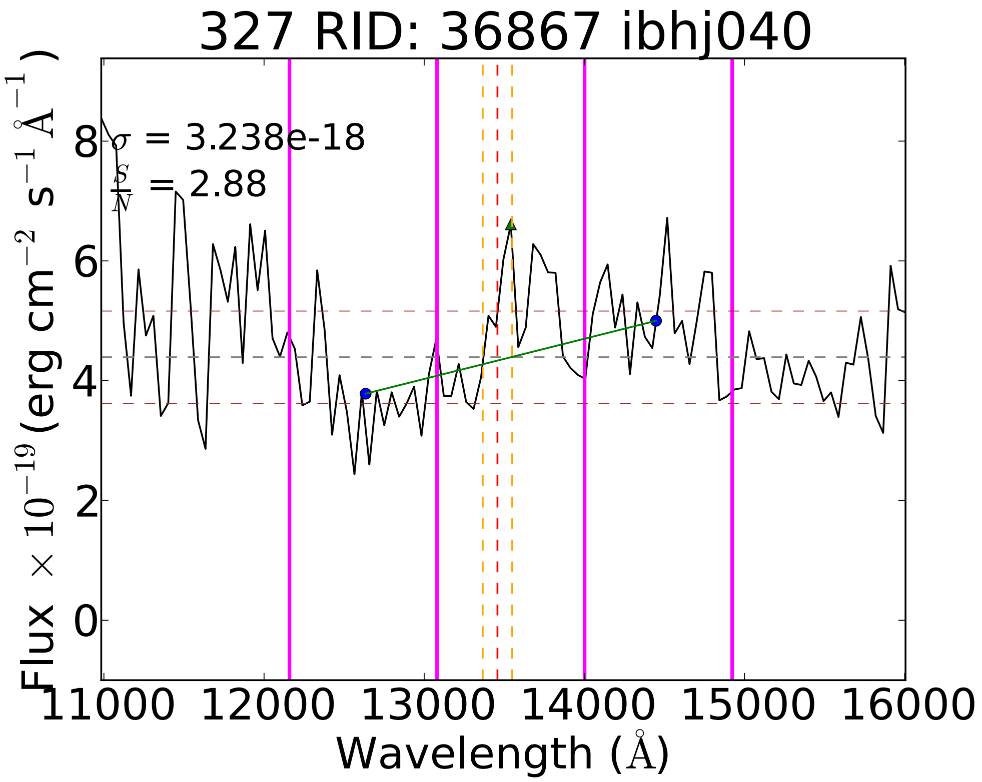
327 RID: 36867 ibhj040
σ = 3.238e-18
$\frac{S}{N}$ = 2.88
Flux $\times 10^{-19}$ (erg cm^{-2} s^{-1} Å^{-1})
0
2
4
6
8
11000
12000
13000
14000
15000
16000
Wavelength (Å)

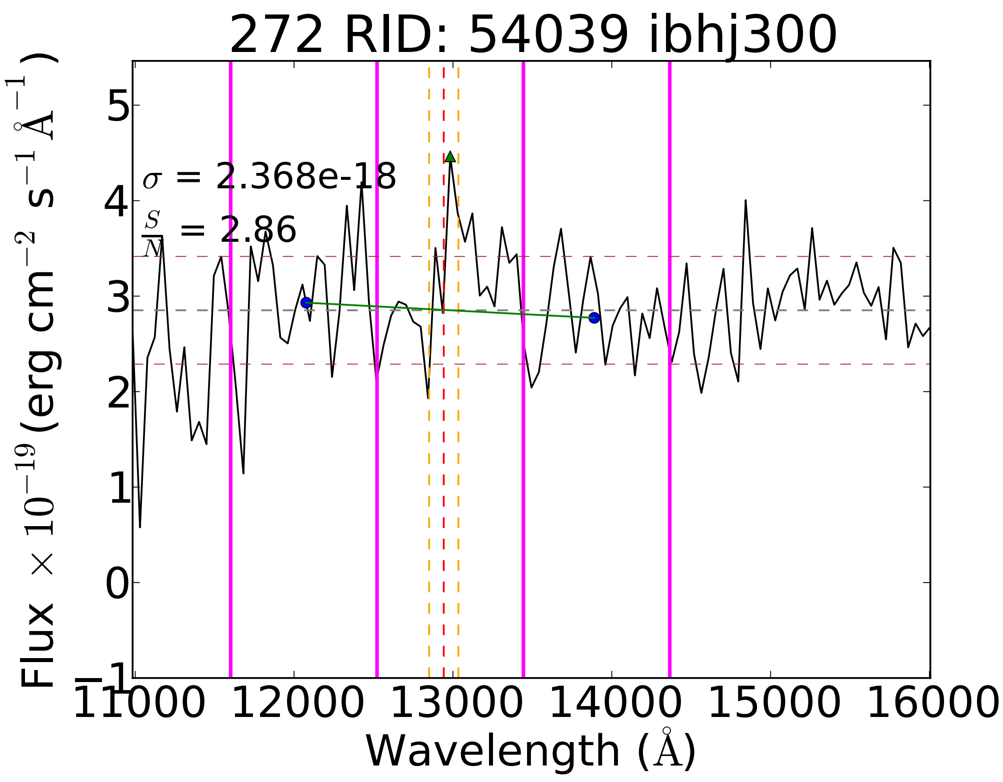
272 RID: 54039 ibhj300
σ = 2.368e-18
$\frac{S}{N}$ = 2.86
Flux $\times 10^{-19}$ (erg cm^{-2} s^{-1} Å^{-1})
−1
0
1
2
3
4
5
11000
12000
13000
14000
15000
16000
Wavelength (Å)

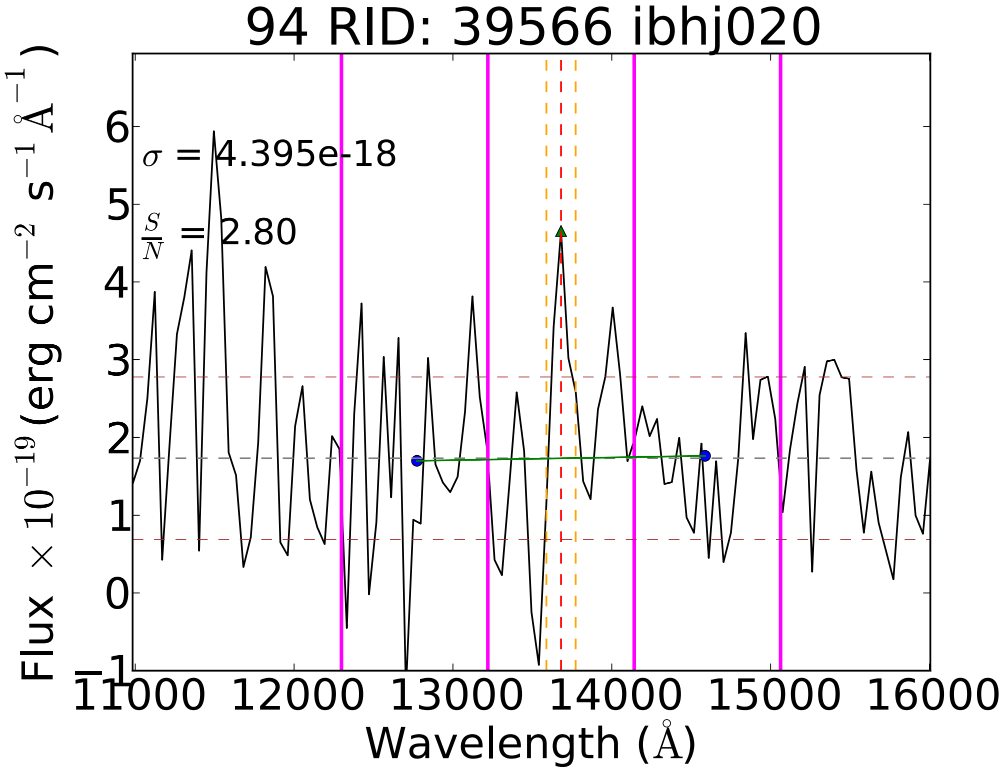
94 RID: 39566 ibhj020

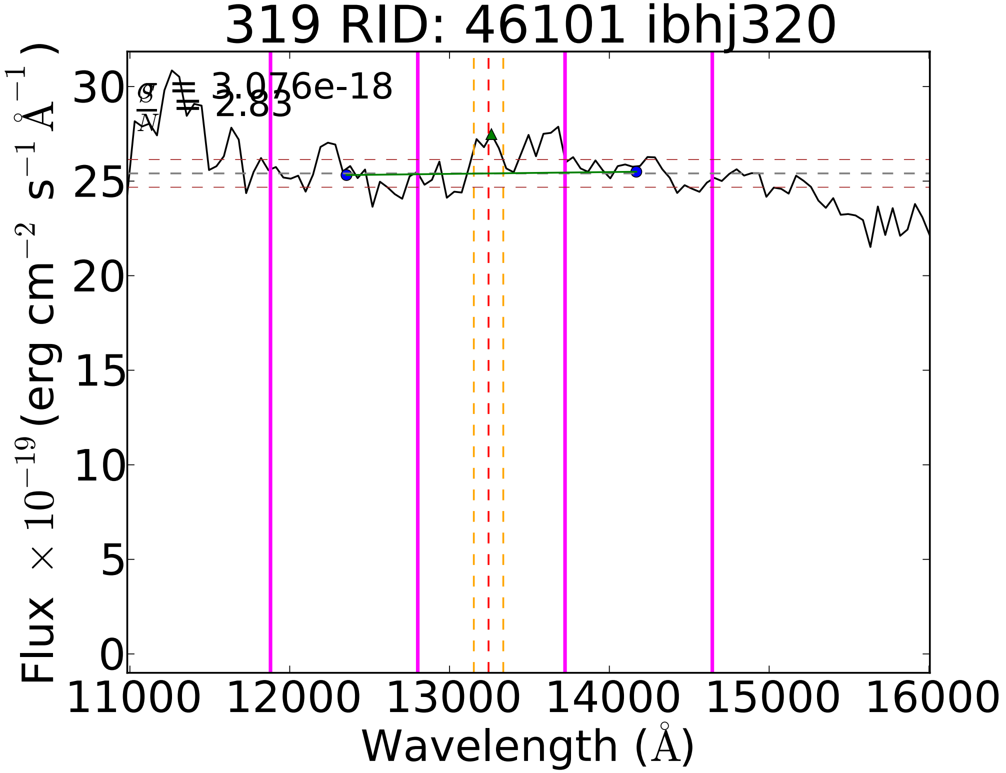
319 RID: 46101 ibhj320

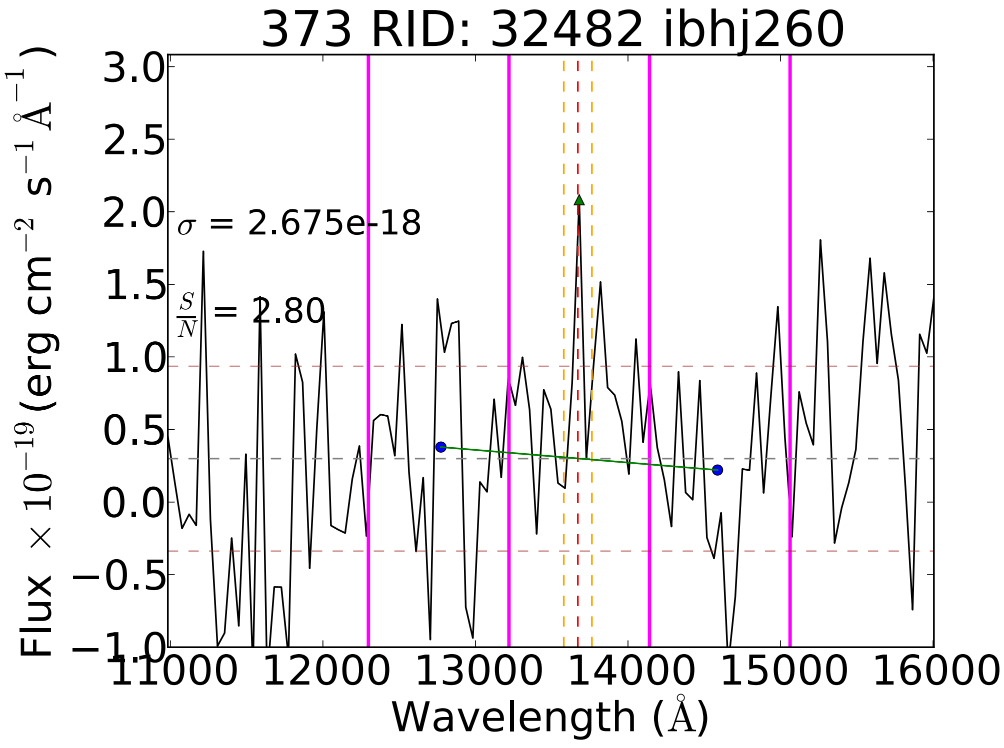
373 RID: 32482 ibhj260

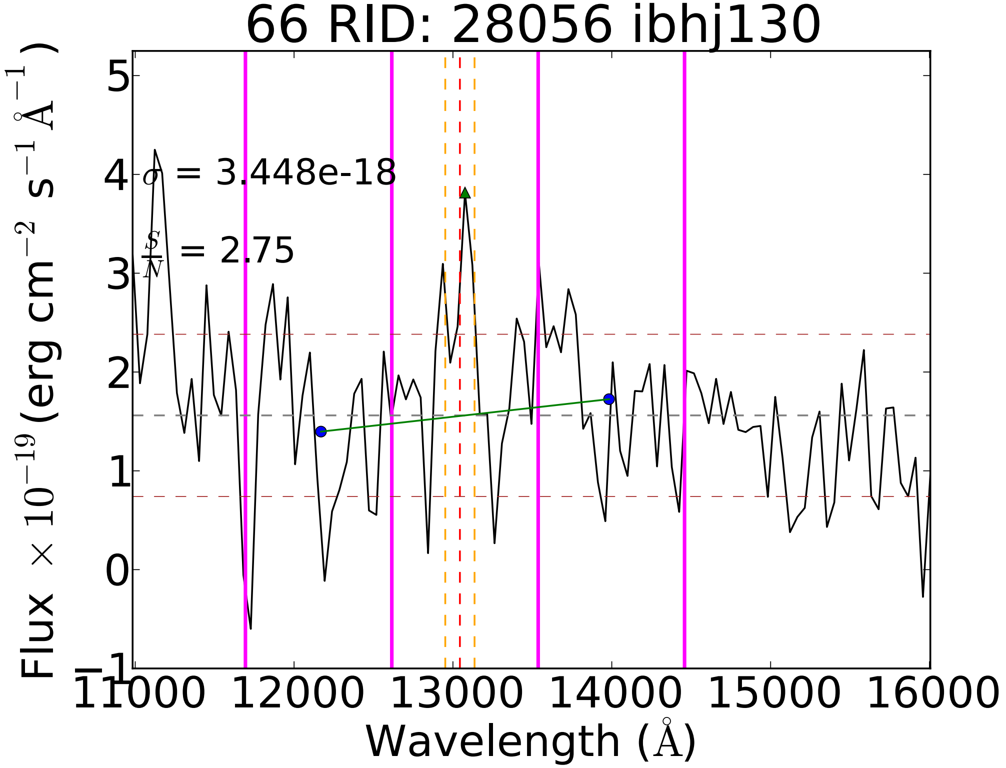
66 RID: 28056 ibhj130

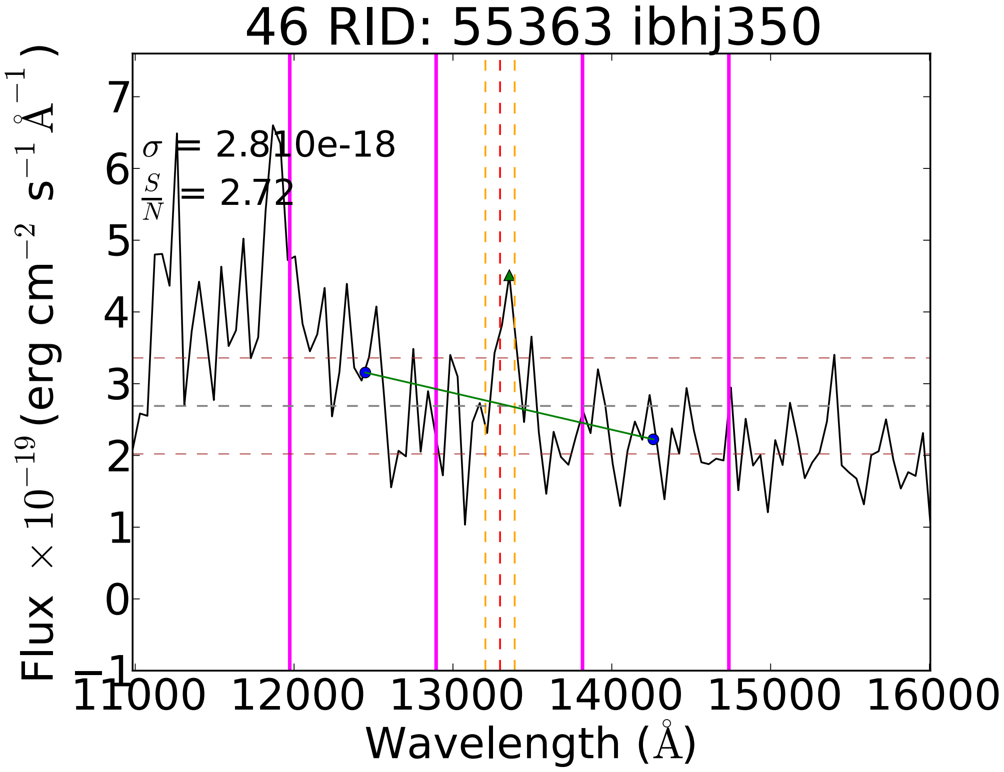
46 RID: 55363 ibhj350
σ = 2.810e-18
$\frac{S}{N}$ = 2.72
Flux $\times 10^{-19}$ (erg cm^{-2} s^{-1} Å^{-1})
Wavelength (Å)
−1
0
1
2
3
4
5
6
7
11000
12000
13000
14000
15000
16000

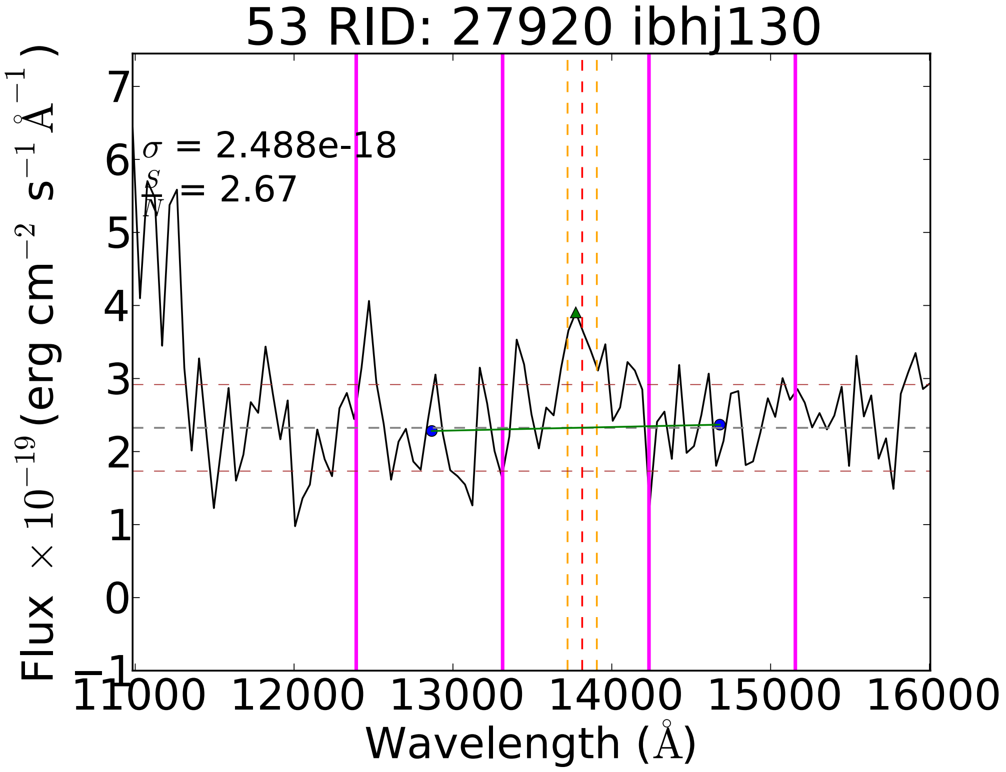
53 RID: 27920 ibhj130
σ = 2.488e-18
$\frac{S}{N}$ = 2.67
Flux $\times 10^{-19}$ (erg cm^{-2} s^{-1} Å^{-1})
Wavelength (Å)
−1
0
1
2
3
4
5
6
7
11000
12000
13000
14000
15000
16000

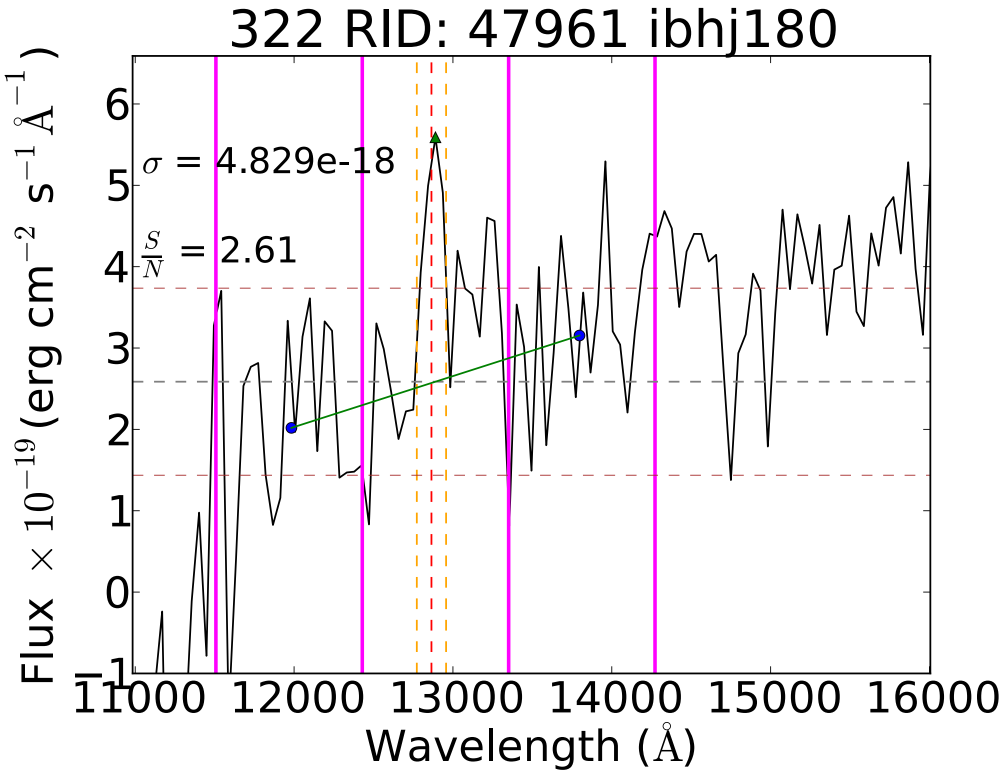
322 RID: 47961 ibhj180
σ = 4.829e-18
$\frac{S}{N}$ = 2.61
Flux $\times 10^{-19}$ (erg cm^{-2} s^{-1} Å^{-1})
Wavelength (Å)
−1
0
1
2
3
4
5
6
11000
12000
13000
14000
15000
16000

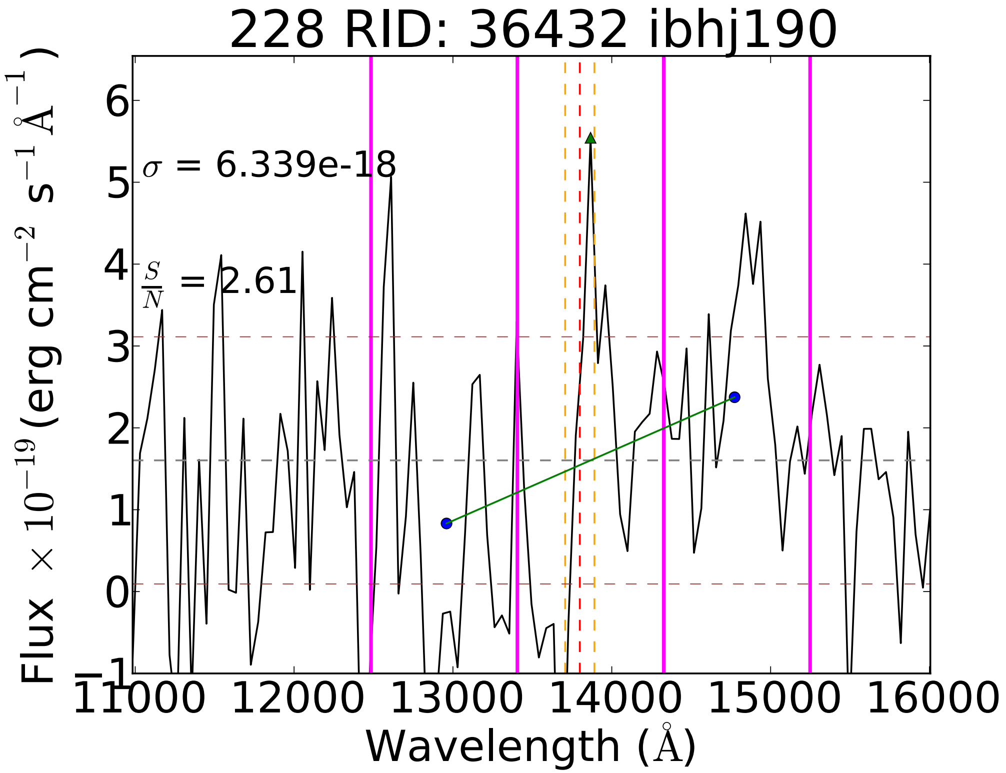
228 RID: 36432 ibhj190
σ = 6.339e-18
$\frac{S}{N}$ = 2.61
Flux $\times 10^{-19}$ (erg cm^{-2} s^{-1} Å^{-1})
Wavelength (Å)
−1
0
1
2
3
4
5
6
11000
12000
13000
14000
15000
16000

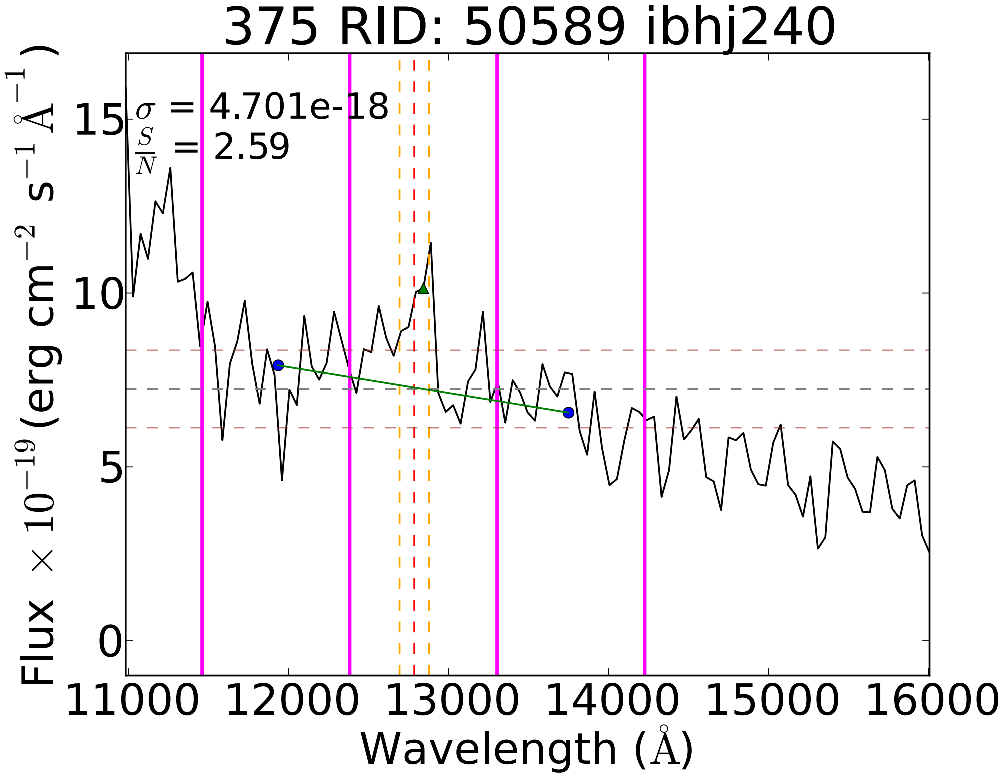
375 RID: 50589 ibhj240

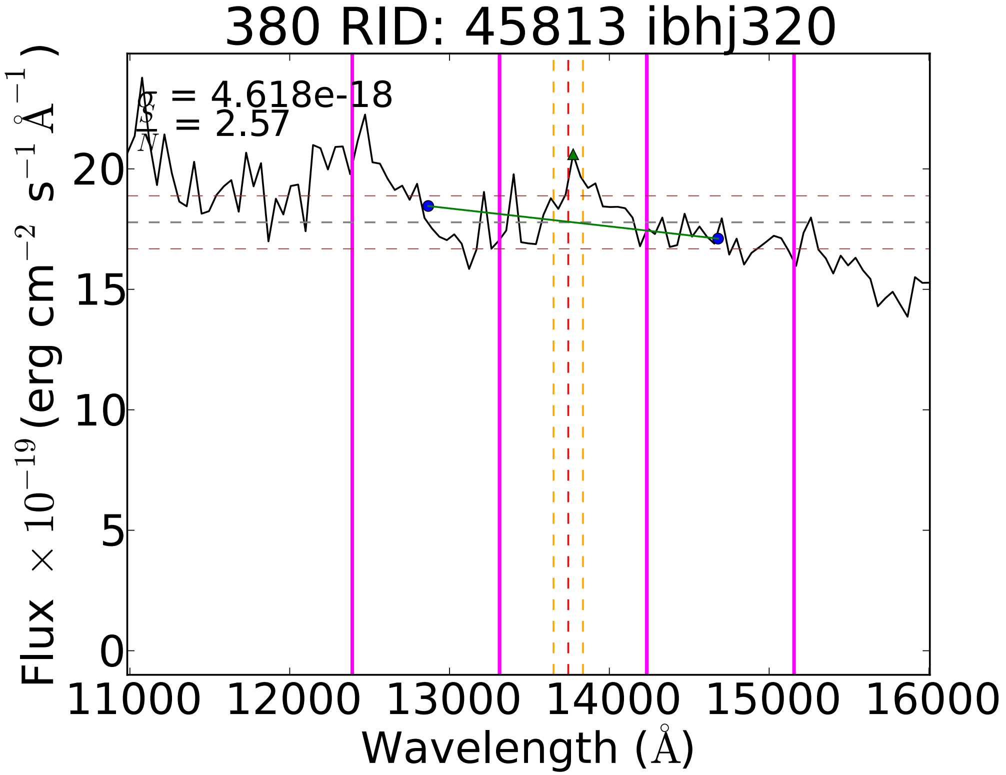
380 RID: 45813 ibhj320

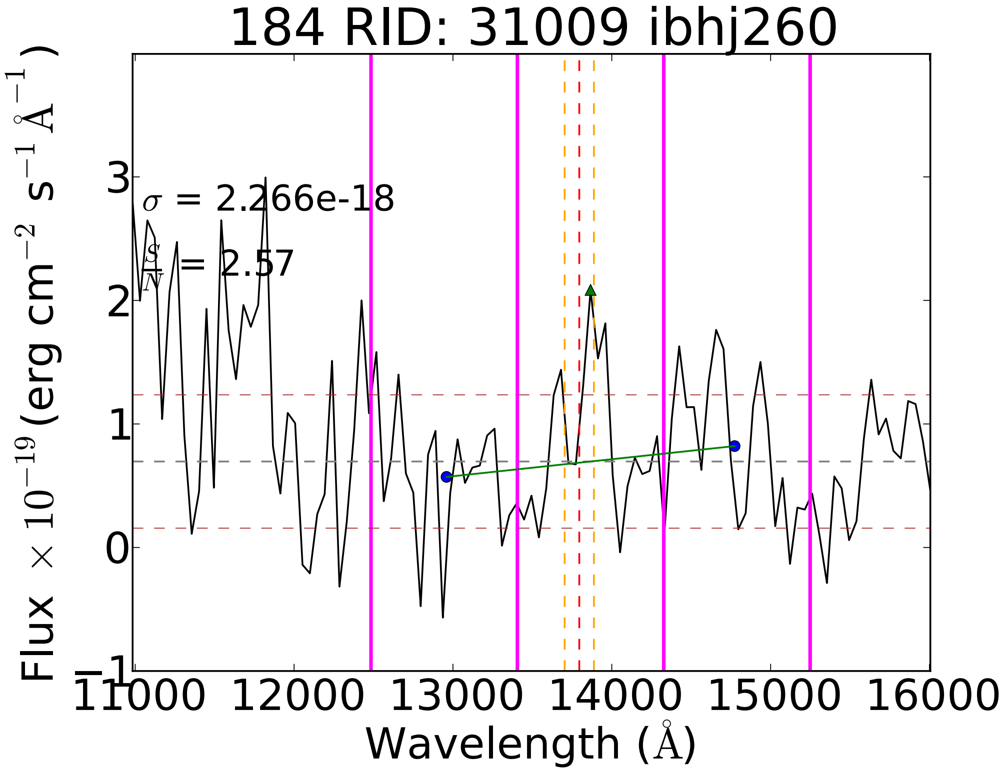
184 RID: 31009 ibhj260

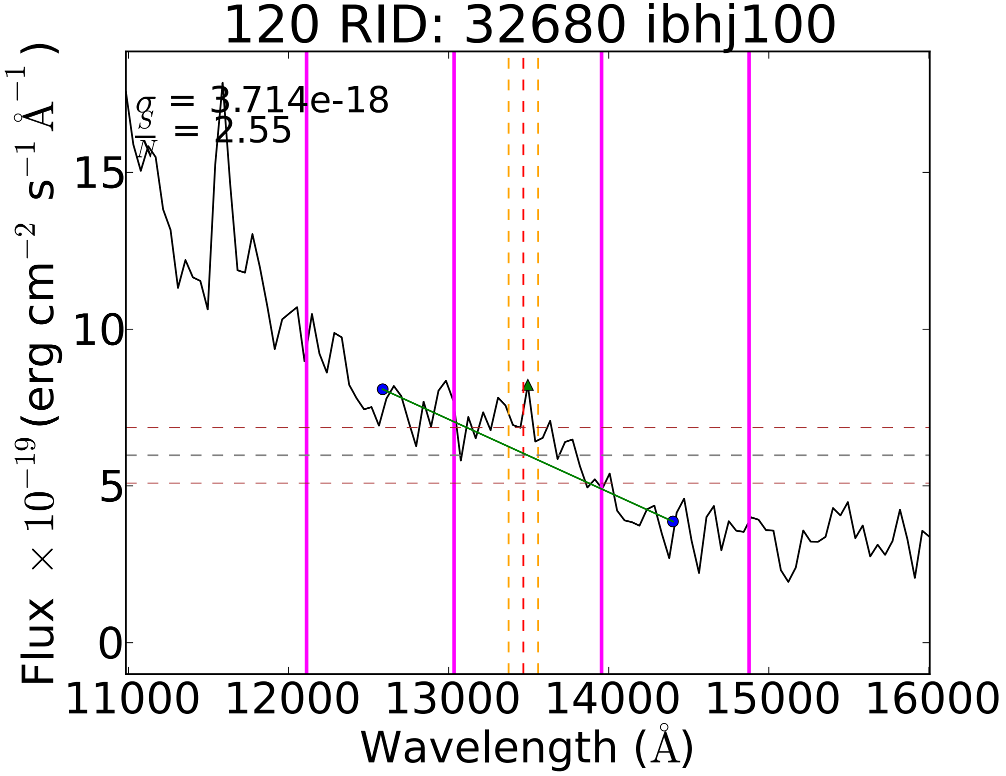
120 RID: 32680 ibhj100

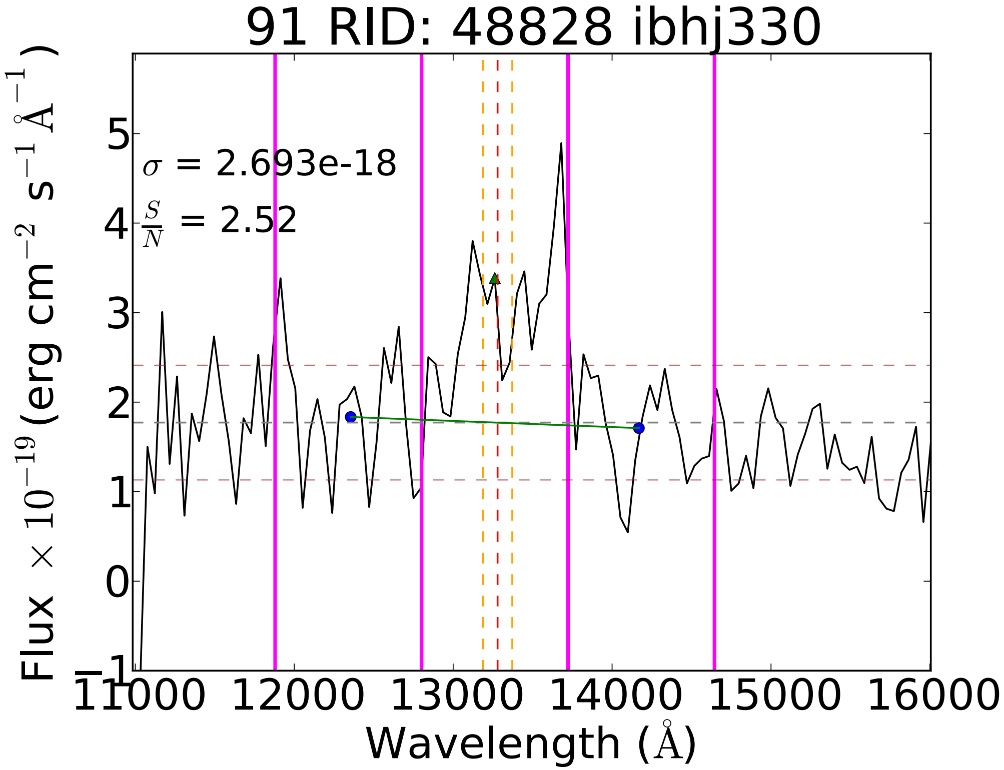
91 RID: 48828 ibhj330

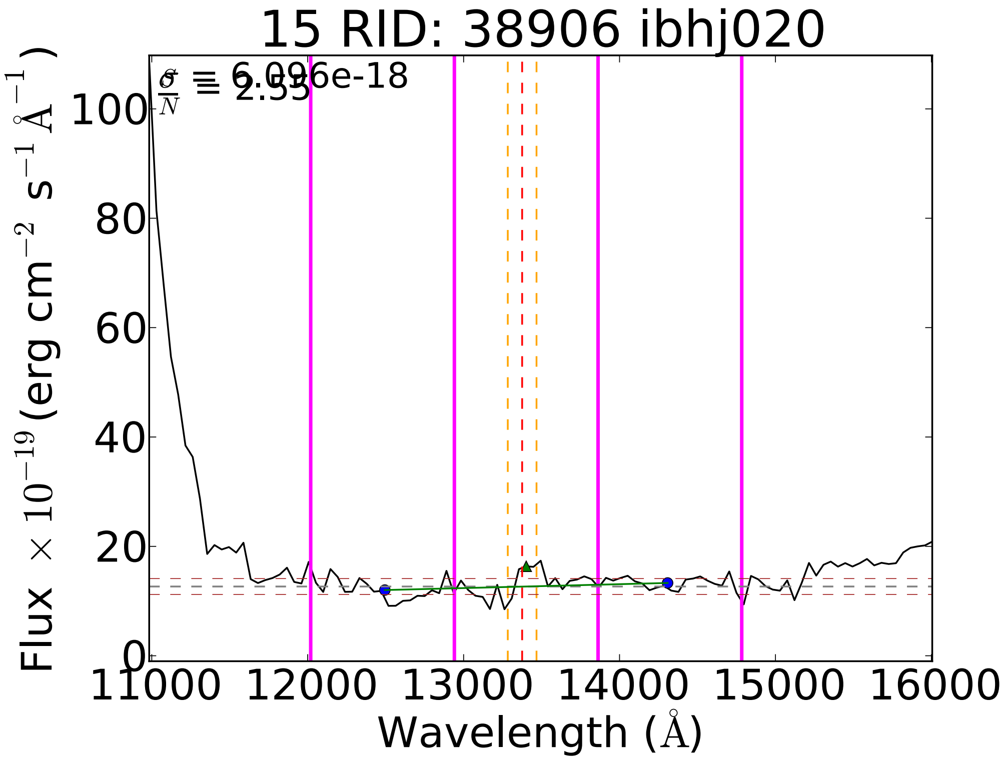
15 RID: 38906 ibhj020

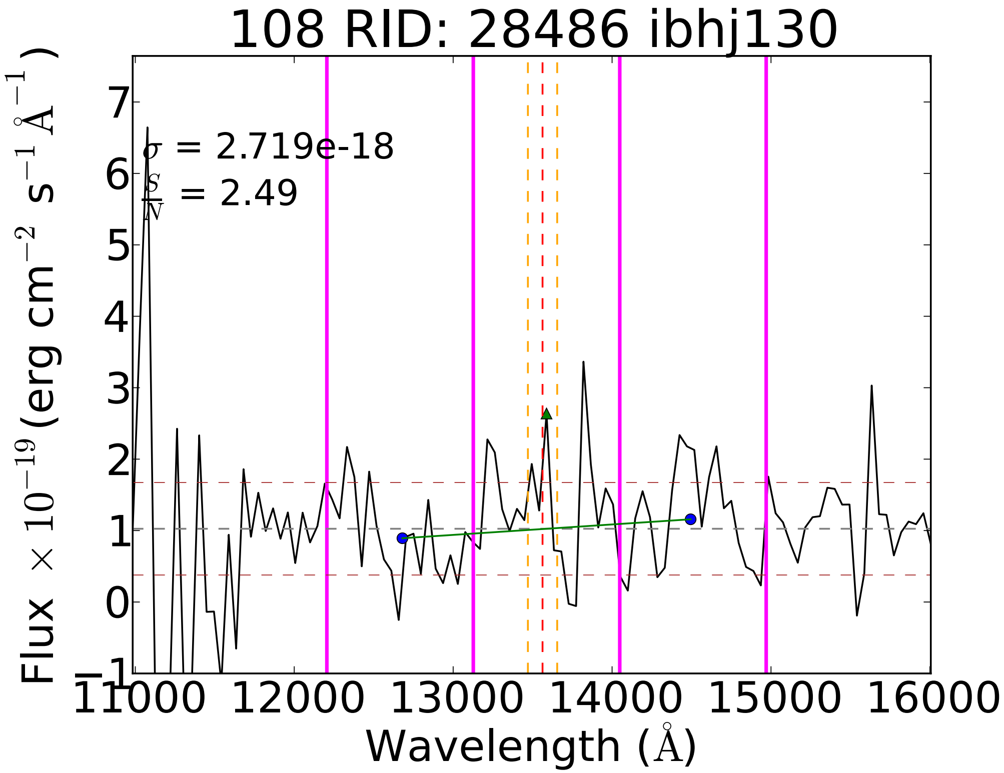
108 RID: 28486 ibhj130

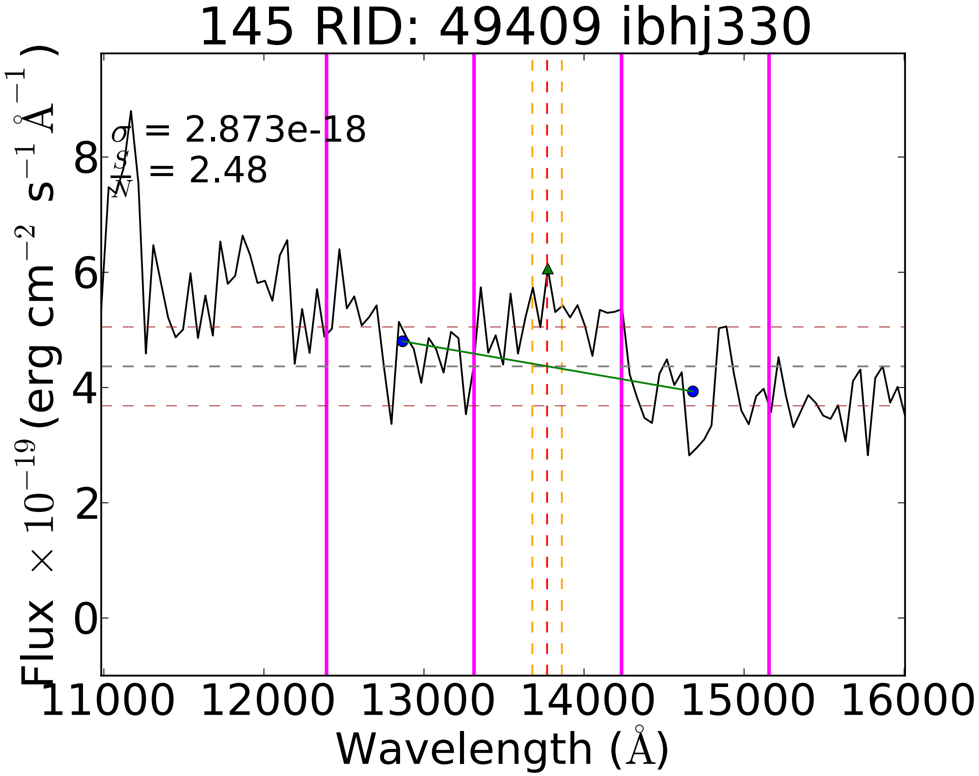
145 RID: 49409 ibhj330

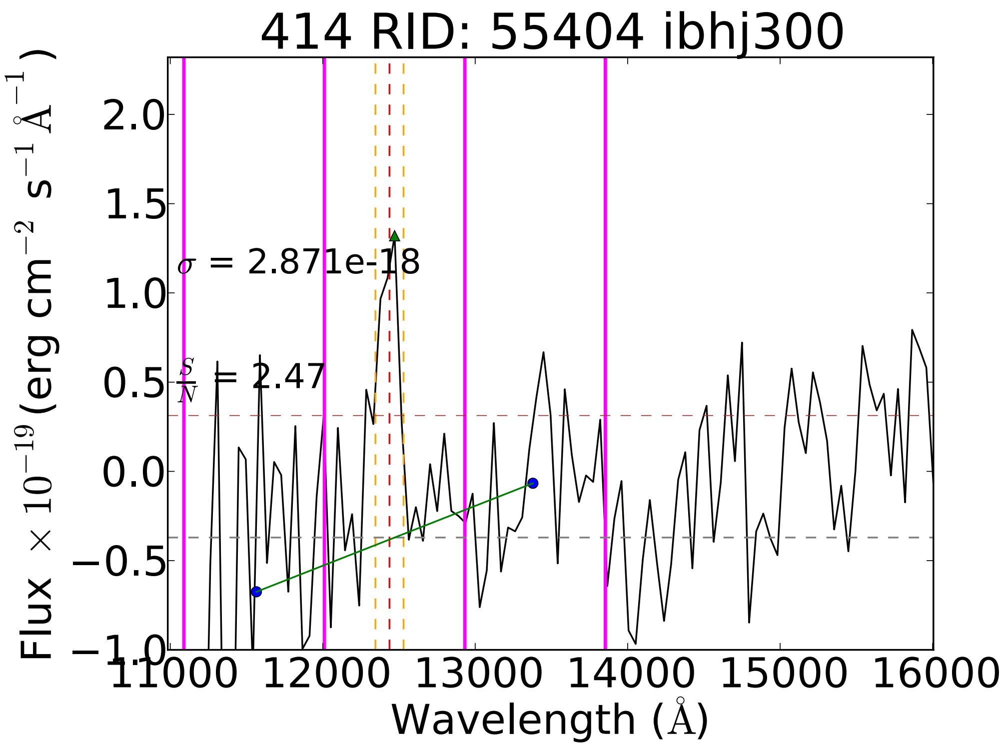
414 RID: 55404 ibhj300

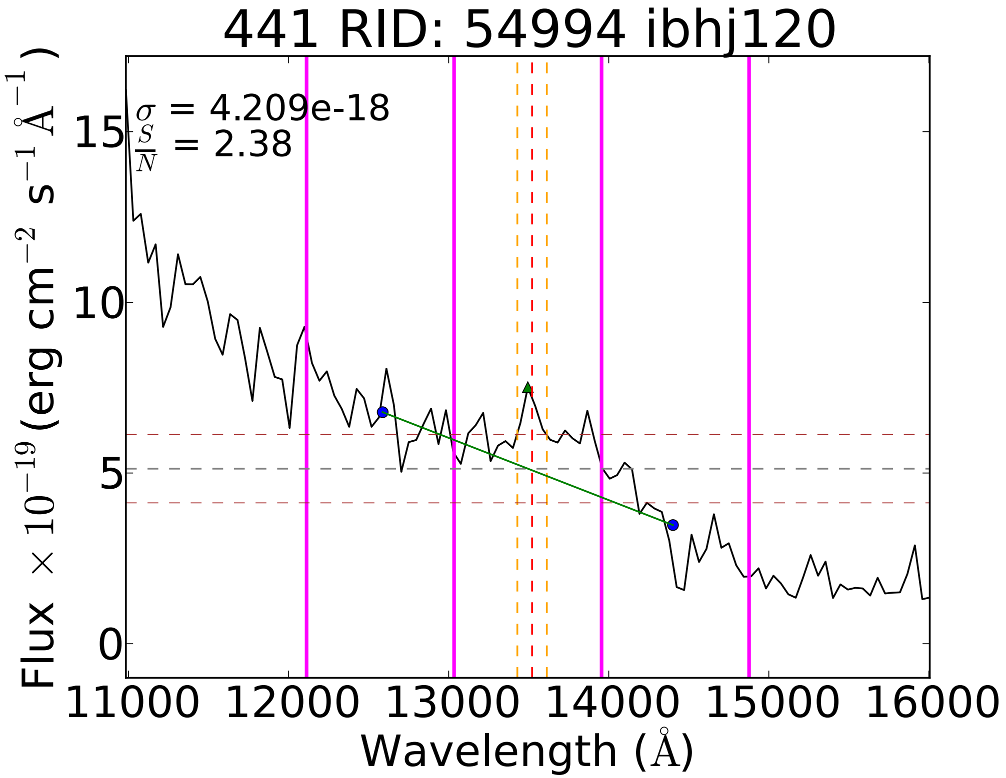
441 RID: 54994 ibhj120

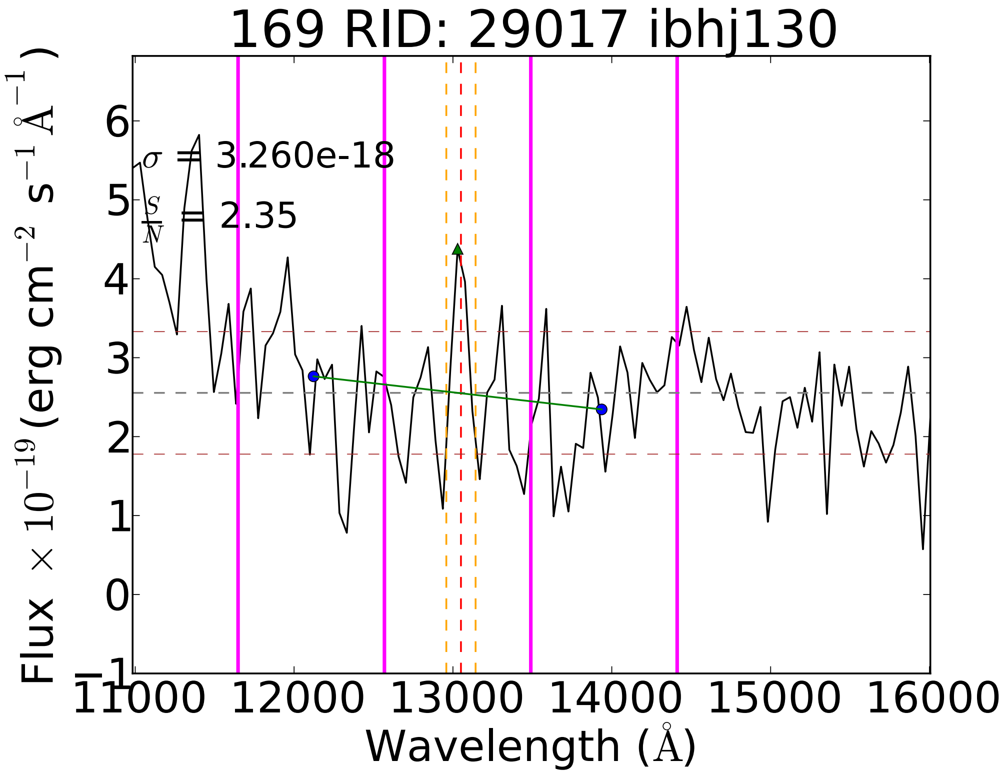
169 RID: 29017 ibhj130

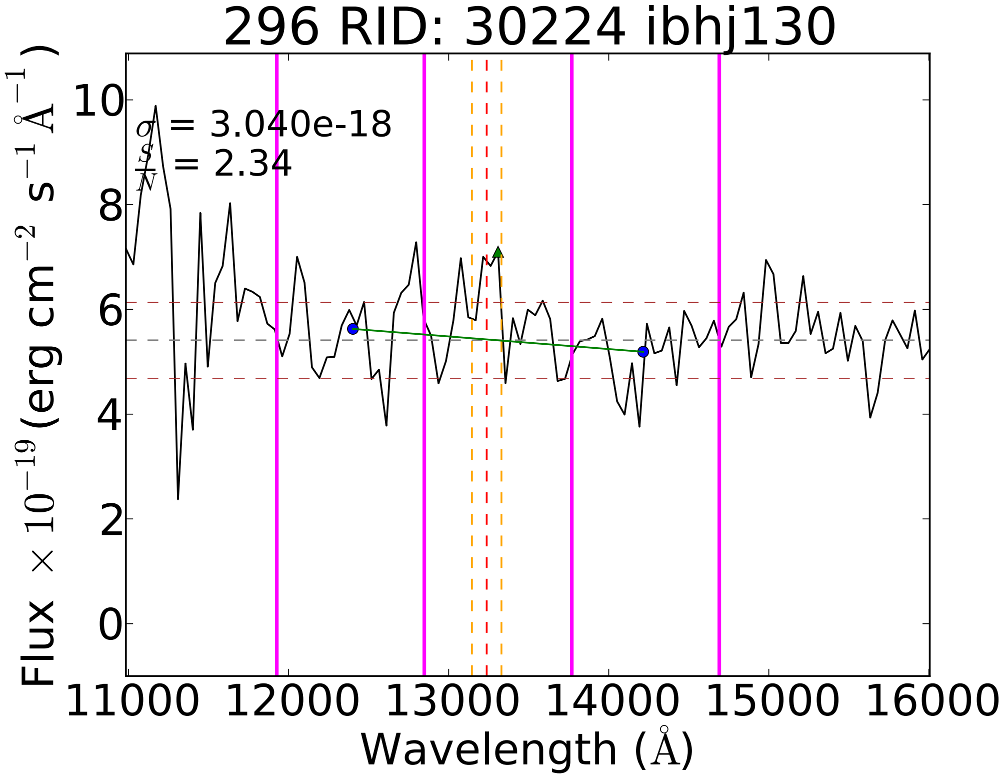
296 RID: 30224 ibhj130

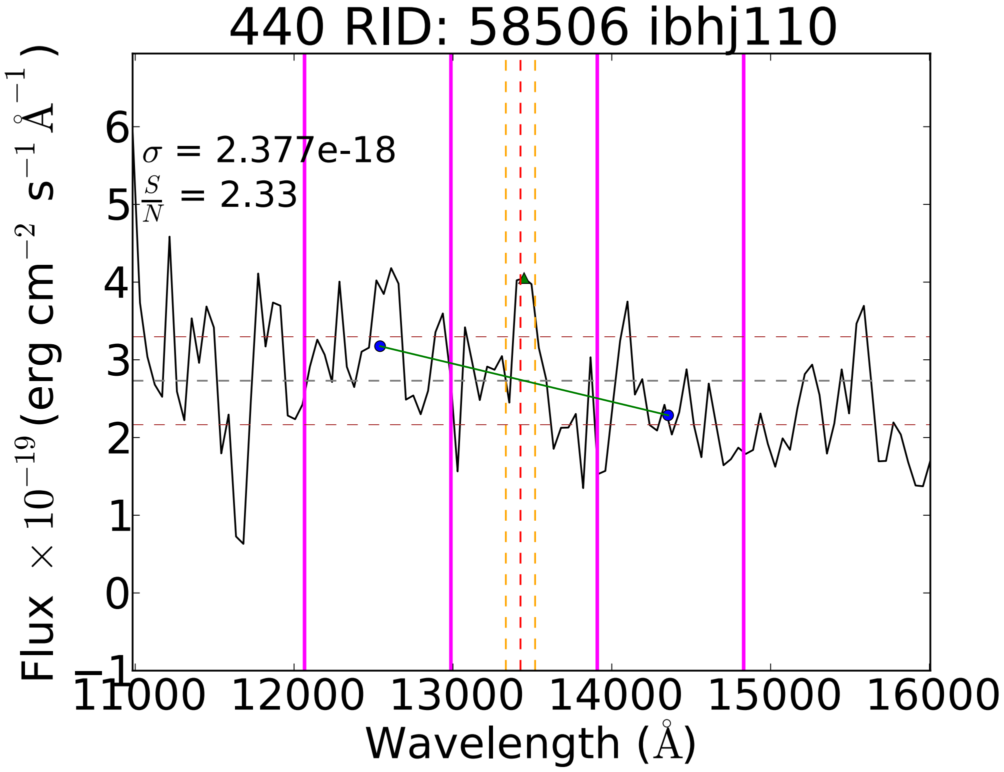

440 RID: 58506 ibhj110

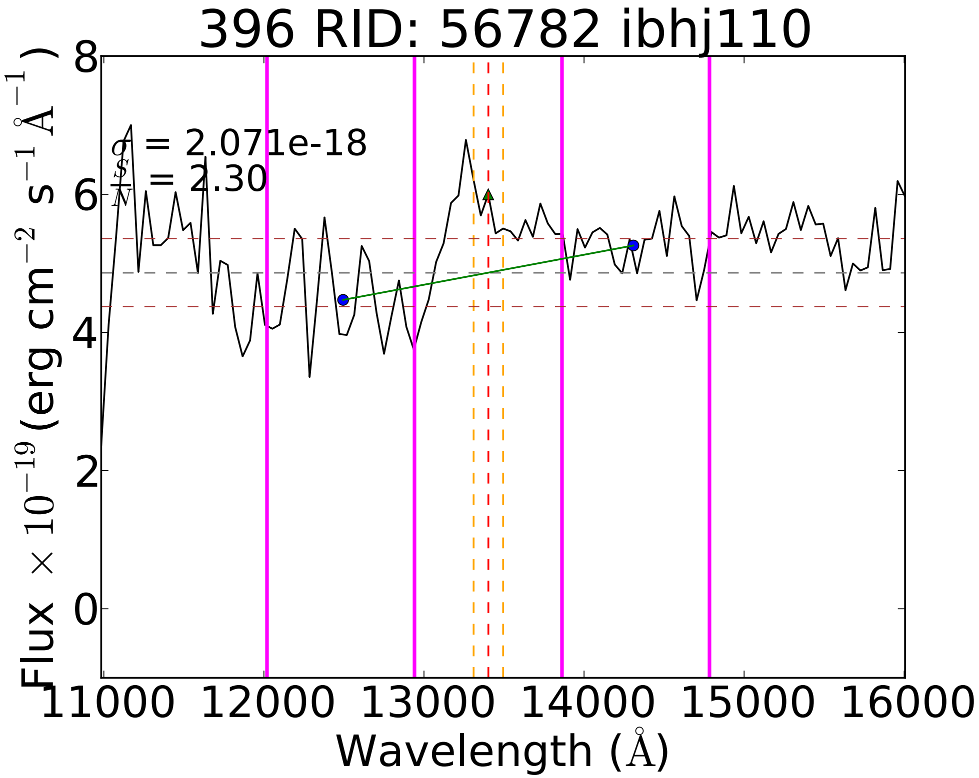

396 RID: 56782 ibhj110

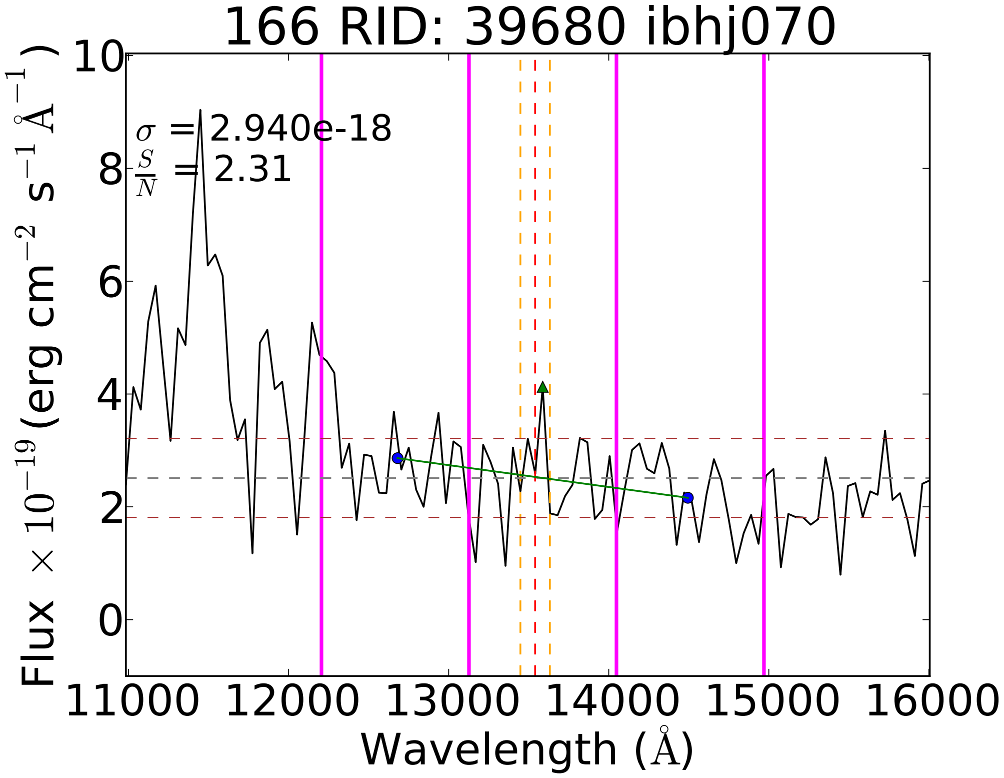

166 RID: 39680 ibhj070

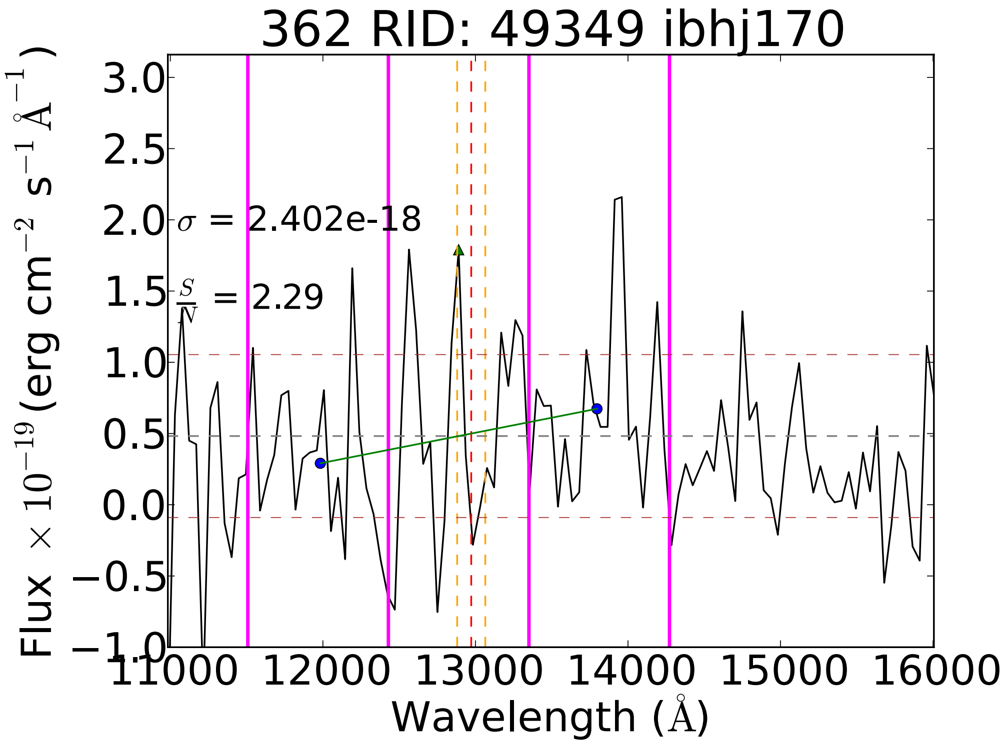

362 RID: 49349 ibhj170

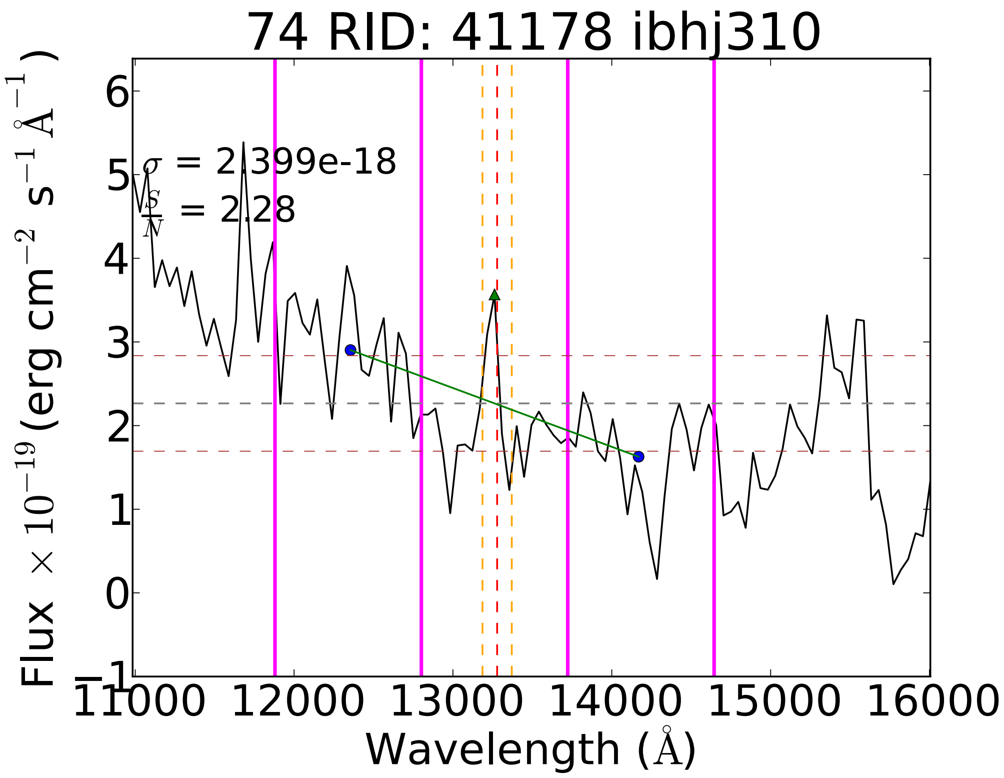
74 RID: 41178 ibhj310
σ = 2.399e-18
S/N = 2.28
Flux × 10^-19 (erg cm^-2 s^-1 Å^-1)
-1
0
1
2
3
4
5
6
11000
12000
13000
14000
15000
16000
Wavelength (Å)

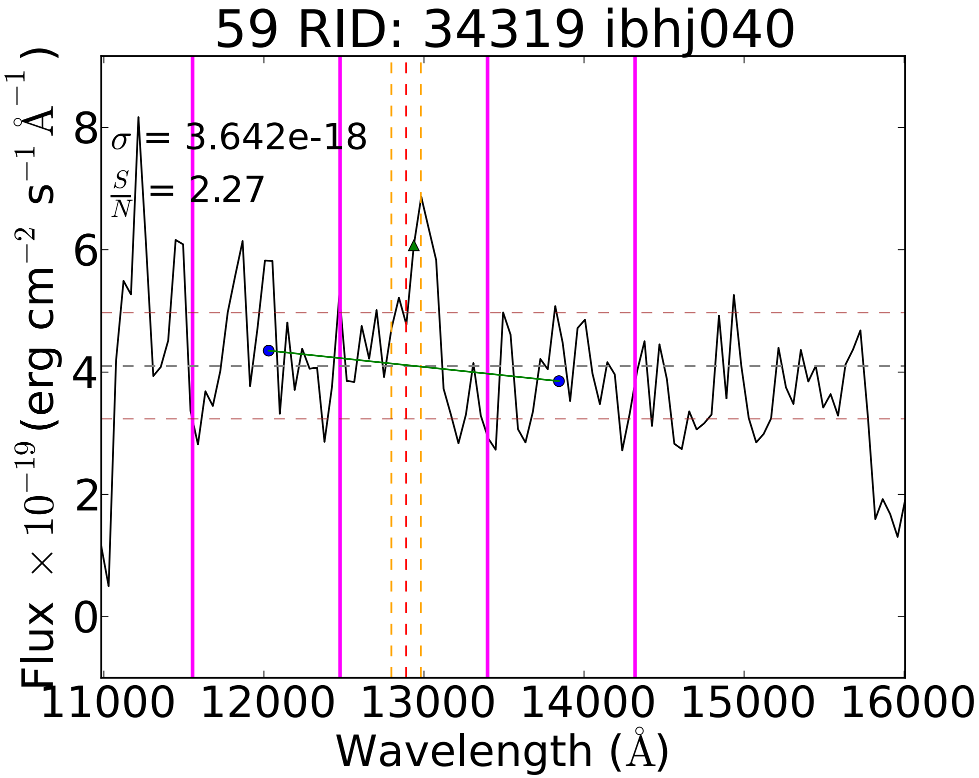
59 RID: 34319 ibhj040
σ = 3.642e-18
S/N = 2.27
Flux × 10^-19 (erg cm^-2 s^-1 Å^-1)
0
2
4
6
8
11000
12000
13000
14000
15000
16000
Wavelength (Å)

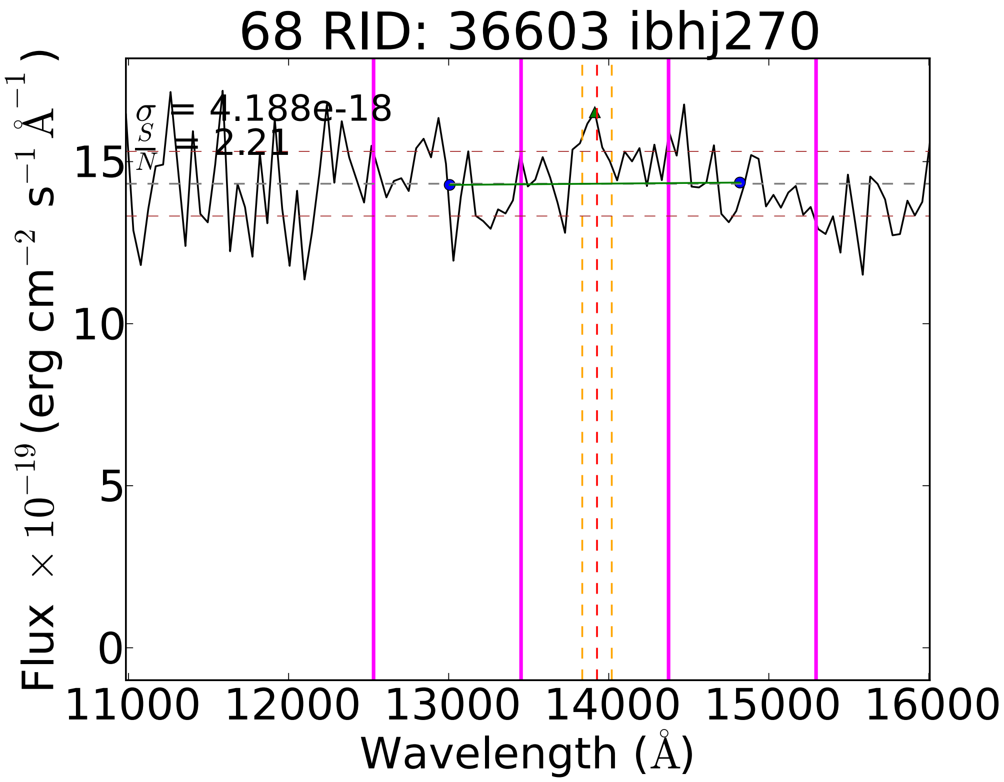
68 RID: 36603 ibhj270
σ = 4.188e-18
S/N = 2.21
Flux × 10^-19 (erg cm^-2 s^-1 Å^-1)
0
5
10
15
11000
12000
13000
14000
15000
16000
Wavelength (Å)

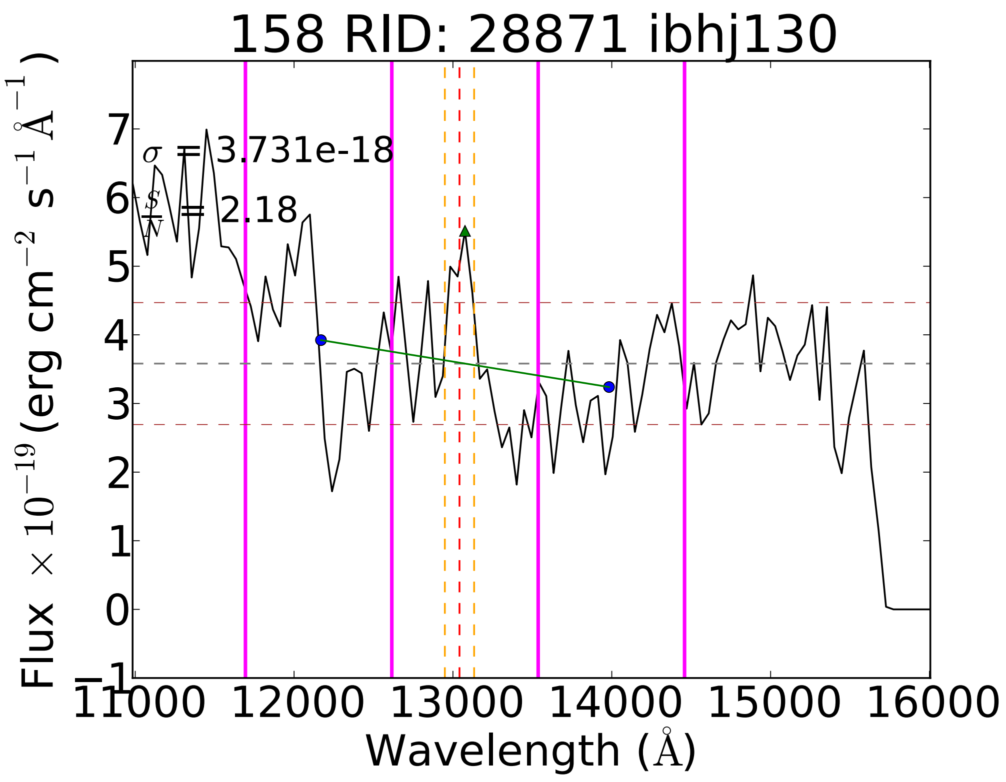
158 RID: 28871 ibhj130
σ = 3.731e-18
S/N = 2.18
Flux × 10^-19 (erg cm^-2 s^-1 Å^-1)
-1
0
1
2
3
4
5
6
7
11000
12000
13000
14000
15000
16000
Wavelength (Å)

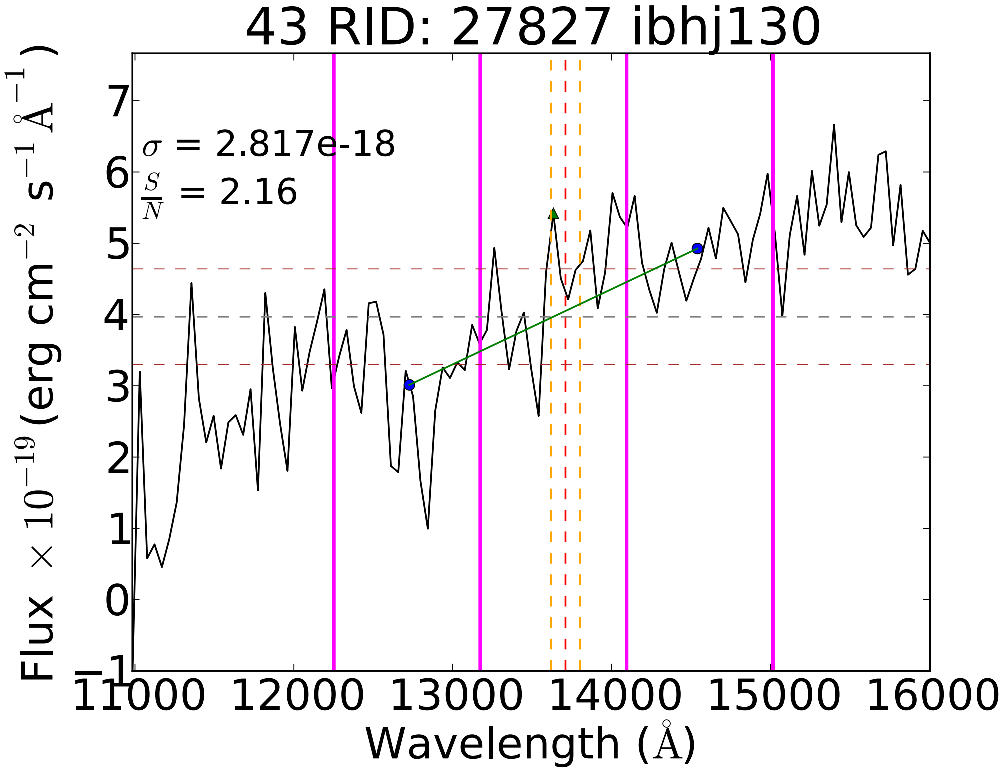
43 RID: 27827 ibhj130

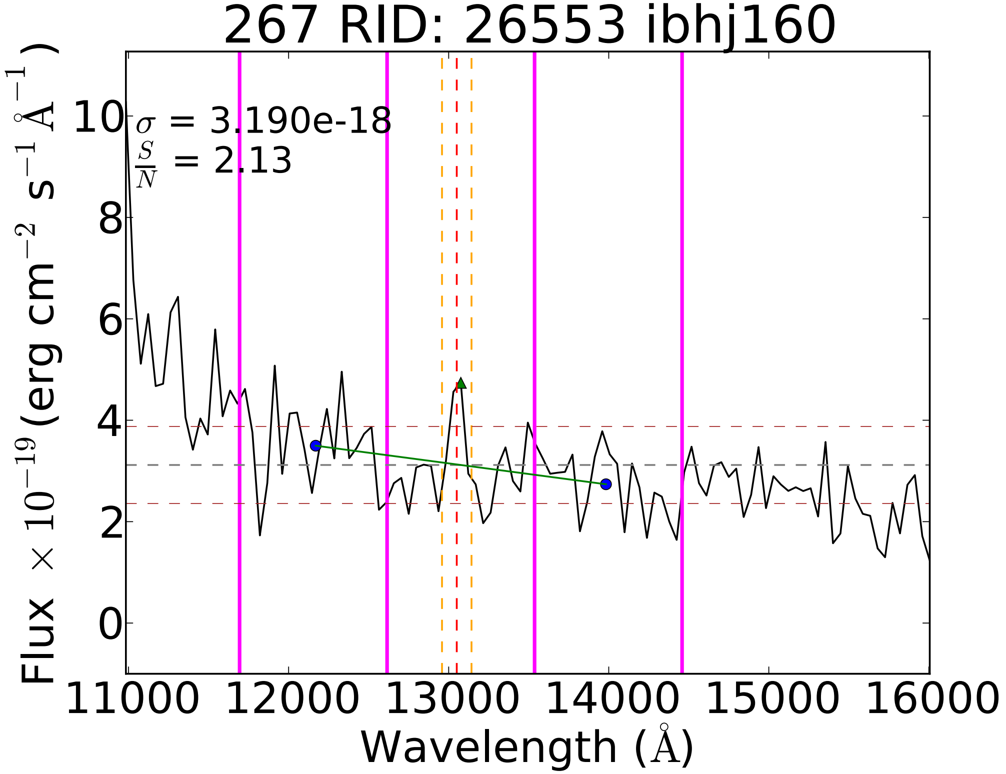
267 RID: 26553 ibhj160

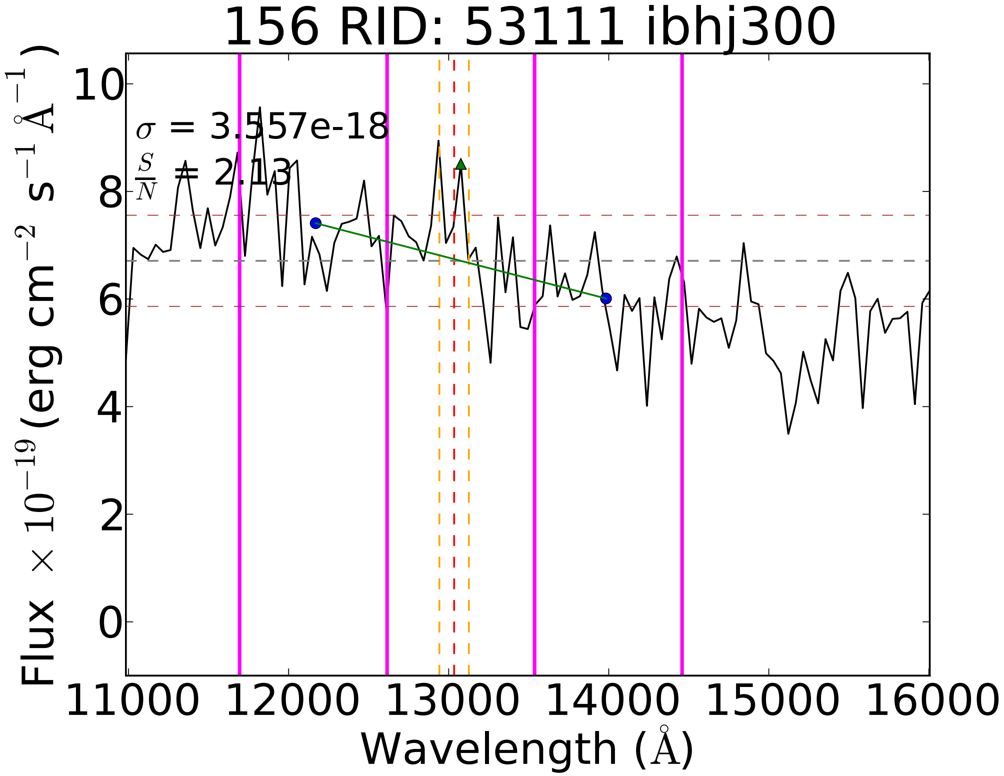
156 RID: 53111 ibhj300

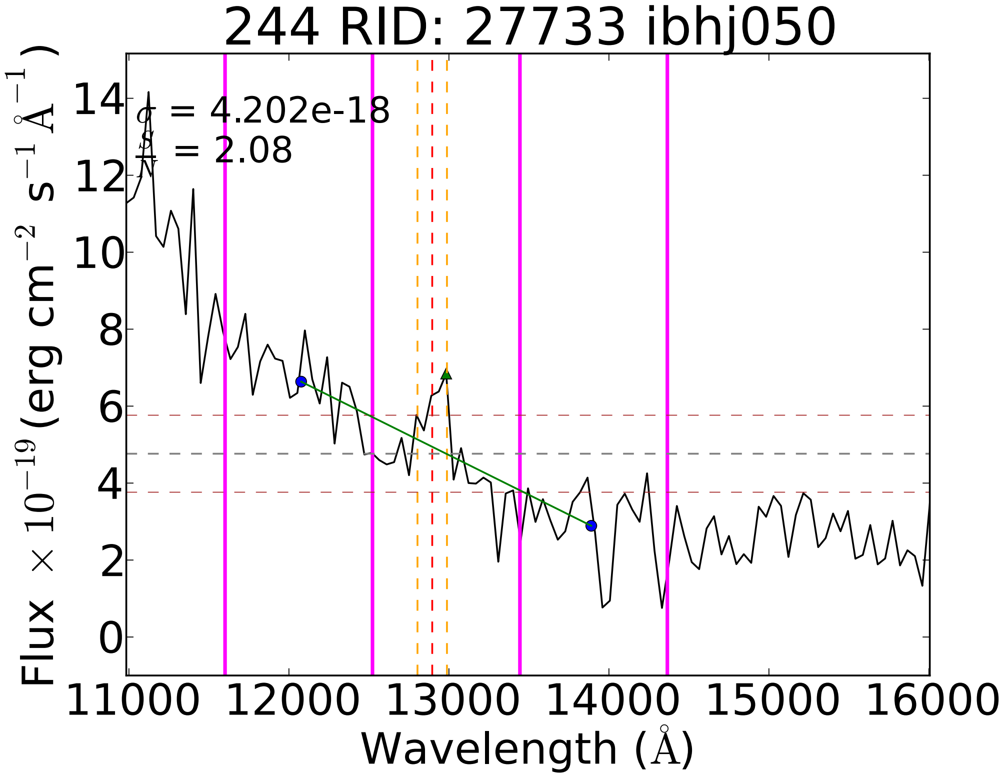
244 RID: 27733 ibhj050

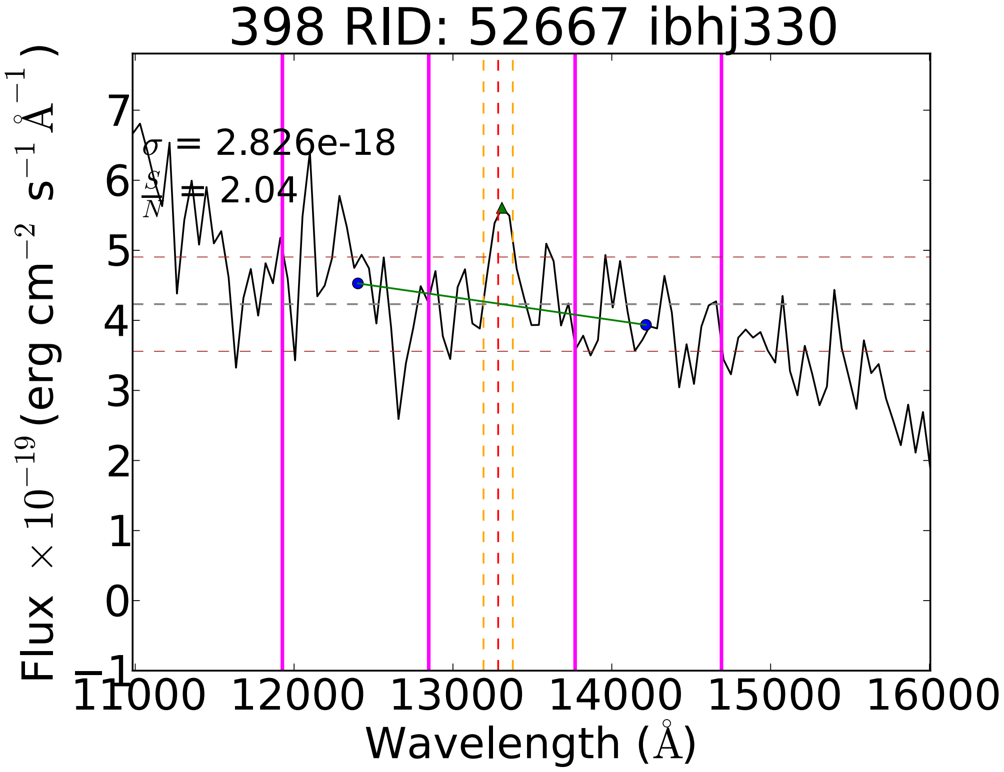
398 RID: 52667 ibhj330
σ = 2.826e-18
S/N = 2.04
Flux × 10^−19 (erg cm^−2 s^−1 Å^−1)
−1
0
1
2
3
4
5
6
7
11000
12000
13000
14000
15000
16000
Wavelength (Å)

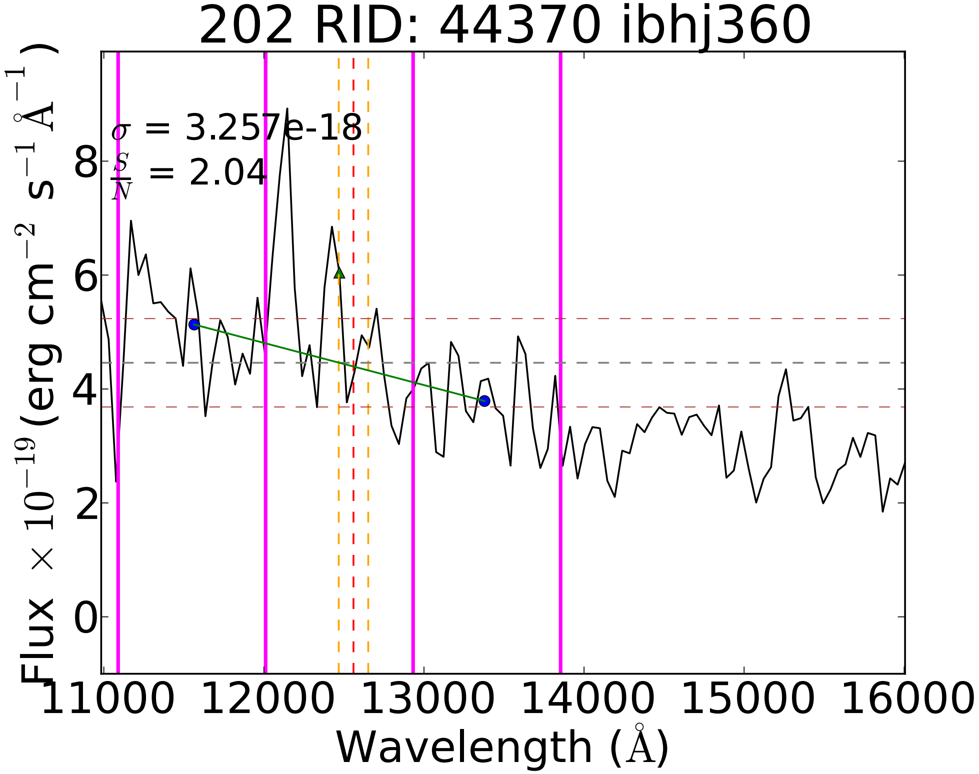
202 RID: 44370 ibhj360
σ = 3.257e-18
S/N = 2.04
Flux × 10^−19 (erg cm^−2 s^−1 Å^−1)
0
2
4
6
8
11000
12000
13000
14000
15000
16000
Wavelength (Å)

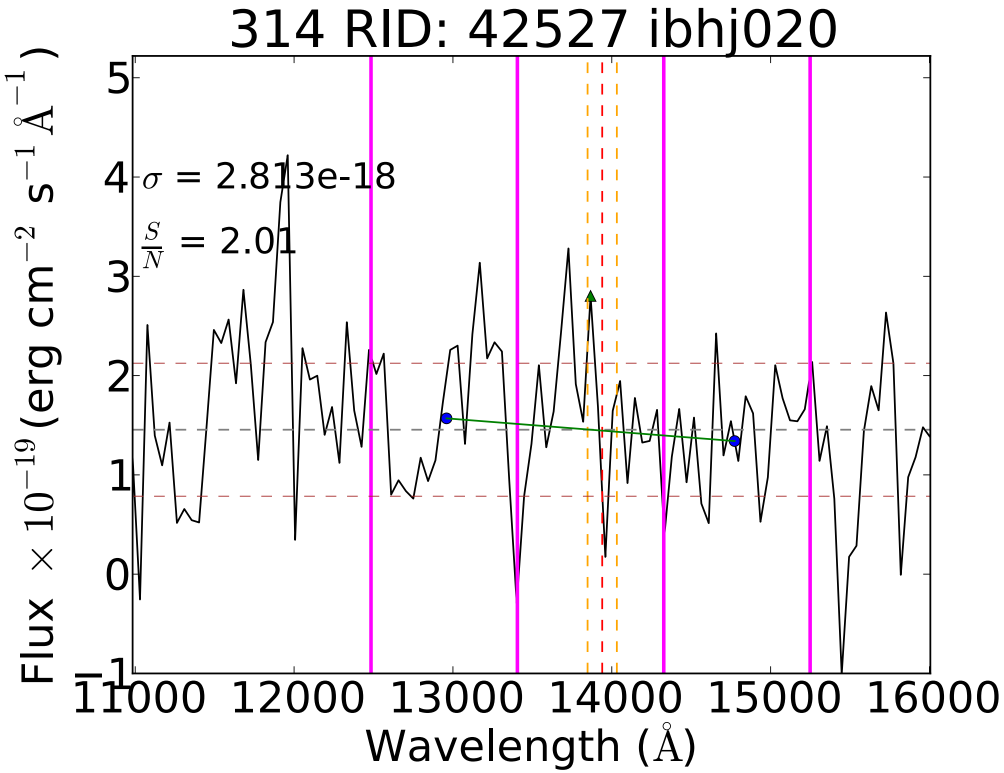
314 RID: 42527 ibhj020
σ = 2.813e-18
S/N = 2.01
Flux × 10^−19 (erg cm^−2 s^−1 Å^−1)
−1
0
1
2
3
4
5
11000
12000
13000
14000
15000
16000
Wavelength (Å)

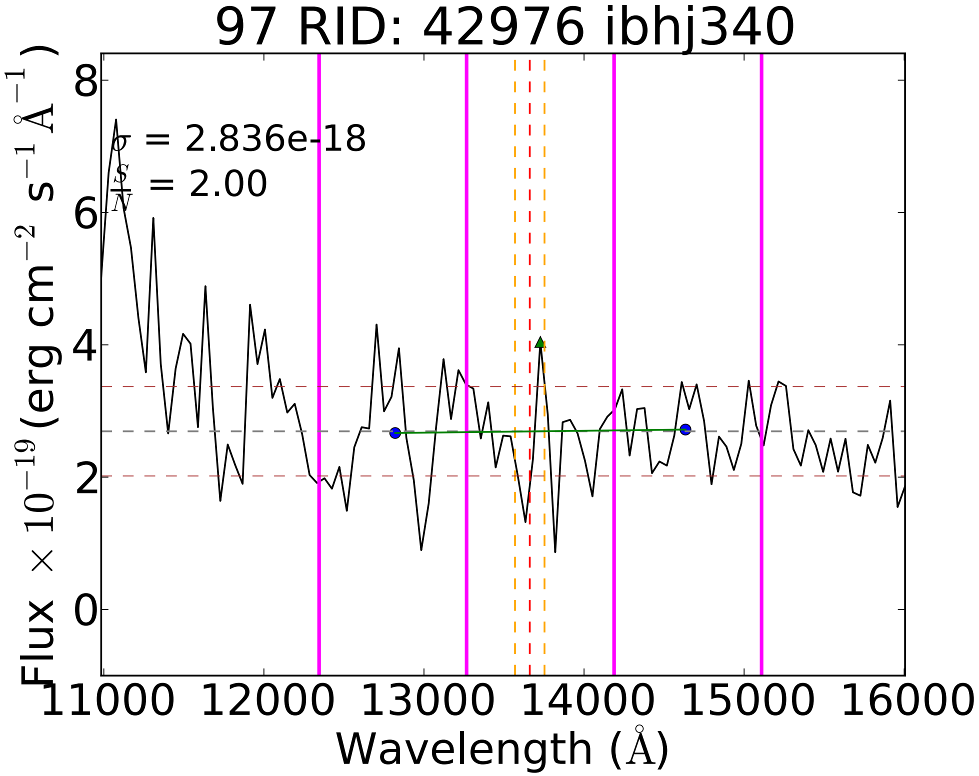
97 RID: 42976 ibhj340
σ = 2.836e-18
S/N = 2.00
Flux × 10^−19 (erg cm^−2 s^−1 Å^−1)
0
2
4
6
8
11000
12000
13000
14000
15000
16000
Wavelength (Å)

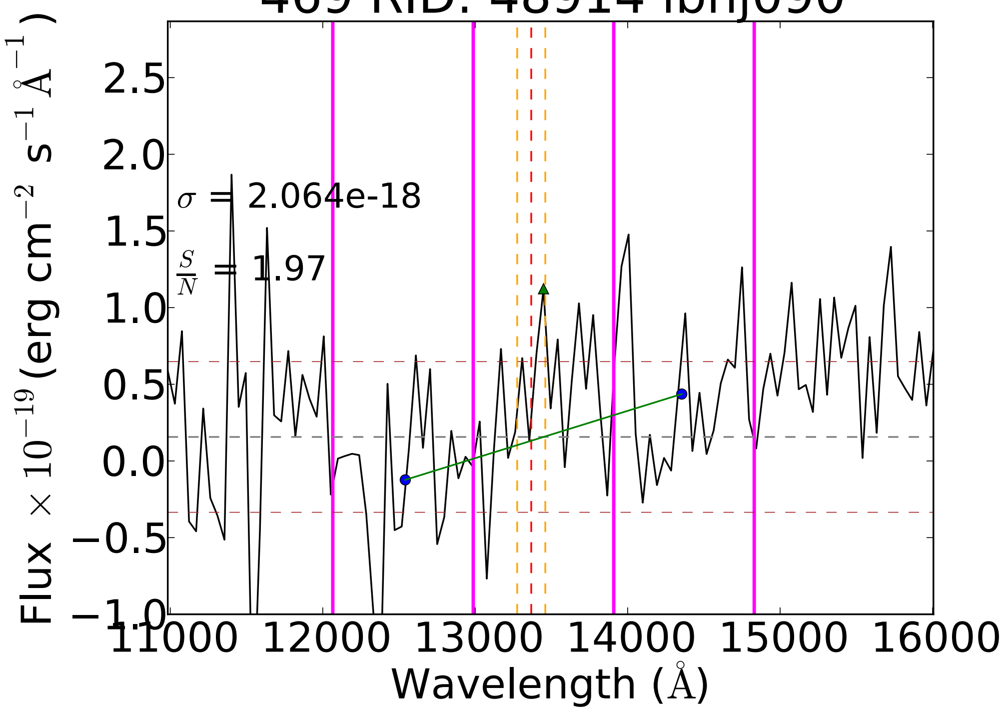
469 RID: 48914 ibhj090

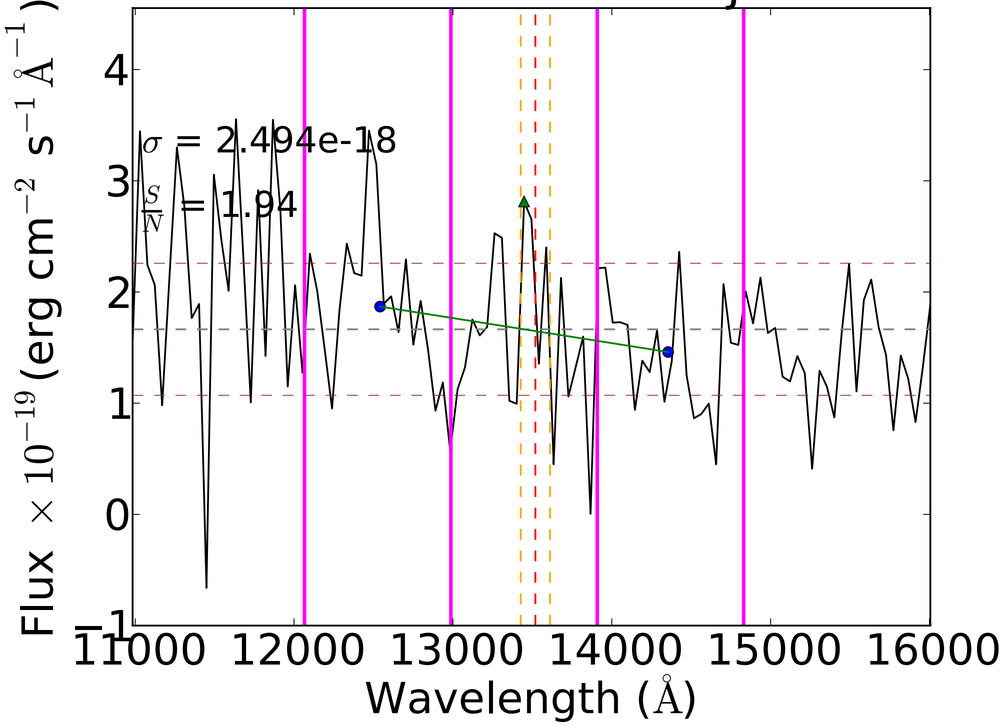
116 RID: 50413 ibhj120

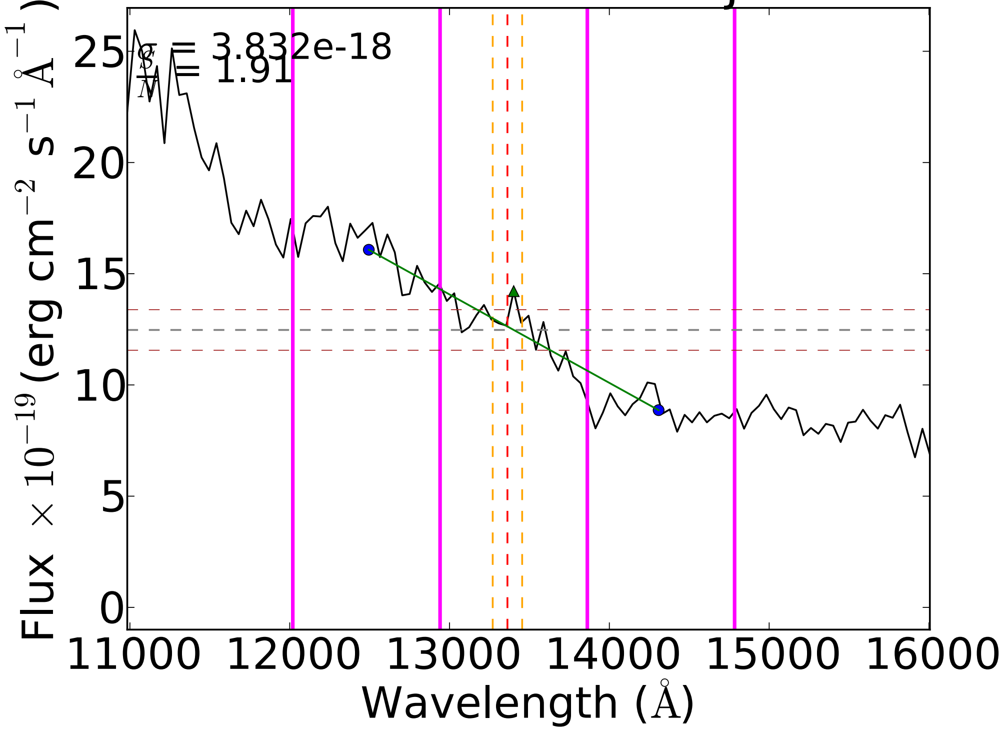
216 RID: 54117 ibhj300

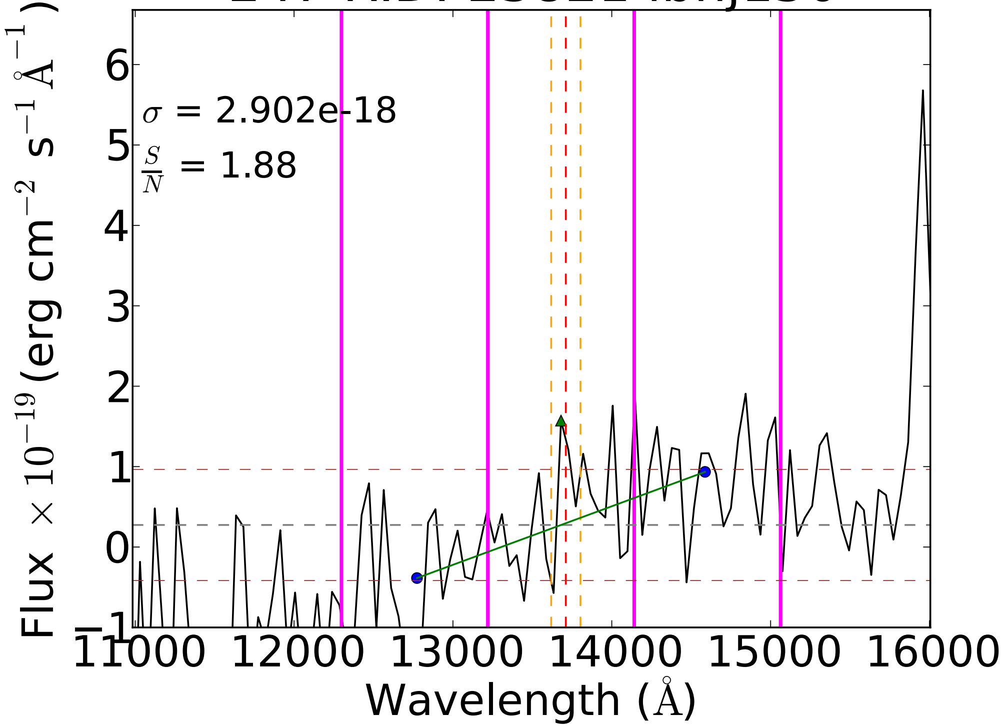
247 RID: 23821 ibhj150

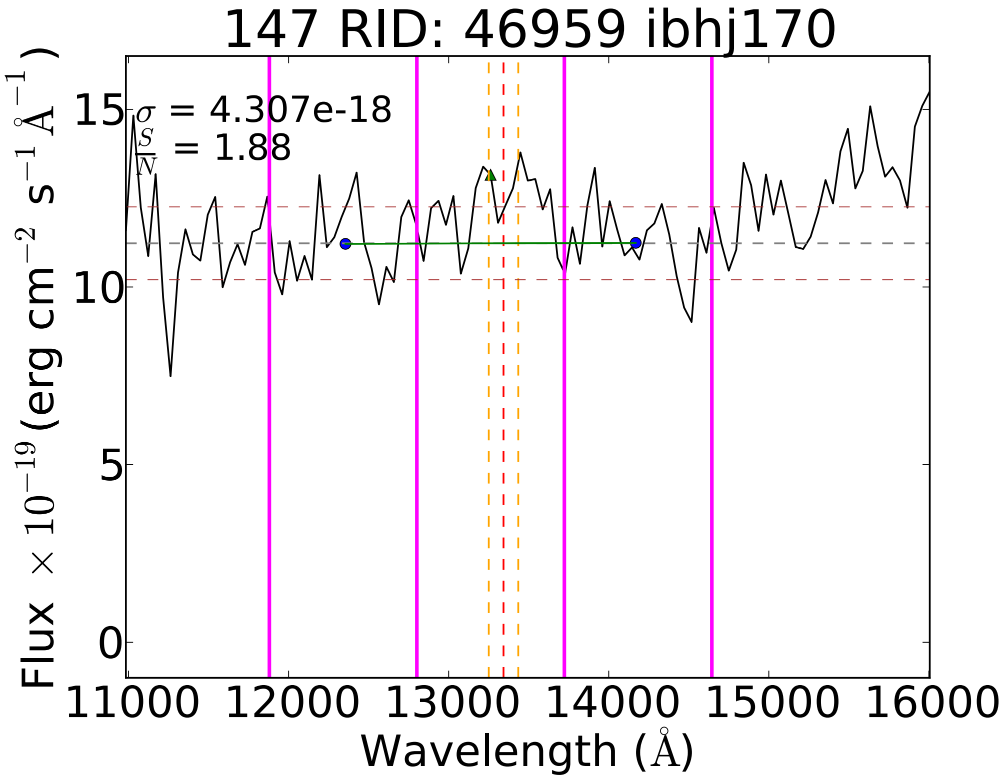

147 RID: 46959 ibhj170

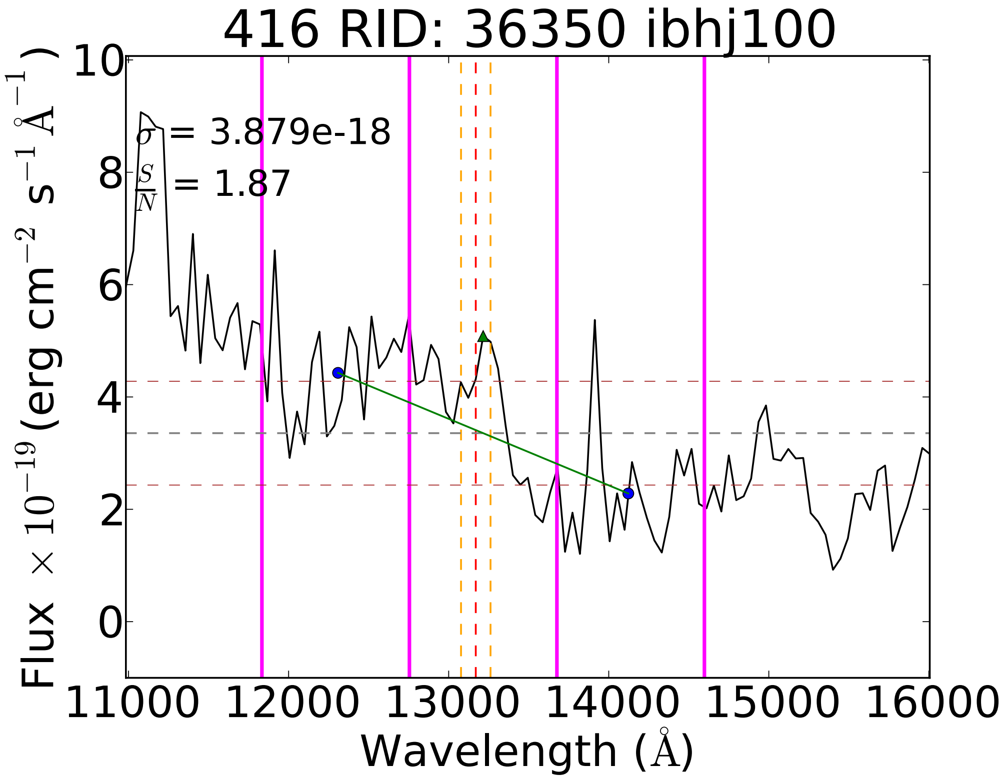

416 RID: 36350 ibhj100

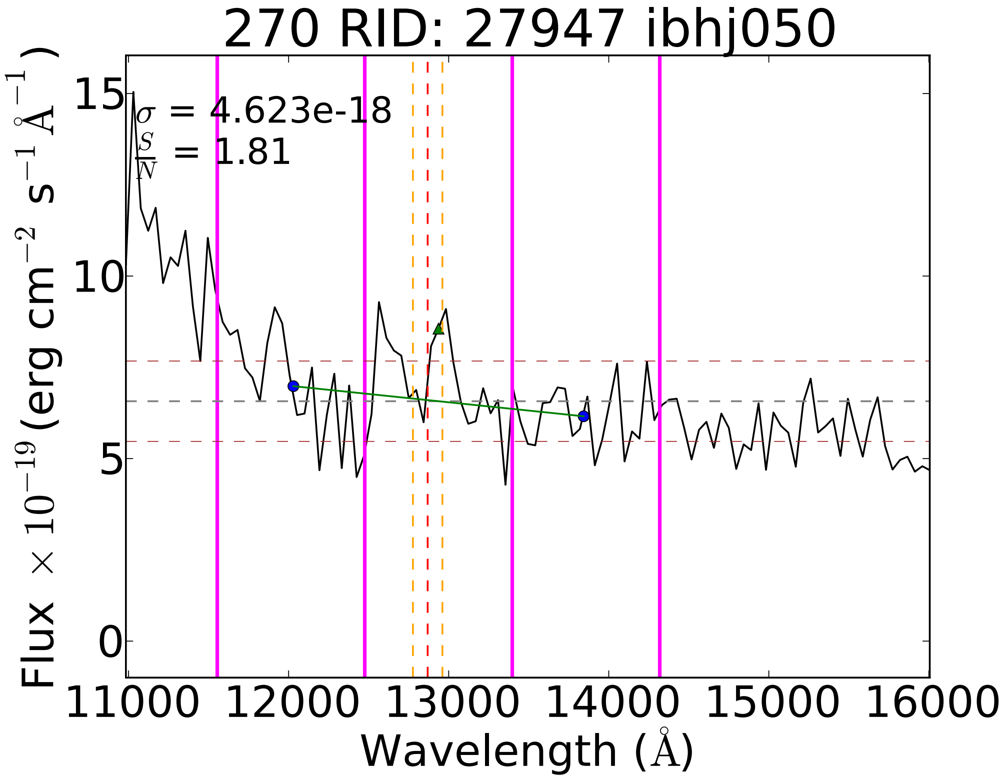

270 RID: 27947 ibhj050

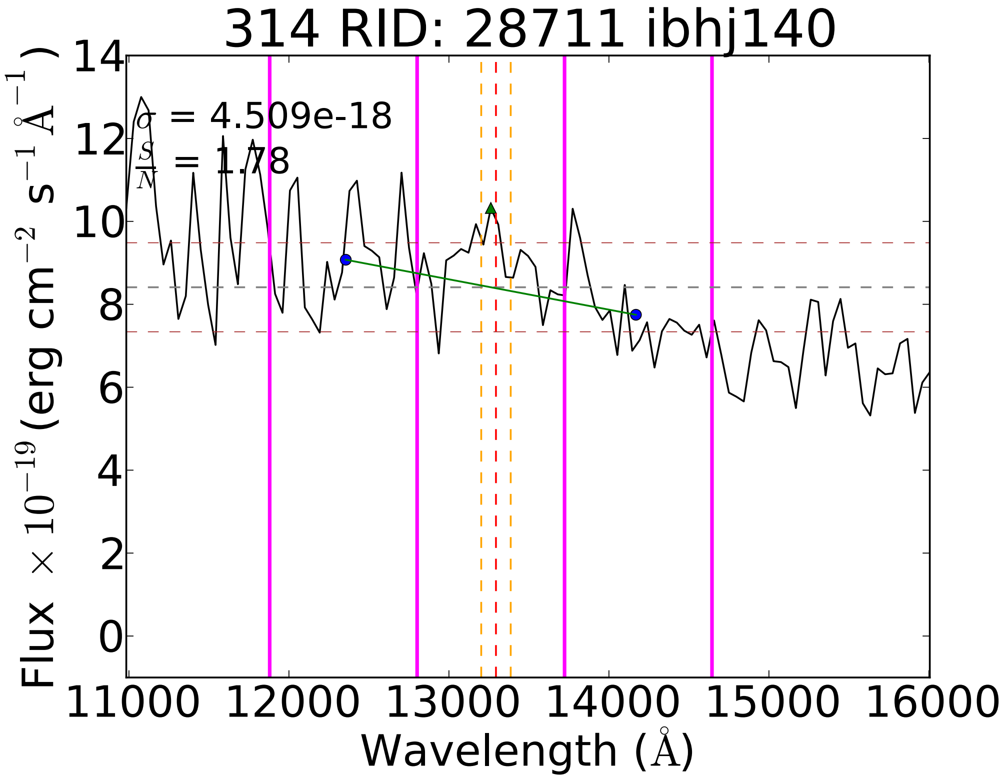

314 RID: 28711 ibhj140

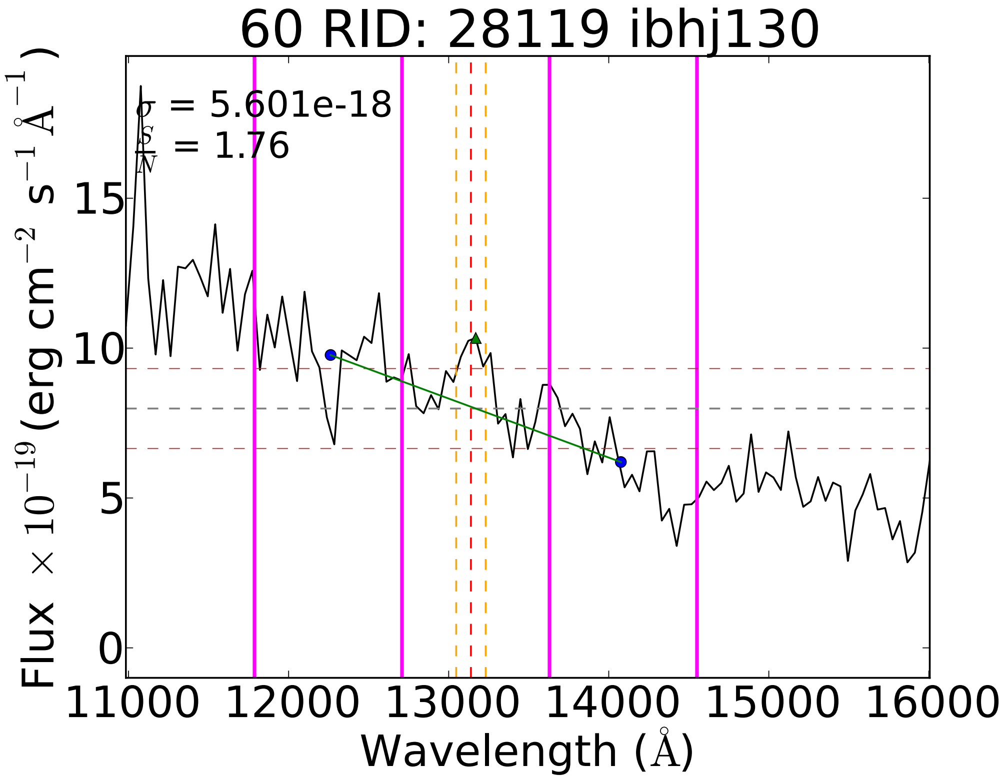
60 RID: 28119 ibhj130
σ = 5.601e-18
$\frac{S}{N}$ = 1.76
Flux $\times 10^{-19}$ (erg cm^{-2} s^{-1} Å^{-1})
Wavelength (Å)
0
5
10
15
11000
12000
13000
14000
15000
16000

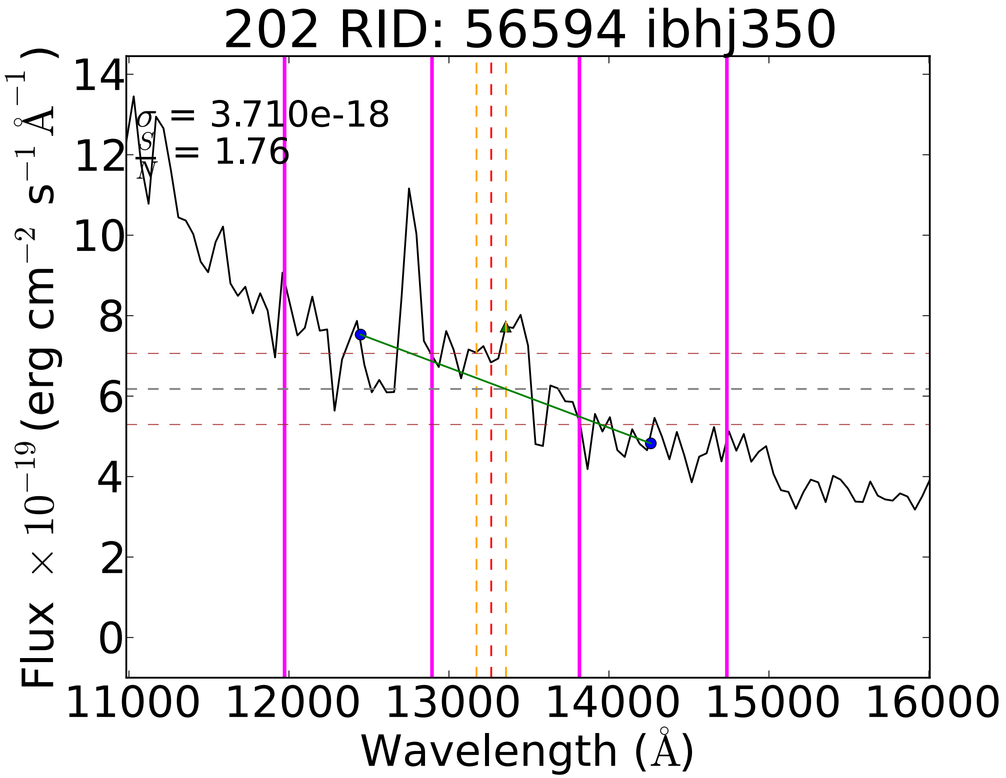
202 RID: 56594 ibhj350
σ = 3.710e-18
$\frac{S}{N}$ = 1.76
Flux $\times 10^{-19}$ (erg cm^{-2} s^{-1} Å^{-1})
Wavelength (Å)
0
2
4
6
8
10
12
14
11000
12000
13000
14000
15000
16000

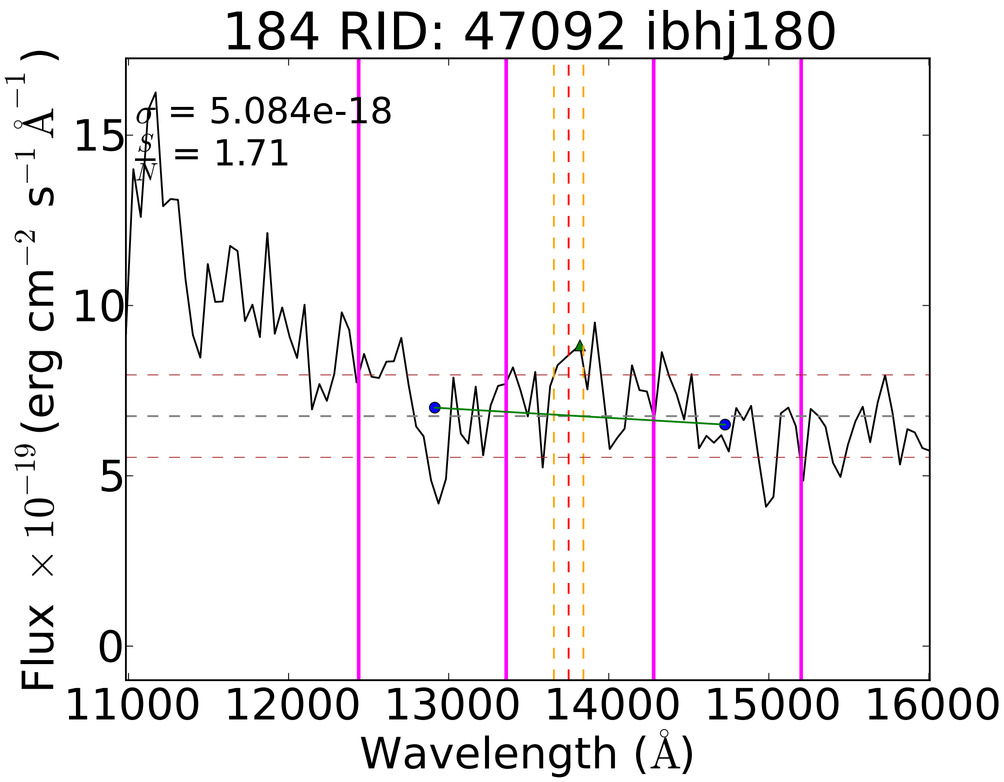
184 RID: 47092 ibhj180
σ = 5.084e-18
$\frac{S}{N}$ = 1.71
Flux $\times 10^{-19}$ (erg cm^{-2} s^{-1} Å^{-1})
Wavelength (Å)
0
5
10
15
11000
12000
13000
14000
15000
16000

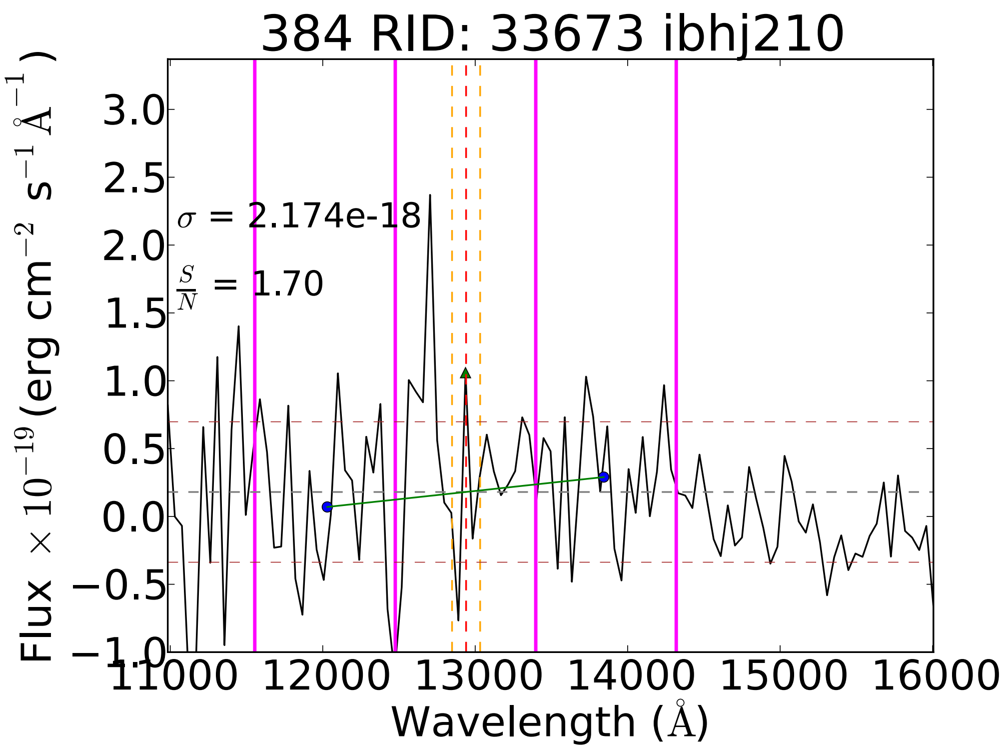
384 RID: 33673 ibhj210
σ = 2.174e-18
$\frac{S}{N}$ = 1.70
Flux $\times 10^{-19}$ (erg cm^{-2} s^{-1} Å^{-1})
Wavelength (Å)
−1.0
−0.5
0.0
0.5
1.0
1.5
2.0
2.5
3.0
11000
12000
13000
14000
15000
16000

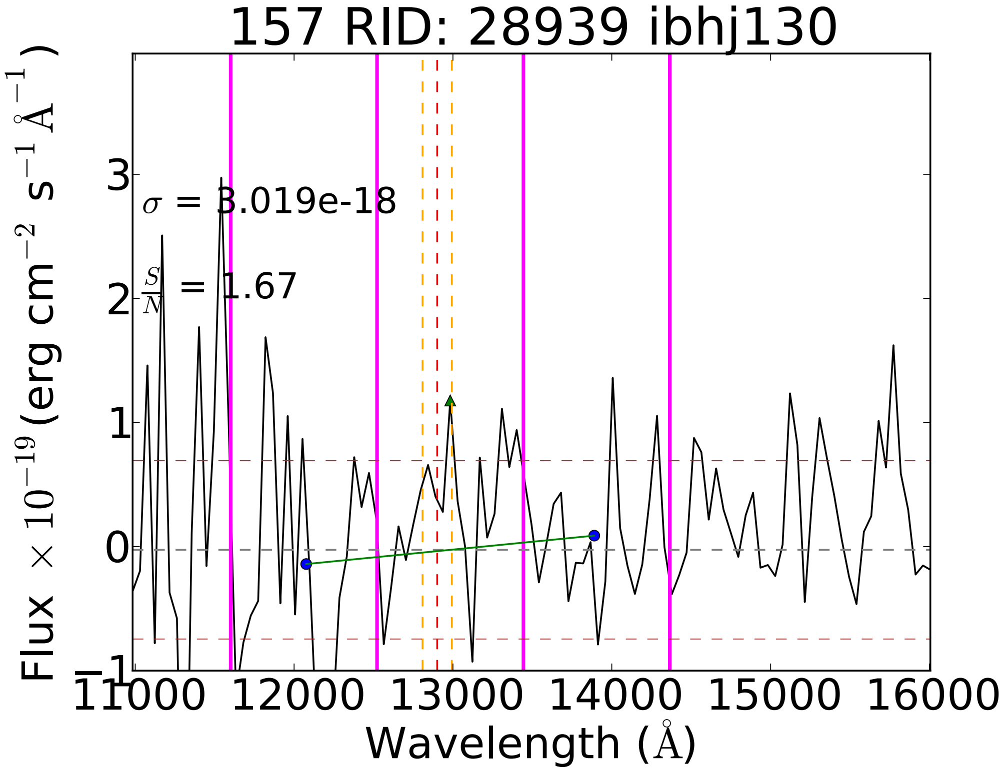
157 RID: 28939 ibhj130
σ = 3.019e-18
S/N = 1.67
Flux × 10^−19 (erg cm^−2 s^−1 Å^−1)
Wavelength (Å)
−1
0
1
2
3
11000
12000
13000
14000
15000
16000

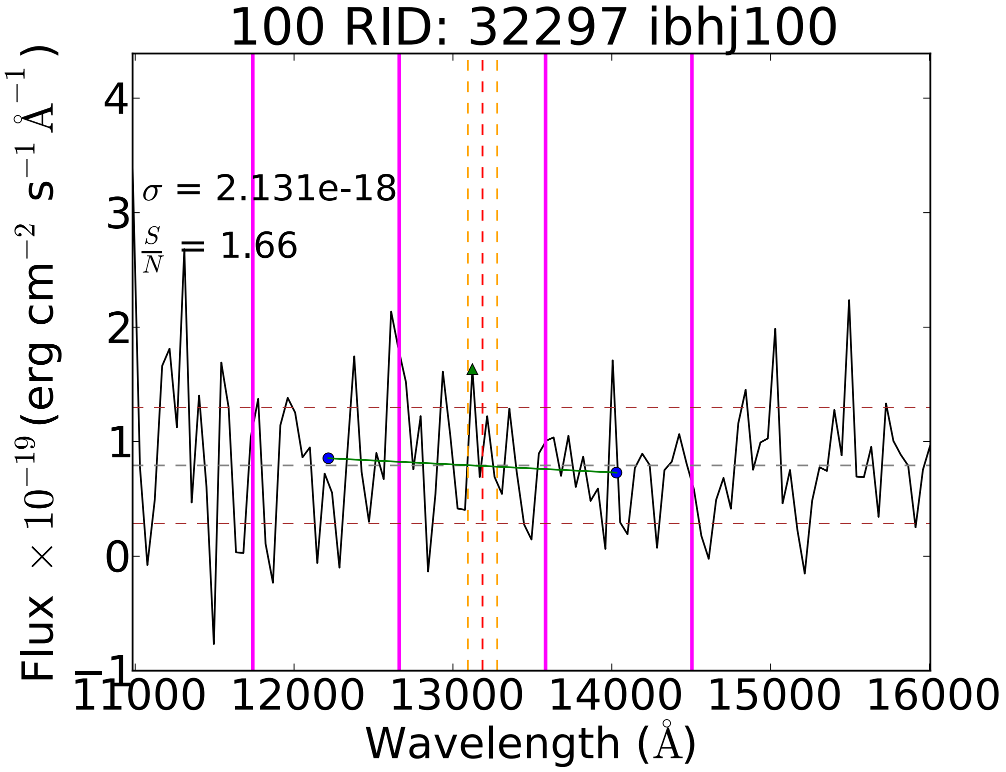
100 RID: 32297 ibhj100
σ = 2.131e-18
S/N = 1.66
Flux × 10^−19 (erg cm^−2 s^−1 Å^−1)
Wavelength (Å)
−1
0
1
2
3
4
11000
12000
13000
14000
15000
16000

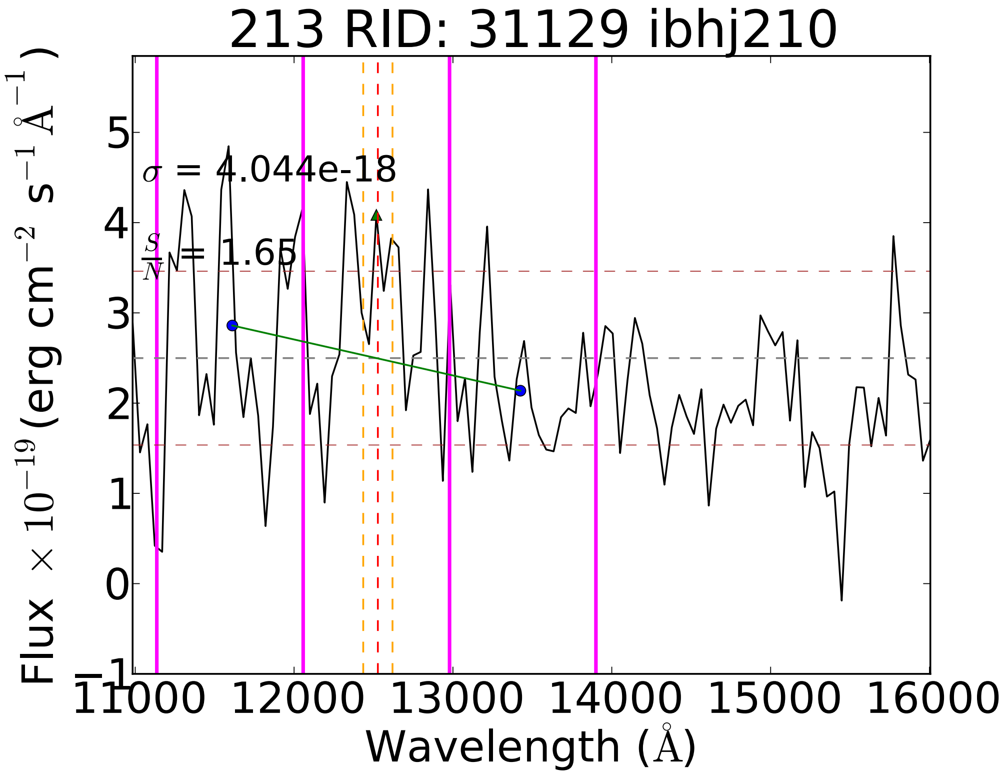
213 RID: 31129 ibhj210
σ = 4.044e-18
S/N = 1.65
Flux × 10^−19 (erg cm^−2 s^−1 Å^−1)
Wavelength (Å)
−1
0
1
2
3
4
5
11000
12000
13000
14000
15000
16000

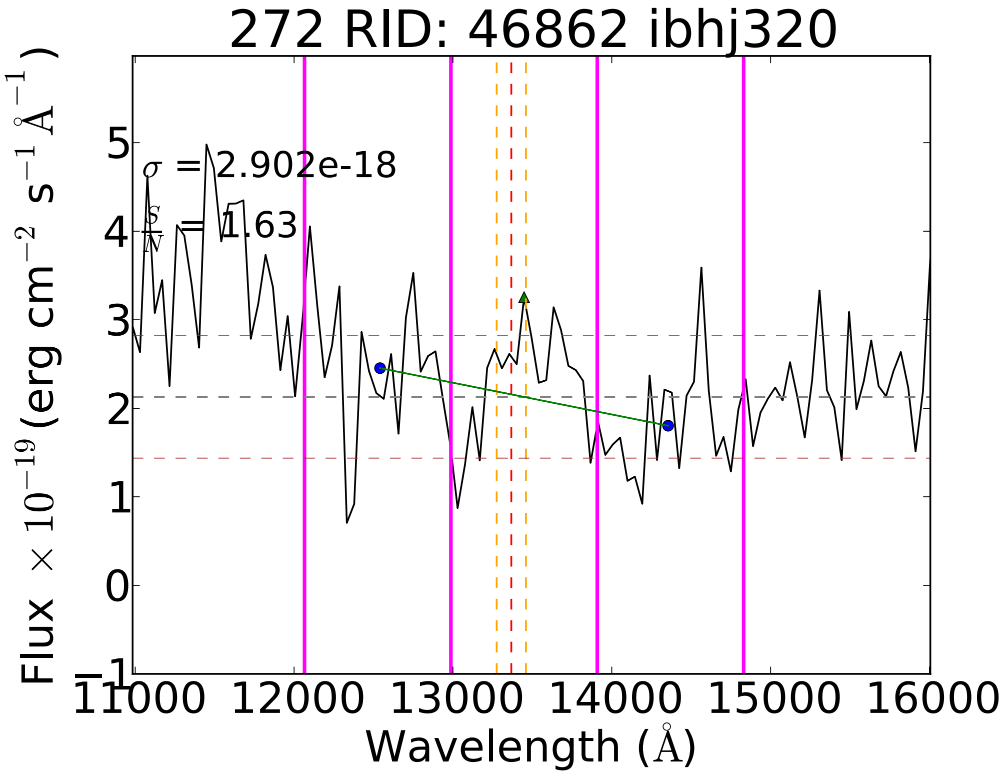
272 RID: 46862 ibhj320
σ = 2.902e-18
S/N = 1.63
Flux × 10^−19 (erg cm^−2 s^−1 Å^−1)
Wavelength (Å)
−1
0
1
2
3
4
5
11000
12000
13000
14000
15000
16000

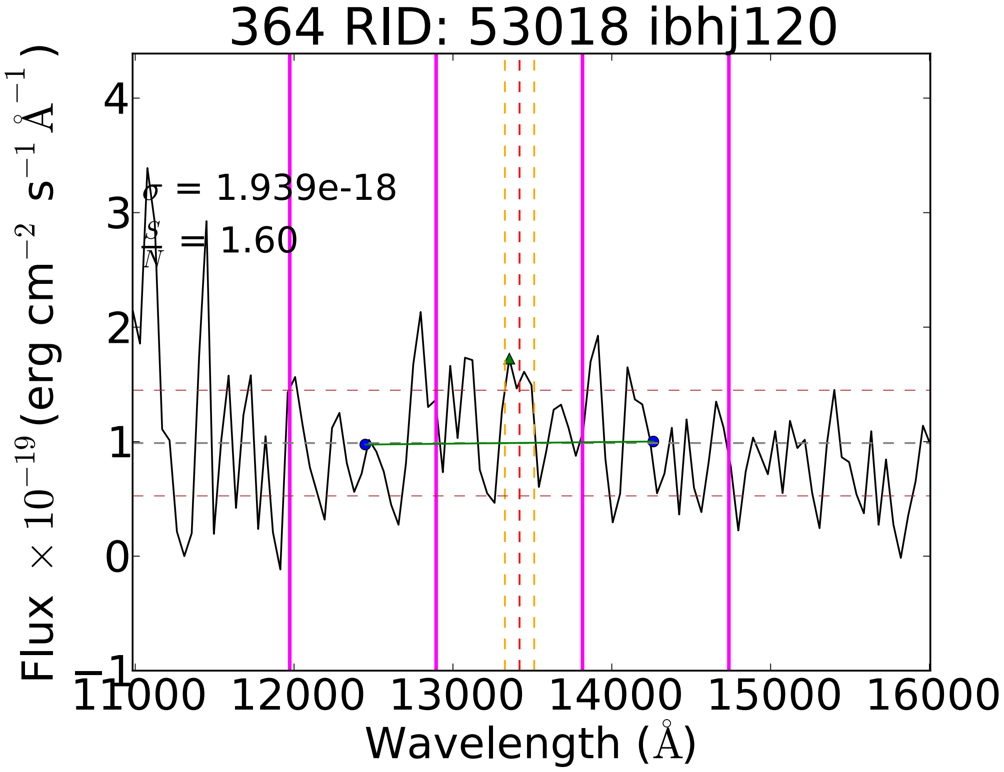
364 RID: 53018 ibhj120
σ = 1.939e-18
$\frac{S}{N}$ = 1.60
Flux × 10^{-19} (erg cm^{-2} s^{-1} Å^{-1})
Wavelength (Å)
-1
0
1
2
3
4
11000
12000
13000
14000
15000
16000

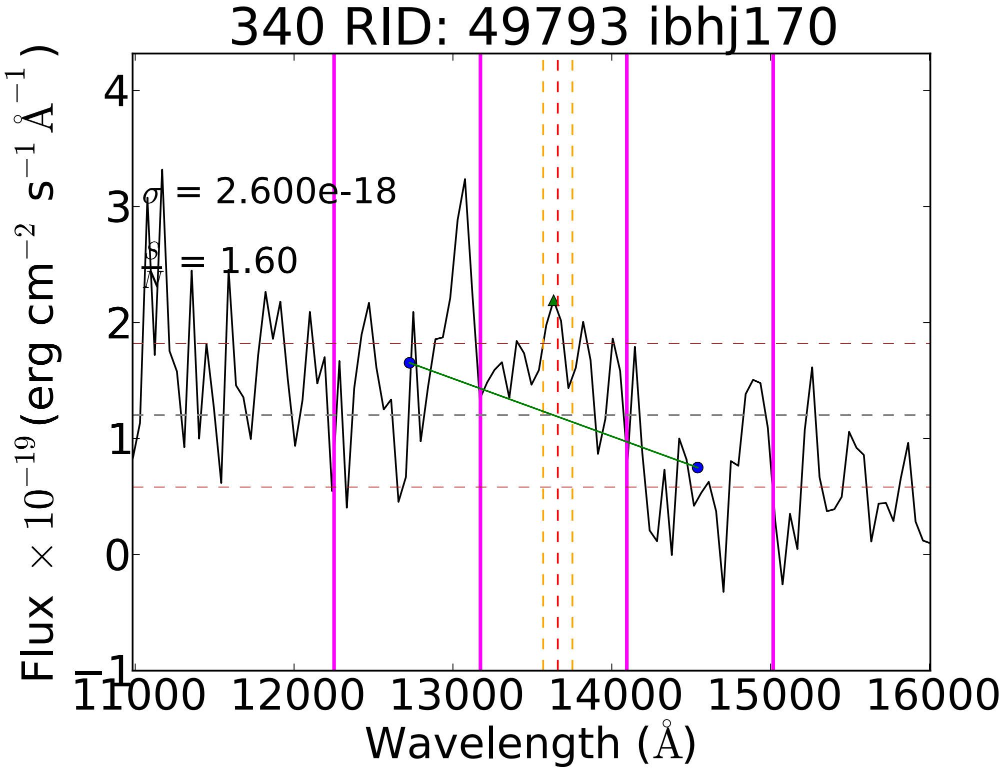
340 RID: 49793 ibhj170
σ = 2.600e-18
$\frac{S}{N}$ = 1.60
Flux × 10^{-19} (erg cm^{-2} s^{-1} Å^{-1})
Wavelength (Å)
-1
0
1
2
3
4
11000
12000
13000
14000
15000
16000

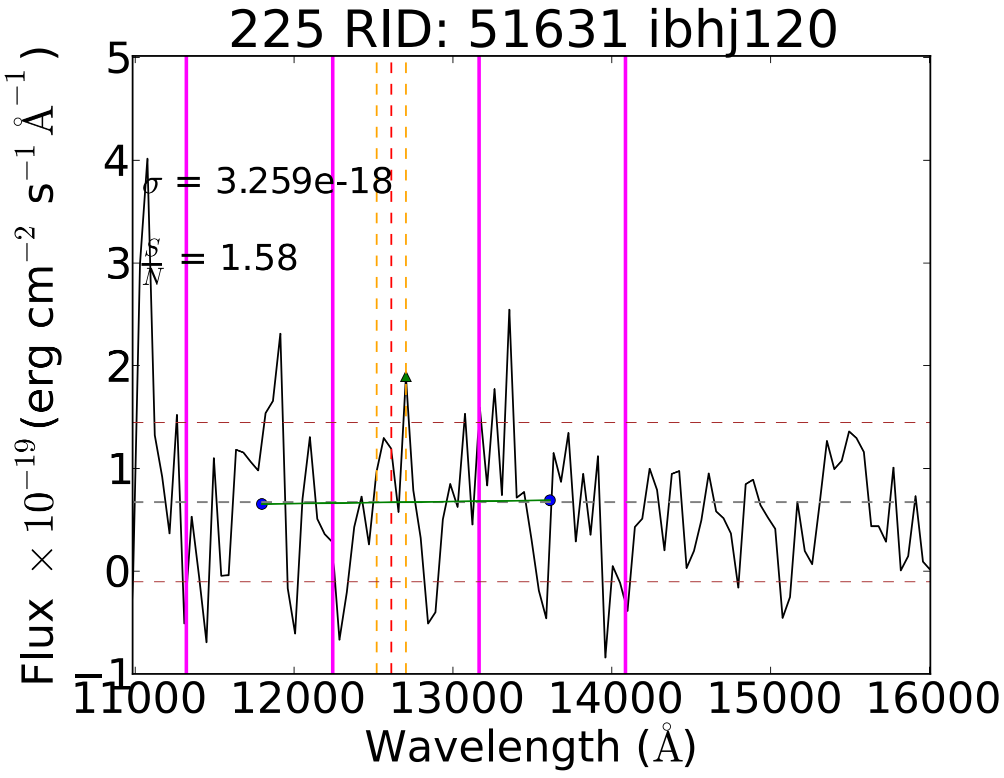
225 RID: 51631 ibhj120
σ = 3.259e-18
$\frac{S}{N}$ = 1.58
Flux × 10^{-19} (erg cm^{-2} s^{-1} Å^{-1})
Wavelength (Å)
-1
0
1
2
3
4
5
11000
12000
13000
14000
15000
16000

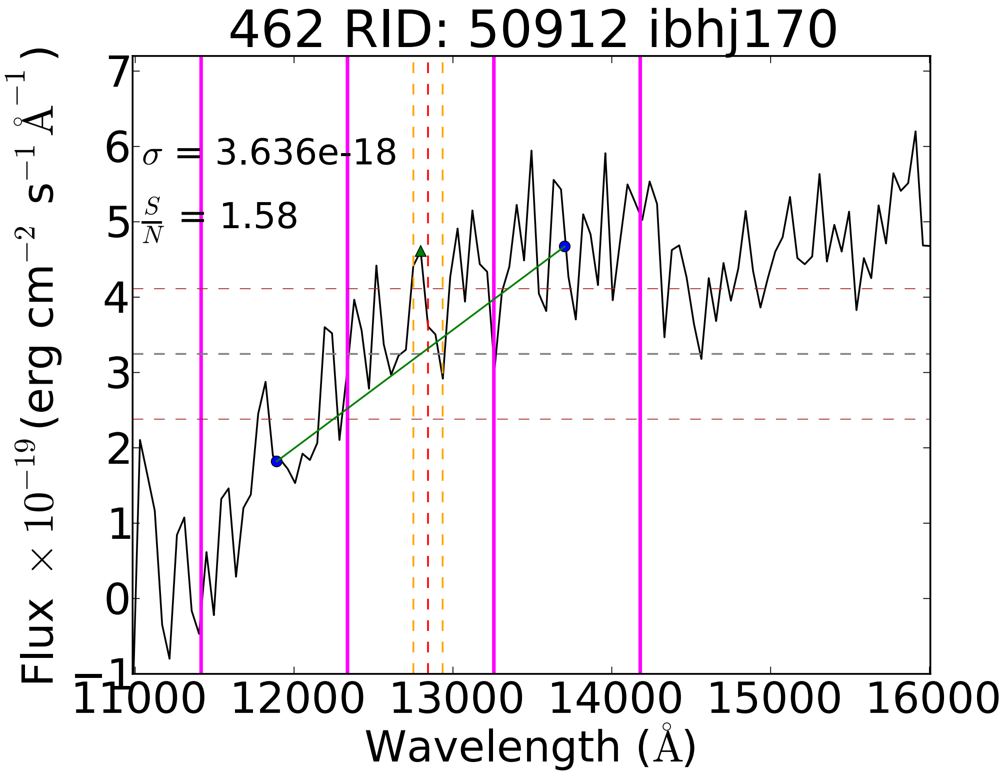
462 RID: 50912 ibhj170
σ = 3.636e-18
$\frac{S}{N}$ = 1.58
Flux × 10^{-19} (erg cm^{-2} s^{-1} Å^{-1})
Wavelength (Å)
-1
0
1
2
3
4
5
6
7
11000
12000
13000
14000
15000
16000

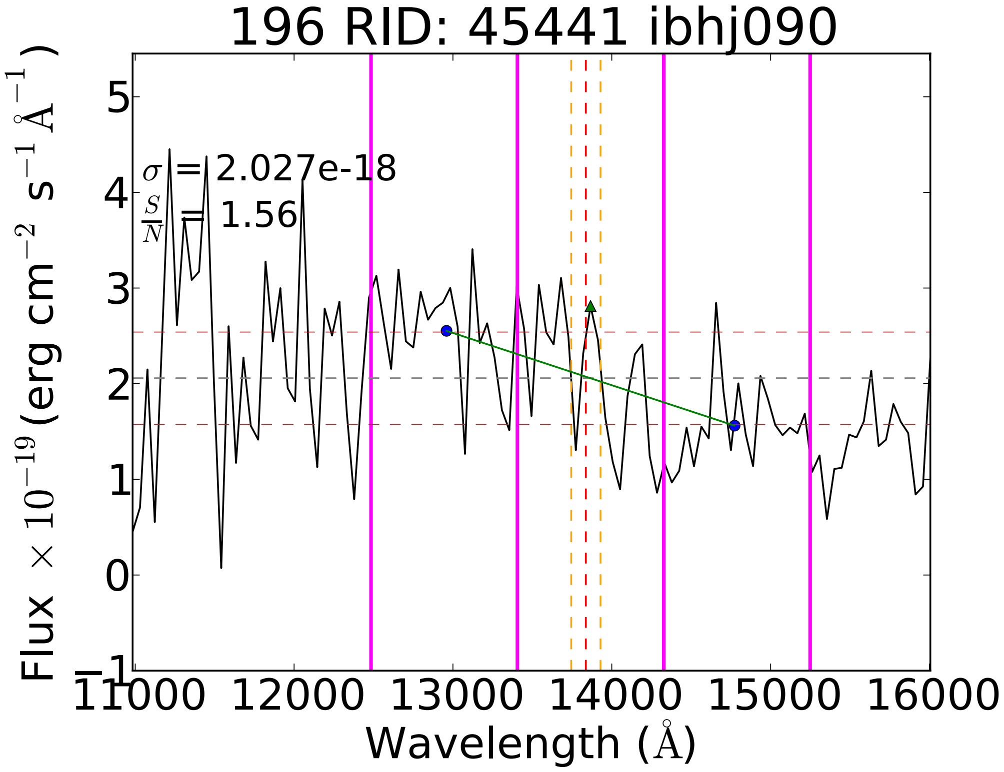
196 RID: 45441 ibhj090
σ = 2.027e-18
$\frac{S}{N}$ = 1.56
Flux $\times 10^{-19}$ (erg cm^{-2} s^{-1} Å^{-1})
−1
0
1
2
3
4
5
11000
12000
13000
14000
15000
16000
Wavelength (Å)

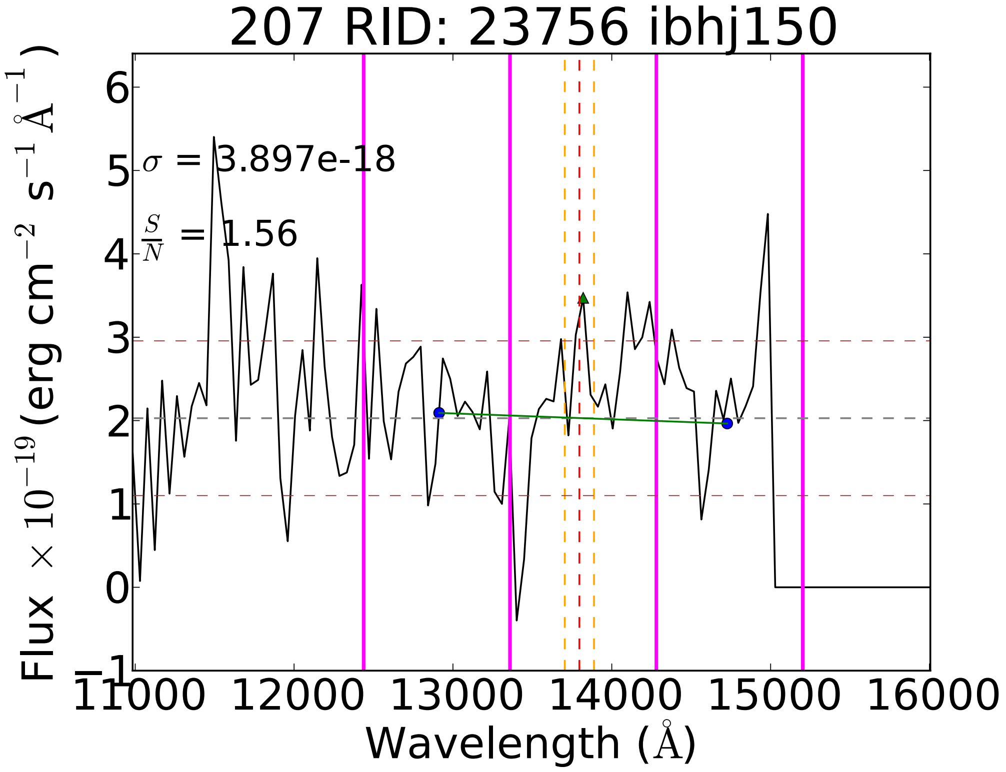
207 RID: 23756 ibhj150
σ = 3.897e-18
$\frac{S}{N}$ = 1.56
Flux $\times 10^{-19}$ (erg cm^{-2} s^{-1} Å^{-1})
−1
0
1
2
3
4
5
6
11000
12000
13000
14000
15000
16000
Wavelength (Å)

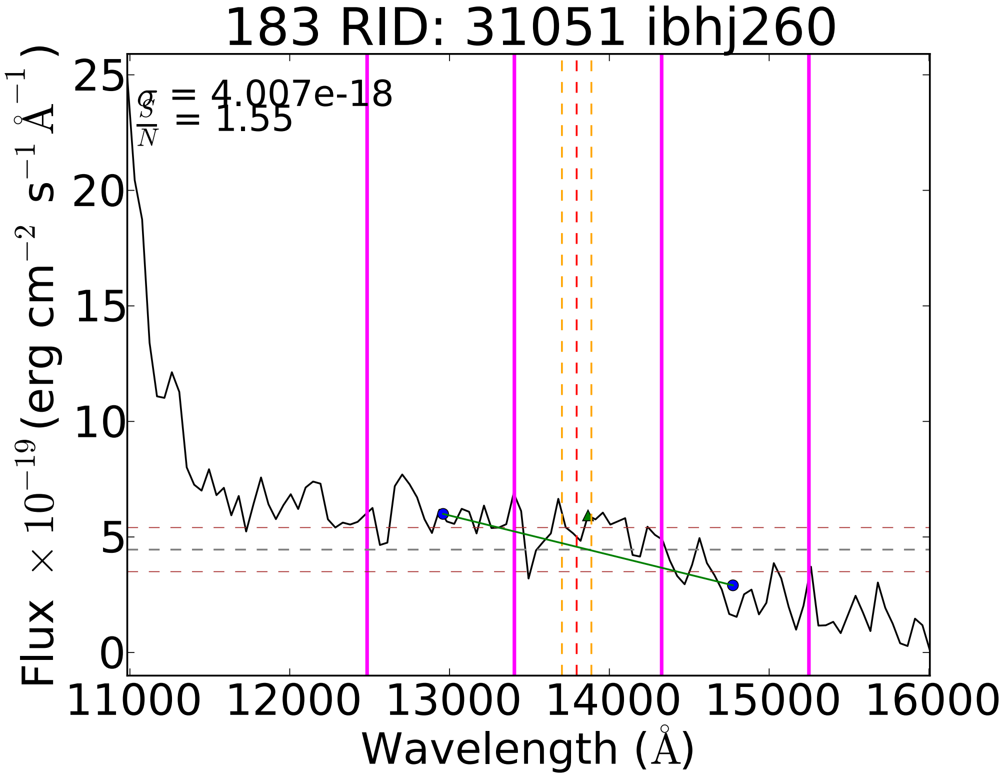
183 RID: 31051 ibhj260
σ = 4.007e-18
$\frac{S}{N}$ = 1.55
Flux $\times 10^{-19}$ (erg cm^{-2} s^{-1} Å^{-1})
0
5
10
15
20
25
11000
12000
13000
14000
15000
16000
Wavelength (Å)

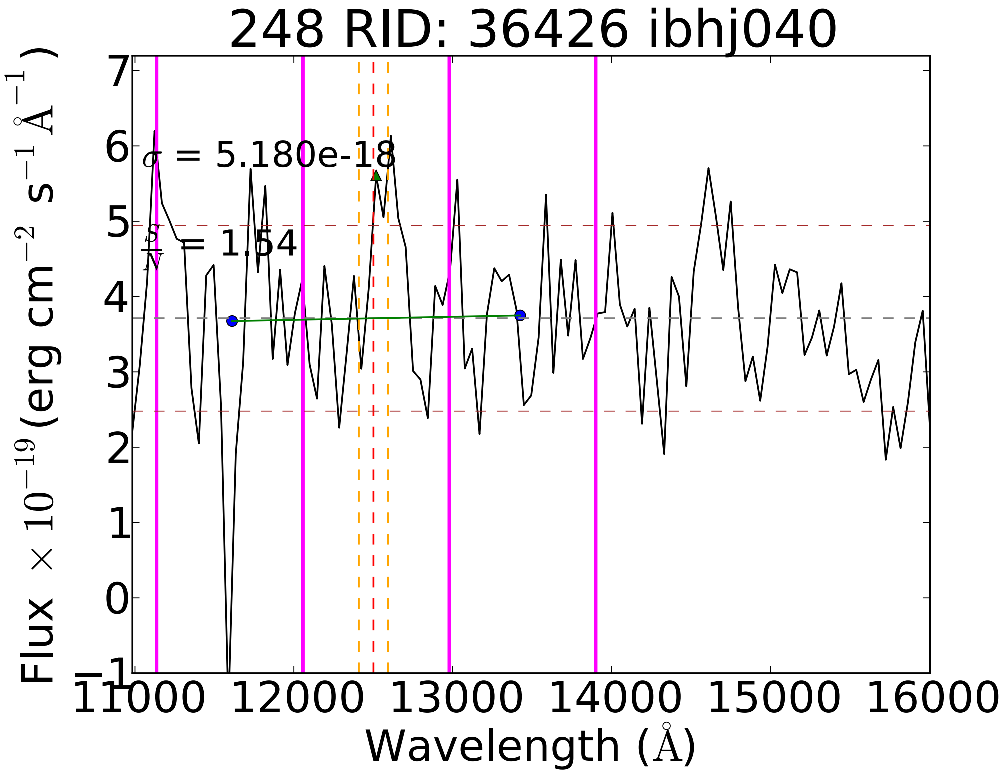
248 RID: 36426 ibhj040
σ = 5.180e-18
$\frac{S}{N}$ = 1.54
Flux $\times 10^{-19}$ (erg cm^{-2} s^{-1} Å^{-1})
−1
0
1
2
3
4
5
6
7
11000
12000
13000
14000
15000
16000
Wavelength (Å)

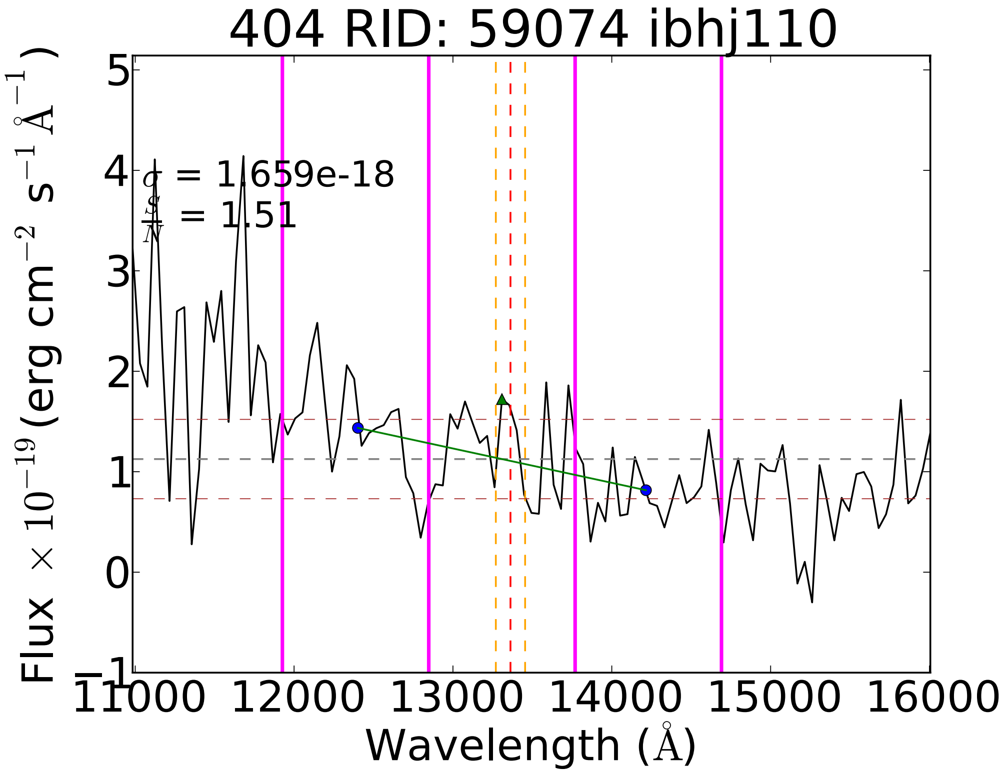
404 RID: 59074 ibhj110
σ = 1.659e-18
$\frac{S}{N}$ = 1.51
Flux $\times 10^{-19}$ (erg cm^{-2} s^{-1} Å^{-1})
Wavelength (Å)
-1
0
1
2
3
4
5
11000
12000
13000
14000
15000
16000

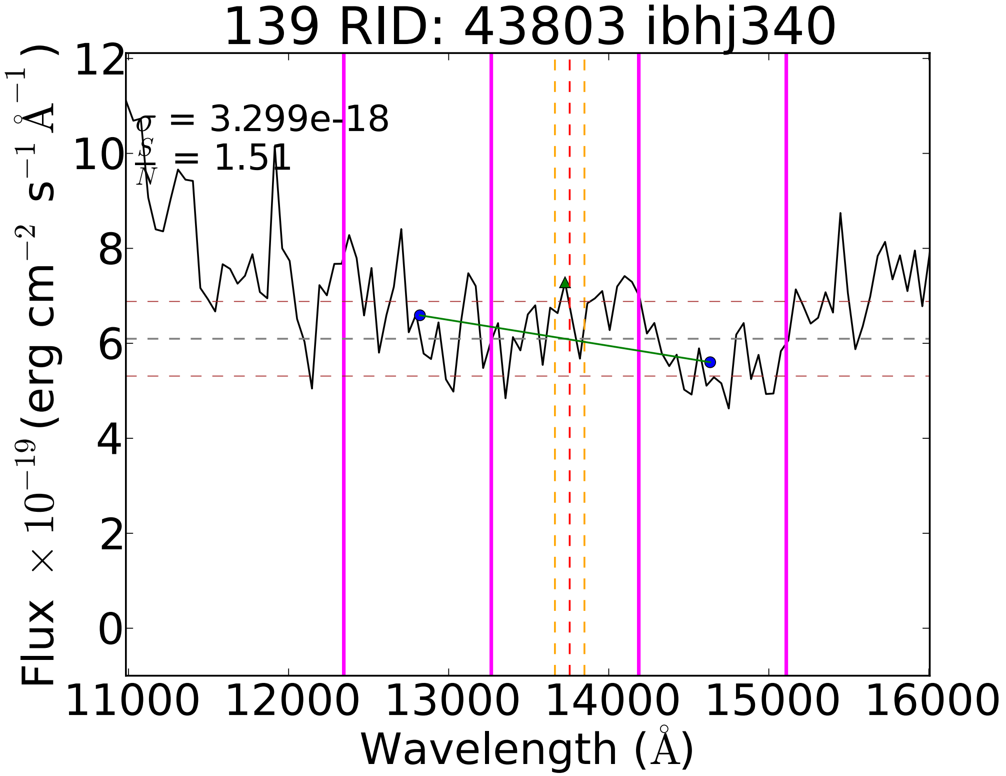
139 RID: 43803 ibhj340
σ = 3.299e-18
$\frac{S}{N}$ = 1.51
Flux $\times 10^{-19}$ (erg cm^{-2} s^{-1} Å^{-1})
Wavelength (Å)
0
2
4
6
8
10
12
11000
12000
13000
14000
15000
16000

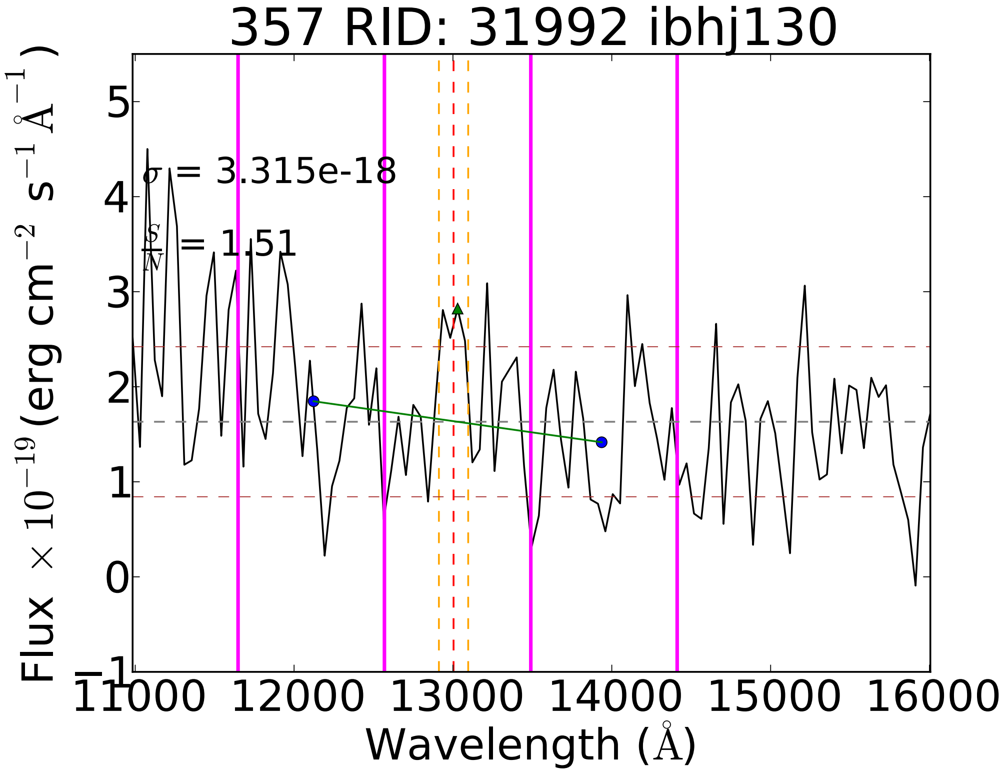
357 RID: 31992 ibhj130
σ = 3.315e-18
$\frac{S}{N}$ = 1.51
Flux $\times 10^{-19}$ (erg cm^{-2} s^{-1} Å^{-1})
Wavelength (Å)
-1
0
1
2
3
4
5
11000
12000
13000
14000
15000
16000

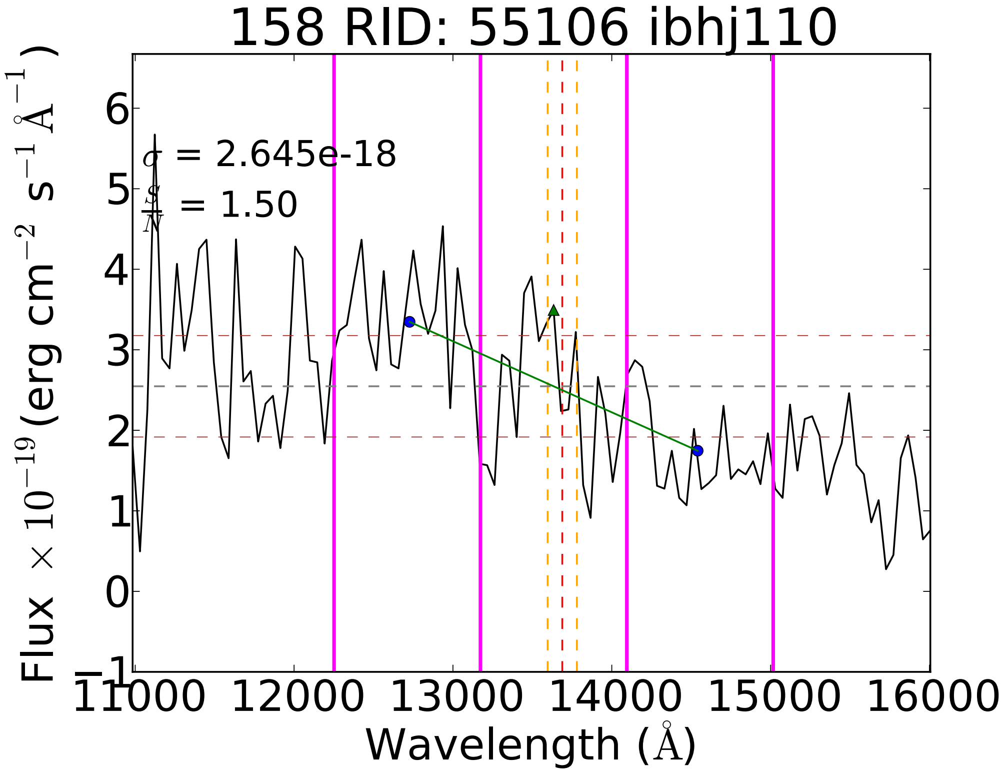
158 RID: 55106 ibhj110
σ = 2.645e-18
$\frac{S}{N}$ = 1.50
Flux $\times 10^{-19}$ (erg cm^{-2} s^{-1} Å^{-1})
Wavelength (Å)
-1
0
1
2
3
4
5
6
11000
12000
13000
14000
15000
16000

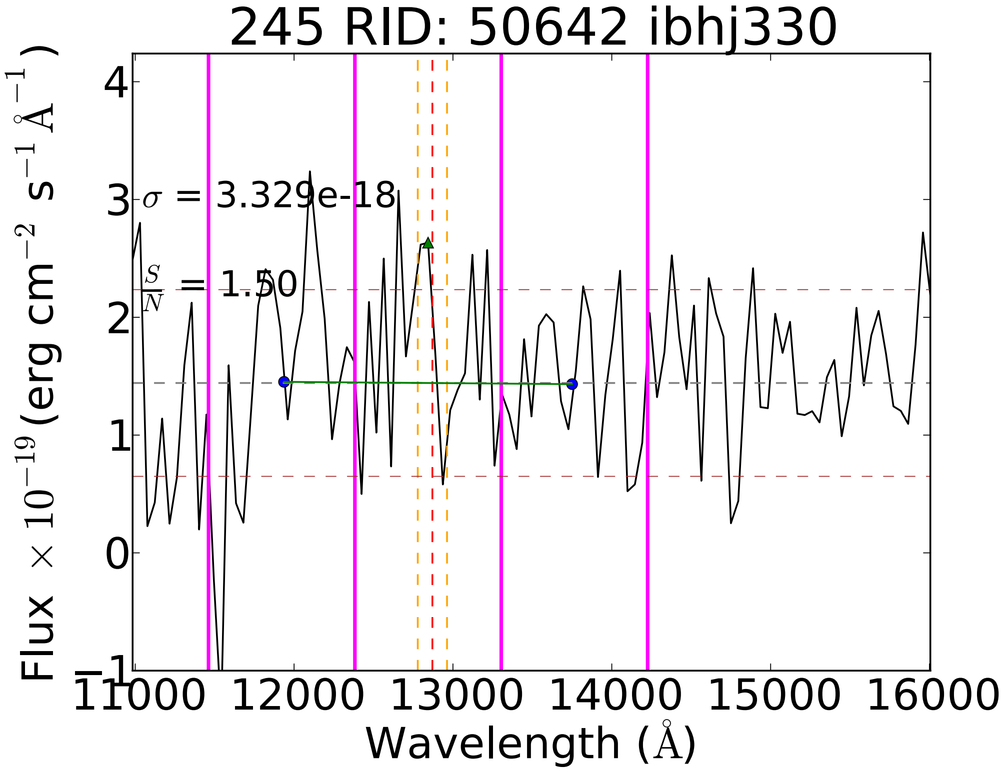
245 RID: 50642 ibhj330

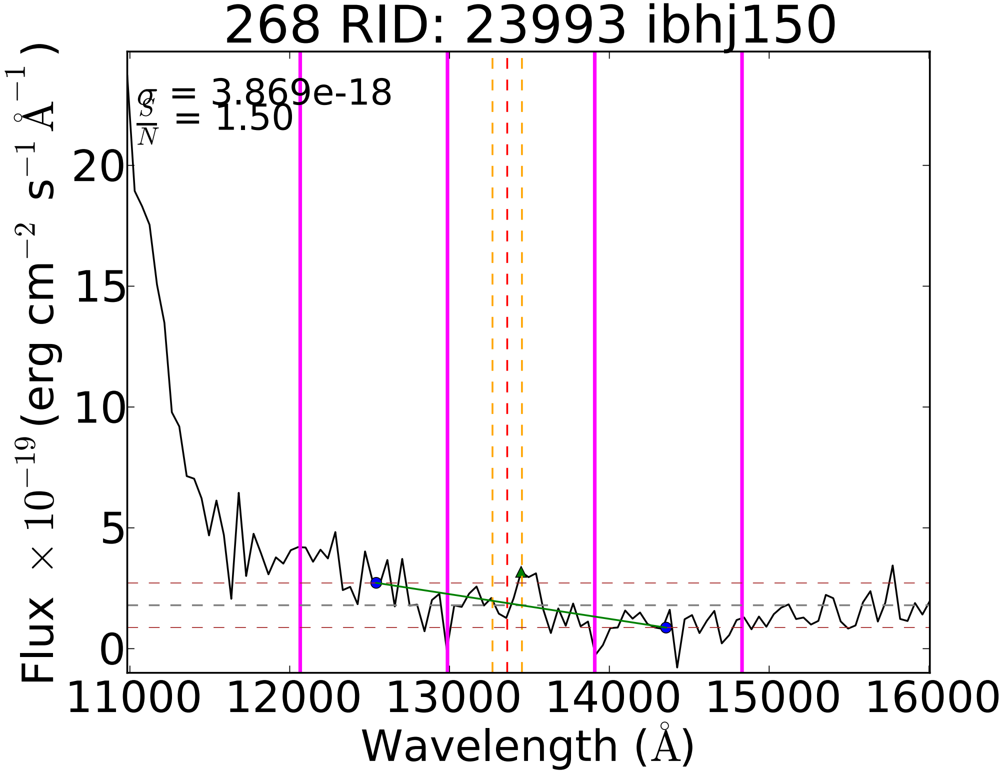
268 RID: 23993 ibhj150

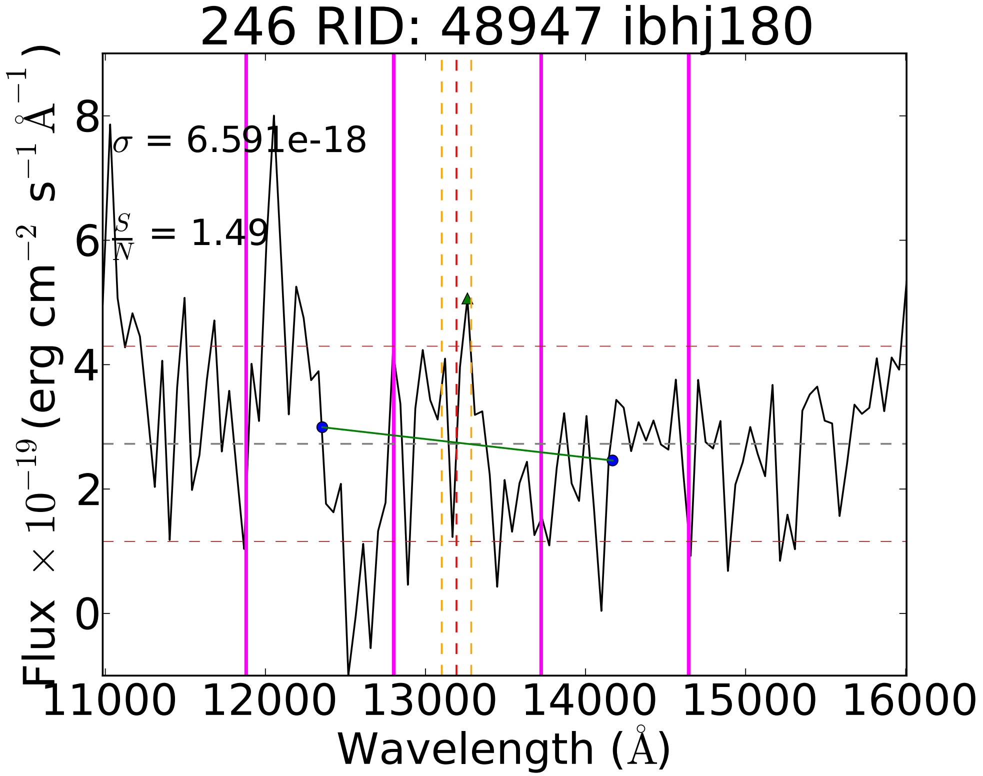
246 RID: 48947 ibhj180

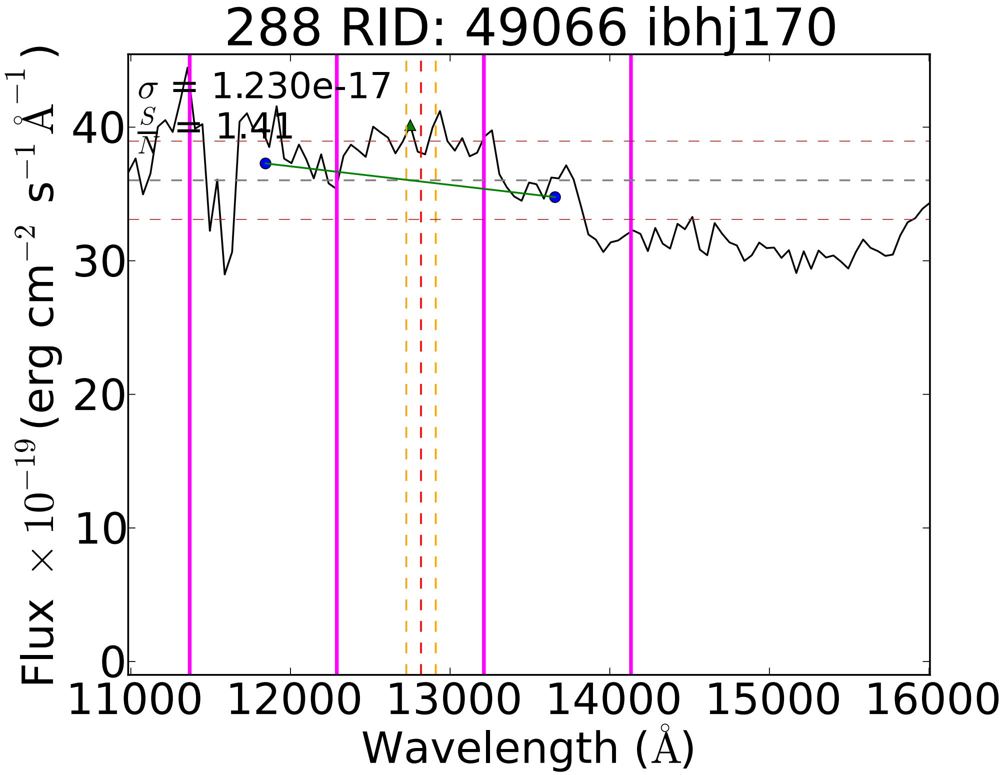
288 RID: 49066 ibhj170

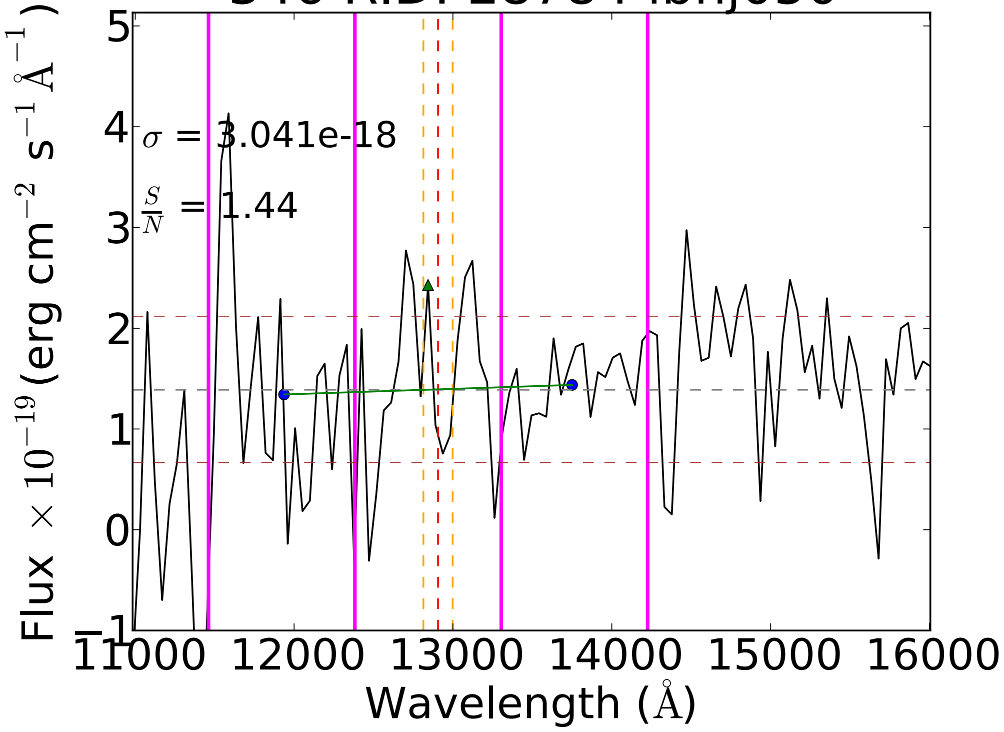
346 RID: 28784 ibhj050

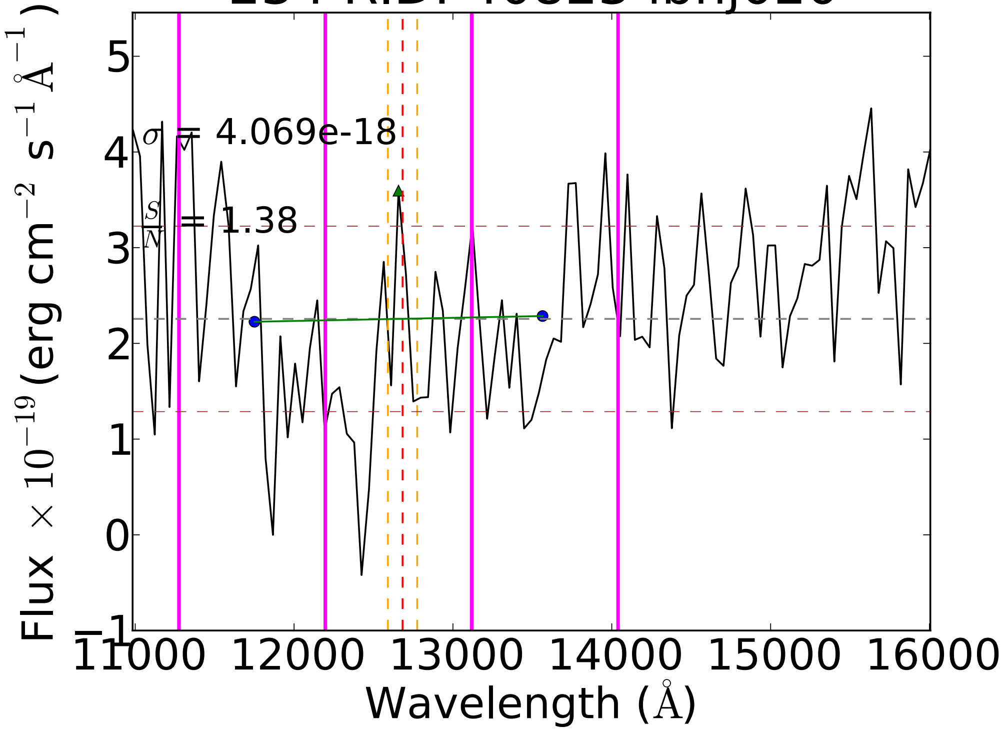
234 RID: 40823 ibhj020

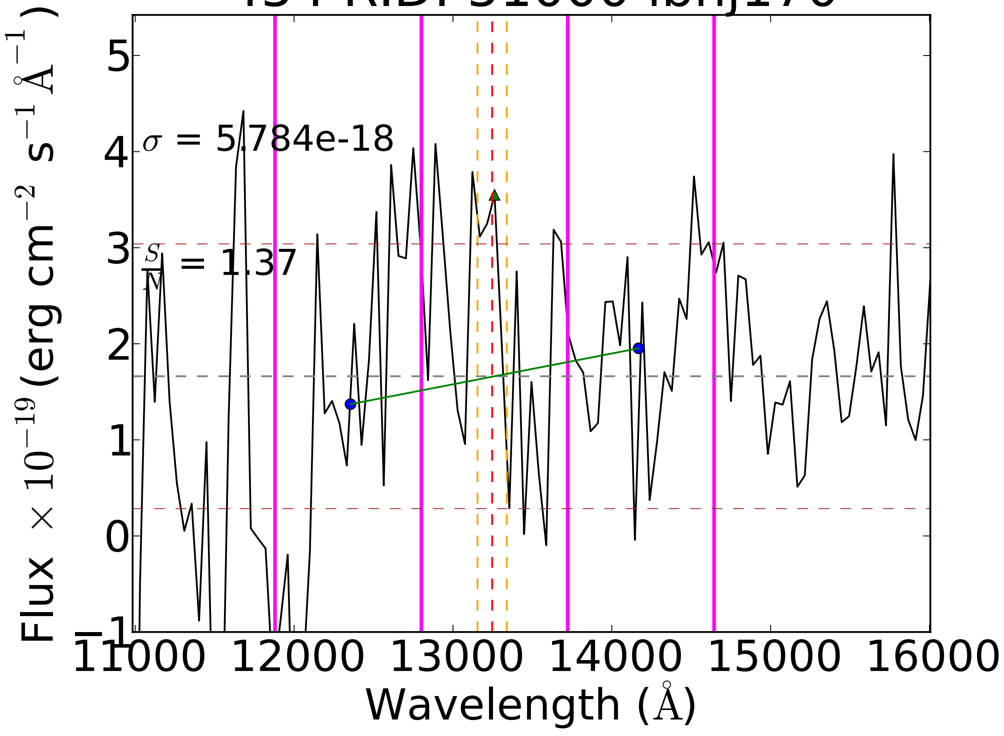
454 RID: 51000 ibhj170

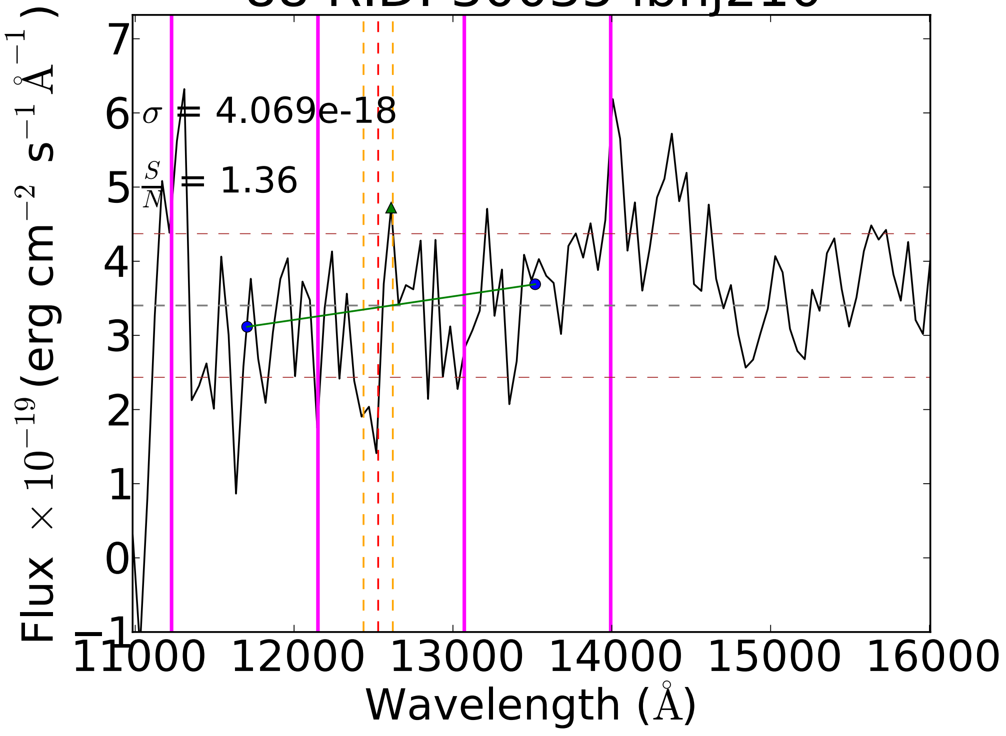
88 RID: 30035 ibhj210

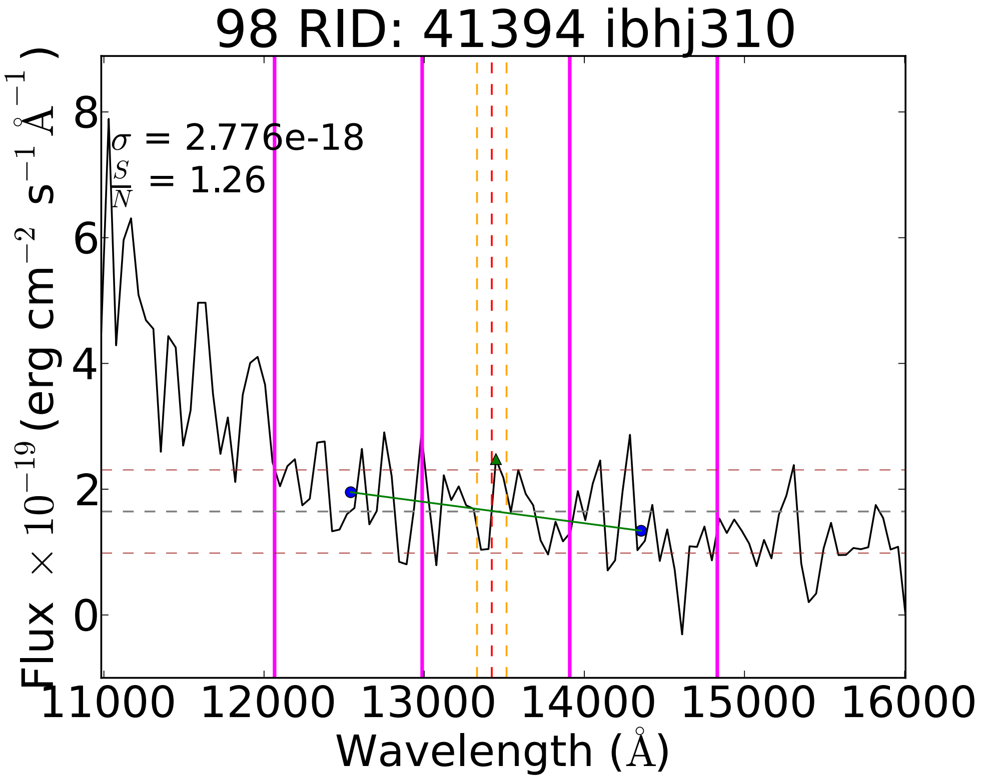
98 RID: 41394 ibhj310

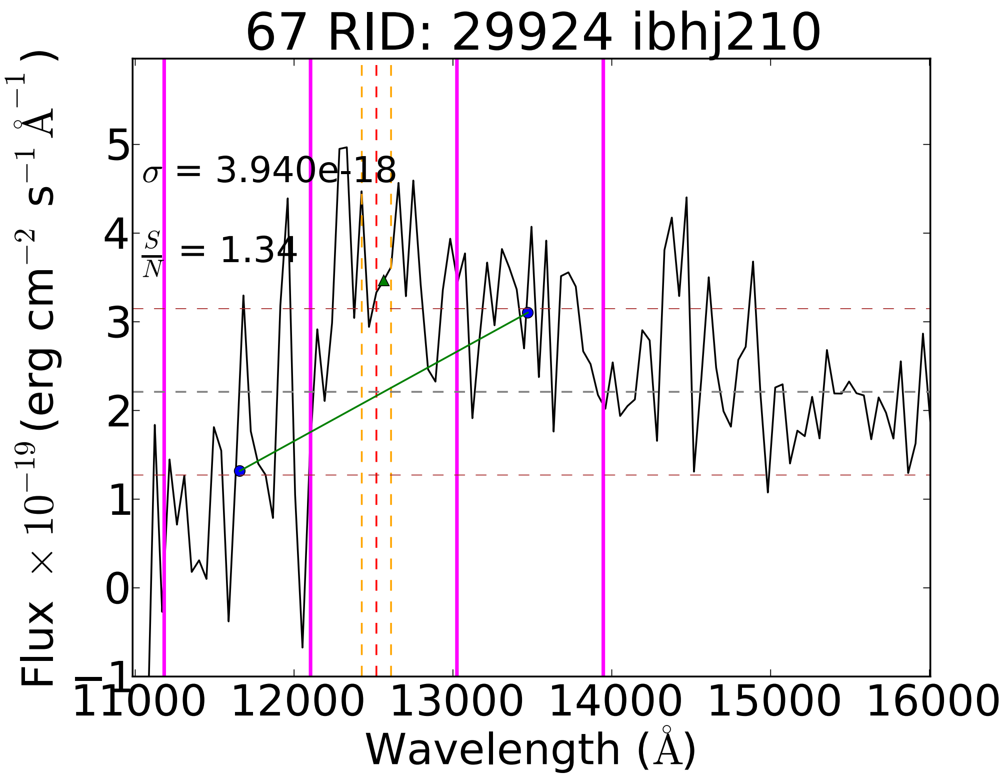
67 RID: 29924 ibhj210

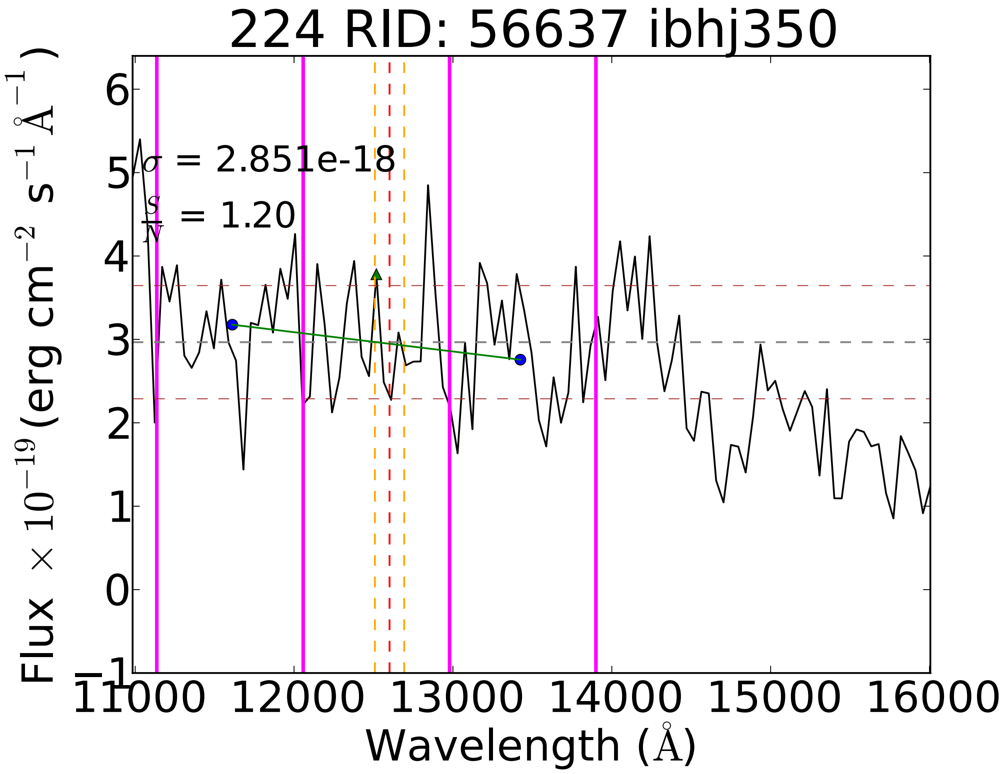
224 RID: 56637 ibhj350

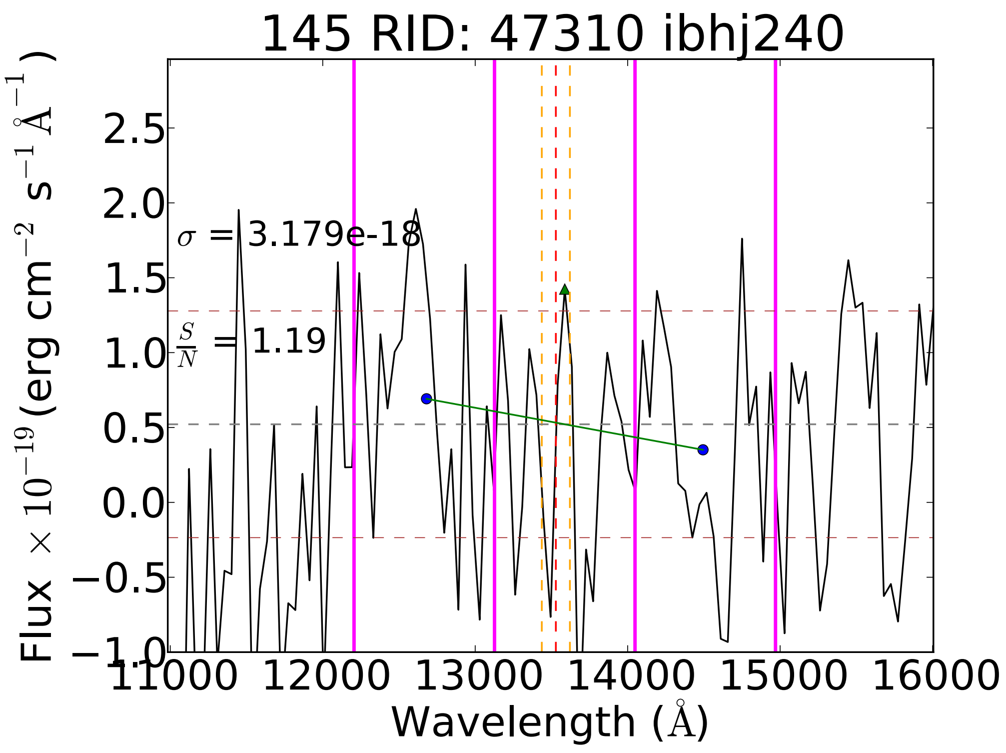
145 RID: 47310 ibhj240

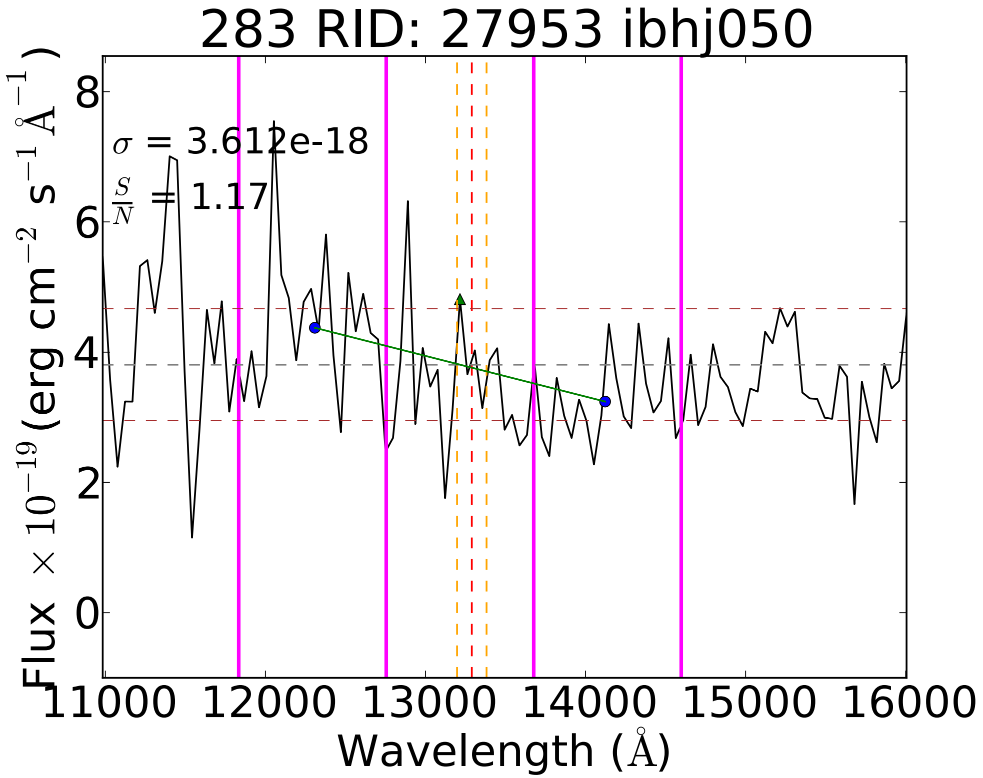
283 RID: 27953 ibhj050
σ = 3.612e-18
$\frac{S}{N}$ = 1.17
Flux $\times 10^{-19}$ (erg cm^{-2} s^{-1} Å^{-1})
Wavelength (Å)
0
2
4
6
8
11000
12000
13000
14000
15000
16000

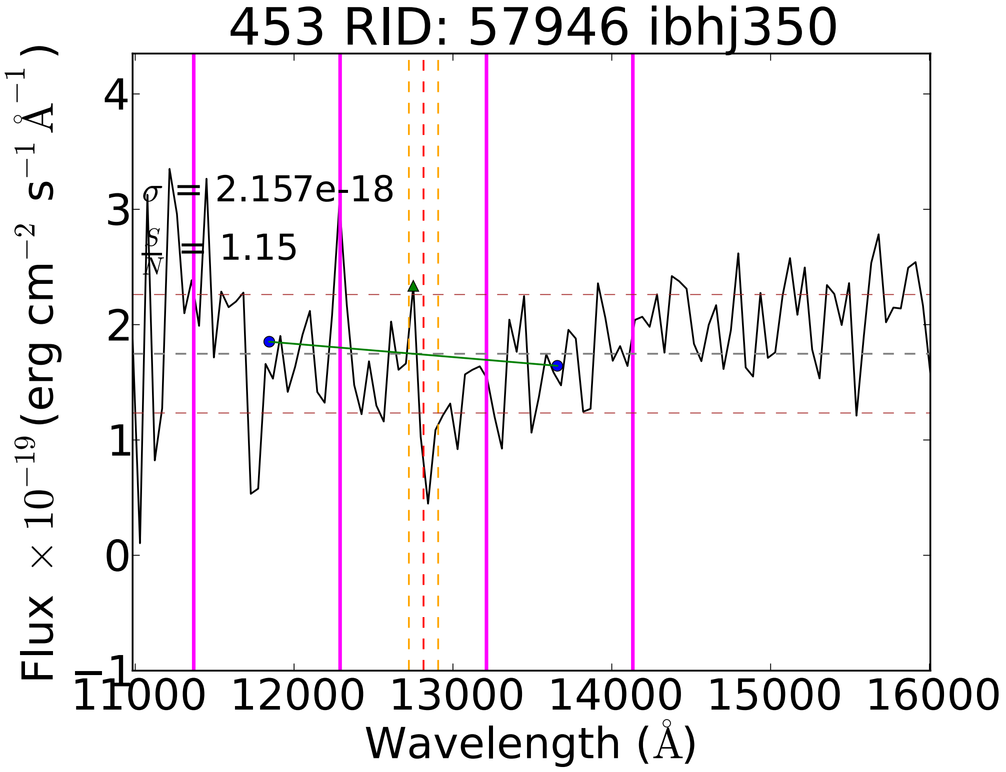
453 RID: 57946 ibhj350
σ = 2.157e-18
$\frac{S}{N}$ = 1.15
Flux $\times 10^{-19}$ (erg cm^{-2} s^{-1} Å^{-1})
Wavelength (Å)
−1
0
1
2
3
4
11000
12000
13000
14000
15000
16000

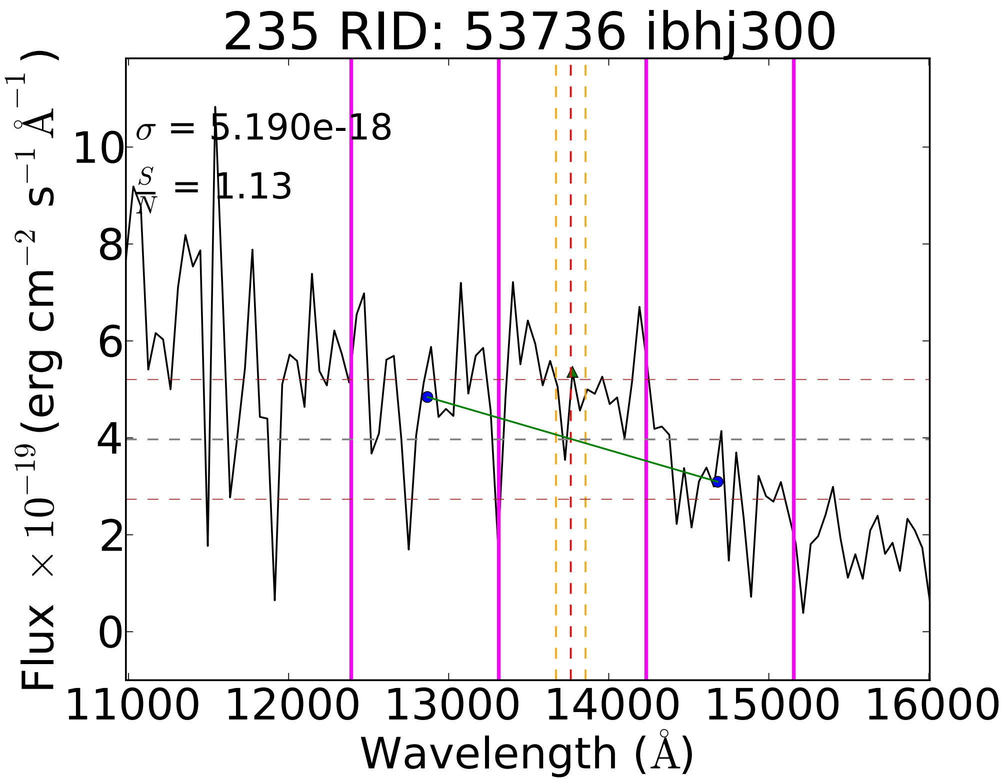
235 RID: 53736 ibhj300
σ = 5.190e-18
$\frac{S}{N}$ = 1.13
Flux $\times 10^{-19}$ (erg cm^{-2} s^{-1} Å^{-1})
Wavelength (Å)
0
2
4
6
8
10
11000
12000
13000
14000
15000
16000

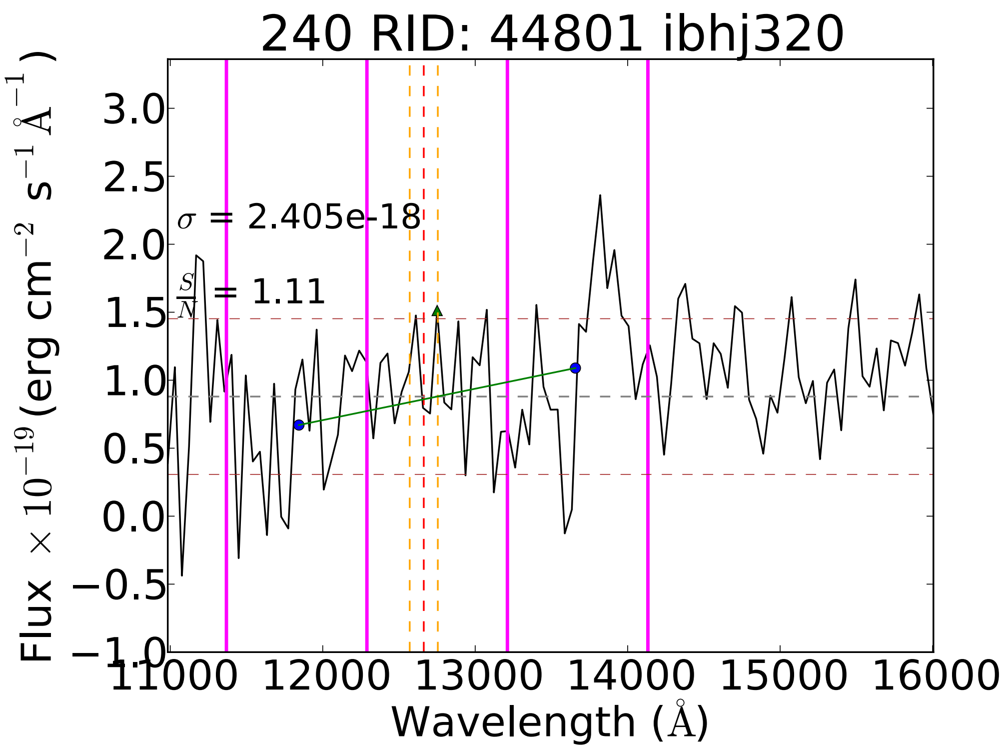
240 RID: 44801 ibhj320
σ = 2.405e-18
$\frac{S}{N}$ = 1.11
Flux $\times 10^{-19}$ (erg cm^{-2} s^{-1} Å^{-1})
Wavelength (Å)
−1.0
−0.5
0.0
0.5
1.0
1.5
2.0
2.5
3.0
11000
12000
13000
14000
15000
16000

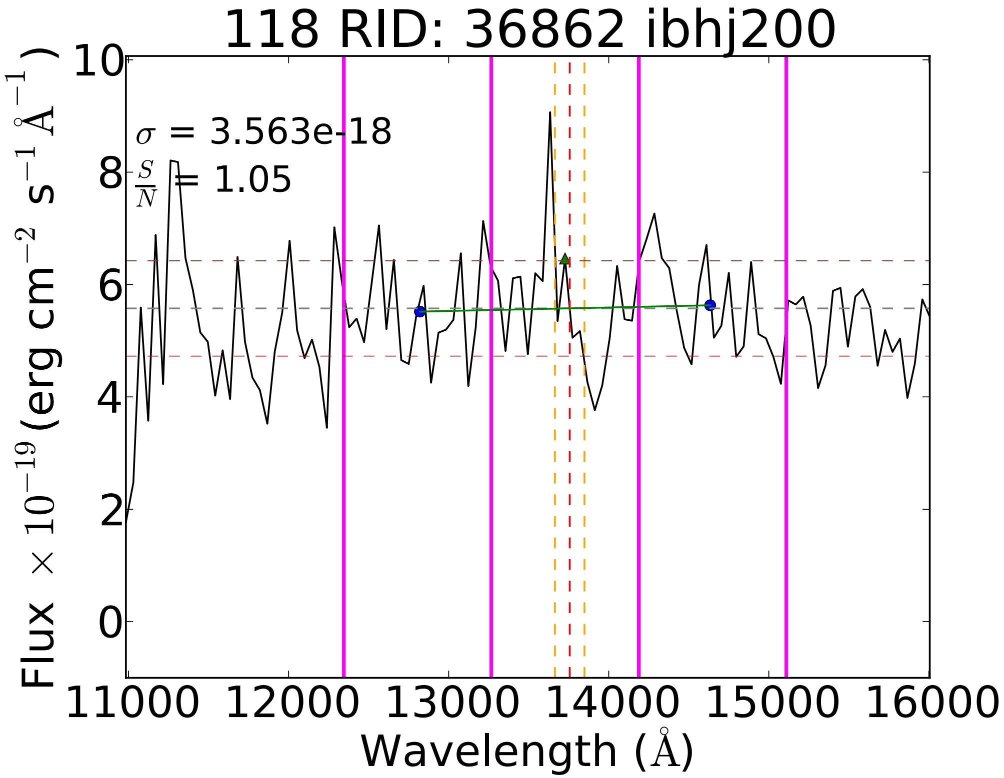
118 RID: 36862 ibhj200
σ = 3.563e-18
S/N = 1.05
Flux × 10^-19 (erg cm^-2 s^-1 Å^-1)
Wavelength (Å)
0
2
4
6
8
10
11000
12000
13000
14000
15000
16000

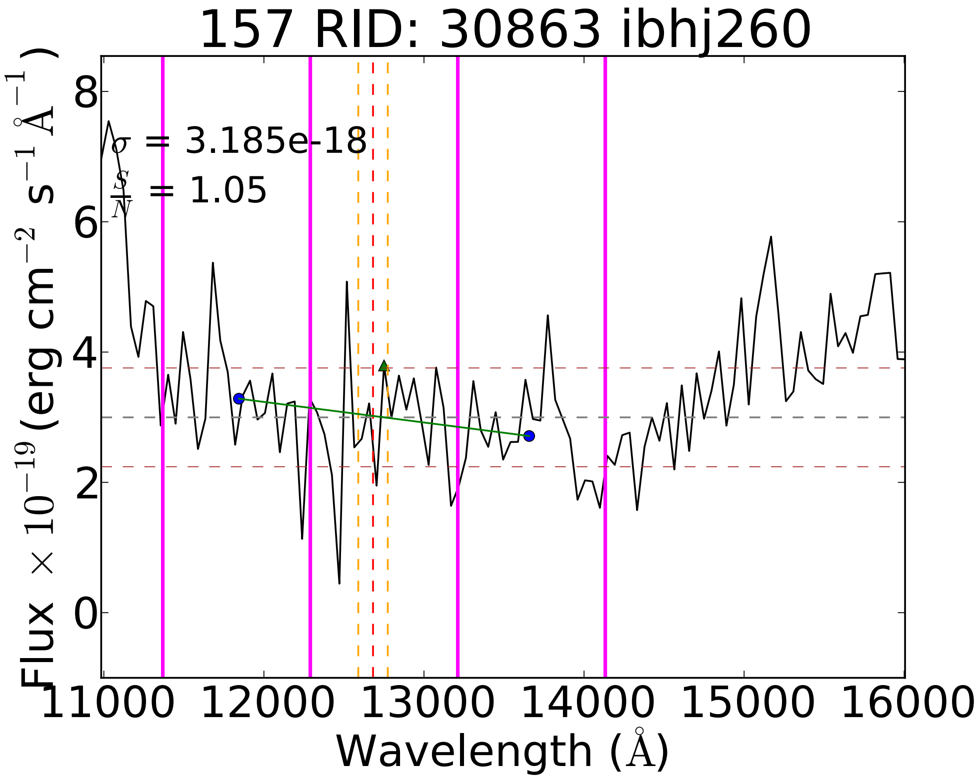
157 RID: 30863 ibhj260
σ = 3.185e-18
S/N = 1.05
Flux × 10^-19 (erg cm^-2 s^-1 Å^-1)
Wavelength (Å)
0
2
4
6
8
11000
12000
13000
14000
15000
16000

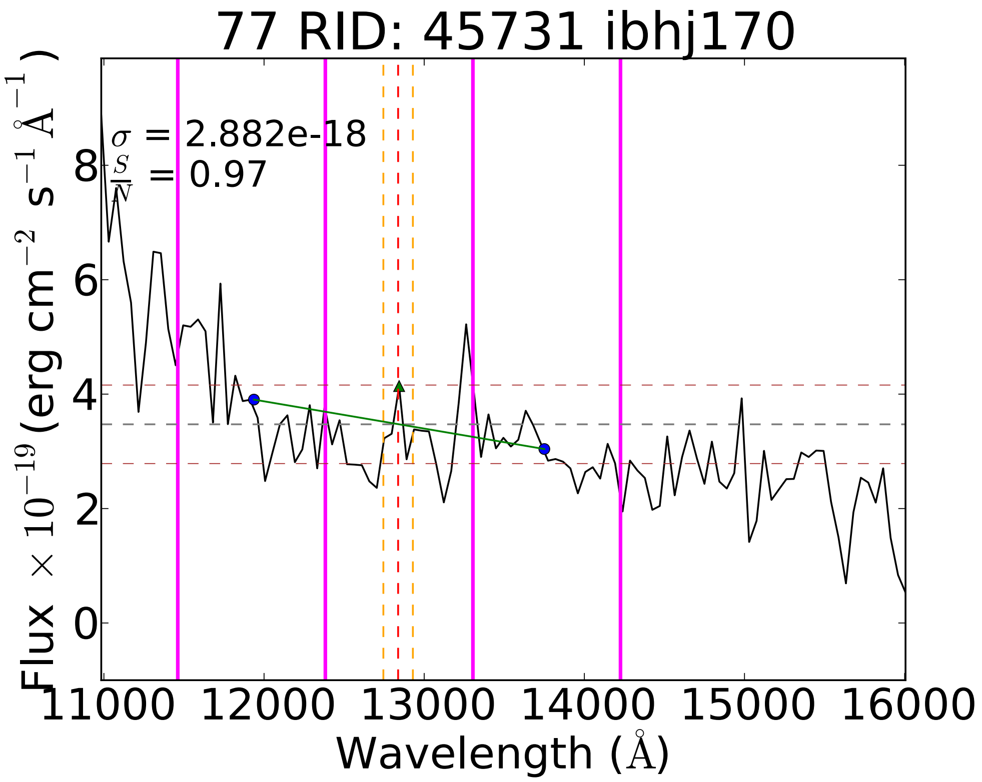
77 RID: 45731 ibhj170
σ = 2.882e-18
S/N = 0.97
Flux × 10^-19 (erg cm^-2 s^-1 Å^-1)
Wavelength (Å)
0
2
4
6
8
11000
12000
13000
14000
15000
16000

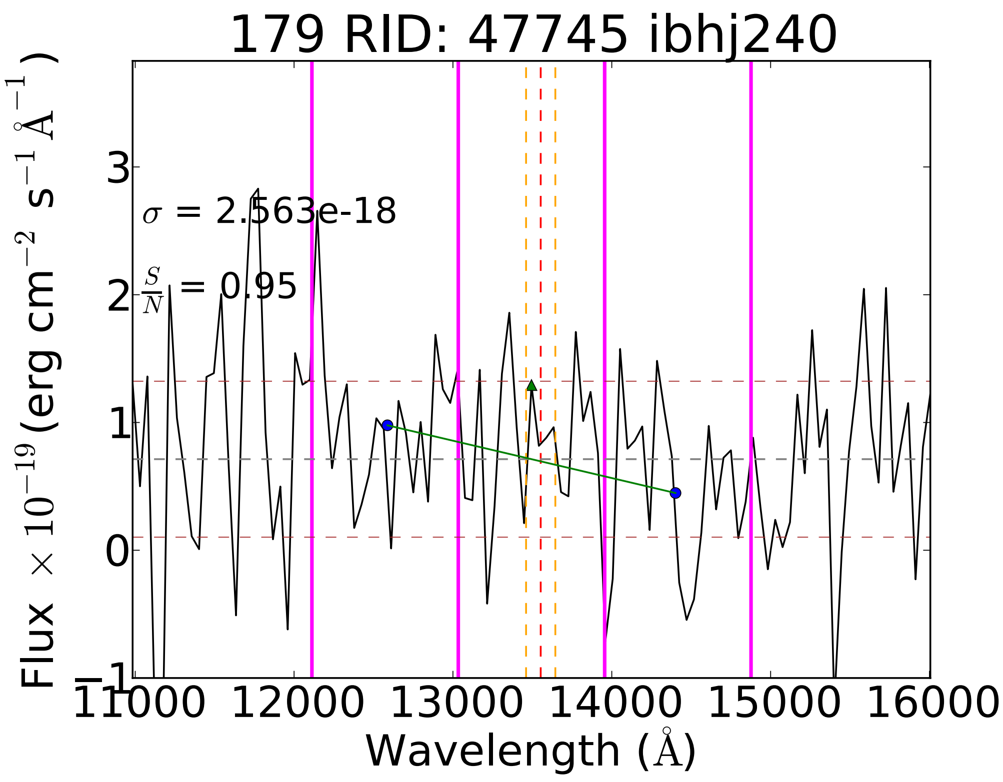
179 RID: 47745 ibhj240
σ = 2.563e-18
S/N = 0.95
Flux × 10^-19 (erg cm^-2 s^-1 Å^-1)
Wavelength (Å)
−1
0
1
2
3
11000
12000
13000
14000
15000
16000

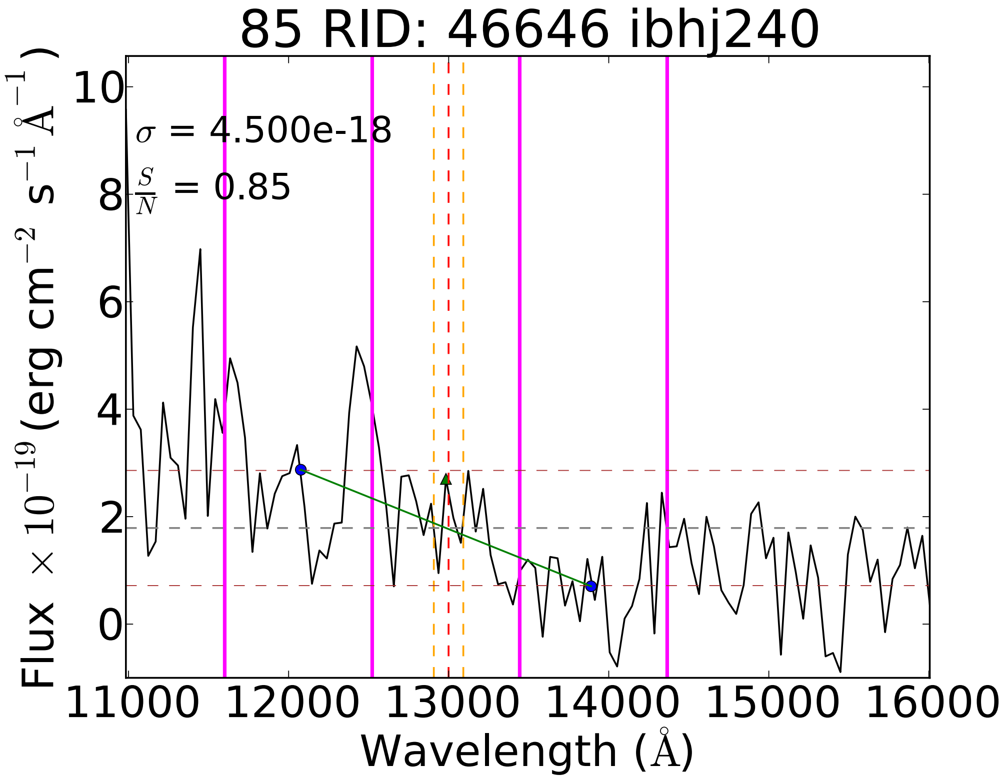
85 RID: 46646 ibhj240
σ = 4.500e-18
S/N = 0.85
Flux × 10^-19 (erg cm^-2 s^-1 Å^-1)
Wavelength (Å)
0
2
4
6
8
10
11000
12000
13000
14000
15000
16000

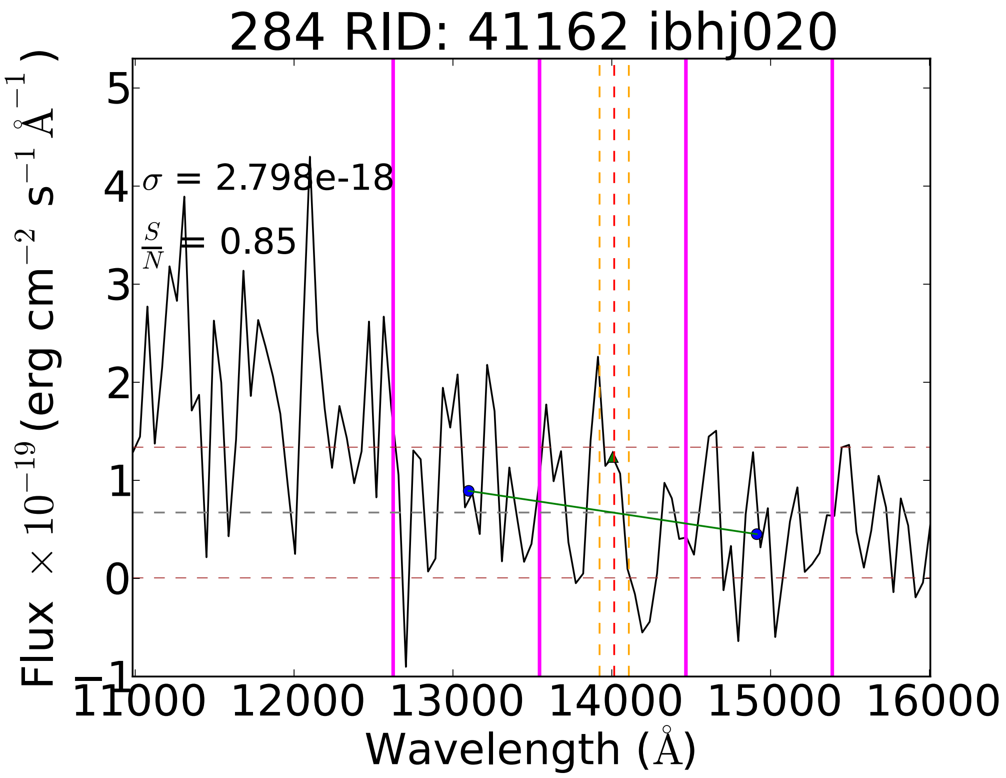
284 RID: 41162 ibhj020
σ = 2.798e-18
S/N = 0.85
Flux × 10^-19 (erg cm^-2 s^-1 Å^-1)
Wavelength (Å)
−1
0
1
2
3
4
5
11000
12000
13000
14000
15000
16000

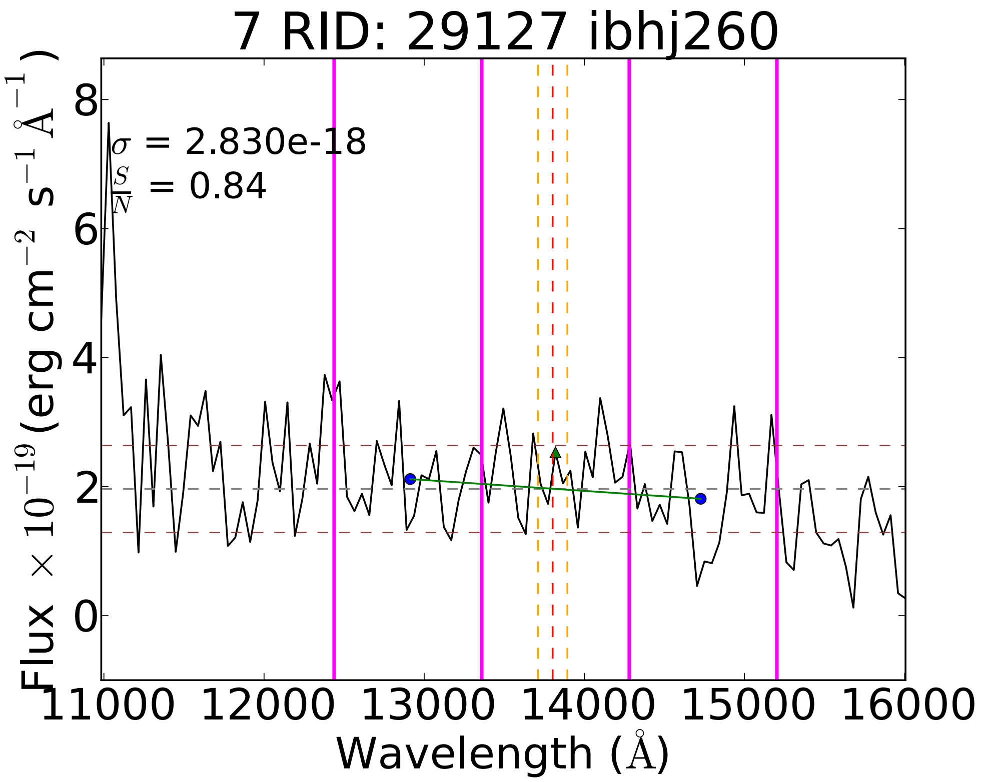
7 RID: 29127 ibhj260
σ = 2.830e-18
S/N = 0.84
Flux × 10^-19 (erg cm^-2 s^-1 Å^-1)
Wavelength (Å)
0
2
4
6
8
11000
12000
13000
14000
15000
16000

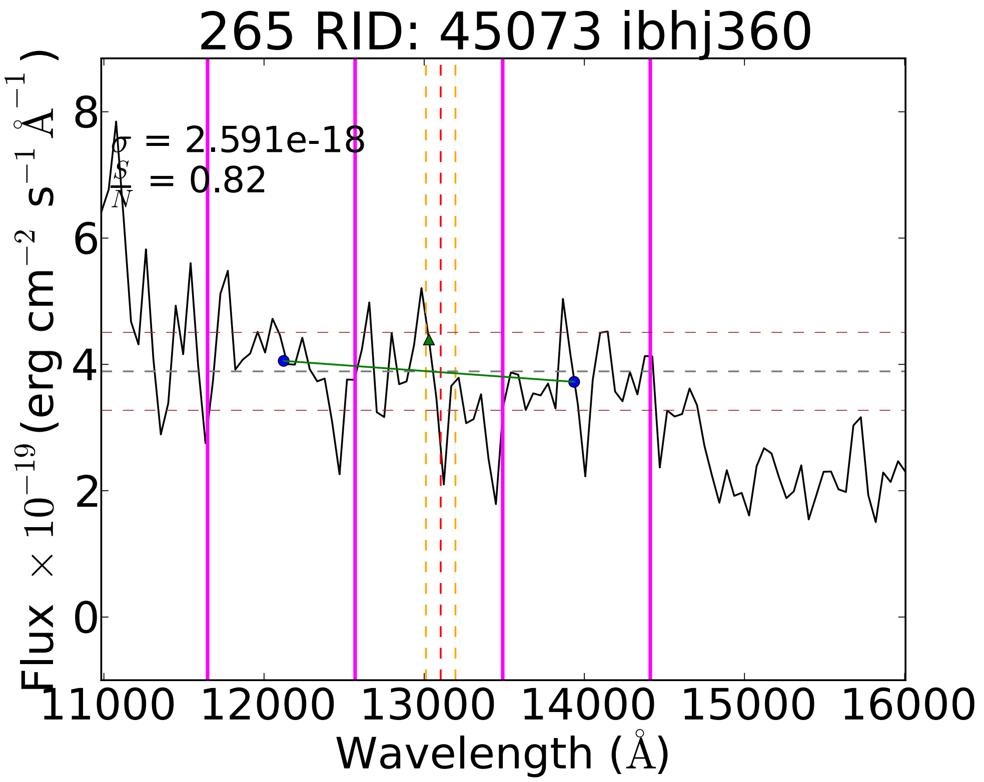
265 RID: 45073 ibhj360
σ = 2.591e-18
S/N = 0.82
Flux × 10^-19 (erg cm^-2 s^-1 Å^-1)
Wavelength (Å)
0
2
4
6
8
11000
12000
13000
14000
15000
16000

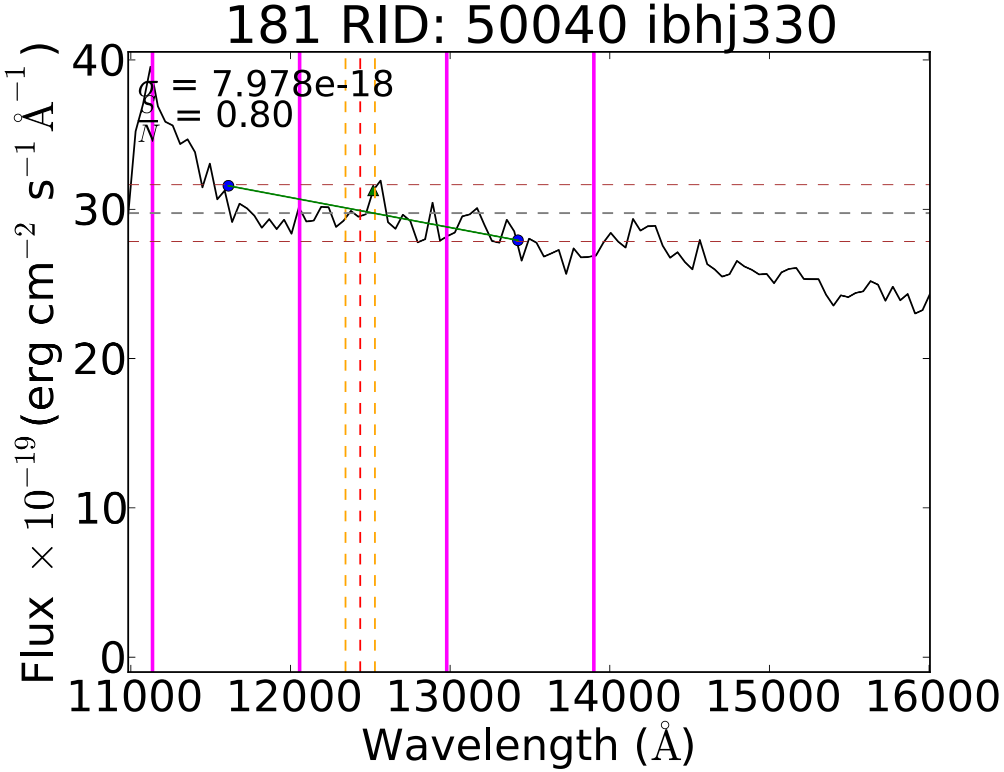
181 RID: 50040 ibhj330
σ = 7.978e-18
S/N = 0.80
Flux × 10^−19 (erg cm^−2 s^−1 Å^−1)
0
10
20
30
40
11000
12000
13000
14000
15000
16000
Wavelength (Å)

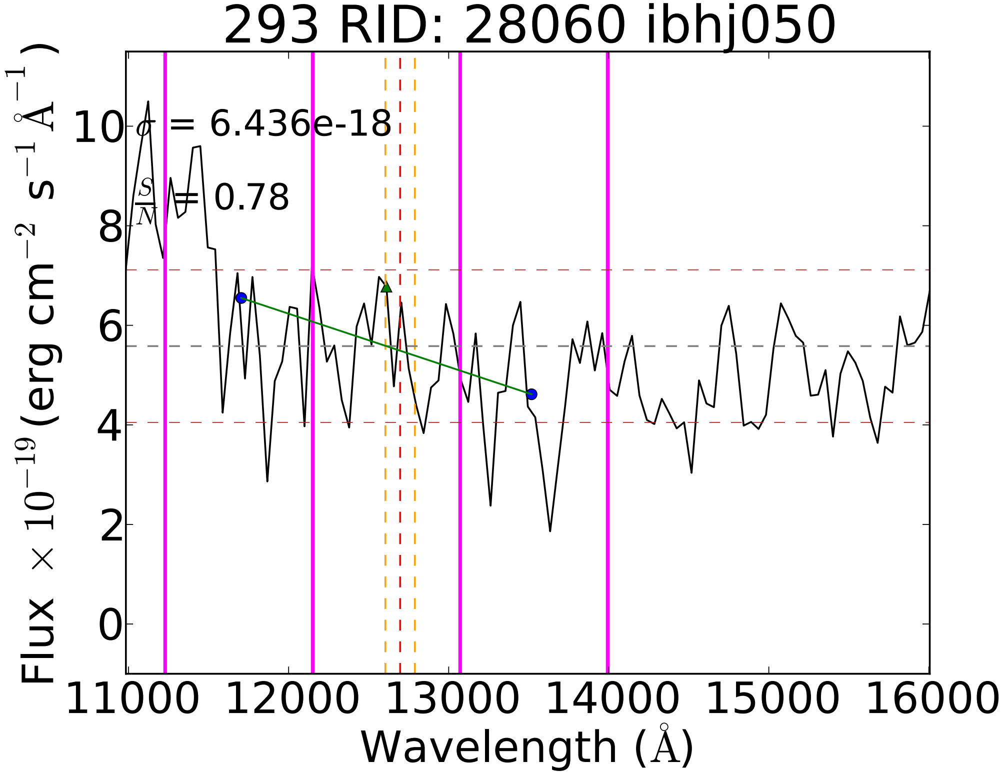
293 RID: 28060 ibhj050
σ = 6.436e-18
S/N = 0.78
Flux × 10^−19 (erg cm^−2 s^−1 Å^−1)
0
2
4
6
8
10
11000
12000
13000
14000
15000
16000
Wavelength (Å)

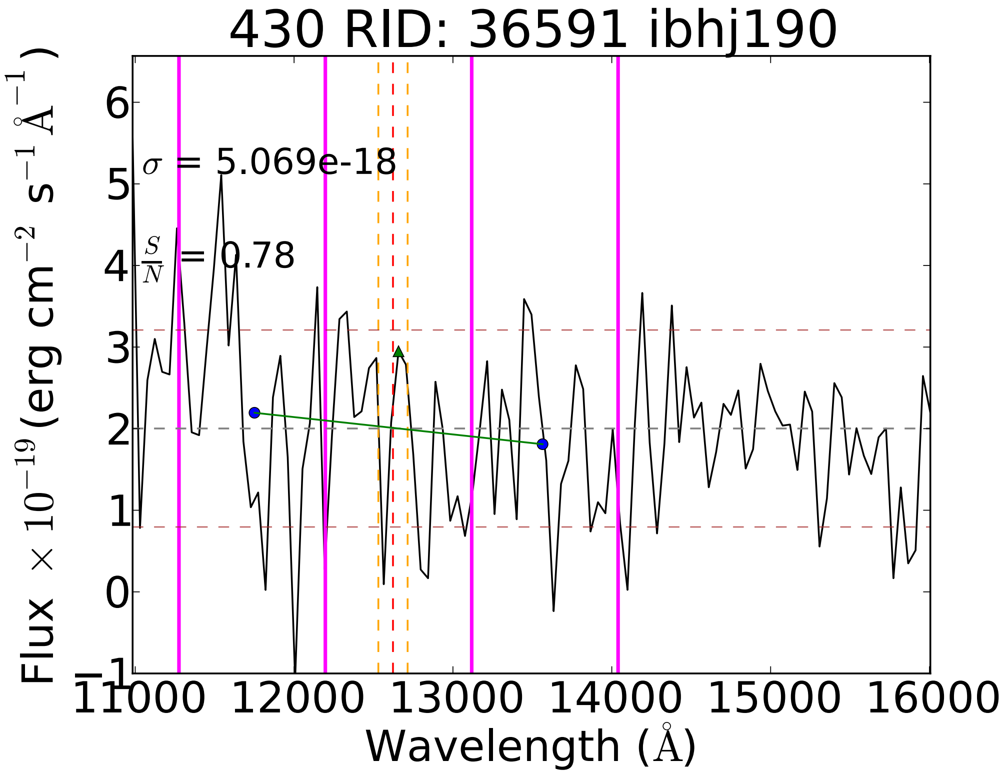
430 RID: 36591 ibhj190
σ = 5.069e-18
S/N = 0.78
Flux × 10^−19 (erg cm^−2 s^−1 Å^−1)
−1
0
1
2
3
4
5
6
11000
12000
13000
14000
15000
16000
Wavelength (Å)

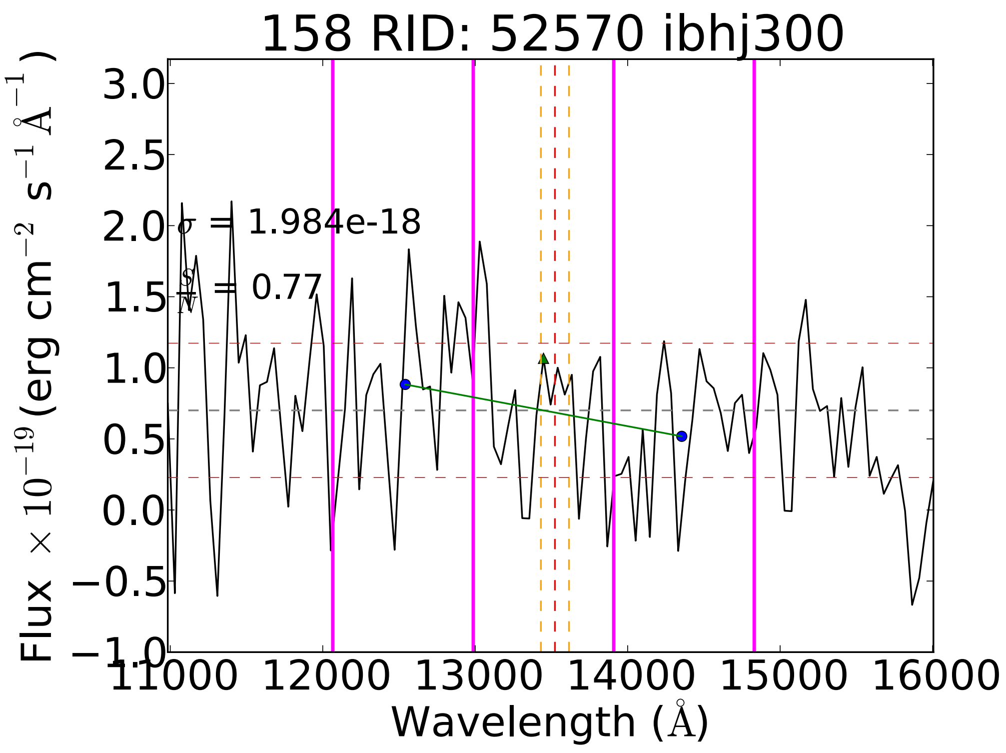
158 RID: 52570 ibhj300
σ = 1.984e-18
S/N = 0.77
Flux × 10^−19 (erg cm^−2 s^−1 Å^−1)
−1.0
−0.5
0.0
0.5
1.0
1.5
2.0
2.5
3.0
11000
12000
13000
14000
15000
16000
Wavelength (Å)

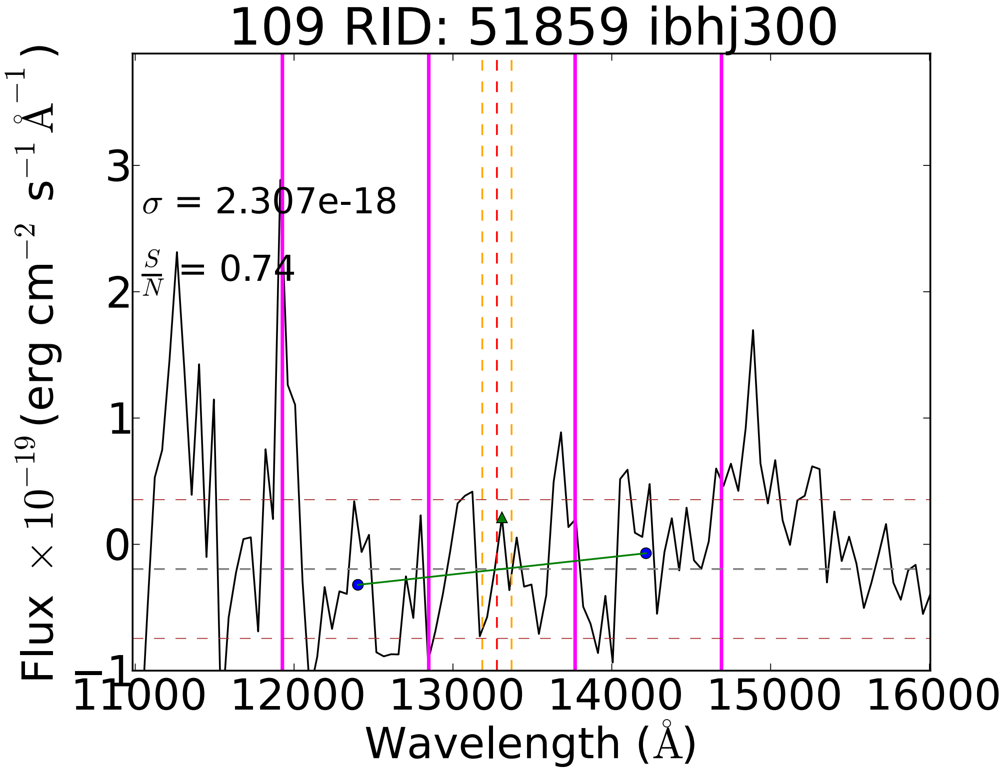

109 RID: 51859 ibhj300

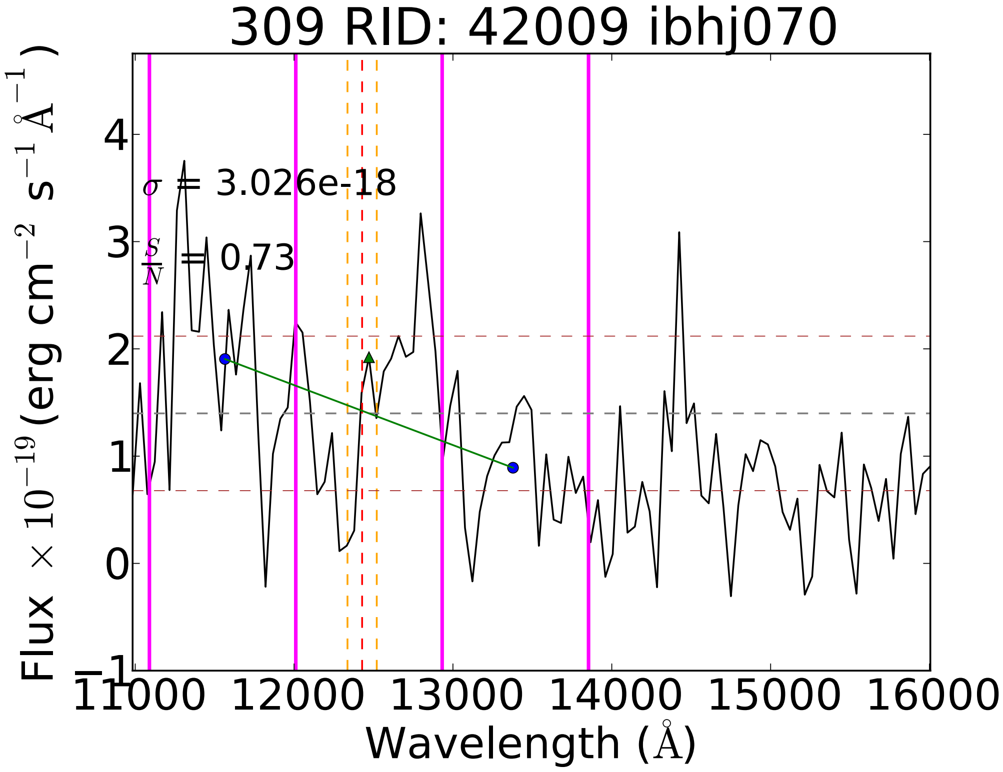

309 RID: 42009 ibhj070

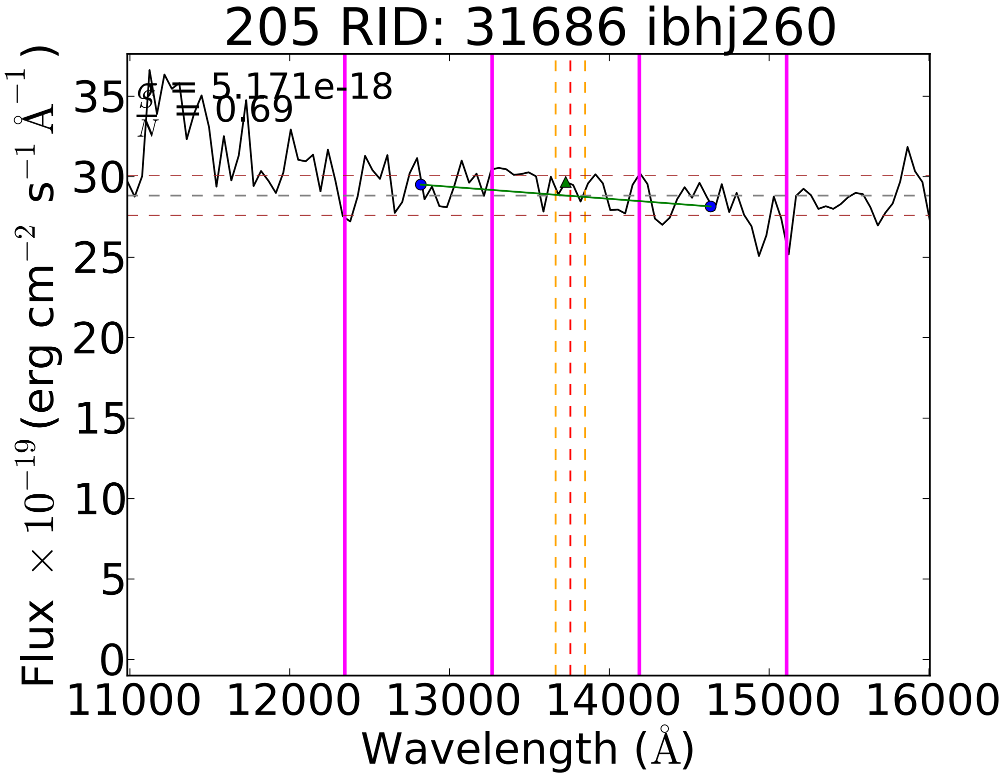

205 RID: 31686 ibhj260

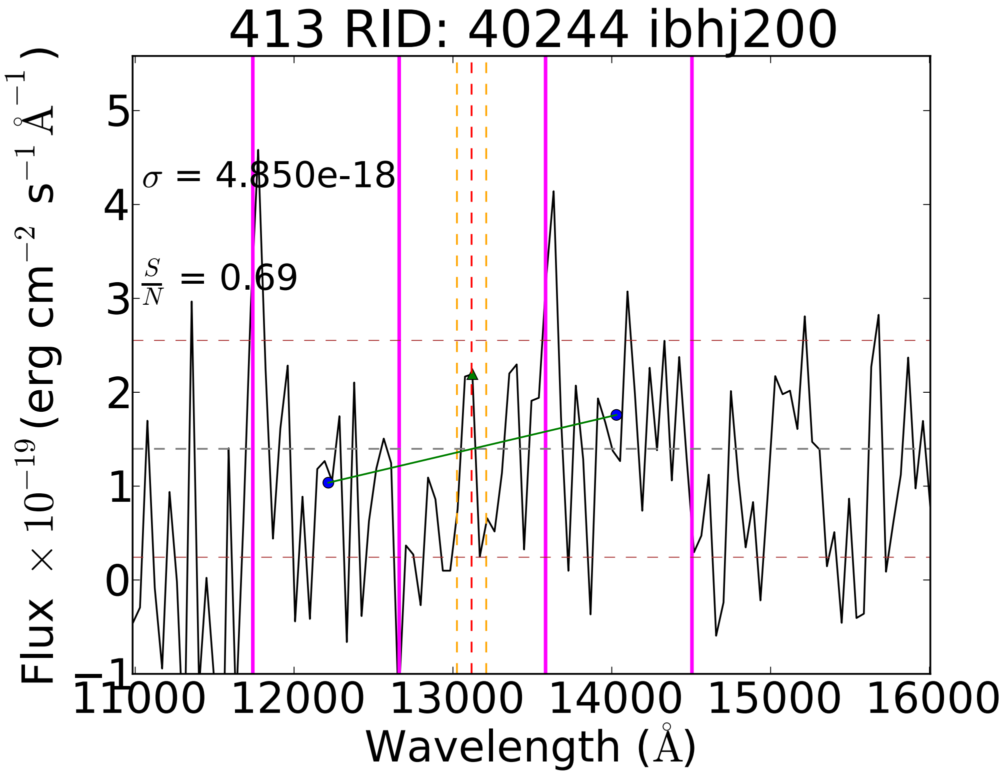

413 RID: 40244 ibhj200

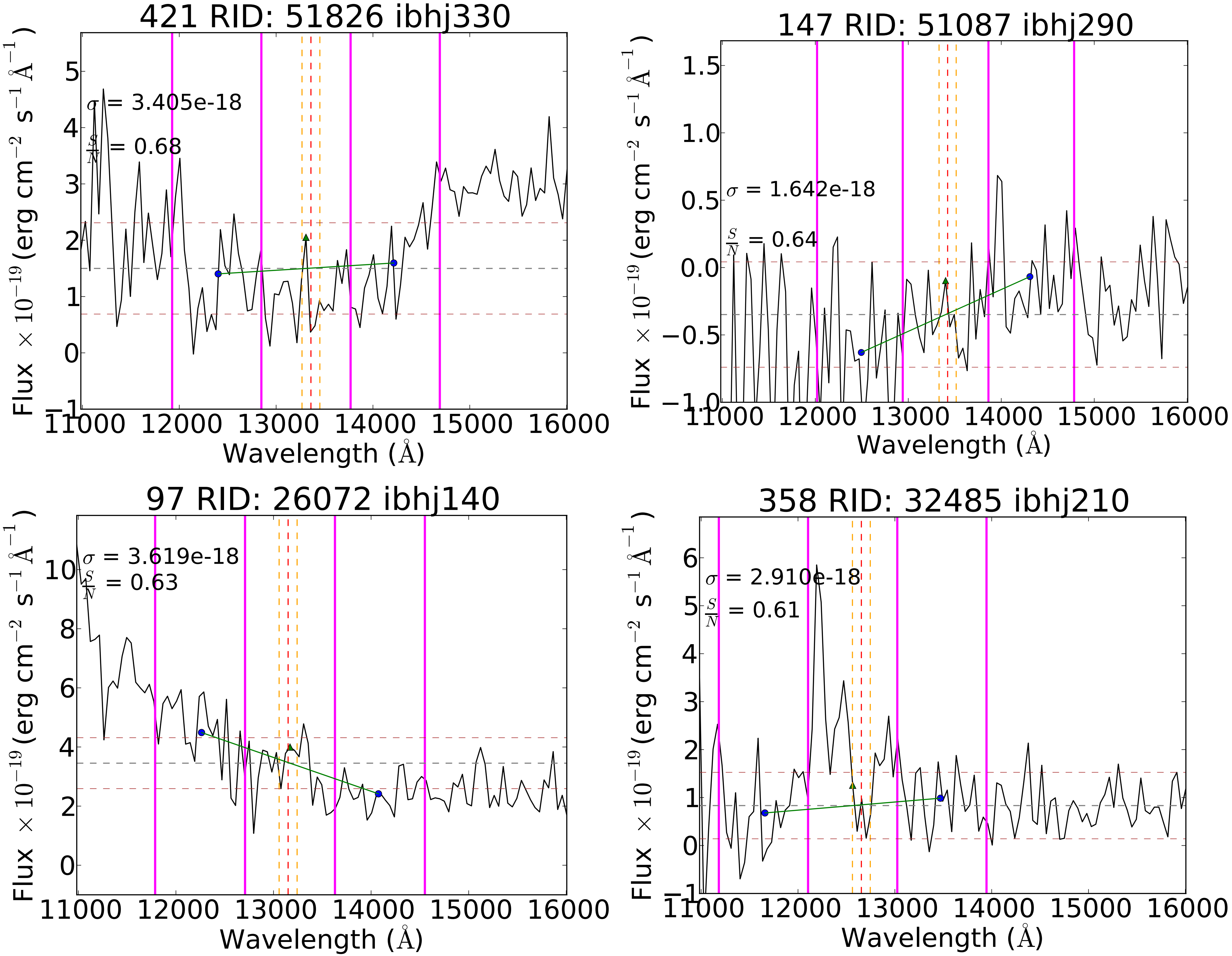
421 RID: 51826 ibhj330
σ = 3.405e-18
$\frac{S}{N}$ = 0.68
Flux $\times 10^{-19}$ (erg cm^{-2} s^{-1} Å^{-1})
Wavelength (Å)
−1
0
1
2
3
4
5
11000
12000
13000
14000
15000
16000
147 RID: 51087 ibhj290
σ = 1.642e-18
$\frac{S}{N}$ = 0.64
Flux $\times 10^{-19}$ (erg cm^{-2} s^{-1} Å^{-1})
Wavelength (Å)
−1.0
−0.5
0.0
0.5
1.0
1.5
11000
12000
13000
14000
15000
16000
97 RID: 26072 ibhj140
σ = 3.619e-18
$\frac{S}{N}$ = 0.63
Flux $\times 10^{-19}$ (erg cm^{-2} s^{-1} Å^{-1})
Wavelength (Å)
0
2
4
6
8
10
11000
12000
13000
14000
15000
16000
358 RID: 32485 ibhj210
σ = 2.910e-18
$\frac{S}{N}$ = 0.61
Flux $\times 10^{-19}$ (erg cm^{-2} s^{-1} Å^{-1})
Wavelength (Å)
−1
0
1
2
3
4
5
6
11000
12000
13000
14000
15000
16000

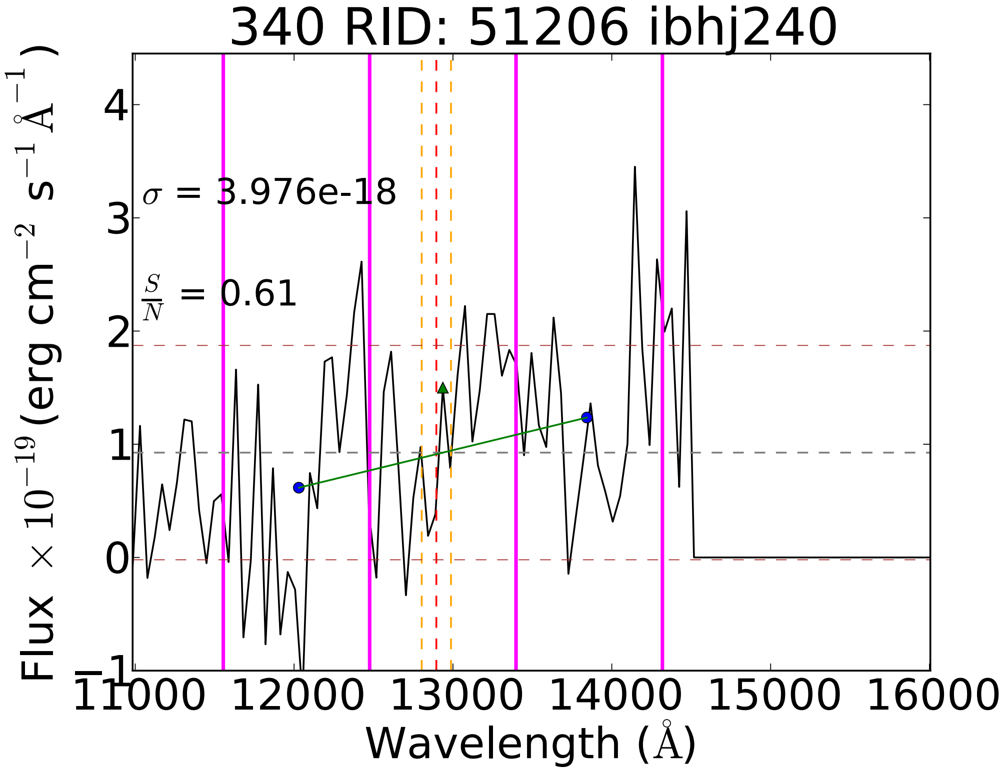
340 RID: 51206 ibhj240
σ = 3.976e-18
S/N = 0.61
Flux × 10^-19 (erg cm^-2 s^-1 Å^-1)
Wavelength (Å)
−1
0
1
2
3
4
11000
12000
13000
14000
15000
16000

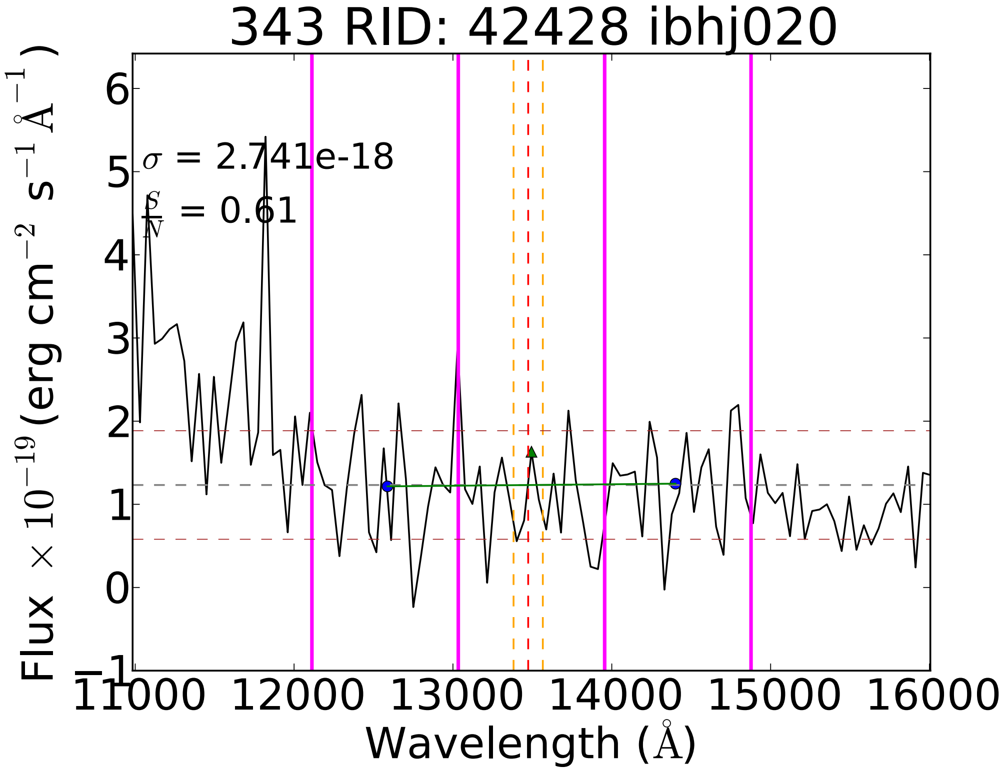
343 RID: 42428 ibhj020
σ = 2.741e-18
S/N = 0.61
Flux × 10^-19 (erg cm^-2 s^-1 Å^-1)
Wavelength (Å)
−1
0
1
2
3
4
5
6
11000
12000
13000
14000
15000
16000

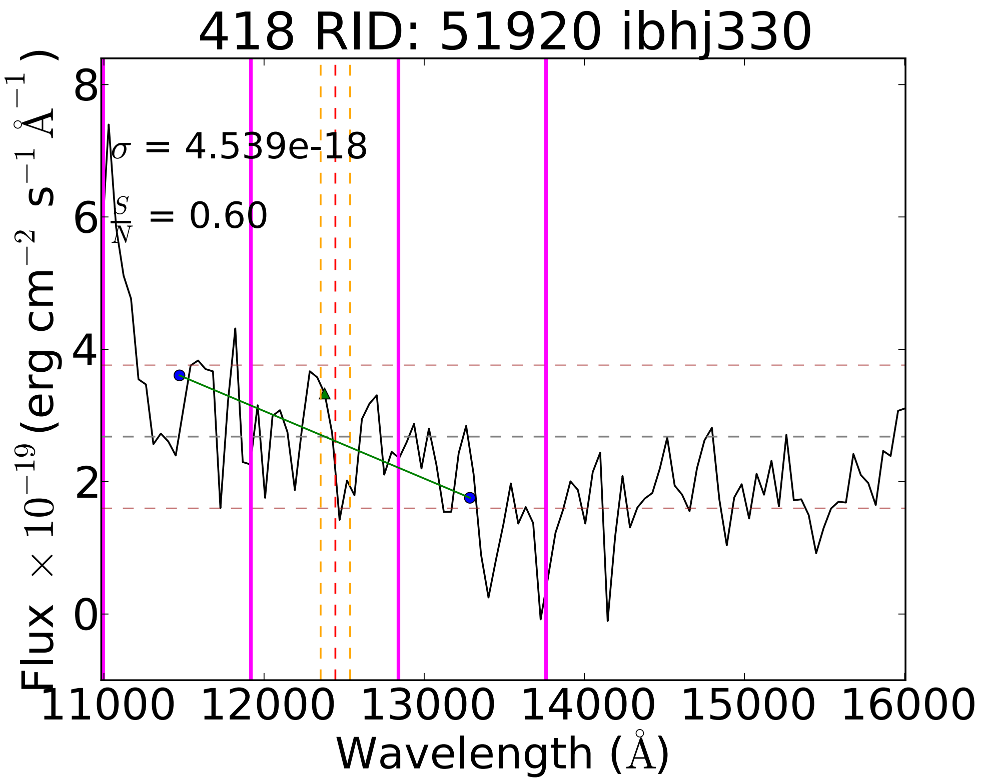
418 RID: 51920 ibhj330
σ = 4.539e-18
S/N = 0.60
Flux × 10^-19 (erg cm^-2 s^-1 Å^-1)
Wavelength (Å)
0
2
4
6
8
11000
12000
13000
14000
15000
16000

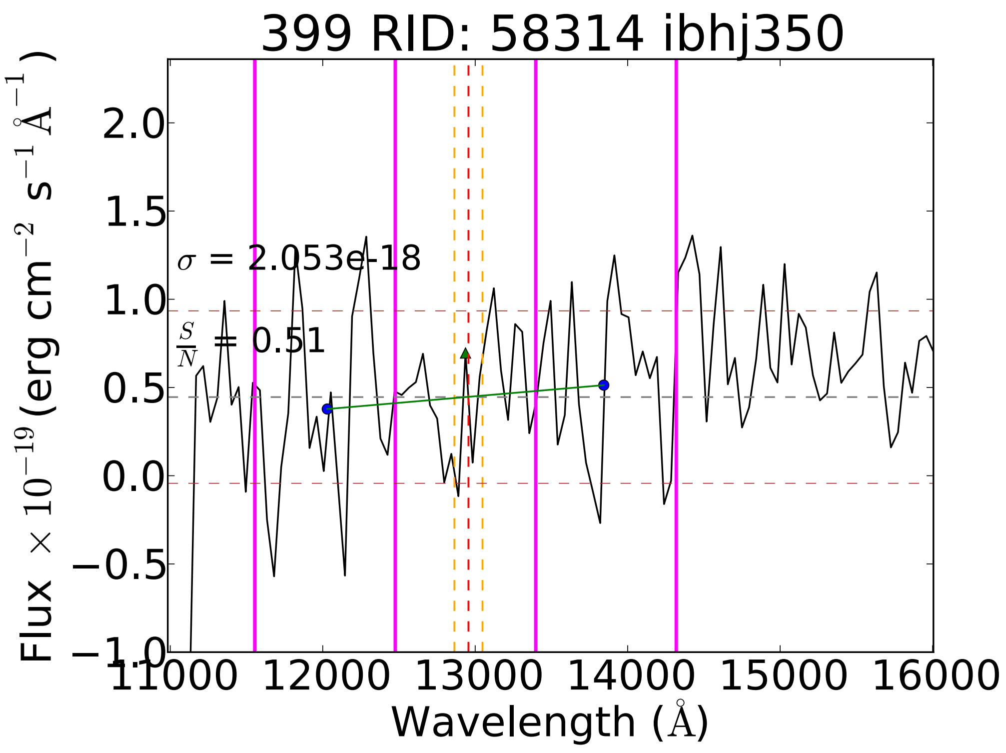
399 RID: 58314 ibhj350
σ = 2.053e-18
S/N = 0.51
Flux × 10^-19 (erg cm^-2 s^-1 Å^-1)
Wavelength (Å)
−1.0
−0.5
0.0
0.5
1.0
1.5
2.0
11000
12000
13000
14000
15000
16000

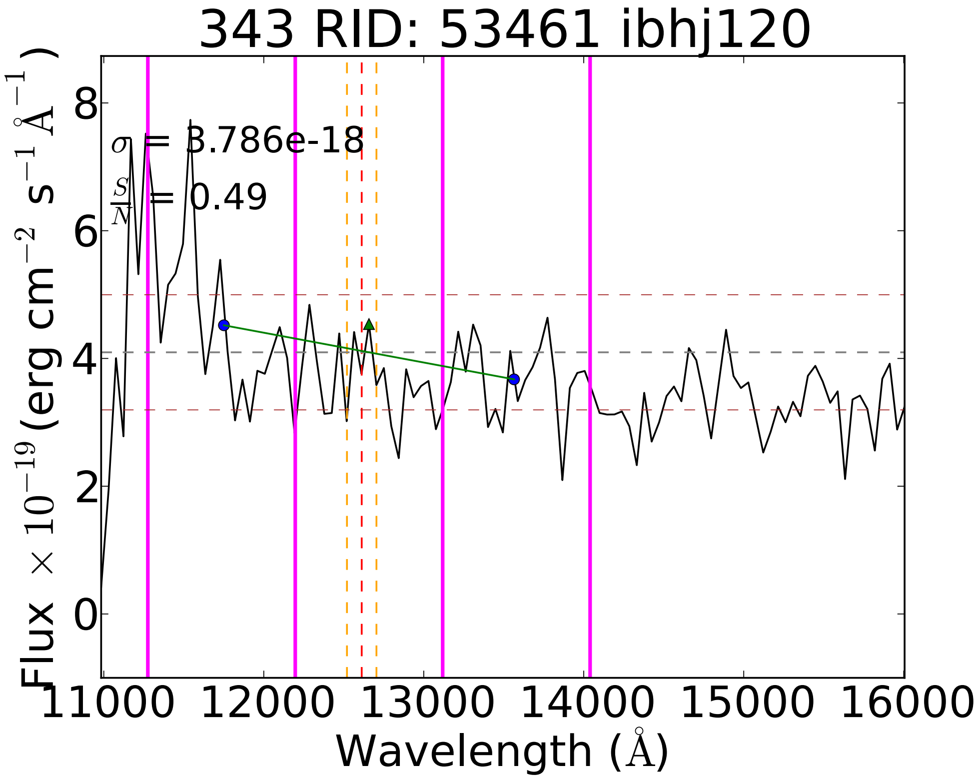
343 RID: 53461 ibhj120
σ = 3.786e-18
S/N = 0.49
Flux × 10^−19 (erg cm^−2 s^−1 Å^−1)
Wavelength (Å)
0
2
4
6
8
11000
12000
13000
14000
15000
16000

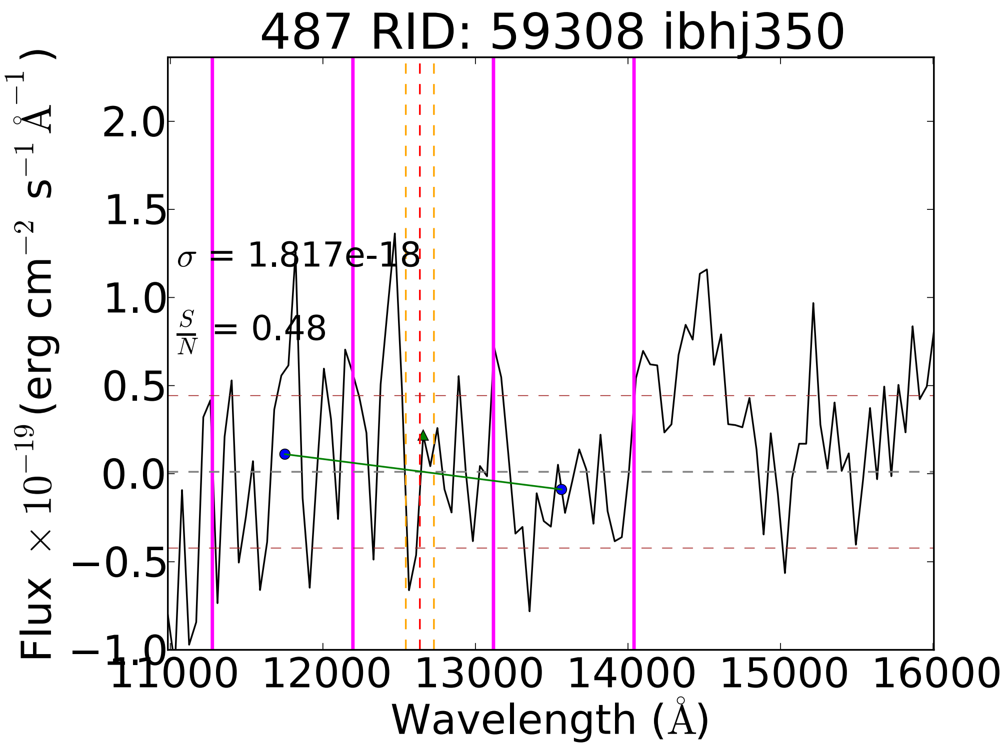
487 RID: 59308 ibhj350
σ = 1.817e-18
S/N = 0.48
Flux × 10^−19 (erg cm^−2 s^−1 Å^−1)
Wavelength (Å)
−1.0
−0.5
0.0
0.5
1.0
1.5
2.0
11000
12000
13000
14000
15000
16000

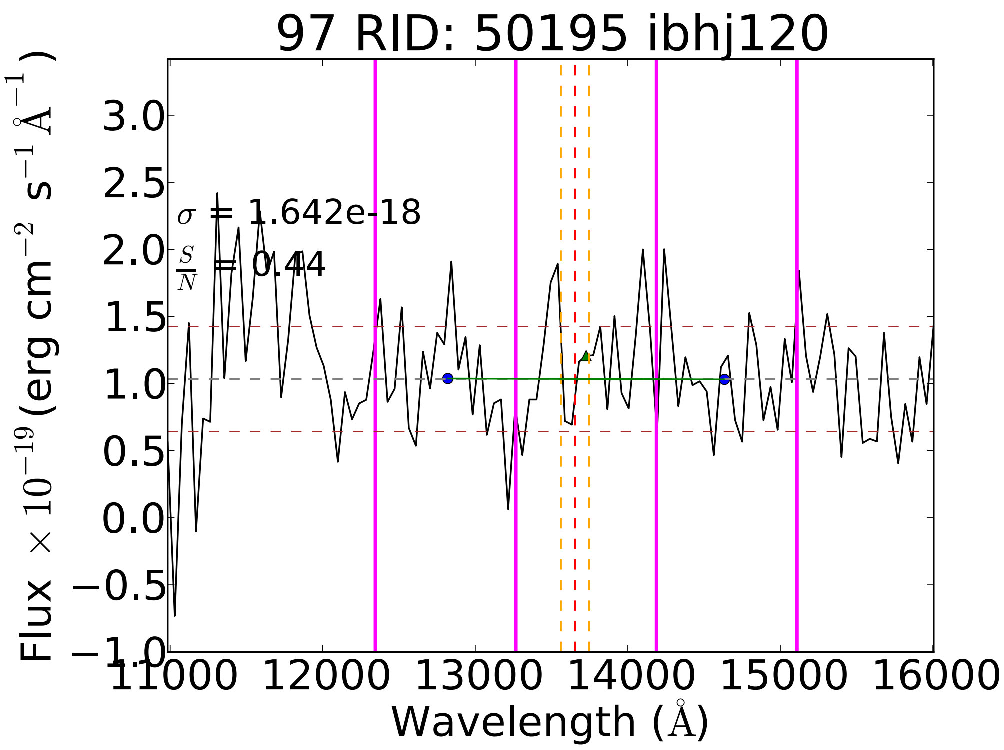
97 RID: 50195 ibhj120
σ = 1.642e-18
S/N = 0.44
Flux × 10^−19 (erg cm^−2 s^−1 Å^−1)
Wavelength (Å)
−1.0
−0.5
0.0
0.5
1.0
1.5
2.0
2.5
3.0
11000
12000
13000
14000
15000
16000

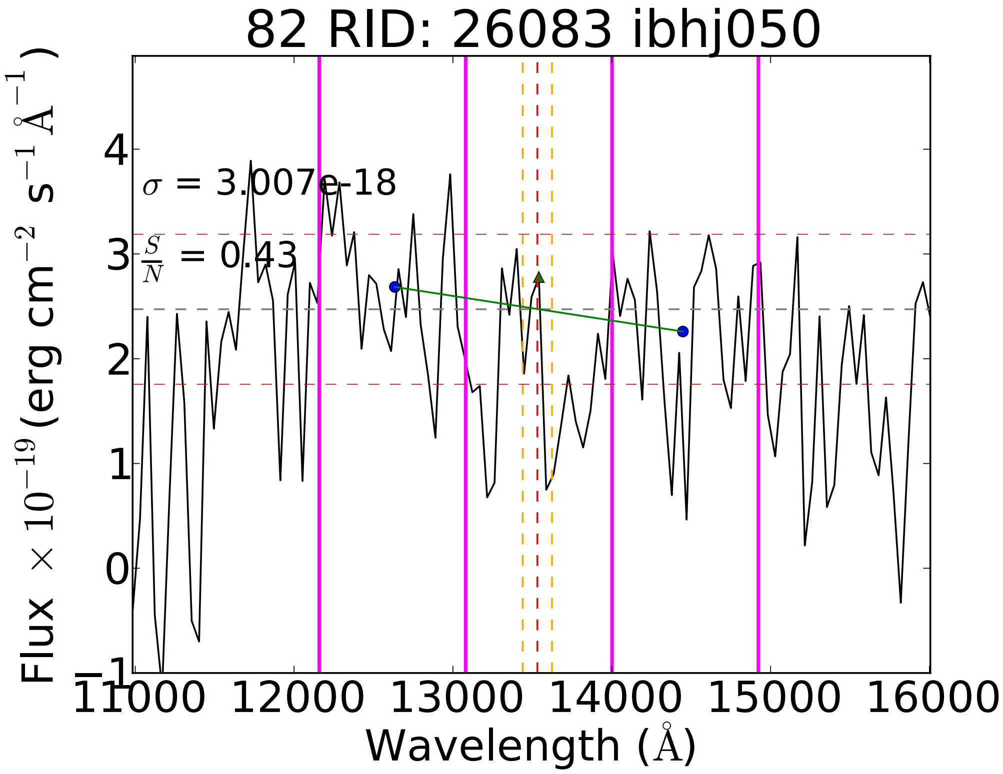
82 RID: 26083 ibhj050
σ = 3.007e-18
S/N = 0.43
Flux × 10^−19 (erg cm^−2 s^−1 Å^−1)
Wavelength (Å)
−1
0
1
2
3
4
11000
12000
13000
14000
15000
16000

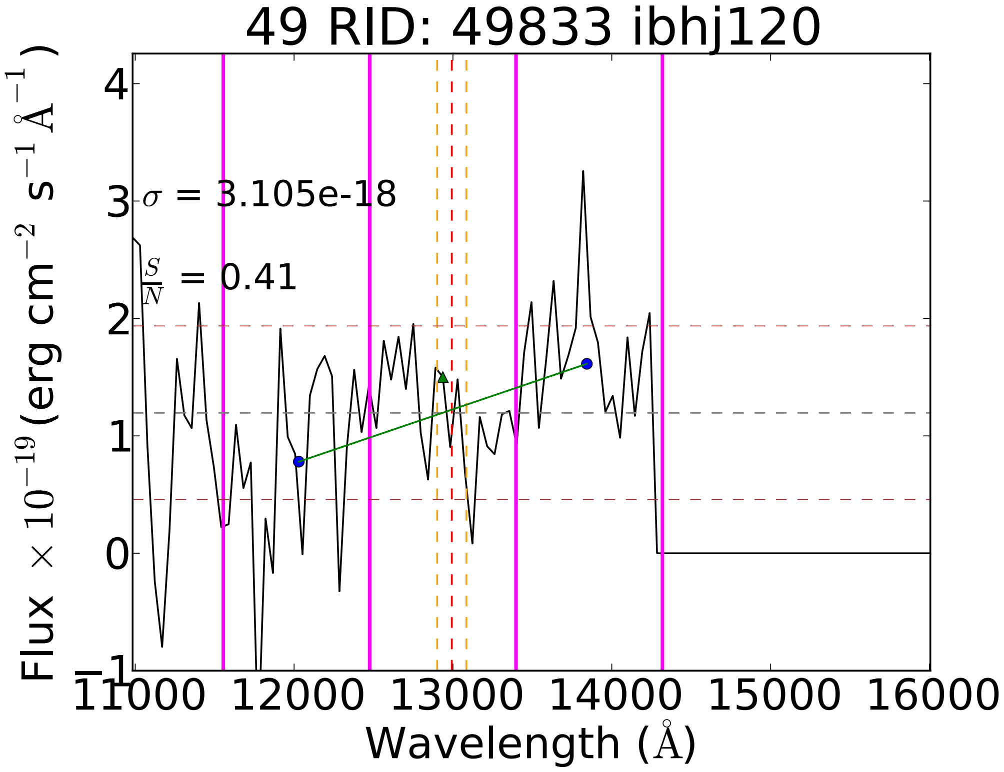
49 RID: 49833 ibhj120
σ = 3.105e-18
$\frac{S}{N}$ = 0.41
Flux $\times 10^{-19}$ (erg cm^{-2} s^{-1} Å^{-1})
Wavelength (Å)
−1
0
1
2
3
4
11000
12000
13000
14000
15000
16000

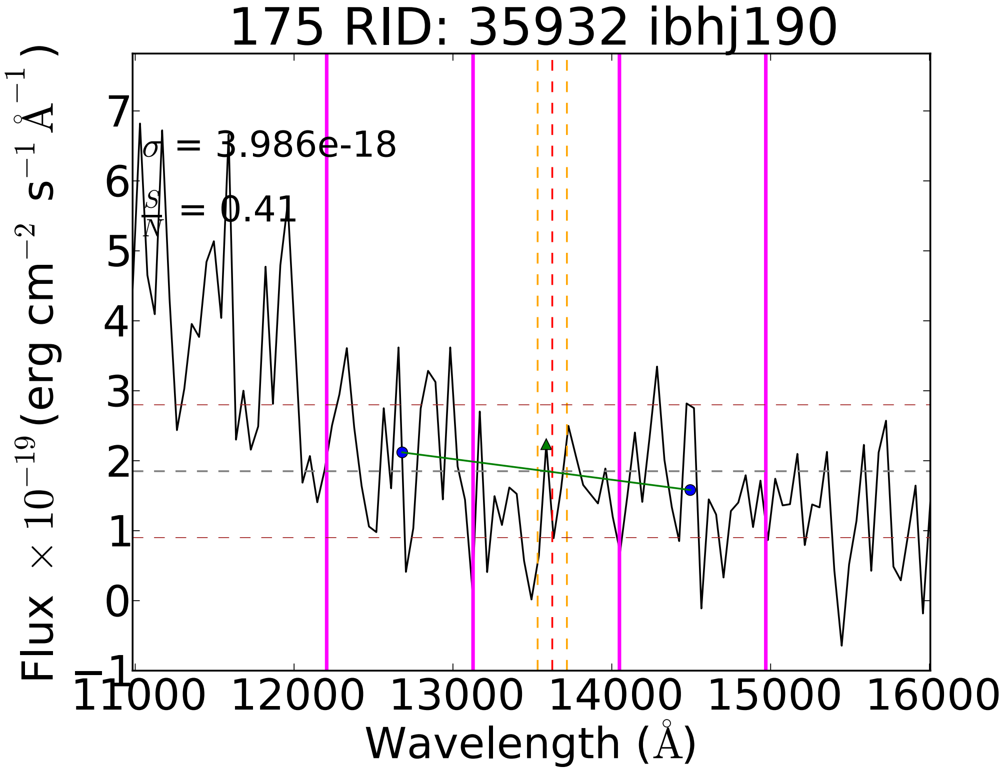
175 RID: 35932 ibhj190
σ = 3.986e-18
$\frac{S}{N}$ = 0.41
Flux $\times 10^{-19}$ (erg cm^{-2} s^{-1} Å^{-1})
Wavelength (Å)
−1
0
1
2
3
4
5
6
7
11000
12000
13000
14000
15000
16000

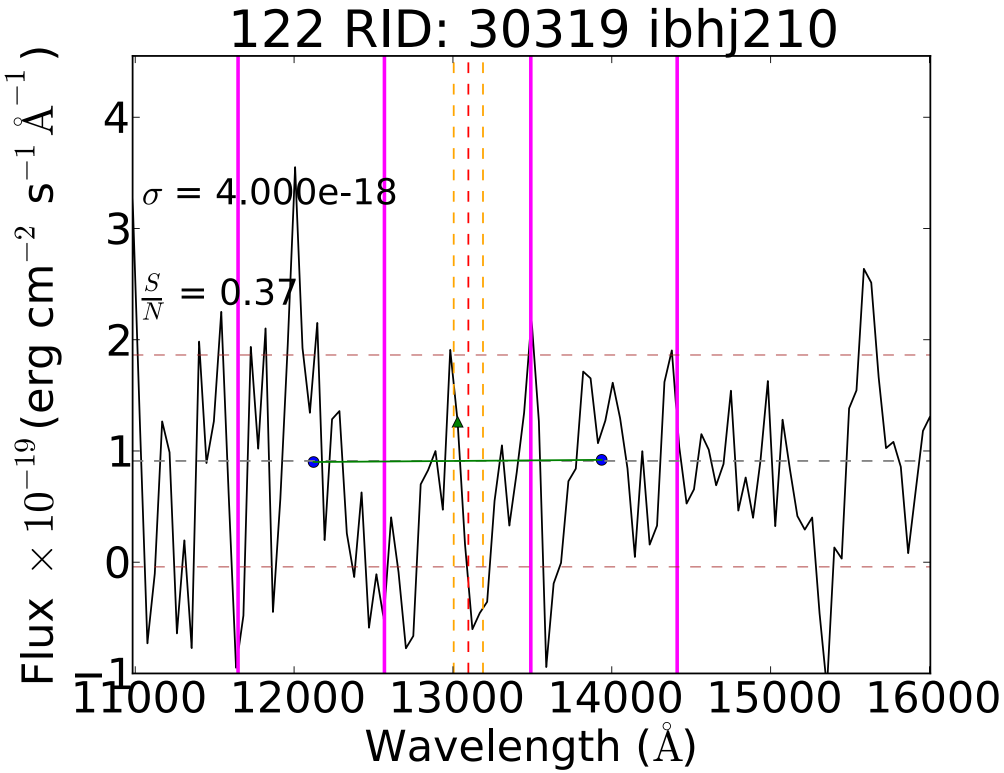
122 RID: 30319 ibhj210
σ = 4.000e-18
$\frac{S}{N}$ = 0.37
Flux $\times 10^{-19}$ (erg cm^{-2} s^{-1} Å^{-1})
Wavelength (Å)
−1
0
1
2
3
4
11000
12000
13000
14000
15000
16000

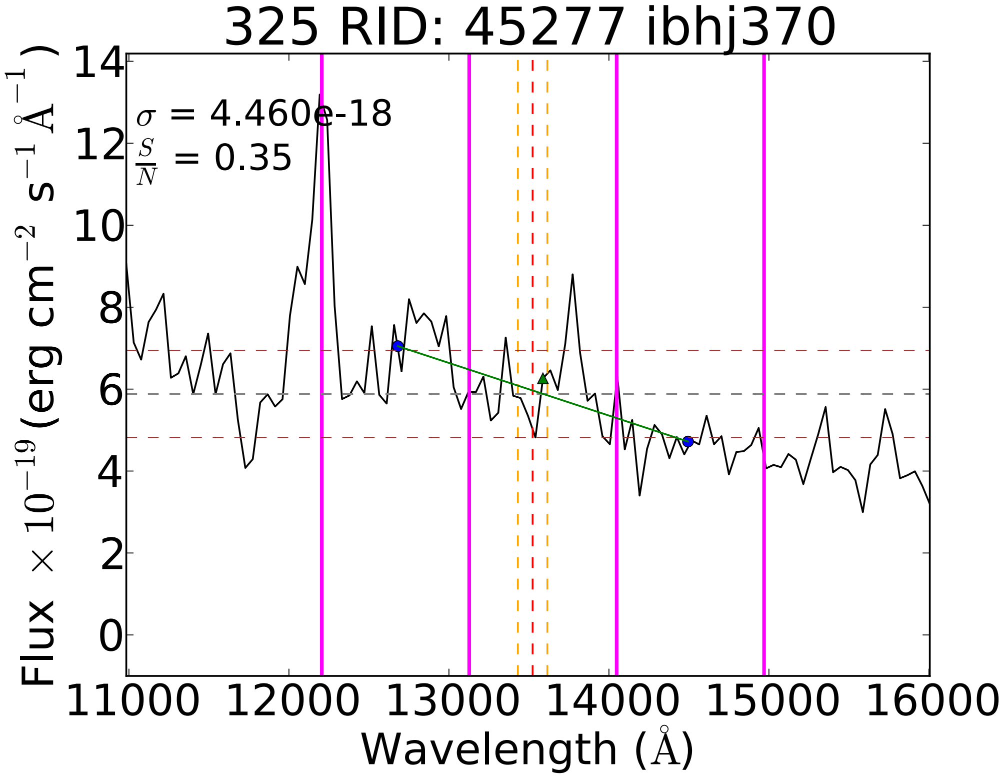
325 RID: 45277 ibhj370
σ = 4.460e-18
$\frac{S}{N}$ = 0.35
Flux $\times 10^{-19}$ (erg cm^{-2} s^{-1} Å^{-1})
Wavelength (Å)
0
2
4
6
8
10
12
14
11000
12000
13000
14000
15000
16000

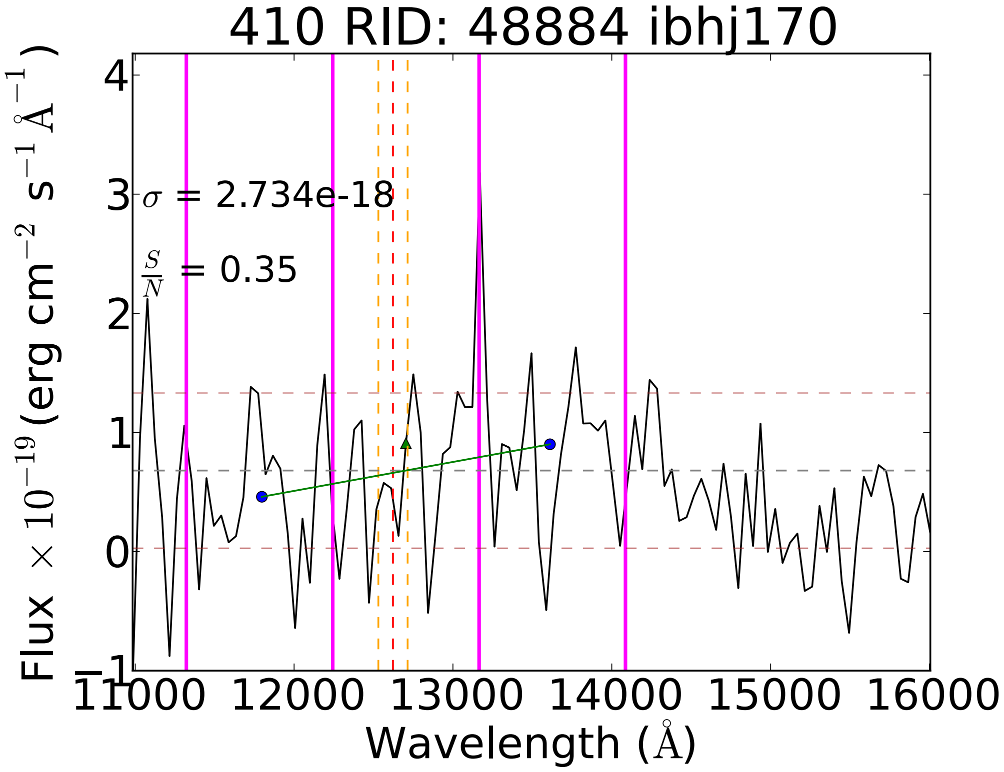
410 RID: 48884 ibhj170

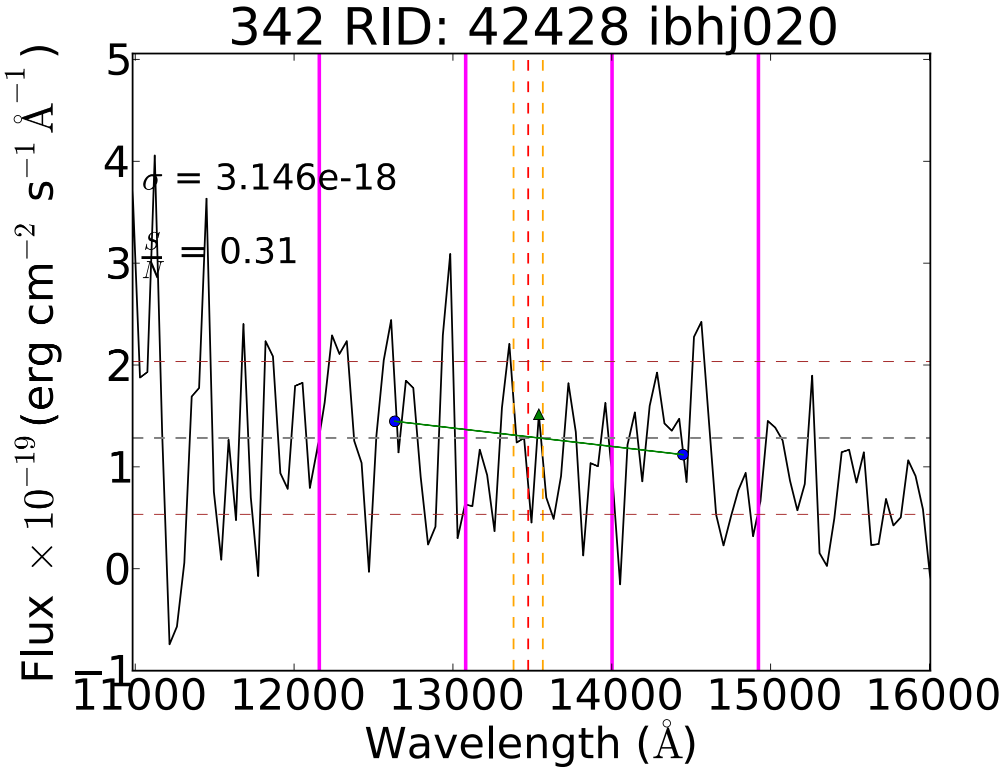
342 RID: 42428 ibhj020

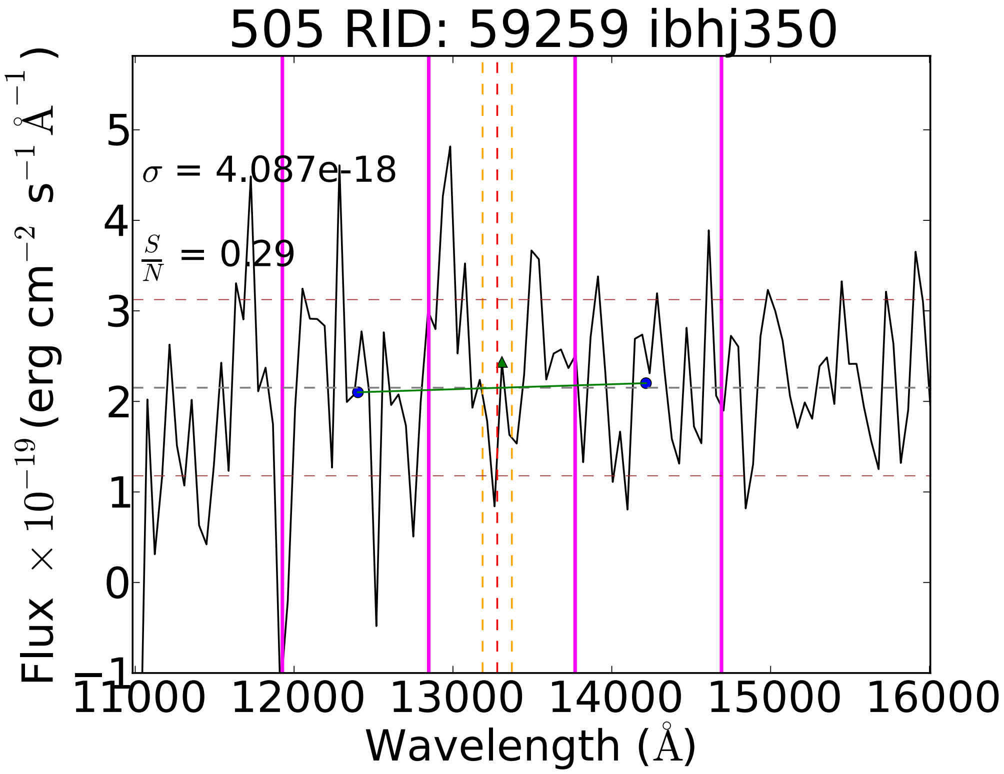
505 RID: 59259 ibhj350

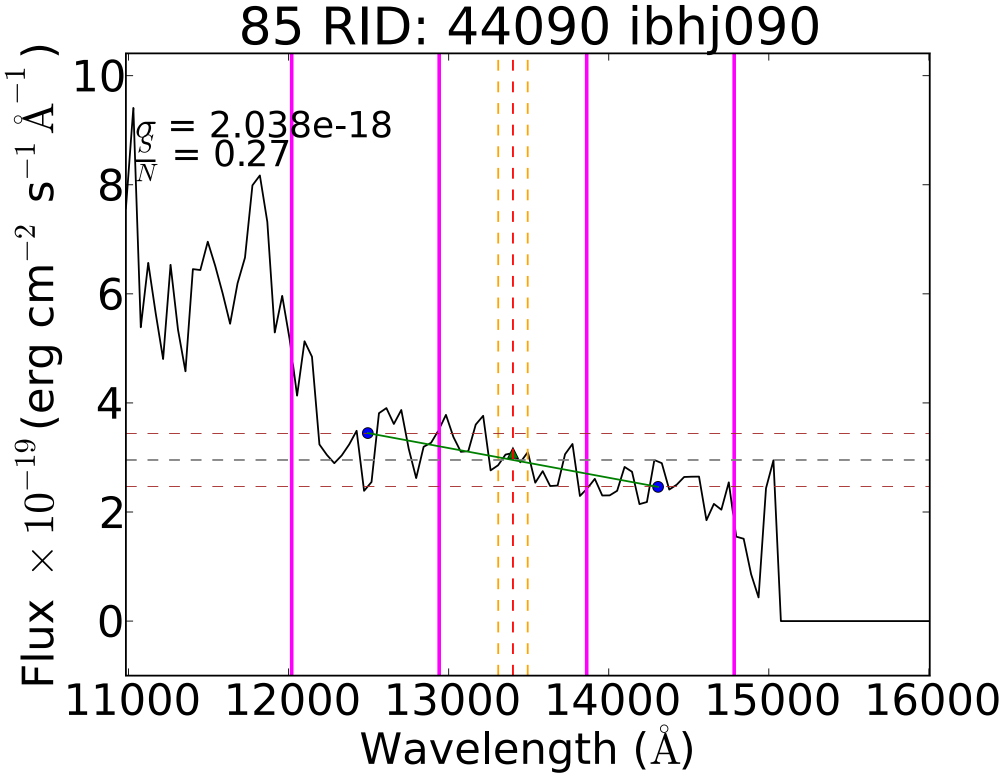
85 RID: 44090 ibhj090

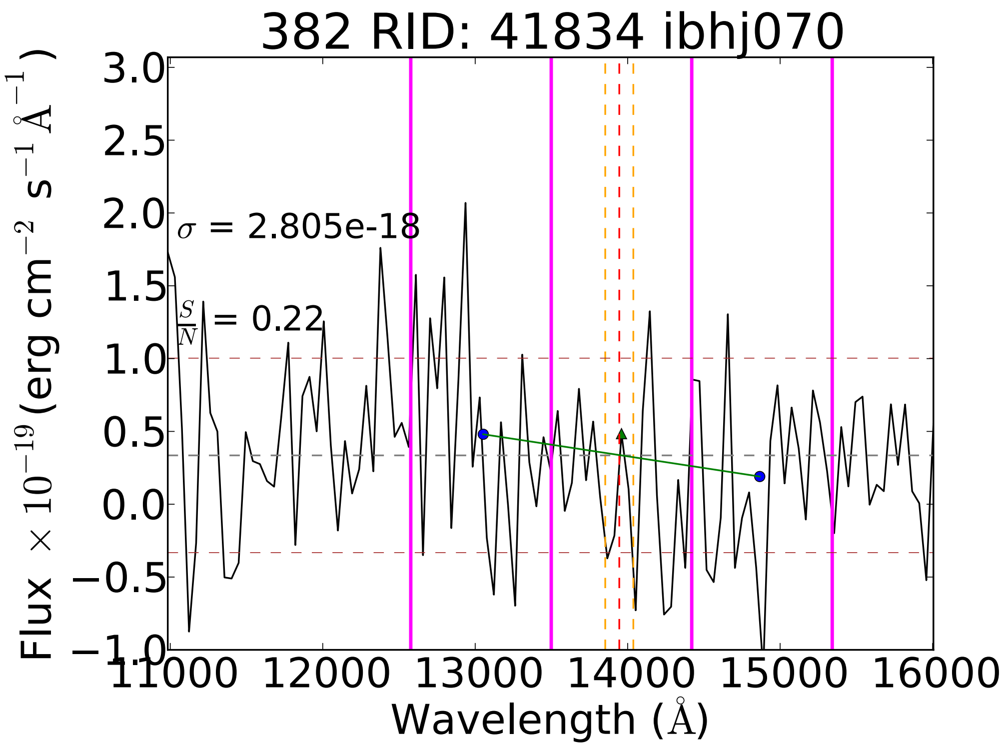
382 RID: 41834 ibhj070
σ = 2.805e-18
S/N = 0.22
Flux × 10^-19 (erg cm^-2 s^-1 Å^-1)
Wavelength (Å)
3.0
2.5
2.0
1.5
1.0
0.5
0.0
−0.5
−1.0
11000
12000
13000
14000
15000
16000

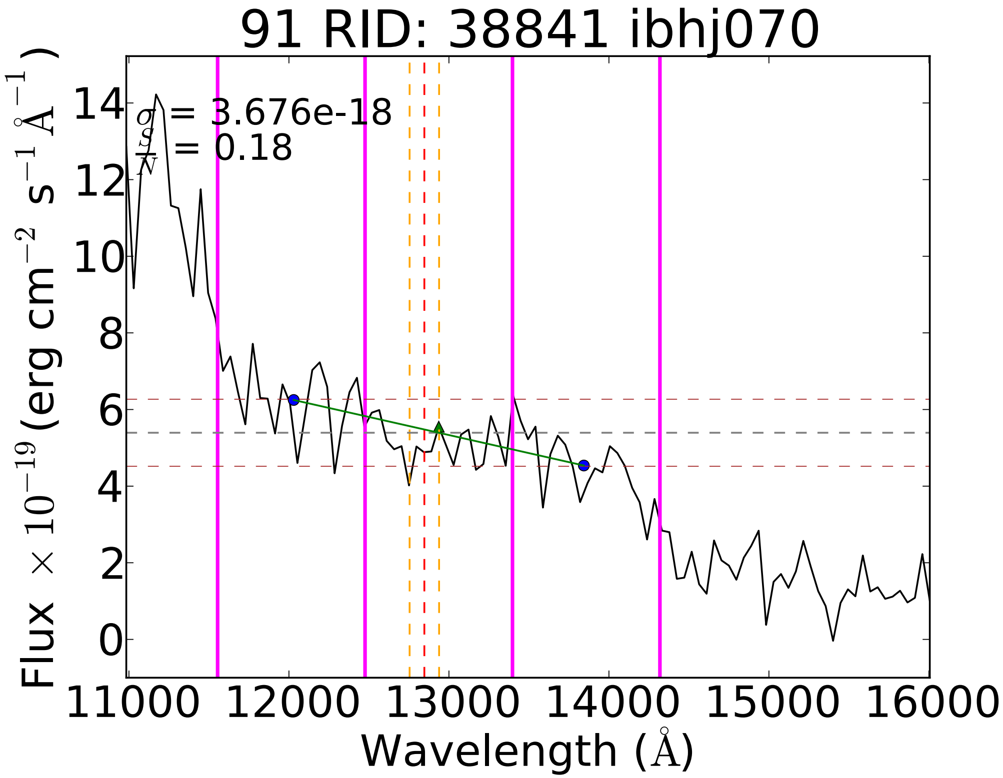
91 RID: 38841 ibhj070
σ = 3.676e-18
S/N = 0.18
Flux × 10^-19 (erg cm^-2 s^-1 Å^-1)
Wavelength (Å)
14
12
10
8
6
4
2
0
11000
12000
13000
14000
15000
16000

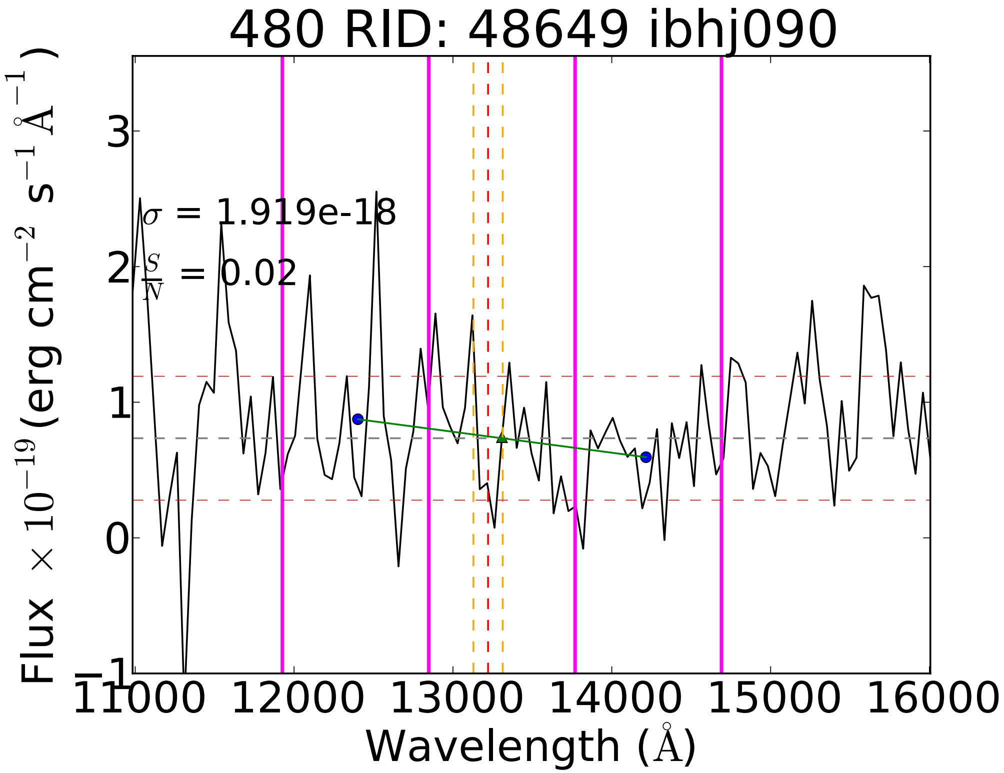
480 RID: 48649 ibhj090
σ = 1.919e-18
S/N = 0.02
Flux × 10^-19 (erg cm^-2 s^-1 Å^-1)
Wavelength (Å)
3
2
1
0
−1
11000
12000
13000
14000
15000
16000

Appendix B

Multiple Spectra

Presented here are plots of all the spectra observed multiple times in different pointings. The lines and symbols have the same meaning as in the previous appendix.

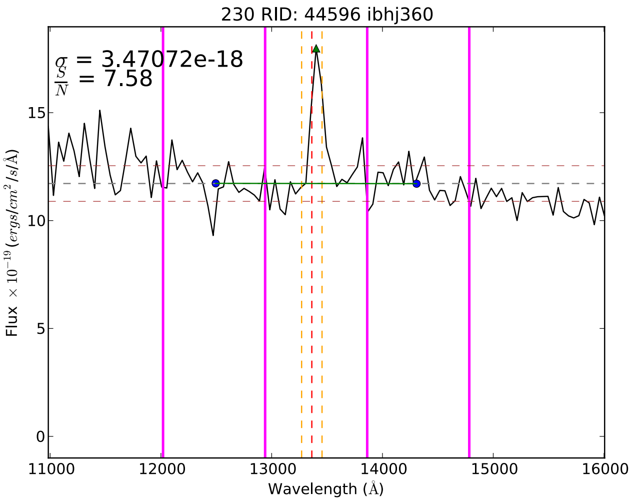
230 RID: 44596 ibhj360
σ = 3.47072e-18
$\frac{S}{N}$ = 7.58
Flux × 10^{-19} (ergs/cm^2/s/Å)
0
5
10
15
11000
12000
13000
14000
15000
16000
Wavelength (Å)

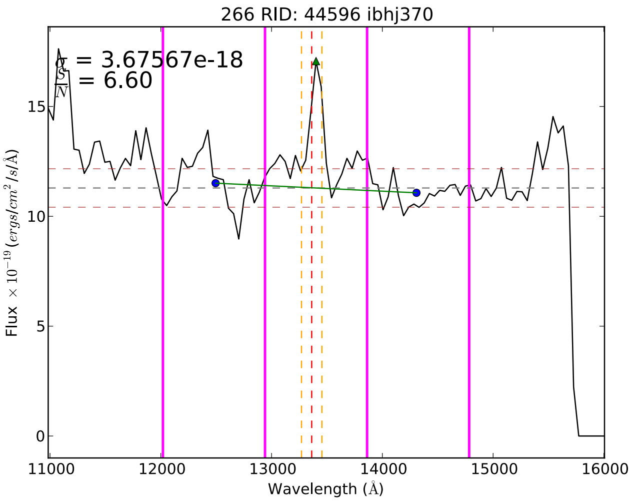
266 RID: 44596 ibhj370
σ = 3.67567e-18
$\frac{S}{N}$ = 6.60
Flux × 10^{-19} (ergs/cm^2/s/Å)
0
5
10
15
11000
12000
13000
14000
15000
16000
Wavelength (Å)

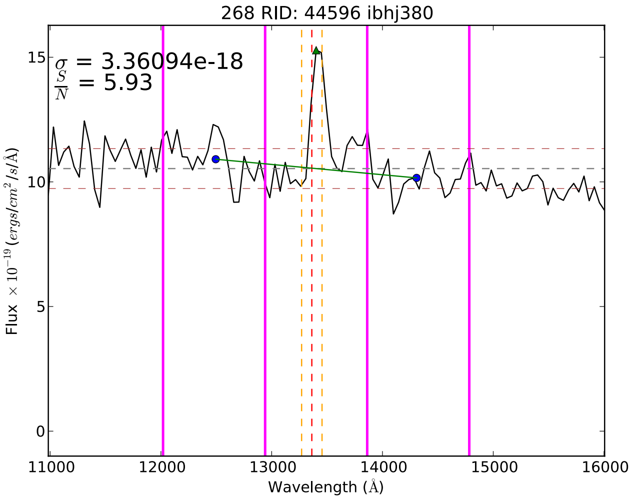
268 RID: 44596 ibhj380
σ = 3.36094e-18
$\frac{S}{N}$ = 5.93
Flux × 10^{-19} (ergs/cm^2/s/Å)
0
5
10
15
11000
12000
13000
14000
15000
16000
Wavelength (Å)

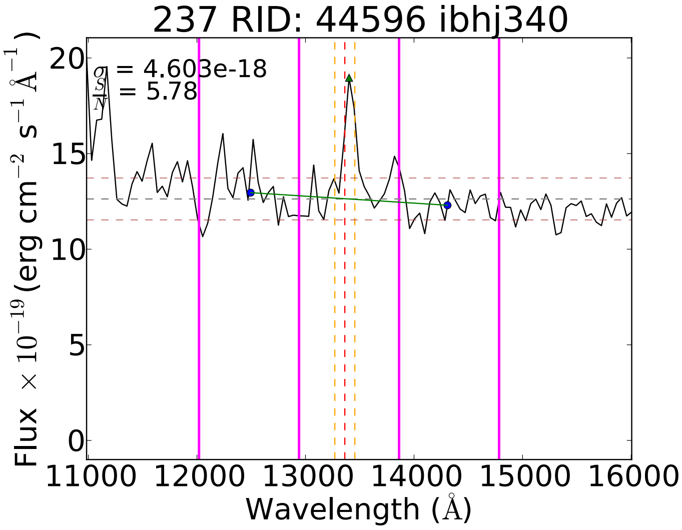
237 RID: 44596 ibhj340
σ = 4.603e-18
$\frac{S}{N}$ = 5.78
Flux × 10^{-19} (erg cm^{-2} s^{-1} Å^{-1})
0
5
10
15
20
11000
12000
13000
14000
15000
16000
Wavelength (Å)

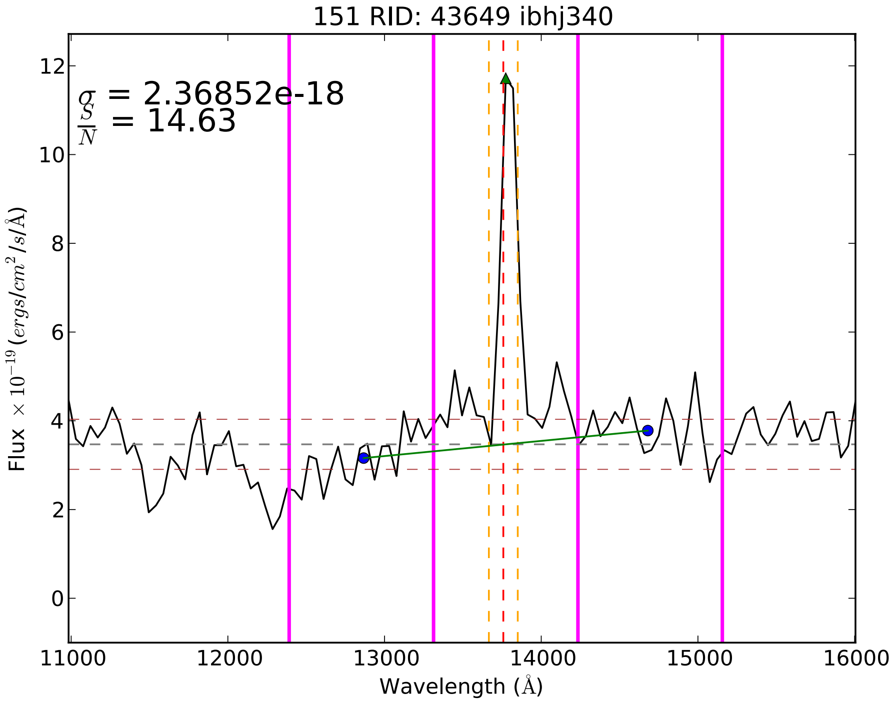
151 RID: 43649 ibhj340
σ = 2.36852e-18
S/N = 14.63
Flux × 10^-19 (ergs/cm^2/s/Å)
0
2
4
6
8
10
12
11000
12000
13000
14000
15000
16000
Wavelength (Å)

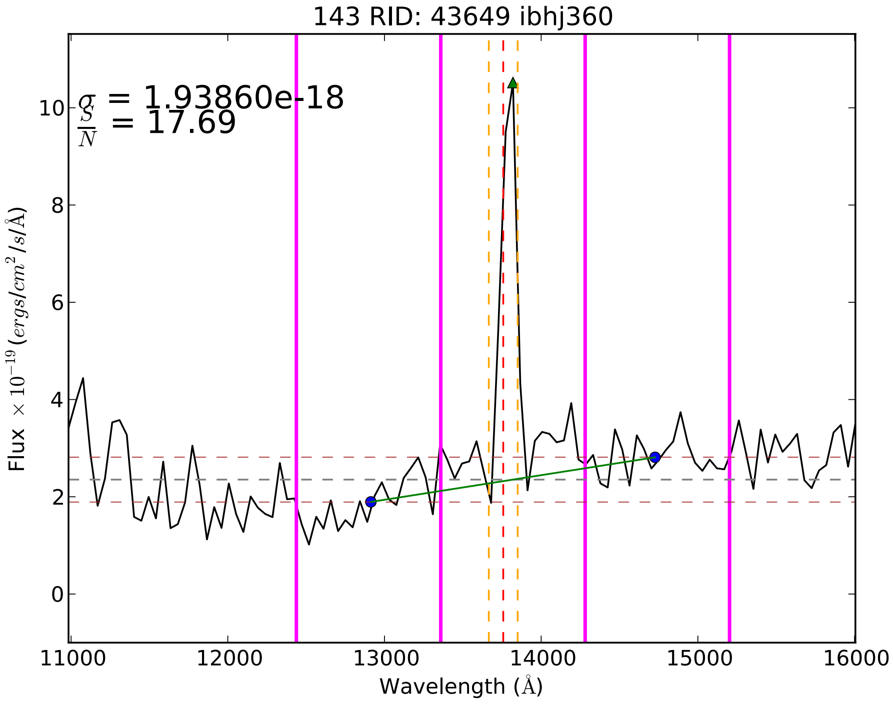
143 RID: 43649 ibhj360
σ = 1.93860e-18
S/N = 17.69
Flux × 10^-19 (ergs/cm^2/s/Å)
0
2
4
6
8
10
11000
12000
13000
14000
15000
16000
Wavelength (Å)

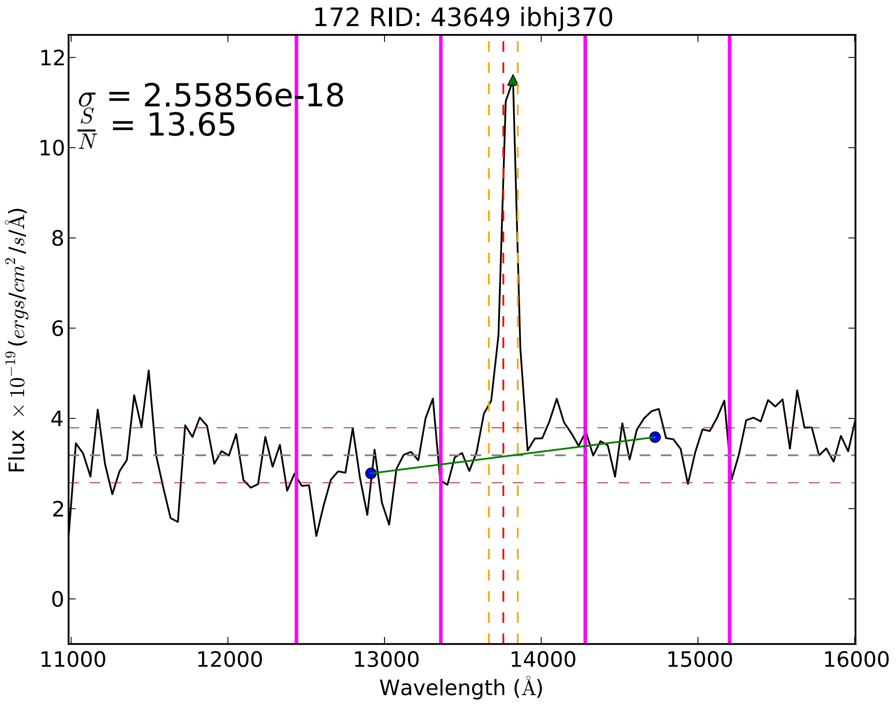
172 RID: 43649 ibhj370
σ = 2.55856e-18
S/N = 13.65
Flux × 10^-19 (ergs/cm^2/s/Å)
0
2
4
6
8
10
12
11000
12000
13000
14000
15000
16000
Wavelength (Å)

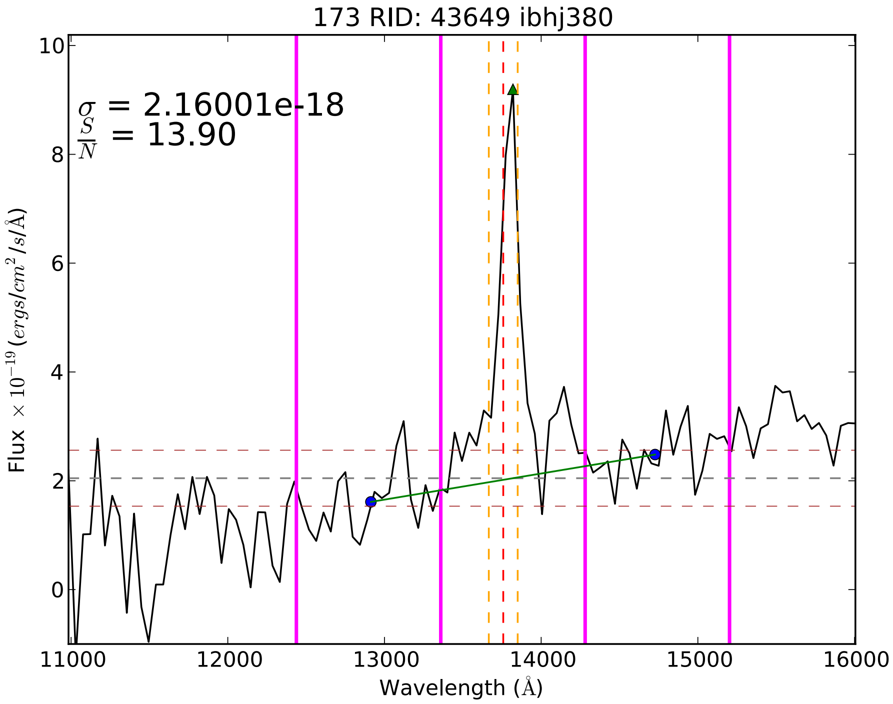
173 RID: 43649 ibhj380
σ = 2.16001e-18
S/N = 13.90
Flux × 10^-19 (ergs/cm^2/s/Å)
0
2
4
6
8
10
11000
12000
13000
14000
15000
16000
Wavelength (Å)

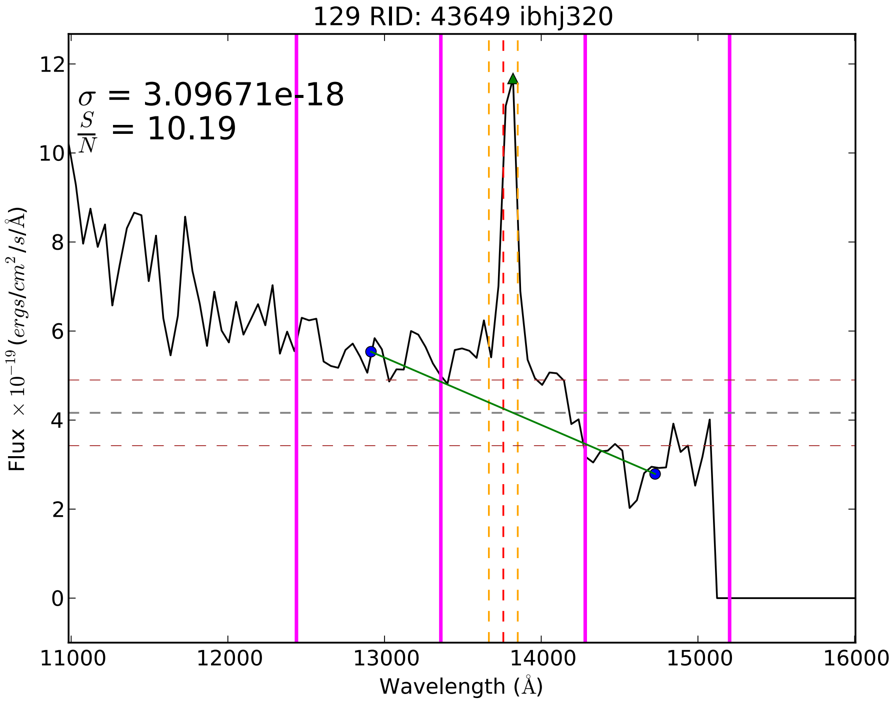
129 RID: 43649 ibhj320

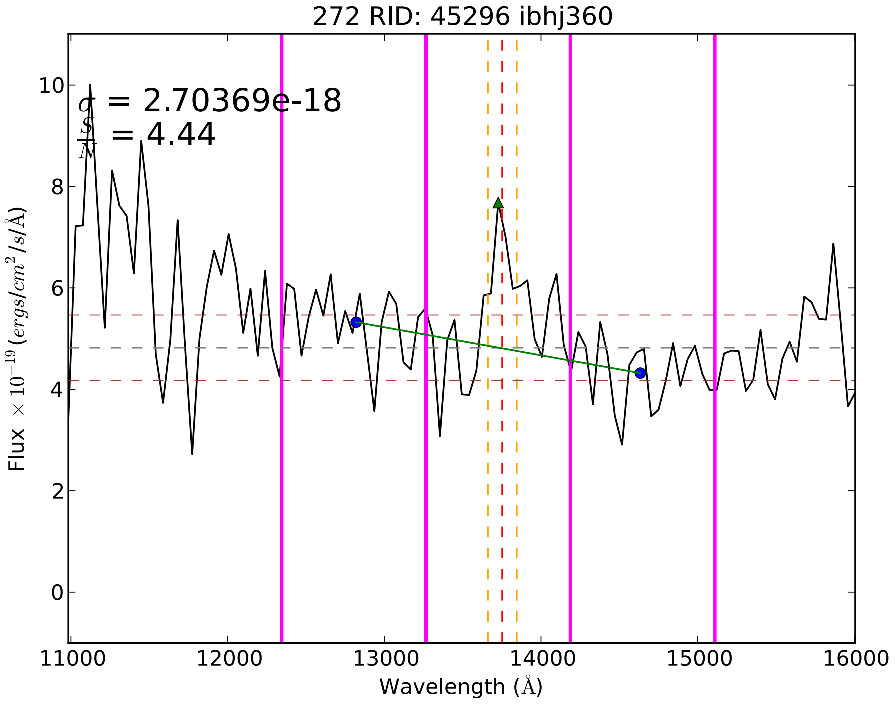
272 RID: 45296 ibhj360
σ = 2.70369e-18
S/N = 4.44
Flux × 10^-19 (ergs/cm^2/s/Å)
Wavelength (Å)
0
2
4
6
8
10
11000
12000
13000
14000
15000
16000

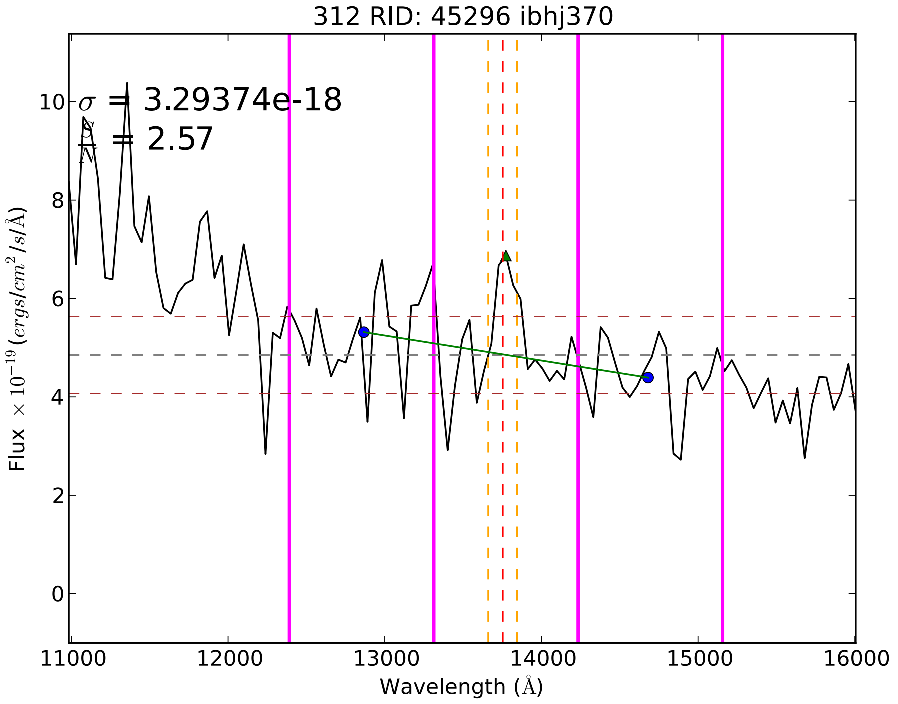
312 RID: 45296 ibhj370
σ = 3.29374e-18
S/N = 2.57
Flux × 10^-19 (ergs/cm^2/s/Å)
Wavelength (Å)
0
2
4
6
8
10
11000
12000
13000
14000
15000
16000

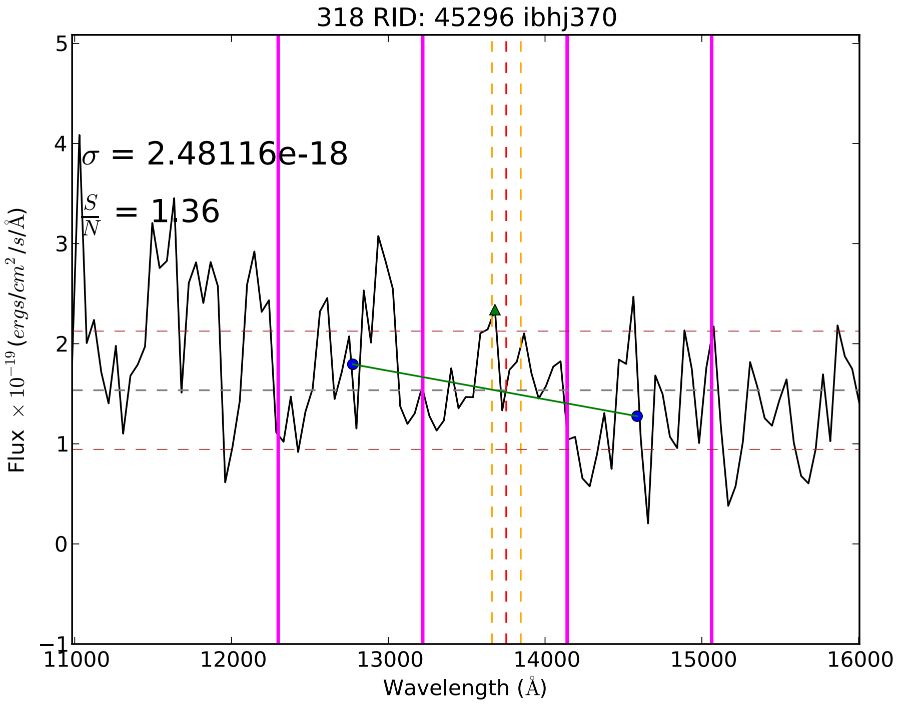
318 RID: 45296 ibhj370
σ = 2.48116e-18
S/N = 1.36
Flux × 10^-19 (ergs/cm^2/s/Å)
Wavelength (Å)
−1
0
1
2
3
4
5
11000
12000
13000
14000
15000
16000

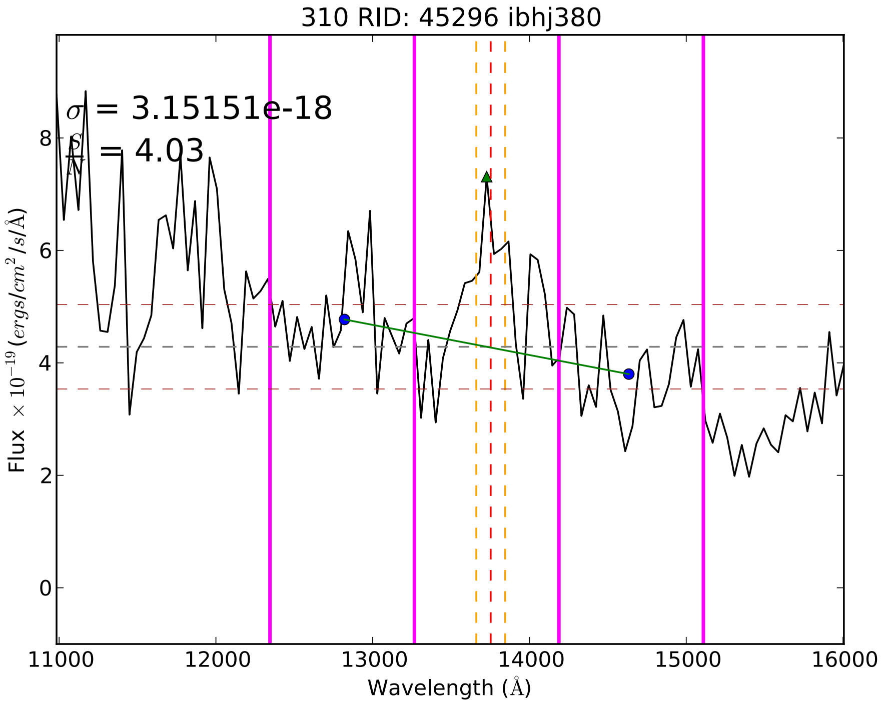
310 RID: 45296 ibhj380
σ = 3.15151e-18
S/N = 4.03
Flux × 10^-19 (ergs/cm^2/s/Å)
Wavelength (Å)
0
2
4
6
8
11000
12000
13000
14000
15000
16000

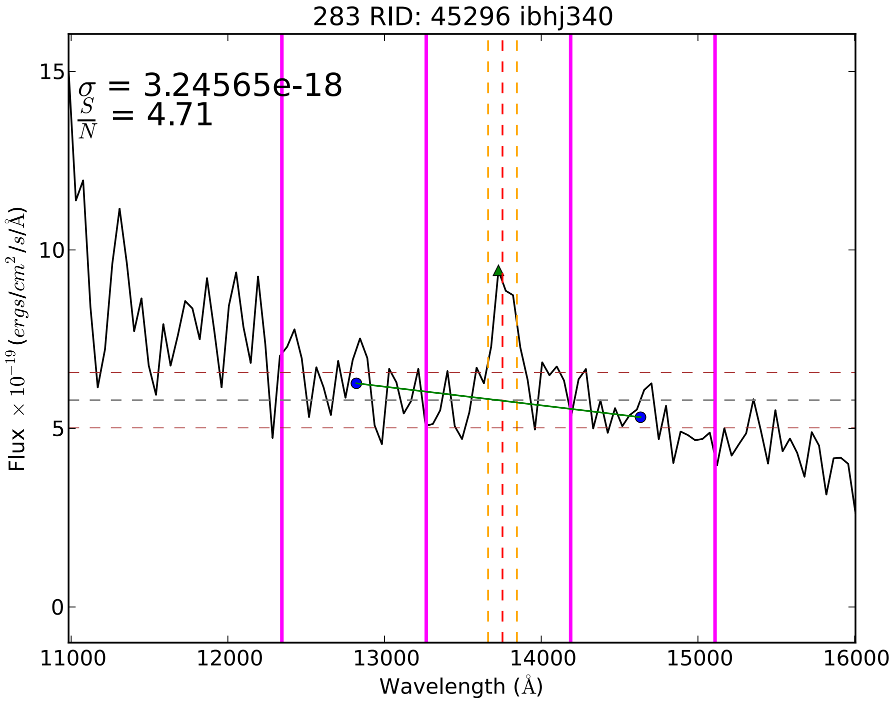
283 RID: 45296 ibhj340
σ = 3.24565e-18
$\frac{S}{N}$ = 4.71
Flux × 10^{-19} $(ergs/cm^2/s/\AA)$
Wavelength (Å)
0
5
10
15
11000
12000
13000
14000
15000
16000

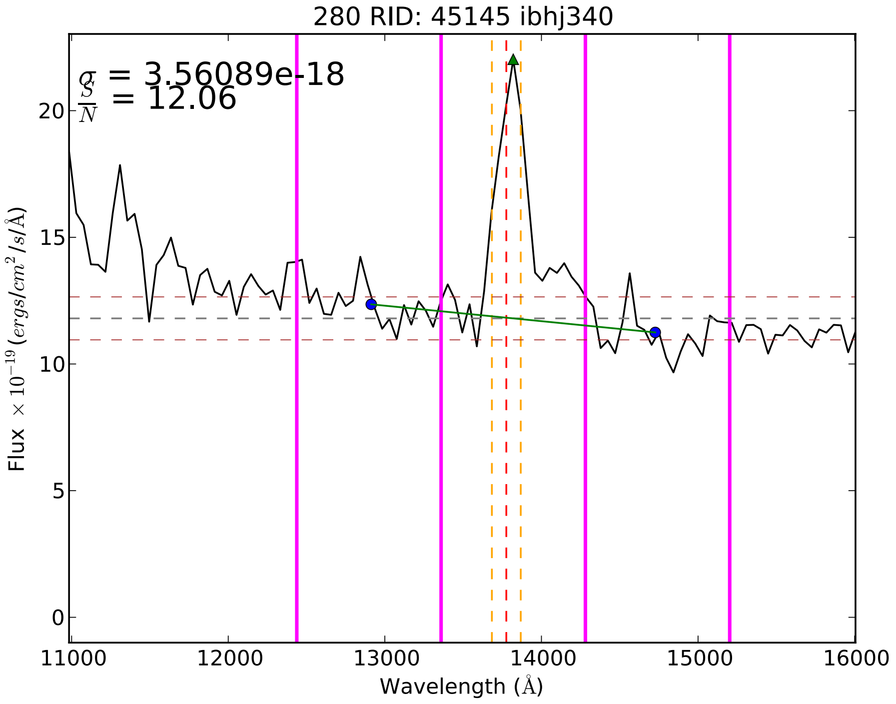
280 RID: 45145 ibhj340
σ = 3.56089e-18
$\frac{S}{N}$ = 12.06
Flux $\times 10^{-19}\,(ergs/cm^2/s/\text{Å})$
Wavelength (Å)
0
5
10
15
20
11000
12000
13000
14000
15000
16000

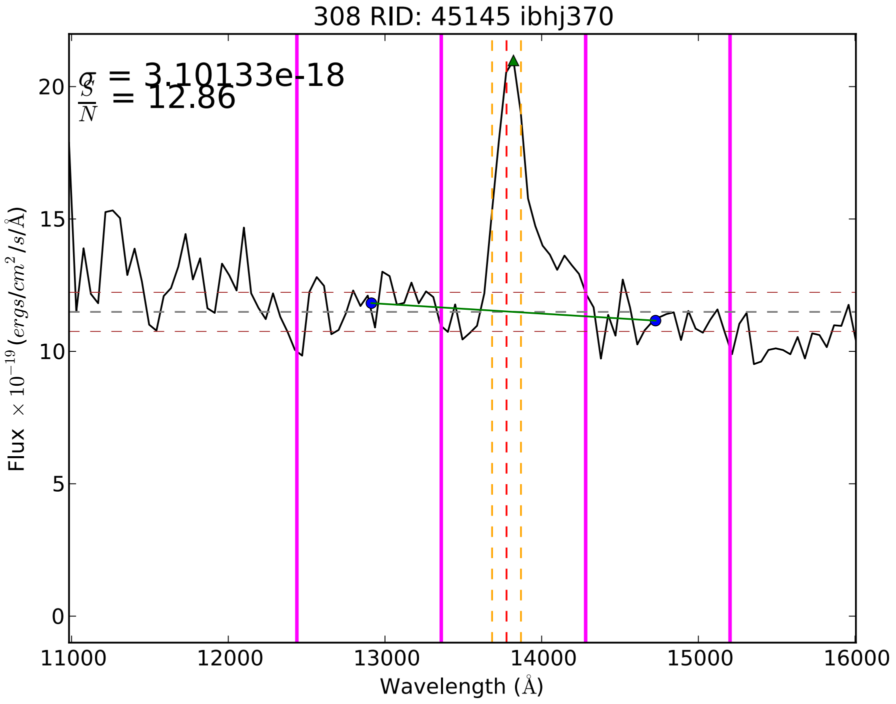
308 RID: 45145 ibhj370
σ = 3.10133e-18
$\frac{S}{N}$ = 12.86
Flux $\times 10^{-19}\,(ergs/cm^2/s/\text{Å})$
Wavelength (Å)
0
5
10
15
20
11000
12000
13000
14000
15000
16000

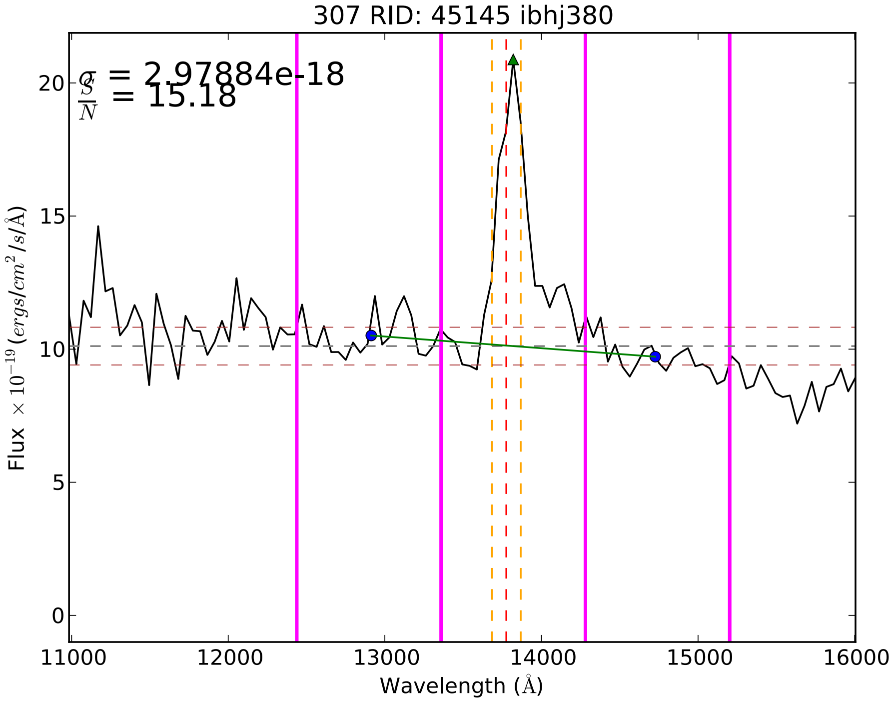
307 RID: 45145 ibhj380
σ = 2.97884e-18
$\frac{S}{N}$ = 15.18
Flux $\times 10^{-19}\,(ergs/cm^2/s/\text{Å})$
Wavelength (Å)
0
5
10
15
20
11000
12000
13000
14000
15000
16000

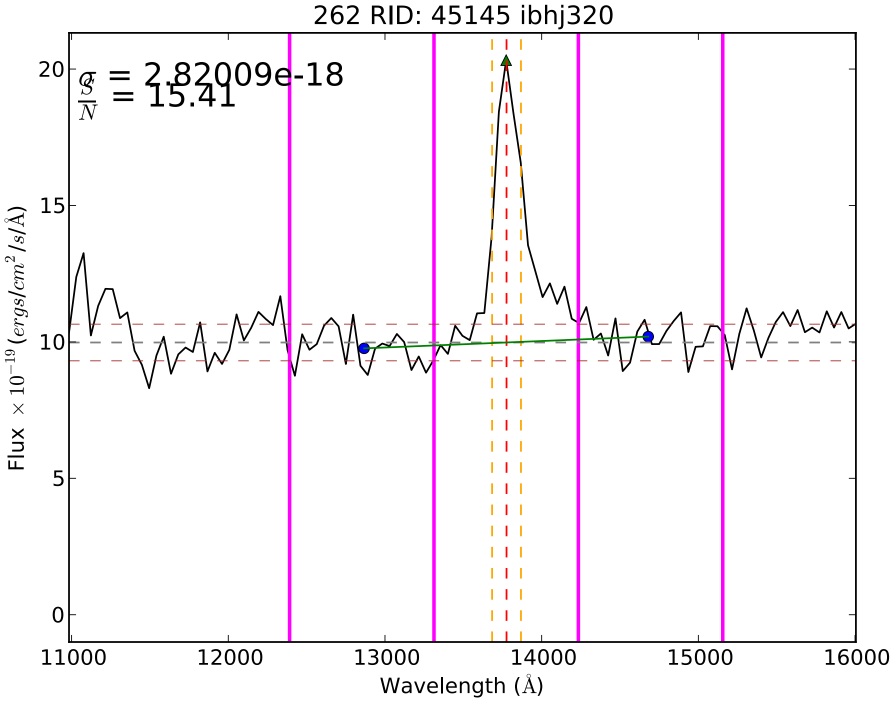
262 RID: 45145 ibhj320
σ = 2.82009e-18
$\frac{S}{N}$ = 15.41
Flux $\times 10^{-19}\,(ergs/cm^2/s/\text{Å})$
Wavelength (Å)
0
5
10
15
20
11000
12000
13000
14000
15000
16000

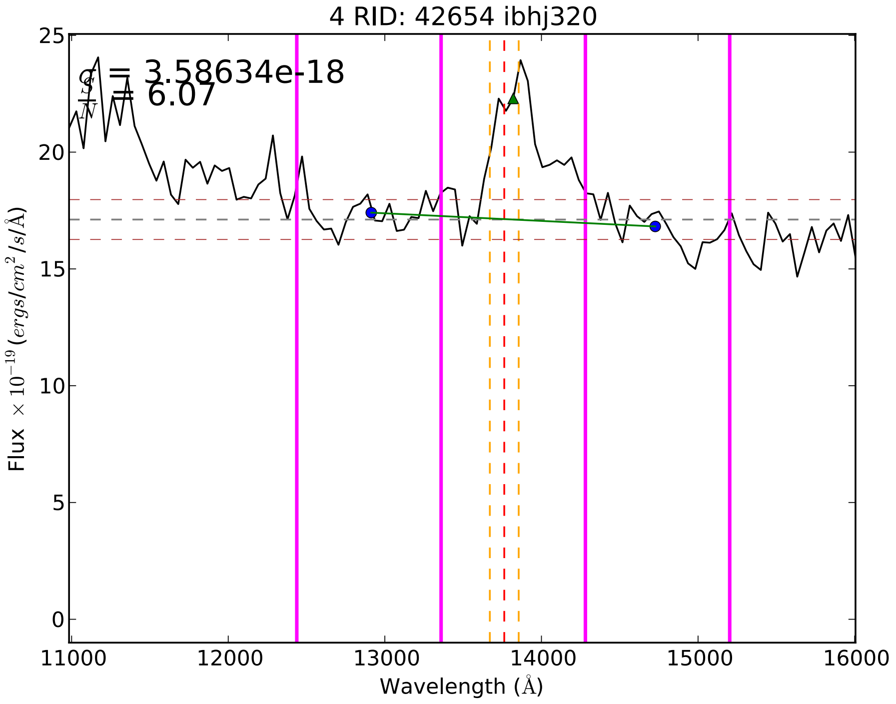
4 RID: 42654 ibhj320
σ = 3.58634e-18
S/N = 6.07
Flux × 10^-19 (ergs/cm^2/s/Å)
Wavelength (Å)
0
5
10
15
20
25
11000
12000
13000
14000
15000
16000

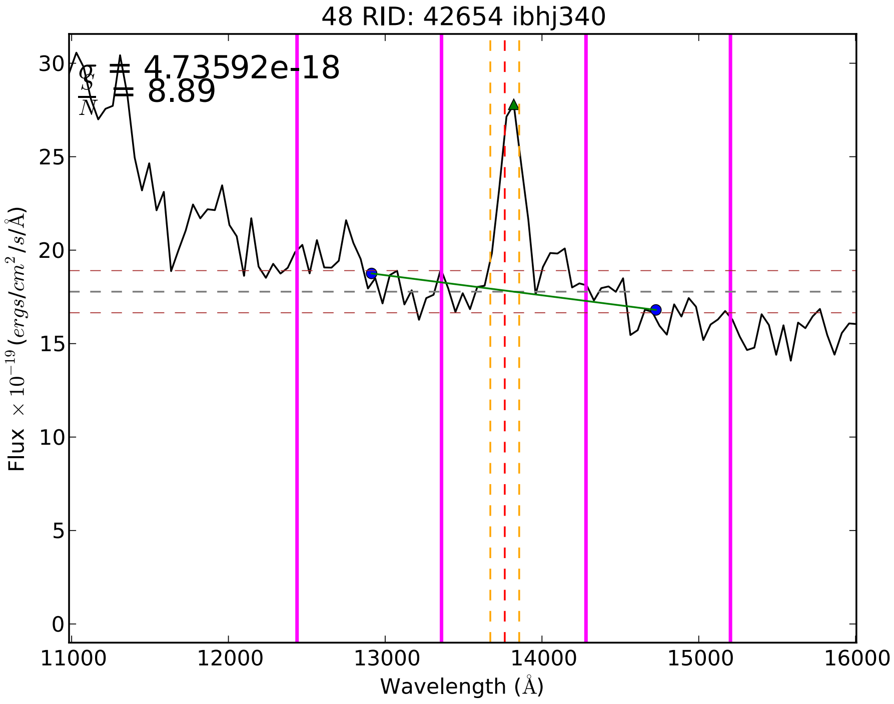
48 RID: 42654 ibhj340
σ = 4.73592e-18
S/N = 8.89
Flux × 10^-19 (ergs/cm^2/s/Å)
Wavelength (Å)
0
5
10
15
20
25
30
11000
12000
13000
14000
15000
16000

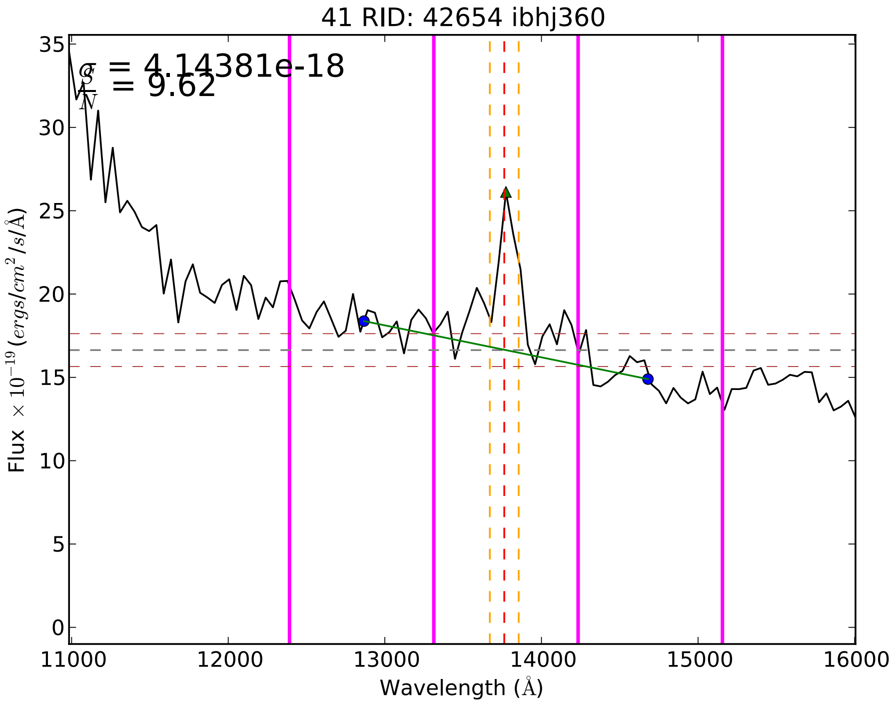
41 RID: 42654 ibhj360
σ = 4.14381e-18
S/N = 9.62
Flux × 10^-19 (ergs/cm^2/s/Å)
Wavelength (Å)
0
5
10
15
20
25
30
35
11000
12000
13000
14000
15000
16000

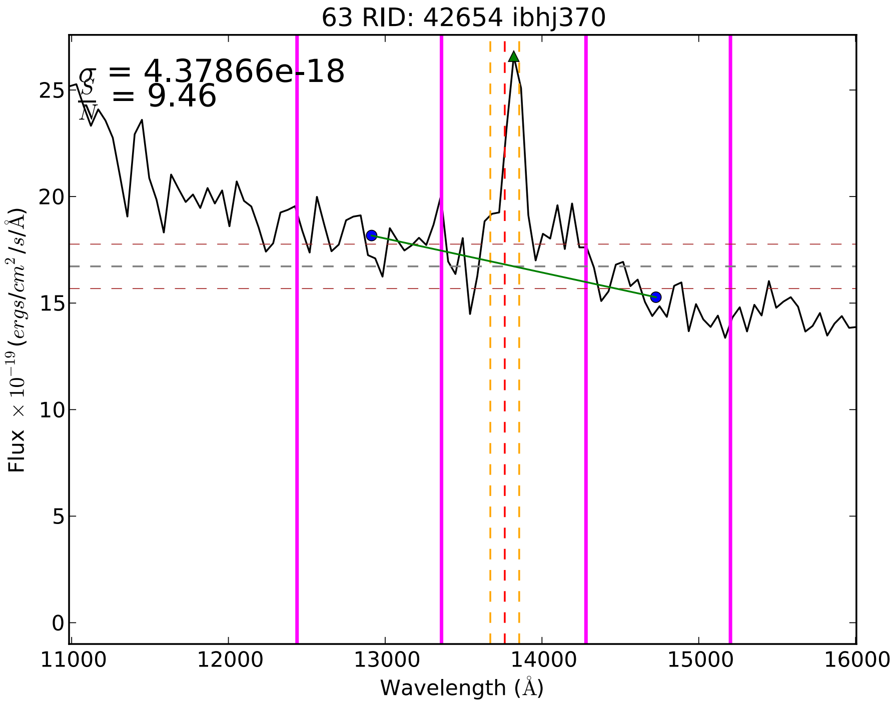
63 RID: 42654 ibhj370
σ = 4.37866e-18
S/N = 9.46
Flux × 10^-19 (ergs/cm^2/s/Å)
Wavelength (Å)
0
5
10
15
20
25
11000
12000
13000
14000
15000
16000

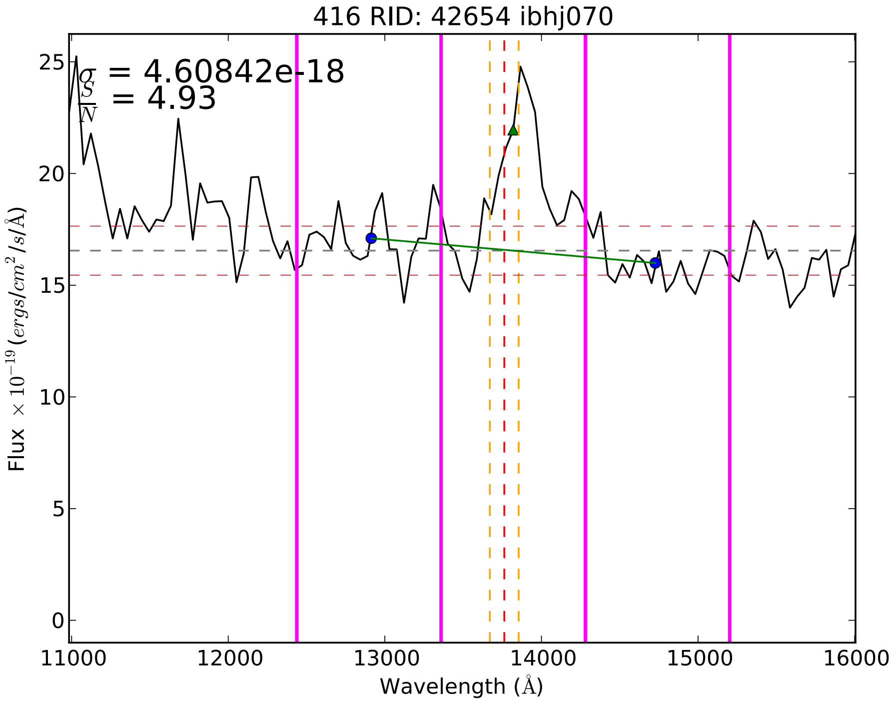
416 RID: 42654 ibhj070
σ = 4.60842e-18
S/N = 4.93
Flux × 10^-19 (ergs/cm^2/s/Å)
Wavelength (Å)
0
5
10
15
20
25
11000
12000
13000
14000
15000
16000

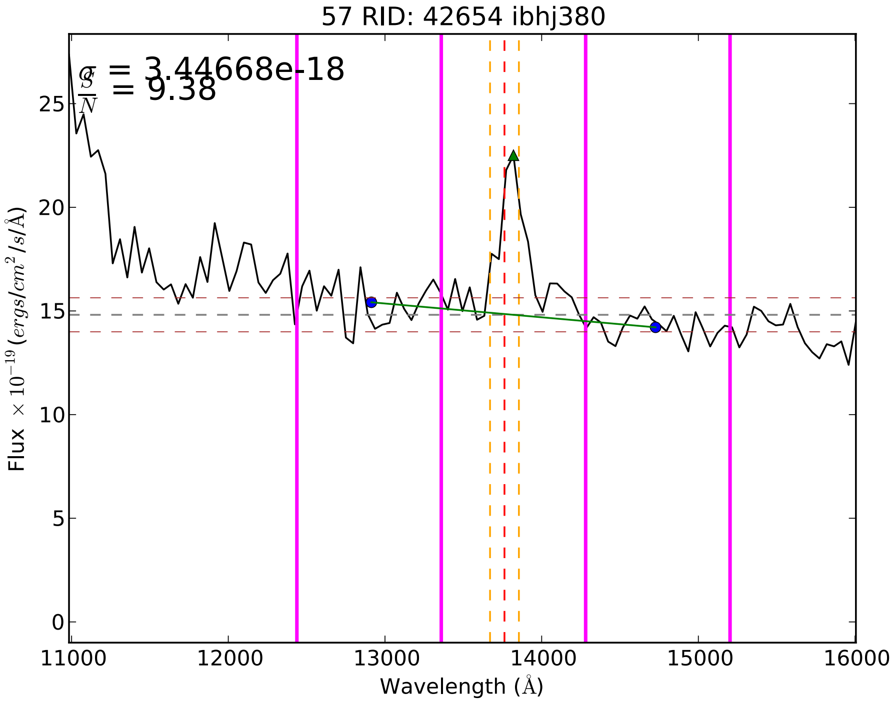
57 RID: 42654 ibhj380
σ = 3.44668e-18
S/N = 9.38
Flux × 10^-19 (ergs/cm^2/s/Å)
Wavelength (Å)
0
5
10
15
20
25
11000
12000
13000
14000
15000
16000

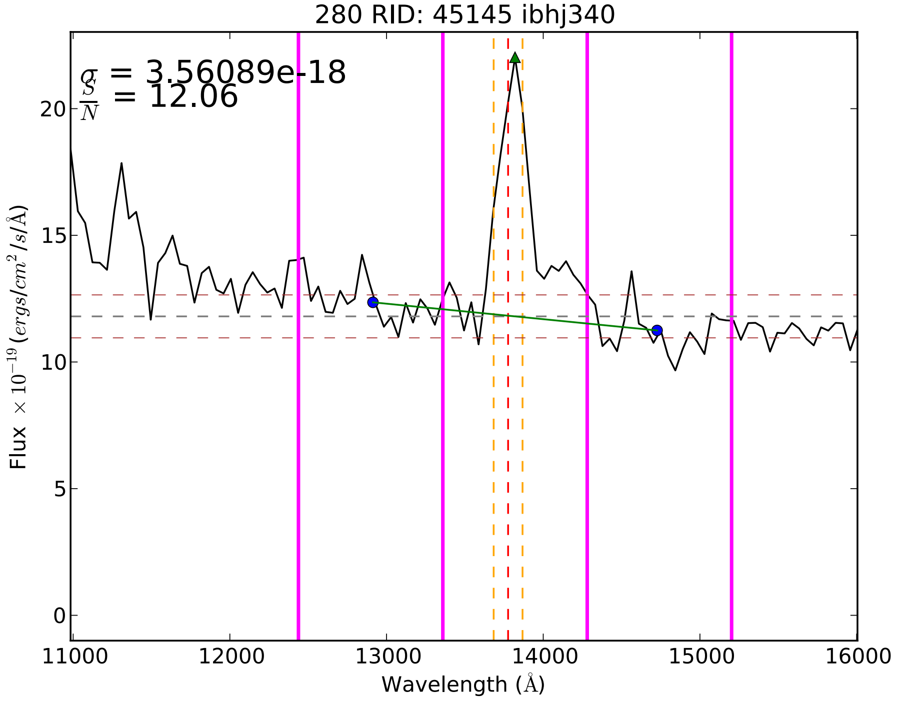
280 RID: 45145 ibhj340
σ = 3.56089e-18
$\frac{S}{N}$ = 12.06
Flux $\times 10^{-19}$ $(ergs/cm^2/s/Å)$
Wavelength (Å)
0
5
10
15
20
11000
12000
13000
14000
15000
16000

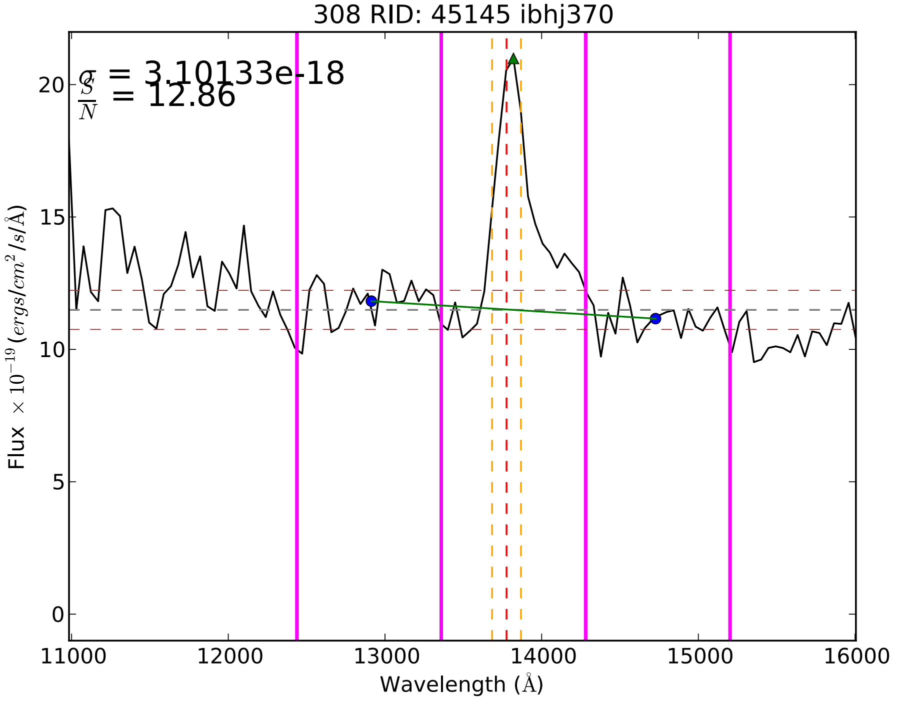
308 RID: 45145 ibhj370
σ = 3.10133e-18
$\frac{S}{N}$ = 12.86
Flux $\times 10^{-19}$ $(ergs/cm^2/s/Å)$
Wavelength (Å)
0
5
10
15
20
11000
12000
13000
14000
15000
16000

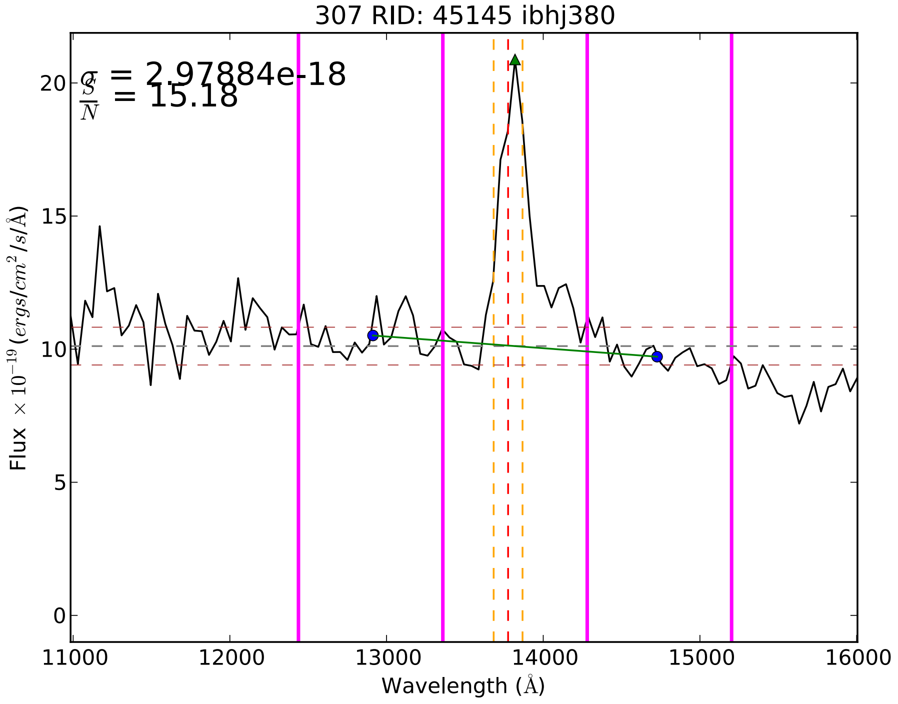
307 RID: 45145 ibhj380
σ = 2.97884e-18
$\frac{S}{N}$ = 15.18
Flux $\times 10^{-19}$ $(ergs/cm^2/s/Å)$
Wavelength (Å)
0
5
10
15
20
11000
12000
13000
14000
15000
16000

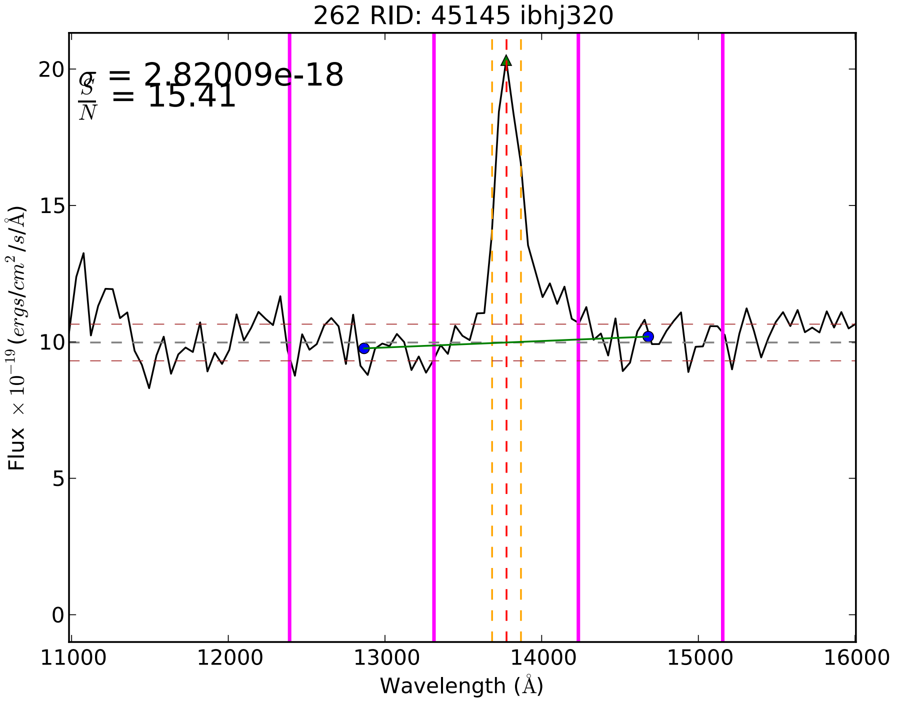
262 RID: 45145 ibhj320
σ = 2.82009e-18
$\frac{S}{N}$ = 15.41
Flux $\times 10^{-19}$ $(ergs/cm^2/s/Å)$
Wavelength (Å)
0
5
10
15
20
11000
12000
13000
14000
15000
16000

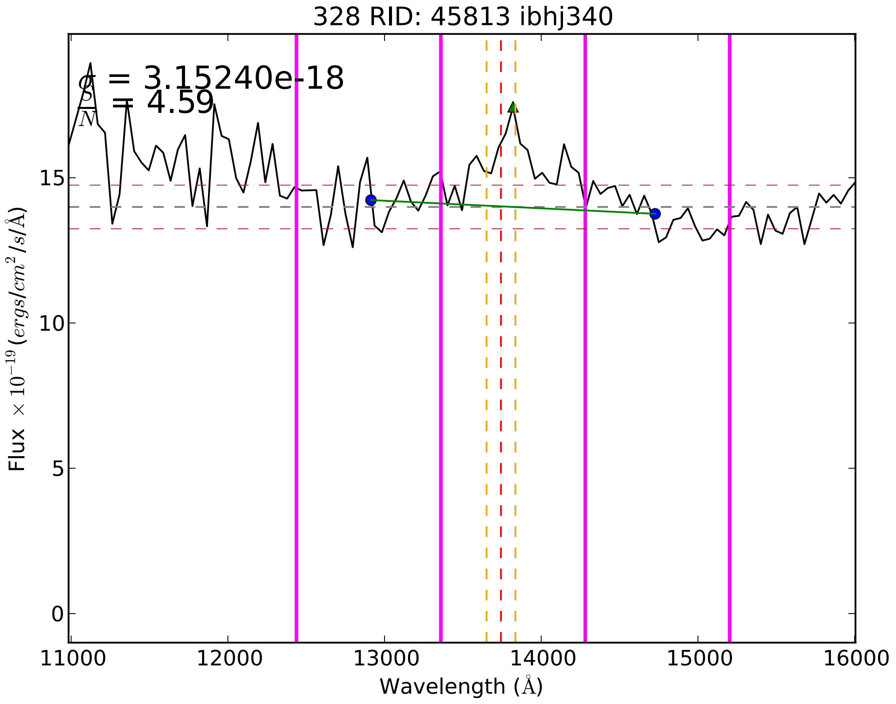
328 RID: 45813 ibhj340
σ = 3.15240e-18
$\frac{S}{N}$ = 4.59
Flux × 10^{-19} $(ergs/cm^2/s/Å)$
Wavelength (Å)
0
5
10
15
11000
12000
13000
14000
15000
16000

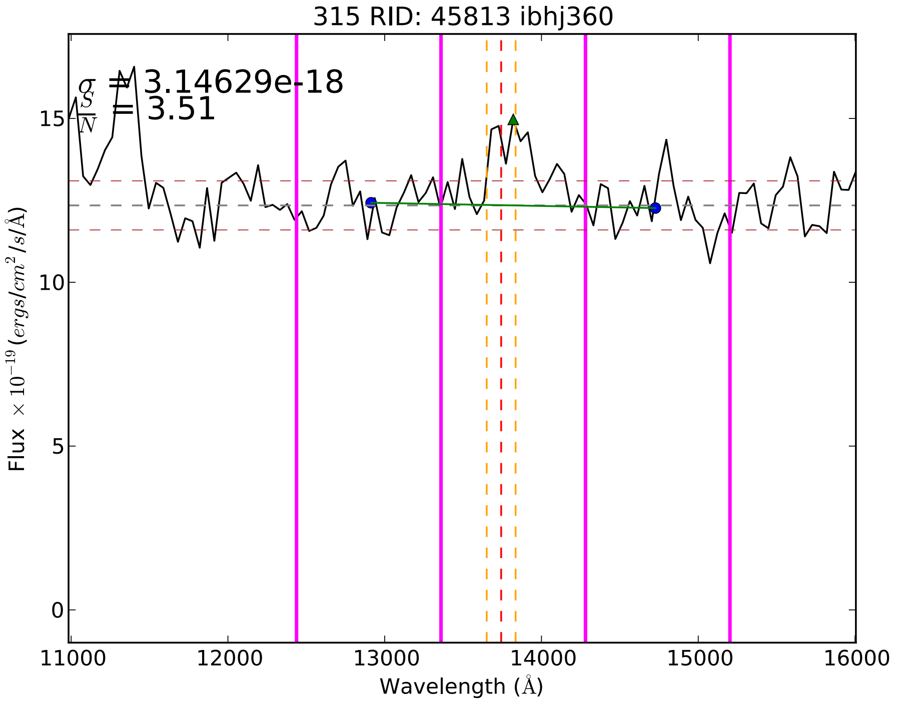
315 RID: 45813 ibhj360
σ = 3.14629e-18
$\frac{S}{N}$ = 3.51
Flux × 10^{-19} $(ergs/cm^2/s/Å)$
Wavelength (Å)
0
5
10
15
11000
12000
13000
14000
15000
16000

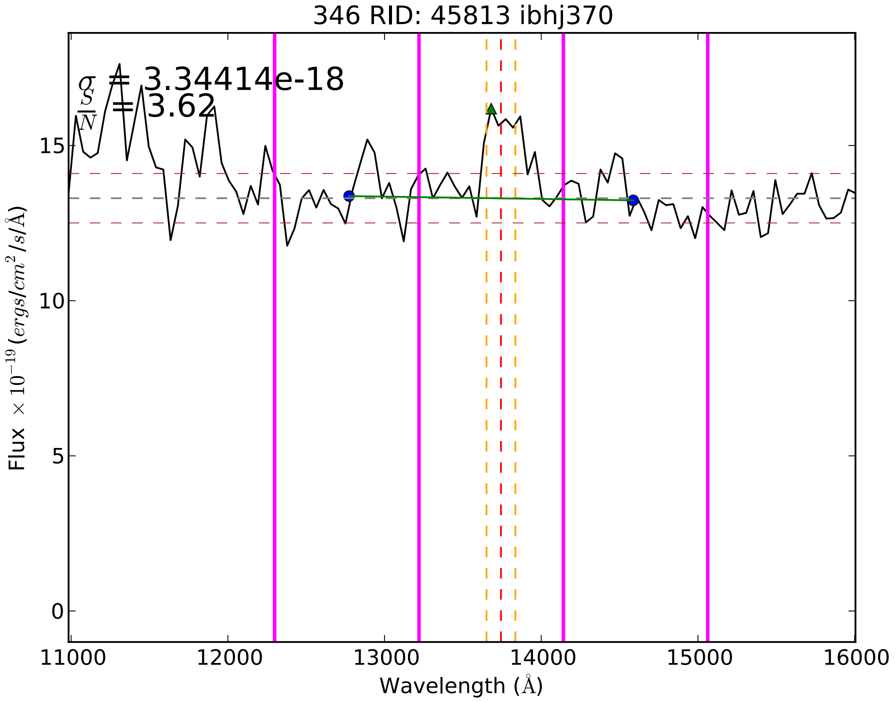
346 RID: 45813 ibhj370
σ = 3.34414e-18
$\frac{S}{N}$ = 3.62
Flux × 10^{-19} $(ergs/cm^2/s/Å)$
Wavelength (Å)
0
5
10
15
11000
12000
13000
14000
15000
16000

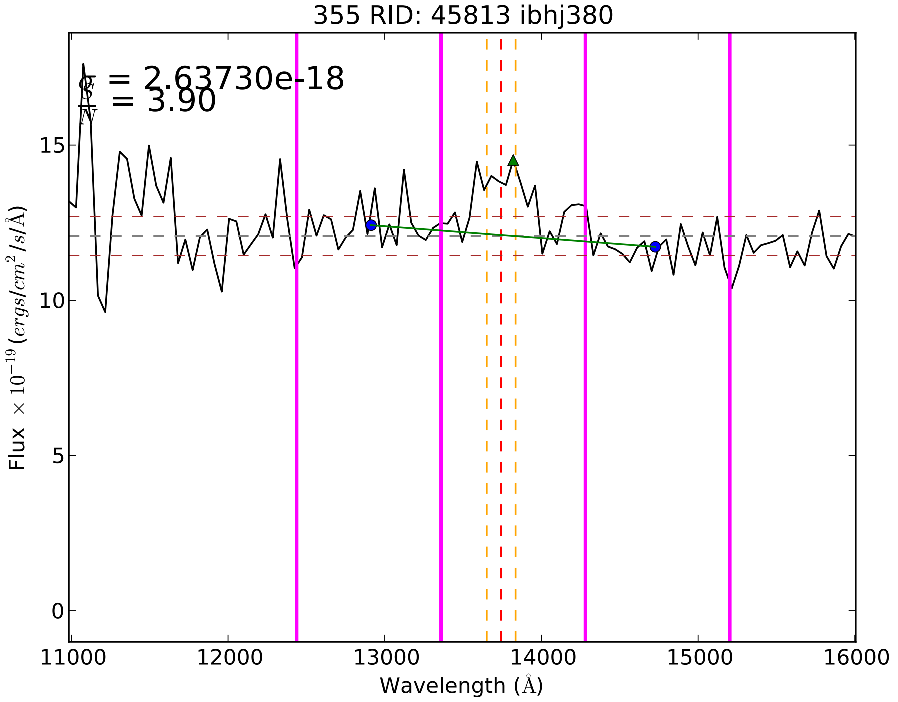
355 RID: 45813 ibhj380
σ = 2.63730e-18
$\frac{S}{N}$ = 3.90
Flux × 10^{-19} $(ergs/cm^2/s/Å)$
Wavelength (Å)
0
5
10
15
11000
12000
13000
14000
15000
16000

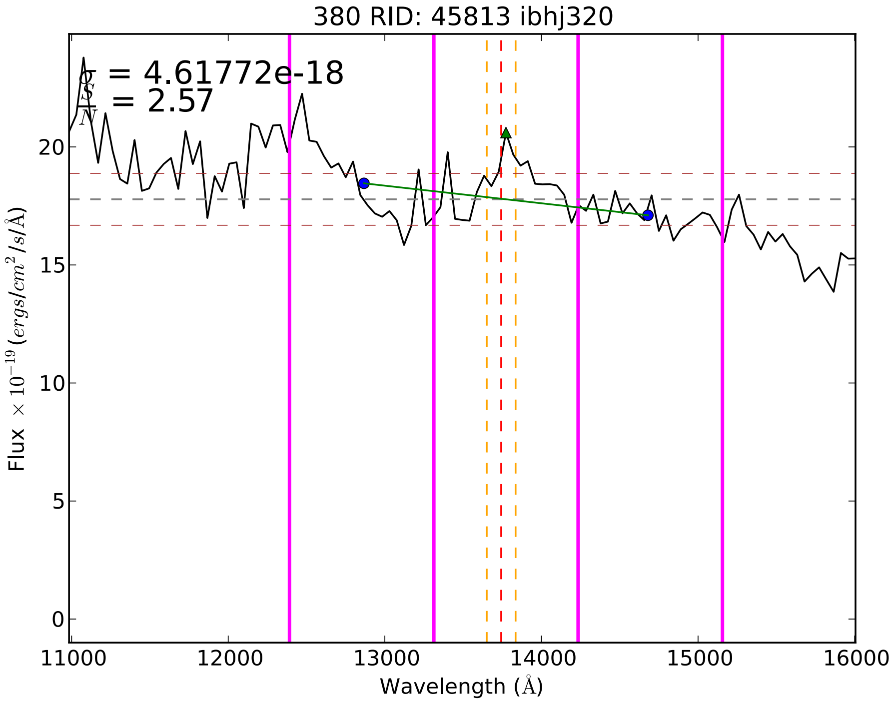

380 RID: 45813 ibhj320
σ = 4.61772e-18
$\frac{S}{N}$ = 2.57
Flux $\times 10^{-19}$ $(ergs/cm^2/s/\AA)$
Wavelength (Å)
0
5
10
15
20
11000
12000
13000
14000
15000
16000

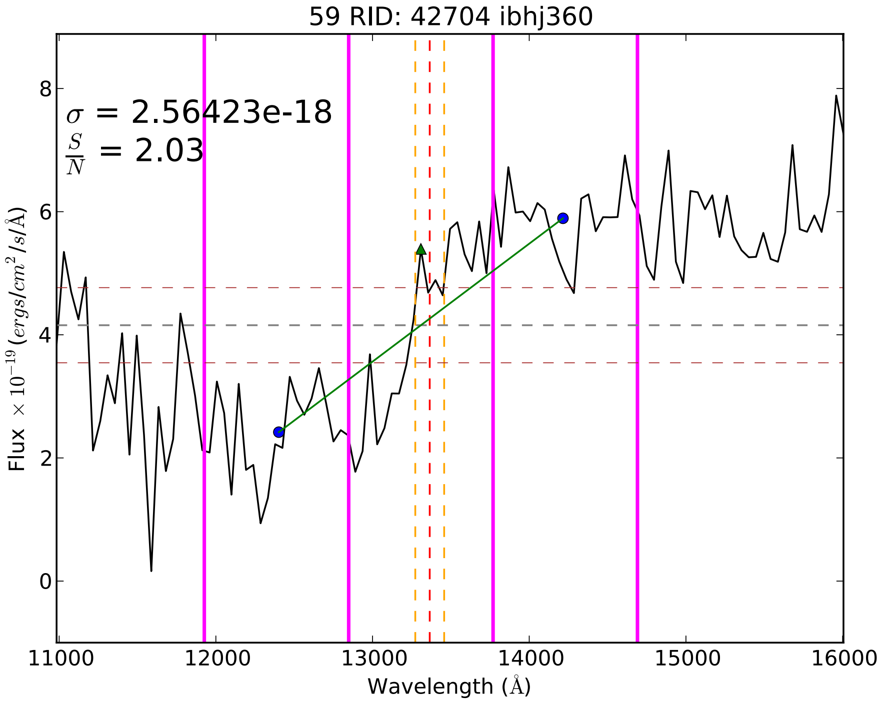
59 RID: 42704 ibhj360
σ = 2.56423e-18
$\frac{S}{N}$ = 2.03
Flux $\times 10^{-19}$ $(ergs/cm^2/s/Å)$
Wavelength (Å)
0
2
4
6
8
11000
12000
13000
14000
15000
16000

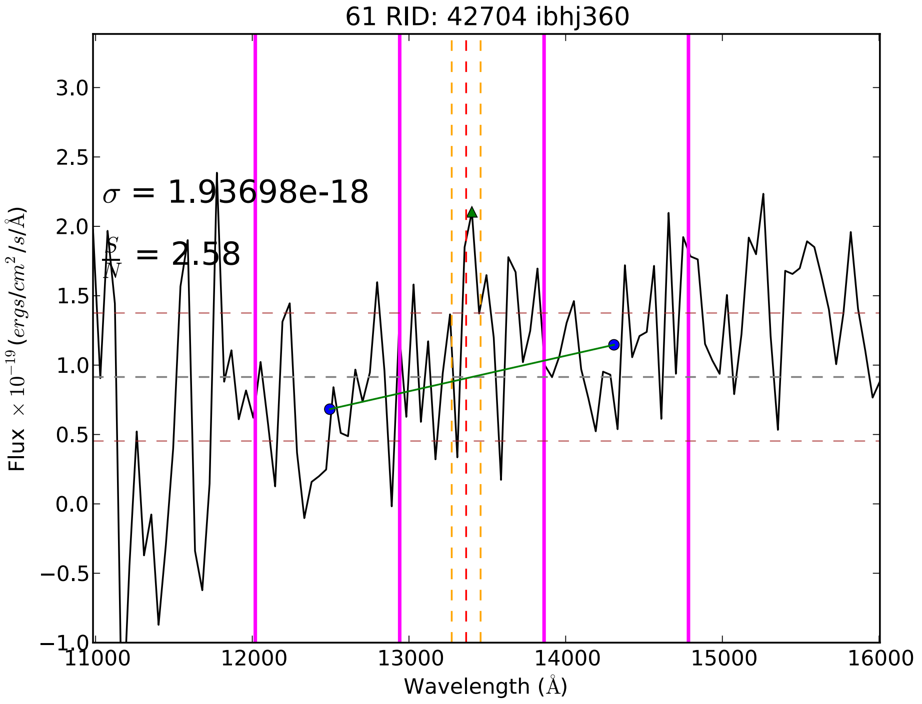
61 RID: 42704 ibhj360
σ = 1.93698e-18
$\frac{S}{N}$ = 2.58
Flux $\times 10^{-19}$ $(ergs/cm^2/s/Å)$
Wavelength (Å)
−1.0
−0.5
0.0
0.5
1.0
1.5
2.0
2.5
3.0
11000
12000
13000
14000
15000
16000

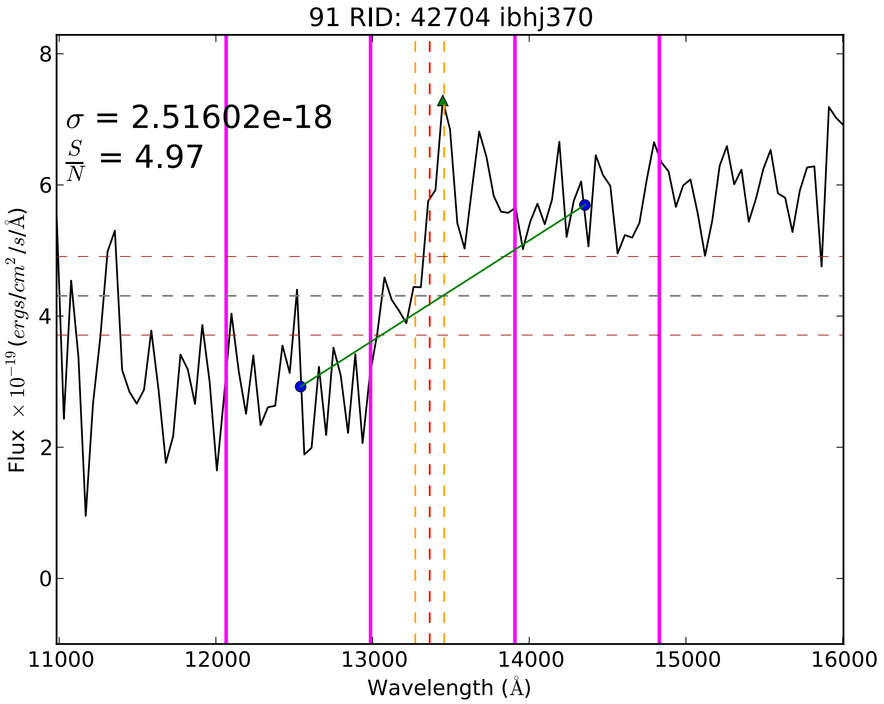
91 RID: 42704 ibhj370
σ = 2.51602e-18
$\frac{S}{N}$ = 4.97
Flux $\times 10^{-19}$ $(ergs/cm^2/s/Å)$
Wavelength (Å)
0
2
4
6
8
11000
12000
13000
14000
15000
16000

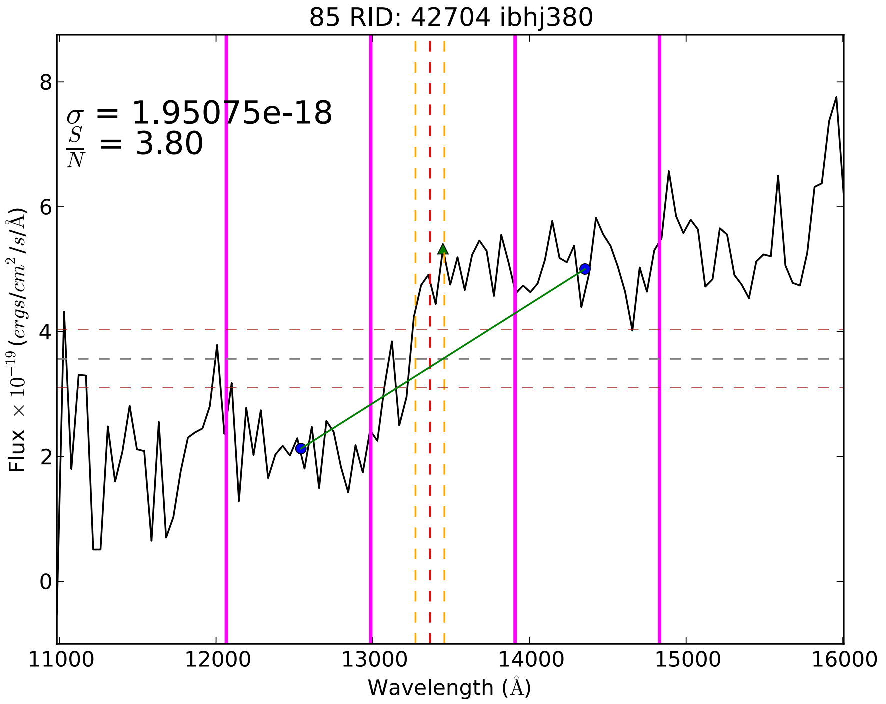
85 RID: 42704 ibhj380
σ = 1.95075e-18
$\frac{S}{N}$ = 3.80
Flux $\times 10^{-19}$ $(ergs/cm^2/s/Å)$
Wavelength (Å)
0
2
4
6
8
11000
12000
13000
14000
15000
16000

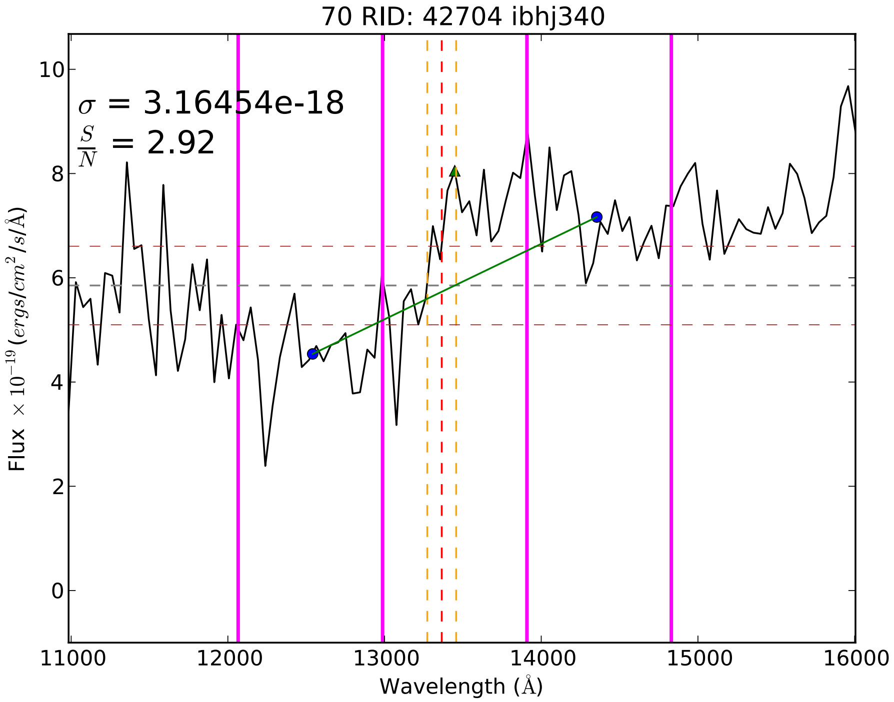
70 RID: 42704 ibhj340
σ = 3.16454e-18
$\frac{S}{N}$ = 2.92
Flux × 10^{-19} $(ergs/cm^2/s/Å)$
Wavelength (Å)
0
2
4
6
8
10
11000
12000
13000
14000
15000
16000

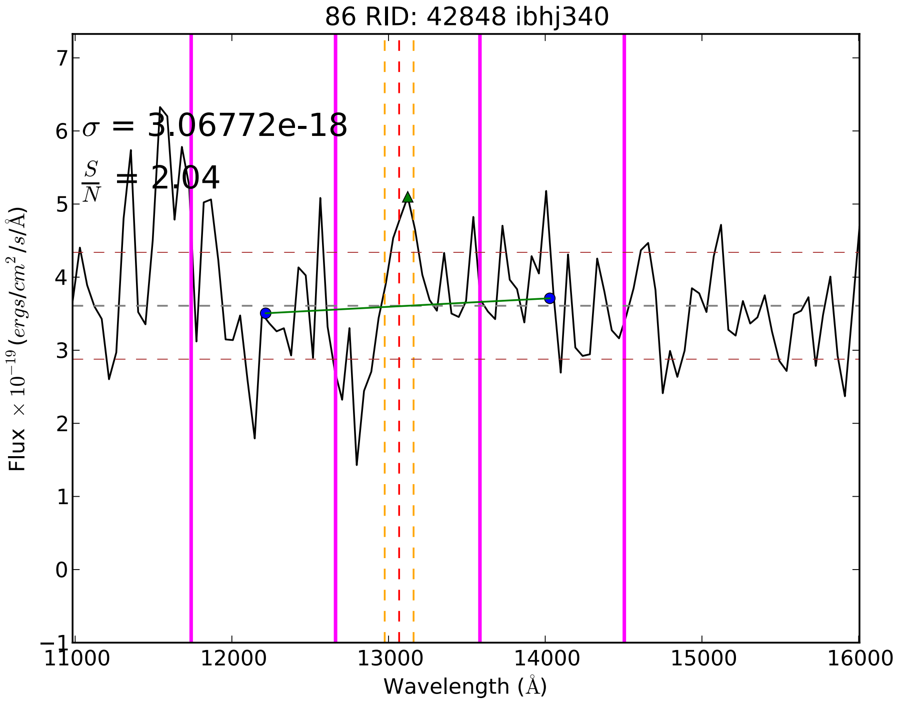
86 RID: 42848 ibhj340

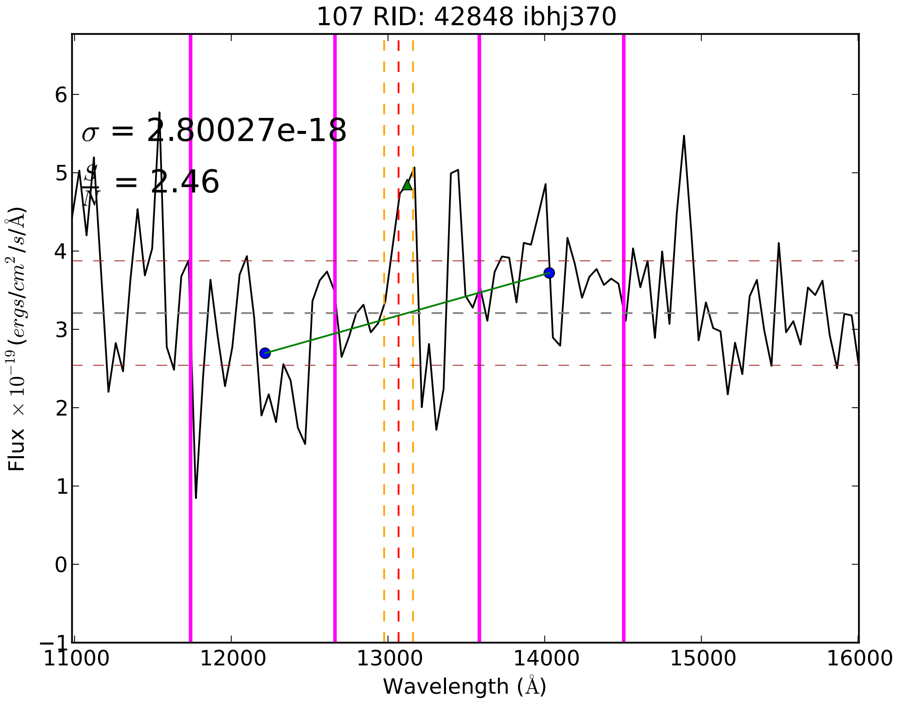
107 RID: 42848 ibhj370

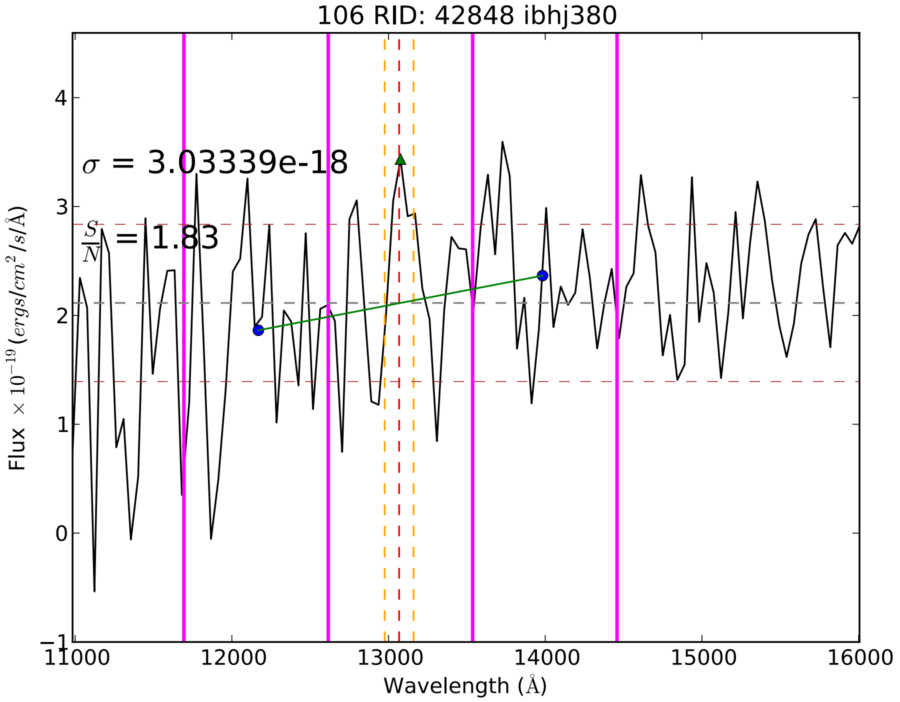
106 RID: 42848 ibhj380

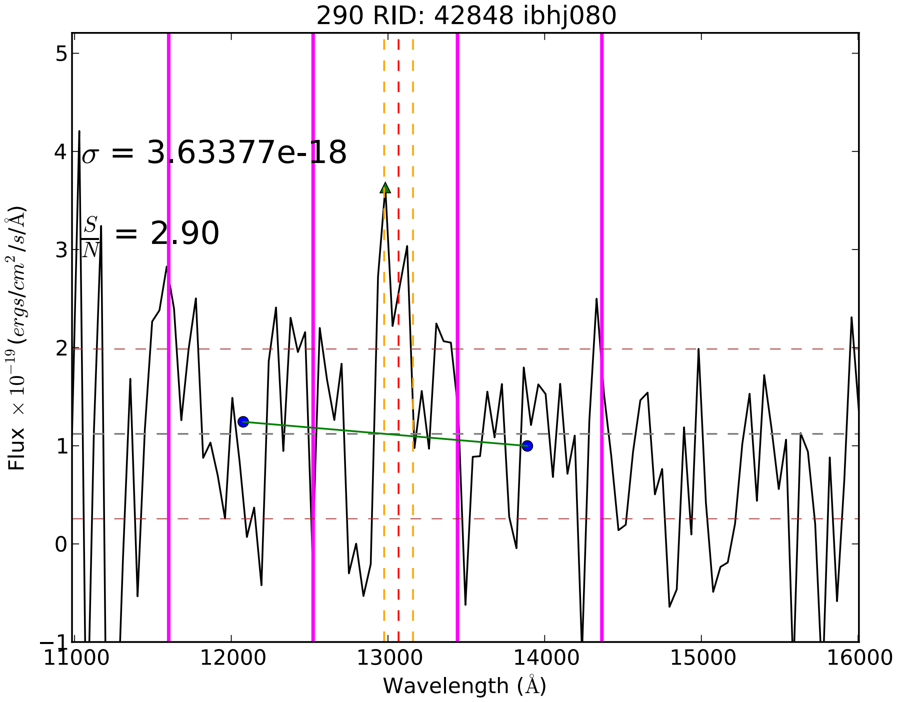
290 RID: 42848 ibhj080

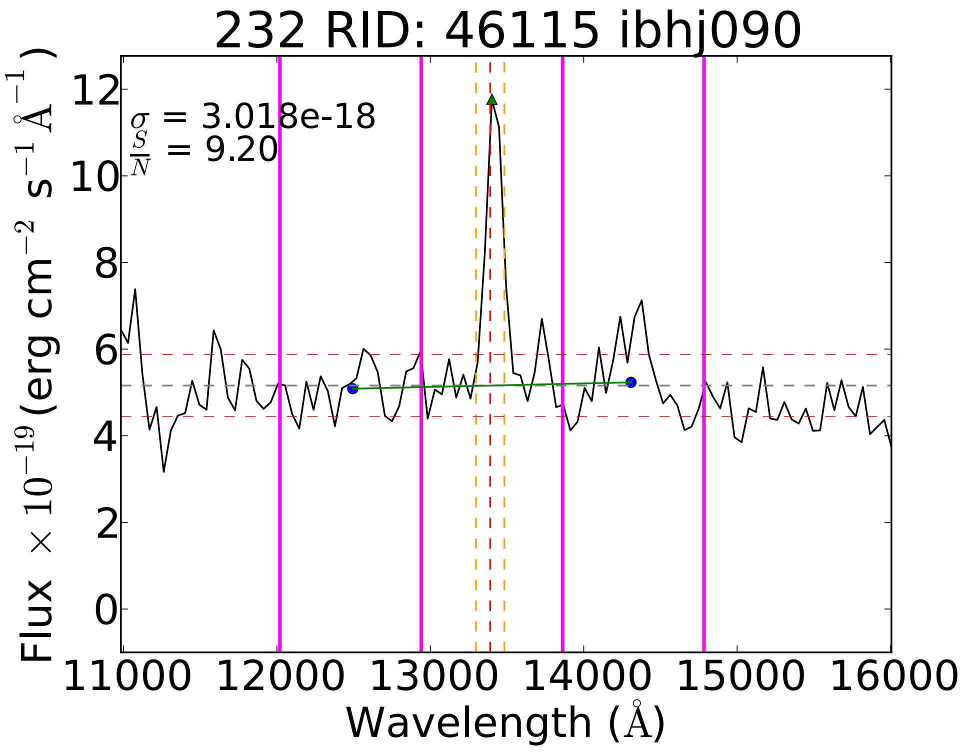
232 RID: 46115 ibhj090
σ = 3.018e-18
S/N = 9.20
Flux × 10⁻¹⁹ (erg cm⁻² s⁻¹ Å⁻¹)
Wavelength (Å)
0
2
4
6
8
10
12
11000
12000
13000
14000
15000
16000

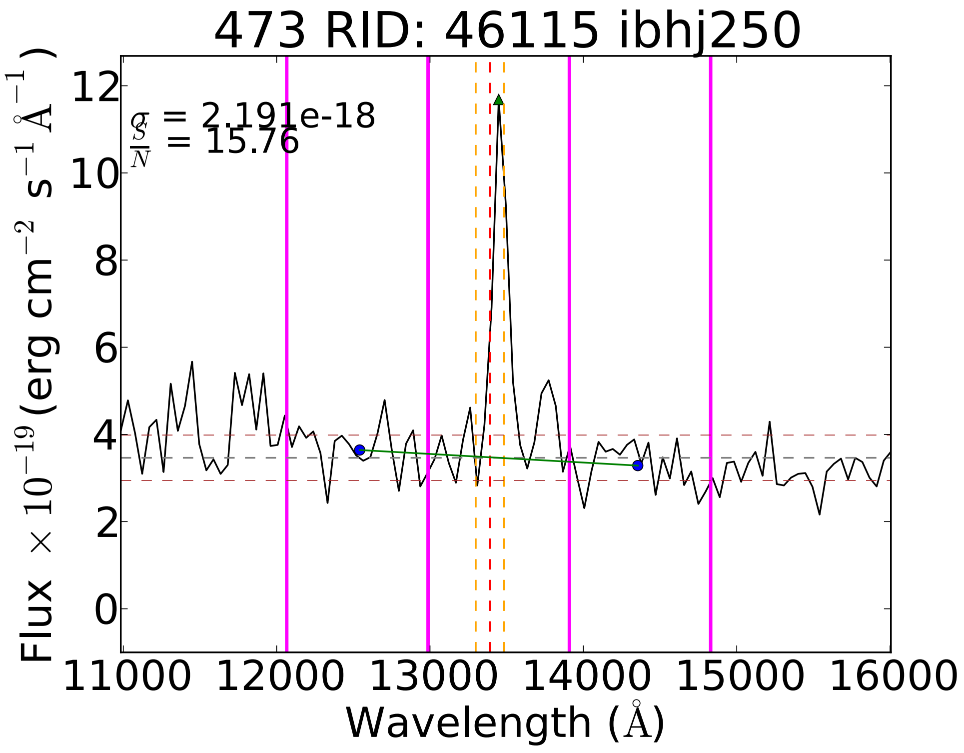
473 RID: 46115 ibhj250
σ = 2.191e-18
S/N = 15.76
Flux × 10⁻¹⁹ (erg cm⁻² s⁻¹ Å⁻¹)
Wavelength (Å)
0
2
4
6
8
10
12
11000
12000
13000
14000
15000
16000

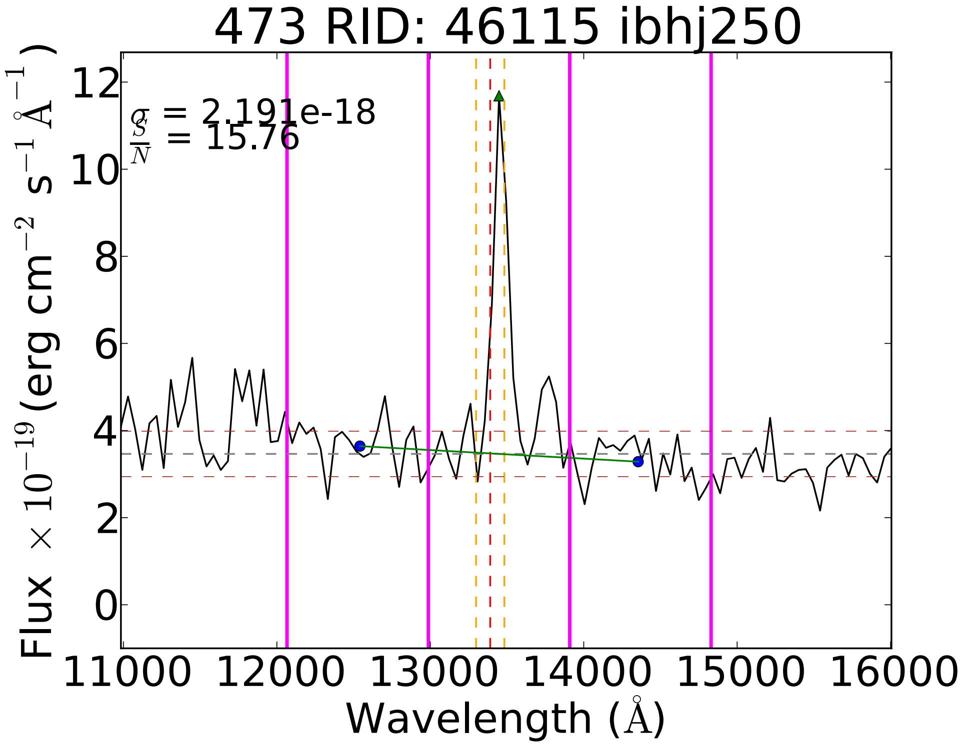
473 RID: 46115 ibhj250
σ = 2.191e-18
S/N = 15.76
Flux × 10⁻¹⁹ (erg cm⁻² s⁻¹ Å⁻¹)
Wavelength (Å)
0
2
4
6
8
10
12
11000
12000
13000
14000
15000
16000

Appendix C

Rejected Spectra

Presented here are plots of all the spectra that were rejected from our sample. The lines and symbols have the same meaning as in the previous appendix.

C1: The following spectra were rejected because the continuum was skew:

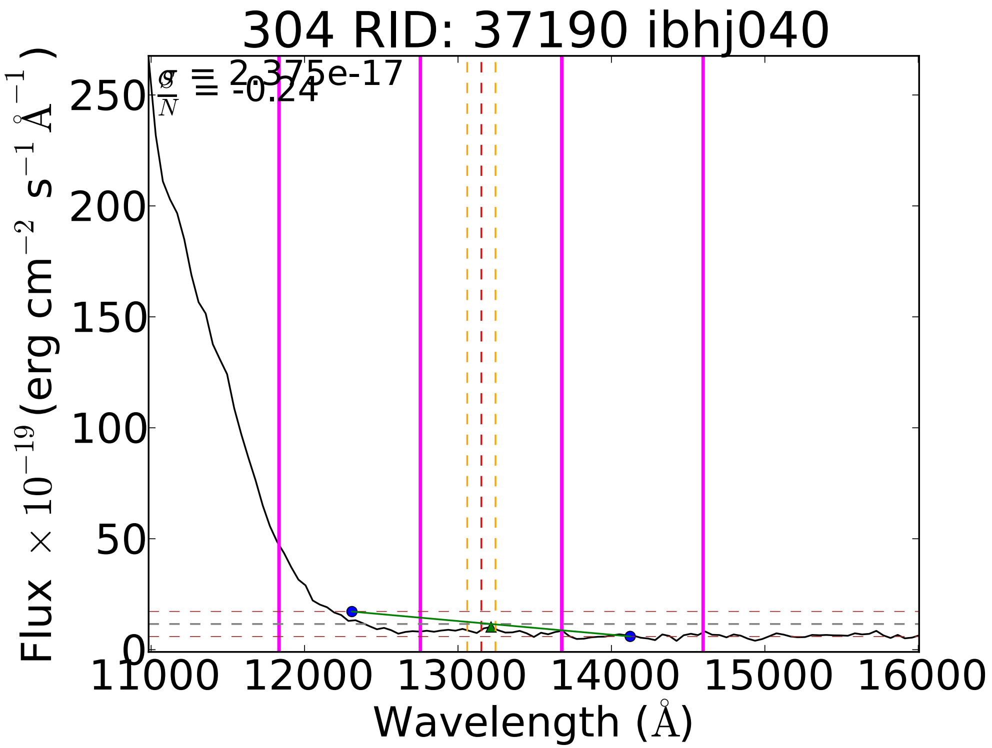
304 RID: 37190 ibhj040

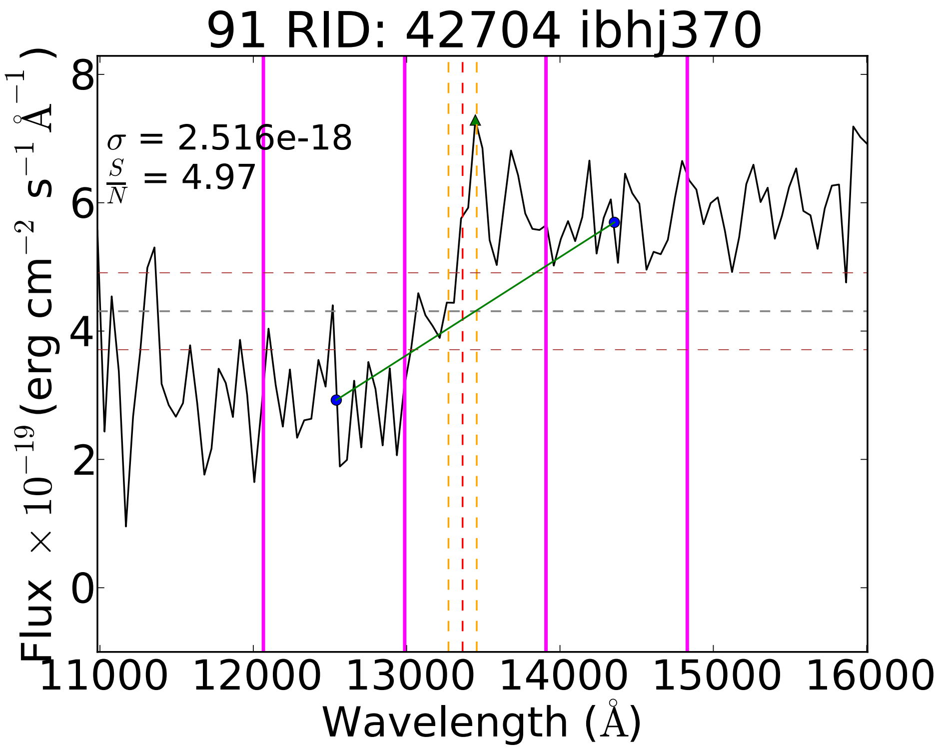
91 RID: 42704 ibhj370

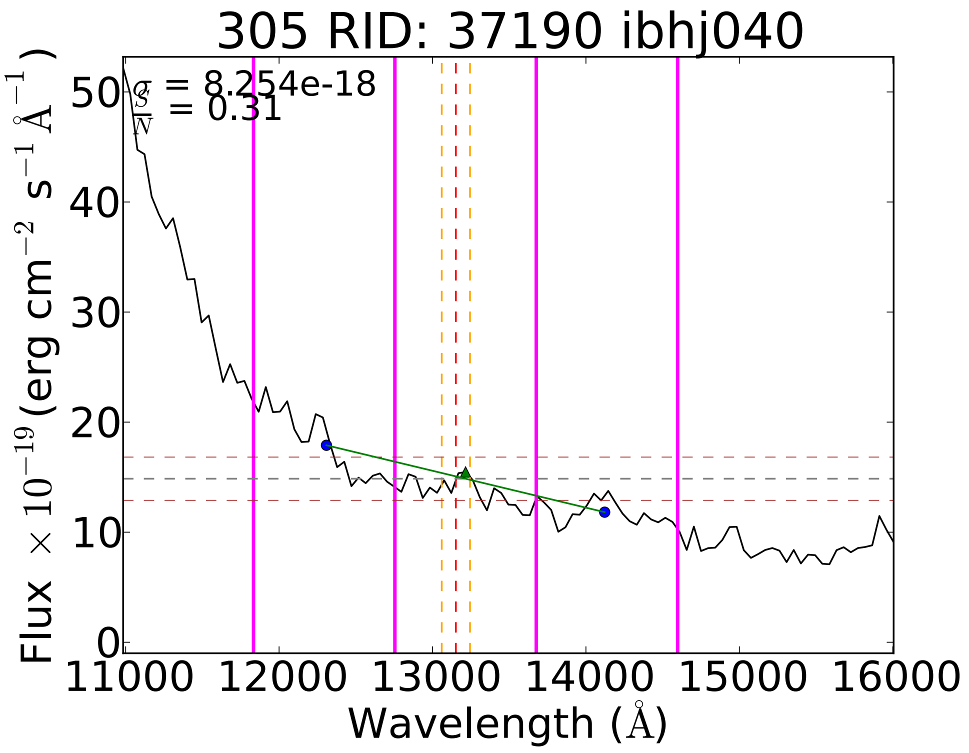
305 RID: 37190 ibhj040

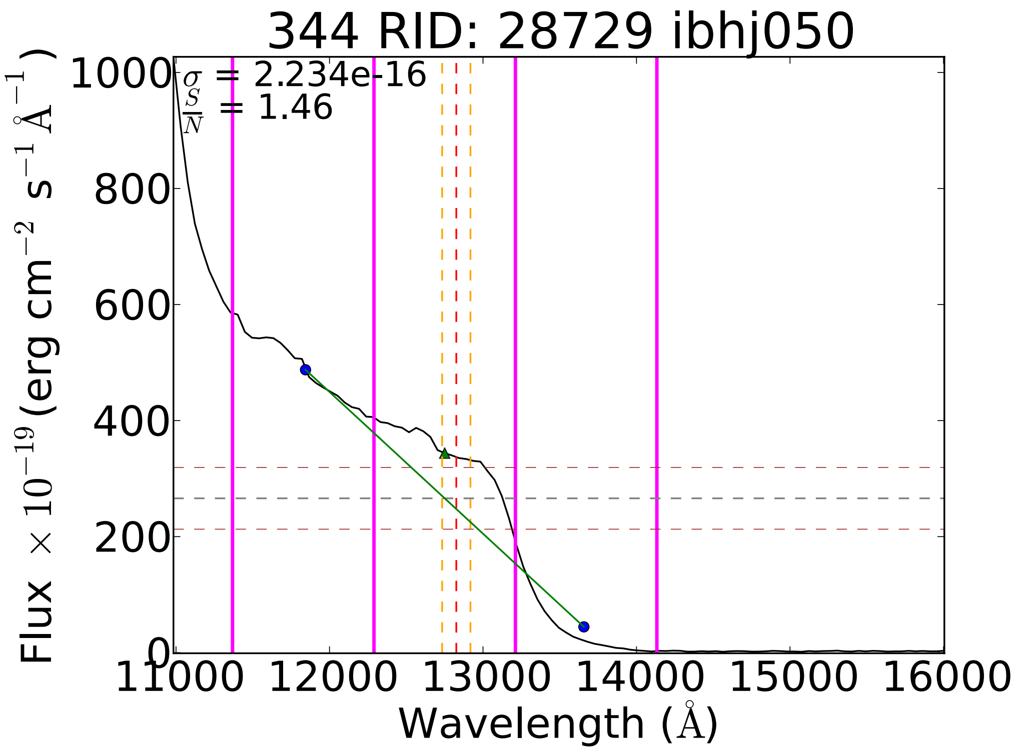
344 RID: 28729 ibhj050

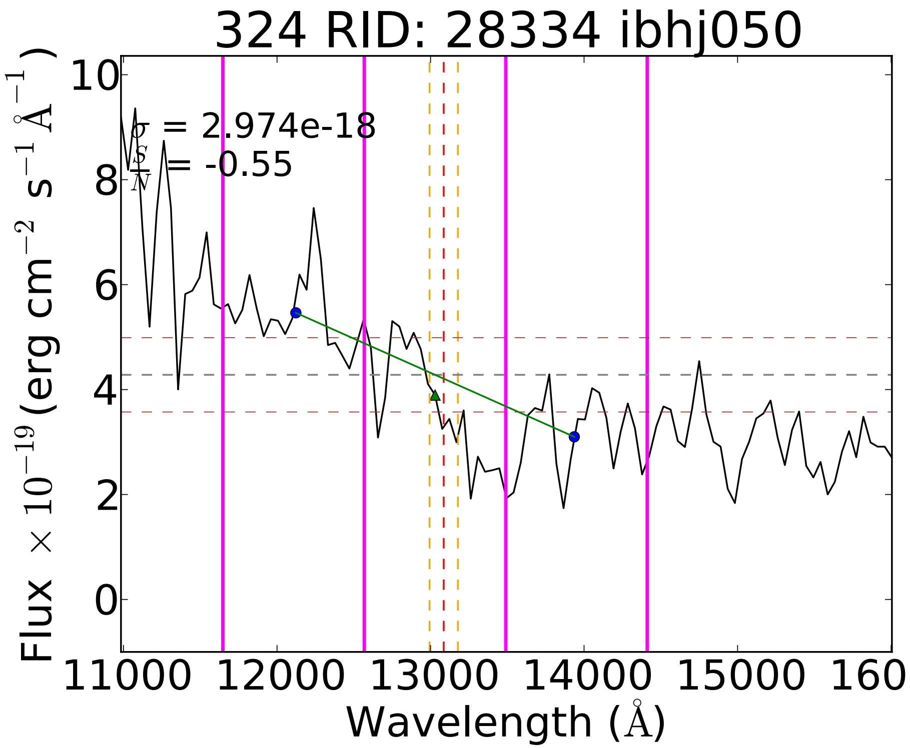
324 RID: 28334 ibhj050
σ = 2.974e-18
S/N = -0.55
Flux × 10^-19 (erg cm^-2 s^-1 Å^-1)
Wavelength (Å)
0
2
4
6
8
10
11000
12000
13000
14000
15000
16000

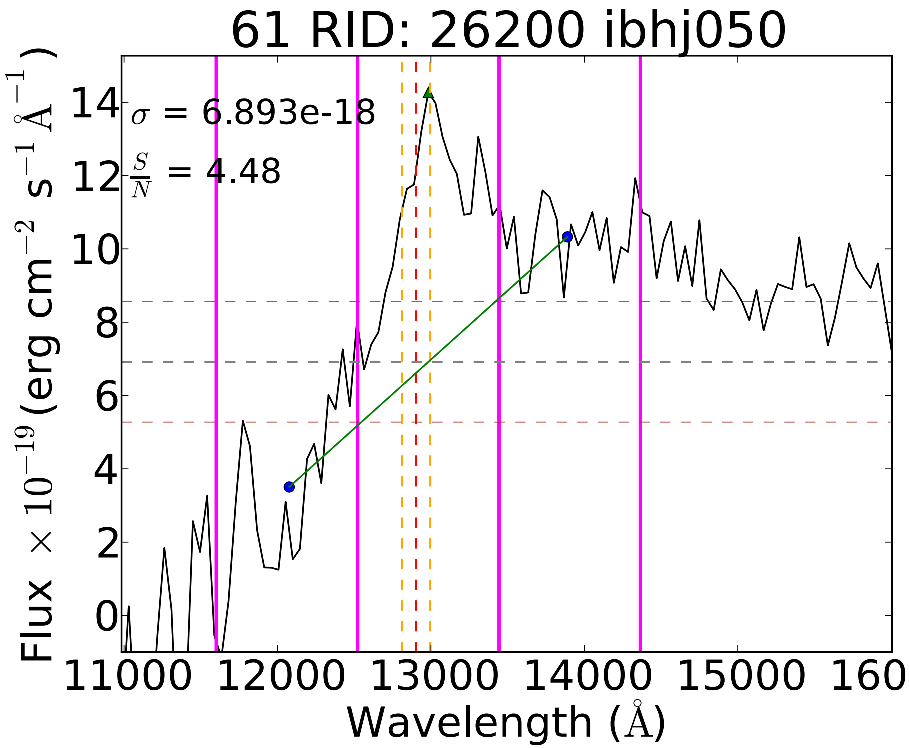
61 RID: 26200 ibhj050
σ = 6.893e-18
S/N = 4.48
Flux × 10^-19 (erg cm^-2 s^-1 Å^-1)
Wavelength (Å)
0
2
4
6
8
10
12
14
11000
12000
13000
14000
15000
16000

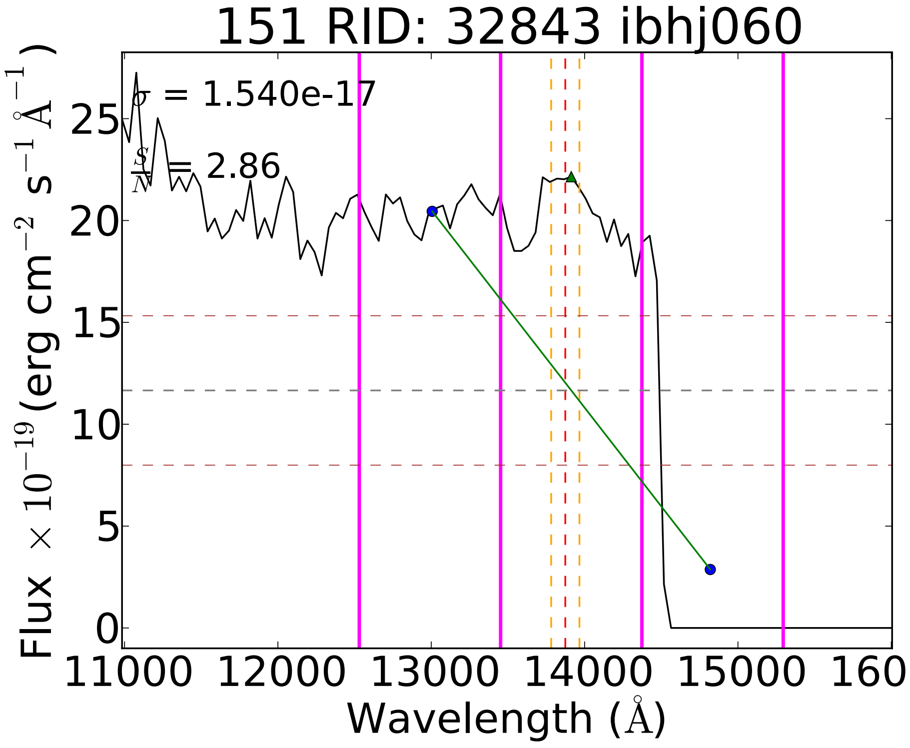
151 RID: 32843 ibhj060
σ = 1.540e-17
S/N = 2.86
Flux × 10^-19 (erg cm^-2 s^-1 Å^-1)
Wavelength (Å)
0
5
10
15
20
25
11000
12000
13000
14000
15000
16000

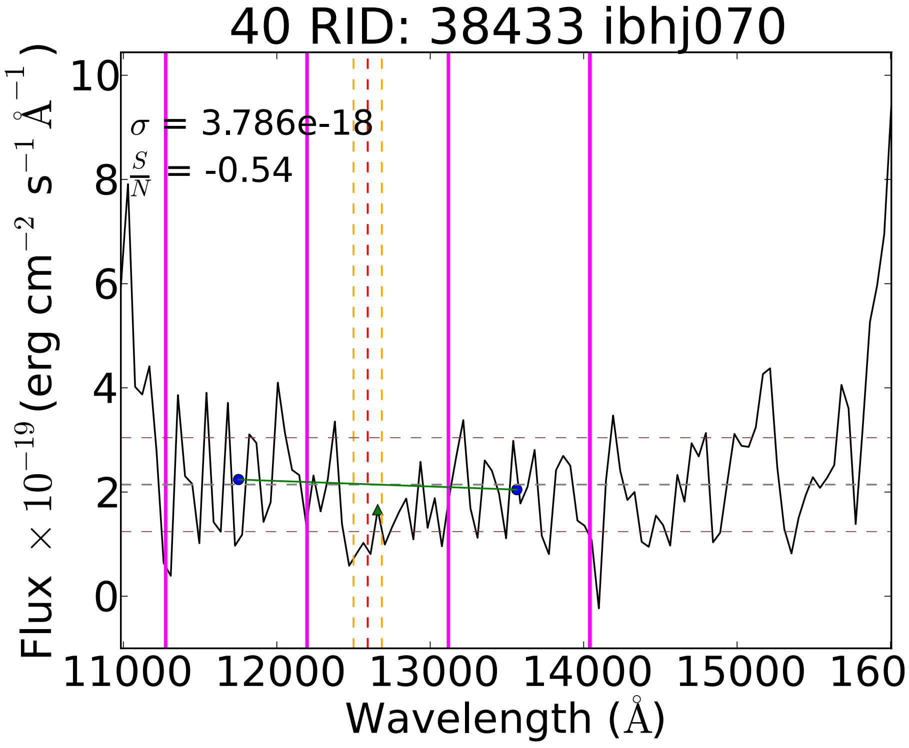
40 RID: 38433 ibhj070
σ = 3.786e-18
S/N = -0.54
Flux × 10^-19 (erg cm^-2 s^-1 Å^-1)
Wavelength (Å)
0
2
4
6
8
10
11000
12000
13000
14000
15000
16000

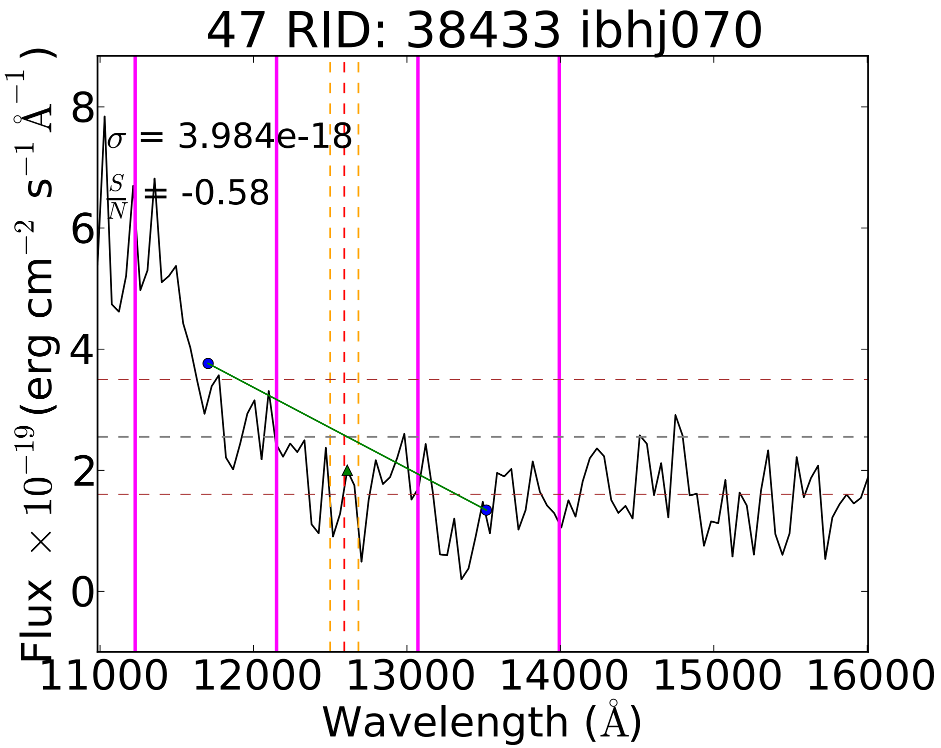
47 RID: 38433 ibhj070
σ = 3.984e-18
S/N = -0.58
Flux × 10^-19 (erg cm^-2 s^-1 Å^-1)
Wavelength (Å)
0
2
4
6
8
11000
12000
13000
14000
15000
16000

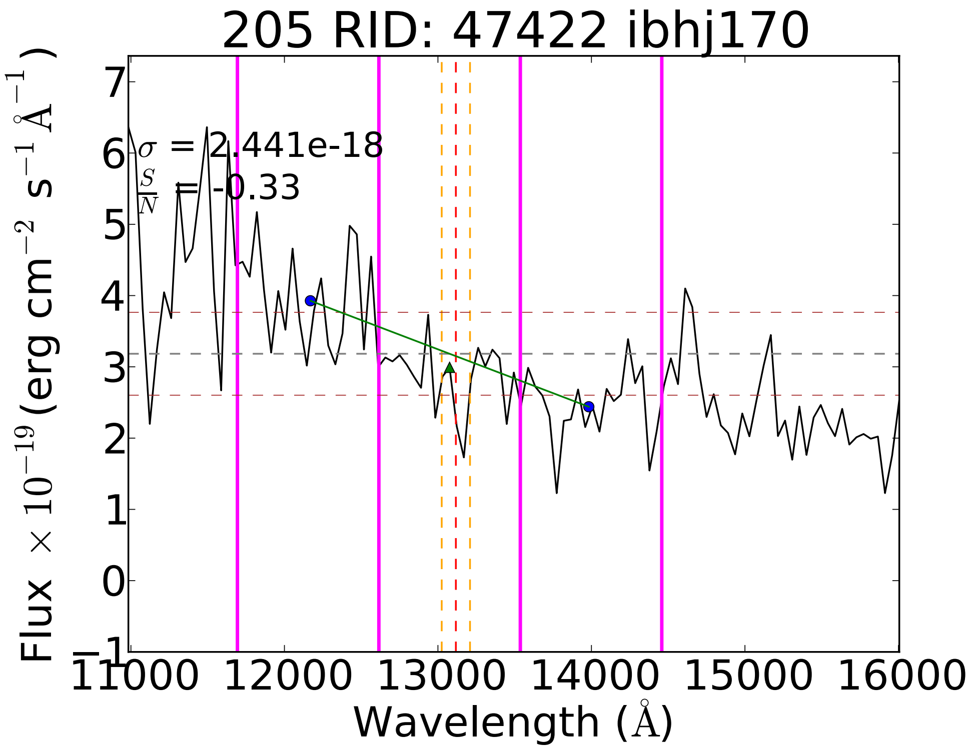
205 RID: 47422 ibhj170
σ = 2.441e-18
S/N = -0.33
Flux × 10^-19 (erg cm^-2 s^-1 Å^-1)
Wavelength (Å)
−1
0
1
2
3
4
5
6
7
11000
12000
13000
14000
15000
16000

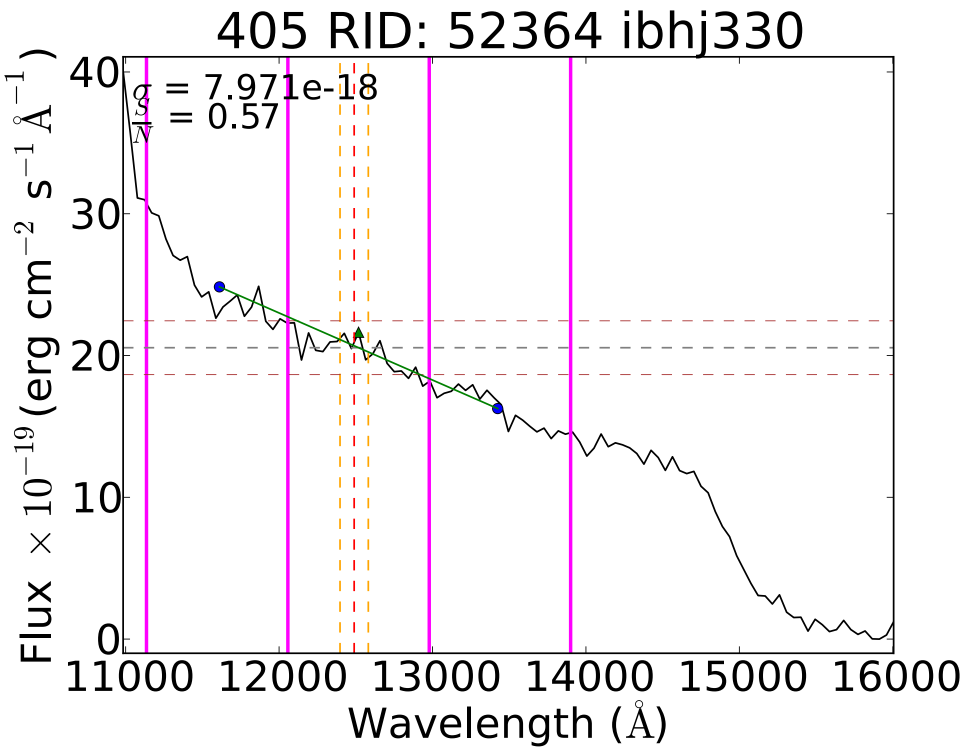
405 RID: 52364 ibhj330
σ = 7.971e-18
S/N = 0.57
Flux × 10^-19 (erg cm^-2 s^-1 Å^-1)
Wavelength (Å)
0
10
20
30
40
11000
12000
13000
14000
15000
16000

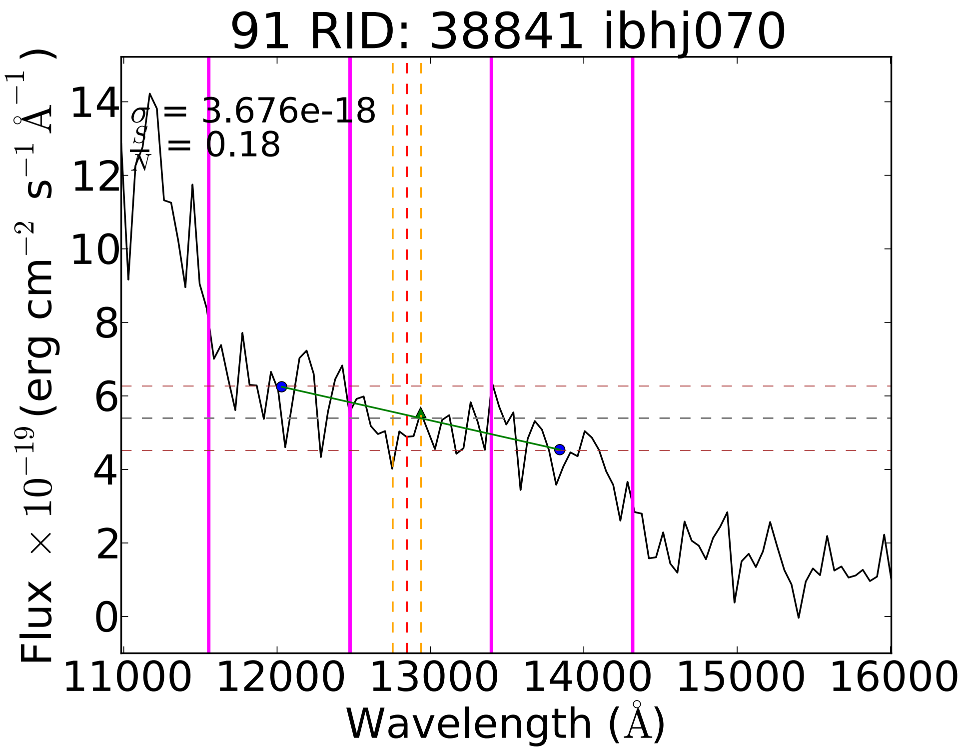
91 RID: 38841 ibhj070
σ = 3.676e-18
S/N = 0.18
Flux × 10^-19 (erg cm^-2 s^-1 Å^-1)
Wavelength (Å)
0
2
4
6
8
10
12
14
11000
12000
13000
14000
15000
16000

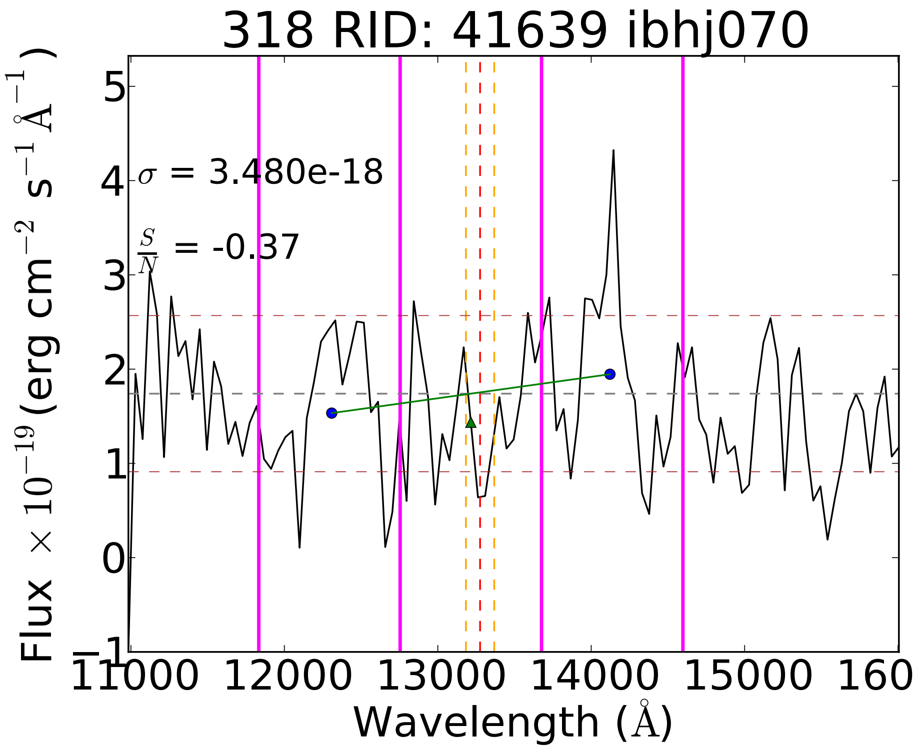
318 RID: 41639 ibhj070

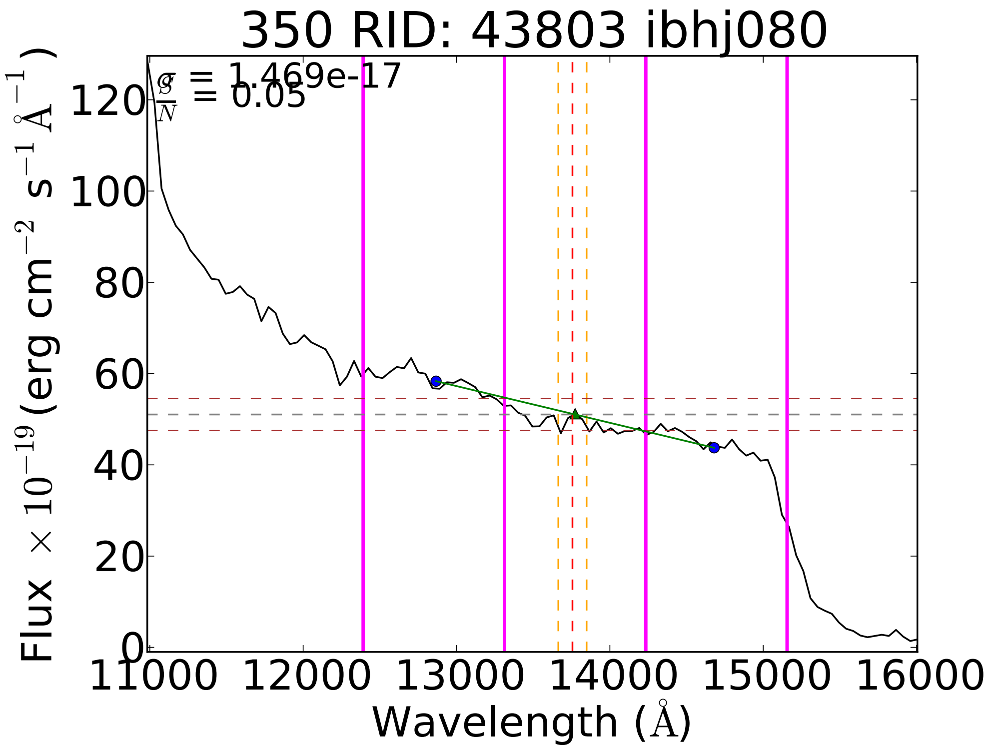
350 RID: 43803 ibhj080

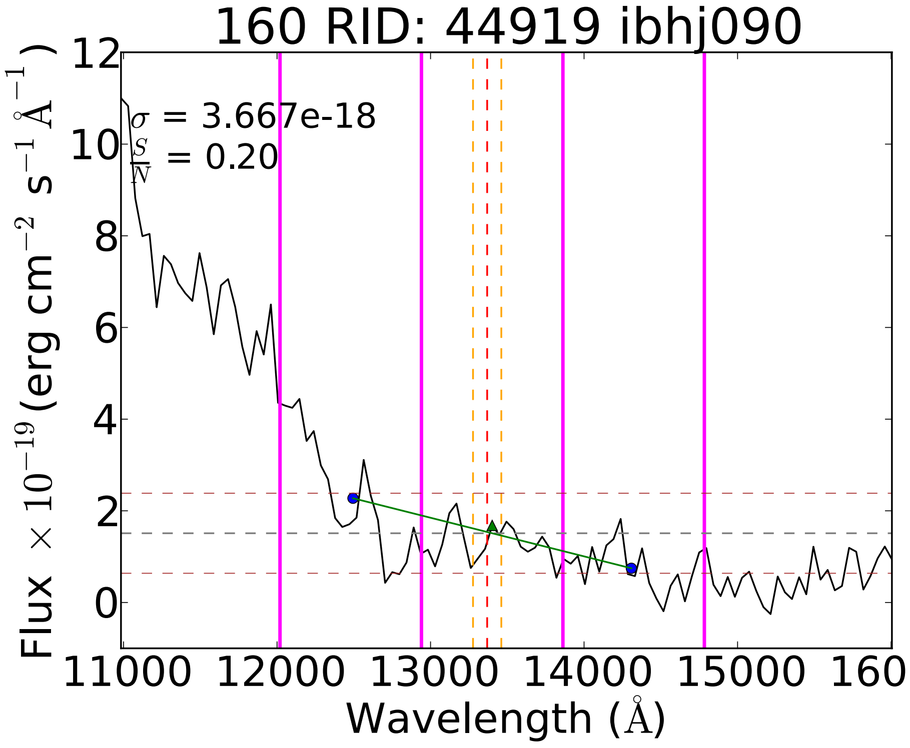
160 RID: 44919 ibhj090

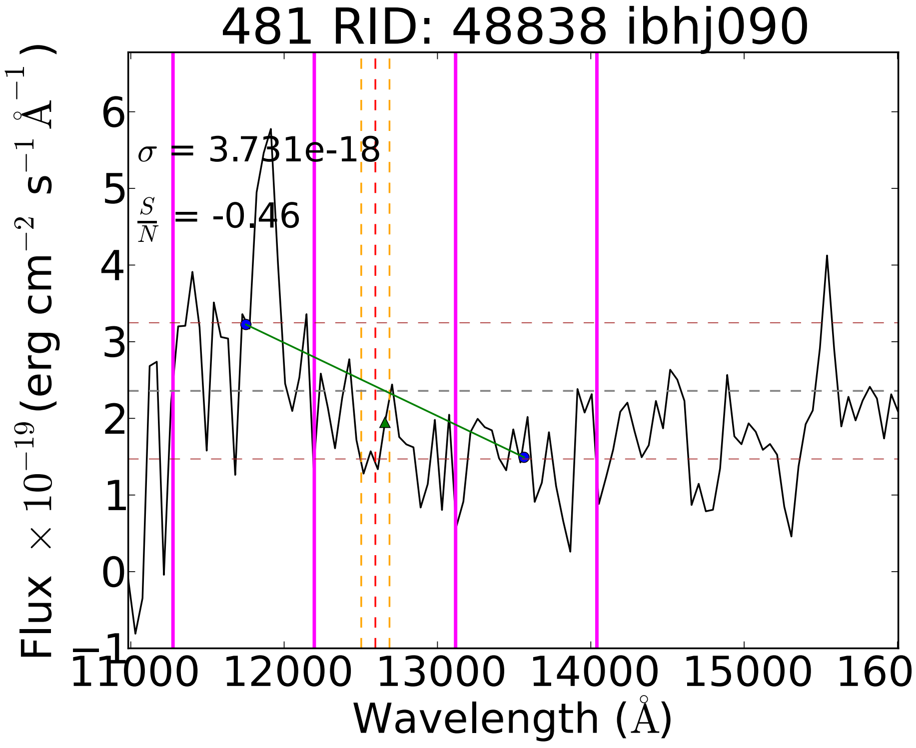
481 RID: 48838 ibhj090

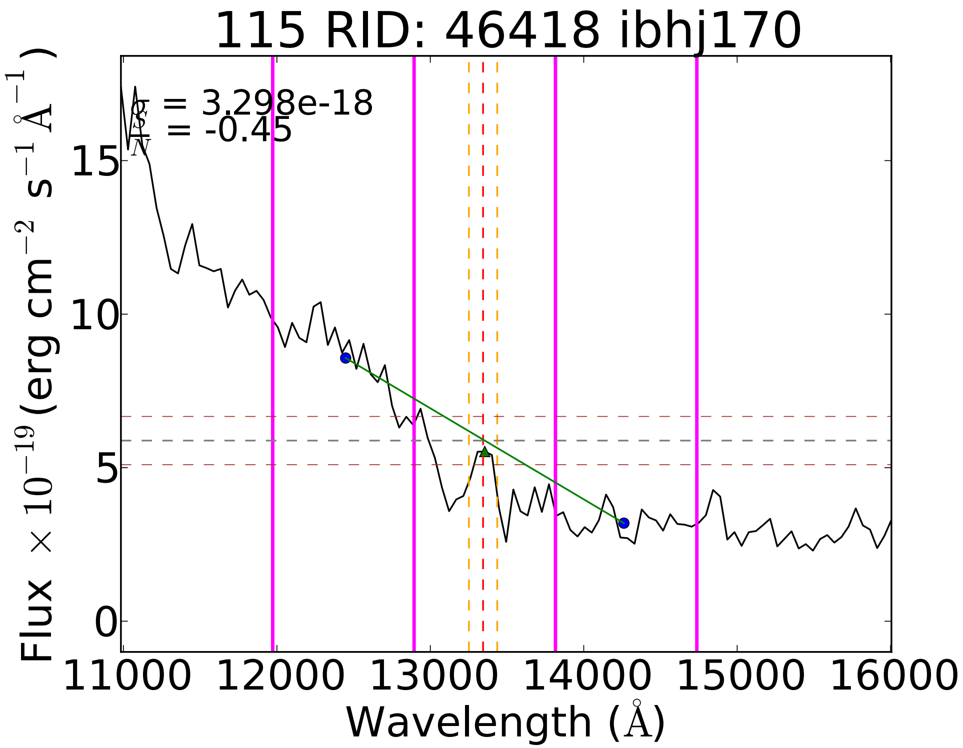
115 RID: 46418 ibhj170

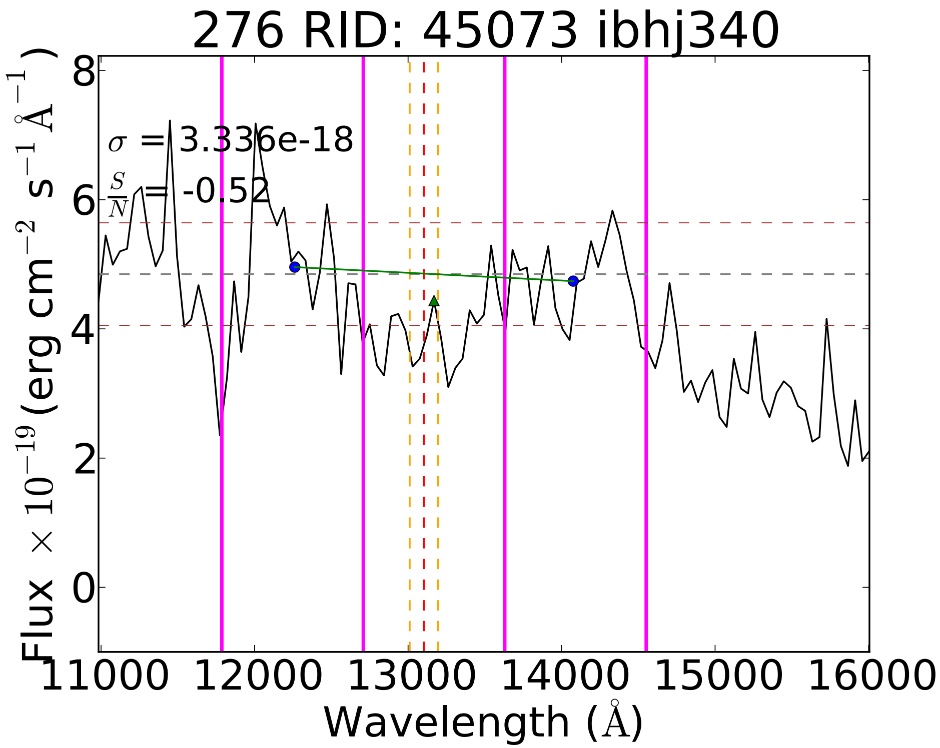
276 RID: 45073 ibhj340

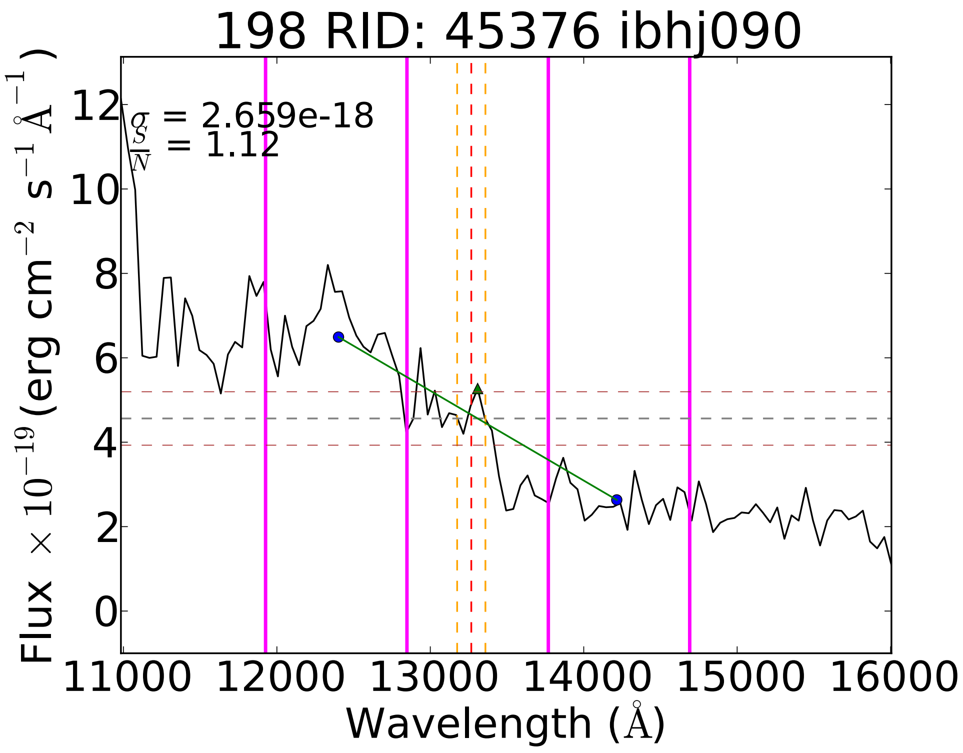
198 RID: 45376 ibhj090

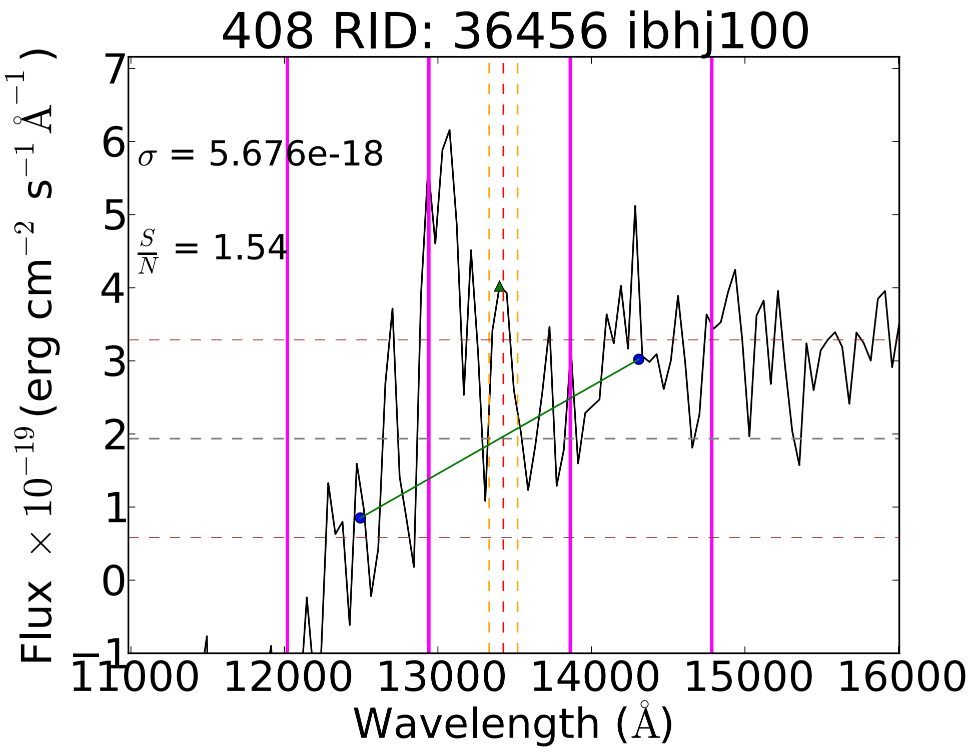
408 RID: 36456 ibhj100

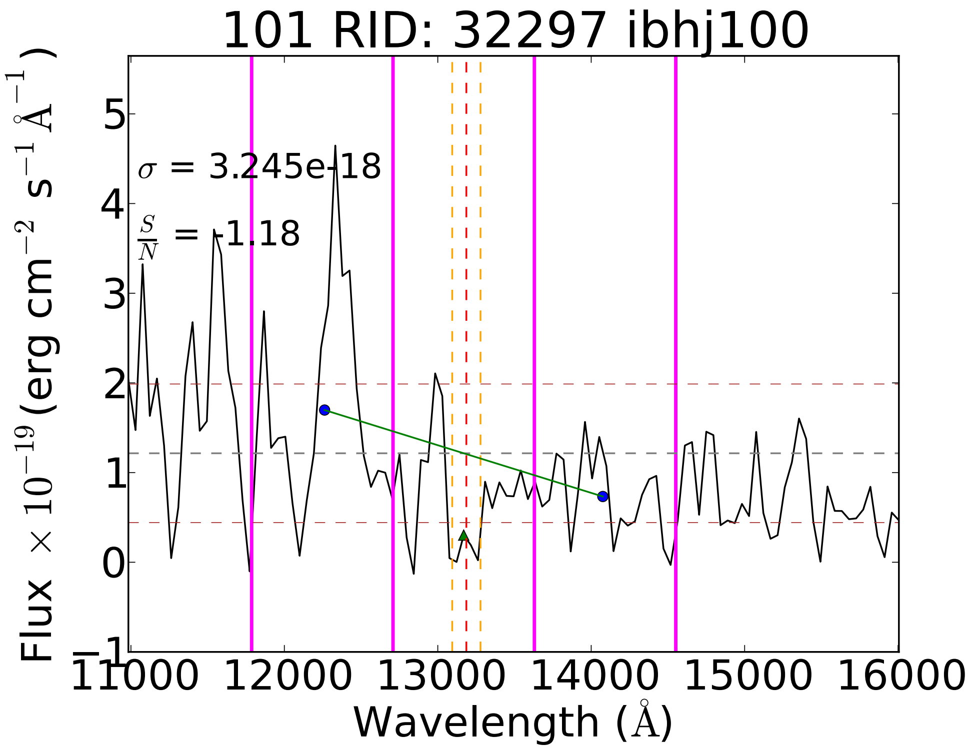
101 RID: 32297 ibhj100

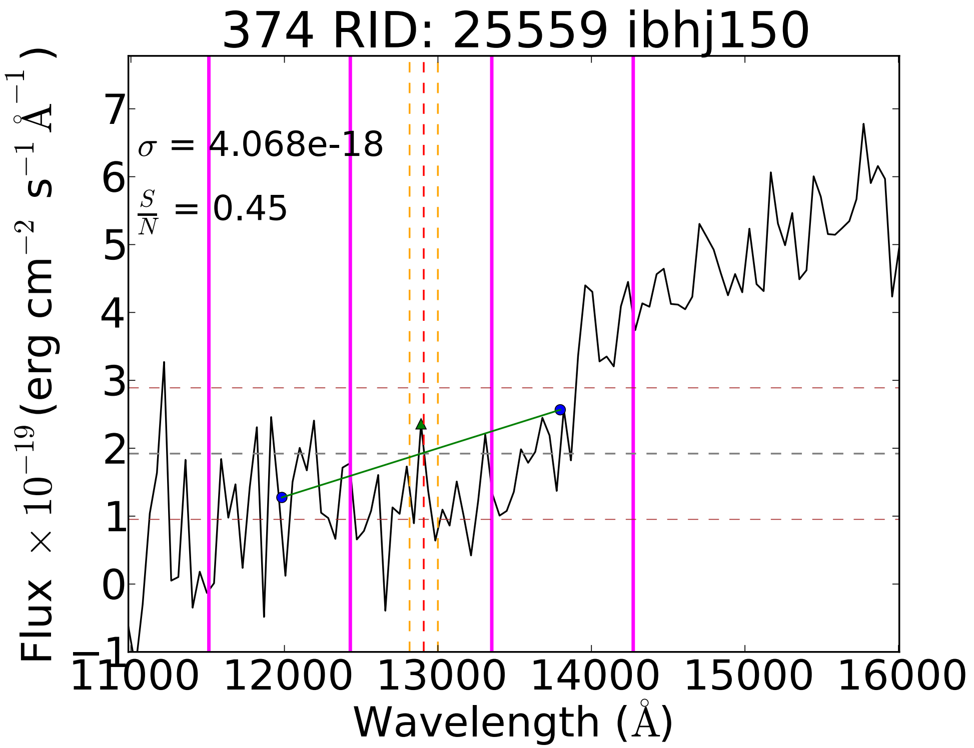
374 RID: 25559 ibhj150

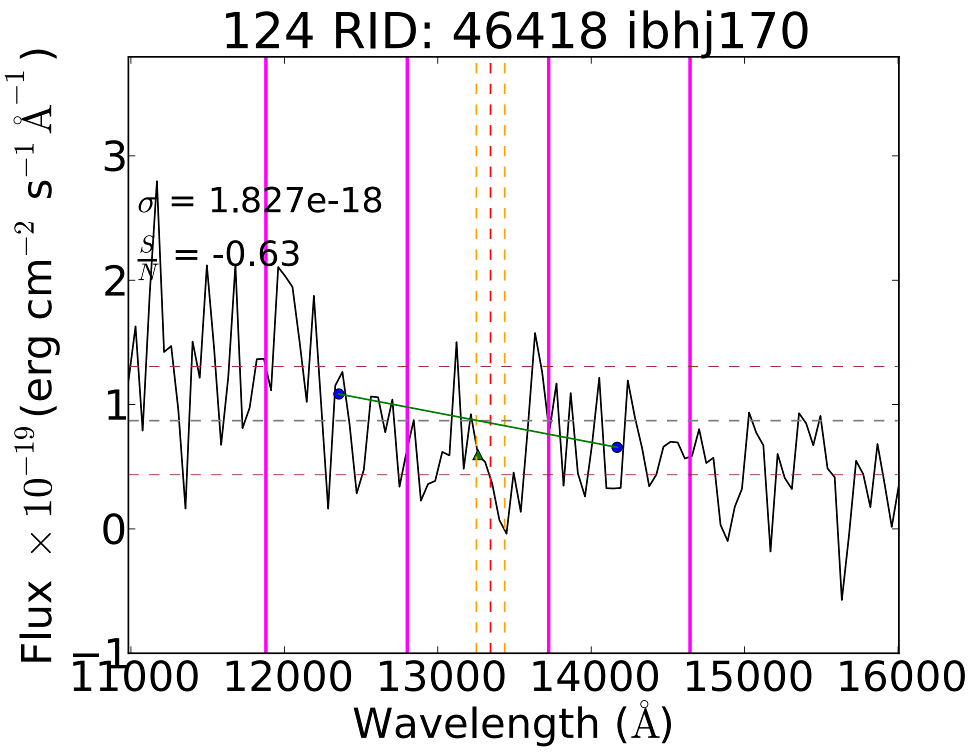
124 RID: 46418 ibhj170

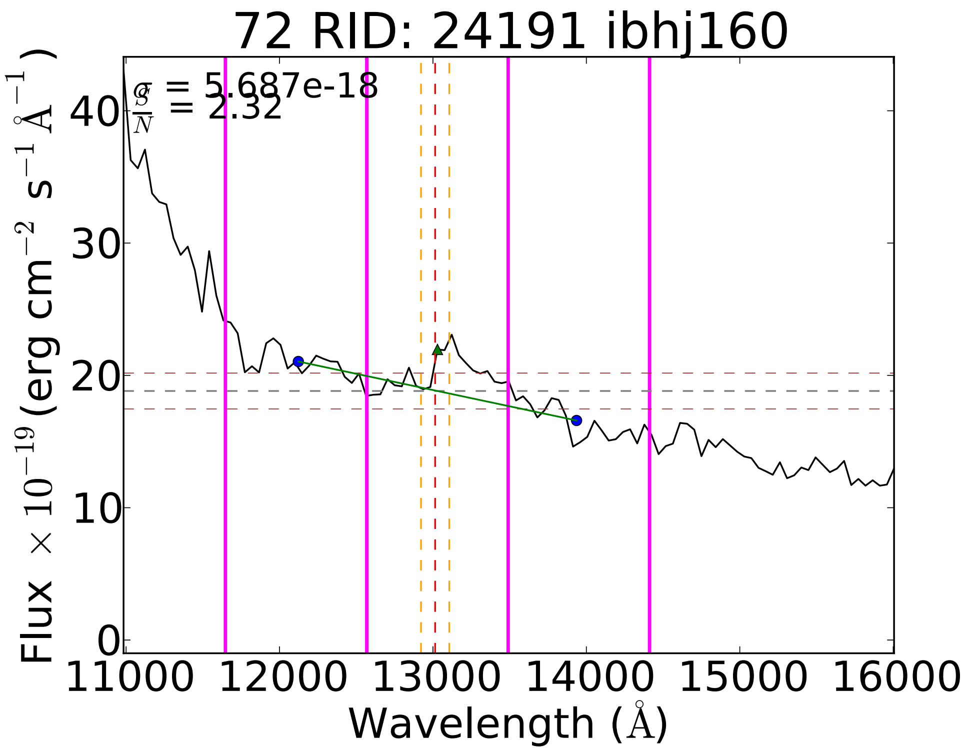
72 RID: 24191 ibhj160

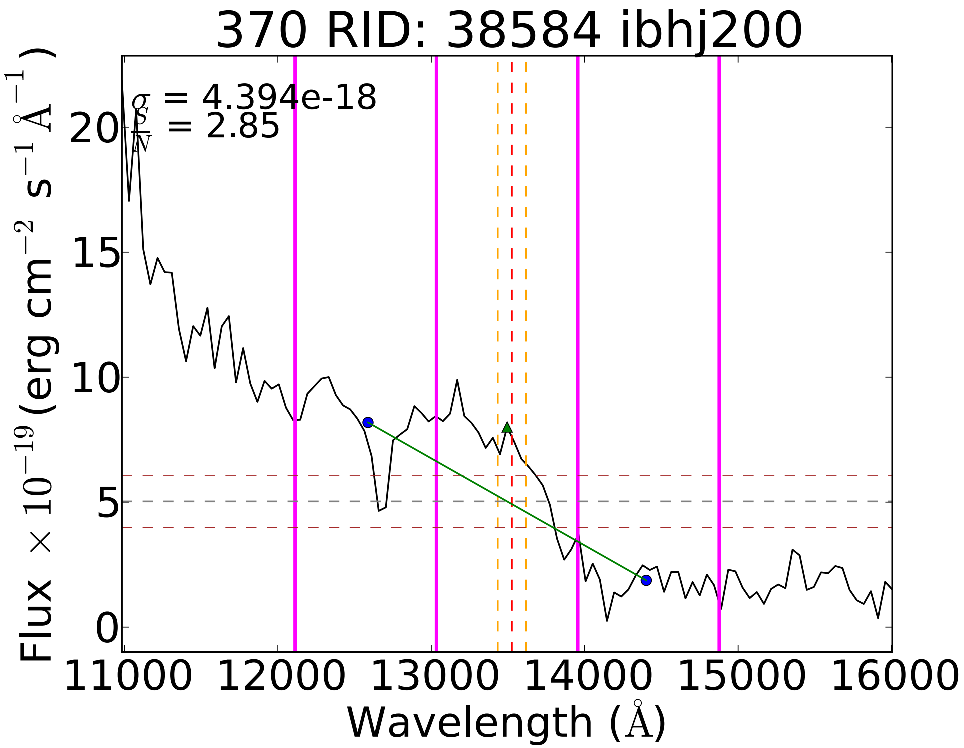

370 RID: 38584 ibhj200

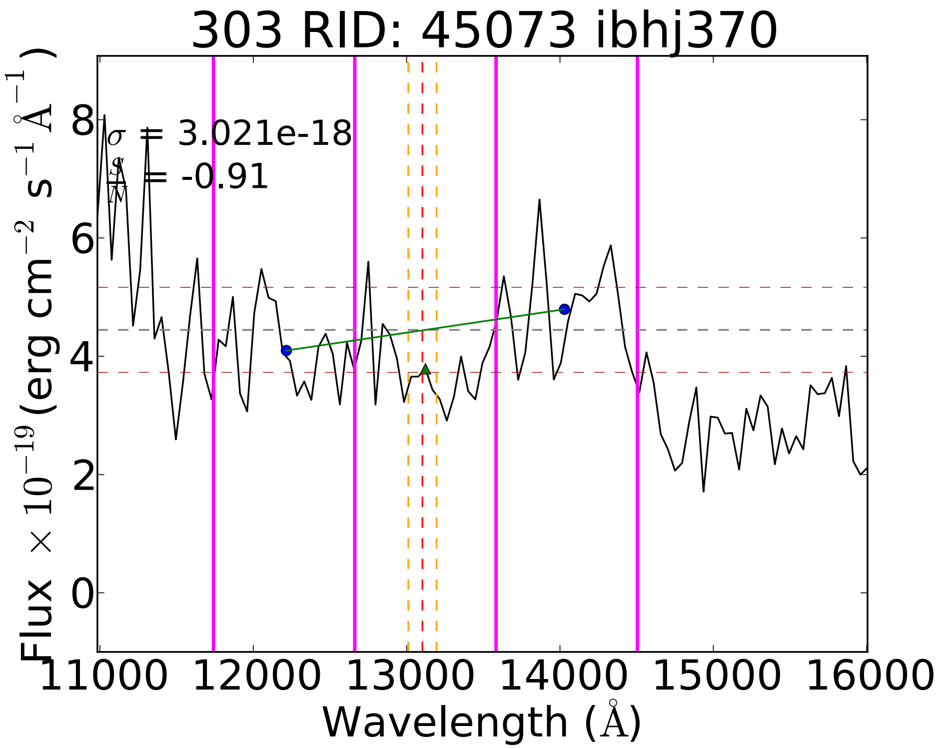

303 RID: 45073 ibhj370

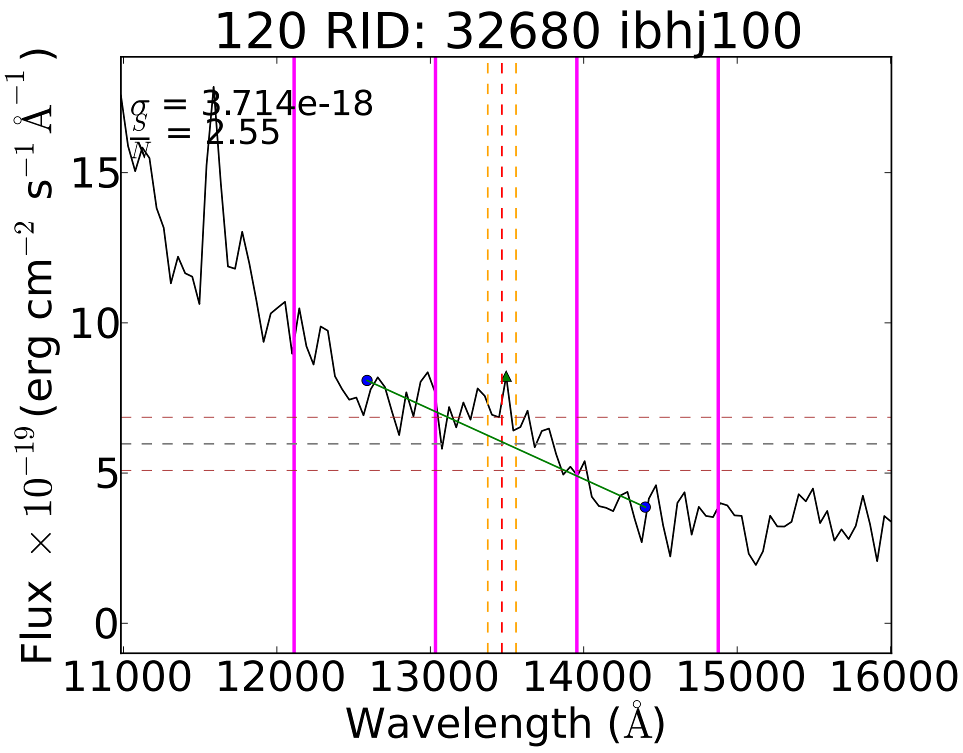

120 RID: 32680 ibhj100

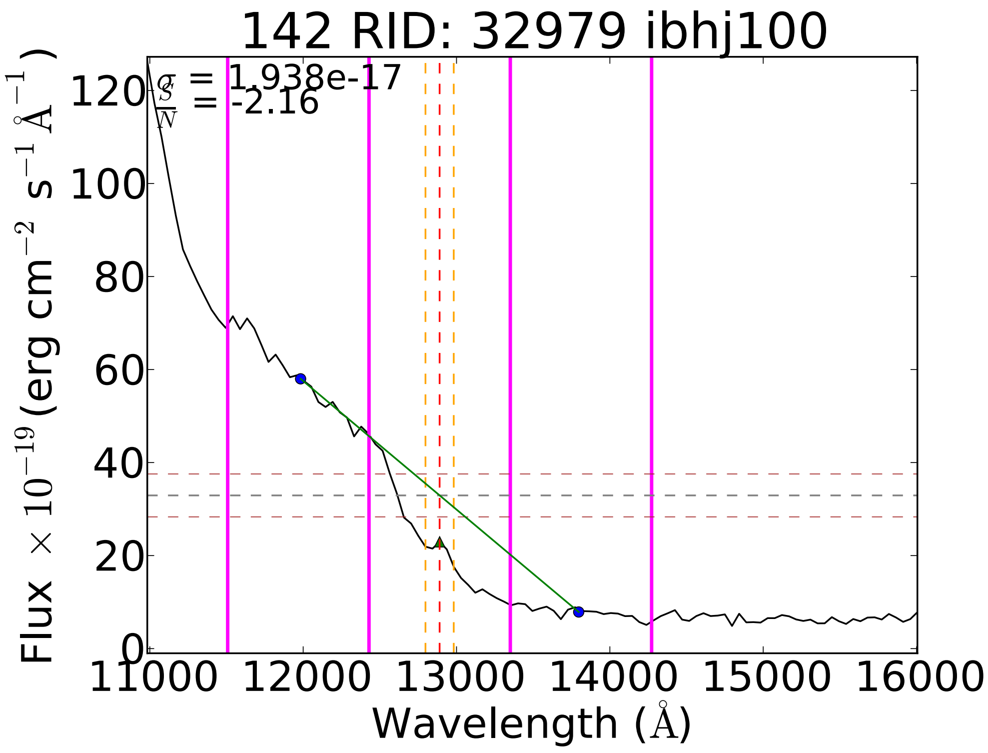

142 RID: 32979 ibhj100

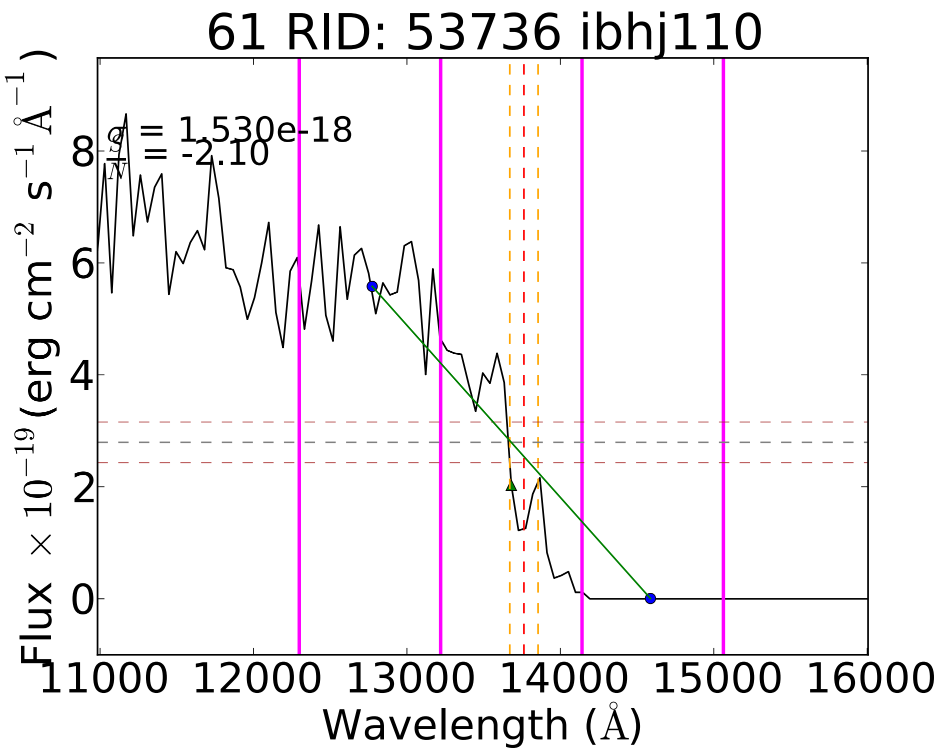
61 RID: 53736 ibhj110
σ = 1.530e-18
S/N = -2.10
Flux × 10^−19 (erg cm^−2 s^−1 Å^−1)
Wavelength (Å)
0
2
4
6
8
11000
12000
13000
14000
15000
16000

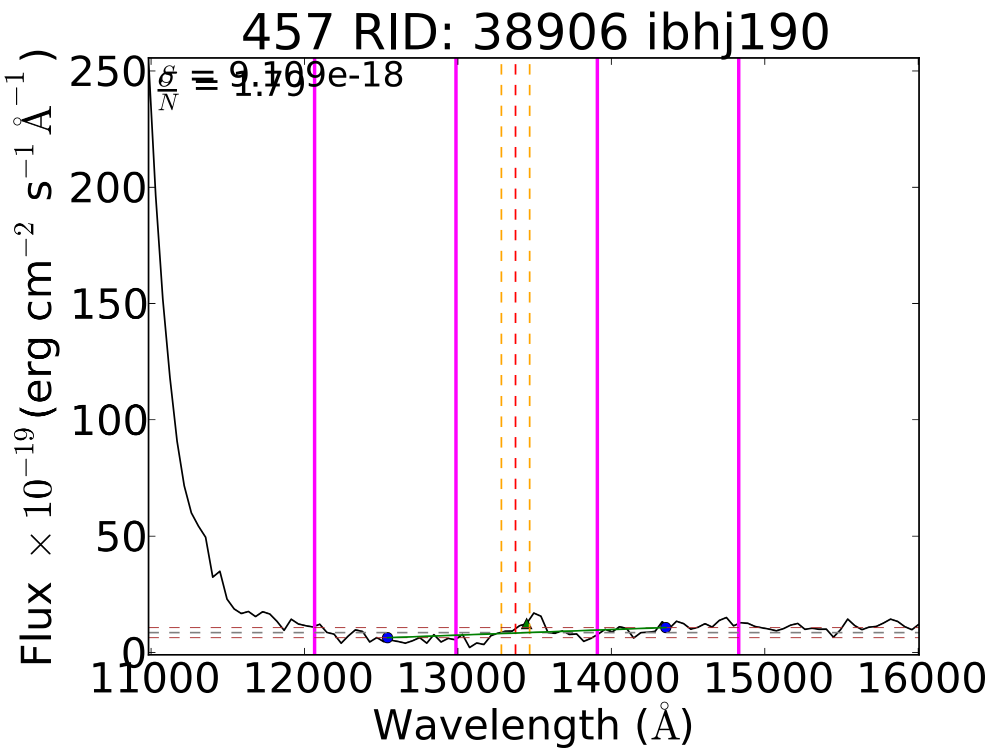
457 RID: 38906 ibhj190
σ = 9.169e-18
S/N = 1.79
Flux × 10^−19 (erg cm^−2 s^−1 Å^−1)
Wavelength (Å)
0
50
100
150
200
250
11000
12000
13000
14000
15000
16000

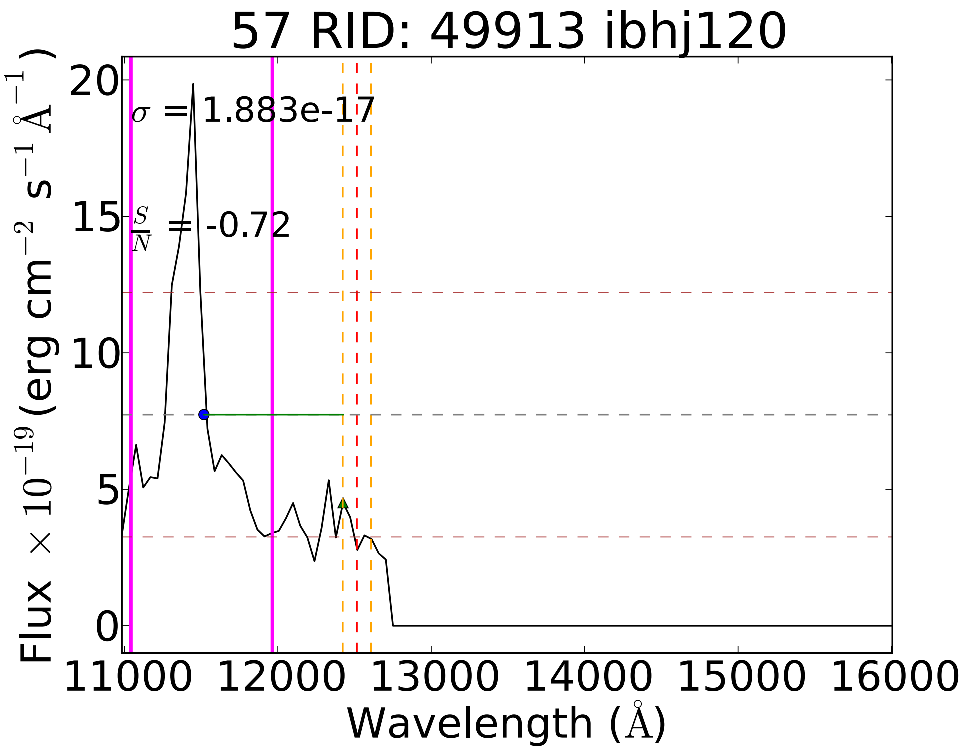
57 RID: 49913 ibhj120
σ = 1.883e-17
S/N = -0.72
Flux × 10^−19 (erg cm^−2 s^−1 Å^−1)
Wavelength (Å)
0
5
10
15
20
11000
12000
13000
14000
15000
16000

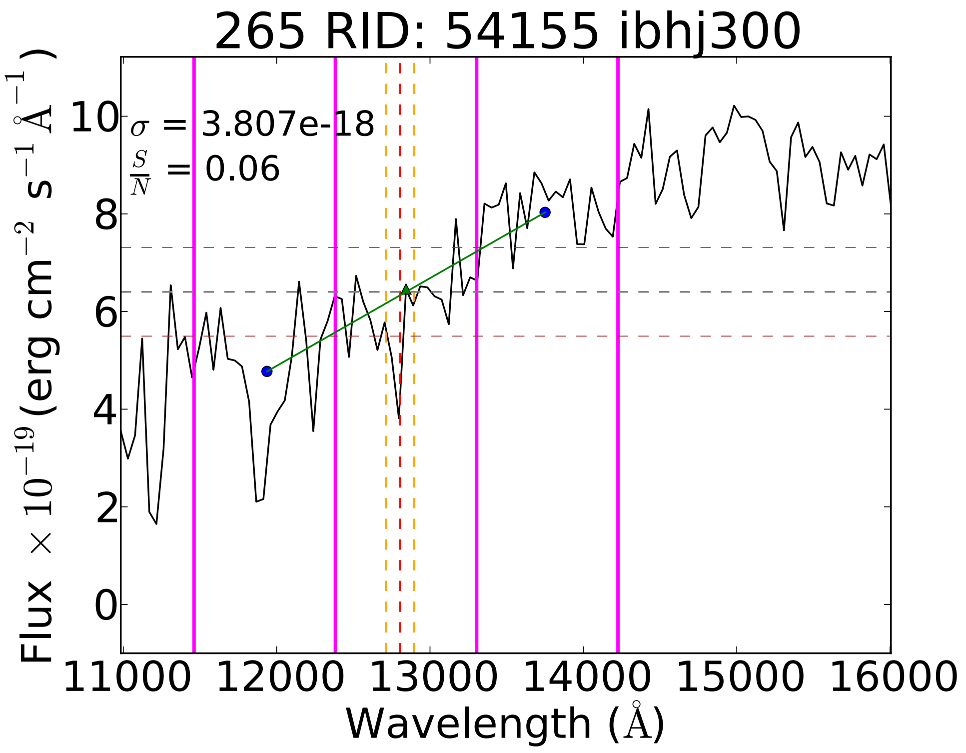
265 RID: 54155 ibhj300
σ = 3.807e-18
S/N = 0.06
Flux × 10^−19 (erg cm^−2 s^−1 Å^−1)
Wavelength (Å)
0
2
4
6
8
10
11000
12000
13000
14000
15000
16000

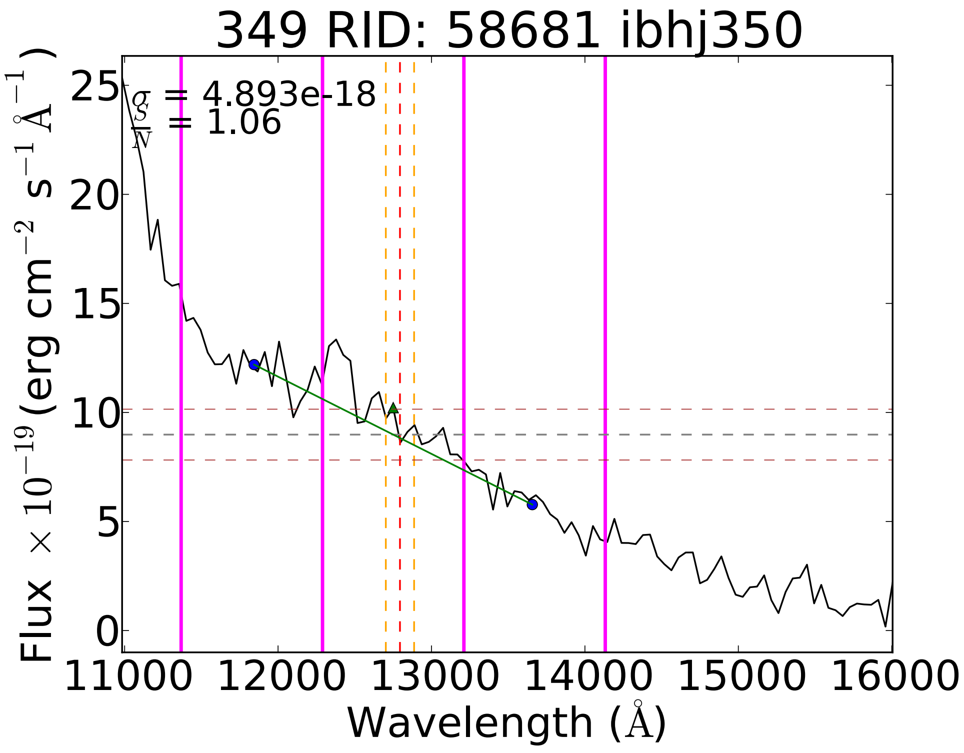
349 RID: 58681 ibhj350
σ = 4.893e-18
S/N = 1.06
Flux × 10^−19 (erg cm^−2 s^−1 Å^−1)
0
5
10
15
20
25
11000
12000
13000
14000
15000
16000
Wavelength (Å)

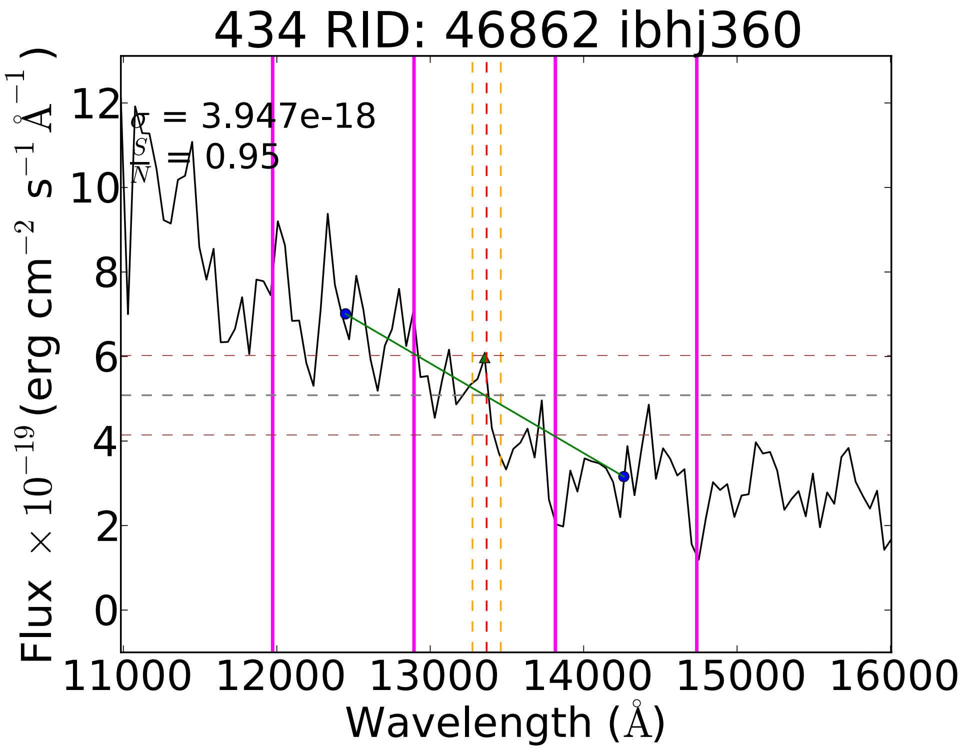
434 RID: 46862 ibhj360
σ = 3.947e-18
S/N = 0.95
Flux × 10^−19 (erg cm^−2 s^−1 Å^−1)
0
2
4
6
8
10
12
11000
12000
13000
14000
15000
16000
Wavelength (Å)

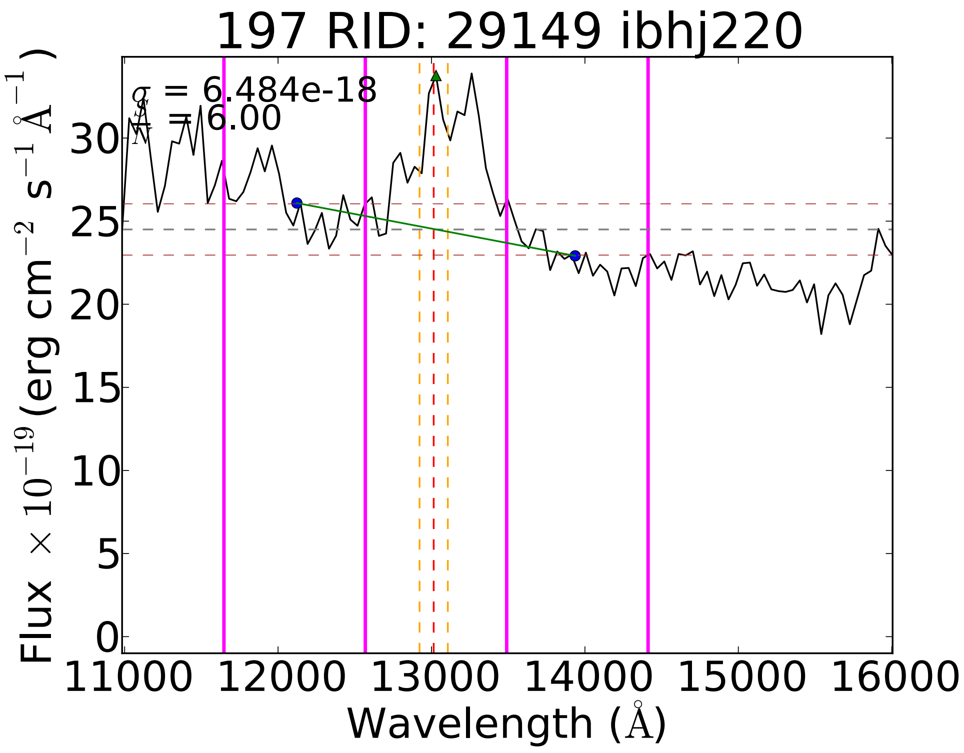
197 RID: 29149 ibhj220
σ = 6.484e-18
S/N = 6.00
Flux × 10^−19 (erg cm^−2 s^−1 Å^−1)
0
5
10
15
20
25
30
11000
12000
13000
14000
15000
16000
Wavelength (Å)

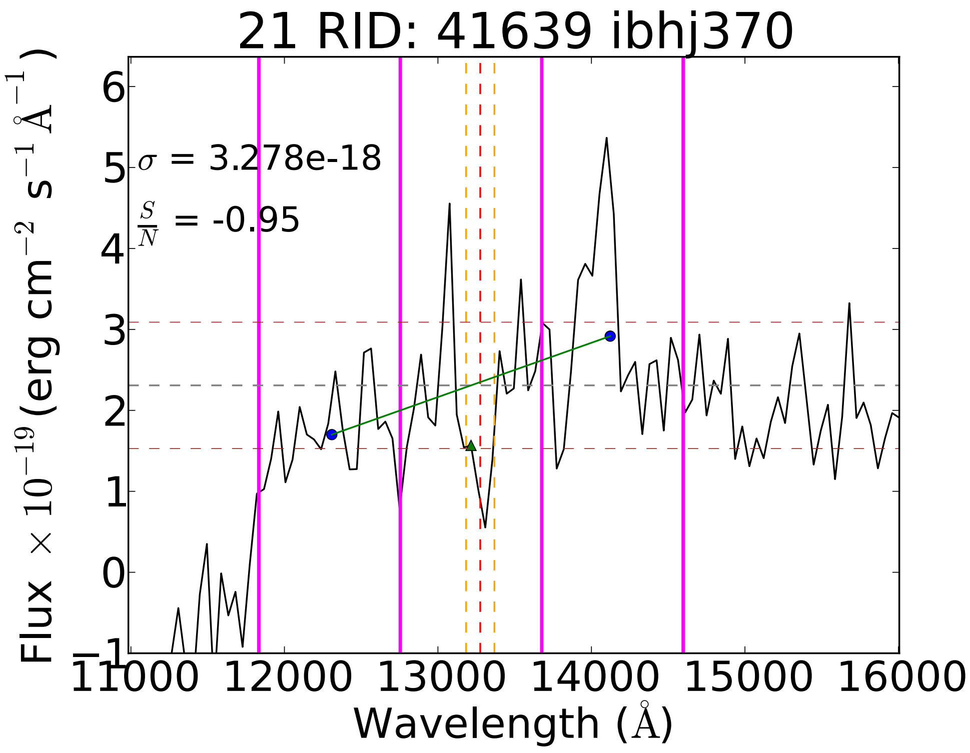
21 RID: 41639 ibhj370
σ = 3.278e-18
S/N = -0.95
Flux × 10^−19 (erg cm^−2 s^−1 Å^−1)
−1
0
1
2
3
4
5
6
11000
12000
13000
14000
15000
16000
Wavelength (Å)

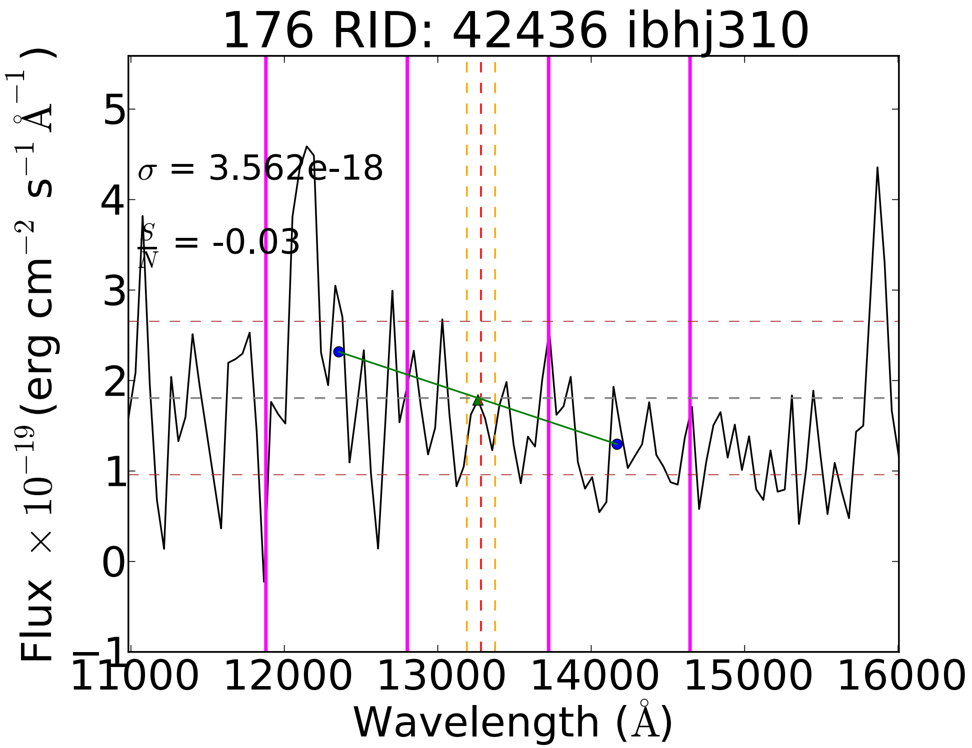
176 RID: 42436 ibhj310
σ = 3.562e-18
$\frac{S}{N}$ = -0.03
Flux $\times 10^{-19}$ (erg cm^{-2} s^{-1} Å^{-1})
Wavelength (Å)
5
4
3
2
1
0
−1
11000
12000
13000
14000
15000
16000

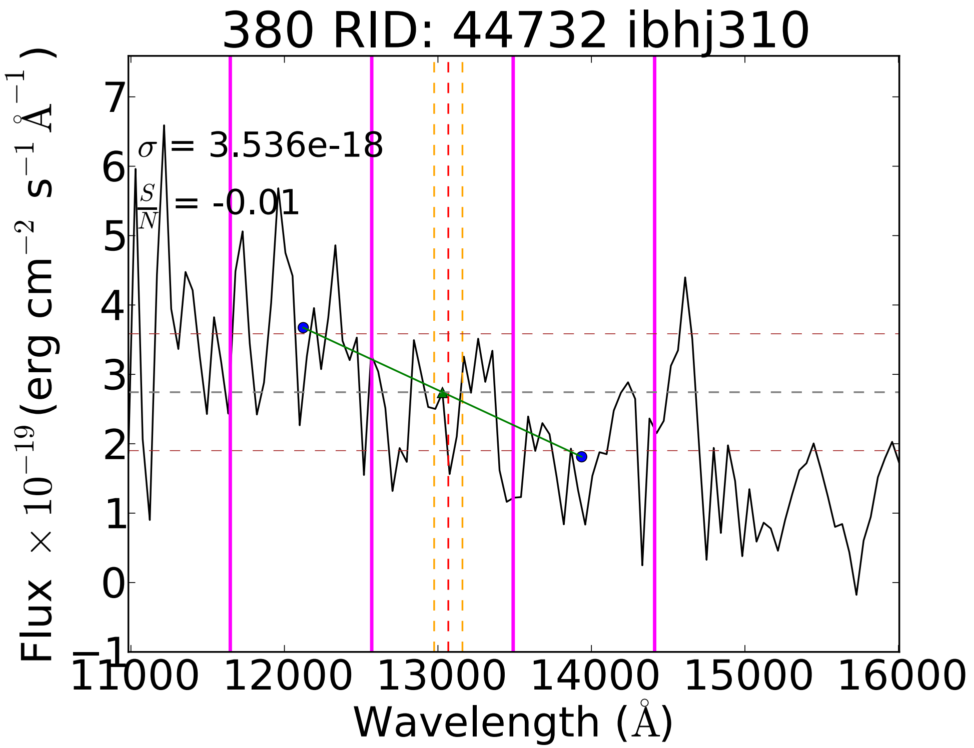
380 RID: 44732 ibhj310
σ = 3.536e-18
$\frac{S}{N}$ = -0.01
Flux $\times 10^{-19}$ (erg cm^{-2} s^{-1} Å^{-1})
Wavelength (Å)
7
6
5
4
3
2
1
0
−1
11000
12000
13000
14000
15000
16000

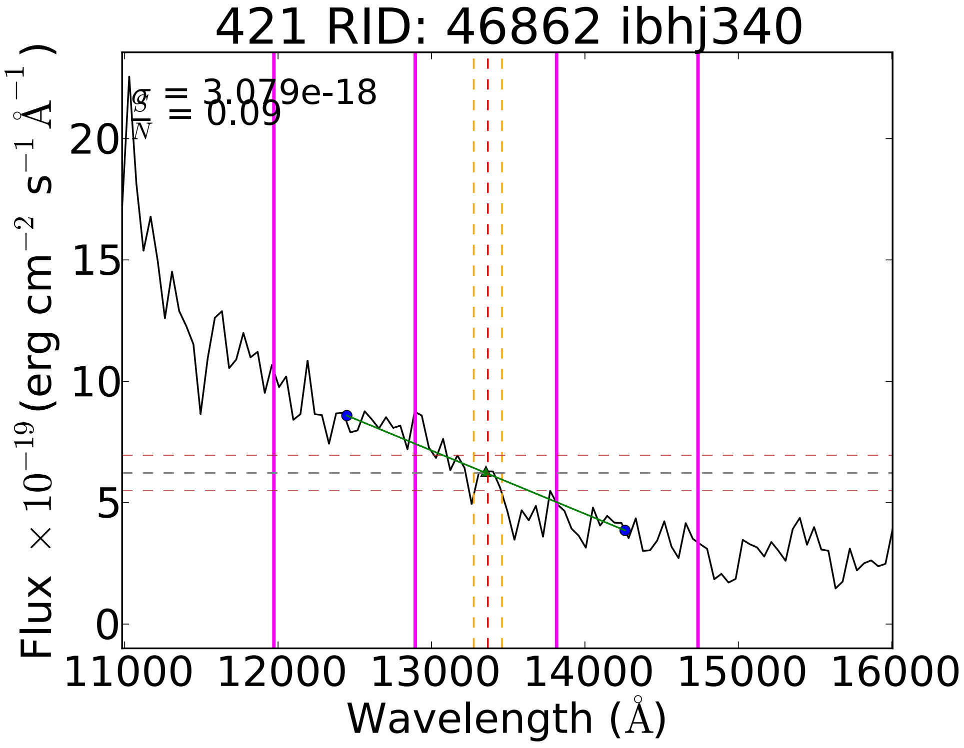
421 RID: 46862 ibhj340
σ = 3.079e-18
$\frac{S}{N}$ = 0.09
Flux $\times 10^{-19}$ (erg cm^{-2} s^{-1} Å^{-1})
Wavelength (Å)
20
15
10
5
0
11000
12000
13000
14000
15000
16000

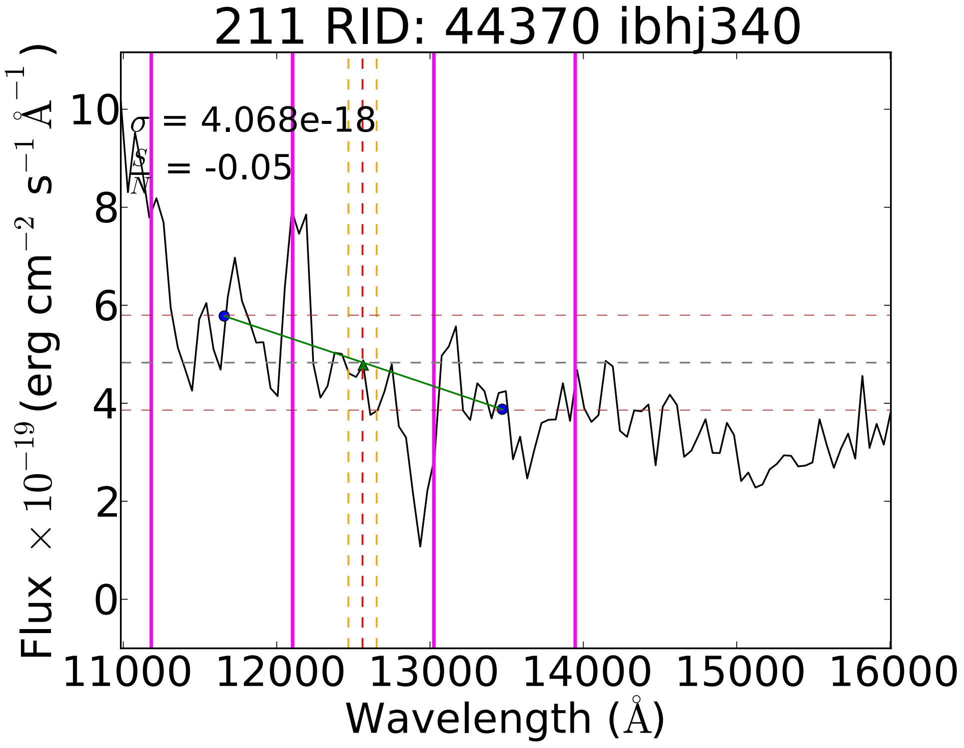
211 RID: 44370 ibhj340
σ = 4.068e-18
$\frac{S}{N}$ = -0.05
Flux $\times 10^{-19}$ (erg cm^{-2} s^{-1} Å^{-1})
Wavelength (Å)
10
8
6
4
2
0
11000
12000
13000
14000
15000
16000

C2: The following spectra were rejected because they were cut-off and did not have an Hα emission line:

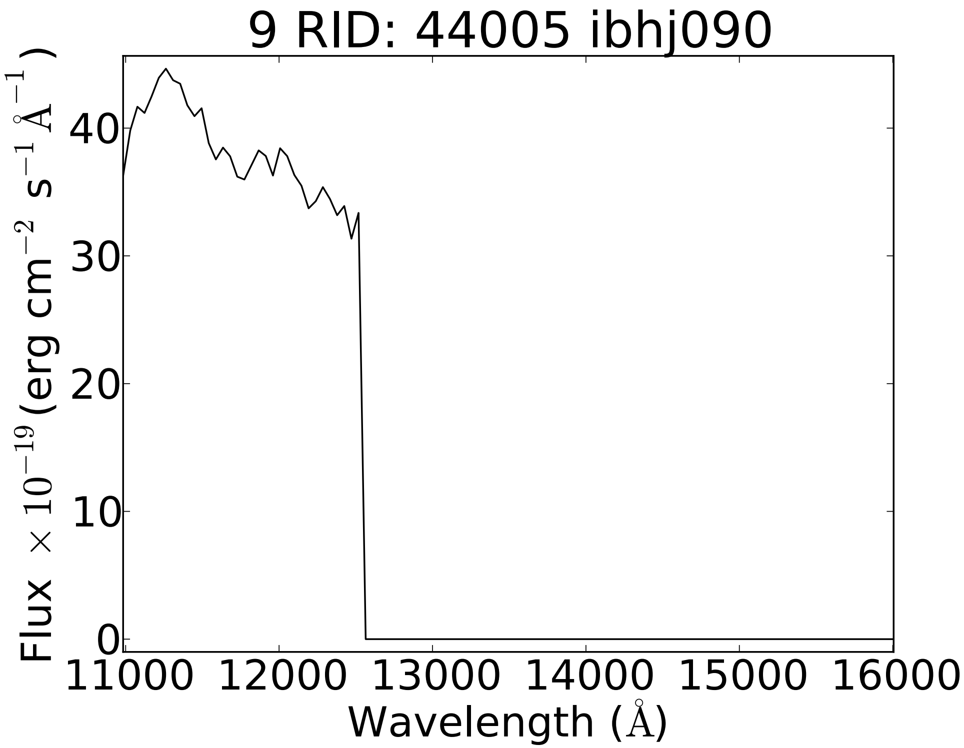
9 RID: 44005 ibhj090
Flux × 10^{-19} (erg cm^{-2} s^{-1} Å^{-1})
0
10
20
30
40
11000
12000
13000
14000
15000
16000
Wavelength (Å)

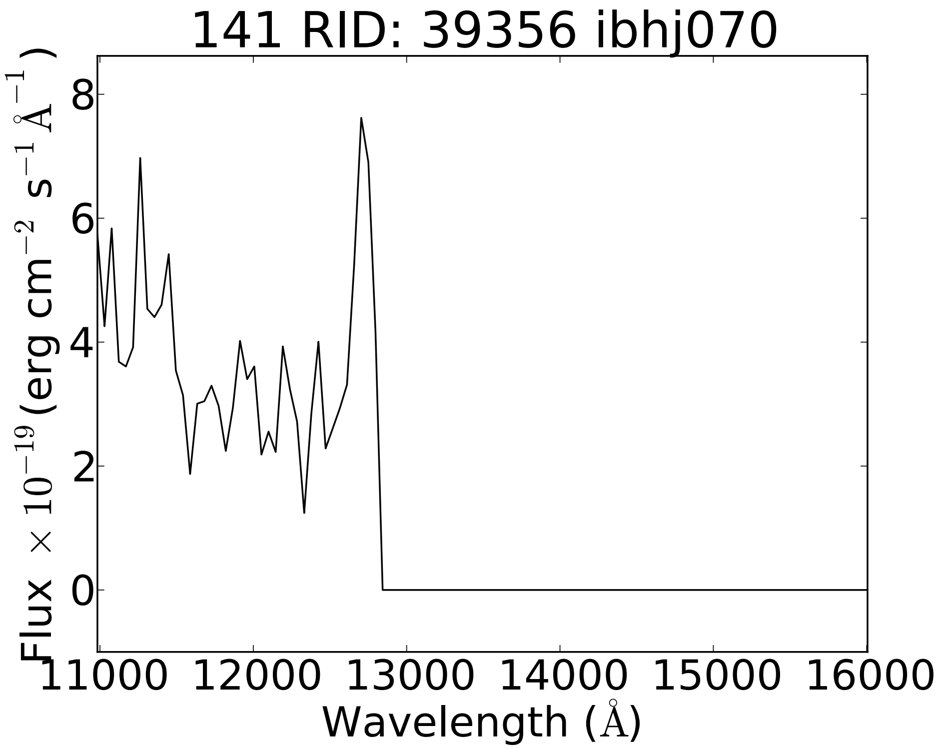
141 RID: 39356 ibhj070
Flux × 10^{-19} (erg cm^{-2} s^{-1} Å^{-1})
0
2
4
6
8
11000
12000
13000
14000
15000
16000
Wavelength (Å)

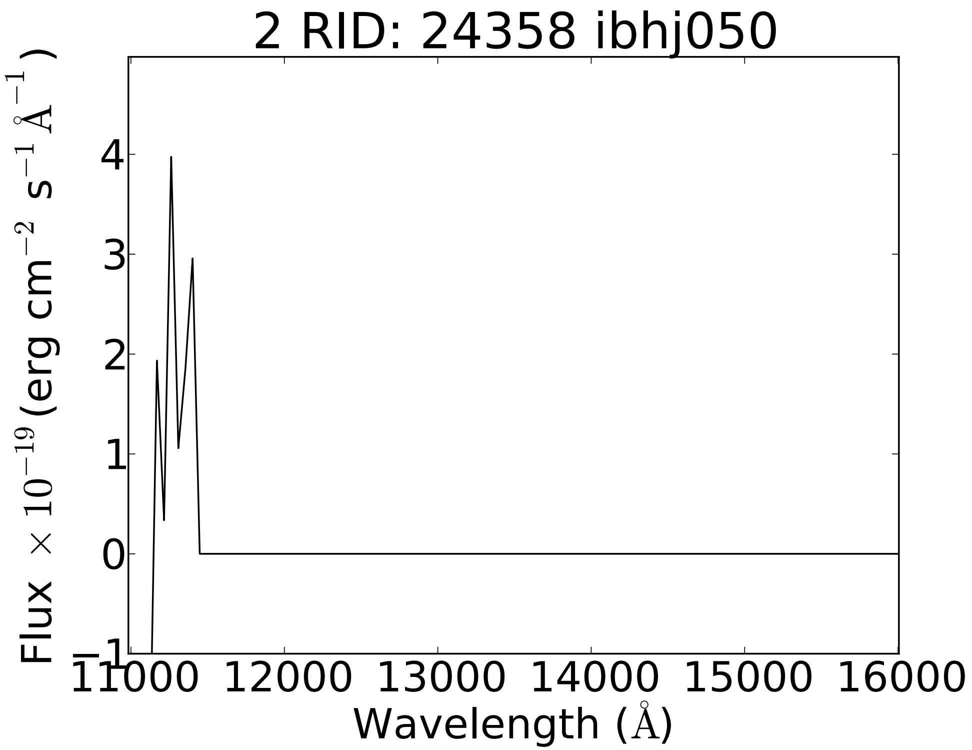
2 RID: 24358 ibhj050
Flux × 10^{-19} (erg cm^{-2} s^{-1} Å^{-1})
−1
0
1
2
3
4
11000
12000
13000
14000
15000
16000
Wavelength (Å)

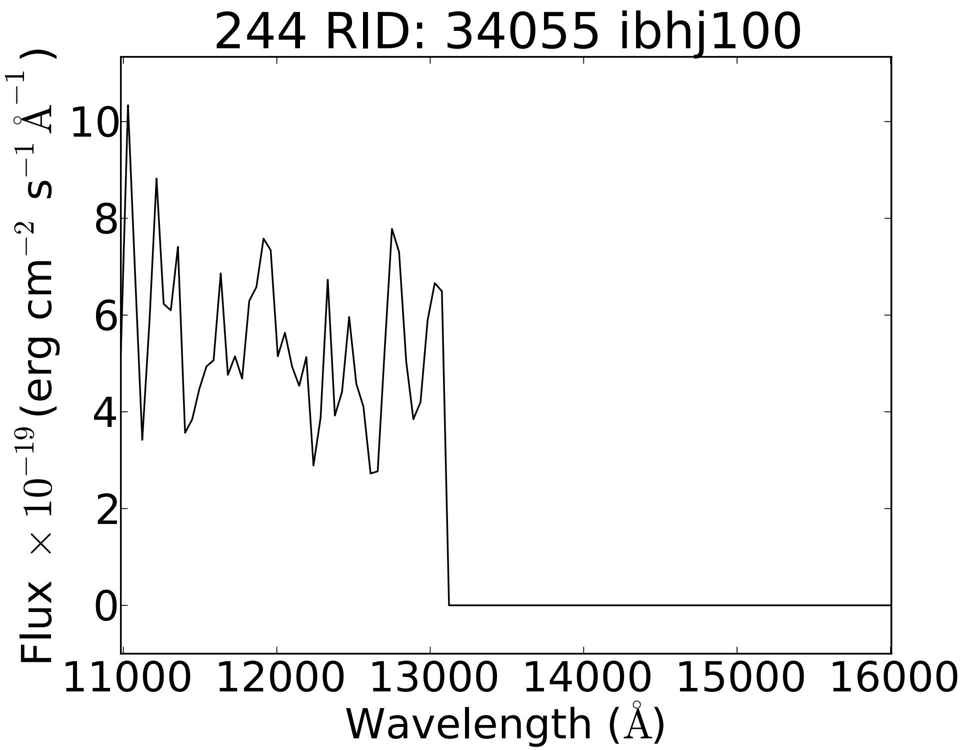
244 RID: 34055 ibhj100
Flux × 10^{-19} (erg cm^{-2} s^{-1} Å^{-1})
0
2
4
6
8
10
11000
12000
13000
14000
15000
16000
Wavelength (Å)

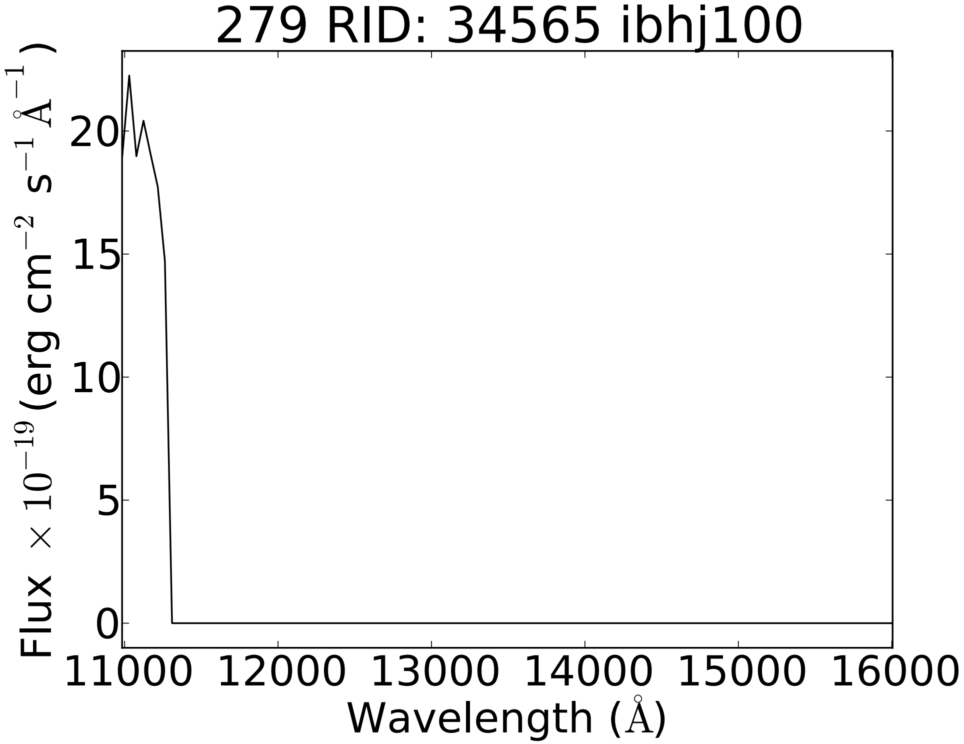
279 RID: 34565 ibhj100
Flux $\times 10^{-19}$ (erg cm^{-2} s^{-1} Å^{-1})
0
5
10
15
20
11000
12000
13000
14000
15000
16000
Wavelength (Å)

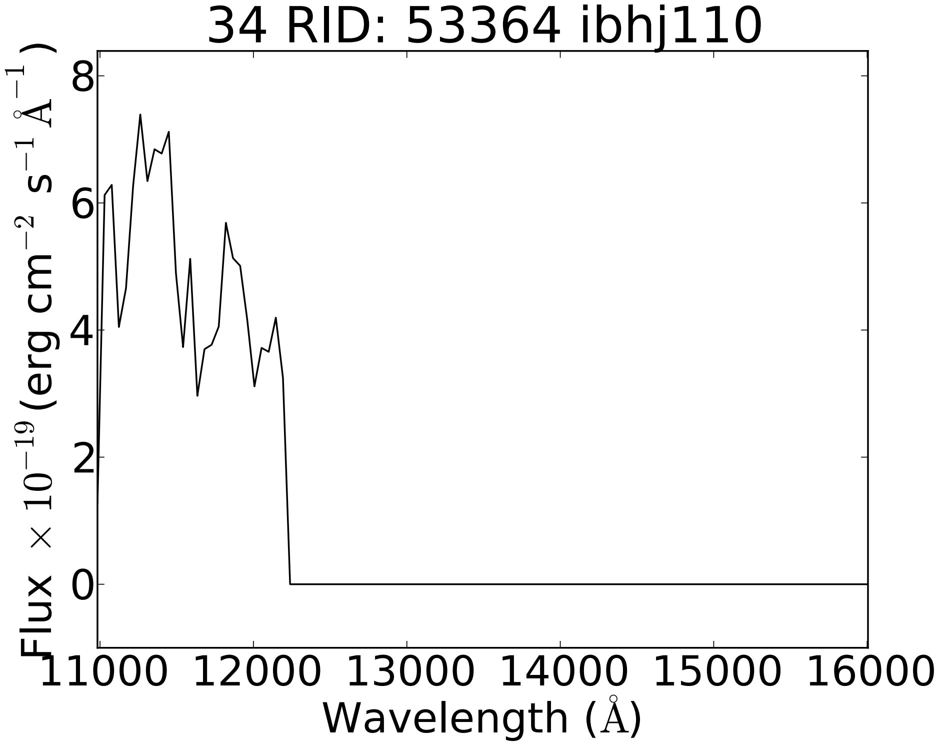
34 RID: 53364 ibhj110
Flux $\times 10^{-19}$ (erg cm^{-2} s^{-1} Å^{-1})
0
2
4
6
8
11000
12000
13000
14000
15000
16000
Wavelength (Å)

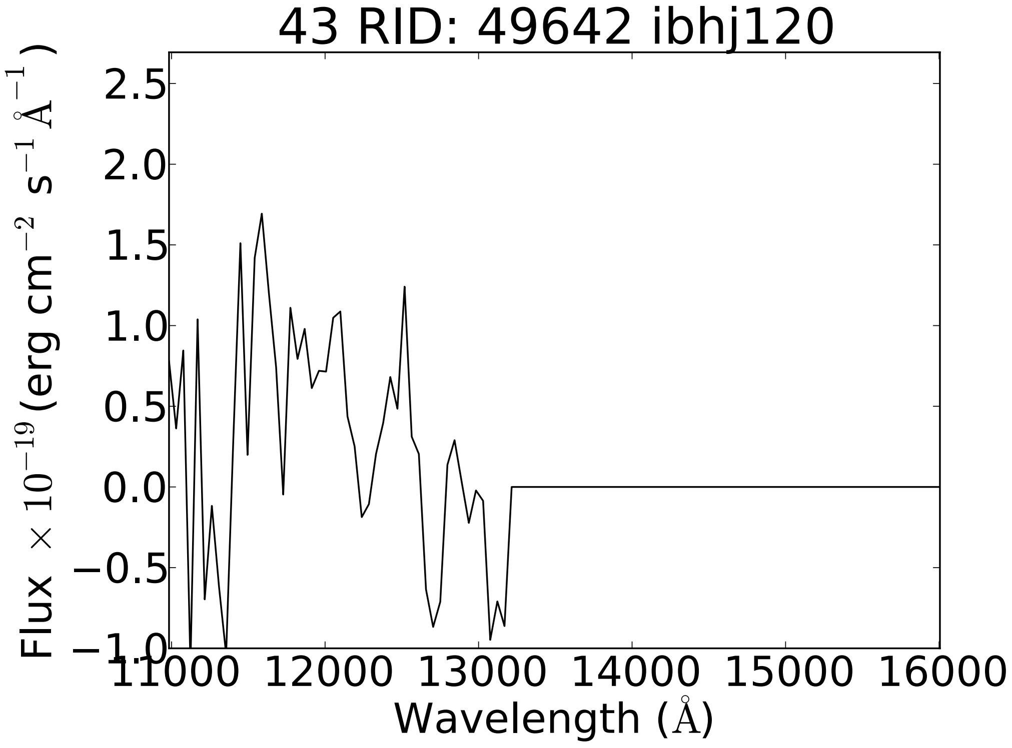
43 RID: 49642 ibhj120
Flux $\times 10^{-19}$ (erg cm^{-2} s^{-1} Å^{-1})
−1.0
−0.5
0.0
0.5
1.0
1.5
2.0
2.5
11000
12000
13000
14000
15000
16000
Wavelength (Å)

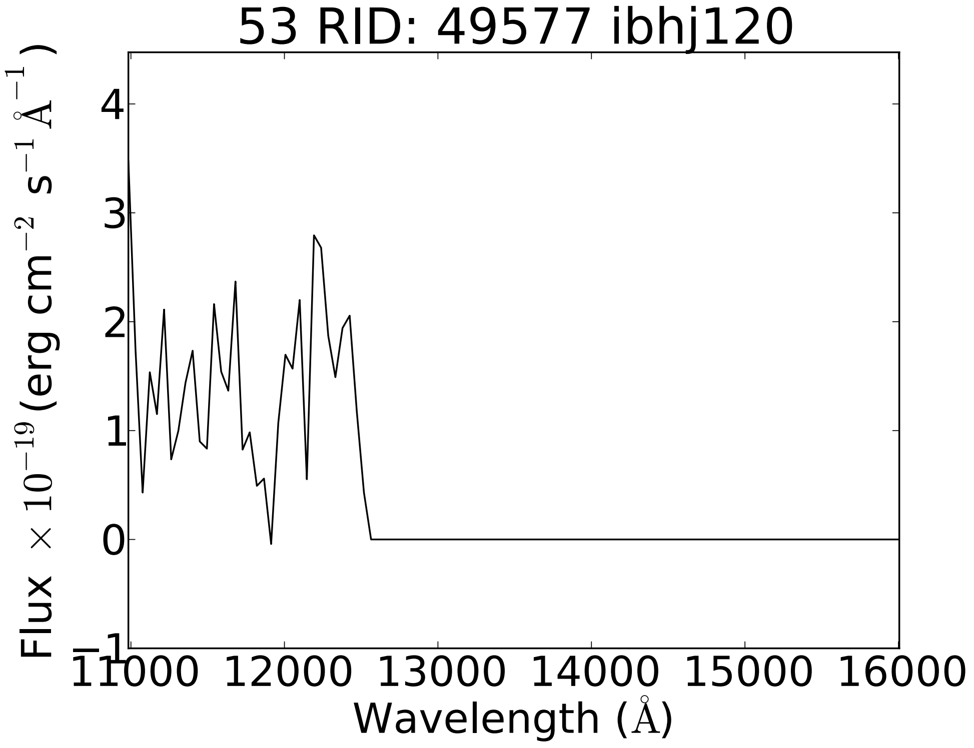
53 RID: 49577 ibhj120
Flux $\times 10^{-19}$ (erg cm^{-2} s^{-1} Å^{-1})
−1
0
1
2
3
4
11000
12000
13000
14000
15000
16000
Wavelength (Å)

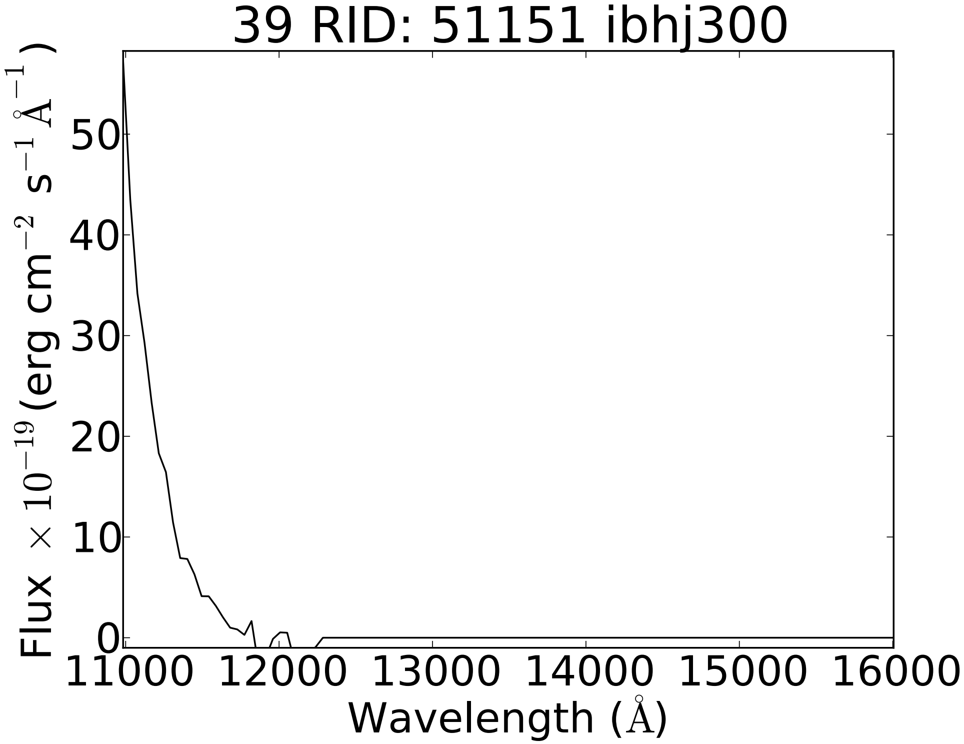
39 RID: 51151 ibhj300
Flux × 10^{-19} (erg cm^{-2} s^{-1} Å^{-1})
0
10
20
30
40
50
11000
12000
13000
14000
15000
16000
Wavelength (Å)

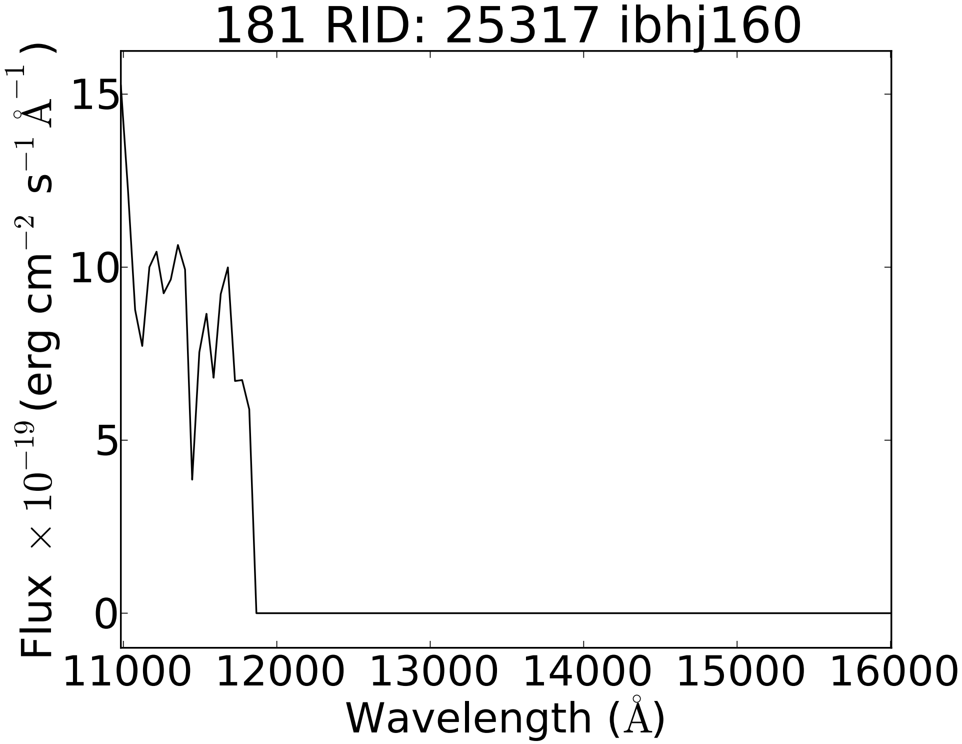
181 RID: 25317 ibhj160
Flux × 10^{-19} (erg cm^{-2} s^{-1} Å^{-1})
0
5
10
15
11000
12000
13000
14000
15000
16000
Wavelength (Å)

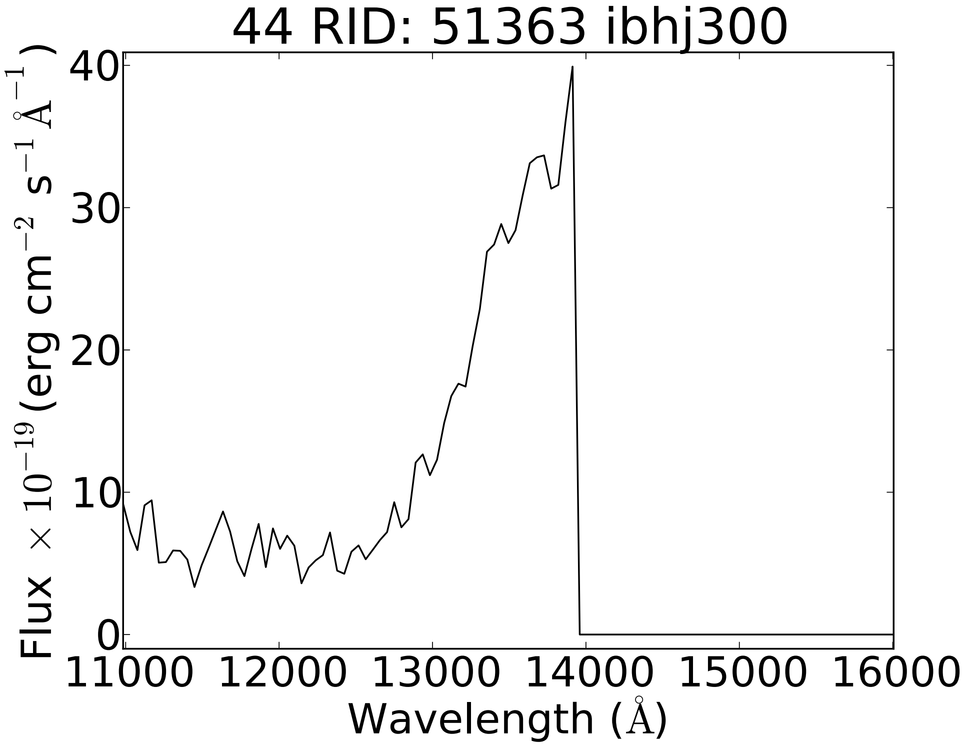
44 RID: 51363 ibhj300
Flux × 10^{-19} (erg cm^{-2} s^{-1} Å^{-1})
0
10
20
30
40
11000
12000
13000
14000
15000
16000
Wavelength (Å)

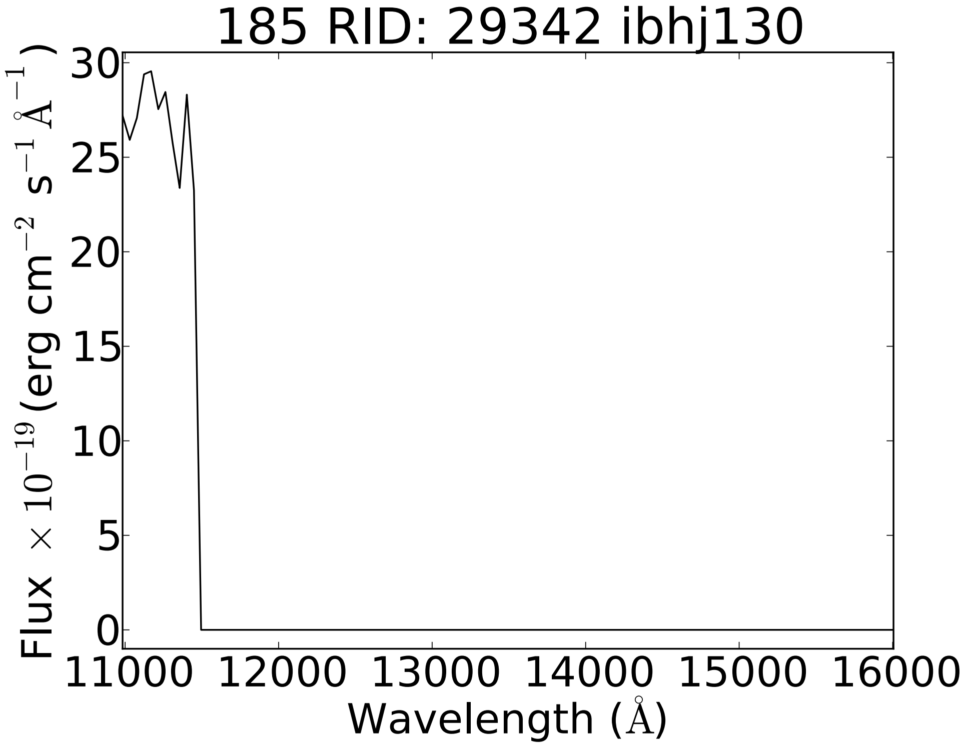
185 RID: 29342 ibhj130
Flux × 10^{-19} (erg cm^{-2} s^{-1} Å^{-1})
0
5
10
15
20
25
30
11000
12000
13000
14000
15000
16000
Wavelength (Å)

36 RID: 49642 ibhj120

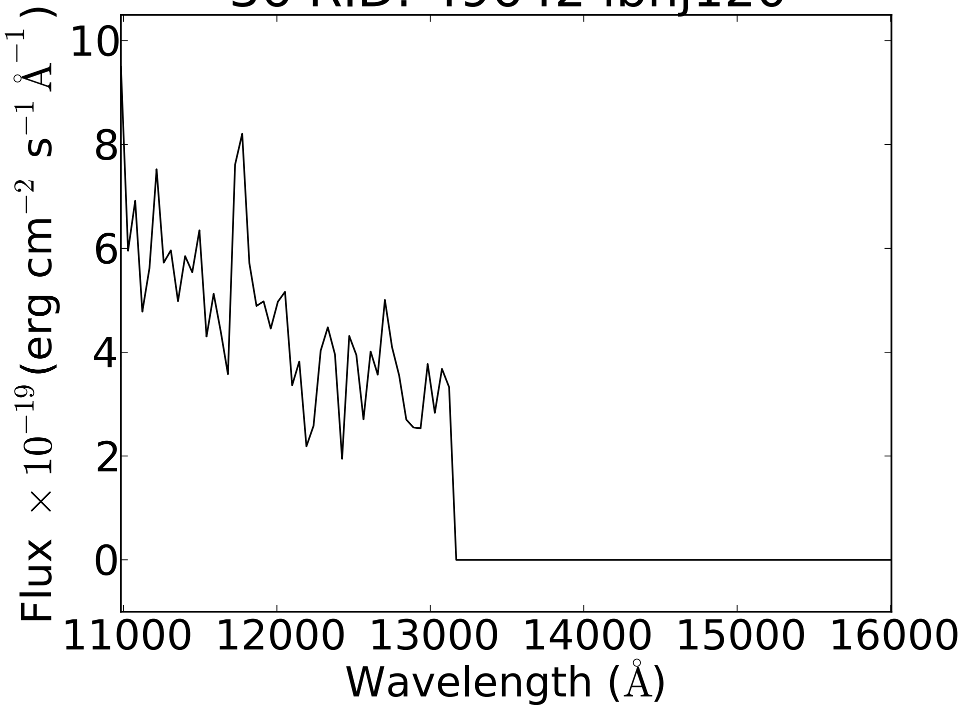

310 RID: 39349 ibhj200

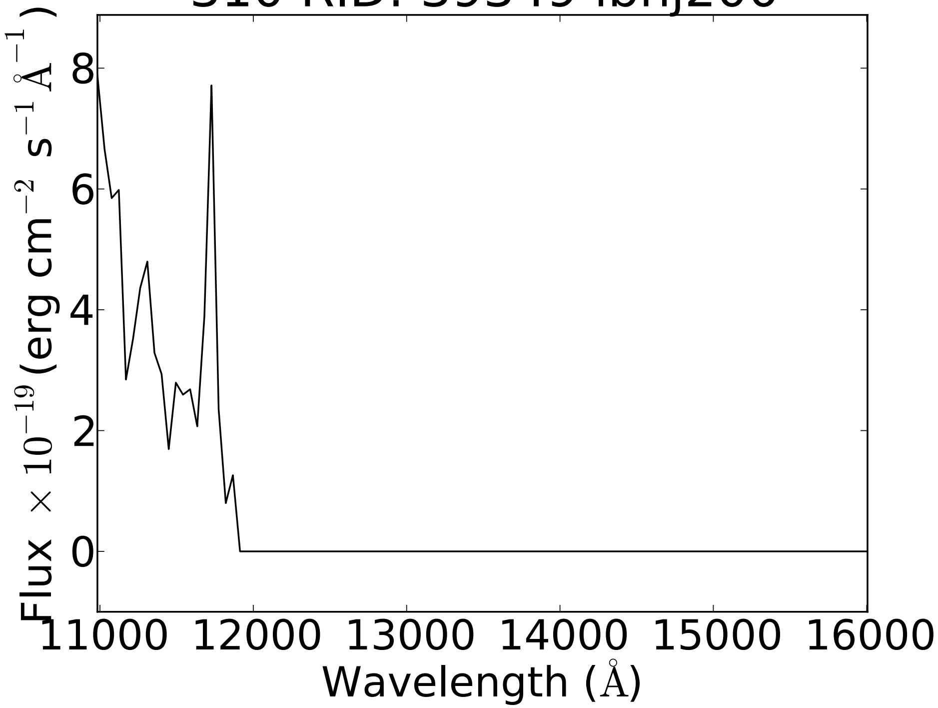

481 RID: 38360 ibhj190

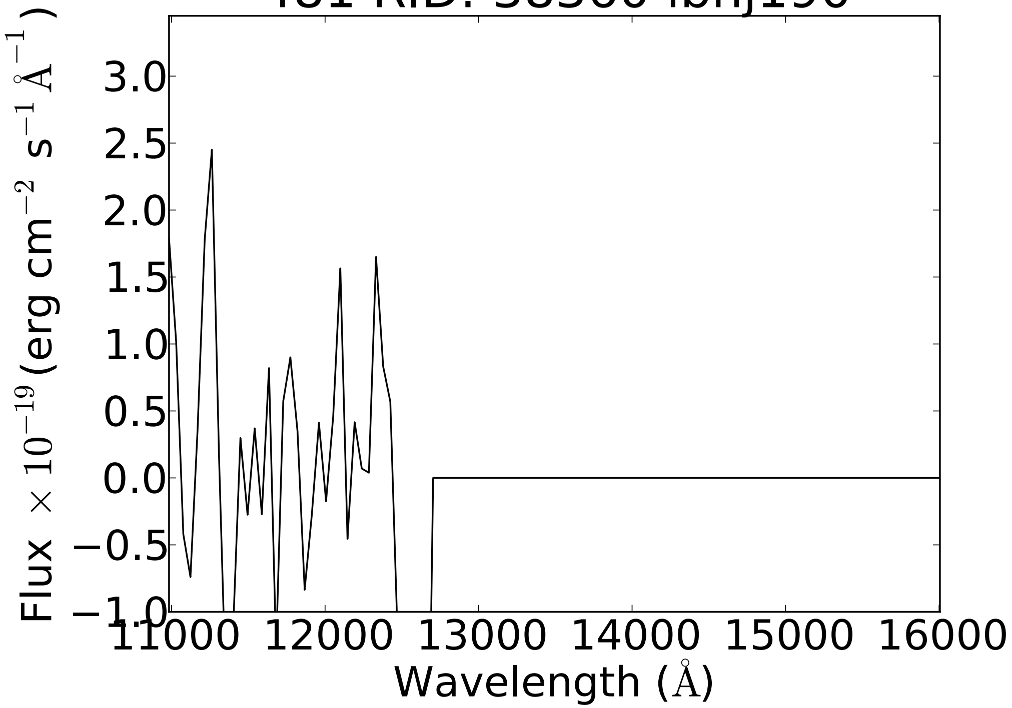

418 RID: 34055 ibhj260

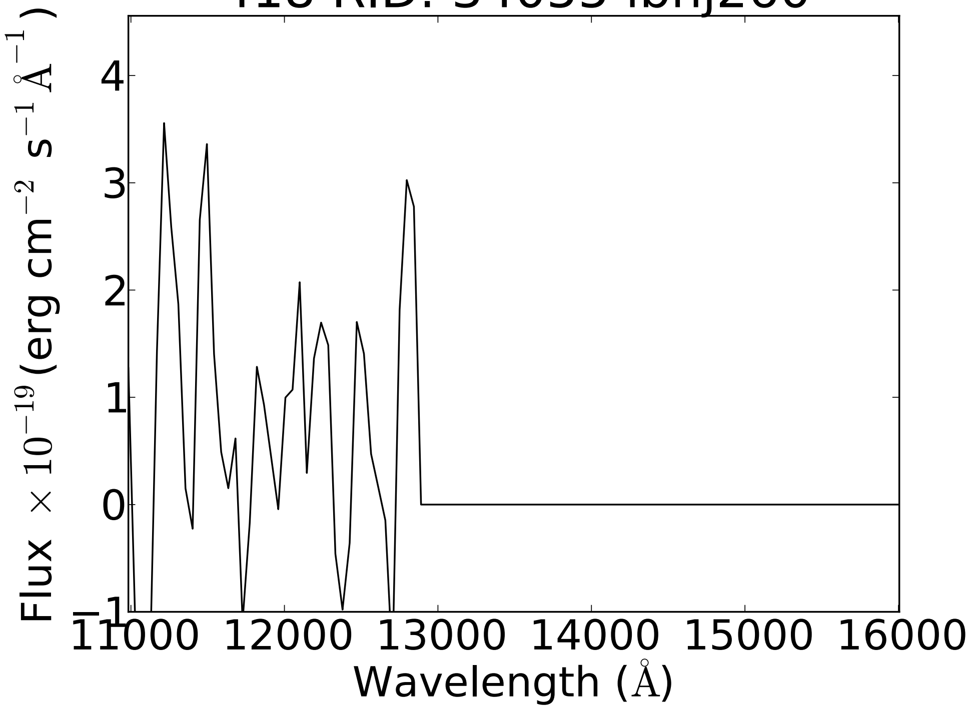

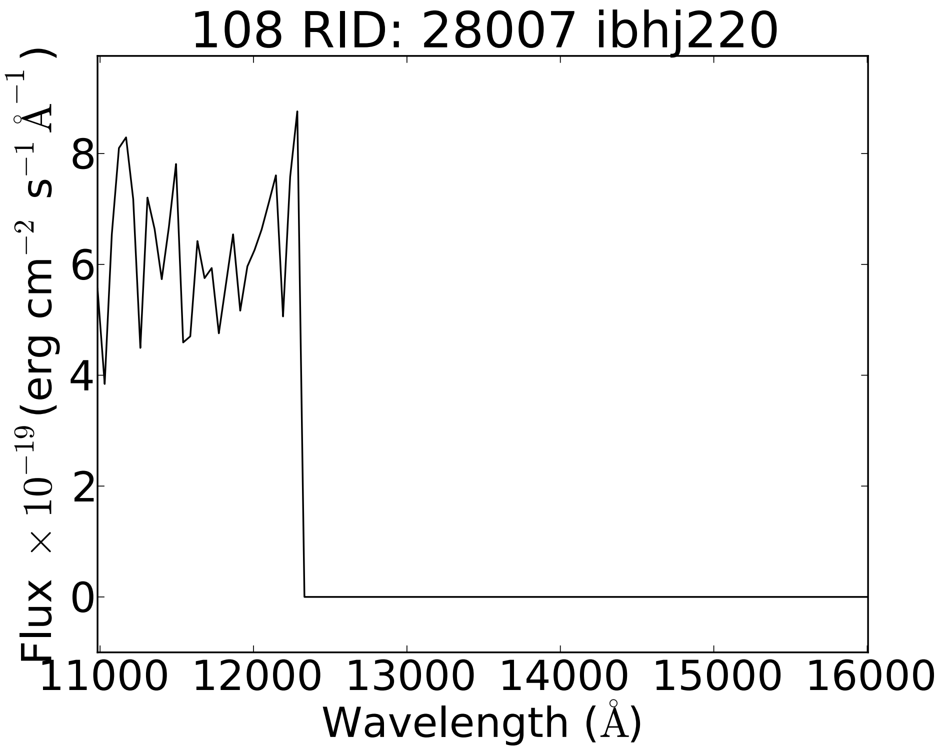
108 RID: 28007 ibhj220
Flux $\times 10^{-19}$ (erg cm^{-2} s^{-1} Å^{-1})
0
2
4
6
8
11000
12000
13000
14000
15000
16000
Wavelength (Å)

C3: The following spectra were rejected because a bright emission line is seen at a position away from Hα is expected. Since we have tested the wavelength calibration and found it to be accurate to within 1 pixel, we know that these galaxies are not at the wrong redshift.

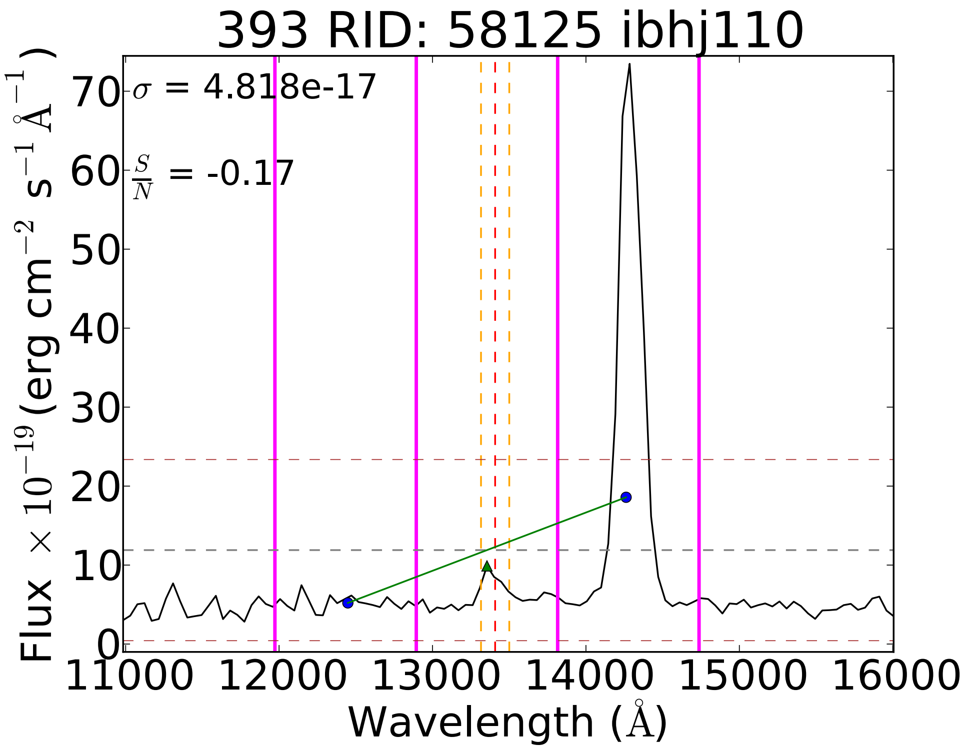
393 RID: 58125 ibhj110
σ = 4.818e-17
$\frac{S}{N}$ = -0.17
Flux $\times 10^{-19}$ (erg cm^{-2} s^{-1} Å^{-1})
Wavelength (Å)
0
10
20
30
40
50
60
70
11000
12000
13000
14000
15000
16000

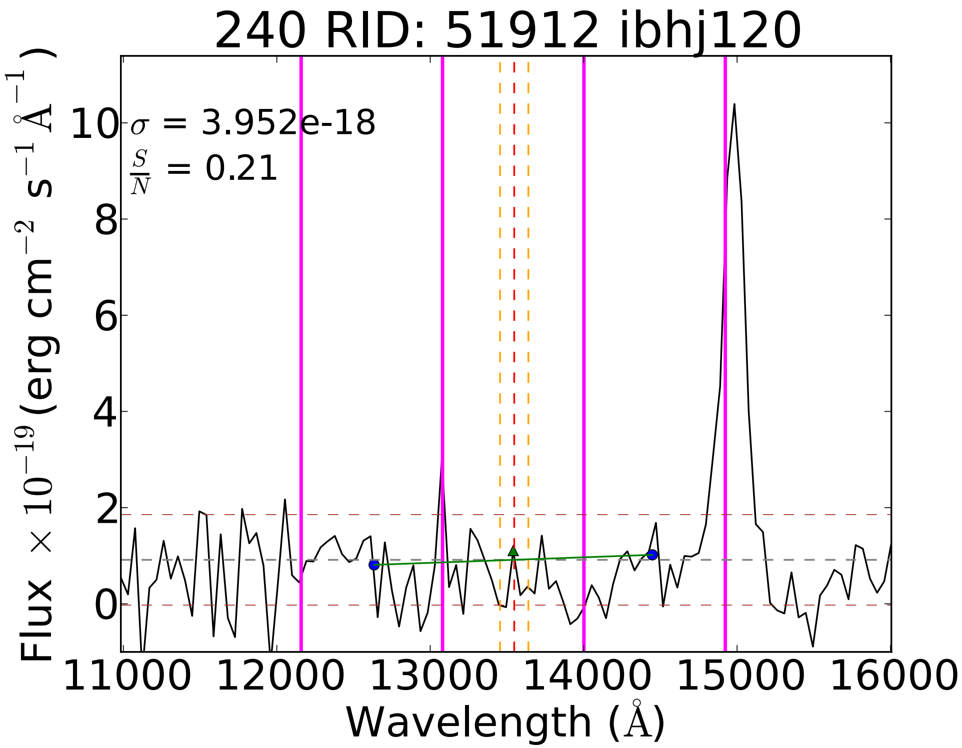
240 RID: 51912 ibhj120
σ = 3.952e-18
$\frac{S}{N}$ = 0.21
Flux $\times 10^{-19}$ (erg cm^{-2} s^{-1} Å^{-1})
Wavelength (Å)
0
2
4
6
8
10
11000
12000
13000
14000
15000
16000

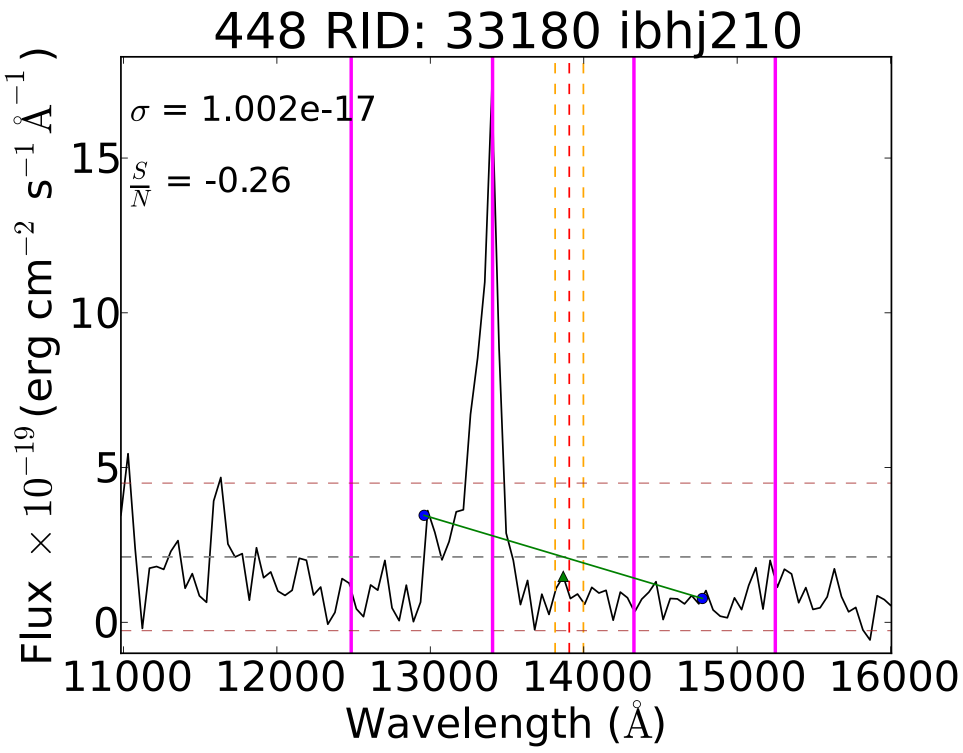
448 RID: 33180 ibhj210
σ = 1.002e-17
$\frac{S}{N}$ = -0.26
Flux $\times 10^{-19}$ (erg cm^{-2} s^{-1} Å^{-1})
Wavelength (Å)
0
5
10
15
11000
12000
13000
14000
15000
16000

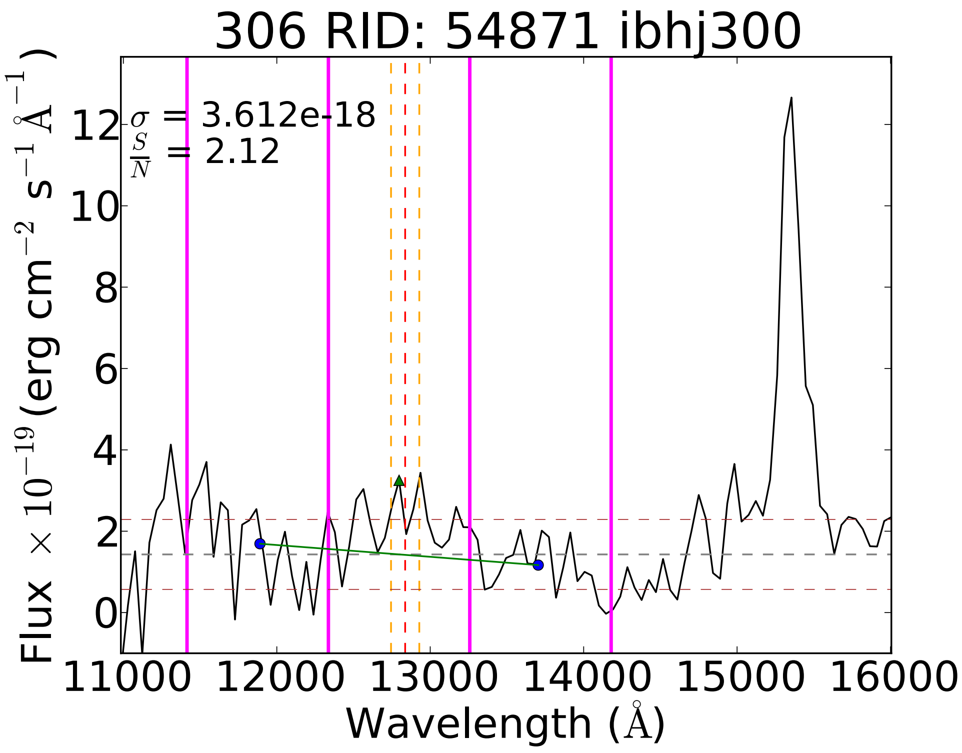
306 RID: 54871 ibhj300
σ = 3.612e-18
$\frac{S}{N}$ = 2.12
Flux $\times 10^{-19}$ (erg cm^{-2} s^{-1} Å^{-1})
Wavelength (Å)
0
2
4
6
8
10
12
11000
12000
13000
14000
15000
16000

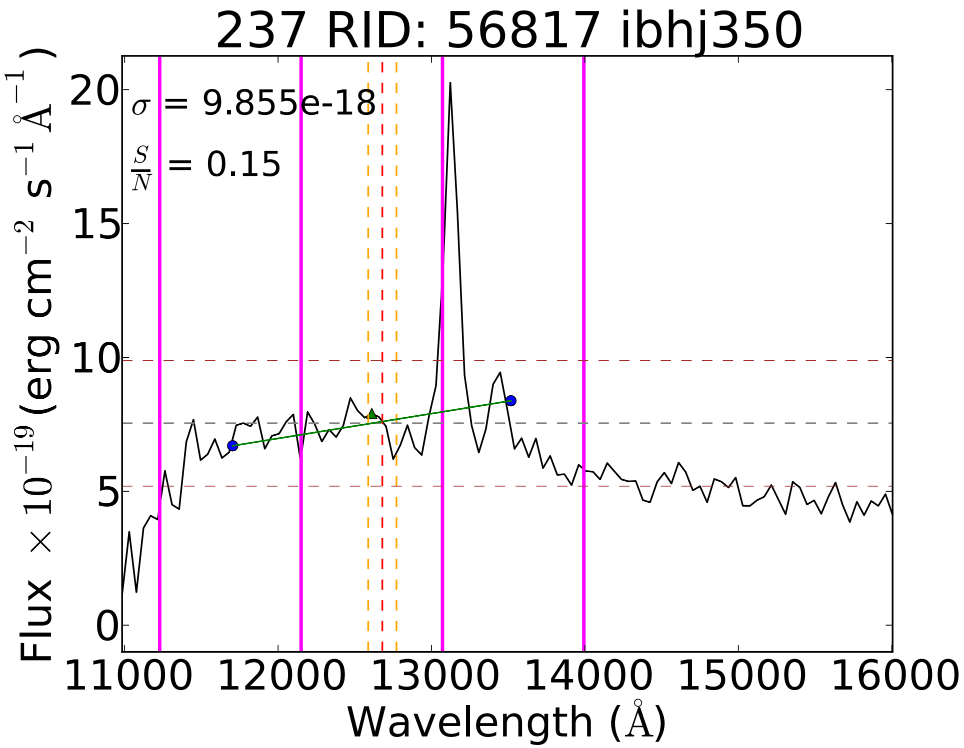
237 RID: 56817 ibhj350
σ = 9.855e-18
$\frac{S}{N}$ = 0.15
Flux $\times 10^{-19}$ (erg cm^{-2} s^{-1} Å^{-1})
0
5
10
15
20
11000
12000
13000
14000
15000
16000
Wavelength (Å)

C4: The following spectra were the special cases (§.2.6) that were rejected because the match could not pick out the correct WFC-OII galaxy since there were two galaxies close together:

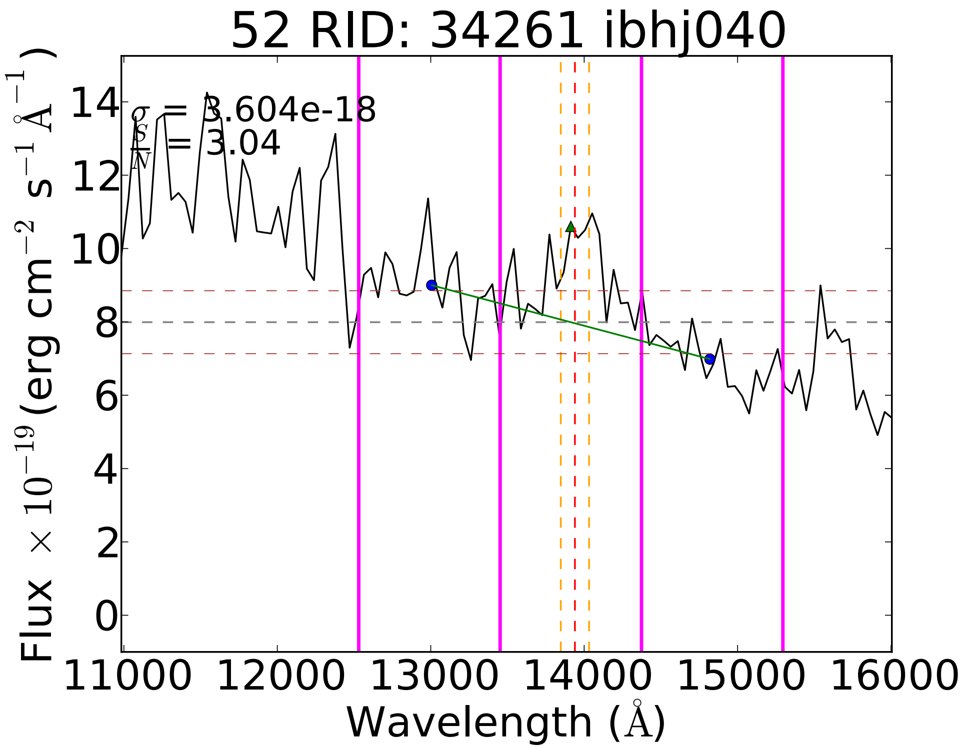
52 RID: 34261 ibhj040
σ = 3.604e-18
$\frac{S}{N}$ = 3.04
Flux $\times 10^{-19}$ (erg cm^{-2} s^{-1} Å^{-1})
Wavelength (Å)
0
2
4
6
8
10
12
14
11000
12000
13000
14000
15000
16000

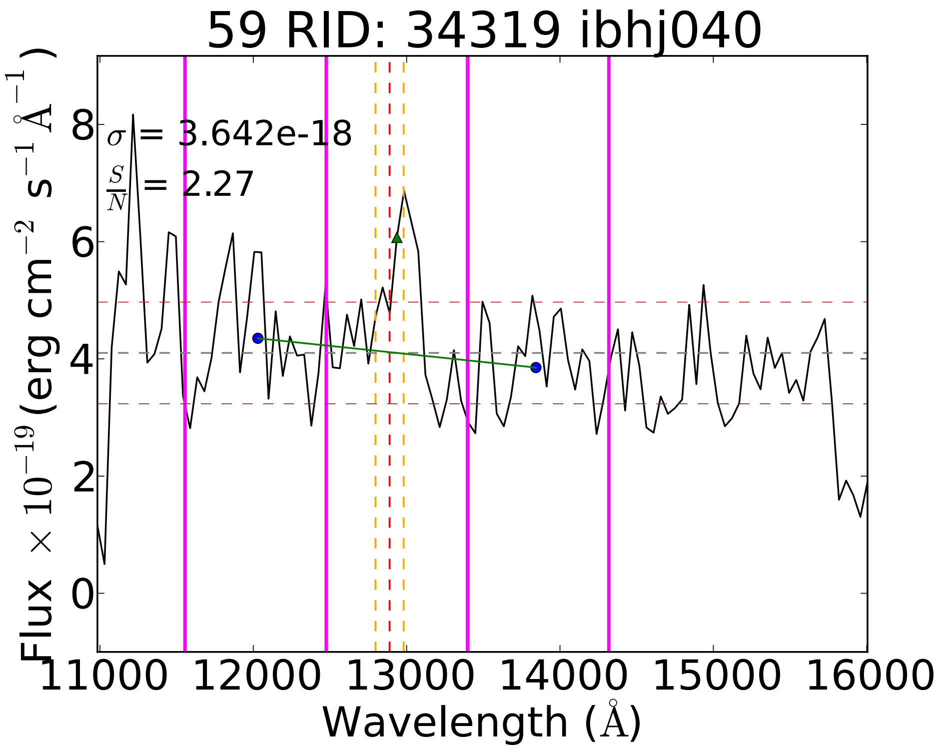
59 RID: 34319 ibhj040
σ = 3.642e-18
$\frac{S}{N}$ = 2.27
Flux $\times 10^{-19}$ (erg cm^{-2} s^{-1} Å^{-1})
Wavelength (Å)
0
2
4
6
8
11000
12000
13000
14000
15000
16000

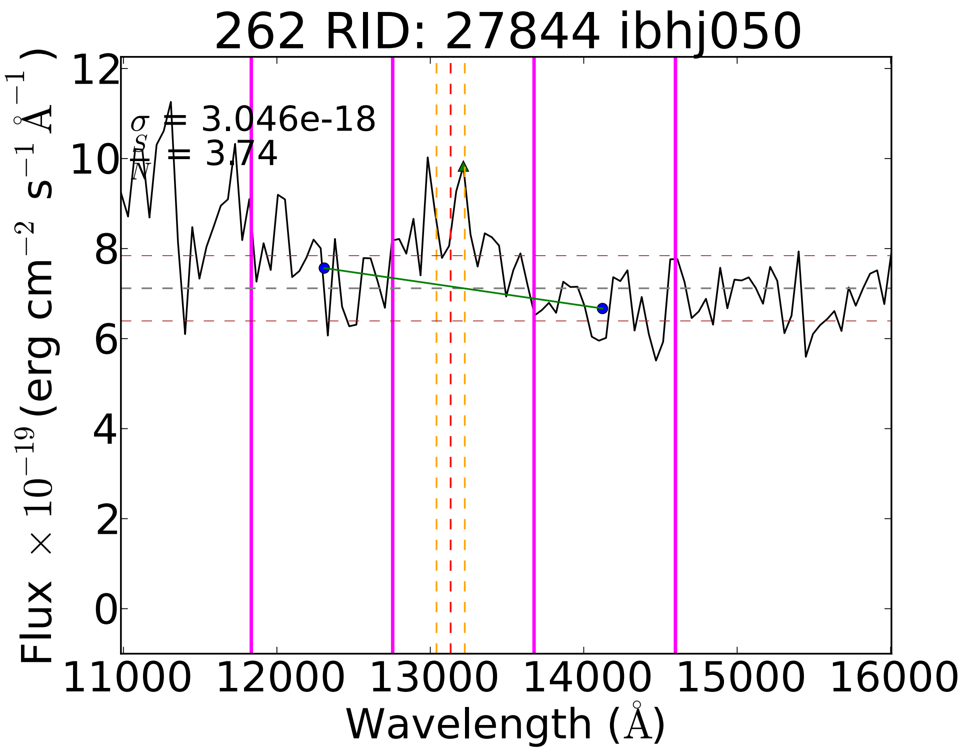
262 RID: 27844 ibhj050
σ = 3.046e-18
$\frac{S}{N}$ = 3.74
Flux $\times 10^{-19}$ (erg cm^{-2} s^{-1} Å^{-1})
Wavelength (Å)
0
2
4
6
8
10
12
11000
12000
13000
14000
15000
16000

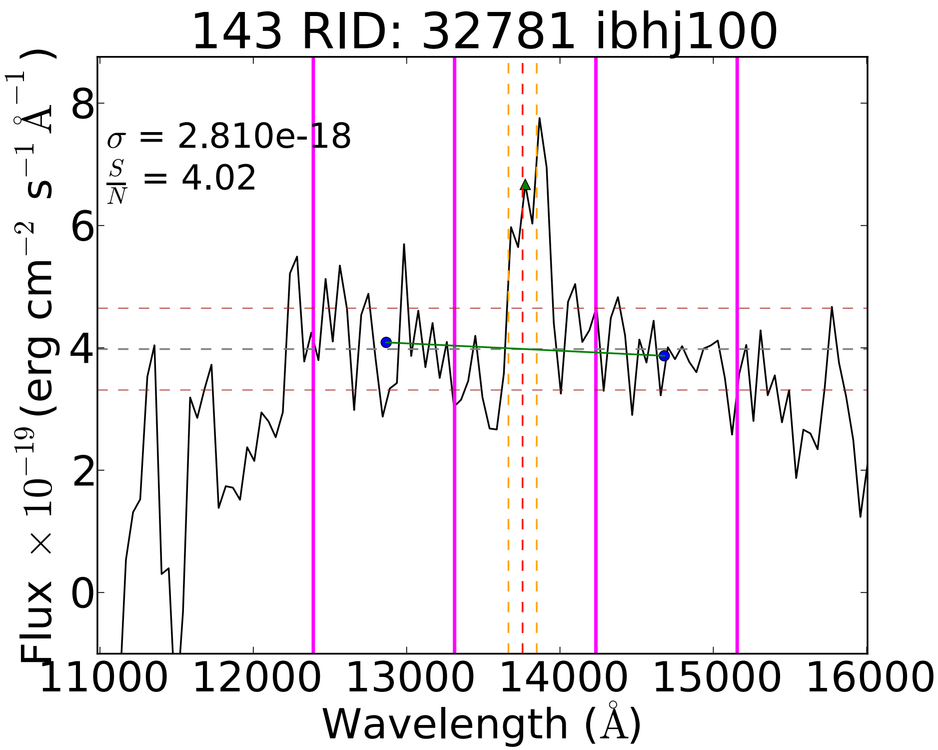
143 RID: 32781 ibhj100
σ = 2.810e-18
$\frac{S}{N}$ = 4.02
Flux $\times 10^{-19}$ (erg cm^{-2} s^{-1} Å^{-1})
Wavelength (Å)
0
2
4
6
8
11000
12000
13000
14000
15000
16000

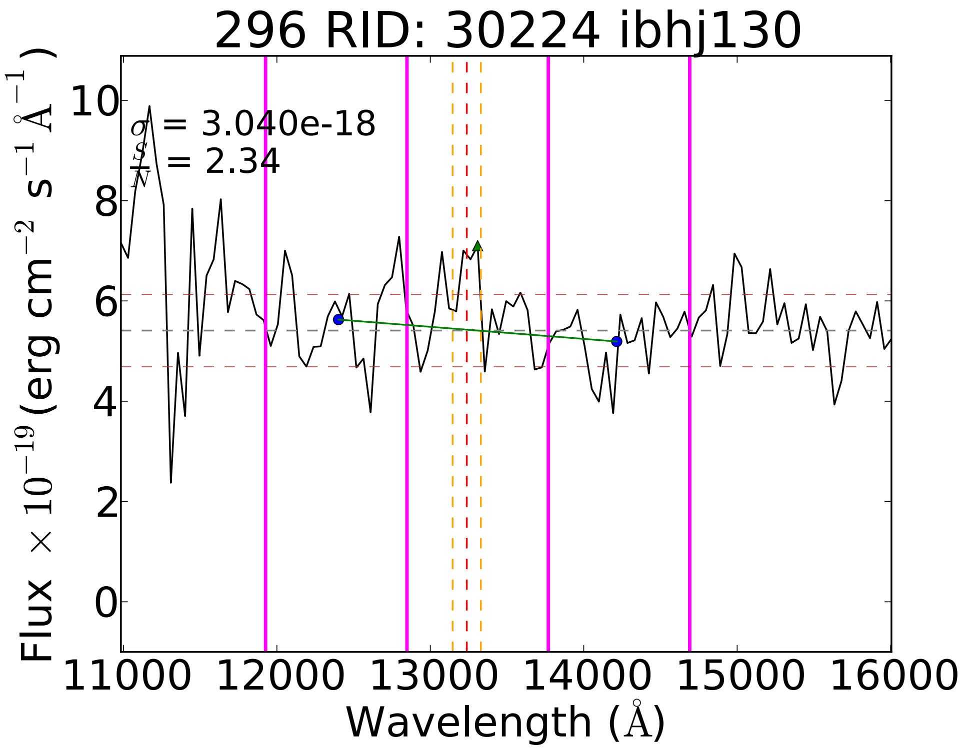
296 RID: 30224 ibhj130
σ = 3.040e-18
$\frac{S}{N}$ = 2.34
Flux $\times 10^{-19}$ (erg cm^{-2} s^{-1} Å^{-1})
Wavelength (Å)
0
2
4
6
8
10
11000
12000
13000
14000
15000
16000

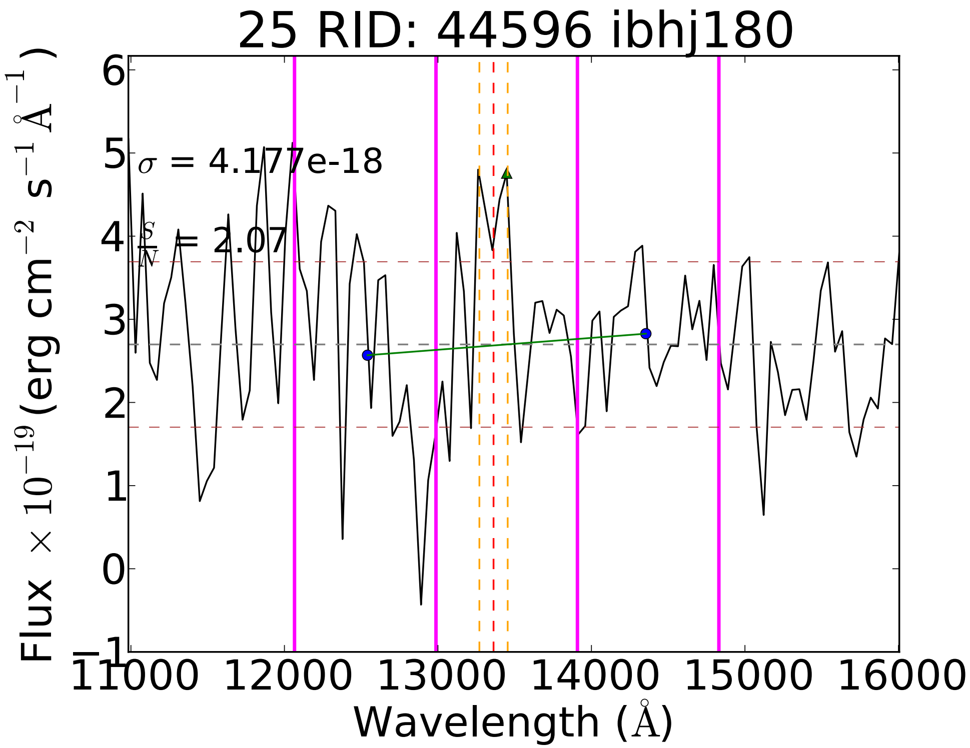
25 RID: 44596 ibhj180
σ = 4.177e-18
$\frac{S}{N}$ = 2.07
Flux $\times 10^{-19}$ (erg cm^{-2} s^{-1} Å^{-1})
Wavelength (Å)
−1
0
1
2
3
4
5
6
11000
12000
13000
14000
15000
16000

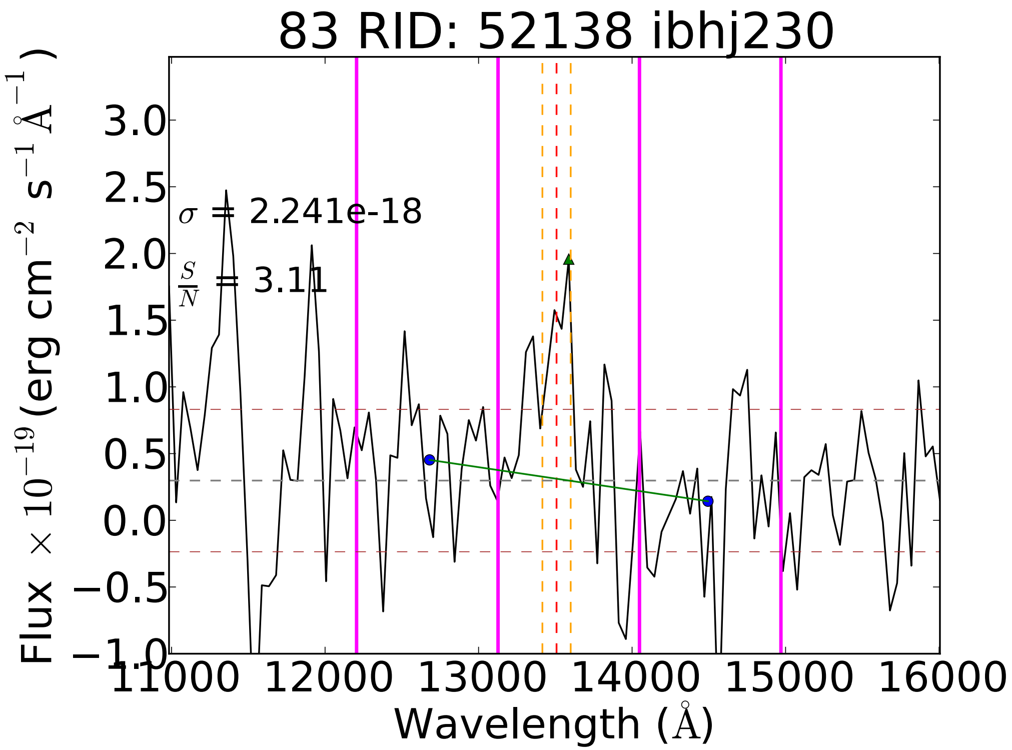
83 RID: 52138 ibhj230
σ = 2.241e-18
$\frac{S}{N}$ = 3.11
Flux $\times 10^{-19}$ (erg cm^{-2} s^{-1} Å^{-1})
Wavelength (Å)
−1.0
−0.5
0.0
0.5
1.0
1.5
2.0
2.5
3.0
11000
12000
13000
14000
15000
16000

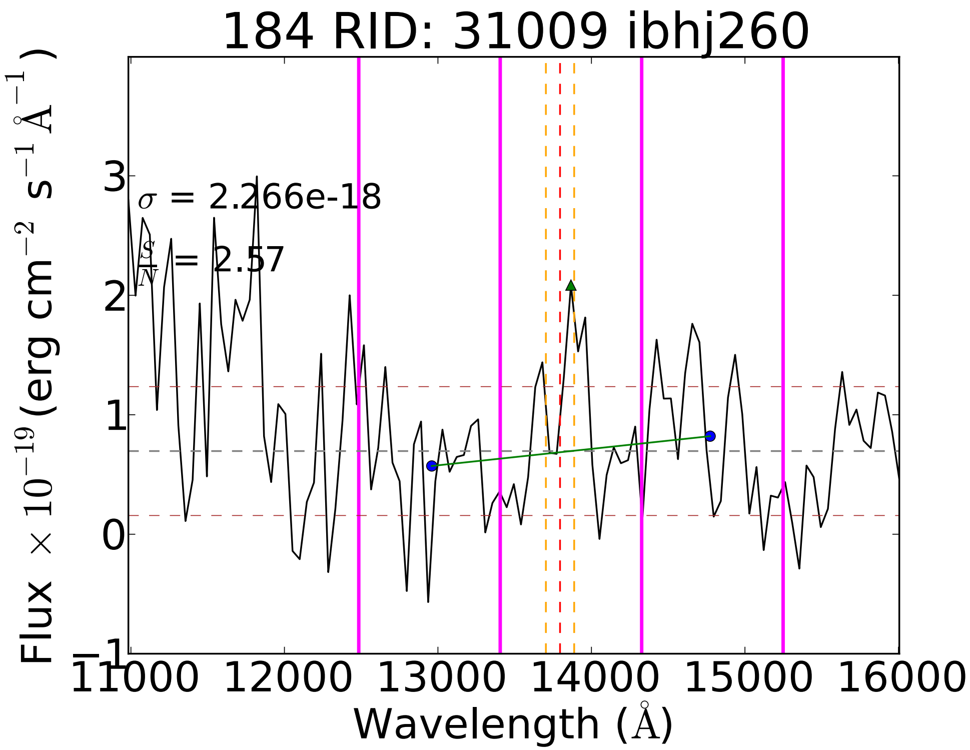
184 RID: 31009 ibhj260
σ = 2.266e-18
$\frac{S}{N}$ = 2.57
Flux $\times 10^{-19}$ (erg cm^{-2} s^{-1} Å^{-1})
Wavelength (Å)
−1
0
1
2
3
11000
12000
13000
14000
15000
16000

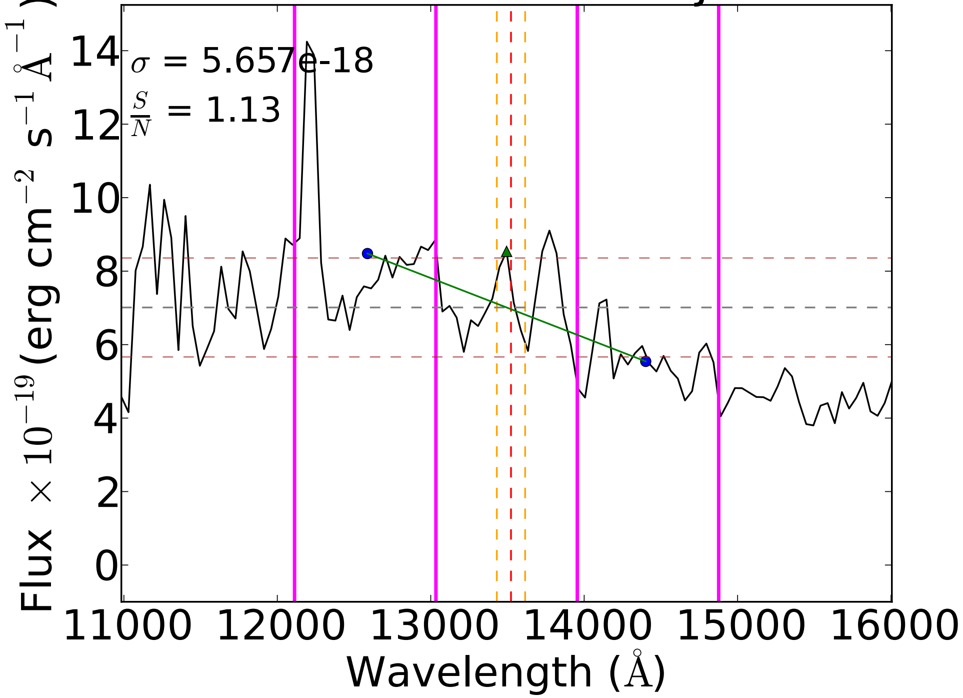
301 RID: 45277 ibhj340

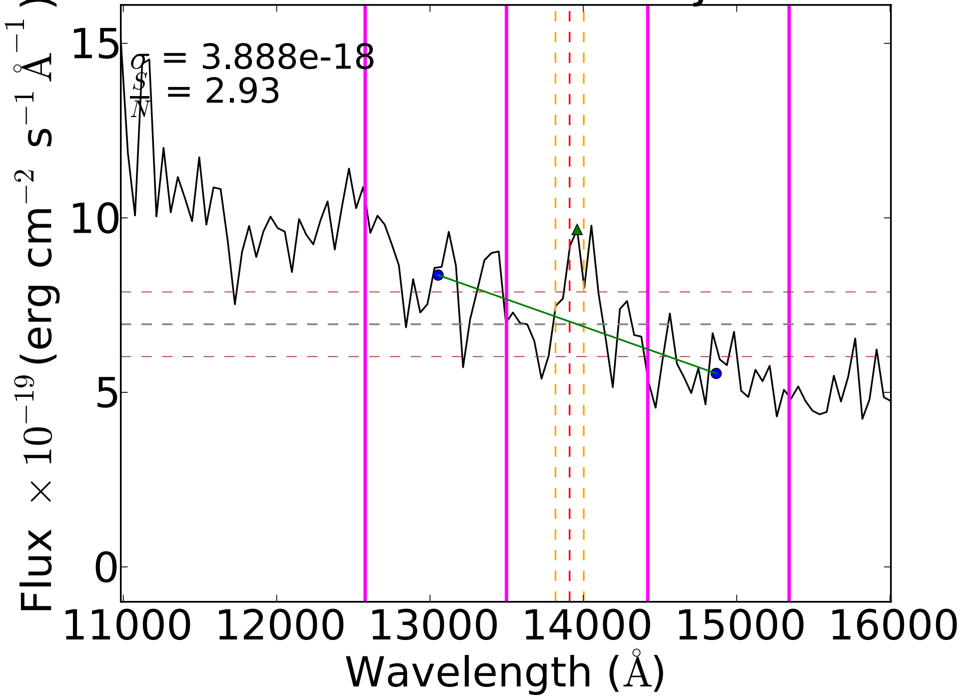
228 RID: 44349 ibhj370

Bibliography

Atek, H., Malkan, M., McCarthy, P., Teplitz, H. I., Scarlata, C., Siana, B., Henry, A., Colbert, J. W., Ross, N. R., Bridge, C., Bunker, A. J., Dressler, A., Fosbury, R. A. E., Martin, C., & Shim, H. 2010, ApJ, 723, 104

Baldry, I. K., Balogh, M. L., Bower, R. G., Glazebrook, K., Nichol, R. C., Bamford, S. P., & Budavari, T. 2006, MNRAS, 373, 469

Baldry, I. K., Glazebrook, K., Brinkmann, J., Ivezić, Ž., Lupton, R. H., Nichol, R. C., & Szalay, A. S. 2004, ApJ, 600, 681

Balogh, M., Navarro, J., & Morris, S. 2000, in KITP Conference: Galaxy Formation and Evolution

Baugh, C. M. 2006, Astronomy and Geophysics, 47, 020000

Bayliss, K. D., McMahon, R. G., Venemans, B. P., Ryan-Weber, E. V., & Lewis, J. R. 2011, MNRAS, 413, 2883

Bell, E. F., Papovich, C., Wolf, C., Le Floc'h, E., Caldwell, J. A. R., Barden, M., Egami, E., McIntosh, D. H., Meisenheimer, K., Pérez-González, P. G., Rieke, G. H., Rieke, M. J., Rigby, J. R., & Rix, H.-W. 2005, ApJ, 625, 23

Bertin, E. & Arnouts, S. 1996, A&AS, 117, 393

Blumenthal, G. R., Faber, S. M., Primack, J. R., & Rees, M. J. 1984, Nature, 311, 517

Brammer, G. B., van Dokkum, P. G., Franx, M., Fumagalli, M., Patel, S., Rix, H.-W., Skelton, R. E., Kriek, M., Nelson, E., Schmidt, K. B., Bezanson, R., da Cunha, E., Erb, D. K., Fan, X., Förster Schreiber, N., Illingworth, G. D., Labbé, I., Leja, J., Lundgren, B., Magee, D., Marchesini, D., McCarthy, P., Momcheva, I., Muzzin, A., Quadri, R., Steidel, C. C., Tal, T., Wake, D., Whitaker, K. E., & Williams, A. 2012, ApJS, 200, 13

Brinchmann, J., Charlot, S., White, S. D. M., Tremonti, C., Kauffmann, G., Heckman, T., & Brinkmann, J. 2004, MNRAS, 351, 1151

Buat, V., Boselli, A., Gavazzi, G., & Bonfanti, C. 2002, A&A, 383, 801

Buat, V., Iglesias-Páramo, J., Seibert, M., Burgarella, D., Charlot, S., Martin, D. C., Xu, C. K., Heckman, T. M., Boissier, S., Boselli, A., Barlow, T., Bianchi, L., Byun, Y.-I., Donas, J., Forster, K., Friedman, P. G., Jelinski, P., Lee, Y.-W., Madore, B. F., Malina, R., Milliard, B., Morissey, P., Neff, S., Rich, M., Schiminovitch, D., Siegmund, O., Small, T., Szalay, A. S., Welsh, B., & Wyder, T. K. 2005, ApJ, 619, L51

Bundy, K., Ellis, R. S., Conselice, C. J., Taylor, J. E., Cooper, M. C., Willmer, C. N. A., Weiner, B. J., Coil, A. L., Noeske, K. G., & Eisenhardt, P. R. M. 2006, ApJ, 651, 120

Calzetti, D. 2001, PASP, 113, 1449

Calzetti, D., Armus, L., Bohlin, R. C., Kinney, A. L., Koornneef, J., & Storchi-Bergmann, T. 2000, ApJ, 533, 682

Caputi, K. I., Lilly, S. J., Aussel, H., Sanders, D., Frayer, D., Le Fèvre, O., Renzini, A., Zamorani, G., Scodeggio, M., Contini, T., Scoville, N., Carollo, C. M., Hasinger, G., Iovino, A., Le Brun, V., Le Floc'h, E., Maier, C., Mainieri, V., Mignoli, M., Salvato, M., Schiminovich, D., Silverman, J., Surace, J., Tasca, L., Abbas, U., Bardelli, S., Bolzonella, M., Bongiorno, A., Bottini, D., Capak, P., Cappi, A., Cassata, P., Cimatti, A., Cucciati, O., de la Torre, S., de Ravel, L., Franzetti, P., Fumana, M., Garilli, B., Halliday, C., Ilbert, O., Kampczyk, P., Kartaltepe, J., Kneib, J.-P., Knobel, C., Kovac, K., Lamareille, F., Leauthaud, A., Le Borgne,

J. F., Maccagni, D., Marinoni, C., McCracken, H., Meneux, B., Oesch, P., Pellò, R., Pérez-Montero, E., Porciani, C., Ricciardelli, E., Scaramella, R., Scarlata, C., Tresse, L., Vergani, D., Walcher, J., Zamojski, M., & Zucca, E. 2008, ApJ, 680, 939

Cardelli, J. A., Clayton, G. C., & Mathis, J. S. 1989, ApJ, 345, 245

Carroll, B. W. & Ostlie, D. A. 2006, An introduction to modern astrophysics and cosmology

Chabrier, G. 2003, PASP, 115, 763

Charlot, S. & Longhetti, M. 2001, MNRAS, 323, 887

Colless, M., Peterson, B. A., Jackson, C., Peacock, J. A., Cole, S., Norberg, P., Baldry, I. K., Baugh, C. M., Bland-Hawthorn, J., Bridges, T., Cannon, R., Collins, C., Couch, W., Cross, N., Dalton, G., De Propris, R., Driver, S. P., Efstathiou, G., Ellis, R. S., Frenk, C. S., Glazebrook, K., Lahav, O., Lewis, I., Lumsden, S., Maddox, S., Madgwick, D., Sutherland, W., & Taylor, K. 2003, ArXiv Astrophysics e-prints

Condon, J. J. 1992, ARA&A, 30, 575

Conroy, C. 2013, ArXiv e-prints

Cowie, L. L., Songaila, A., Hu, E. M., & Cohen, J. G. 1996, AJ, 112, 839

Dale, D. A., Barlow, R. J., Cohen, S. A., Cook, D. O., Johnson, L. C., Kattner, S. M., Moore, C. A., Schuster, M. D., & Staudaher, S. M. 2010, ApJ, 712, L189

Davies, G. T., Gilbank, D. G., Glazebrook, K., Bower, R. G., Baldry, I. K., Balogh, M. L., Hau, G. K. T., Li, I. H., McCarthy, P., & Savaglio, S. 2009, MNRAS, 395, L76

Davis, M., Efstathiou, G., Frenk, C. S., & White, S. D. M. 1985, ApJ, 292, 371

Davis, M., Huchra, J., Latham, D. W., & Tonry, J. 1982, ApJ, 253, 423 de Lapparent, V., Geller, M. J., & Huchra, J. P. 1986, ApJ, 302, L1

Dicke, R. H., Peebles, P. J. E., Roll, P. G., & Wilkinson, D. T. 1965, ApJ, 142, 414

Dreyer, J. L. E. 1888, MmRAS, 49, 1

Elbaz, D., Daddi, E., Le Borgne, D., Dickinson, M., Alexander, D. M., Chary, R.-R., Starck, J.-L., Brandt, W. N., Kitzbichler, M., MacDonald, E., Nonino, M., Popesso, P., Stern, D., & Vanzella, E. 2007, A&A, 468, 33

Erb, D. K., Shapley, A. E., Pettini, M., Steidel, C. C., Reddy, N. A., & Adelberger, K. L. 2006, ApJ, 644, 813

Feulner, G., Gabasch, A., Salvato, M., Drory, N., Hopp, U., & Bender, R. 2005, ApJ, 633, L9

Foot, C. J. 2005, Atomic Physics (Oxford University Press)

Frenk, C. S., White, S. D. M., Efstathiou, G., & Davis, M. 1985, Nature, 317, 595

Freudling, W., Kümmel, M., Haase, J., Hook, R., Kuntschner, H., Lombardi, M., Micol, A., Stoehr, F., & Walsh, J. 2008, A&A, 490, 1165

Fumagalli, M., Patel, S. G., Franx, M., Brammer, G., van Dokkum, P., da Cunha, E., Kriek, M., Lundgren, B., Momcheva, I., Rix, H.-W., Schmidt, K. B., Skelton, R. E., Whitaker, K. E., Labbe, I., & Nelson, E. 2012, ApJ, 757, L22

Garn, T. & Best, P. N. 2010, MNRAS, 409, 421

Garn, T., Sobral, D., Best, P. N., Geach, J. E., Smail, I., Cirasuolo, M., Dalton, G. B., Dunlop, J. S., McLure, R. J., & Farrah, D. 2010, MNRAS, 402, 2017

Geach, J. E., Smail, I., Best, P. N., Kurk, J., Casali, M., Ivison, R. J., & Coppin, K. 2008, MNRAS, 388, 1473

Gilbank, D. G., Baldry, I. K., Balogh, M. L., Glazebrook, K., & Bower, R. G. 2010a, MNRAS, 405, 2594

Gilbank, D. G., Balogh, M. L., Glazebrook, K., Bower, R. G., Baldry, I. K., Davies, G. T., Hau, G. K. T., Li, I. H., & McCarthy, P. 2010b, MNRAS, 405, 2419

Gilbank, D. G., Bower, R. G., Glazebrook, K., Balogh, M. L., Baldry, I. K., Davies, G. T., Hau, G. K. T., Li, I. H., McCarthy, P., & Sawicki, M. 2011, MNRAS, 414, 304

Glazebrook, K., Abraham, R. G., McCarthy, P. J., Savaglio, S., Chen, H.-W., Crampton, D., Murowinski, R., Jørgensen, I., Roth, K., Hook, I., Marzke, R. O., & Carlberg, R. G. 2004, Nature, 430, 181

Glazebrook, K., Blake, C., Economou, F., Lilly, S., & Colless, M. 1999, MNRAS, 306, 843

Hawking, S. W. 1982, Physics Letters B, 115, 295

Herschel, W. 1785, Royal Society of London Philosophical Transactions Series I, 75, 213

—. 1786, Royal Society of London Philosophical Transactions Series I, 76, 457

Hogg, D. W. 1999, ArXiv Astrophysics e-prints

Holwerda, B. W., Blyth, S.-L., & Baker, A. J. 2012, in IAU Symposium, Vol. 284, IAU Symposium, ed. R. J. Tuffs & C. C. Popescu, 496–499

Hopkins, A. M. & Beacom, J. F. 2006, ApJ, 651, 142

Hopkins, A. M., Connolly, A. J., Haarsma, D. B., & Cram, L. E. 2001, AJ, 122, 288

Hubble, E. 1929, Proceedings of the National Academy of Science, 15, 168

Juneau, S., Glazebrook, K., Crampton, D., McCarthy, P. J., Savaglio, S., Abraham, R., Carlberg, R. G., Chen, H.-W., Le Borgne, D., Marzke,

R. O., Roth, K., Jørgensen, I., Hook, I., & Murowinski, R. 2005, ApJ, 619, L135

Kashino, D., Silverman, J. D., Rodighiero, G., Renzini, A., Arimoto, N., Daddi, E., Lilly, S. J., Sanders, D. B., Kartaltepe, J., Zahid, H. J., Nagao, T., Sugiyama, N., Capak, P., Carollo, C. M., Chu, J., Hasinger, G., Ilbert, O., Kajisawa, M., Kewley, L. J., Koekemoer, A. M., Kovač, K., Le Fèvre, O., Masters, D., McCracken, H. J., Onodera, M., Scoville, N., Strazzullo, V., Symeonidis, M., & Taniguchi, Y. 2013, ArXiv e-prints

Kennicutt, Jr., R. C. 1992, ApJ, 388, 310

—. 1998a, ARA&A, 36, 189

—. 1998b, ApJ, 498, 541

Kennicutt, Jr., R. C. & Kent, S. M. 1983, AJ, 88, 1094

Kewley, L. J., Geller, M. J., & Jansen, R. A. 2004, AJ, 127, 2002

Koekemoer, A. M., Fruchter, A. S., Hook, R. N., Hack, W., & Hanley, C. 2006, in The 2005 HST Calibration Workshop: Hubble After the Transition to Two-Gyro Mode, ed. A. M. Koekemoer, P. Goudfrooij, & L. L. Dressel, 423

Kroupa, P. 2001, MNRAS, 322, 231

Kümmel, M., Walsh, J. R., Pirzkal, N., Kuntschner, H., & Pasquali, A. 2009, PASP, 121, 59

Kurk, J. D., Cimatti, A., di Serego Alighieri, S., Vernet, J., Daddi, E., Ferrara, A., & Ciardi, B. 2004, A&A, 422, L13

Leavitt, H. S. & Pickering, E. C. 1912, Harvard College Observatory Circular, 173, 1

Leitner, S. N. 2012, ApJ, 745, 149

Li, I. H., Glazebrook, K., Gilbank, D., Balogh, M., Bower, R., Baldry, I., Davies, G., Hau, G., & McCarthy, P. 2011, MNRAS, 411, 1869

Lilly, S. J., Le Fevre, O., Hammer, F., & Crampton, D. 1996, ApJ, 460, L1

Ly, C., Malkan, M. A., Kashikawa, N., Shimasaku, K., Doi, M., Nagao, T., Iye, M., Kodama, T., Morokuma, T., & Motohara, K. 2007, ApJ, 657, 738

Madau, P., Ferguson, H. C., Dickinson, M. E., Giavalisco, M., Steidel, C. C., & Fruchter, A. 1996, MNRAS, 283, 1388

Maier, C., Lilly, S. J., Zamorani, G., Scodeggio, M., Lamareille, F., Contini, T., Sargent, M. T., Scarlata, C., Oesch, P., Carollo, C. M., Le Fèvre, O., Renzini, A., Kneib, J.-P., Mainieri, V., Bardelli, S., Bolzonella, M., Bongiorno, A., Caputi, K., Coppa, G., Cucciati, O., de la Torre, S., de Ravel, L., Franzetti, P., Garilli, B., Iovino, A., Kampczyk, P., Knobel, C., Kovač, K., Le Borgne, J.-F., Le Brun, V., Mignoli, M., Pello, R., Peng, Y., Perez Montero, E., Ricciardelli, E., Silverman, J. D., Tanaka, M., Tasca, L., Tresse, L., Vergani, D., Zucca, E., Abbas, U., Bottini, D., Cappi, A., Cassata, P., Cimatti, A., Fumana, M., Guzzo, L., Halliday, C., Koekemoer, A. M., Leauthaud, A., Maccagni, D., Marinoni, C., McCracken, H. J., Memeo, P., Meneux, B., Porciani, C., Pozzetti, L., & Scaramella, R. 2009, ApJ, 694, 1099

McCarthy, P. J., Yan, L., Freudling, W., Teplitz, H. I., Malumuth, E. M., Weymann, R. J., Malkan, M. A., Fosbury, R. A. E., Gardner, J. P., Storrie-Lombardi, L. J., Thompson, R. I., Williams, R. E., & Heap, S. R. 1999, ApJ, 520, 548

Messier, C. & Niles, P. H. 1981, The Messier catalogue of Charles Messier

Mo, H. J., Mao, S., & White, S. D. M. 1998, MNRAS, 295, 319

Mok, A., Balogh, M. L., McGee, S. L., Wilman, D. J., Finoguenov, A., Tanaka, M., Giodini, S., Bower, R. G., Connelly, J. L., Hou, A., Mulchaey, J. S., & Parker, L. C. 2013, MNRAS, 431, 1090

Momcheva, I. G., Lee, J. C., Ly, C., Salim, S., Dale, D. A., Ouchi, M., Finn, R., & Ono, Y. 2013, AJ, 145, 47

Mostek, N., Coil, A. L., Moustakas, J., Salim, S., & Weiner, B. J. 2012, ApJ, 746, 124

Moster, B. P., Somerville, R. S., Maulbetsch, C., van den Bosch, F. C., Macciò, A. V., Naab, T., & Oser, L. 2010, ApJ, 710, 903

Moustakas, J., Kennicutt, Jr., R. C., & Tremonti, C. A. 2006, ApJ, 642, 775

Navarro, J. F., Frenk, C. S., & White, S. D. M. 1997, ApJ, 490, 493

Noeske, K. G., Faber, S. M., Weiner, B. J., Koo, D. C., Primack, J. R., Dekel, A., Papovich, C., Conselice, C. J., Le Floc'h, E., Rieke, G. H., Coil, A. L., Lotz, J. M., Somerville, R. S., & Bundy, K. 2007a, ApJ, 660, L47

Noeske, K. G., Weiner, B. J., Faber, S. M., Papovich, C., Koo, D. C., Somerville, R. S., Bundy, K., Conselice, C. J., Newman, J. A., Schiminovich, D., Le Floc'h, E., Coil, A. L., Rieke, G. H., Lotz, J. M., Primack, J. R., Barmby, P., Cooper, M. C., Davis, M., Ellis, R. S., Fazio, G. G., Guhathakurta, P., Huang, J., Kassin, S. A., Martin, D. C., Phillips, A. C., Rich, R. M., Small, T. A., Willmer, C. N. A., & Wilson, G. 2007b, ApJ, 660, L43

Osterbrock, D. E. 1989, Astrophysics of gaseous nebulae and active galactic nuclei

Peng, Y.-j., Lilly, S. J., Kovač, K., Bolzonella, M., Pozzetti, L., Renzini, A., Zamorani, G., Ilbert, O., Knobel, C., Iovino, A., Maier, C., Cucciati, O., Tasca, L., Carollo, C. M., Silverman, J., Kampczyk, P., de Ravel, L., Sanders, D., Scoville, N., Contini, T., Mainieri, V., Scodeggio, M., Kneib, J.-P., Le Fèvre, O., Bardelli, S., Bongiorno, A., Caputi, K., Coppa, G., de la Torre, S., Franzetti, P., Garilli, B., Lamareille, F., Le Borgne, J.-F., Le Brun, V., Mignoli, M., Perez Montero, E., Pello, R., Ricciardelli, E., Tanaka, M., Tresse, L., Vergani, D., Welikala, N., Zucca, E., Oesch, P., Abbas, U., Barnes, L., Bordoloi, R., Bottini, D., Cappi, A., Cassata, P., Cimatti, A., Fumana, M., Hasinger, G., Koekemoer, A., Leauthaud, A., Maccagni, D., Marinoni, C., McCracken, H., Memeo, P., Meneux, B., Nair, P., Porciani, C., Presotto, V., & Scaramella, R. 2010, ApJ, 721, 193

Penzias, A. A. & Wilson, R. W. 1965, ApJ, 142, 419

Pérez-González, P. G., Zamorano, J., Gallego, J., Aragón-Salamanca, A., & Gil de Paz, A. 2003, ApJ, 591, 827

Pirzkal, N., Xu, C., Malhotra, S., Rhoads, J. E., Koekemoer, A. M., Moustakas, L. A., Walsh, J. R., Windhorst, R. A., Daddi, E., Cimatti, A., Ferguson, H. C., Gardner, J. P., Gronwall, C., Haiman, Z., Kümmel, M., Panagia, N., Pasquali, A., Stiavelli, M., di Serego Alighieri, S., Tsvetanov, Z., Vernet, J., & Yan, H. 2004, ApJS, 154, 501

Press, W. H. & Schechter, P. 1974, ApJ, 187, 425

Price, S. H., Kriek, M., Brammer, G. B., Conroy, C., Forster Schreiber, N. M., Franx, M., Fumagalli, M., Lundgren, B., Momcheva, I., Nelson, E. J., Rix, H.-W., Skelton, R. E., van Dokkum, P. G., Whitaker, K. E., & Wuyts, S. 2013, ArXiv e-prints

Rajan, A. e. 2011, WFC3 Data Handbook v. 2.1

Rees, M. J. & Ostriker, J. P. 1977, MNRAS, 179, 541

Salpeter, E. E. 1955, ApJ, 121, 161

Santini, P., Fontana, A., Grazian, A., Salimbeni, S., Fiore, F., Fontanot, F., Boutsia, K., Castellano, M., Cristiani, S., de Santis, C., Gallozzi, S., Giallongo, E., Menci, N., Nonino, M., Paris, D., Pentericci, L., & Vanzella, E. 2009, A&A, 504, 751

Scalo, J. M. 1986, Fund. Cosmic Phys., 11, 1

Schiminovich, D., Wyder, T. K., Martin, D. C., Johnson, B. D., Salim, S., Seibert, M., Treyer, M. A., Budavári, T., Hoopes, C., Zamojski, M., Barlow, T. A., Forster, K. G., Friedman, P. G., Morrissey, P., Neff, S. G., Small, T. A., Bianchi, L., Donas, J., Heckman, T. M., Lee, Y.-W., Madore, B. F., Milliard, B., Rich, R. M., Szalay, A. S., Welsh, B. Y., & Yi, S. 2007, ApJS, 173, 315

Schmitt, H. R., Calzetti, D., Armus, L., Giavalisco, M., Heckman, T. M., Kennicutt, Jr., R. C., Leitherer, C., & Meurer, G. R. 2006, ApJ, 643, 173

Sheth, R. K., Mo, H. J., & Tormen, G. 2001, MNRAS, 323, 1

Shim, H., Colbert, J., Teplitz, H., Henry, A., Malkan, M., McCarthy, P., & Yan, L. 2009, ApJ, 696, 785

Silk, J. & Mamon, G. A. 2012, Research in Astronomy and Astrophysics, 12, 917

Sobral, D., Best, P. N., Geach, J. E., Smail, I., Kurk, J., Cirasuolo, M., Casali, M., Ivison, R. J., Coppin, K., & Dalton, G. B. 2009, MNRAS, 398, 75

Sobral, D., Best, P. N., Matsuda, Y., Smail, I., Geach, J. E., & Cirasuolo, M. 2012, MNRAS, 420, 1926

Sobral, D., Best, P. N., Smail, I., Geach, J. E., Cirasuolo, M., Garn, T., & Dalton, G. B. 2011, MNRAS, 411, 675

Sobral, D., Smail, I., Best, P. N., Geach, J. E., Matsuda, Y., Stott, J. P., Cirasuolo, M., & Kurk, J. 2013, MNRAS, 428, 1128

Springel, V., Frenk, C. S., & White, S. D. M. 2006, Nature, 440, 1137

Starobinsky, A. A. 1982, Physics Letters B, 117, 175

Straughn, A. N., Meurer, G. R., Pirzkal, N., Cohen, S. H., Malhotra, S., Rhoads, J., Windhorst, R. A., Gardner, J. P., Hathi, N. P., Xu, C., Gronwall, C., Koekemoer, A. M., Walsh, J., & di Serego Alighieri, S. 2008, AJ, 135, 1624

Tresse, L., Maddox, S. J., Le Fèvre, O., & Cuby, J.-G. 2002, MNRAS, 337, 369

Twite, J. W., Conselice, C. J., Buitrago, F., Noeske, K., Weiner, B. J., Acosta-Pulido, J. A., & Bauer, A. E. 2012, MNRAS, 420, 1061

van den Bosch, F. C., Aquino, D., Yang, X., Mo, H. J., Pasquali, A., McIntosh, D. H., Weinmann, S. M., & Kang, X. 2008, MNRAS, 387, 79 van Dokkum, P. G., Brammer, G., Fumagalli, M., Nelson, E., Franx, M., Rix, H.-W., Kriek, M., Skelton, R. E., Patel, S., Schmidt, K. B., Bezanson, R., Bian, F., da Cunha, E., Erb, D. K., Fan, X., Förster Schreiber, N., Illingworth, G. D., Labbé, I., Lundgren, B., Magee, D., Marchesini, D., McCarthy, P., Muzzin, A., Quadri, R., Steidel, C. C., Tal, T., Wake, D., Whitaker, K. E., & Williams, A. 2011, ApJ, 743, L15

Vanzella, E., Cristiani, S., Dickinson, M., Giavalisco, M., Kuntschner, H., Haase, J., Nonino, M., Rosati, P., Cesarsky, C., Ferguson, H. C., Fosbury, R. A. E., Grazian, A., Moustakas, L. A., Rettura, A., Popesso, P., Renzini, A., Stern, D., & GOODS Team. 2008, A&A, 478, 83

Villar, V., Gallego, J., Pérez-González, P. G., Pascual, S., Noeske, K., Koo, D. C., Barro, G., & Zamorano, J. 2008, ApJ, 677, 169

Weiner, B. J., Papovich, C., Bundy, K., Conselice, C. J., Cooper, M. C., Ellis, R. S., Ivison, R. J., Noeske, K. G., Phillips, A. C., & Yan, R. 2007, ApJ, 660, L39

Weinmann, S. M., van den Bosch, F. C., Yang, X., & Mo, H. J. 2006, MNRAS, 366, 2

White, S. D. M. & Frenk, C. S. 1991, ApJ, 379, 52

Wisotzki, L., Koehler, T., Groote, D., & Reimers, D. 1996, A&AS, 115, 227

Worseck, G., Wisotzki, L., & Selman, F. 2008, A&A, 487, 539

Wuyts, S., Labbé, I., Schreiber, N. M. F., Franx, M., Rudnick, G., Brammer, G. B., & van Dokkum, P. G. 2008, ApJ, 682, 985

Zheng, X. Z., Bell, E. F., Papovich, C., Wolf, C., Meisenheimer, K., Rix, H.-W., Rieke, G. H., & Somerville, R. 2007, ApJ, 661, L41

Zhu, G., Moustakas, J., & Blanton, M. R. 2009, ApJ, 701, 86